Innovative Materials and Techniques in Concrete Construction

Michael N. Fardis
Editor

Innovative Materials and Techniques in Concrete Construction

ACES Workshop

Springer

Editor
Michael N. Fardis
Department of Civil Engineering
University of Patras
P.O. Box 1424
26504 Patras
Greece
fardis@upatras.gr

ISBN 978-94-007-1996-5 e-ISBN 978-94-007-1997-2
DOI 10.1007/978-94-007-1997-2
Springer Dordrecht Heidelberg London New York

Library of Congress Control Number: 2011937478

Preface

Concrete is ubiquitous in the modern world. It is claimed to be the material that humankind uses most (in volume terms), after water of course. The position of structural concrete as the prime structural material seems unchallenged nowadays. However, to remain so and to continue serving well the world, concrete has to continuously adapt to the economic, social and technical developments around the globe: the demand for sustainable use and re-use of material resources, the threat of climate change, the pressures in the developing world for more affordable housing, the need of the developed world to extend the lifetime of its infrastructures or to build better and more efficient ones, the desire for safety in a world of increased natural and man-made hazards, etc.

To rise to the challenge, concrete should be used ingeniously and be combined more often and better with other materials, profiting from recent advances in their science and technology. The emergence of new types of concrete and of novel combinations with other materials holds great promise for application. Indeed, recent years have seen enormous advances in the technology of concrete as a material, through which its strength, compactness and ductility can reach levels never dreamed of before. Thanks to these improved material properties, the strength and the durability of concrete structures is greatly improved, their weight and dimensions reduced, the scope of concrete as a structural material is widened and – despite the higher material costs – overall economy is possible, with positive impacts on sustainability as well. Similar advances are underway in reinforcing materials, notably high strength steel and fibre-reinforced polymers, and in the way they are combined with concrete into high performance structures. Developments in materials and equipment, as well as new concepts, have lead to innovative construction techniques, reducing cost and construction time and making possible the application of concrete under extreme conditions of construction or environment. These are leading in turn to new design concepts, answering a critique often heard nowadays that great innovations in concrete construction seem to be a thing of the past.

Top experts in the field of concrete structures, active in the leading and truly international scientific and technical association in Structural Concrete – the International Federation of Structural Concrete (*fib*) – gathered on the Greek island

of Corfu in early October 2010 for the Workshop on "Innovative Materials and Concepts in Concrete Construction".

The Workshop has been organized in the framework and with the financial support of Grant FP7-REGPOT-2007-1, no. 204697, of the European Community to the University of Patras within the Regional Potential part of its seventh Framework Programme (2007–2013). The Grant, titled: "Advanced Centre of Excellence in Structural and Earthquake Engineering (ACES)" www.aces.upatras.gr, supports the Structures Group of the Civil Engineering Department at the University of Patras to develop further its material and human resources, enhance its international reputation and pave the way for its younger generation of faculty. A first ACES Workshop, "Advances in Performance-Based Earthquake Engineering", had taken place again in Corfu in July 2009. Its Proceedings have also been published by Springer, as Vol. 13 of the Geotechnical, Geological and Earthquake Engineering series (ISBN 978-90-481-8745-4).

The International Scientific Committee of ACES, representing the networking partners of the University of Patras in the project, and composed of:

Michel Bouchon,	Univ. J. Fourier, Grenoble (FR)
Michel Géradin,	JRC, Ispra (IT)
Haig Gulvanessian,	BRE (UK)
Giuseppe Mancini,	Politecnico di Torino (IT)
Urs Meier,	EMPA, Zurich (Ch)
Artur Pinto,	JRC, Ispra (IT)
Jean-Claude Quéval,	CEA, Saclay (FR)
Joost Walraven,	Technical University Delft (NL)

have greatly assisted the organizers of the Corfu Workshop and contributed to its success, as they have done for the first ACES Workshop in 2009. They have effectively been the Scientific Committee of both Workshops. Our thanks go to all of them.

The editor of this volume and co-ordinator of ACES project gratefully acknowledges the support of his co-worker Dr. Dionysis Biskinis for the organization of the 2010 ACES Workshop and his help for this Volume. Special thanks are also due to Ms. Vassia Vayenas for her exemplary work for the preparation of these Proceedings.

Department of Civil Engineering
University of Patras, Patras

Michael N. Fardis

Contents

Contributors

Emmanuel Annerel Faculty of Engineering and Architecture, Department of Structural Engineering, Magnel Laboratory for Concrete Research, Ghent University, Technologiepark-Zwijnaarde 904, B-9052 Zwijnaarde, Belgium, emmanuel.annerel@ugent.be

György L. Balázs Budapest University of Technology and Economics, Faculty of Civil Engineering, Department of Construction Materials and Engineering Geology, Muegyetem rkp 3, H-1111, Budapest, Hungary, balazs@vbt.bme.hu

Josée Bastien Département de génie civil, CRIB, Université Laval, Québec, QC G1K 7P4, Canada, josee.bastien@gci.ulaval.ca

Idris Bedirhanoglu Department of Civil Engineering, Structural Engineering Laboratory, Engineering Faculty, Dicle University, 21280 Diyarbakir, Turkey, ibedirhanoglu@dicle.edu.tr

Erez Berkover Department of Structural Engineering and Construction Management, National Building Research Institute, Technion – Israel Institute of Technology, Technion City, Haifa 32000, Israel, eberk@technion.ac.il

Gabriele Bertagnoli Dipartimento di Ingegneria Strutturale e Geotecnica, Politecnico di Torino, C.so Duca degli Abruzzi 24, 10127 Torino, Italy, gabriele.bertagnoli@polito.it

Mario Alex Biagini Dipartimento di Ingegneria Strutturale e Geotecnica, Politecnico di Torino, C.so Duca degli Abruzzi 24, 10127 Torino, Italy, mario_alex.biagini@libero.it

Benoît Bissonnette Département de génie civil, CRIB, Université Laval, Québec, QC G1K 7P4, Canada, benoit.bissonnette@gci.ulaval.ca

Pierre-Vincent Certain Département de génie civil, LCM, École Polytechnique Fédérale de Lausanne, 1015 Lausanne, Switzerland, pierre-vincent.certain@epfl.ch

Hugo Corres-Peiretti FHECOR Ingenieros Consultores, C/Barquillo, 23 2ª Planta, 28004 Madrid, Spain, hcp@fhecor.es

Jian-Guo Dai Department of Civil and Structural Engineering, The Hong Kong Polytechnic University, Hung Hom, Hong Kong, cejgdai@polyu.edu.hk

Avraham N. Dancygier Department of Structural Engineering and Construction Management, National Building Research Institute, Technion – Israel Institute of Technology, Technion City, Haifa 32000, Israel, avidan@technion.ac.il

Pieter Desnerck Department of Structural Engineering, Magnel Laboratory for Concrete Research, Ghent University, Technologiepark-Zwijnaarde 904, B-9052 Zwijnaarde, Belgium, pieter.desnerck@ugent.be

Marco di Prisco Department of Structural Engineering, Politecnico di Milano, Piazza Leonardo da Vinci, 32, Milano 20133, Italy, marco.diprisco@polimi.it

Sebastián Dieste FHECOR Ingenieros Consultores, C/Barquillo, 23 2ª Planta, 28004 Madrid, Spain, sdb@fhecor.es

Liberato Ferrara Department of Structural Engineering, Politecnico di Milano, Piazza Leonardo da Vinci, 32, Milano 20133, Italy, liberato.ferrara@polimi.it

Stephen J. Foster Centre for Infrastructure Engineering and Safety, School of Civil and Environmental Engineering, The University of New South Wales, UNSW, Sydney, NSW 2052, Australia, s.foster@unsw.edu.au

Michael Haist Department of Building Materials, Institute of Concrete Structures and Building Materials, Karlsruhe Institute of Technology (KIT), Kaiserstrasse 12, D-76131 Karlsruhe, Germany, michael.haist@kit.edu

Ivan S. Ignjatović Faculty of Civil Engineering, University of Belgrade, Bulevar kralja Aleksandra 73, Belgrade 11000, Serbia, ivani@imk.grf.bg.ac.rs

Alper Ilki Faculty of Civil Engineering, Istanbul Technical University, Ayazaga Campus, 34469 Maslak, Istanbul, Turkey, ailki@itu.edu.tr

Marc Jolin Département de génie civil, CRIB, Université Laval, Québec, QC G1K 7P4, Canada, marc.jolin@gci.ulaval.ca

Tsutomu Kadotani Hanamizuki Bridge Planning, INC, 2-13-16-504, Kamitsuruma Honcho, Minami-ward, Sagamihara City 228-0818, Japan, tsutomukadotani@gmail.com

Michael Kaffetzakis Civil Engineering Department, University of Patras, 26504 Patras, Greece, mkaffetzakis@upatras.gr

Nahit Kumbasar Faculty of Civil Engineering, Istanbul Technical University, Ayazaga Campus, 34469 Maslak, Istanbul, Turkey, kumbasarn@itu.edu.tr

Marco Lamperti Department of Structural Engineering, Politecnico di Milano, Piazza Leonardo da Vinci, 32, Milano 20133, Italy, lamperti@stru.polimi.it

Simone Lapolla Department of Structural Engineering, Politecnico di Milano, Piazza Leonardo da Vinci, 32, Milano 20133, Italy, simone.lapolla@gmail.com

Javier León FHECOR Ingenieros Consultores, C/Barquillo, 23 2ª Planta, 28004 Madrid, Spain, jlg@fhecor.es

Marc'Antonio Liotta Department of Structural Engineering and Geotechnics, Sapienza University of Rome, via A. Gramsci, 53, I-00197 Rome, Italy, liotta@uniroma1.it

Koichi Maekawa Department of Civil Engineering, The University of Tokyo, 7-3-1 Hongo, Bunkyo-ku, Tokyo 113-8656, Japan, maekawa@concrete.t.u-tokyo.ac.jp

Anna Magri Department of Structural Engineering, Politecnico di Milano, Piazza Leonardo da Vinci, 32, Milano 20133, Italy, magri@stru.polimi.it

Mirjana M. Malešev Department for Civil Engineering, Faculty of Technical Sciences, University of Novi Sad, Trg Dositeja Obradovića 6, Novi Sad 21000, Serbia, miram@uns.ac.rs

Giuseppe Mancini Dipartimento di Ingegneria Strutturale e Geotecnica, Politecnico di Torino, C.so Duca degli Abruzzi 24, 10127 Torino, Italy, giuseppe.mancini@polito.it

Jacques Marchand Département de génie civil, CRIB, Université Laval, Québec, QC G1K 7P4, Canada, jacques.marchand@gci.ulaval.ca

Snežana B. Marinković Faculty of Civil Engineering, University of Belgrade, Bulevar kralja Aleksandra 73, Belgrade 11000, Serbia, sneska@imk.grf.bg.ac.rs

Stijn Matthys Department of Structural Engineering, Magnel Laboratory for Concrete Research, Ghent University, Technologiepark-Zwijnaarde 904, B-9052 Zwijnaarde, Belgium, stijn.matthys@ugent.be

Takeju Matsuka Technical Research Institute, Hazama Corporation, 515-1 Karima, Tsukuba, Ibaraki 305-0822, Japan, matsuka@hazama.co.jp

Urs Meier Swiss Federal Laboratories for Materials Science and Technology, EMPA, Dübendorf, Switzerland, urs.meier@empa.ch

Marco Menegotto Department of Structural Engineering and Geotechnics, Sapienza University of Rome, via A. Gramsci, 53, I-00197 Rome, Italy, marco.menegotto@uniroma1.it

Giorgio Monti Department of Structural Engineering and Geotechnics, Sapienza University of Rome, via A. Gramsci, 53, I-00197 Rome, Italy, giorgio.monti@uniroma1.it

Harald S. Müller Department of Building Materials, Institute of Concrete Structures and Building Materials, Karlsruhe Institute of Technology (KIT), Kaiserstrasse 12, D-76131 Karlsruhe, Germany, sekretariat-bt@imb.kit.edu

Kohei Nagai Department of Civil Engineering, The University of Tokyo, 7-3-1 Hongo, Bunkyo-ku, Tokyo 113-8656, Japan, nagai@concrete.t.u-tokyo.ac.jp

Tabea Neumann Department of Building Materials, Institute of Concrete Structures and Building Materials, Karlsruhe Institute of Technology (KIT), Kaiserstrasse 12, D-76131 Karlsruhe, Germany, sekretariat-bt@imb.kit.edu

Tian Sing Ng Centre for Infrastructure Engineering and Safety, School of Civil and Environmental Engineering, The University of New South Wales, UNSW, Sydney, NSW 2052, Australia, tian.ng@unsw.edu.au

Tor Ole Olsen Dr.techn.Olav Olsen a.s., Dicks vei 10, 1325 Lysaker, Norway, too@olavolsen.no

Catherine Papanicolaou Civil Engineering Department, University of Patras, 26504 Patras, Greece, kpapanic@upatras.gr

Alejandro Pérez FHECOR Ingenieros Consultores, C/Barquillo, 23 2ª Planta, 28004 Madrid, Spain, apc@fhecor.es

Vlastimir S. Radonjanin Department for Civil Engineering, Faculty of Technical Sciences, University of Novi Sad, Trg Dositeja Obradovića 6, Novi Sad 21000, Serbia, radonv@uns.ac.rs

Koji Sakai Safety Systems Construction Engineering, Kagawa University, 2217-20 Hayashi-cho, Takamatsu, Kagawa 761-0396, Japan, sakai@eng.kagawa-u.ac.jp

Julio Sánchez FHECOR Ingenieros Consultores, C/Barquillo, 23 2ª Planta, 28004 Madrid, Spain, jsd@fhecor.es

Cristina Sanz FHECOR Ingenieros Consultores, C/Barquillo, 23 2ª Planta, 28004 Madrid, Spain, csm@fhecor.es

Benny Suryanto Department of Civil Engineering, The University of Tokyo, 7-3-1 Hongo, Bunkyo-ku, Tokyo 113-8656, Japan, benny@concrete.t.u-tokyo.ac.jp

Yasunori Suzuki Cement/Concrete Research Laboratory, Sumitomo Osaka Cement Co., Ltd, 585 Houfu-cho, Funabashi, Chiba, Japan, yasuzuki@soc.co.jp

Luc Taerwe Faculty of Engineering and Architecture, Department of Structural Engineering, Magnel Laboratory for Concrete Research, Ghent University, Technologiepark-Zwijnaarde 904, B-9052 Zwijnaarde, Belgium, luc.taerwe@ugent.be

Thanasis Triantafillou Department of Civil Engineering, University of Patras, 26504 Patras, Greece, ttriant@upatras.gr

Tamon Ueda Division of Engineering and Policy for Sustainable Environment, Faculty of Engineering, Hokkaido University, Sapporo 060-8628, Japan, ueda@eng.hokudai.ac.jp

Lander Vasseur ECC NV Belgium, Terbekehofdreef 50-52, B-2610 Antwerp, Belgium, lander.vasseur@ecc-belgium.be

Michael Vogel Department of Building Materials, Institute of Concrete Structures and Building Materials, Karlsruhe Institute of Technology (KIT), Kaiserstrasse 12, D-76131 Karlsruhe, Germany, michael.vogel@kit.edu

Yen Lei Voo Dura Technology Sdn Bhd, Lot 304993, Jalan Chepor 11/8, Pusat Seramik, Fasa 2, Ulu Chepor, 31200 Chemor, Perak, Malaysia, vooyenlei@dura.com.my

Jun Yamazaki Department of Civil Engineering, Nihon University, Kanda-Surugadai 1-8-14, Chiyoda-ku, Tokyo 101-308, Japan, yamazaki@civil.cst.nihon-u.ac.jp

Giulio Zani Department of Structural Engineering, Politecnico di Milano, Piazza Leonardo da Vinci, 32, Milano 20133, Italy, zani@stru.polimi.it

Chapter 1
Non Finito: Challenges in Rehabilitation

Urs Meier

Abstract "Non Finito" is a sculpting technique literally meaning that the work is unfinished. Non finito sculptures appear unfinished because the artist only sculpts part of the block, leaving the figure appearing to be stuck within the block of material. The idea of post-strengthening civil structures with carbon fiber reinforced polymer (CFRP) tapes was for the first time unveiled in an oral presentation at ETH Zurich in 1985. An appropriate feasibility study was published 2 years later. The reactions of the listening and reading audience were mixed. Most found the concept very crazy and absolutely not practicable. The method is meanwhile state-of-the-art. The goal of this paper is to discuss the very promising system of CFRP straps as active external reinforcement in present time and to list three examples of new "crazy" ideas which might be interesting for future R&D work and might show successful applications in 10, 20 or 30 years. (i) More and more lacy and very slender structural components of historic structures like in the matter of the dome of Milan are suffering cracking. Internal, post-tensioning along three-dimensional boreholes with thin CFRP wires could be powerful tool to close the cracks. (ii) After all the severe earthquakes within the last few years seismic retrofitting gained dramatically relevance. CFRP post-strengthening is a successful mean in many cases however not always applicable. For example in the case of a mosque with golden mosaic ceilings there is no possibility to adhere black CFRP strips to the surface. Why should we not work with huge airbags, corresponding gas generators and sensors? How could we avoid that such airbags kill people? (iii) In modern architecture it is more and more fashionable to design and construct lean high raised towers. Already in the past some of them faced oscillation problems due to aerodynamic excitations. Instead of the subsequent installation of tuned mass dampers an adaptive outer skin

U. Meier (✉)
Swiss Federal Laboratories for Materials Science and Technology, EMPA,
Dübendorf, Switzerland
e-mail: urs.meier@empa.ch

M.N. Fardis (ed.), *Innovative Materials and Techniques in Concrete Construction: ACES Workshop*, DOI 10.1007/978-94-007-1997-2_1,

made of electro-active polymers might resolve this problem. “Non Finito” in this paper means only to sculpt ideas and leave the realization to the next generation of researchers and engineers.

1.1 An Example of a Challenge in the Past

The challenge of post-strengthening civil structures with carbon fiber reinforced polymer (CFRP) strips was for the first time addressed in an oral presentation at ETH, the Swiss Federal Institute of Technology in Zurich in 1985 by the author. An appropriate feasibility study was published 2 years later (Meier 1987). The reactions of the listening and reading audiences were mixed. CFRP strips were first applied in 1991 to strengthen the Ibach Bridge near Lucerne. Consumption of the material at that time totaled a mere 6 kg per annum. Today about one quart of the worldwide carbon fiber production is used in construction, mostly for post-strengthening purposes, i.e. approximately 7,000 ton per annum. Considering the tonnages of steel used in construction, this seems extremely little. However we have to keep in mind that the strength of such strips is above 3,000 MPa and the density is only 1.5 t/m^3. The sentence “Never before has a post-strengthening method done so much with so little” coined by the writer during a lecture tour trough the Unites States in 1997 for the promotion of CFRP rehabilitation systems symbolizes the situation. The material’s excellent corrosion resistance, extremely high strength, high stiffness, good fatigue performance and low bulk density have already enabled it to supplant steel for these applications in much of Europe, Asia and the Americas. In most cases, 1 kg of CFRP can match 30–35 kg of steel in terms of strength. The material’s low density makes its application so straightforward compared to steel that the additional cost (CFRP composites are some ten times more expensive per unit volume) is more than recouped by labor savings due to the extreme ease of handling. The first-rate material properties are effectively thrown in as an added value. CFRP strip or wet lay-up is best applied as “structural wallpaper” using a rubber roller; unlike externally bonded steel plate, it does not require support or contact pressure while the resin cures. The overcoming of this challenge brought construction industry a modern, meaningful method for post-strengthening of structures.

1.2 A Selected “Non Finito” Challenge in the Present Time

The focus of the research by Lees, Winistörfer and Meier (1999, 2002) was the development of post-tensioned non-laminated CFRP straps as active external reinforcement. At the beginning the emphasis was on shear-strengthening for concrete. The use of an active system has several advantages compared with a passive reinforcement system. In particular, the post-tensioned CFRP straps provide confinement and enhance the performance of the concrete.

Fig. 1.1 Conceptual design of pin-loaded strap elements. On the *left side* there is a laminated and on the *right side* a non-laminated strap

The current section seeks to discuss reliability aspects of this tendon system which is based on a brittle material and therefore theoretically subject to a large variability of strength properties. Experimental results of static short-term tensile tests and creep tests under severe loading conditions prove its high reliability.

A carbon fiber reinforced laminated pin-loaded strap, as shown in Fig. 1.1 on the left side, might provide a practical tension element for the shear enhancement of concrete. Such an element can consist of a unidirectional fiber reinforced plastic, having a fiber volume fraction of about 60%, wound around two cylindrical pins in a racetrack shape. However the maximum number of layers is limited by technical considerations in the manufacturing process (Winistoerfer 1999). No machining of holes is required to make a strap. The two pins transfer tensile load between the structure, and the fully consolidated strap.

Laminated straps have desirable characteristics of relative high tensile strength, low weight, low thermal conductivity, and, crucial, high durability. The US-Army has therefore investigated laminated CFRP tendons for temporary bridge deployment (Bauersfeld 1984). However, laboratory experiments and analytical modeling by Winistoerfer (1999) have shown that there are severe stress concentrations in the region where the strap and the pin meet. The tensile resistance of the strap is therefore limited to about 60% or less of the material's expected unidirectional strength. This is attributed to stress concentrations, which lead to premature failure. Furthermore, the production process for multi-layered laminated straps is not straightforward, if fiber misalignment is to be eliminated where the stress concentrations occur.

An alternative option to reduce the undesirable stress concentrations, overcome the manufacturing difficulties and reduce the cost is the use of a non-laminated strap. The concept which has been patented by Meier and Winistoerfer (1998) is shown on the right side of Fig. 1.1.

The CFRP strap now comprises a number of unidirectional reinforced layers, formed from a single, continuous, thermoplastic tape of about 0.13 mm thickness. The tape is wound around the two pins and only the end of the outermost layer is fusion bonded to the next outermost layer to form a closed loop.

Table 1.1 Summary of experimental investigation on non-laminated pin-loaded straps

(a)					
Number of layers, N	1	10	20	30	40
Specimens tested, n	6	6	6	6	7
Pin diameter, D	30	30	30	30	50
Length, L	700	700	700	700	700
Ultimate load F_{ult} [kN]	6.2	50.0	101.2	157.8	207.4
Standard deviation s [kN]	0.3	1.2	2.8	3.4	3.8
Coefficient of variation [%]	5.5	2.5	2.8	2.1	1.8
Weibull modulus, m	16.0	33.6	32.0	40.9	49.2
(b)					
Number of layers, N	40	40	50	60	70
Specimens tested, n	6	3	7	4	2
Pin diameter, D	50	50	50	50	50
Length, L	350	1,500	700	700	700
Ultimate load F_{ult} [kN]	173.8	204.0	249.0	269.8	278.0
Standard deviation s [kN]	12.0	3.6	4.9	10.2	14.1
Coefficient of variation [%]	6.9	1.8	2.0	3.8	5.1
Weibull modulus, m	12.5	43.7	47.2	21.6	13.8

The non-laminated strap element enables the individual layers to move relative to each other which allow an equalization of forces in the layers as the strap is tensioned (Winistoerfer 1999). The stress concentrations are reduced since the new structural form is more compliant than the laminated equivalent. Control of the initial tensioning process reduces interlaminar shear stresses so that a more uniform strain distribution in all layers can be achieved. The approach allows greater flexibility in terms of the geometry of the tendon, and it can be manufactured on site. Moreover, the concept is going to be less expensive because there is no consolidation process required.

An important aspect of non-laminated pin-loaded straps is the brittle nature of the carbon fibers. The stress at which brittle fibers fail usually depends on the presence of flaws, which may occur randomly along the length of a fiber. A statistical approach of this situation involves conceptually dividing a length of fiber into a number of incremental lengths. The fiber fractures when it has at least one incremental element containing a flaw sufficient to cause failure under a given stress. This analysis is known as the Weakest Link Theory (WLT) (Hull and Clyne 1996).

The Weibull modulus m is an important parameter for characterizing the strength distribution of brittle solids. A low value of m (e.g. <10) implies considerable uncertainty about the strength of a specimen. In practice, many ceramic materials exhibit Weibull moduli in the range 2–15. Sommer et al. (1996) reported values of m = 5.25 for strength properties of single carbon fiber filaments of the type Sigrafil C.

Fifty-three straps were produced from 12 mm wide carbon fiber tape with a polyamide 12 matrix and Toray T700 fibers. Various configurations in terms of number of layers, N, length, L, and pin diameter, D, were investigated. The tensile tests for the smaller pin diameters, summarized in the Table 1.1a and b, were performed on an Instron 1251 universal testing machine. The larger pin diameter straps were

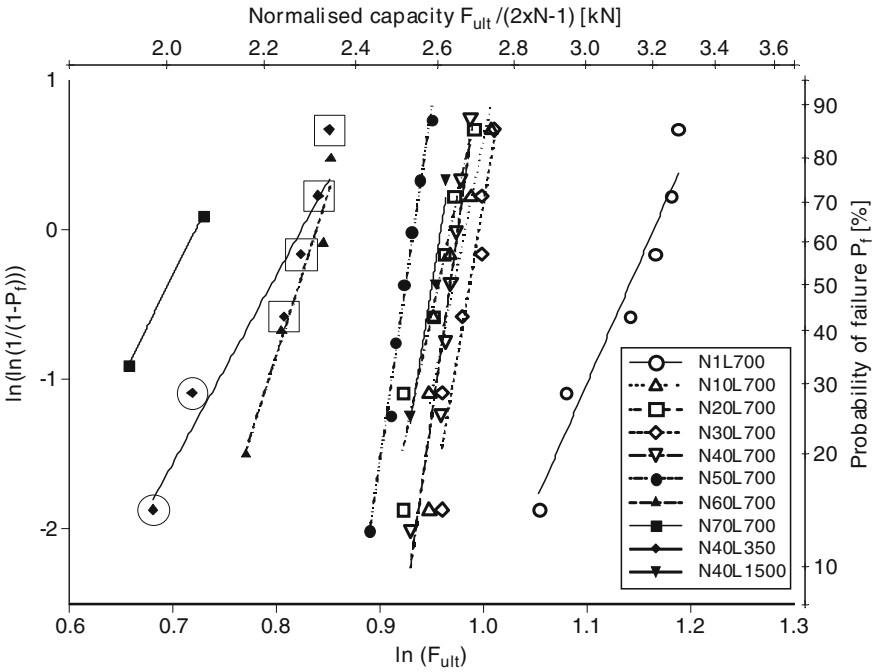

Fig. 1.2 Weibull plots of load carrying capacities of non-laminated pin-loaded straps with different numbers of layers and lengths (Winistoerfer 1999)

tested on an Instron 1346. The pin diameter had to be increased for the straps consisting of 40 or more layers to prevent failure of the steel pin due to extensive bending and shear stresses. Load carrying capacities, F_{ult}, are given instead of stresses because of variations in the tape dimensions, hence inaccurate measurements of the cross-sectional area.

The Weibull plots of the experimentally determined F_{ult} and the corresponding linear curve fits to resolve the gradients (Weibull moduli m) are presented in Fig. 1.2. The capacities are normalized with the total number of tapes present in each strap.

The highest mean strength was attained with a single layer containing a fusion bonded joint. Failure occurred in the joint, which may be the reason for the large variability. Only minor differences in the capacity per tape were observed for straps consisting of 10 up to 50 layers. Furthermore, the variability of these sets was considerably reduced. Specimens consisting of less than 30 layers failed in a brittle manner, whereas those with 30 or more layers started to fail with localized fractures in the pin region starting with the innermost layer. Substantial, clearly visible, damage was accumulated in the pin region before the final failure occurred. This experimental observation is also reflected by the increase of the Weibull moduli m, given in the Table 1.1a and b. A considerable reduction of the capacity per tape was observed in specimens consisting of 60 and more layers. It suggests that failure of such straps is dominated by excessive through-thickness stress components.

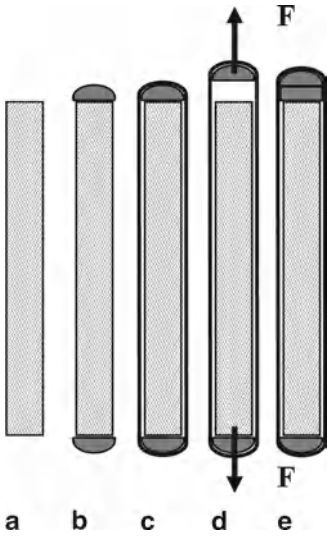

Fig. 1.3 Conception for post-tensioning with CFRP straps shown on the example of a steel rebar reinforced concrete shear wall: (**a**) cross section of shear wall, (**b**) addition of semi-elliptical interface pad elements that are placed on the *bottom* and *top* faces of the shear wall, (**c**) the layers of the CFRP tapes are wound around the pads and shear wall, (**d**) the straps are tensioned by lifting the top interface pad using a jacking system, (**e**) the post-tensioning force is applied to the concrete by overstressing the straps, inserting spacers between the interface pad and the shear wall and then releasing the tensioning force

Similarly, the short specimens (L = 350 mm) exhibited a considerable reduction of the load carrying capacity (Table 1.1b). This is attributed to an uneven strain distribution between individual layers because a reduced length requires increased relative displacement to attain an even strain distribution. The large variability in the set N = 40 and L = 350 mm indicates a difference in the tape qualities since the specimens marked in Fig. 1.2 with large circles and square boxes are made from different production batches.

The dramatic increase of the Weibull moduli presented in the Table 1.1a and b compared to the values mentioned above for single fibers is attributed to the large number of filaments present in the composite and the ability of the matrix to transfer load into the fibers across the interface, thus resulting in load redistribution effects in the vicinity of cracks. The consequence is a much more reliable material than expected from tensile strength properties of single fibers.

A key issue in determining the effectiveness of an active shear strengthening system for steel reinforced concrete is the capability of the system to enhance the shear resistance of a reinforced concrete beam or a shear wall. This shear resistance is generally thought to be comprised of a combination of aggregate interlock, dowel action, the concrete compressive zone and the internal shear reinforcement (where present).

The strengthening system consists of external pre-stressed non-laminated CFRP straps as outlined above. The straps are made up of 5–40 layers of 0.13 mm thick tapes which are wrapped around semi-elliptical interface pad elements that are placed on the bottom and top faces of the beam, membrane or wall to be strengthened (see Fig. 1.3).

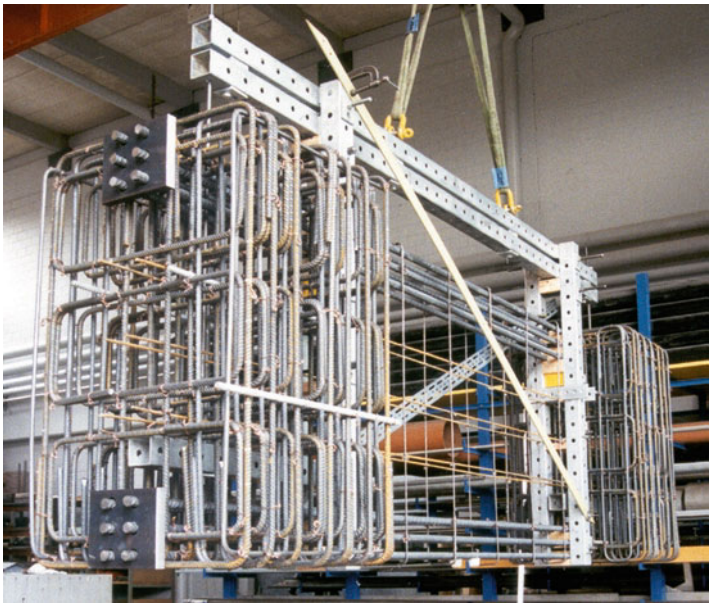

Fig. 1.4 Steel reinforcement of shear wall. The total length of a wall is 3,840 mm, the depth 1,200 mm and the thickness in the central part 150 mm and at the clamps 800 mm. The dimensions of the observed shear zone are 2,240 mm in length, 1,200 in depth and 150 mm in thickness

The strap is tensioned by lifting the top interface pad using a jacking system. The transverse post-tensioning force is applied to the concrete by overstressing the strap, inserting a spacer between the interface pad and the beam and then releasing the tensioning force.

The straps connect the concrete compression and tension zones, and such connection is felt to be important for the concrete shear resistance. Another benefit of the closed loop configuration is that the unexpected reversal of load paths can be accommodated. However, perhaps the most important advantage of the system is the ability to provide active confinement to the concrete and therefore increase the shear capacity of a beam, membrane or shear wall. The CFRP straps proved to be an extremely effective means to strengthen beams. A load carrying capacity enhancement of approximately 50% was obtained and the addition of the external straps resulted for certain beam configurations in a change from a brittle shear failure to a ductile flexural failure due to yielding of the longitudinal steel reinforcement (Lees et al. 2002).

Stenger (2001) demonstrated in a comprehensive study the efficiency of shear strengthening with post-tensioned CFRP straps for shear walls. His thesis covers five large scale experiments. All five steel reinforced concrete walls had the same dimensions and the same internal reinforcement as shown in Fig. 1.4. Four of these five walls have been post-strengthened each with four vertically applied external CFRP straps as described above. The walls were on both sides rigidly clamped and loaded in a large "Beam-Element-Tester" developed by Prof. Peter Marti at ETH Zurich (Stenger 2001). The CFRP straps used for the shear wall experiments were built up

Table 1.2 Results of shear experiments on reinforced concrete elements

Wall element number	Cracking shear load [kN]	Ultimate shear load [kN]	Max. vertical displacement [mm]
ST1: 70 kN-post-tensioned	−305	−703	−13.01
ST2: Reference, not strengthened	−210	−465	−3.85
ST3: 5 kN-post-tensioned	−250	−479	−11.10

of tapes with a thermoplastic PA12-matrix. The tapes had the following properties: elastic modulus E: 130 GPa, strain at failure: 1.2%, width 12 mm, thickness 0.16 mm, cross section: 1.92 mm^2. The load carrying capacity of the each strap wound of 25 layers was 125 kN and the cross section (twice 25 layers) 96.0 mm^2.

The flexural internal steel reinforcement consisted of twice 6 rebars diameter 26 mm symmetrically on bottom and on top. The steel stirrups of diameter 6 mm had a distance of 375 mm in the shear zone.

In Table 1.2 selected results of the shear experiments are presented. The wall element number ST2 was the reference and was not post-strengthened with CFRP straps. ST3 was post-strengthened with 4 CFRP straps with a distance of 500 mm. Each strap was post-tensioned with only 5 kN. ST1 had a similar arrangement like ST3, however each strap was post-tensioned with 70 kN.

The general failure mode was in the case of all three shear walls brittle. However in the case of the post-tensioned walls the failure of the external CFRP straps was of a progressive type, mostly starting from the innermost layer. Gradual longitudinal splitting of CFRP tapes and breaking of fiber bundles could easily be observed and heard quite a while before the abrupt and noisy collapse.

Remarkable within the results of Table 1.2 is the difference between the post-tensioned (70 kN each strap) and the not really post-tensioned (only 5 kN each strap) application. 70 kN-post-tensioning helped to increase the ultimate shear load for 51%. The same amount of CFRP in the same arrangement reached in the "not" post-tensioned (in reality 5 kN) shear wall only an increase of 3%. This demonstrates the high effectivity of post-tensioned applications. Figure 1.5 shows exemplarily the test setup, the theoretical stress field and the crack distribution for the shear wall ST1.

In the experimental phase the pins and the semi-elliptical pads were made of steel. It does not make much sense to propagate CFRP as a non-corroding material and to use steel for the anchorage of such elements. Meanwhile very powerful pins made of CFRP are available. Also the semi-elliptical steel pads have been successfully replaced by pads made of CFRP reinforced mortar (Fig. 1.6), polyethylene or GFRP (glass fiber reinforced polymers).

In 2007 such CFRP straps were applied for the first time as post-strengthening tendons to improve the seismic resistance of a masonry wall of a three floor administration-building (Fig. 1.7). The EMPA spin-off company Carbo-Link Ltd. was responsible for the production, installation and post-tensioning of five CFRP-elements of 13 m in length and 34 mm in diameter (Fig. 1.8). The pre-tensioning force on each tendon is 360 kN and the ultimate load amounts to 1,050 kN. Due to easy installation purposes the tendons are placed on the outside of the façade. The

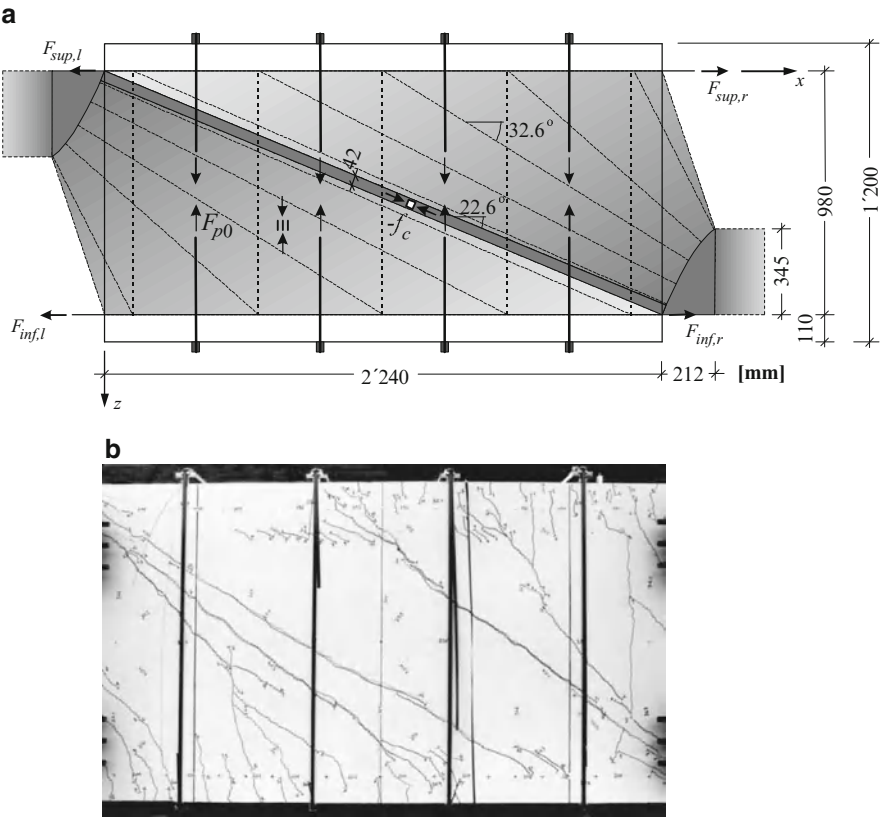

Fig. 1.5 Shear wall ST1 loaded up to −635 kN: (*top*) discontinuous stress field; (*bottom*) crack distribution

Fig. 1.6 Semi-elliptical CFRP reinforced mortar pad

advantages of these tendons are the low weight and therefore very easy handling during installation, high tensile strength and outstanding corrosion resistance. Similar elements have been used for Liebherr cranes with extreme cantilevers and for shovel dredgers of the same manufacturer. In mechanical engineering the steel cable substitution with CFRP tendons is resulting in considerable weight savings and an outperforming fatigue life.

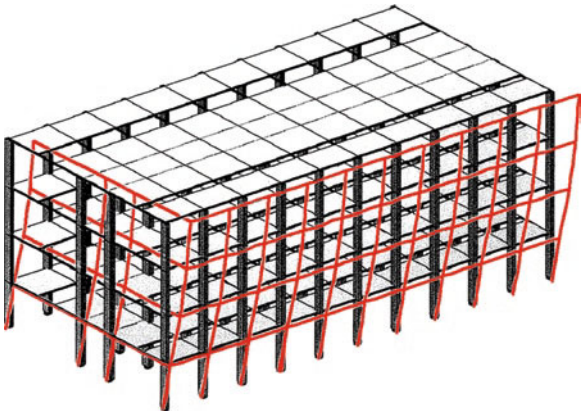

Fig. 1.7 Structure of three floor administration-building made of masonry. The wall on the *left side* had to be post-strengthened

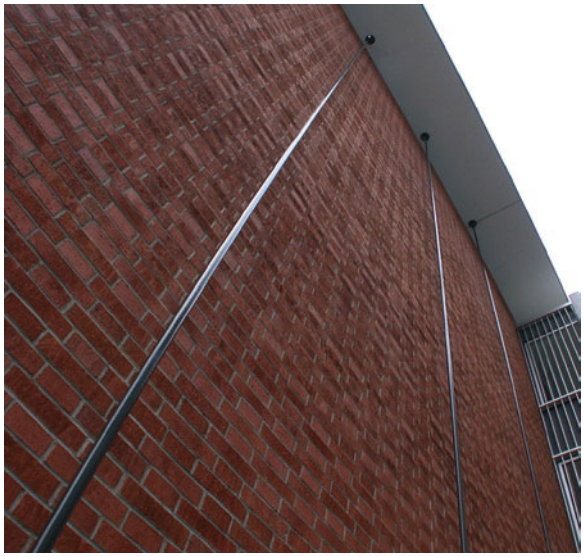

Fig. 1.8 Masonry wall post-tensioned with external CFRP tendons each of 1,050 kN ultimate load and 34 mm diameter

The described CFRP-strap-tendons were originally designed for rehabilitation of structures, especially post-strengthening in shear. Nowadays they are also used in new construction, e.g. for a bowstring arch bridge (Meier et al. 2009) realized with six longitudinal arranged CFRP bowstrings and glulam for the finally arch shaped bridge deck. This deck is stress-laminated as a flat plate. It is constructed by placing sawn lumber laminations on edge and stressing the laminations laterally together on the wide face with thin high-strength thermoplastic CFRP tapes (Fig. 1.9). It is causing the deck to act as a large orthotropic wooden plate. The bowstrings are composed of non-laminated pin loaded thermoplastic CFRP strap elements. These elements enable the individual layers to move relative to each other which allow an equalization of forces in the layers as the strap is tensioned. The approach allows excellent

Fig. 1.9 Glulam plate orthotropic post-tensioned with CFRP strap elements

use of the strength of CFRP and great flexibility in terms of the geometry of the strap elements as tendons. After prefabrication of the flat glulam plate and the CFRP straps the bow has been drawn. The bridge deck, which has the arch function, was axially loaded with the CFRP straps and elastically bent with a deflection of 1/75 of the span. The described bowstring arch concept allows an extremely slender and therefore very elegant bridge design. The first bridge of this kind with a span of 12 m was built at the end of 2006. A similar application in concrete is absolutely feasible. This kind of tendons would be predestined for a concrete stress ribbon bridge.

1.3 Selected "Non Finito" Challenges for the Future

1.3.1 Three Dimensional Post-tensioning

Especially in the case of rehabilitation of historic structures it would be ideal to be able to drill three dimensional curved holes of small diameters (typically 5 mm) into components of a structure to be able to post-tension such a component with mono wires or strands of CFRP or stainless steel. This would be a very effective and efficient way for the rehabilitation of pinnacles and spires especially on gothic churches. It could also be used to repair cracked stones of monuments. It would be a very interesting technique for seismic retrofitting of masonry walls of historic buildings. Post-tensioning could be optimized according to the stress trajectories of a structure.

To the best knowledge of the author there are no such tools available today in construction industry. Oil industry is drilling curved bore holes since decades. It is only a question of miniaturizing such systems for construction. Following the US Patent 4,442,908 (Steenbock 1984) such a system could be described as subsequent: a drilling tool having a motor-driven drill bit which can be turned at an angle to the axis of the primary hole to produce lateral holes branching from the primary hole. The bit that is rotatable mounted in a series of pivotally articulated links at the end

of the drill pipe string. The deviation of the drill bit from the axis is controlled by pivoting the last link with respect to the penultimate link. The last link includes a sliding surface which bears against the wall of the hole to effect the pivoting.

1.3.2 Could Airbags Prevent Structural Collapses Due to Earthquakes?

The airbag for automotive applications traces its origin to air-filled bladders outlined as early as 1941. Patented ideas on airbag safety devices began appearing in the early 1950s. U.S. patent 2,649,311 was granted on August 18, 1953, to John W. Hetrick for an inflated safety cushion to be used in automotive vehicles. Early air bag systems were large and bulky, primarily using tanks of compressed air, compressed nitrogen gas (N_2), freon, or carbon dioxide (CO_2).

The first use of large airbags for landing of space vehicles were Luna 9 and Luna 13, which landed on the Moon in 1966. The Mars Pathfinder lander employed an innovative airbag landing system. This prototype successfully tested the concept, and the two Mars Exploration Rover Mission landers employed similar landing systems. The US Army has incorporated airbags in its Black Hawk and Kiowa Warrior helicopter fleets. Airbags have been proven very effective in preventing motor vehicle accident injuries. Why should they not also be used in the case of earthquakes to protect lives and prevent structural collapses?

In 2002 Hans-Joachim Kuempel was awarded the US Patent 6,360,384 B1 "Earthquake proof sleeping place". This place comprises a base frame with arcuate guiding tubes. From each guiding tube, an arcuate supporting bar may be telescoped. The supporting bars are connected by a longitudinal bar and form a protective frame therewith. Two protective frames can be raised out from the guiding tubes from opposite sides to close above the bed. The protective device requires little space since the base frame is mostly arranged under the bed. An earthquake sensor causes the protective device to be triggered, in which event the protective frames come up. This proposed system does not use airbags, however, similar to those the protection is initiated by a sensor system.

In 2005 Amir Hashem Shahidi Bonjar (2005) coined the expression Earthquake Airbag (EA). Based on many scientific reports, fatality rates are lower in automobiles equipped with airbags than unequipped ones. Accordingly, it was postulated that similar devices can be adopted in buildings to protect people and lower human casualties in building crashes. The safety advantage of EAs would be that they can reduce impact injuries upon indoor people from falling debris in earthquakes.

Why one should not try to avoid building crashes and thereby save lives and buildings at the same time? The author was in 2003 member of a peer review committee of the DFG (German Research Foundation) concerning structural investigations on the Hagia Sophia in Istanbul and visited this monument in 2004. During this visit the idea was born to think about the use of airbags to protect structures from earthquakes.

The current structure of Hagia Sophia was completed in 537. But it suffered under severe seismic loadings, e.g. in the years 553, 557, 865, 869, 986, 989, 1344, 1346, 1462, 1500, 1509, 1719, 1754, 1766, 1894 and 1999. The dome had to be reconstructed several times during the centuries. Based on recent seismic activity and the history of the North Anatolian fault south of Istanbul there is a high probability that Istanbul with the Hagia Sophia will be hit with a major earthquake over the next three decades. In Istanbul many structures have been post-strengthened against seismic loading with advanced composite materials. In the case of Hagia Sophia, e.g. it is impossible to cover the golden mosaics with black carbon fiber reinforced polymers. Seismic retrofitting of historic structures is anyway being between the poles of curators of monuments and structural engineers a difficult task.

Many wonder how Hagia Sophia will fare in the next great earthquake. The region just south of Istanbul is expected to experience tremors of equal or greater magnitude to the Izmit earthquake in the next few decades (Hughes 2006; Hubert-Ferrari et al. 2000). In 1991, a team of Turkish and US researchers fitted Hagia Sofia with several vibration sensors. From data gathered during micro earthquakes, Çakmak created three-dimensional computer simulations that could predict how the building might move during a large earthquake (Çakmak et al. 1995). Results obtained using LUSAS finite element modelling indicate that damage will occur initially in the west and east semi-domes before proceeding to the arches and main dome. The model shows also that when hit by a magnitude 7.5 tremor, the walls of Hagia Sophia will tremble and sway dramatically back and forth. The tops of its arches will feel the most stress. But the dome will remain unscathed, and the heritage structure will stand. If the earthquake is greater than 7.5, there is a high risk for a collapse.

How can this most valuable structure be preserved with airbags in the case of such a severe earthquake? Even if it would be possible from a technical point of view to have, e.g. for the central part of Hagia Sophia, one huge powerful airbag being folded on the ground this cannot work. In the case of an earthquake in presence of visitors inside the building the airbag's deployment might protect the structure; however it would kill the persons being between the airbag and the dome. Therefore a steel support structure is needed to carry the folded airbags. For the central dome this could be a centrically arranged horizontal circular steel ring with a large U-profile supported by telescope like columns. The opening of the U-profile would be on top. Inside the U-profile there are large folded tubular airbags. The initial height of this ring would be about 3 m above the ground floor. It would only little disturb the appearance of the wonderful architecture. As soon as the seismic sensors identify a strong earthquake they trigger the gas generators and deploy the airbag tubes. At the same time the telescopic columns would lift up the whole system. The system would perform as an adaptive structural support and damping the oscillations caused by the seismic activity. For the semi-domes and the arches (Fig. 1.10) semicircular ring U-profiles and linear U-profiles respectively would be used.

These systems could not fully prevent the falling of single stones between the tubes. The feasibility of the application of such earthquake airbags had first to be checked on the existing computer models. If the answer is positive experiments on smaller scale had to be provided. If all these investigations should give positive

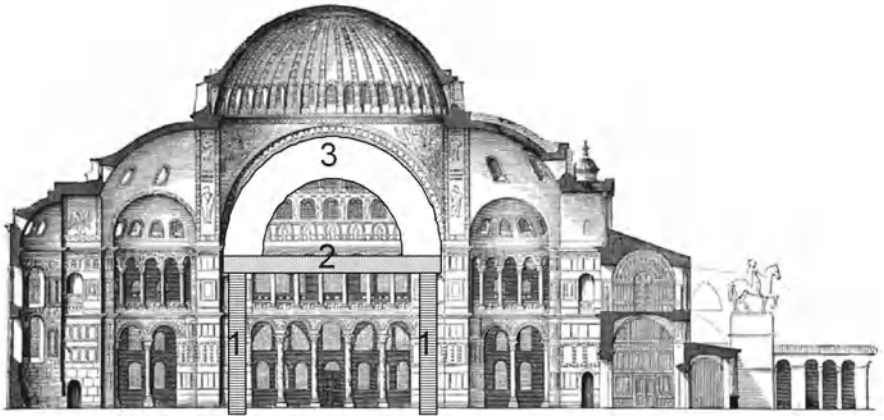

Fig. 1.10 Cross section of Hagia Sophia: Example for the seismic protection of an arch. *1* telescopic columns; *2* linear U-profile, open on the top; *3* deployed tubular earthquake airbag

answers the great advantage of earthquake airbags would be a fast installation and that there is no irreversible intervention on the historic structure needed. For the first application of this kind of "rehabilitation" the cost would be high due to elevated R&D expenses. However further applications should be very fairly priced. A special challenge would be the design of stable telescopic columns.

1.3.3 Adaptive Wind Fairings?

Due to low structural damping and relatively low mass, long-span suspended bridges become susceptible to vibrations caused by winds. That was the reason for the collapse of the Tacoma Bridge in 1940. The Bronx–Whitestone Bridge in New York used the same general design as the Tacoma Narrows Bridge. In 1943 6,000 ton of heavy trusses were installed on the Bronx–Whitestone Bridge on both sides of the deck to weigh down and stiffen the bridge in an effort to reduce oscillations after the Tacoma Narrows Bridge disaster. These trusses detracted from the former streamlined looking span. In 2003, the Metropolitan Transit Authority restored the classic lines of the bridge by removing the stiffening trusses and installing instead glass fiber reinforced polymer (GFRP) wind fairings along both sides of the bridge deck. The lightweight GFRP fairings are triangular in shape giving it an aerodynamic profile. The removal of the trusses and other changes to the decking cut the bridge's weight by 6,000 ton, some 25% of the mass suspended by the cables (Meier 2003).

In future similar cases an innovative wind-induced vibration mitigation strategy based on active control of the bridge's aerodynamic profile might be applied. An array of adjustable flaps might be installed along both edges of the girder and their angular position controlled as a function of the current dynamic state of the structure and

the local wind field measurement. This information is shared with other similar units distributed over the whole length of the bridge through wireless networking (Bischoff et al. 2009). The characteristics of the interaction between the wind field and the underlying structure with the additional degrees of freedom introduced by the flap system result in complex models and associated control strategies. The need for real-time coordination between various units, leading to an active control of the global aerodynamic profile of the full bridge model with the constraints introduced by the mechanical structure makes the problem of mitigating vibrations at the perturbation source extremely challenging. Also for this challenge the cost for the first application of this kind of "rehabilitation" would be high due to soaring R&D expenses. However, further applications should be very fairly priced.

In modern architecture it is more and more fashionable to design and construct lean high raised towers. Already in the past some of them faced oscillation problems due to aerodynamic excitations. Instead of the subsequent installation of tuned mass dampers an adaptive outer skin made of electro-active polymers might resolve this problem (Jordi et al. 2010). Such an outer skin may not only improve the aerodynamic properties but also serve as a curtain wall with special thermal and optical properties. Such multifunctional materials will play an important role in construction in the future.

1.4 Conclusions

Today's state-of-the-art in civil engineering is the accumulation of past innovations. As engineers, we must be innovative so tomorrow's world will be better. Innovation starts with the questions "Why?" and "Why not?". The question "Why?" gives us the opportunity to challenge the status quo. "Why not?" gives us the opportunity to introduce new ideas or overcome restrictions. The question "What if?" keeps us humble and conservative. How can we overcome these barriers? We have to accept challenges. We have to overcome them. It is what makes civil engineering meaningful. General George S. Patton said: "Accept challenges, so that you may feel the exhilaration of victory".

References

Bauersfeld D-W (1984) Composite graphite/epoxy tensile element. In: Report 2404, United States Army, Belvoir Research & Development Center, Fort Belvoir, pp 1–62

Bischoff R, Meyer J, Feltrin G (2009) Wireless sensor network platforms. In: Boller C, Chang F, Fujino Y (eds) Encyclopedia of structural health monitoring. Wiley, Chichester, pp 1229–1238

Bonjar A-H-S (2005) Earthquake airbags, new devices to save lives in earthquakes, tornados and similar disasters resulting from building crashes. Am J Appl Sci 2:774–777

Çakmak A, Moropoulou A, Mullen C-L (1995) Interdisciplinary study of dynamic behavior and earthquake response of Hagia Sophia. Soil Dyn Earthq Eng 14:125–133

Hubert-Ferrari A et al (2000) Seismic hazard in the Marmara Sea region following the 17 August 1999 Izmit earthquake. Nature 404:269–273

Hughes V (2006) Shaken, not stirred. Nature 443:390–391

Hull D, Clyne T-W (1996) An introduction to composite materials. Cambridge solid state science series, 2nd edn. Cambridge University Press, Cambridge

Jordi C, Dürager C, Michel S (2010) Dielectric-elastomer-driven airship uses fish-like propulsion. SPI 30 April 2010, http://spie.org/x39863.xml?ArticleID=x39863. Accessed 23 Feb 2011

Lees J-M, Winistoerfer A-U, Meier U (1999) Non-laminated pin-loaded CFRP straps for the shear enhancement of concrete. In: Dolan C-W, Rizkalla S-H, Nanni A (eds) Fiber reinforced polymer reinforcement for reinforced concrete structures. ACI SP-188, Baltimore, pp 985–993

Lees J-M, Winistoerfer A, Meier U (2002) External prestressed CFRP straps for the shear enhancement of concrete. ASCE J Compos Constr 6:249–256

Meier U (1987) Brückensanierungen mit Hochleistungs-Faserverbund-Werkstoffen. Mater Tech 15:125–128

Meier U (2003) Auf dem Weg zu intelligenten Baumaterialien: adaptive Werkstoffsysteme – Eine aktuelle Übersicht. tec21 129:6–9

Meier U, Winistoerfer A (1998) Multilayer traction element in the form of a loop. European Patent 0,815,329, 7 Jan 1998

Meier U, Brönnimann R, Widmann R, Winistörfer A, Irniger Ph (2009) Bowstring-Arch Bridge Made of CFRP, GFRP and Glulam. In: Proceedings second Asia-pacific conference on FRP in structures (APFIS), Seoul, pp 557–562

Sommer U, Kainer K-U, Böhm E, Krüger G (1996) Charakterisierung von Hochleistungsfasern für die Verstärkung von Metallmatrix-Verbundwerkstoffen. In: Ziegler G (ed) Verbundwerkstoffe und Werkstoffverbunde, DGM Informationsgesellschaft, pp 375–378

Steenbock A (1984) Tool for drilling curved sections of well holes. US Patent 4,442,908

Stenger F (2001) Tragverhalten von Stahlbetonscheiben mit vorgespannter externer Kohlenstofffaser-Schubbewehrung. Dissertation No 24589, ETH Zürich

Winistoerfer A (1999) Development of non-laminated advanced composite straps for civil engineering applications. Dissertation, University of Warwick

Chapter 2
New Materials and Construction Techniques in Bridge and Building Design

Hugo Corres-Peiretti, Sebastián Dieste, Javier León, Alejandro Pérez, Julio Sánchez, and Cristina Sanz

Abstract This paper demonstrates a series of exemplary works which have introduced innovations in concepts, materials and execution processes. These projects embody proposals for improvement that make suitable use of different uncommon or recent technologies, taking maximum advantage of the possibilities they offer.

2.1 Introduction

Structural engineering is a profession extraordinarily open to creativity, where technological possibilities do play an essential role in the development of good ideas, together with imagination and deep understanding of structural problems, as well as knowledge of previous contributions, that is, of the History of structural engineering. However, it becomes more and more difficult to conceive new structural shapes, neither already defined nor used in the past. This is noticed when carefully studying the innovations of the great architects-engineers-builders throughout history (Heinle and Schlaich 1996).

Nevertheless, it is possible today to recover old brilliant proposals updated according to present technological opportunities. This is a great challenge for today's professionals, a sort of deconstruction that enables the production of old ideas with new possibilities.

The authors of this paper consider the Pantheon in Rome as an extraordinary work of structural engineering and architecture; perhaps the most outstanding

H. Corres-Peiretti (✉) • S. Dieste • J. León • A. Pérez • J. Sánchez • C. Sanz
FHECOR Ingenieros Consultores, C/Barquillo, 23 2ª Planta, 28004 Madrid, Spain
e-mail: hcp@fhecor.es; sdb@fhecor.es; jlg@fhecor.es; apc@fhecor.es; jsd@fhecor.es; csm@fhecor.es

M.N. Fardis (ed.), *Innovative Materials and Techniques in Concrete Construction: ACES Workshop*, DOI 10.1007/978-94-007-1997-2_2,

Fig. 2.1 Pantheon in Rome. Apolodorus of Damascus. Second Century AD

masterpiece of all times, a good example of how to profit, in a pioneering way, from the technological possibilities available at that time, new materials, notably concrete, new shapes, i.e. a spherical dome of variable depth, developed after a clever, brilliant geometrical arrangement, with an oculus not intuitively safe, a system of coffers that optimises the self-weight effect, an excellent construction procedure avoiding double formwork, etc. Going into such a marvellous example, which was built when masters had great intuition but limited technological possibilities, leads ineluctably to bow to the genius and braveness of our predecessors. Furthermore, we must humbly admit how much less we innovate nowadays, taking into account the infinite technological possibilities available to us today (Fig. 2.1).

2.2 Intesa-San Paolo Tower in Turin

This tower is a complex building (Corres et al. 2008a; Corres and Gómez 2010; Bertagnoli et al. 2010), currently under construction in Torino, Italy, after an architectural project by Renzo Piano and a structural design by FHECOR Ingenieros Consultores and SINTECNA.

It is a 170.0 m tall building, vertically supported by an internal concrete core, eccentrically arranged in plan, and six mega-columns that bear, through a transfer structure located at the 7th floor, i.e., about 34 m above ground level, all the upper storeys, up to level L38. Underneath this transfer structure and hanging from it, five storeys house an auditorium (Fig. 2.2).

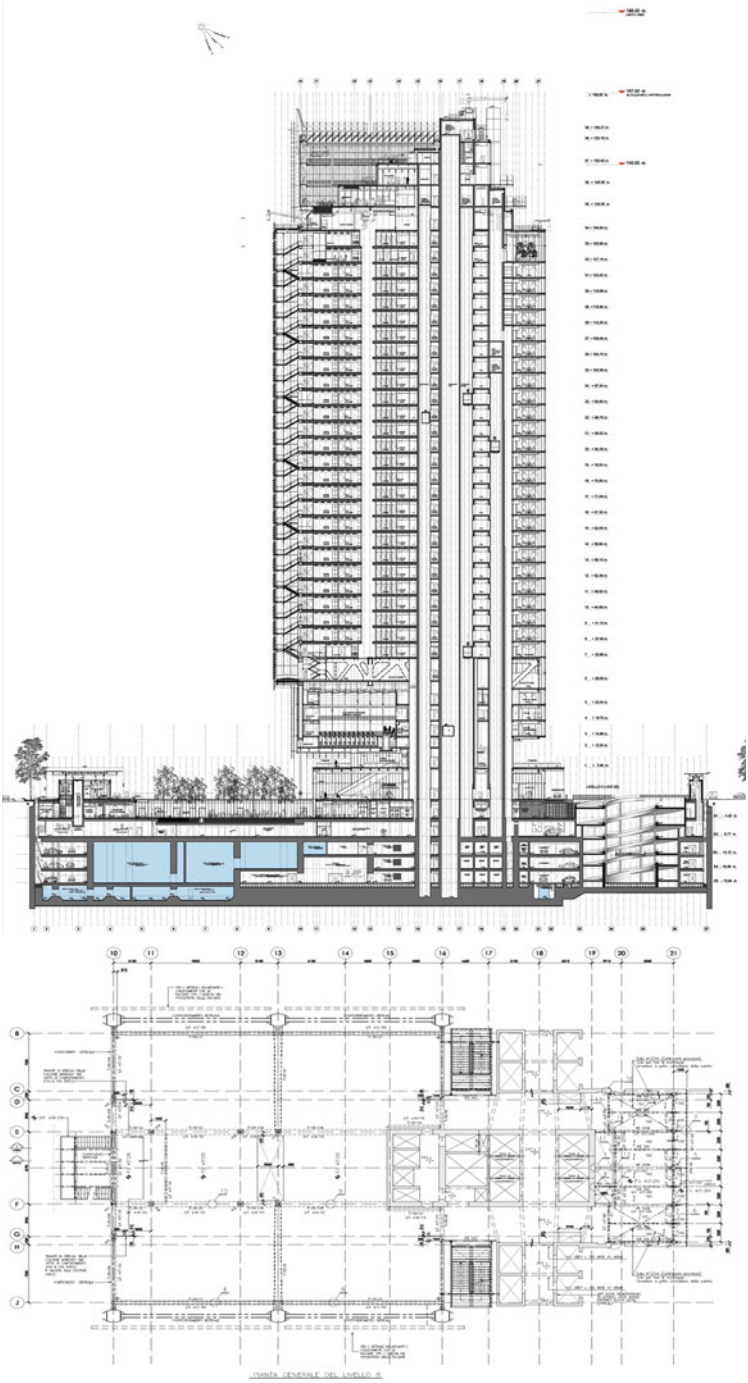

Fig. 2.2 Longitudinal south-north section and plan view of the Intesa-San Paolo Tower in Torino

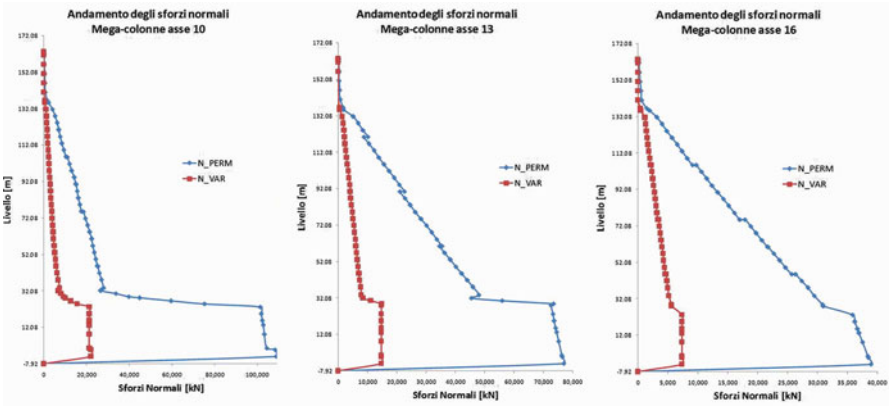

Fig. 2.3 Axial forces in the mega-columns on axis 10, 13 and 16

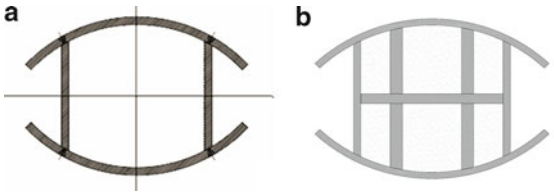

Fig. 2.4 Mega-columns' section: (**a**) original design's section; (**b**) proposed alternative

Figure 2.3 shows the axial force distribution of three mega-columns. Axial forces increase more or less linearly up to level L6, where the transfer structure is located, increasing then significantly the value of the axial force.

Mega-columns are external to the building and, therefore, are directly submitted to ambient temperature, whereas the internal concrete core is placed inside the building, conditioned and, thus, at an almost constant temperature. This situation induces a differential movement between the part of the building directly supported by the mega-columns, with temperature changes rising from −10°C to +60°C, while the part of the building on the concrete core is at constant temperature.

The original design conceived plain steel mega-columns, with plates up to 120 mm thickness, protected by an intumescent painting, 8 mm thick, as shown in Fig. 2.4a, to guarantee a fire protection of up to 120 min.

The alternative proposal consists of a composite section built up of external 30 mm thick plates, unprotected against fire since such plates are not considered as resistant in case of fire. The thickest plates are located inside, protected by concrete from the fire action. Concrete has been designed self-compacting, to ensure adequate casting, with $f_{ck} = 70$ MPa. Additionally, the new composite proposal isolates the mega-column, alleviating its maximum and minimum temperatures relative to the extreme exterior values (Fig. 2.5).

This solution allowed reduction of about 25% of the steel section due to the contribution of concrete. In addition, it has been possible to eliminate the intumescent painting of the external plates and, also, to decrease the range maximum-minimum

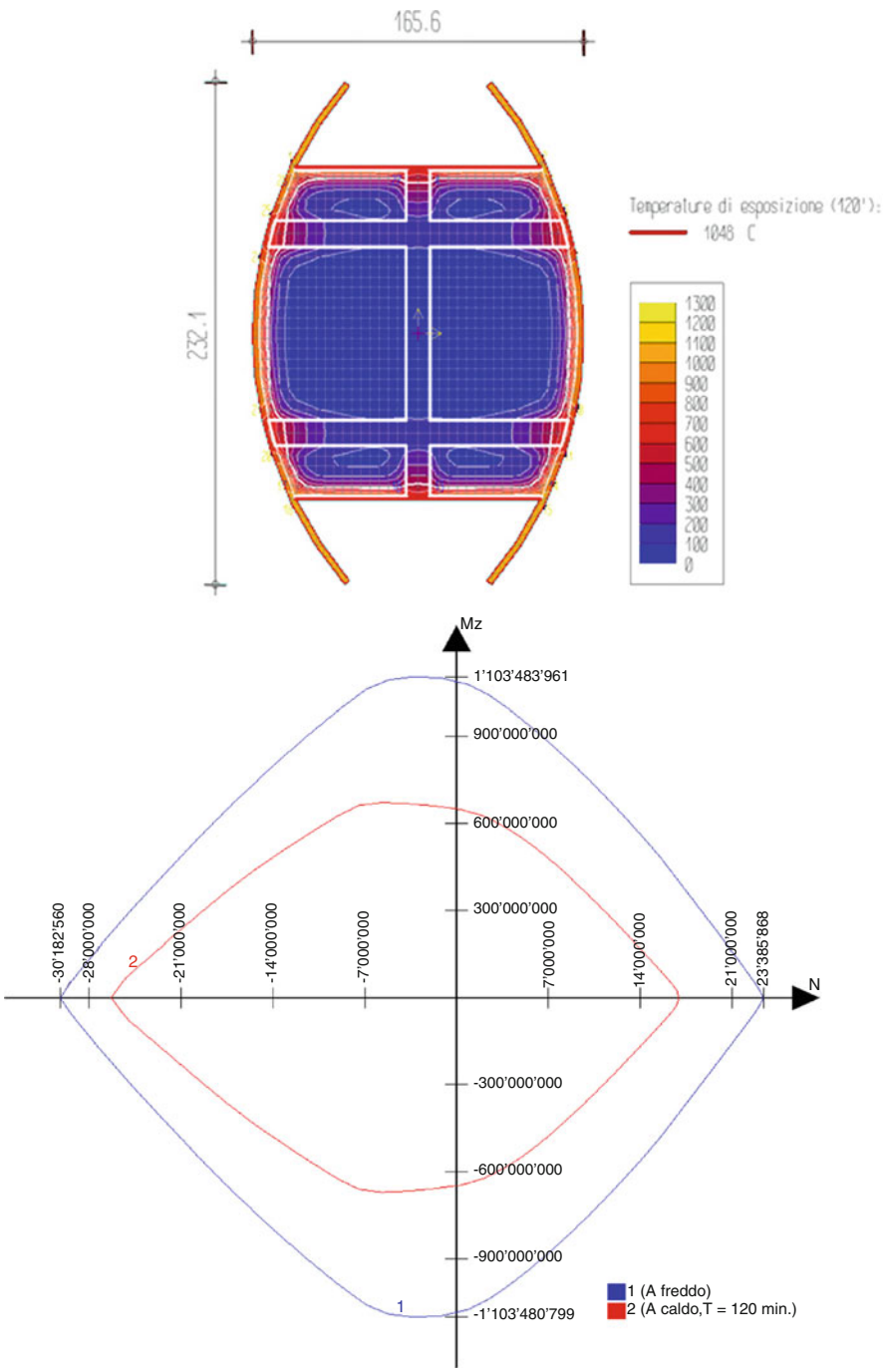

Fig. 2.5 Temperature distribution in the composite section of the mega-column (*top*) and interaction diagram for Ultimate Limit State with and without fire action (*bottom*)

ambient temperatures and, therefore, to diminish the differential deformations between the part of the building lying on the external mega-columns and the internal zone on the concrete core, at almost constant interior temperature.

The foundation of the central part of the building, beneath the tower, is a 75.0 × 43.0 × 4.3 m concrete slab, which represents a concrete total volume of 13,870 m³. The operation of pouring concrete in this element was not easy since, on the one hand, it took long time in the schedule of construction and, on the other hand, it required a big quantity of connecting reinforcement at concreting joints. To minimize these problems, a continuous pouring was proposed as an alternative.

In order to fulfil such requirements, a special low-heat and self-compacting mix was designed. Since this structural element would not require its full bearing capacity till a year after casting, a slow-rate strength concrete was accepted, in such a way that the specified strength would be attained at 60 days, instead of the conventional 28 days (Figs. 2.6–2.10).

Once the adequate mix has been defined, several tests were carried out to calibrate the distribution of temperatures while hardening of concrete, the evolution of compressive and tensile strength, modulus of elasticity, shrinkage and creep at very early stages. All this information served as a basis to estimate a theoretical evolution of temperature within the concrete mass and its structural influence: the build-up of tensile stresses (Bertagnoli et al. 2010). A conclusion drawn was that some additional reinforcement was required at the outermost slab surfaces.

The result of this proposal was a continuous casting of 13,870 m³ of concrete in 3 days with three pumps. This layout allowed a reduction in execution time, as well as a substantial reduction in the amount of reinforcement, since connecting reinforcement at the joints was avoided (Fig. 2.11).

2.3 Widening of the Los Santos Viaduct in Spain

This viaduct was erected with the free cantilever method in the mid-1980s. It has spans of 75 + 3 × 150 + 75 m, variable depth and single-cell box cross section, with a 12.0 m wide deck (Fig. 2.12).

The new traffic requirements made it necessary to widen the viaduct to 24 m. The environmental requirements did not allow a twin viaduct or a new foundation. Moreover, the great difficulties of detouring the traffic to facilitate the construction forced to conceive a solution compatible with maintaining the traffic during widening the platform.

Taking into account the referred requirements, and after a deep analysis of different possibilities, a decision was made for a solution according to a concept described in the following.

The concept of the widening solution was based on the idea of minimizing the total weight of the broadened viaduct and at the same time strengthening it (Corres et al. 2008b).

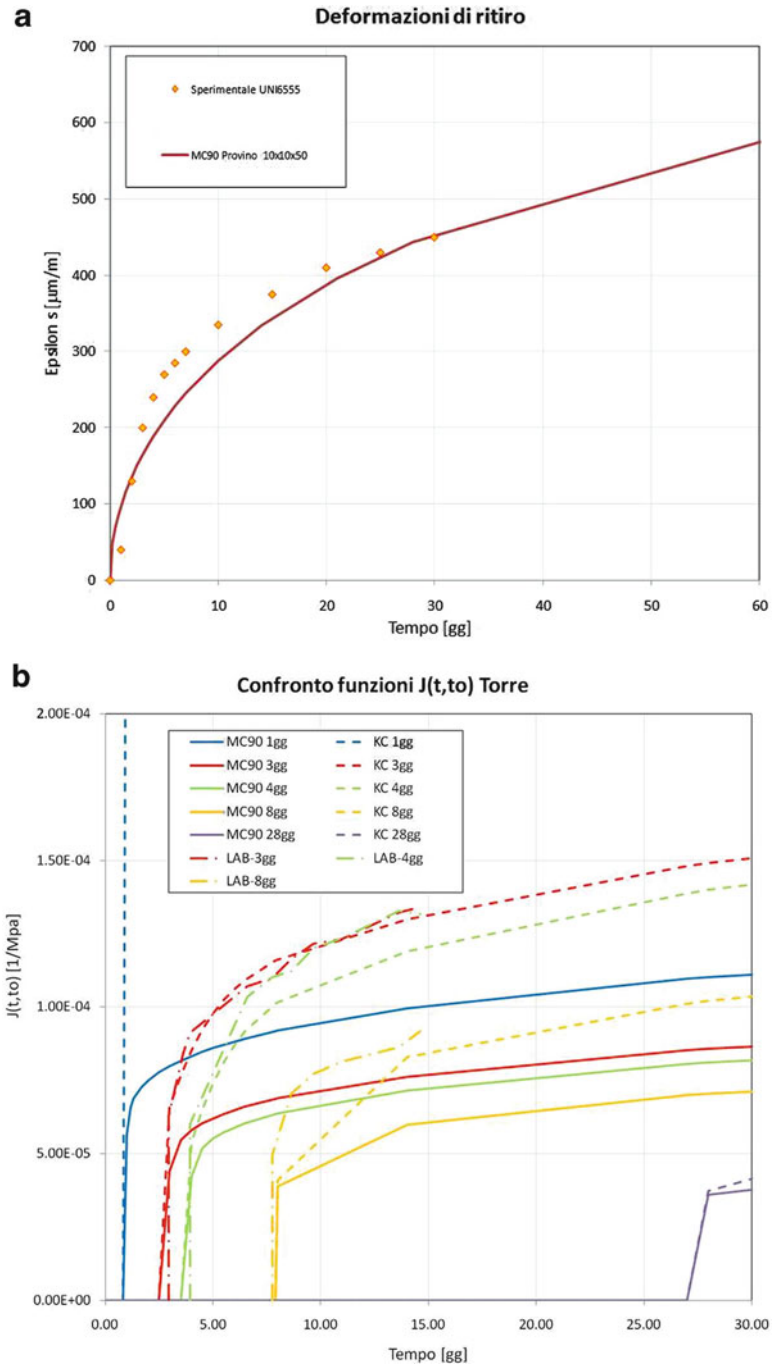

Fig. 2.6 Theoretical estimation and experimental results on shrinkage and creep of the concrete selected for the foundation slab (Bertagnoli et al. 2010)

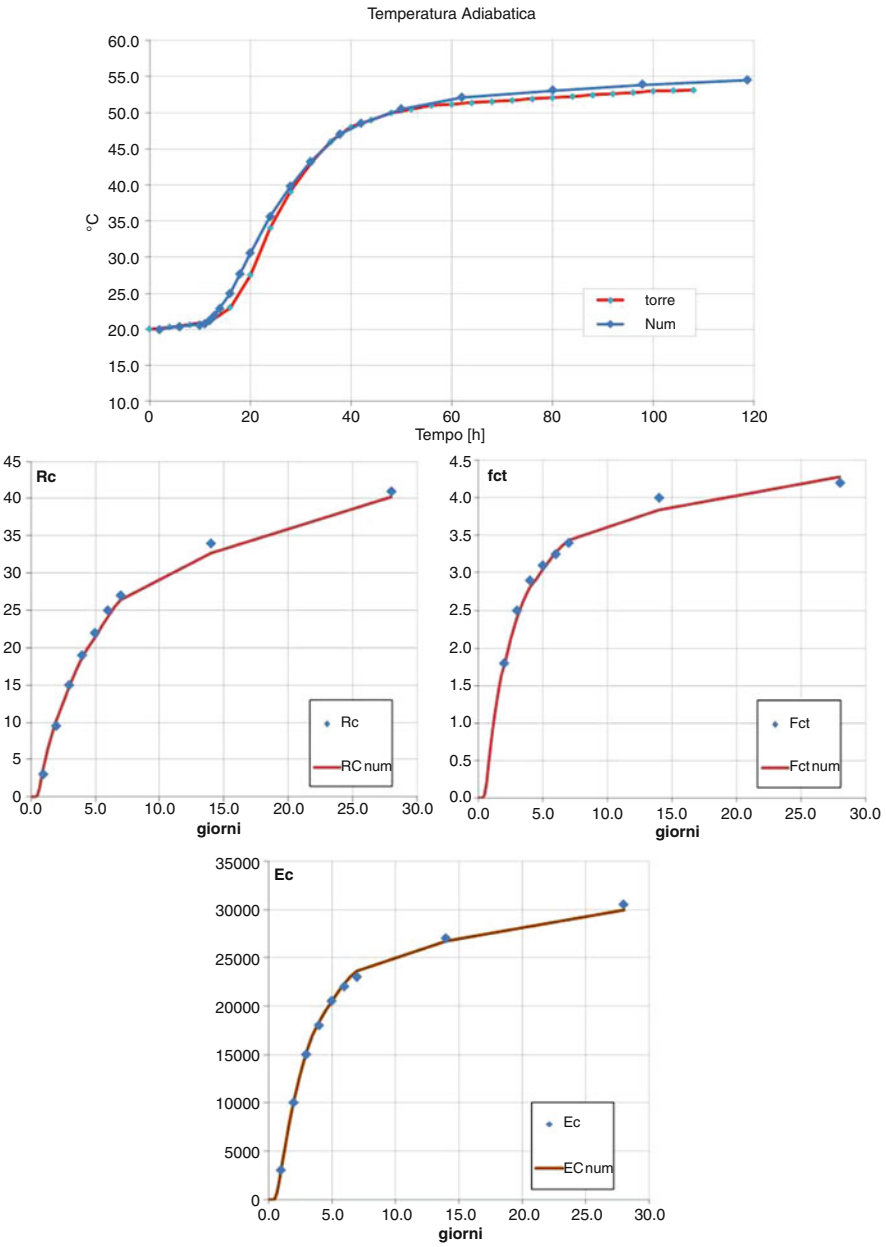

Fig. 2.7 Theoretical estimation and experimental results of the adiabatic temperature, compressive and tensile strength and E-modulus of concrete chosen for the foundation slab (Bertagnoli et al. 2010)

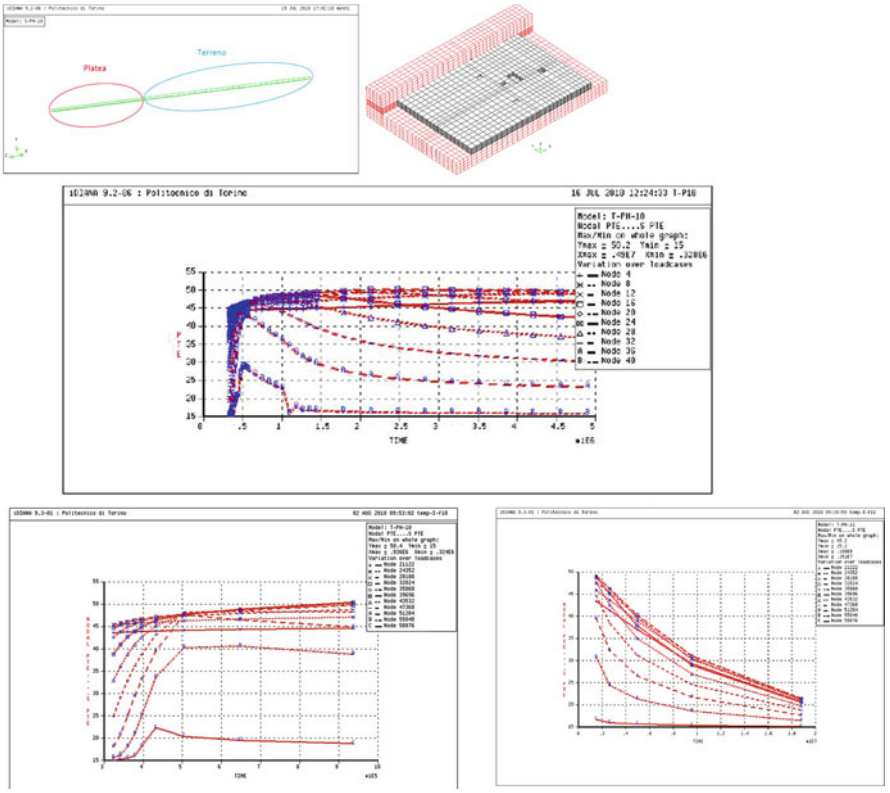

Fig. 2.8 Models and theoretical results for the stress distribution of the slab foundation during casting

Fig. 2.9 Some views of the casting operation and equipment

Fig. 2.10 Reinforcement layout and density, and views of casting the self-compacting concrete and of surface finishing

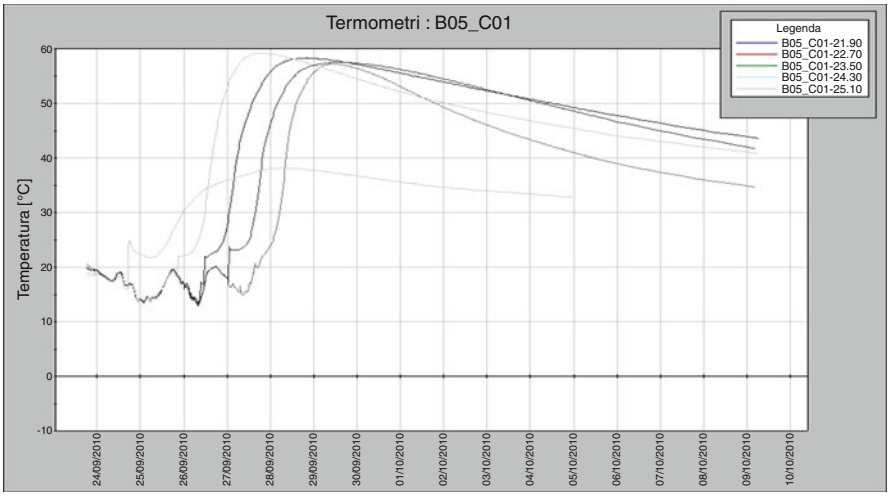

Fig. 2.11 Evolution of measured concrete temperature at different depths of the foundation slab

The foundations of the outer piers rest directly on rock, whose loadbearing properties were sufficient for the new loads. Interior piers were on piles down to a competent depth with sufficient loadbearing capacity, as derived after new drillings carried out directly from the pier cap to the interface with the rock. However, pier caps and foundation slabs required strengthening.

Fig. 2.12 General view of the viaduct before the intervention

The piers exhibited sufficient load-bearing capacity for the widening. This can be understood by the circumstance that that piers of this type of bridge, built using the free cantilever method, are strongly conditioned by the erection process. Thus, in the final state, the piers' bearing capacity is greater than strictly required for nominal loading in the final stage. However, the deck required strengthening, as it did not have the capacity to take over the full additional loading of the widened platform (dead plus live loads).

Since the existing bridge was the fundamental basis of the broadened structure, an intensive and extensive inspection campaign was undertaken. Tests to infer the conditions of resistance and, especially, of the durability of the structure were made: intensity and potential of corrosion, carbonation, chloride profile, sulphates, concrete cover, density, porosity, etc. (Fig. 2.13). It was concluded that the bridge had adequate remaining durability to allow an increase in lifespan of at least 50 years.

Figure 2.14 shows the structural concept of the intervention. It was decided that the widening would be symmetrical, at both sides of the existing box section, with a lightweight concrete slab of variable depth. This slab was lying on, basically, a system of light steel props, conceived to direct the new vertical loads to a vertical central web to be added at the interior of the existing box section. This new web should be of self-compacting concrete (Fig. 2.15).

The existing transverse section would be strengthened by means of a steel box filled with self-compacting high performance concrete, linking the aforementioned props and other elements that support the widening slabs. Besides, an external intradosed prestressing was added inside the box. The tendons have a straight horizontal layout, due to the longitudinal variable depth, providing a rather modest contribution to vertical bending. However, this prestressing supplies compression to the box, improving the shear and torsion resistance of the outer webs of the box.

Another novelty was the construction process, which was rather complex, since it referred to an existing structure with lots of uncertainties and the additional extraordinary complexity due to the need of maintaining the traffic. Thus, it became

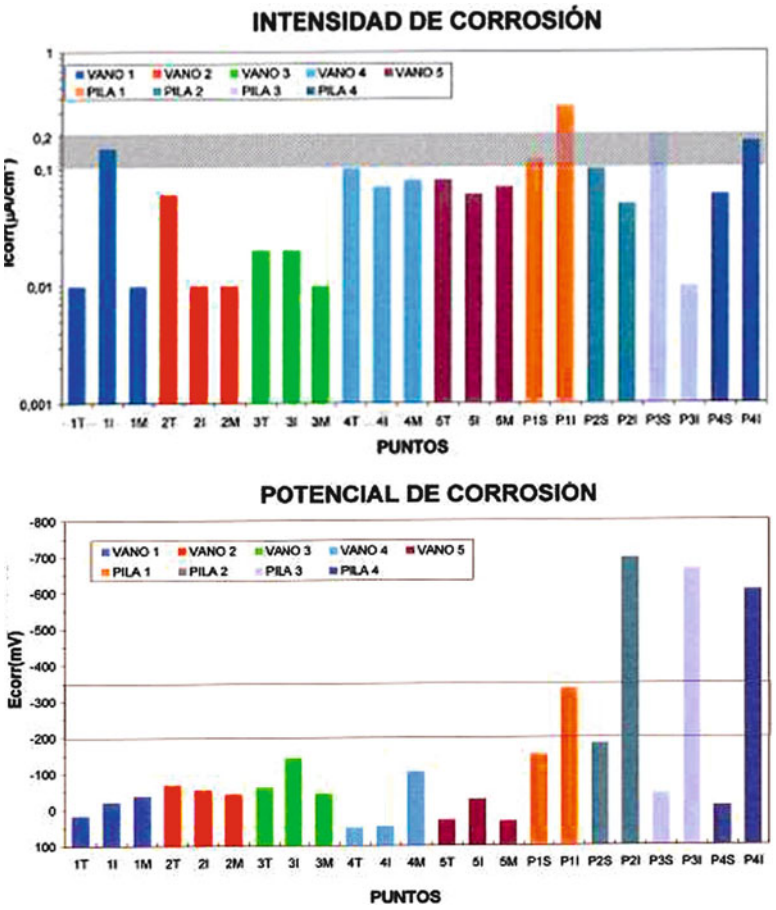

Fig. 2.13 Results of tests for intensity and potential of corrosion

necessary to make use of extraordinary auxiliary equipment. Such an intervention requires minimizing the effect on the existing structure, in the context of very special working conditions. To provide an idea of the processes and equipment required, Figs. 2.16 and 2.17 show three operations: erection of the intermediate web, construction of deviators and assembly of the internal prestressing within the box section.

In addition, three movable platforms were specifically developed, the first to install part of the steel structure (the bottom chord and transverse struts); the second to allow demolition of the old transverse cantilevers without fall of debris and the third one to assemble the inclined struts and to cast the widened transverse slabs

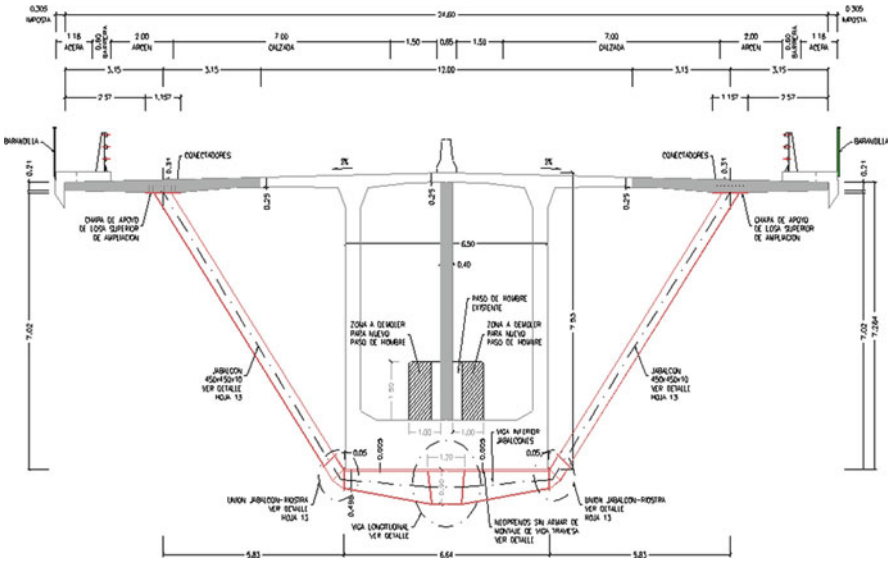

Fig. 2.14 Transverse section of the widened box from 12.0 to 24.0 m

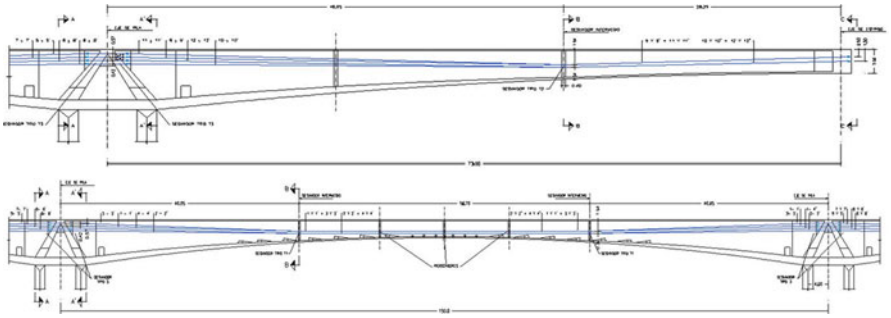

Fig. 2.15 External strengthening prestressing arranged at the interior of the existing box section

(Fig. 2.16). All the equipment used and the processes involved must allow the traffic to pass on the existing platform (Fig. 2.18).

Figure 2.19 shows views of the completed bridge. Red painting expresses that a widening operation like this is similar to an intervention on a historical building, where valuable existing elements must be respectfully kept and new elements are explicitly highlighted: again the debate about the capacity of engineers to understand the aesthetic implications of an intervention on an existing structure; in particular whether engineers are able to handle appropriate use of colours or not, a valuable resource in the hands of engineering activity.

Fig. 2.16 Inner web with self-compacting concrete: drilling to place reinforcement at *top slab*, with hydrodemolition to avoid damage to existing reinforcement; in *bottom slab*, conventional drilling, accepting a certain percentage of affected bars; assembly of mild and prestressing steel

2.4 Shell Pedestrian Bridge in Madrid

The Matadero and Invernadero pedestrian bridges (Fig. 2.20) are part of the overall refurbishment and new public spaces created on the banks of Manzanares River in Madrid, within the framework of a process started by the Municipality of Madrid in 2003 to depress underground the urban expressway M-30. The expressway, built in the late 1960s, had really caused a deep wound splitting the south-west zone of the city. This operation constitutes a huge engineering work with profound social and urban implications.

In 2005, the Municipality of Madrid organized an international competition and called for ideas proposing alternatives for the town planning to be applied to the vacant area resulting from depressing the expressway underground. The purpose

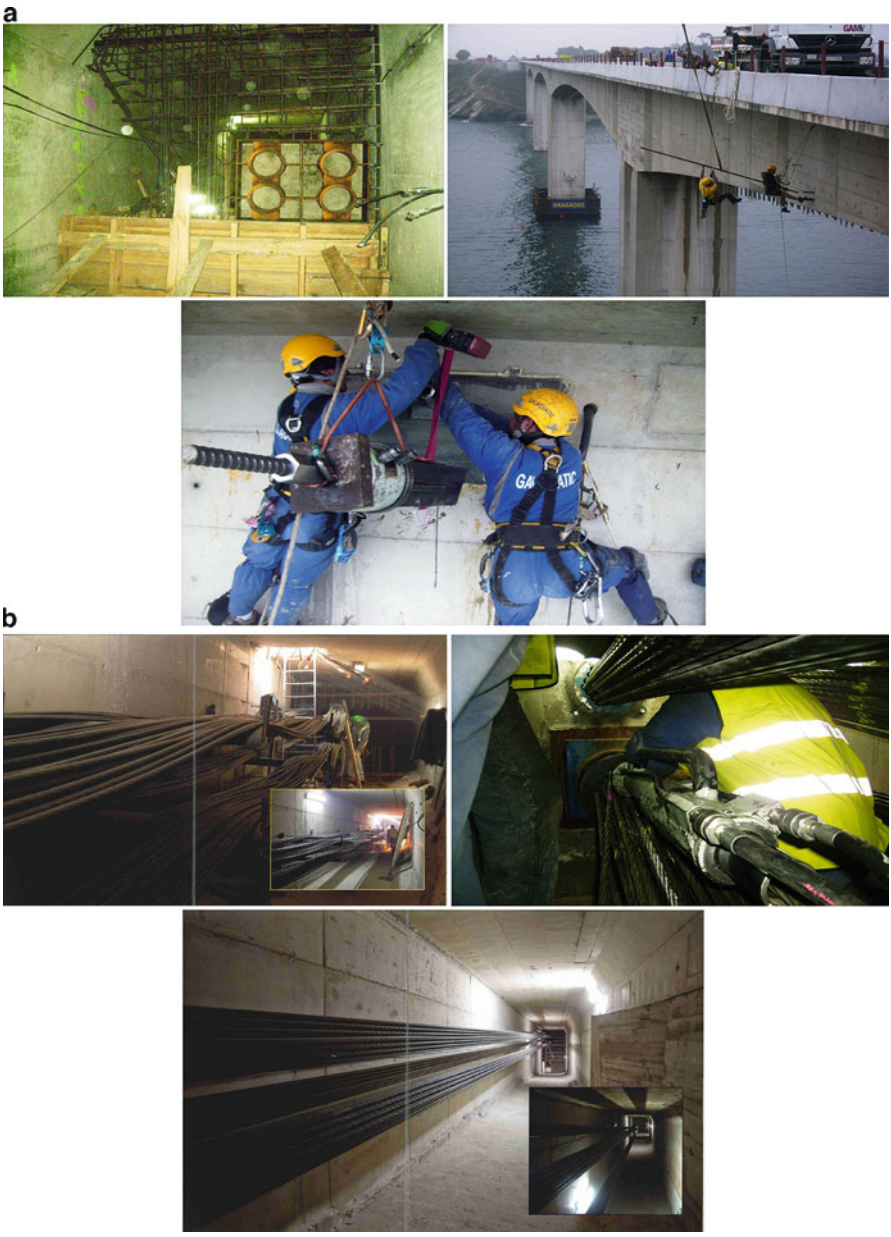

Fig. 2.17 Erection of inner web of self-compacting concrete. (**a**) Execution of deviators; Arrangement of connecting reinforcement to the existing box section. (**b**) Assembly of external prestressing

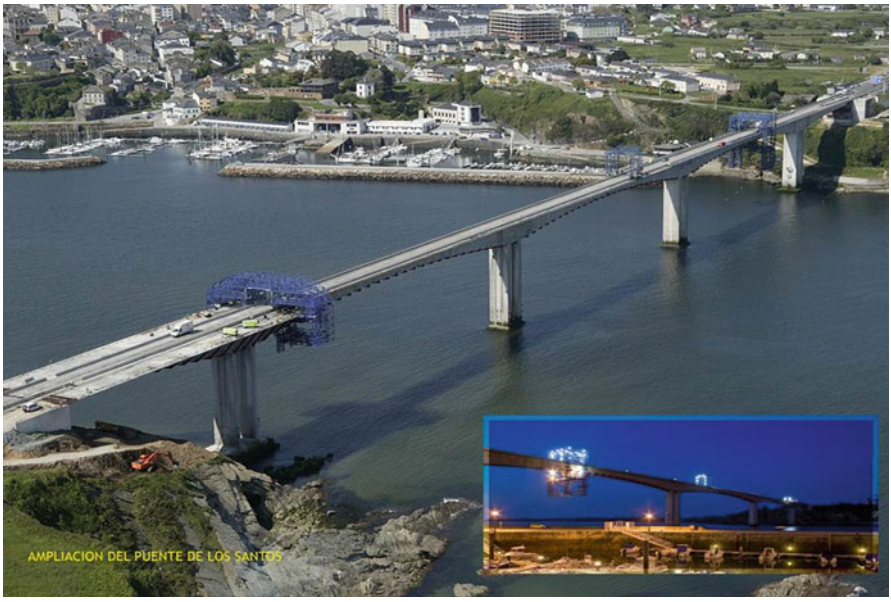

Fig. 2.18 View of the three platforms used on different parts of the bridge

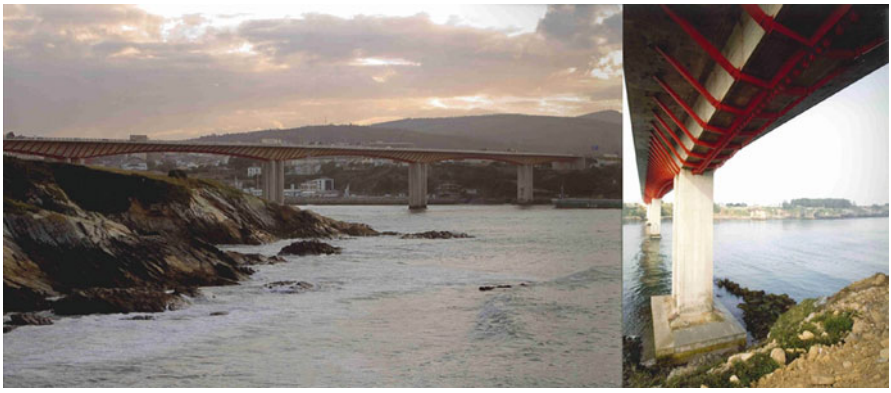

Fig. 2.19 General and bottom view of the completed structure

was to create a huge urban park, 6 km long and with an area of 1,200,000 m², flanking left and right the banks of the river.

The winner proposal was given by Mrio Arquitectos, a joint venture of the architects' teams from Madrid Burgos & Garrido, Porras & La Casta, Rubio & Álvarez-Sala, with the cooperation of the Dutch artist-landscape specialists West8 (MRio 2010).

The leitmotiv of the project's conception was to establish a communication gate between downtown Madrid and its south-west surrounding neighbourhoods. Prior to the intervention, the complex set of rings and other infrastructures made impos-

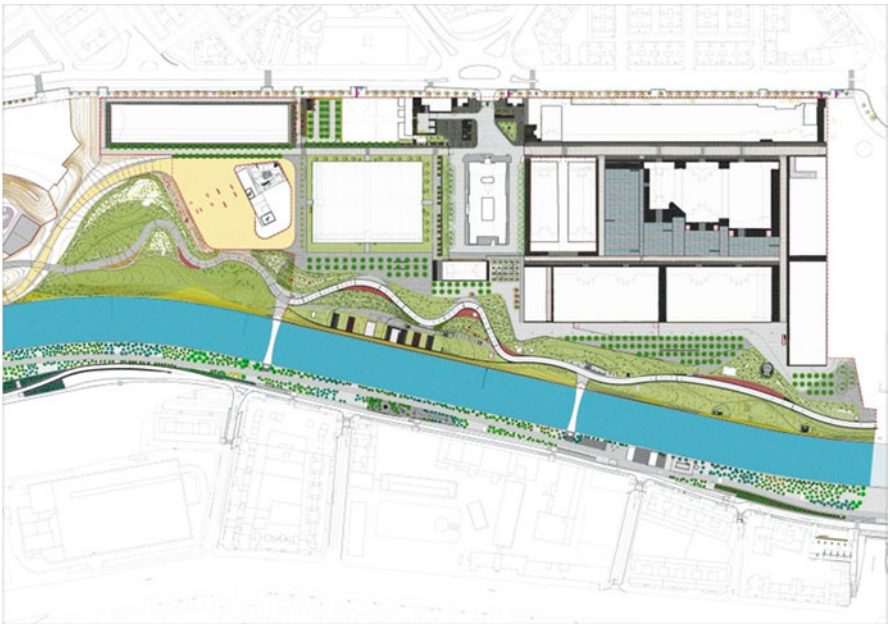

Fig. 2.20 Location of Matadero and Invernadero pedestrian bridges

sible a fluid connection between the city and the natural environment surrounding it. The developed idea converts the river into the desired link with nature, by creating a green corridor and several viaducts and pedestrian bridges that connect transversally the banks in a more efficient and sustainable way.

The proposal builds up three landscape units: first, the corridor along the right bank of Manzanares; second, the new monumental scenario connecting in a definitive way the historic centre and the biggest park of the city (Casa de Campo); and third, the New Arganzuela Park, including the Matadero Contemporary Creativity Center.

The twin Matadero and Invernadero pedestrian bridges become, due to their size and plastic configuration, true opening gates to the Arganzuela Park and the Matadero Contemporary Creativity Center. They solve the transverse communication between both sides of the river and, simultaneously, constitute vaulted spaces floating over the river, giving support to covered paths, being at times pavilions incorporated to the park. An additional unique aspect is that these works required the intimate and fruitful cooperation of several persons: architects, engineers, artists and builders, unlike the recent past, when these profiles were concentrated in a single person: the master.

Figures 2.21–2.24 show some data defining the rather complex geometry of the shell.

Externally, the vaults are the most outstanding elements from which a composite deck hangs by means of a fine curtain of ties. The inner spaces are dominated by two great mosaics by the artist Daniel Canogar. Such mosaics deepen and highlight a basic idea: the pedestrian must associate the fact of crossing the river underneath the vaults to a unique experience. Two photographic images, different to each other in

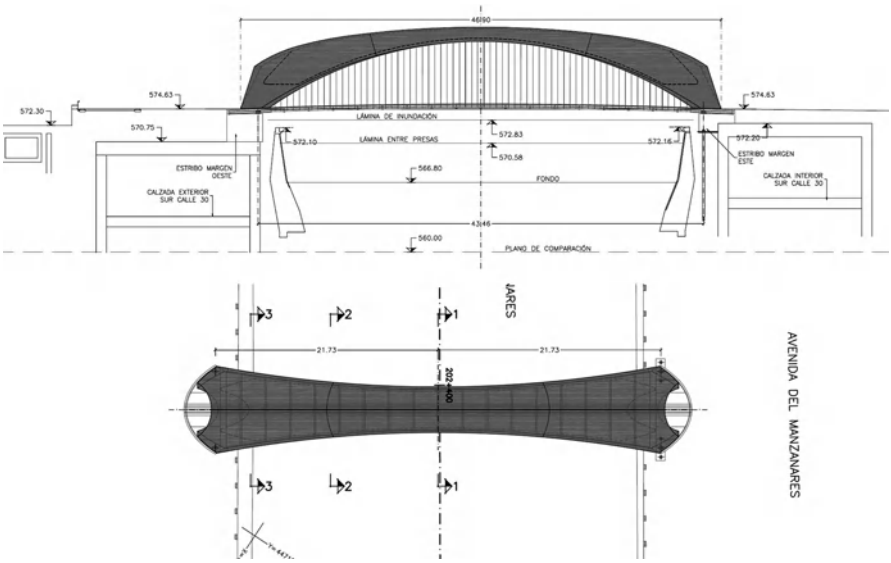

Fig. 2.21 Elevation and plan view of the adopted solution

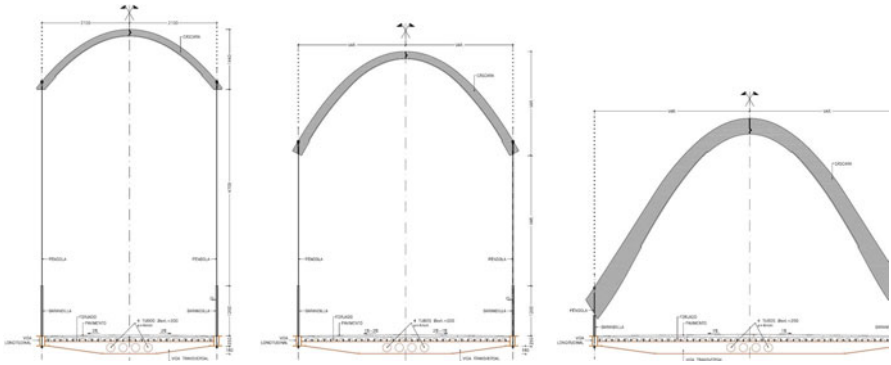

Fig. 2.22 Transverse cross sections

both structures, are embedded at the interior face, as a tattoo, showing contemporary figures: children, young and older people, real citizens living in the neighbourhoods that were separated for decades by the expressway. The mosaic is made up with tesserae, tiles 7×7 mm and 4 mm thick, grouped into plates 300×300 mm that were placed at the concrete vault's interior face. 6,615,000 tiles were used.

As stated above, the structural solution is a concrete shell (Corres et al. 2010, 2011a, b; AAVV 2011). The deck hangs from its contour by means of two families of fine, closely spaced, ties.

The project conceived a multiple purpose for the vaulted shell. On one hand, it provides support to a work of art. On the other, it serves as an entrance gate to a site. Additionally, its morphology has a structural meaning. Last but not least, the vault

Fig. 2.23 Virtual images of the pedestrian bridge

had to be erectable at a reasonable cost. Not all these conditions, that had to be fulfilled anyway, had the same weight: a typical situation in debates like this. Aesthetics was the conditioning argument.

During the project, the possibility of precasting the pedestrian bridge was considered. This solution seemed to be interesting since two pedestrian bridges had to be erected. Thus, the vault would be split in six parts, by a section through the longitudinal axis and two along transverse sections. Due to the symmetry, only three different formworks would be needed to produce all the elements. Moulds would have been of great geometrical complexity and required a sophisticated definition system. With this purpose, different materials, composites among them, were considered for the formwork. This solution considered only moulds for the exterior face, implying a casting of the concrete with variable depth. Once hardened, pieces would be turned over to place them in their final position. The layout of the reinforcement was of great difficulty, since the variable geometry in the three directions required a careful study of the distribution of re-bars. Furthermore, the finishing of the surfaces was also a matter of controversy. It is common practice in the world of architecture to afford several finishing tests. Here, during the design phase, distinct solutions were analysed in order to ensure compatibility with the precast solution.

Unfortunately, once the moment of prefabrication arrived, the suppliers that had taken part in the study of precasting possibilities lost interest, claiming fabrication, transport, and assembly difficulties. The shells were, then, cast in situ.

The structural solution consists of a reinforced concrete arch-vault with a suspended composite deck spanning 43.50 m (total length of 49.10 m) and 7.7 m rise (Fig. 2.25). The deck is suspended by means of two families of 8.1 mm diameter ties arranged every 0.60 m at both sides.

The vault is of variable dimensions. Thickness increases from the crown to the abutments, but decreases from the axial longitudinal plane to the lateral edges. The minimum thickness, at the crown axis, is 0.15 m and the maximum 0.57 m at

Fig. 2.24 Views of a completed pedestrian bridge

the connection of the vault with the deck. Concrete quality is f_{ck} = 40 MPa and reinforcement is a mesh ∅12 mm at100 mm centres.

The composite deck is made up of two 0.25 m deep longitudinal girders and transverse steel beams every 2.4 m (Fig. 2.26). The concrete topping is 100 mm thick. Therefore, the slenderness ratio is 1/124. The width of the deck is variable, coinciding in plan with the vertical projection of the edges of the vault, ranging from 4.5 m at mid-span to 8.4 m at the abutments.

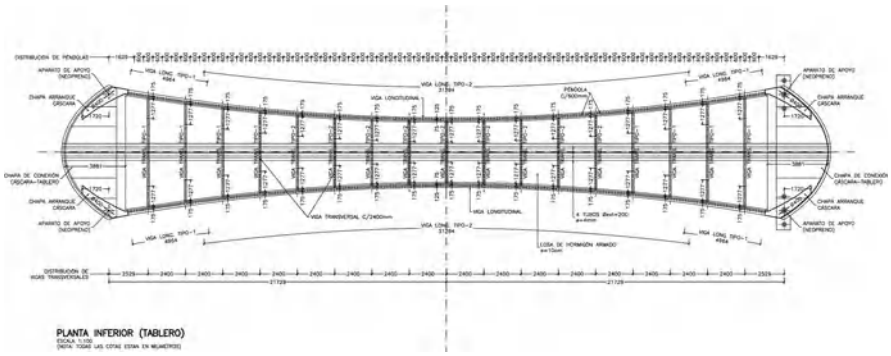

Fig. 2.25 Definition of the steel grillage of the deck

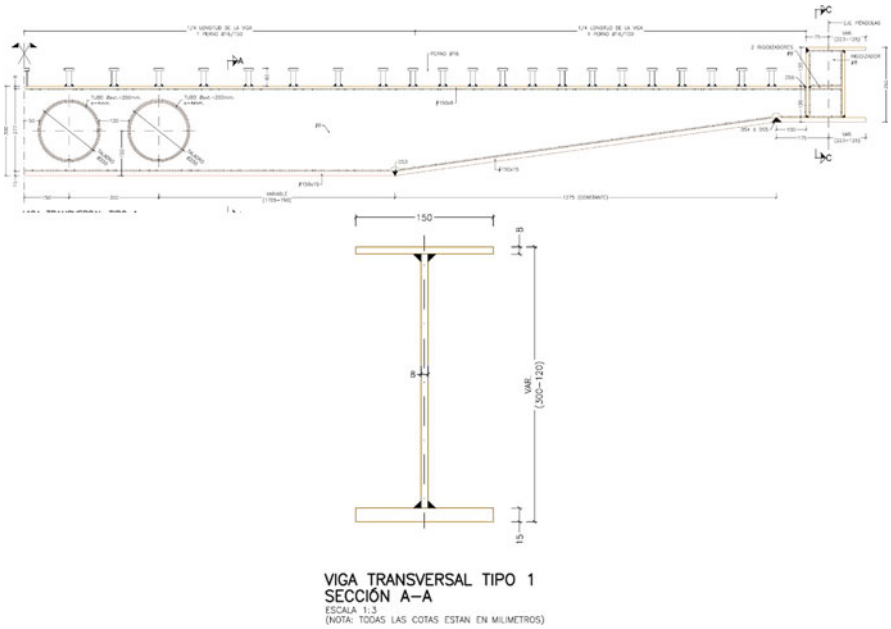

Fig. 2.26 Transverse sections of the deck

The solution given to the foundations is different at the right bank (west) and at the left bank (east). West abutments are supported by foundation beams that distribute loading on the existing retaining walls belonging to the new tunnel for the depressed expressway. The rest of the abutment is cellular, of reinforced lightweight concrete, in order not to exceed the pressure limit of 30 kN/m² on the top slab of the tunnel. The east abutments are not subject to geometrical restrictions; they transmit the vertical loads through six micro-piles, 225 mm in diameter (Fig. 2.27). The top of the micro-piles is fixed to a pile-cap connected to the top slab of the tunnel to transmit the horizontal thrusts.

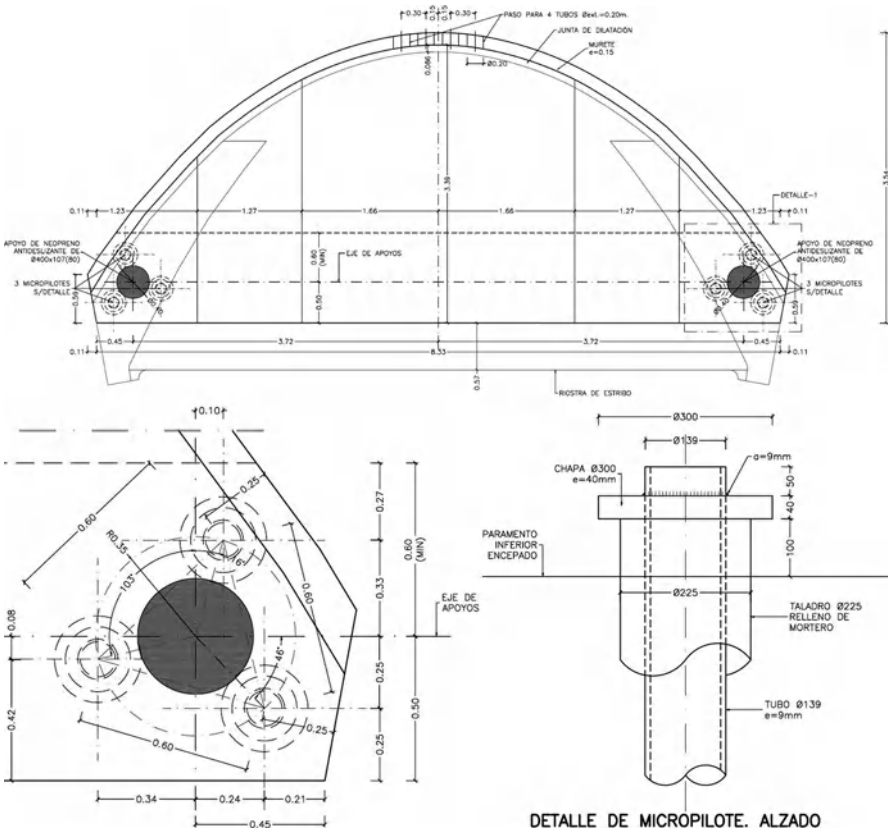

Fig. 2.27 Foundation of abutments with micro-piles (Plans and detail of micro-pile top)

The structural behaviour of the pedestrian bridges is clearly spatial. Shells are conceived to work essentially under compression but, in this case, the way the loads are applied to them mobilises other structural patterns. The deck transmits the loads, through the suspension ties, directly to the edges of the shell which, by transverse bending, leads them to the overall longitudinal arch system. Nevertheless, the transverse shears in the shells are moderate (Fig. 2.28).

The erection of the composite deck required the arrangement of temporary props supported on foundations distributed on a knee of the river bank.

The main problems that arose during the construction had to do with that of the shells. Once the idea of prefabrication was abandoned and the decision of casting in-situ was made, it was decided to use self-compacting concrete. The vaults were cast on a wooden double-sided formwork, on scaffolding that rested on the already erected deck, still supported by the propping arranged on the river knee (Fig. 2.29).

The uniqueness of the shell's shape conditioned fabrication and assembly of the formwork (Fig. 2.30), of the reinforcement cages and of casting the concrete as

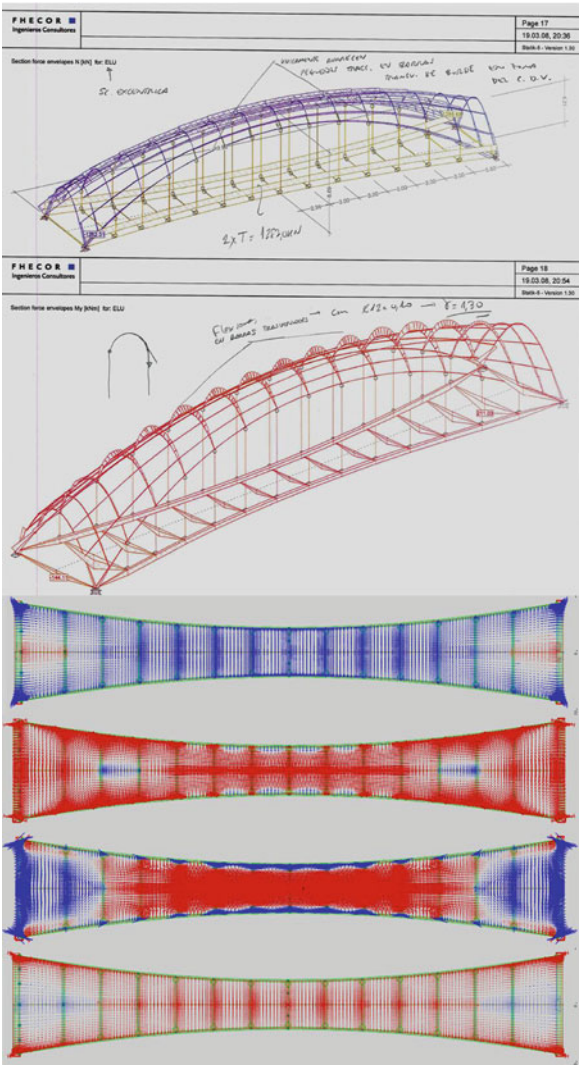

Fig. 2.28 Structural behaviour of the shell

well, since the shell depth was very strict (150 mm). Most of the work was, therefore, done manually.

The large amount of suspension ties, distributed every 600 mm, complicated immensely the stressing operation, due to the high static redundancy of the system. Initially, prestressing forces were applied in groups of ties, in order to ensure a level of stress at the end of the process in the range of 80–100 N/mm². The final introduction of loading was completed after a programmed decentring of the deck.

Fig. 2.29 Structure during construction

2.5 Final Remarks

Progress in technological capabilities now constitutes the best basis for innovation in structural engineering. The use of classical ideas, updated according to the new possibilities offered by the latest technology, is a source of new resources for structural engineering.

Often, new technologies emerge in fields quite far away from structural engineering, in complementary and sometimes marginal applications. The use of these techniques does not exploit their possibilities in an optimal way, since engineers still apply them to traditional shapes and ideas, omitting the hidden possibilities they bring. This is, in fact, the big challenge: seeking for optimal available opportunities.

Rather commonly, new technologies normally involve knowledge that, in principle, is not available to structural engineers, who should continuously bear in mind that an adequate use of a tool requires a deep study of its basis and field of application. In addition, structural engineers must be aware that it is their responsibility to go deep in this study, as it is not enough to delegate this task to others.

Fig. 2.30 Some details of the formwork

References

AAVV (2011) Las Pasarelas Cáscara. MadridRío. Un proyecto de transformación urbana. ISBN: 978-84-7506-978-4

Bertagnoli G, Mancini G, Tondolo F (2010) Comportamento termo-meccanico della platea della Torre Intesa S. Paolo: analisi delle fasi di getto per il controllo della fessurazione, Torino

Corres H, Gómez M (2010) El hormigón en edificios de gran altura: realizaciones en Madrid, Revista Zuncho 26

Corres H, Romo J, Romero E (2008a) High rise buildings. The challenge of a new field of possibilities for the use of structural concrete. fib Symposium, Amsterdam

Corres H, Pérez A, Romo J, León J, Prieto F, Sánchez J, Sisí D, Espeche A, García-Arango I (2008b) The widening of Los Santos Bridge. A case study of a Taylor-made structure. fib Symposium, Amsterdam

Corres H, García JD, Calvo I, Grávalos J, Chozas V, Lample R, Viñola A (2010) Aplicación de Tecnologías Avanzadas del Hormigón en las pasarelas en Cáscara sobre el río Manzanares para el proyecto Madrid Río. Revista Obras Públicas 3.515

Corres H, Romo J, Sánchez J, Sanz C (2011a) Matadero and Invernadero Shell pedestrian bridges built over the Manzanares River in Madrid. Civil Eng Mag Am Soc Civil Eng (ASCE) 81(6)

Corres H, Romo J, Sánchez J, Sanz C (2011b) Pasarelas Cáscara del Matadero y del Invernadero sobre el río Manzanares. Revista Obras Públicas 3.520

Heinle E, Schlaich J (1996) Kuppeln aller Zeiten, aller Kulturen. Deutsche Verlags-Anstalt, Stuttgart. ISBN 3-421-03062-6

MRio Arquitectos (2010) Jugar en el Bosque. Diseño de la Ciudad

Chapter 3
New Types of High Performance Concretes – Potentials for Innovations in Concrete Construction

Harald S. Müller and Michael Haist

Abstract Among the new types of high performance concretes this paper deals with self-compacting concrete (SCC) and ultra high strength concrete (UHPC). Both types of self-compacting concrete, the powder type SCC and the stabilizer type SCC, are presented. Differences in the mix design and composition as well as the properties in the fresh and in the hardened state are indicated. While most of the properties of SCC are roughly similar to normal concrete (NC) – apart from the self-compacting property – this holds by far not true for UHPC. Not only the mechanical properties but also the durability of UHPC deviates significantly from normal concrete. In addition, it is shown that UHPC is more sustainable than normal concrete if the ecological impact is considered in relation to the performance of the concrete.

3.1 Introduction

In the last two decades considerable progress in concrete technology has taken place. New types of concrete, such as self-compacting concrete (SCC) and high strength concrete (HSC), are produced and applied in practice on a routine basis. Today even ultra high strength concrete (UHPC), reaching compressive strength values above 200 MPa, may be produced and applied for precast concrete elements. Further, promising trends towards the development of ultra ductile concrete, ecological concrete (green concrete) and textile concrete are under way. Besides, also the strengthening of concrete by the use of carbon nanotubes reveals a remarkable potential for the improvement of concrete performance.

H.S. Müller (✉) • M. Haist
Department of Building Materials, Institute of Concrete Structures and Building Materials, Karlsruhe Institute of Technology (KIT), Kaiserstrasse 12, D-76131 Karlsruhe, Germany
e-mail: sekretariat-bt@imb.kit.edu; michael.haist@kit.edu

M.N. Fardis (ed.), *Innovative Materials and Techniques in Concrete Construction: ACES Workshop*, DOI 10.1007/978-94-007-1997-2_3,

It is not possible to treat the above mentioned special concretes in detail here. Hence, this paper concentrates on self-compacting concrete and ultra high strength concrete. These two types of concrete may be roughly characterized as follows:

- *self-compacting concrete (SCC)*: a type of structural concrete which strongly deviates from normal concrete (NC) in the fresh state, as it de-aerates and flows without the application of additional compaction energy;
- *ultra high strength concrete (UHPC)*: a type of structural concrete with a compressive strength above 120 MPa and a very high durability, achieved by an optimized packing density of all granular raw materials.

As the very high strength of UHPC is always associated with a very high durability, i.e. excellent performance characteristics, this type of concrete is usually termed as ultra high performance concrete.

Mix design, composition and properties in the fresh and the hardened state of these special concretes deviate considerably from those of conventional structural concrete, as will be shown in the subsequent sections. Moreover, the related governing parameters and effects are dealt with in the following.

3.2 Self-Compacting Concrete

3.2.1 General

Self-compacting concrete (SCC) is a concrete that de-aerates and flows without the application of compaction energy, while staying homogenous during the whole placing process until hardening. To understand the underlying mechanisms, one has to focus on the rheological behaviour of concrete at the fresh state. Hereby it has to be kept in mind that concrete, i.e. the cement paste as the governing component, is a non-Newtonian material where the viscosity depends strongly on the shear rate. This is indicated in Fig. 3.1 where the viscosity of normal concrete and of self-compacting concrete is shown as a function of the shear rate.

For very low shear rates, or when it is at rest, concrete shows a very high dynamic viscosity, which continuously reduces with increasing shear rate and approaches a final value, the so-called plastic viscosity (Fig. 3.1). In order to compact a concrete after placing, it is subjected to high shear rates using a vibrator-poker. This reduces the viscosity of the concrete and minimizes the viscous flow resistance, allowing air bubbles to escape. At rest, however, the viscosity instantly regains its previous high value, preventing segregation effects (Haist 2009).

In order to facilitate the concrete to de-aerate properly without any additional compaction work during the placing process, i.e. by flowing in the formwork at moderate shear rates, the dynamic viscosity of the mixture at these shear rates must be low enough to enable the entrapped air bubbles to rise to the concrete surface. Today, two procedures are available to achieve this, i.e. to produce self-compacting concrete, as described subsequently.

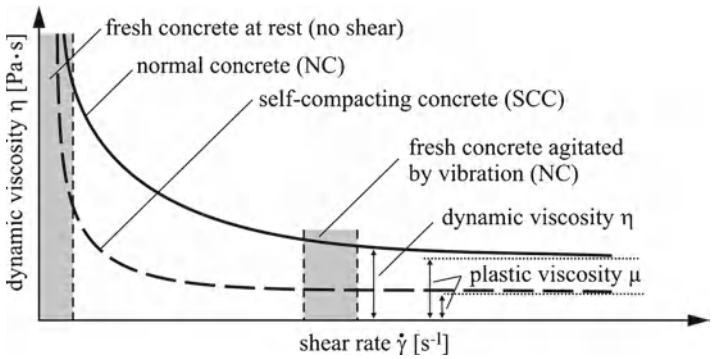

Fig. 3.1 Rheological behaviour of fresh normal (conventional) concrete and self-compacting concrete as a function of the shear rate during placing

The so-called *powder type self-compacting concretes* are characterized by an approximately 30% higher paste content compared to conventional concrete. This ensures a high fluidity of the mix. The paste itself consists of cement, large amounts of mineral additives such as fly ash or limestone powder, water and chemical admixtures (above all superplasticizers). In order to prevent segregation, the water/cement ratio and the water/binder ratio are kept very low, leading to high strength values at the hardened state. Due to the high paste content, powder type SCC generally exhibits a reduced modulus of elasticity in comparison to conventional concretes of equal strength.

In contrast to powder type SCC, *stabilizer type self-compacting concretes* have lower paste content (approximately 10% higher than conventional concrete) but a significantly higher water/binder ratio. By adding superplasticizer, the viscosity of the mixes, especially at low shear rates, is markedly reduced, hence allowing the entrapped air to leave the concrete. At rest, however, strong segregation would occur unless this is prevented by adding stabilizing admixtures, so-called viscosity modifying agents (VMA). At the hardened state stabilizer type SCC has only insignificant differences from conventional concrete of equal strength. The increased water/binder ratio allows for the production of low and normal strength concretes with self-compacting properties.

3.2.2 Mix Design

The mix design process of SCC is still exclusively focused on ensuring self-compacting properties while neglecting other important mix design criteria, such as the compressive strength or the durability. Usually this disadvantage is accepted, as the most commonly used powder type SCC normally results in compressive strength values above 60 MPa at very low water/binder-ratios, ensuring a high durability. However, it should be considered that exceeding the strength class projected by the designer might be associated with significant changes in the concrete's modulus of elasticity and its long-time deformation behaviour, i.e. creep and shrinkage.

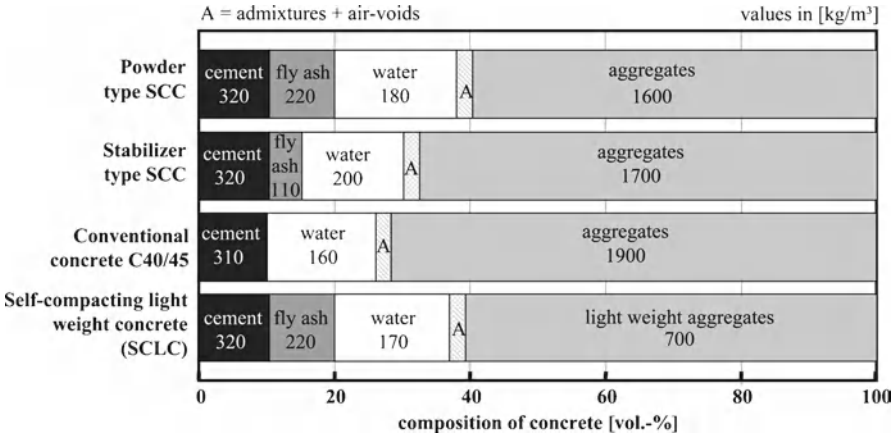

Fig. 3.2 Composition of a powder type SCC, a stabilizer type SCC and a conventional vibrated concrete C40/45, as well as of a self-compacting light weight concrete (*SCLC*)

3.2.2.1 Powder Type SCC

As has already been pointed out, by increasing the powder and thus the paste content in the concrete, its workability can be significantly improved. However, this measure alone is not sufficient to achieve the desired self-compactability. In order for the paste to flow properly and to be able to transport coarse aggregate grains, it must have a sufficient viscosity at high shear rates. On the other hand, at low shear rates the viscosity should not be too high, in order to enable sufficient de-aering and to flow in common placing conditions. This behaviour is usually ensured by using modern superplasticizers, which allow for a targeted adjustment of the paste's viscosity at low shear rates, without significantly influencing the flow behaviour at high shear rates. Prerequisite for such a systematic adjustment of the fresh paste properties is that the water/binder ratio of the paste is kept at a minimum value, the so-called water demand level. In order to prevent segregation of the concrete – i.e. sedimentation of the coarse aggregates in the fresh concrete – the grading curve of the aggregates should be adjusted to have a high fines or sand content. The sand grains hinder the coarser aggregates from sinking and thus prevent sedimentation.

Based on these principles, Okamura and Ozawa (1995) developed a mix design procedure for powder type SCC. Further details on this subject may also be found in (Müller and Haist 2010). A typical composition of a powder type SCC is shown in Fig. 3.2.

3.2.2.2 Stabilizer Type SCC

Today, no standardized mix design procedure for stabilizer type SCC exists. This is due to the fact that the stabilizers and superplasticizers available on the market have

a highly diverse working regime, which makes it very difficult to follow standardized approaches.

Stabilizer type SCC normally has a paste content of approximately 32–36% by volume, to be contrasted with 27–32% in conventional concrete. In contrast to powder type SCC, the paste usually contains a much higher water content. This leads to a pronounced reduction of the viscosity of the mix at the fresh state over the full range of shear rates (cf. Fig. 3.1). In order to prevent segregation at rest and to avoid blockage of coarse aggregates in confined reinforcement layouts, stabilizing admixtures are added. These stabilizers significantly influence the viscosity of the concrete at low and medium shear rates.

Similar to the powder type SCC, the grain size distribution of stabilizer type SCC is characterized by a comparatively high sand content, which helps to prevent segregation phenomena. A typical composition of a stabilizer type SCC is also shown in Fig. 3.2.

3.2.3 Composition and Fresh Concrete Properties

As can be seen in Fig. 3.2, mixes based on the powder type formulation are characterized by volumetric powder contents approximately twice as high as those of a conventional structural concrete. When using fly ash as a filler, it should be noted, many national codes allow regarding only parts of this amount as cement replacement (e.g. maximum of 33% by mass in Germany) and hence taking it into account in the equivalent water/cement ratio (e.g., a k-value of 0.4 applying in Germany). The rest of the fly ash is normally considered as pure filler, even though it reacts in the same manner as the fly ash considered as a cement replacement. This explains why powder type self-compacting concretes containing fly ash usually show very high strengths and have hardened concrete properties corresponding to a high strength concrete rather than to a conventional concrete.

When using limestone or other inert mineral powders, it should be noted that for the contents considered here, these fillers do not contribute actively to the hydration process. The increased paste content of the concrete might therefore have adverse effects on the hardened state properties and especially on the durability of the concrete. With respect to the use of limestone powders, it is recommended to use powders with low total organic contents (TOC) and high fineness, i.e. powders of LL-quality according to European standard EN 197-1:2004.

The maximum aggregate size for the production of self-compacting concrete should be limited to approximately 16–20 mm. In order to prevent segregation at rest and blocking behaviour during flow, the grading curve of the aggregates should be characterized by a high content in fines. It is possible to produce self-compacting concrete with rounded or crushed aggregates. In the latter case, normally higher paste contents might be required in order to get equivalent flow properties. When using aggregates sensitive to alkali silica reaction, it should be borne in mind that the high paste content of SCC, as well as the high superplasticizer content – which may provide large amounts of alkalis – form unfavourable conditions for such a concrete.

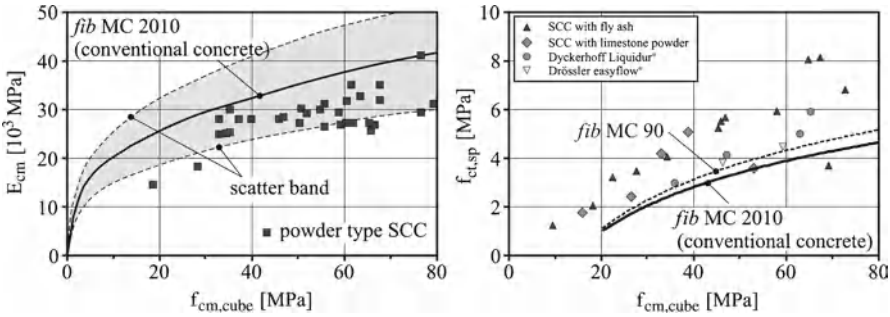

Fig. 3.3 Modulus of elasticity E_{cm} (*left*) and splitting tensile strength $f_{ct,sp}$ (*right*) as a function of the mean concrete compressive (*cube*) strength $f_{cm,cube}$ for various self-compacting concretes; experimental data and *fib* MC 2010 predictions

Testing of the fresh concrete properties of SCC is, among others, covered by the European standard EN 206-9:2008. In contrast to conventional concrete, the complex fresh concrete behaviour of SCC required the introduction of several new test methods, such as the slump flow test (see European standards EN 12350-8:2009 and EN 12350-12:2008 with or without J-Ring), the V-funnel test (see European standard EN 12350-9:2008-01) or the sedimentation test (see EN 12350-11:2008).

The primary goals of the test procedures are to guarantee that the concrete de-aerates properly, stays homogenous during flow and rest until hardening and has suitable flow behaviour in order to fill a given formwork. The last requirement mentioned clarifies that the required flow behaviour is a function of the formwork geometry. On this background the flow properties must vary, depending, e.g., on whether a long wall element with extensive flow passages is cast or whether a slender column is filled with SCC.

3.2.4 Properties at the Hardened State

The differences in the composition of self-compacting concrete in comparison to conventional (vibrated) concrete may lead to deviations in the hardened state behaviour. Especially for powder type SCC, the increased paste content normally results in a reduced modulus of elasticity E_{cm}. From experimental results, this deviation can be estimated to be between 10% and 20% below the prediction of e.g. *fib* MC 2010 for a conventionally compacted concrete of equal compressive strength. However, as can be seen from Fig. 3.3 (left), this deviation is still within the scatter band known from conventional concretes. When using pozzolanic additives, like fly ash, the reduced modulus of elasticity at the age of 28 days is outweighed to some extent by an increased gain in stiffness due to the pozzolanic reaction of the fly ash at higher concrete age. The designer should, however, keep in mind that for structures sensitive to the deformation behaviour of the concrete, additional testing of the self-compacting concrete to be used is highly recommended.

Regarding the tensile strength, the increased binder content of SCC may lead to higher values, depending on the type of filler used (see Fig. 3.3, right). Note in this context that *fib* MC 2010 predicts a slightly lower splitting tensile strength $f_{ct,sp}$ for concretes of equal mean compressive strength f_{cm} than the CEB/FIP MC 90. This is due to the fact that, in *fib* MC 2010 the conversion factor to calculate the tensile strength from the splitting tensile strength was changed from 0.9 to 1.0. For structures sensitive to cracking, further attention should be paid to the development of the tensile strength beyond the design age of 28 days. Especially when using large amounts of pozzolanic additives, like fly ash or silica fume, a pronounced growth of the tensile strength at higher concrete ages might be observed.

Similarly to the modulus of elasticity, the creep and shrinkage behaviour of powder type SCC is also affected by the high paste content of such concretes. The limited data regarding the shrinkage behaviour of powder type SCC suggest that the ultimate shrinkage deformation can be expected to be approximately 20% higher than for a conventional concrete of equal strength. The same tendency holds true for the creep behaviour of such concretes. Powder type SCC in general exhibits an increase of approximately 10–20% in creep deformations.

Both creep and shrinkage deformations of SCC are well within the scatter band e.g. of *fib* MC 2010 predictions, which is defined to be ±30%. It should be noted, however, that for structures which are sensitive to variations in the modulus of elasticity as well as the creep and shrinkage behaviour, the deviations mentioned above for SCC occur systematically. In case of doubt it is therefore highly recommended to measure the actual short- and long-time deformation behaviour.

The bond behaviour of SCC, being comparable to NC, is less dependent on the position of the reinforcing bar, i.e. whether the bar is embedded at the top or the bottom of a formwork.

The durability of SCC is characterized by an identical or improved behaviour than conventional concrete of equal strength regarding the carbonation and chloride diffusion behaviour. The freeze-thaw resistance of powder type SCC strongly depends on the type of filler used. For SCC containing fly-ash, an equivalent or even higher freeze-thaw resistance has been observed. However, concretes containing limestone powder have shown increased weathering in the freeze-thaw test. Further, it should be taken into account that SCC has higher paste content, which in general has an adverse effect on the freeze-thaw behaviour.

3.3 Ultra High Strength Concrete

3.3.1 Introduction

Ultra high strength concrete is usually defined as a concrete having a characteristic compressive strength above the strength grade C100/115. One may distinguish between two types:

- the reactive powder concrete (RPC), characterised by a maximum aggregate size of approximately 0.5 mm and
- the ultra high performance concrete (UHPC), with coarse aggregates normally up to an aggregate size of 8 mm.

The water/cement ratios of such concretes are usually below 0.25 and highly reactive additions, such as silica fume, have to be added to the mix. The workability of the concrete can only be ensured by applying large amounts of superplasticizer. Thus a compressive strength of approximately 200 MPa may be achieved. Depending on the type of curing, e.g. with additional heat treatment without or with mechanical pressure, this concrete may reach a compressive strength of up to 800 MPa, provided a proper selection of the aggregates is carried out.

No standard has been adopted yet for this type of concrete, which significantly exceeds the strength range specified in EN 206-1:2001. Nevertheless UHPC might become interesting for a broader application in practice. The reason is that the very high strength allows a significant reduction of the cross-section of members, while retaining a high load bearing capacity. This is accompanied by a significant mass reduction, allowing in principle much longer spans compared to those realized when ordinary structural concrete is used. Mass reduction also decreases the loads on the foundation, as well as inertia and seismic forces in earthquake-resistant construction. In addition, savings in materials affect positively sustainability and make UHPC superior to ordinary structural concrete, despite the significantly higher cement content of UHPC, see below and e.g. (Müller and Scheydt 2009).

Considering the practical application of UHPC, major problems result from the fact that this concrete shows a significant autogenous shrinkage during the early hardening process. As a consequence, construction with UHPC in practice is realised mostly by precasting. However, research is under way to overcome this deficiency, e.g. through addition of super-absorbent polymers.

3.3.2 Mix Design

UHPC is composed of aggregates, cement, water, additives and admixtures. Aggregates that may be used include the materials referred to as “aggregates for concrete” in EN 12620:2008. The particle strength should be sufficiently high and the grain size distribution should guarantee a high packing density.

Regarding the cement type used in UHPC, Portland cements with a low C_3A content are recommendable, as these cements have a low water demand. This is also advantageous in view of the risk of a secondary ettringite formation in case of curing at high temperatures. The strength classes of the cements applied is 42.5 or 52.5. Blast furnace slag cement of strength class 52.5 has also been successfully used. The cement contents in UHPC are normally very high and range from 600 to 1,000 kg/m^3. The fineness of the cement should be between 3,000 and 4,500 cm^2/g.

In order to produce UHPC, it is important to achieve the maximum possible packing density of all granular constituents. The voids between the cement particles

(diameter from 1 to 20 μm) are filled by silica fume (SF) particles (0.1–0.3 μm). For this purpose, the required silica fume quantity is between 10 and 30% of the cement by mass.

The second major effect expected from the addition of silica fume, beyond the increase in packing density, is a reduction of the amount of calcium hydroxide in the interfacial transition zone between the aggregate grains and the cement paste matrix. The almost pure SiO_2 of silica fume consumes $Ca(OH)_2$, which is created during the hydration of cement clinker, and forms calcium silicate hydrates (CSH). This means that the $Ca(OH)_2$, which has lower strength, is replaced by CSH of much higher strength. The porosity decreases in the bulk and in particular in the interfacial zone. All these effects result in a significant increase in strength.

Quartz powder with particle sizes similar to cement is predominantly used in heat-treated UHPC. The quartz particles are inert at room temperature but, together with $Ca(OH)_2$, they react at high temperatures to form CSH phases.

Fresh UHPC is not workable without the addition of large quantities of high performance plasticizers (up to 5% of the cement by mass). Only third generation plasticizers (polycarboxylate ethers, PCE) allow saving a sufficient amount of water while making UHPC workable. Their mechanism of action relies on the adsorption of the PCE molecules to the surface of the clinker phases and of hydration products, which results in a steric repulsion. This leads to a dispersion of the cement particles, which creates in turn the plasticizing effect.

Like dense natural stone, UHPC shows an elastic and brittle behaviour. Fibres are added to the concrete to compensate for this disadvantage in construction practice. It has been proven that approximately 2.5% of steel fibres by volume, at an aspect ratio *l*/*d* between 40 and 60, lead to best results, both in view of fresh and hardened concrete properties. The fibre length should be adjusted to the maximum aggregate diameter. For powder type UHPC (i.e. with limited maximum grain size), the fibre length should be at least ten times the maximum aggregate diameter.

The water content of the mix is the crucial parameter to ensure optimal properties. Water/binder ratios from 0.15 to 0.25 seem to ensure a reasonable balance between the flow properties of the fresh concrete and the strength of the hardened concrete.

3.3.3 Properties of the Fresh Concrete

UHPC is characterized by high powder content, in excess of 1,000 kg/m³, in combination with high dosages of superplasticizers. Its properties at the fresh state are thus comparable to self-compacting concrete of the powder type. For this reason, the workability of this type of concrete should rather be measured with the test set-up used for SCC, i.e. slump flow and V-funnel flow test. The slump flow of UHPC normally ranges from 650 to 800 mm and the V-funnel flow time from 15 to 40 s. Superplasticizers strongly reduce the flow resistance of the concrete and lead to a normalization of the dynamic viscosity over the whole range of shear rates (Fig. 3.4).

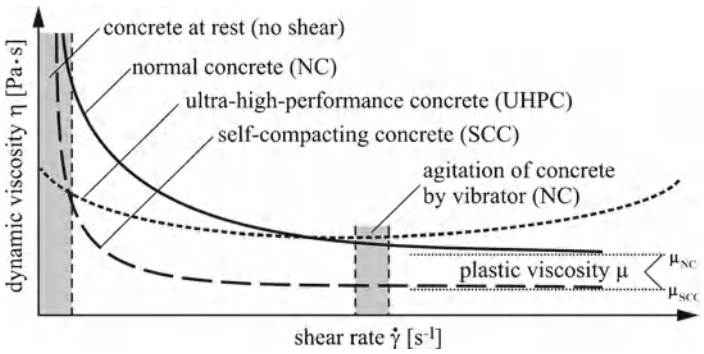

Fig. 3.4 Dynamic viscosity of fresh UHPC, conventional concrete (*NC*) and self-compacting concrete (*SCC*), as a function of the externally applied shear rate

As can be seen from Fig. 3.4, the dynamic viscosity of UHPC remains nearly constant – even though at a very high level – no matter whether the concrete is at rest or it is agitated, for example by a vibrator. For UHPC, the de-airing process therefore cannot be enhanced significantly by vibrating the concrete. At rest, however, for concretes with a very low dynamic viscosity, sedimentation may be observed, which must be prevented in UHPC by optimizing the grain size distribution of the aggregates, thus ensuring an interlocking of the particles. At high shear rates, UHPC normally shows a dilatant material behaviour, i.e. an increase of the dynamic viscosity.

The air content in UHPC ranges from 1% to 5% by volume, with the lower ratios observed in low viscosity mixes. In addition, there is a trend towards an air ratio increase that occurs in line with the increasing length of the steel fibres used.

Plastic (capillary) shrinkage and autogenous deformation are promoted by high cement paste content and a low water/cement ratio. For this reason, the immediate curing of UHPC is basically very important.

3.3.4 Properties of Hardened Concrete

3.3.4.1 Strength Characteristics

The compressive and the tensile strength which may be achieved by UHPC depend strongly on the concrete composition, in particular with regard to the type and amount of binders and the fine aggregates (micro- fillers) as well as the type and duration of curing. If ordinary curing, at room temperature of 20°C, is applied a maximum compressive strength of UHPC of approximately 200 MPa can be achieved. If the curing temperature is increased to 100°C, the strength will reach approximately 250 MPa. A further increase of the curing temperature to 250°C is accompanied by a strength gain to almost 400 MPa. A compressive strength value of approximately 800 MPa may be achieved, if mechanical pressure is applied in addition.

Similarly to ordinary fibre reinforced concrete, the addition of fibres (mostly steel fibres) causes a small improvement of the compressive strength of UHPC, but may significantly affect the strain capacity of the concrete. The investigations on the effect of the volume content of fibres of up to 6% by volume, point to an optimum fibre content of approximately 2.5%.

The uniaxial tensile strength and the flexural tensile strength of UHPC reach values ranging approximately from 10 to 60 MPa. When special binders and techniques are applied, a tensile strength of 150 MPa may be attained. It should be noted that, unlike the compression characteristics, the tensile strength of UHPC may be doubled when fibres (1.5–3.0% by volume) are added to the mix. This may be attributed to a large extent to the reduction of the brittleness of non-reinforced UHPC, where minor flaws and cracks may tremendously reduce the tensile strength.

Concerning the fracture energy and the characteristic length of UHPC, the available knowledge is still very insufficient. It appears that for UHPC made without fibres these values are somewhat lower than for high strength concrete. Of course, the addition of fibres may increase the fracture energy up to a factor of approximately 100.

3.3.4.2 Deformation Behaviour

The stress-strain behaviour of non-reinforced UHPC shows a linearly elastic pattern almost up to the ultimate load level. Most of the commonly used testing equipment and specimen sizes do not allow the determination of a descending branch in the stress-strain diagram. An explosive failure occurs, causing a strong impact on the testing equipment. In a fibre reinforced UHPC, the fibres prevent macro-cracking, because they hold the crack edges together already at the micro-cracking stage and thus hinder the cracking progress. As a result, a significant additional strain capacity is obtained while the increase in strength is minor. Similar to ordinary fibre reinforced concrete, the fibre content determines whether this strain results in strain softening or in strain consolidation.

The modulus of elasticity of UHPC reaches approximately 50–60 GPa when the compressive strength is 200 MPa. If reactive powder concrete (RPC) is produced, having a compressive strength of up to 800 MPa, the modulus of elasticity may approach 75 GPa. As it holds for conventional structural concrete, the modulus of elasticity of UHPC also strongly depends on the paste content and the type of aggregates.

The autogenous shrinkage of UHPC is very pronounced and may reach values beyond 0.0012 (1.2 μm/mm). Often much lower values are reported in the literature. However, this is mostly due to the applied measurement technique, in connection with the age of concrete when the measurement starts. When it starts too late, e.g. at a concrete age of one day, most of the autogenous shrinkage, which develops mainly between an age of 8–24 h, has already taken place and is consequently not recorded. As may be seen from Fig. 3.5 (top), autogenous shrinkage observed after a concrete age of one day reaches strain values of approximately 0.3 μm/mm for an UHPC with a compressive strength of 170 MPa (C170).

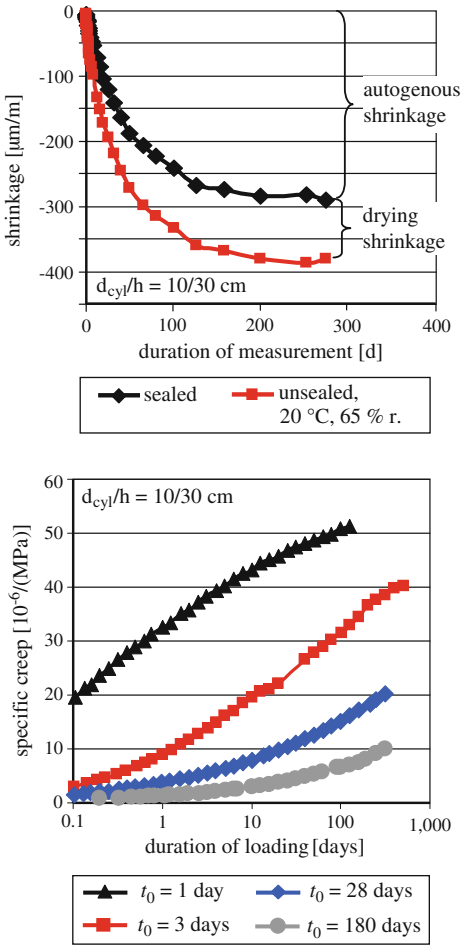

Fig. 3.5 Shrinkage of UHPC under different storage condition (*top*), and creep of UHPC for different ages at loading (*bottom*)

Drying shrinkage of UHPC, obtained from the difference of total shrinkage and autogenous shrinkage, is much lower, even when compared to that in high strength concrete. This may be traced back to the extremely low porosity of UHPC. In studies on autogenous and drying shrinkage of different UHPC starting at the concrete age of 1 day, an autogenous shrinkage of 0.3 µm/mm and a drying shrinkage of 0.1 µm/mm (at a maximum) have been observed (see Fig. 3.5, top). The test results shown in Fig. 3.5 have been obtained on concrete cylinders (with diameter 100 mm and height 300 mm) stored at an ambient temperature of 20 °C, where the specimens were either sealed (water loss prevented) or remained unsealed in an ambient environment of 65% relative humidity.

Figure 3.5 (bottom) exemplarily shows the influence of different concrete ages at loading on the specific creep (creep per unit stress) of an UHPC (C170). The stress level was 30% of strength and the specimens were stored unsealed in a climate of 20°C and 65% relative humidity. As already observed in experiments on normal

strength and high-strength concretes, the magnitude of creep is significantly decreasing with increasing concrete age. However, this effect is much more pronounced for UHPC than for high strength concrete or normal strength concrete. If creep coefficients are calculated from the results shown, for an age at loading of $t_0 = 1$ day or $t_0 = 3$ days, final creep coefficients between approximately $\varphi = 3$ and $\varphi = 2$, respectively, are obtained. Even for an age at loading of $t_0 = 28$ days the final creep coefficient reaches approximately $\varphi = 1.5$. This means that the pronounced decrease of the creep capacity of concrete with the increase in strength of the hardened cement paste is no longer true for UHPC.

The application of high sustained loads showed no significant difference in the sustained load strength of UHPC compared to normal strength concrete.

3.3.4.3 Physical Characteristics

The physical characteristics of concrete are mainly determined by its capillary porosity. Whereas conventional concrete (C35) and high strength concrete (C100) show marked peaks in the pore size distribution between 0.01 and 0.1 μm, these peaks are nearly eliminated in the case of UHPC (C200) and disappear completely in RPC (C500). Absolute porosities then become so low, that transport processes almost come to a halt.

As a consequence carbonation depths measured on UHPC are almost negligible. Chloride penetration was investigated in migration tests where a diffusion coefficient of $0.02 \cdot 10^{12}$ m²/s was measured, which is about 100 times lower than the value for a C30 concrete.

The nitrogen permeability of UHPC decreases to a level that is ten times lower than in a high performance C100 concrete and 100 times lower than in a C30 concrete. The water permeability of a C190 UHPC was found to be in a range between 4 and $5 \cdot 10^{-15}$ m²/s, which corresponds to the permeability of dense natural stone. The same behaviour was found for capillary water absorption.

3.3.4.4 Durability

Structural concrete usually containing capillary pores is often destroyed by mechanisms triggered by frost or by freeze-thaw cycles. If no capillary pores are present, or if only a minimal amount of such pores exist, only a small quantity of water can be absorbed and no saturation will occur. Correspondingly, the concrete shows a very good behaviour when exposed to frost or freeze-thaw cycles.

Tests in sodium sulphate solution have demonstrated a very high chemical resistance. No conclusive findings have been established yet with regard to alkali silica reaction. However, the tightness of the material appears to be one of the crucial factors that determine resistance.

Even though UHPC is exposed to a strong acid attack (pH = 1 and 3) it shows a significantly better performance than ordinary structural concrete. Of course, also

UHPC will be destroyed by a long-term attack of strong acids, as the CSH component of the hydrated cement paste is principally dissolved by acids as a consequence of its chemical nature. However, due to the extreme low porosity of UHPC compared to ordinary structural concrete and even high strength concrete, the rate of damage is much slower, leading to a significant higher durability or life time, respectively (Müller and Scheydt 2009).

Initially UHPC had not been fire-resistant: the tested concrete bursted and the fibres in the fibre reinforced concrete oxidised under heat exposure. Fire resistant UHPC could be successfully produced by adding 0.3–0.6% of polypropylene fibres by volume. It is also helpful to replace quartz with basalt aggregate, which prevents occurrence of the deleterious quartz conversion.

3.3.4.5 Sustainability

Compared to normal strength concrete, ultra high performance concrete is up to three times more expensive, owing to the high binder and fibre content. But beyond cost efficiency, also the mechanical and durability properties of the concretes, as well as their sustainability, should be compared.

For the evaluation of the environmental impact and thus the sustainability, various impact categories are considered, see e.g. (Stengel and Schießl 2008). When entering the values of the material's impact categories in a radar chart, a closed polygon can be drawn. The closer the polygon lines approach the point of origin, the more favourable is the environmental impact of the considered material.

In a direct comparison, i.e. when a volume-based analysis is made, the UHPC (C190) has a significantly more adverse impact than the normal strength concrete NPC (C30), see Fig. 3.6. This is caused in particular by its higher cement, steel fibre and superplasticizer content, compared to NPC. When, by contrast, these environmental impact parameters are related to durability values, e.g. to the permeability, the UHPC demonstrates a clear superiority (Fig. 3.7). Analogous diagrams result if the impact categories are related to other performance parameters, such as the resistance against chemical attack, or also to the concrete strength.

3.4 Summary and Outlook

This paper deals with self-compacting concrete (SCC) and ultra high strength concrete (UHPC). Mix design, composition and properties in the fresh and in the hardened state of these concretes are shown. While practical experience with self-compacting concrete already exists, which is produced as ready mixed concrete, for ultra high strength concrete only a few applications, primarily its use in precast elements, are known so far. In view of the promising properties of these both new types of concrete, a broader application in practice seems to be very likely in the future. Still remaining technical problems, such as the high sensitivity of SCC to minor

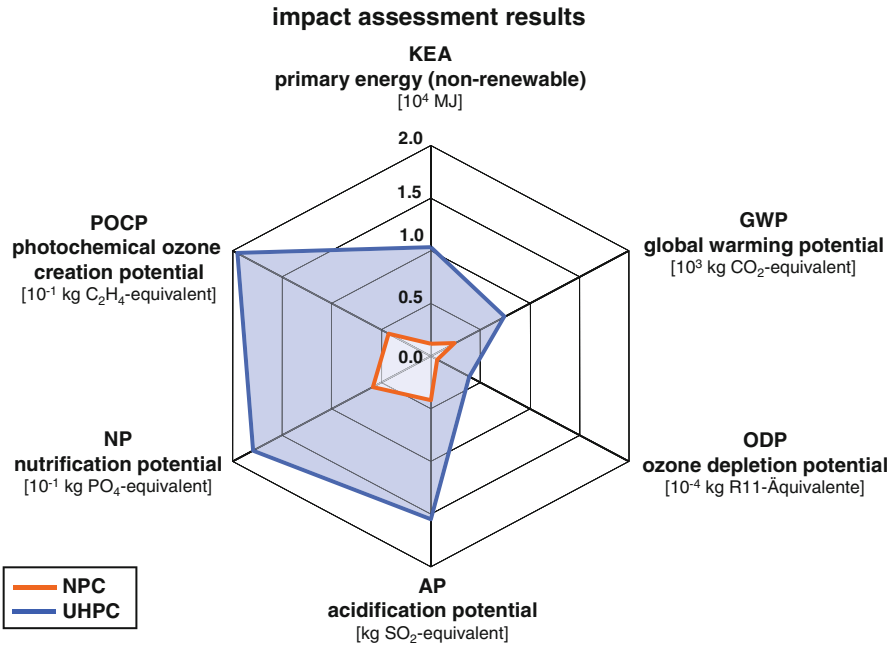

Fig. 3.6 Impact assessment results for 1 m³ of concrete when normal strength concrete (*NPC*) and ultra high performance concrete (*UHPC*) are compared

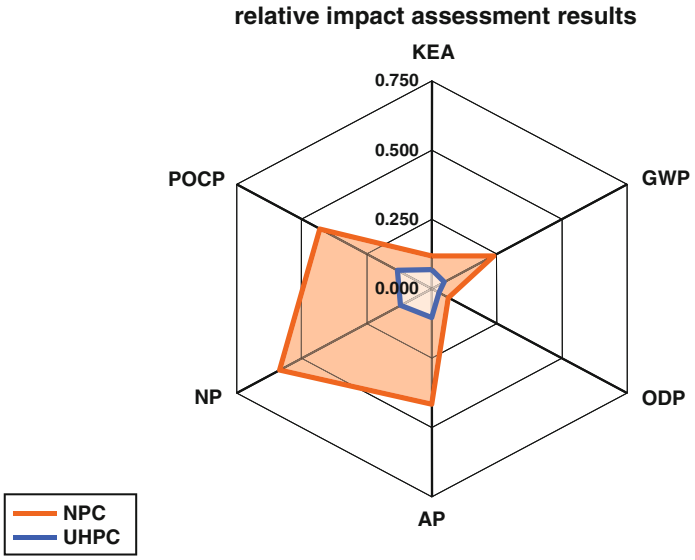

Fig. 3.7 Relative impact assessment results for 1 m³ of normal strength concrete (*NPC*), when NPC and UHPC are compared, referring to the individual values of the permeability

variations in composition and concrete temperature, or the very high autogenous shrinkage of UHPC, have to be solved by continuing research.

Further, promising trends towards the development of ultra ductile concrete, ecological concrete (green concrete) and textile concrete are under way, revealing remarkable potentials for the improvement of the concrete performance. Having a time scale in mind and looking to the recent developments in concrete technology, it becomes clear that the end of innovations may not be seen in the future.

References

Haist M (2009) Zur Rheologie und den physikalischen Wechselwirkungen bei Zementsuspensionen. PhD thesis, University of Karlsruhe, Germany

Müller HS, Haist M (2010) Concrete. In: Structural concrete – textbook on behaviour, design and performance, vol 1, fib Bulletin 51

Müller HS, Scheydt JC (2009) The durability potential of ultra-high-performance concretes – Opportunities for the precast concrete industry. Betonwerk + Fertigteil-Technik 75(2):17–19

Okamura H, Ozawa K (1995) Mix design for self-compacting concrete. Concr Libr JSCE 25(6):107–120

Stengel T, Schießl P (2008) Sustainable construction with UHPC – from life cycle inventory data collection to environmental impact assessment. In: Proceedings of the 2nd international symposium on ultra high performance concrete. Kassel University Press, Kassel, pp 461–468

Chapter 4
Integrated Concept for Service Life Design of Concrete Structures

Harald S. Müller, Michael Vogel, and Tabea Neumann

Abstract With regard to a sustainable development people have to use the existing range of resources in an optimum way. For the building industry this means that the durability of our civil structures is sufficient to withstand the different environmental conditions during a defined service life. Therefore, it is necessary to manage the whole lifetime of a civil structure, from the planning phase to the deconstruction, to avoid cost-intensive maintenance measures and corresponding downtimes. Against this background, the role of lifetime management is briefly shown in this paper. Furthermore, the requirements and tools for the realization of an effective lifetime management are presented. Within these considerations it is taken into account that different deterioration mechanisms occur in combination with each other. These interactions have to be implemented into deterioration time models. Special examples, which clarify some selective elements of the procedure of lifetime management, close this paper.

4.1 Introduction

During the last decade the concept of sustainable development came noticeably into the focus of public and political awareness. The most important principle of the concept is based on the maxim that current ambitions for resource use must not affect the needs of future generations. It is valid for all kind of human activities, and as a consequence the principle of sustainable development should be applied as well to construction and building activities and the building industry, respectively.

H.S. Müller (✉) • M. Vogel • T. Neumann
Department of Building Materials, Institute of Concrete Structures and Building Materials, Karlsruhe Institute of Technology (KIT), Kaiserstrasse 12, D-76131 Karlsruhe, Germany
e-mail: sekretariat-bt@imb.kit.edu; michael.vogel@kit.edu

M.N. Fardis (ed.), *Innovative Materials and Techniques in Concrete Construction: ACES Workshop*, DOI 10.1007/978-94-007-1997-2_4,

This holds particularly true as the construction industry covers a significant percentage of the material and energy use by mankind.

The realisation of the principle of sustainable development requires a successful lifetime management of civil structures. In this context it is very important to predict reliably the changing material behaviour with time and thus the durability of civil concrete structures, which underlie different and complex exposure conditions. Moreover, the deterioration mechanisms usually occur combined and interact among each other. Hence, for a realistic service life prediction these interactions have to be modelled by means of probabilistic tools. In this way, cost minimisation can also be promoted by optimised construction processes and maintenance. The latter involves an effective inspection and assessment management in order to upgrade the repair strategies as well as the preventive and repair work.

4.2 Prediction of the Durability of Civil Concrete Structures

The existing procedure for durability design of civil concrete structures is based on empirical experience in civil engineering. The national and international standards imply special deem-to-satisfy limits in connection with rough environmental classifications to ensure the durability of structures for an approximate defined minimum lifetime, e.g. 50 years according to DIN EN 206 (2001) and DIN 1045-2 (2001), respectively. For instance, the compliance of the regulations on a maximum water/cement ratio of a concrete and a minimum concrete cover is supposed to prevent the concrete and the reinforcement from damaging effects resulting from frost attack or chloride ingress, respectively. Therefore, this concept is a prescriptive approach which considers the different environmental actions on civil structures in a descriptive way.

It is quite evident that the above-mentioned concept is connected with several unfavourable consequences allowing only a rough estimate of the durability. Neither the environmental actions nor the material resistance, i.e. the different deterioration mechanisms in concrete, are considered in a realistic way. Instead of this, the different environmental actions are roughly subdivided in so-called exposure classes which are associated with limiting values for the concrete composition and the concrete compressive strength. The intensity of the different exposure conditions is described in terms like “moderate humidity” or “cyclical wet and dry”. This means that the difference between action S and resistance R, which is a measure of the failure safety, is only estimated by experience (see Fig. 4.1, left). The effective safety margin is unknown to the designer. This descriptive concept is supposed to “guarantee” a sufficient concrete performance for a fixed service life of e.g. 50 years. Hence, it is not possible to quantify, among other things, the necessary concrete properties for a specified lifetime of e.g. 20 or 100 years. In addition, it is also not possible to consider different limit states in view of damage risks, e.g. the time span until the depassivation of the reinforcement occurs.

In contrast, the performance concept based on a probabilistic approach is appropriate to allow for quantitative estimations of the durability of concrete structures. Hereby, the increasing damage process with time, i.e. the interaction of action and

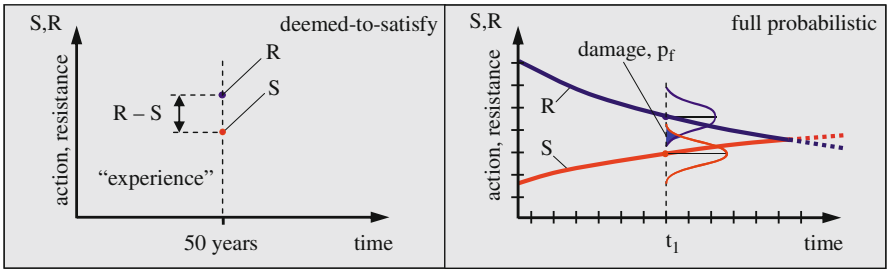

Fig. 4.1 Action and resistance in view of the durability of concrete members. Schema of the descriptive concept (*left*) and the performance concept including a probabilistic approach (*right*)

resistance, affecting the concrete structure is modelled by means of appropriate deterioration time laws, and the material resistance is additionally quantified. Since there are several uncertainties in the action- and resistance-related parameters, it is necessary that the variability and the observable scatter, e.g. for the material parameters, are described by means of related statistical parameters. As a consequence, the safety margin between the well defined functions for the action S and the resistance R can be expressed in terms of the failure probability; see the overlap area between the two curves in Fig. 4.1 on the right side.

By means of the probabilistic performance concept the time-dependent increase of damage and the failure probability according to a defined unintended condition of the structure can be calculated. It is obvious that the application of statistical methods in durability design is – in analogy to the structural design approach – an essential tool in order to quantify the performance of structural concrete. The decisive advantage of the performance concept is based on the fact that the time-dependent durability of concrete structures can be expressed in terms of the failure probability or reliability indices, respectively (see Sect. 4.3.5).

It is already evident that the next generation of standards will include probabilistic methods for durability design.

The required tools have been developed within recent years (The European Union 1997, 1998, 1999, 2000; Sarja and Vesikari 1996). For instance, well established models which describe the degradation process in uncracked concrete for the initiation phase are listed in the fib Model Code for Service Life Design (fib 2006). By means of the developed statistical tools and advanced degradation time laws the prediction of the lifetime of a structure is feasible for civil engineers in practice. This will improve the lifetime management significantly.

4.3 Prediction of Lifetime – Background and Basic Principles

It is evident from the preceding section that the prediction of the lifetime needs time functions for the actions S and the resistance R (see Fig. 4.1, right), including information on the related variability. Further statistical methods to quantify the

interactions of the S and R functions have to be applied. These methods are already well-developed and usually implemented in commercial statistical software tools. In the subsequent paragraphs the essential elements and design steps for the prediction of the lifetime of civil structures are briefly summarised.

4.3.1 Description of the Deterioration Process

The increasing deterioration with time, i.e. the gradual loss of durability due to environmental actions, has to be described by means of deterioration time laws, also called material laws or material models. Such laws should preferably take into consideration real physical or chemical mechanisms. This holds true e.g. for the degradation process caused by carbonation. Of course, carbonation itself does not damage the concrete or the concrete cover, respectively, but if the carbonation front reaches the reinforcement depassivation takes place, which initiates corrosion of the reinforcement in the presence of moisture and oxygen. Considering this process in terms of action S and resistance R, the action is described by means of the material law for the progress of the carbonation front in concrete taking into account environmental and material parameters. The resistance is given by the thickness of the concrete cover.

4.3.2 Statistical Quantification of Parameters

The parameters included in the models for the action S and the resistance R are not exact values but they scatter around average values, see again Fig. 4.1, right. This can be easily observed for the carbonation depth (action) as well as for the concrete cover (resistance) in a concrete member in practice. Hence, the varying parameters are considered as random variables, also called basic variables. If such a basic variable is measured, the corresponding mean value and coefficient of variation as well as the type of the distribution function have to be determined.

4.3.3 Deterioration Process and Limit States

A limit state is understood as a condition at which a civil structure or a structural component ceases to comply with its intended serviceability. In the case of carbonation induced corrosion of the reinforcement, a limit state may be defined by the condition that the carbonation front reaches the reinforcement. Correspondingly, for chloride induced corrosion a limit state is reached if the actual chloride content is equal to the critical chloride content in the depth of the reinforcement. It is self-evident that further limit states may be defined, e.g. the initiation of cracks or any higher level of chloride content.

Table 4.1 Values for the failure probability p_f and the related reliability index β (DIN EN 1990 2002)

p_f	10^{-1}	10^{-2}	10^{-3}	10^{-4}	10^{-5}	10^{-6}	10^{-7}
β	1.28	2.32	3.09	3.72	4.27	4.75	5.20

4.3.4 Intended Service Life of Civil Structures

The loss of durability, i.e. the increase of the deterioration with time, reduces the reliability or the safety of a civil structure. In order to be able to evaluate this reliability or this safety at any age of the structure, a reference period for the service life has to be specified. Reference values of the service life of buildings and structures are listed in relevant standards and guidelines. As an example, the intended service life of residential buildings and other simple engineering structures is 50 years, for hydraulic structures and complex engineering structures it is 100 years (DIN EN 1990 2002).

4.3.5 Failure Probability and Limit State Function

The failure probability p_f is defined as the probability for exceeding a limit state within a defined reference time period. When this occurs an unintentional condition of a considered building component is reached.

The magnitude of the failure probability is closely connected with the interaction of the resistance and the action functions and varies with time (see Fig. 4.1, right). This interaction may be described by means of the so-called limit state function Z which is defined according to Eq. 4.1.

$$Z = R - S \tag{4.1}$$

The function Z represents the elementary form of a limit state function in which R and S are random variables. If the value of Z turns to zero, the limit state will be reached. The stochastical properties of the function Z can be expressed in the form of a distribution function, if this function is considered to be normal distributed and the resistance R as well as the action S are expressed using related mean values μ and standard deviations σ.

By means of the introduction of the so-called reliability index β, a direct correlation between the reliability index β and the failure probability p_f is obtained. In case of a normal distributed limit state function Z, the failure probability p_f can be determined directly by Eq. 4.2.

$$p_f = p\{Z < 0\} = \Phi(-\beta) \tag{4.2}$$

Here, the variable $\Phi(-)$ is the distribution function of the standardised normal distribution. The correlation between various values for the failure probability p_f and the reliability index β is shown in Table 4.1. Note e.g. that the often used 5%

Table 4.2 Target values of the reliability index β according to (DIN EN 1990 2002) and (Rackwitz 1999)

Relative cost of safety measures	Reliability index β (DIN EN 1990 2002)	Reliability index β (Rackwitz 1999)
High	1.3 ($p_f \approx 10\%$)	1.0 ($p_f \approx 16\%$)
Moderate	1.7 ($p_f \approx 5\%$)	1.5 ($p_f \approx 7\%$)
Low	2.3 ($p_f \approx 1\%$)	2.0 ($p_f \approx 2\%$)

quantile in civil engineering is equal to a failure probability of $5 \cdot 10^{-2}$ which corresponds to a reliability index $\beta = 1.645$.

The above given definitions and derivations are generally valid, i.e. for mechanical as well as for physical and chemical actions and resistances which are related to durability. As the durability of concrete is pronouncedly dependent on time t, the functions for S, R and Z are also time-dependent (see Fig. 4.1, right). As a consequence, the reliability index β is also obtained as a function of time, where the value of $\beta = \beta(t)$ is decreasing with time as durability decreases and failure probability increases, respectively.

Table 4.2 indicates target values of the reliability index for building components in the serviceability limit state (SLS) (DIN EN 1990 2002; Rackwitz 1999). Considering the case of depassivation of the reinforcement due to carbonation or chloride ingress the target reliability index is recommended to be $\beta = 1.3$, see (fib 2006).

The calculation of the failure probability p_f for a building component considering a particular mechanism related to durability (e.g. carbonation-induced corrosion of the reinforcement) may be performed by the use of the subsequent Eq. 4.3.

$$p_f = p\{Z < 0\} \leq p_{target} \tag{4.3}$$

As the failure probability increases with time, $p_f = p_f(t)$ approaches $p_{target} = \text{const}$. Finally, $p_f(t = t_{crit}) = p_{target}$ is obtained, where t_{crit} is the time when the failure probability of the member becomes equal to the target failure probability. In practical applications this analysis is done by means of the reliability index β as p_f and p_{target} may be easily expressed as the reliability indices β and β_{target}, see e.g. Fig. 4.4.

4.4 Lifetime Prediction – Application in Practice

The method of lifetime prediction can be applied to a single structural element or component as well as to complex engineering structures like bridges or tunnels. In the latter case additional procedures have to be taken into account. Further, it may be applied for new structures at the stage of planning and also for existing structures, e.g. in order to clarify the remaining lifetime. In the following the application of the procedures of lifetime prediction is shown for some practical cases.

The procedure of lifetime prediction involves the design steps which are summarised in Table 4.3. This overview also indicates the distinction between planned and existing civil structures. In the first case the concrete structure is designed for an intended service life, which is a so-called design for durability. In the latter case the

Table 4.3 Design steps for lifetime prediction

Planned structure	Existing structure
• Identification of action S and resistance R	• Investigation of the structure (ascertainment of the loss of durability and existing damages)
• Ascertainment of material performance (laboratory investigations)	• Identification of action S and resistance R (in situ)
• Definition of appropriate deterioration time laws	• Definition of appropriate deterioration time laws
• Statistical quantification of the model parameters	• Statistical quantification of the model parameters
Requirements for quality and lifetime	
• Definition of limit states with regard to safety and economic boundary conditions • Definition of the target failure probability p_f and the related target reliability index β	
Statistical and analytical investigations	
• Quantification of the failure probability p_f and reliability index β, respectively, according to the given exposure • Assessment of the lifetime of the structure and planning of required maintenance measures	

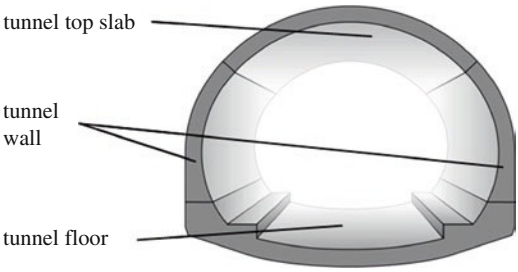

Fig. 4.2 Tunnel structure subdivided in its basic elements

residual lifetime of the structure is determined. Hereby a detailed investigation of the structure is necessary, where non-destructive test methods may help to reduce the costs and to increase the information on the structural status, which in turn improves the accuracy of the prediction of the residual lifetime.

4.4.1 Service Life Prediction of Structural Components

4.4.1.1 Planned Structures – Inner Shell of a Tunnel

In this first example, the developed tools for a probabilistic-based performance design concept for the durability behaviour of a concrete structure are applied considering the inner shell of a tunnel (see Fig. 4.2). The focus is on the question how the intended and designed lifetime changes if an insufficient quality management system was realised during the construction process.

Table 4.4 Lifetime depending on concrete cover

	Concrete cover c		Lifetime analysis		
Case	Mean value [mm]	Standard deviation [mm]	Reliability index β [−]	Failure probability p_f [−]	Achievement of the limit state [years]
A	55	8	1.7	5	100
B	55	16	1.3	11	60
C	45	8	1.0	15	62

For a profound lifetime management it is necessary to implement a quality management system already at the stage of design of the structure. Quality management comprises also the inspection of the planned and built structure with regard to the workmanship. This means that after the construction phase the corresponding material or structural parameters – e.g. the concrete strength or the concrete cover – have to be measured. By means of the determined data and based on the lifetime prediction of the structure – the design for durability – a verification of the planned reliability at the end of the structure's service life can be conducted, or, vice versa, a more precise (updated) lifetime prediction is obtained.

In particular, the concrete cover is subjected to several material dependent and production dependent influences. The most important among them are the form and quality of the bar spacer, the form and quality of the formwork, and the placing and compaction of the concrete.

For the inner shell of a tunnel construction – here the tunnel wall, see Fig. 4.2 – the concrete cover in particular is the focus of attention. The concrete cover is an essential parameter for the durability relevant deterioration process of carbonation-induced corrosion (see Sect. 4.3.1). Deviations from the planned cover thickness exert a pronounced effect on the long term durability. This effect is subsequently studied in more detail.

The intended lifetime of the tunnel is assumed to be 100 years. The target value of the reliability index is set to be $\beta = 1.7$. The limit state is defined as the depassivation of the reinforcement of the tunnel wall. Thus, when the carbonation front reaches the reinforcement, the intended lifetime of the wall ends. During the design process the concrete cover – i.e. the design cover thickness – has been specified in view of its mean value and its related standard deviation. By means of non-destructive testing the realised cover and its variation may be determined.

Table 4.4 shows the corresponding parameter study and the results of the reliability analysis, which was performed applying the software STRUREL (RCP GmbH 2003). Case A represents the design situation. At the end of the intended lifetime of the structure, the calculated maximum failure probability – the probability of depassivation – is about 5%.

For case B – which might represent the results of an investigation after the completion of the construction – it is assumed that during the construction process the mean value of the concrete cover was correctly performed, but the intended standard deviation got doubled (from 8 mm to 16 mm) due to poor workmanship. The effect

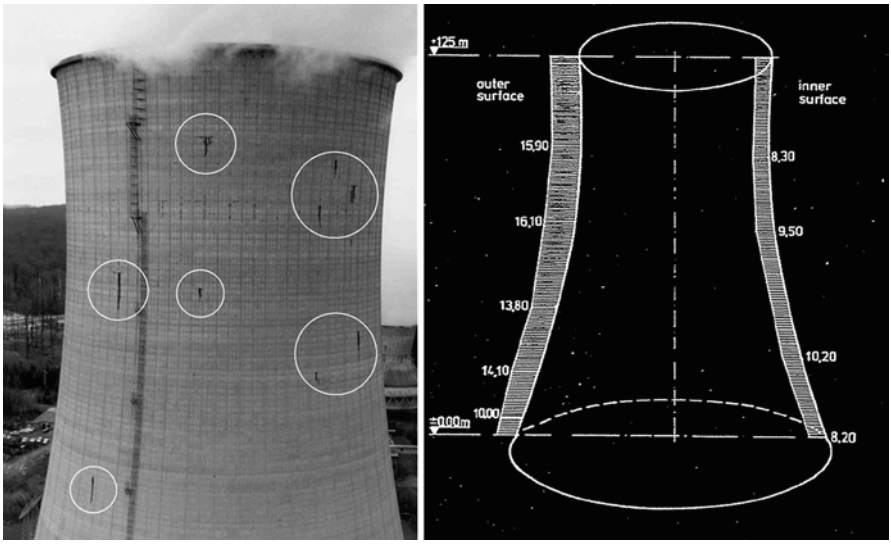

Fig. 4.3 Cooling tower in operation. Shell of the tower with visible rust discolourations (Harte et al. 2006) (*left*) and characteristics of the carbonation depth at the shell in mm (Busch 1991) (*right*)

of this deviation on the lifetime is significant. The probability of depassivation, i.e. the failure probability, is more than doubled (from 5% to 11%), and already after a calculated service life of 60 years appropriate maintenance measures are necessary to avoid further damages. In Case C the workmanship was in accordance with the assumption at the design stage, but a wrong bar spacer was used (mean cover 45 mm instead of 55 mm). For this case the failure probability is tripled compared to the design assumptions. Again, after approx. 60 years of service life, repair measures have to be conducted.

This simple study reveals two main aspects. First, by the application of a probabilistic-based performance concept, deterioration effects are quantified. The designer is not only able to design a structural member for durability, but he is also able to quantify changes in the durability behaviour due to deviations from the planned conditions. Second, it is evident from this study that poor or inaccurate workmanship, which is not identified during initial quality management measures, leads to extensive and expensive repair works.

4.4.1.2 Existing Structure – Cooling Tower

In the following example a cooling tower is considered which is in operation for many years. On the left side of Fig. 4.3, a typical shell of a cooling tower damaged by carbonation-induced corrosion is shown. The white circles mark the areas in

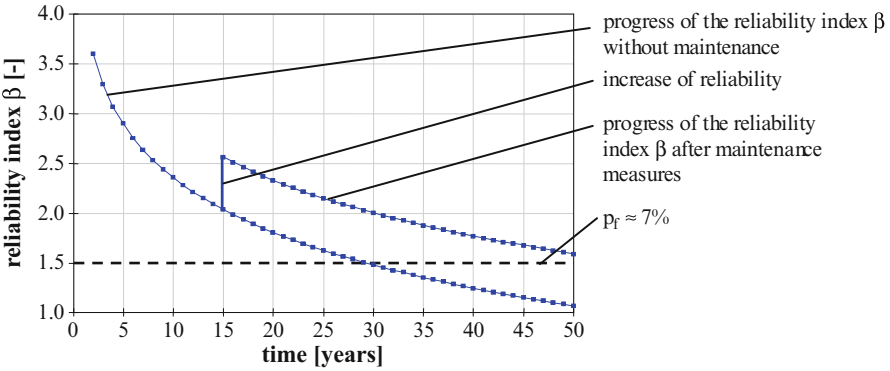

Fig. 4.4 Reliability index β vs. time for calculation "without maintenance" or "with maintenance"

which rust discolourations are visible. The right side in Fig. 4.3 shows schematically the varying carbonation depths in the concrete surface over the height of the cooling tower. It should be noted that especially at cooling towers carbonation depths up to 40 mm were measured after a service life of about 20 years (Harte et al. 2006; Busch 1991). For this structure the residual lifetime should be calculated by means of the probabilistic-based performance concept.

The intended lifetime of the cooling tower is considered to be 50 years. The target value of the reliability index β is set to be 1.5 which corresponds to a failure probability of about 7%. Based on investigations performed prior to this analysis it was found that the concrete cover has a mean thickness of $c = 35$ mm.

The results of the reliability calculations demonstrated in Fig. 4.4 show that the intended reliability index β after a calculated lifetime of 50 years is significantly below 1.5. Already at the age of about 30 years the limit state is reached, which corresponds to the end of the planned lifetime (see Fig. 4.4, lower curve).

For a reconditioning of the damaged shell of the considered cooling tower an appropriate maintenance measure is necessary. This includes the application of repair concrete with a sufficient concrete cover, e.g. $c = 50$ mm. Based on the new boundary conditions with regard to the concrete quality and the concrete cover, a reliability update by means of the Bayesian statistics can be performed (Melchers 2002). The result of this analysis shows that the maximum failure probability does no longer exceed the corresponding probability of the defined limit state after a lifetime period of 50 years. The repair led to a significant improvement of the safety of the structure (see Fig. 4.4, upper curve).

In view of lifetime management of civil structures, it becomes obvious from this example that the necessity of either protective or repair measures can be derived and quantified on the basis of structural investigations so that the intended lifetime may be reached at minimum cost. The decisive advantage of the applied method of probabilistic-based performance design is that a quantitative estimation of protective and maintenance measures is facilitated.

Table 4.5 Design steps for lifetime prediction of structural systems

I	*System analysis*, which includes: – Description of the system – Failure analysis – Fault tree analysis
II	*Failure probability analysis*, considering the individual structural components and the structural system as a whole
III	*Risk assessment*, which includes in particular economical considerations and calculation

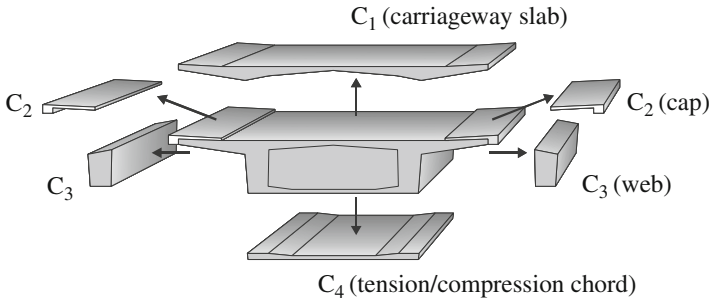

Fig. 4.5 Principle of a component breakdown of a bridge superstructure

4.4.2 Service Life Prediction of Structural Systems

In the previous section the lifetime prediction was performed only for structural components considering single limit states. However, one has to keep in mind that typical civil structures are complex systems. In general, they are composed of numerous structural components which have to satisfy more than one limit state criterion according to the different environmental exposures that stress the structure simultaneously.

In this section a brief introduction into the method of lifetime prediction for complex structural systems is given. Table 4.5 summarises the design steps which have to be considered.

There are three major design steps, namely system analysis, failure probability analysis and risk assessment. In the following paragraphs, system reliability analysis procedures are discussed considering the example of a superstructure of a concrete bridge, which is exposed to several environmental actions (see Fig. 4.5 and Table 4.6).

4.4.2.1 System Analysis

The aim of the system analysis is to understand the function of the structure and to simplify the structure for the reliability analysis. Therefore, it is necessary to describe the system, to analyse the individual failure modes according to the

Table 4.6 Structural components of a bridge superstructure and their exposure

Component	Denotation	Major exposure condition
C_1	Carriageway slab	– Chloride-induced corrosion
C_2	Caps	– Chloride-induced corrosion
		– Frost attack
C_3	Webs	– Carbonation-induced corrosion
		– Frost attack
C_4	Tension/compression chord	– Carbonation-induced corrosion

potential system failure and to perform a fault tree analysis by means of mathematical definitions (Klingmüller and Bourgund 1992). The framework for these design steps is shown in the following.

Description of the System

Within the description of the system it is necessary to identify its main components. Therefore, it is firstly subdivided into its structural components. Figure 4.5 shows the principle of a component breakdown using the example of a bridge superstructure. Here, the main components are the carriageway slab (C_1), the caps (C_2), the webs (C_3) and the tension/compression chord (C_4).

For the component breakdown the appropriate level of detail depends on the given structure itself. It is important to classify the different components according to their function as well as to the different environmental actions, e.g. frost attack. At a later stage, every component of the superstructure has to be assigned to the different exposure conditions which were identified at the structure. Table 4.6 indicates some examples for a reasonable assignment of the exposure conditions (carbonation- or chloride-induced corrosion and frost attack) to the corresponding structural components.

Failure Analysis

The aim of a failure analysis is the identification of the different failure modes of the structural components and their influences on the system. Hence, it is assumed that each component is either in a function state or in a failed state. On this basis, the state of the structure can be expressed in terms of the component functionality.

The building structure usually consists of a large number of components, which are connected in relation to their functions. The interaction of the different components of the structure influences the failure of the systems. The failure mode of one particular component may lead to system failure. For instance, if the carriageway slab fails due to the corrosion of the tendons, the total super-structure of the bridge fails too (see Fig. 4.6).

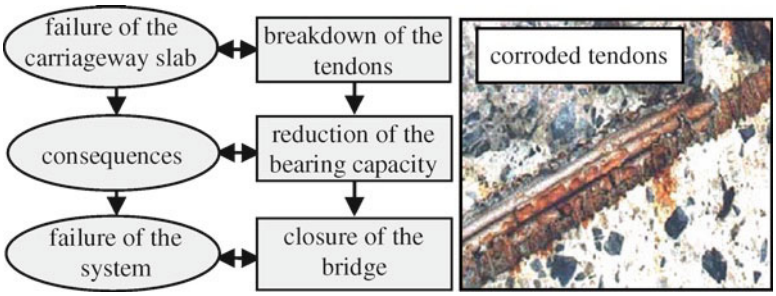

Fig. 4.6 Example of a failure analysis related to a bridge superstructure

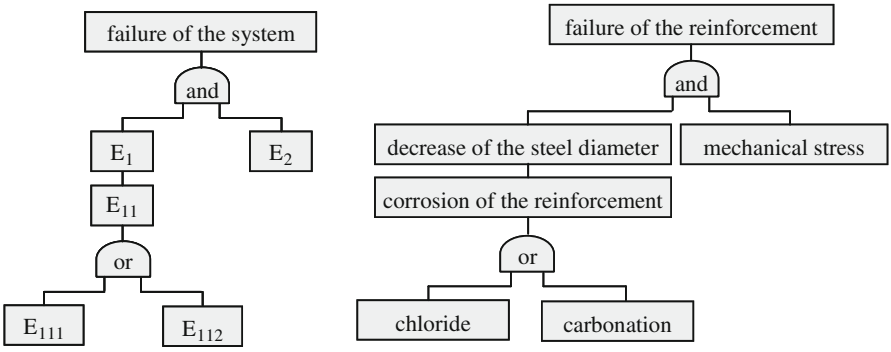

Fig. 4.7 Schema of a fault tree analysis (*left*, E_i = event i) and example of a fault tree according to carbonation- and chloride-induced corrosion (*right*)

Fault Tree Analysis

The fault tree analysis is an analytical method to identify all kinds of events which lead to a "top" event. The top event corresponds to an undesired condition of the structure; hence, it is an adverse event (see Fig. 4.7).

In view of the fault tree analysis there are two basic elementary systems: the series system, termed also weakest link system, and the parallel system, termed also redundant system. A series system fails if any of the system elements fails and a parallel system fails definitively if all elements fail. However, the parallel system does not fail, if just one element does not fail. By means of mathematical rules one can define the lower and upper bounds of the failure probability of the system (Melchers 2002). The simple bounds for the failure probability of a series system can be calculated by means of Eq. 4.4.

$$\max\left[p_{fi}\right] \le p_{f,series\ syst} \le 1-\prod_{i=1}^{n}\left(1-p_{fi}\right) < \sum_{i=1}^{n} p_{fi} \tag{4.4}$$

Table 4.7 Results of the reliability analysis carried out for the components of the bridge superstructure

Exposure	Component	Limit state	Time until the limit state is reached ($\beta = 1.7$)
E_1: chloride	C_1: carriageway slab	Critical chloride content at the reinforcement is reached	27 years
E_2: frost	C_3: webs	2/3 of the concrete cover is destroyed	35 years
E_3: carbonation	C_4: tension/ compression chord	Depassivation of the reinforcement	29 years

The simple bounds for the failure probability of a parallel system can be calculated using Eq. 4.5.

$$\prod_{i=1}^{n} p_{fi} \leq p_{f,parallel\ syst} \leq \min\left[p_{fi}\right] \tag{4.5}$$

The bounds for the failure probability of the above-mentioned bridge superstructure depend on the statistical dependences of the considered failure events.

4.4.2.2 Failure Probability Analysis

This is the second major design step according to Table 4.5, to be subdivided in the analysis of the individual components and of the system as a whole.

Failure of the Components

The failure probability of the components carriageway slab, webs and tension/compression chord (see Fig. 4.5) of the investigated superstructure is determined considering the relevant exposure conditions chloride- and carbonation-induced corrosion and frost attack (see Table 4.6). For this calculation example, the corresponding deterioration time laws have been taken from the literature (fib 2006; Sentler 1983). The magnitude of the necessary parameters and their statistical characteristics have been taken or derived from The European Union (1998, 2000).

The target reliability index β is set to be 1.7 and the considered lifetime is 80 years. Table 4.7 shows the obtained results of the reliability analysis of the components of the superstructure. If it is assumed that the most severe exposure – here the chloride-induced corrosion – controls the failure behaviour, a maintenance measure of the bridge superstructure is necessary after a service life period of 27 years. On the basis of this lifetime prediction, a significant reduction of the lifetime compared to the intended lifetime of the structure is determined.

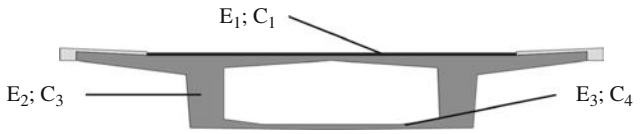

Fig. 4.8 Bridge superstructure with its components and corresponding relevant exposure conditions

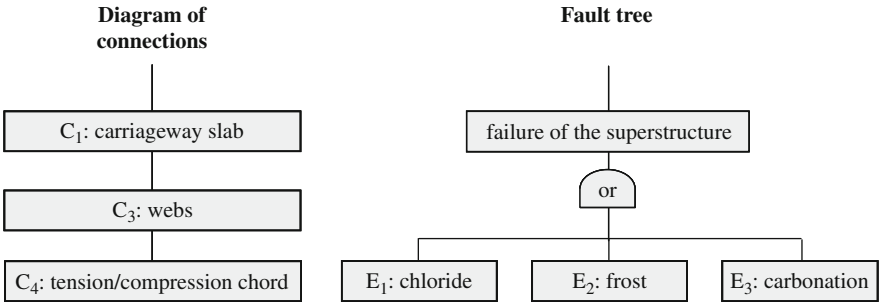

Fig. 4.9 Schema of the series system bridge superstructure

Failure of the System

Figure 4.8 visualises the relevant exposure conditions for the individual components of the bridge superstructure. The chloride-induced corrosion (E_1) is related to the component C_1 (carriageway slab), the frost attack (E_2) is related to the component C_3 (webs) and the carbonation-induced corrosion (E_3) is related to the component C_4 (tension/compression chord).

The superstructure of the bridge represents a series system. As explained above, this system fails – in terms of an undesired condition – when component C_1 or component C_3 or component C_4 fails. Figure 4.9 shows the principle of this series system indicating components and relevant exposure conditions.

The calculated result of the time-dependent system failure probability of the considered series system bridge superstructure with respect to the above-mentioned boundary conditions (see Eqs. 4.4 and 4.5) is shown in Fig. 4.10.

The lower bound curve is the result of the assumption that all failure events are statistically dependent. The upper bound curve is obtained when all failure events are statistically independent. Considering a series system, it should be kept in mind that the system failure probability increases if the correlation between the failure events decreases, since for a decreasing correlation the uncertainties between the failure events are increasing.

In comparison with the results of the lifetime prediction for the individual components (see Table 4.7), the reliability analysis for the system of the superstructure results in a further reduction of the intended lifetime. Hence, the structure has to be repaired

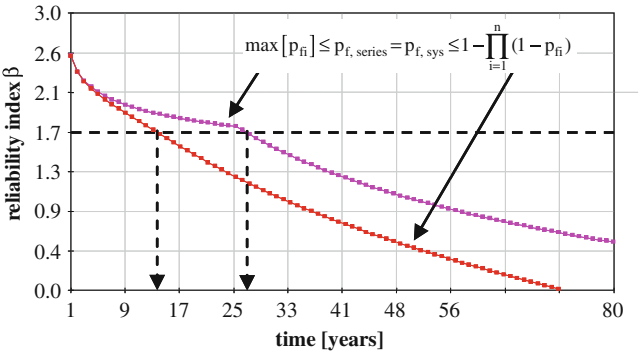

Fig. 4.10 Reliability index β vs. time, determined on the basis of the system reliability investigation of a bridge superstructure

before the calculated lifetime of 27 years; already after 14 years of service life maintenance measures are necessary. This surprising result is based on the fact that the reliability index β is decreasing if the failure events are statistically independent.

4.4.2.3 Risk Assessment

The risk assessment is the third major design step according to Table 4.5. For a risk assessment, the failure probability of a single event $p_{f,i}$ has to be considered in connection with potential consequences c_i, see Eq. 4.6. The potential consequences are usually given in the form of a monetary valuation, e.g. costs due to necessary repair works and corresponding production downtimes. Hence, the risk assessment relates to economical risks.

$$R_{total} = \sum (p_{f,i} \cdot c_i) \tag{4.6}$$

By means of the risk assessment it is possible to identify weak points of the civil concrete structure. On the basis of the risk assessment method, an economical optimisation of the on-site inspections can be achieved. Further, by identifying vulnerable components cost effective protection or repair measures can be undertaken before the occurrence of damages causes high repair costs. It is evident that by means of the risk assessment the lifetime management of civil structures may become very efficient. Material resources, energy and additional expenses may be considerably saved.

4.5 Analysis of Interactions and Singular Risks

The reliability index calculated in the examples beforehand designates the most decisive mechanism. This means that the reliability of a structure can be predicted for carbonation-induced or chloride-induced corrosion or for freeze/thaw attack,

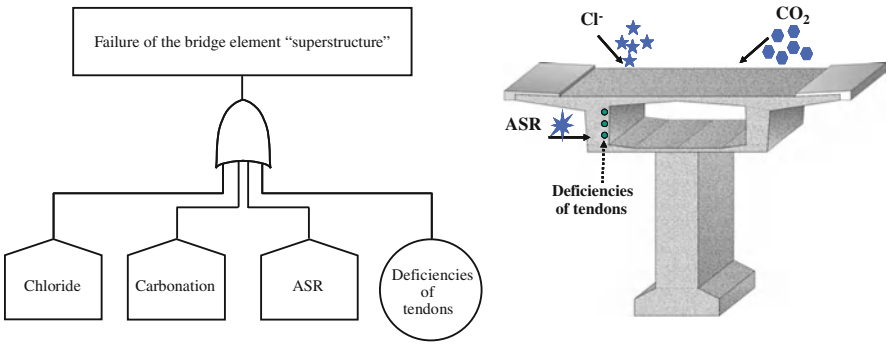

Fig. 4.11 Schema of the series system modelled for a bridge superstructure

considered as physically non-correlated effects. Their interactions with each other are not considered adequately. In practice, however, the exposures occur only in a combined manner (Holt et al. 2009). In contrast to the knowledge about single mechanisms, the knowledge about the impact of combined durability actions on concrete structures is limited to some few investigations. A comprehensive overview of the relevant combined actions does not exist.

Besides, it is even more difficult to quantify durability with these durability-relevant deterioration mechanisms, such as carbonation, chloride ingress and frost/thaw attack, if so-called singular risks occur at the same time. These singular risks can be for example a leaking sealing or cracking due to stress corrosion. The effect of a leaking sealing in durability is considerable but not measurable so far.

Intensive research has shown that the resulting deterioration progress is affected in its intensity by the interactions of various durability actions. This is not only influenced by the intensity of the single deterioration mechanisms, but also by the chronological occurrence of combined exposures, which has an influence on the type of interaction and the resultant deterioration progress, respectively.

The current methods for system and risk analysis do not allow modelling interactions against the background of material science considerations. The characteristic of fault tree analysis is that one only has the choice between a serial ("and") and a parallel ("or") connection of events (see Sect. 4.4.2).

Combined actions can be displayed easily by an "and"-connection, since all actions with their individual failure probability can be incorporated (Müller and Vogel 2008). Interaction may not be introduced by an "and" nor by an "or"-connection of events or mechanisms, respectively.

A suitable way of modelling interactions is the introduction of a dimensionless factor η. By introducing the factor η the material technological characteristics which have an influence on the interactions can be taken into account.

To exemplarily demonstrate the procedure of the new concept for modelling the interactions of combined actions, a reliability analysis was carried out. The following deterioration mechanisms were chosen: carbonation and chloride-induced corrosion, alkali-silica reaction (ASR) and an insufficient grouting of the tendon ducts. Simplifying, it was assumed that ASR and the tendon ducts do not have a significant influence on carbonation and chloride ingress. Figure 4.11 shows the fault tree for

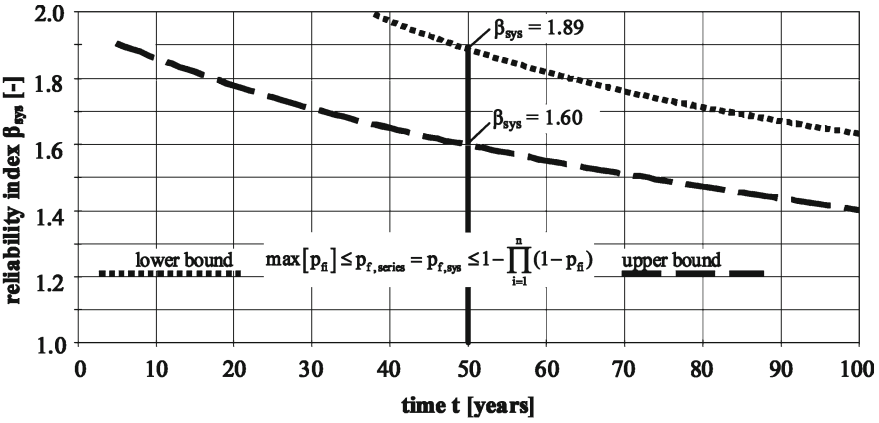

Fig. 4.12 Reliability index β_{sys} vs. time t according to the superstructure of the bridge, see Fig. 4.11

the deterioration of a bridge element superstructure. The superstructure of the bridge represents a series system.

For the actions of carbonation and chloride ingress in this exemplary calculation, the models of the *fib* Model Code 2010 were applied. On this basis, the limit state orientated probabilities were calculated. For the model parameters needed, appropriate values were chosen from the literature (The European Union 1998, 2000; Durable and Reliable Tunnel Structures (DARTS) 2004).

For the deterioration caused by alkali-silica reaction and the insufficient grouting of the tendon ducts, failure probabilities which refer to an example in literature were chosen (Zhu 2008). Therefore, the probability for an alkali-silica reaction was taken as $5 \cdot 10^{-3}$ ($p_f = 0{,}5\%$) and for the insufficient grouting of the tendon ducts the failure probability was assumed to be $2 \cdot 10^{-2}$ ($p_f = 2{,}0\%$).

The prediction of the system failure probability of the bridge structure was performed for a reference period of 100 years. The determination of the time dependent reliability β_{sys} was calculated with the FORM method using the software STRUREL (RCP GmbH 2003). The results are displayed in Fig. 4.12.

For every point in time a range of reliability can be calculated. After 50 years, for example, the reliability index β is expected to be within a range of 1.60 and 1.89. The lower bound indicates the reliability index in case of full correlated failure modes and the upper bound in case of uncorrelated failure modes. The correlation term used in this sense has only a mathematical reason. Material technological correlations or interactions are not considered.

In order to implement the material technological interactions, the factor η_{carbo} is introduced. The fault tree in Fig. 4.13 illustrates descriptively the chosen actions and the meaning of the factor η_{carbo}.

By using the factor η_{carbo} it is possible to take into account an interaction of carbonation and chloride ingress. There are different possible effects an interaction might cause. Due to the carbonation the concrete might have an increased density and

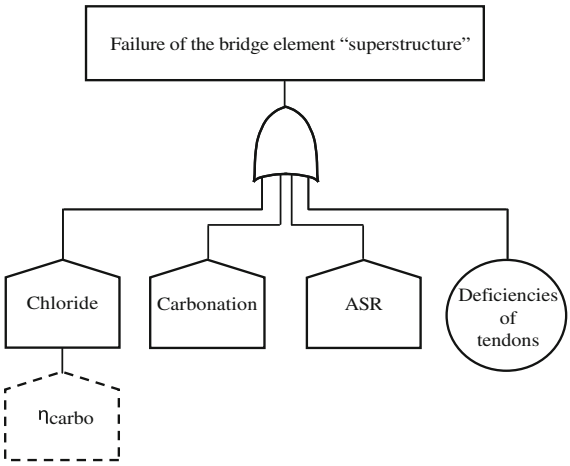

Fig. 4.13 Schema of the series system modelled for a bridge superstructure; the interaction of carbonation and chloride ingress by implementing the factor η_{carbo} is taken into account

lower porosity, which in turn might impede the further ingress of carbonates. On the other hand, the binding capacity of the concrete is lowered due to the carbonation process. The total chloride concentration might be higher than in non-carbonated concrete since the so far bound chlorides are set free. To indicate the influence of carbonation on the chloride ingress, the factor η_{carbo} is annexed to the chloride ingress. The effect simulated can be described simplified with the assumption that the chloride migration coefficient is either increased or decreased. The chronology in which the different actions occur plays an important role within this context, which is not further discussed here.

Although in this example the interaction is limited to the influence of carbonation on the chloride ingress, the principle of the procedure may be demonstrated. The deficiencies of the tendons do not have an impact in the chloride ingress, nor does the carbonation. The ASR may be considered for simplicity to be independent from the other accompanying factors. The only two actions which have an influence on each other are the ingress of chlorides and the carbonation of concrete.

In Table 4.8 the varying ranges of the reliability index β_{sys} and the failure probability $p_{f,sys}$ according to the varying factor η_{carbo} can be seen. The parameter study of the factor η_{carbo} was performed considering a lifetime of 50 years.

The influence of an increasing (>1.0) or decreasing (<1.0) factor η_{Carbo} on the development of the reliability is shown. In the example, a change of the chloride diffusion coefficient by an influence of carbonation was simulated with the factor η_{carbo}. If the average chloride diffusion coefficient is increased with a factor η_{carbo} higher than 1.0, a lower reliability is obtained. Correspondingly the reliability increases with a decreasing chloride diffusion coefficient as a result of a factor η_{carbo} lower than 1.0. The deviation of the reliability index β_{η} adds up to ±7%, which might have a noticeable impact on the service, even if interaction factor η_{carbo} changes only moderately.

Table 4.8 Parameter study on probability p_f and reliability index β_η depending on factor η_{carbo}

η_{carbo} [-]	lower bound		upper bound	
	p_f [%]	β_η [-]	p_f [%]	β_η [-]
0.80	2.1	2.03	4.7	1.68
0.84	2.3	2.00	4.8	1.66
0.88	2.5	1.97	5.0	1.65
0.92	2.6	1.94	5.2	1.63
0.96	2.8	1.91	5.3	1.61
1.00	**3.0**	**1.89**	**5.5**	**1.60**
1.04	3.1	1.86	5.7	1.58
1.08	3.3	1.84	5.8	1.57
1.12	3.5	1.82	6.0	1.55
1.16	3.7	1.79	6.2	1.54
1.20	3.8	1.77	6.4	1.53

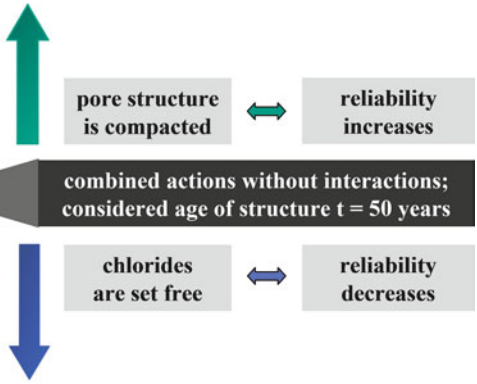

4.6 Conclusions and Outlook

The political emphasis which is paid to the sustainable development in all areas of human activities necessitates the introduction of lifetime management for civil structures. Lifetime management will reduce the consumption of material and energy, and thus it will also reduce the total costs for civil structures. These total costs cover not only the costs for construction itself, but also the costs for maintenance and demolition.

While very often in the past only the investment for a building, i.e. the costs for the construction of a building, were considered, new financial concepts, such as PPP (private financing of public buildings, so-called public private partnership) or BOT (a concept where the contractor builds, operates and finally transfers the civil structure) are entering more and more the market. In these concepts, the total costs are taken into account. Hence, not only the political framework but also economical reasons will facilitate the introduction of the lifetime management of civil structures. This is possible as nowadays the aging process of buildings, i.e. the loss of durability with time, is reasonably well understood and can be described by models which are the core elements of lifetime management.

The procedure for durability design as regulated in the national standards (DIN 1045-2 2001) and e.g. in the *fib* Model Code for Service Life Design (fib 2006) is based on the most decisive deterioration mechanism a concrete structure is exposed to. The knowledge and the design methods established so far have to be extended from single to interacting actions and, therefore, to deterioration models which incorporate related effects. First approaches in regard to modelling of interactions have been developed and shown here.

The results of these investigations are not only relevant for the service life design but also for the prediction of the remaining service life of concrete structures.

During the lifetime of a building, investigations of the material and structural behaviour are necessary from time to time in order to improve the prediction accuracy of the models – for single mechanisms as well as for interactions – for the performance behaviour. These investigations may preferably be carried out by means of non-destructive test methods.

References

Busch D (1991) Schäden und Sanierungsmaßnahmen an Kühlturmschalen aus Beton. In: 2. Fachtagung für Betoninstandsetzung, Konstruktive Instandsetzung, großflächige Erneuerung, vorbeugender Schutz und Instandsetzungs-Sonderverfahren von Stahlbetonbauwerken, Institut für Baustofflehre und Materialprüfung, Universität Innsbruck, 7th–8th February 1991, Innsbruck 1991

DIN 1045-2 (2001) Tragwerke aus Beton, Stahlbeton und Spannbeton. Teil 2: Beton – Festlegung, Eigenschaften, Herstellung und Konformität, Anwendungsregeln zu DIN EN 206–1, Beuth Verlag, Berlin

DIN EN 206-1 (2001) Beton – Teil 1: Festlegung, Eigenschaften, Herstellung und Konformität. Beuth Verlag, Berlin

DIN EN 1990 (2002) Eurocode: Grundlagen der Tragwerksplanung. Deutsche Fassung EN 1990: 2002

Durable and Reliable Tunnel Structures (DARTS) (2004) The Reports (CD Rom) CUR Gouda

fib (2006) Model code for service life design. *fib* bulletin 34. Federation internationale du beton, Lausanne. ISBN 2-88394-074-6

Harte R, Krätzig WB, Lohaus L, Petryna YS (2006) Sicherheit und Restlebensdauer altersgeschädigter Naturzugkühltürme. Beton- und Stahlbetonbau 101(8), Ernst & Sohn Verlag

Holt EE, Kousa HP, Leivo MT, Vesikari EJ (2009) Deterioration by frost, chloride and carbonation interactions based on combining field station and laboratory results. In: 2nd international RILEM workshop on concrete durability and service life planning, 2009, pp 123–130

Klingmüller O, Bourgund U (1992) Sicherheit und Risiko im Konstruktiven Ingenieurbau. Vieweg Verlag, Braunschweig

Melchers RE (2002) Structural reliability analysis and prediction. Wiley, Chichester

Müller HS, Vogel M (2008) Lebenszyklusmanagement im Betonbau. Beton 58(5):206–214

Rackwitz R (1999) Zuverlässigkeitsbetrachtungen bei Verlust der Dauerhaftigkeit von Bauteilen und Bauwerken. Bericht zum Forschungsvorhaben T 2847. Fraunhofer IRB Verlag, Stuttgart

RCP GmbH STRUREL (2003) A structural reliability analysis program system, (STATREL Manual 1999; COMREL & SYSREL Manual, 2003). RCP Consulting GmbH, München

Sarja A, Vesikari E (1996) Durability design of concrete structures. Report of RILEM Technical Committee 130-CSL

Sentler L (1983) Stochastic characterization of concrete deterioration. CEB – RILEM, international workshop: durability of concrete s tructures, Copenhagen, May 1983

The European Union (1997) Brite EuRam III: Design framework. DuraCrete: probabilistic performance based durability design of concrete structures, Contract BRPR-CT95-0132, Project BE95-1347, Document BE95-1347/R1

The European Union (1998) Brite EuRam III: Modelling of degradation. DuraCrete: probabilistic performance based durability design of concrete structures, Contract BRPR-CT95-0132, Project BE95-1347, Document BE95-1347/R4-5

The European Union (1999) Brite EuRam III: Probabilistic methods for durability design. DuraCrete: probabilistic performance based durability design of concrete structures, Contract BRPR-CT95-0132, Project BE95-1347, Document BE95-1347/R0

The European Union (2000) Brite EuRam III: Statistical quantification of the variables in the limit state functions. DuraCrete: probabilistic performance based durability design of concrete structures, Contract BRPR-CT95-0132, Project BE95-1347, Document BE95-1347/R9

Zhu W (2008) An investigation into reliability-based methods to include risk of failure in life cycle cost analysis of reinforced concrete bridge rehabilitation. Master Thesis, School of Civil, Environmental and Chemical Engineering, Science, Engineering and Technology Portfolio, RMIT University

Chapter 5
Sustainability with Ultra-High Performance and Geopolymer Concrete Construction

Tian Sing Ng, Yen Lei Voo, and Stephen J. Foster

Abstract This paper presents an overview on the use of high performance cementitious products and in using cement replacement materials, such as geopolymers in the development of sustainable design and construction. The design approach not only accounts for the limit states design, it also takes into consideration the environmental impact and durability of the designed structure. Two examples of environmental impact calculations, a bridge structure and a retaining wall, are provided for conventional Portland cement concrete, geopolymer concrete and reactive powder concrete solutions. The comparison studies show that many structures constructed of reactive powder concrete and of geopolymer concrete can provide for environmentally sustainable alternatives to the use of conventional concrete construction with respect to the reduction of CO_2 emissions, embodied energy and global warming potential. The enhanced durability of reactive powder concrete and geopolymer concrete also provides for significant improvements in the design life, further supporting the concept of sustainable development.

T.S. Ng (✉) • S.J. Foster
Centre for Infrastructure Engineering and Safety, School of Civil and Environmental Engineering, The University of New South Wales, UNSW, Sydney, NSW 2052, Australia
e-mail: tian.ng@unsw.edu.au; s.foster@unsw.edu.au

Y.L. Voo
Dura Technology Sdn Bhd, Lot 304993, Jalan Chepor 11/8, Pusat Seramik, Fasa 2, Ulu Chepor, 31200 Chemor, Perak, Malaysia
e-mail: vooyenlei@dura.com.my

M.N. Fardis (ed.), *Innovative Materials and Techniques in Concrete Construction: ACES Workshop*, DOI 10.1007/978-94-007-1997-2_5,

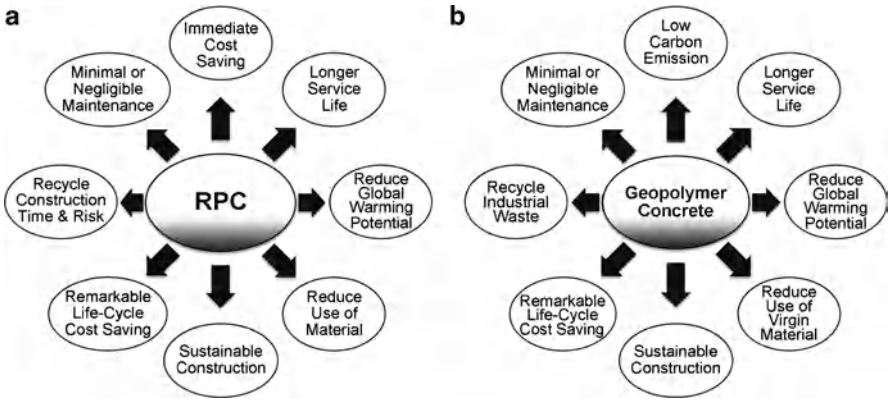

Fig. 5.1 (**a**) RPC and (**b**) Geopolymer concrete towards sustainable construction

5.1 Introduction

From the time when Portland cement was invented, the cement and concrete industry has been confronted with the environmental and energy intensive issues (Fling 1975). Both of these issues have resurfaced as a point of international interest as the world begins to move towards the concept of sustainable development. As governments develop low carbon policies, industries that consume excessive energy and/or resources are likely to be subjected to higher pricing policies to encourage market development of more sustainable solutions. The cement and concrete industry is one of these industries.

Over the last three decades, significant advancements have been achieved in the concrete industry. One of the major breakthroughs in the 1990s was the development of ultra-high performance concrete (UHPC), also known as the reactive powder concrete (RPC), by Richard and Cheyrezy (1994). Compressive strength and flexural strength of over 180 and 30 MPa, respectively, have been reported for RPC. The second advancement was the development of geopolymer and its application in concrete industry as an alternative binder to the Portland cement. Geopolymer is a material resulting from the reaction of a source material that is rich in silica and alumina with alkaline solution. Concrete made from geopolymer has also been found to be more durable than Portland cement concrete, possesses excellent engineering properties and has a lower carbon footprint than conventional Portland cement concrete (Li et al. 2004; Gourley and Johnson 2005; Rangan 2008). In the last decade, or so, extensive research has been undertaken by academics and engineers alike with the view to industrialise these technologies as alternatives for more sustainable construction. The principle of sustainable construction stands on a basis of material optimisation together with structural design optimisation, which results in the lower life-cycle cost. Figure 5.1 shows some of the immediate and long-term benefits that RPC and geopolymer concrete technology is able to provide.

This paper firstly presents an overview on the material characteristics of typical RPC and geopolymer concrete and compares them to conventional normal strength and high strength concretes. Secondly, a sustainability design approach is proposed. This design approach not only accounts for the limit states design of a structure but also takes into consideration the environmental impact and durability of the detailed structure. Examples on the environmental impact calculation (EIC) of conventional concrete structures are compared against comparable structures built using RPC geopolymer concrete. Lastly, durability aspects of each material are discussed and design calculations presented.

5.2 Material Characteristics

Table 5.1 summarises the material characteristics of RPC and geopolymer concrete and is compared against conventional, normal, strength concrete (NSC) and high strength concrete (HSC).

5.2.1 Reactive Powder Concrete

Reactive powder concrete (RPC) is suitable for use in the production of precast elements for civil and structural engineering and architectural applications. The constituent materials of RPC are ordinary Portland cement, silica fume, fine aggregate, water, steel fibres and a superplasticiser admixture. In order to achieve the required performance of RPC, powder materials and fine aggregates are blended or proportioned to an adequate particle size distribution in order to maximise the density or compactness. Table 5.2 presents the mix design for a standard RPC with 2% steel fibres by volume of concrete. The superplasticiser used is Polycarboxylate ether (PCE)-based and no recycled wash water is used in the mixing. In addition, structural members made of RPC are recommended to be heat cured for a minimum of 48 h at a temperature of 90°C by the concrete committee of the Japanese Society of Civil Engineering recommendations for design and construction of ultra-high strength fibre reinforced concrete structures (JSCE 2006).

Reactive powder concrete is a highly homogenous cementitious-based composite without coarse aggregates and, therefore, can achieve ultra-high compressive strengths and high flexural strength. Its blend of very high strength steel fibres and cementitious binders with extremely low water content give RPC extraordinary characteristics of mechanical strengths and high ductility. The durability of RPC is comparable to natural rocks with very low permeability and is resistant to carbonation (Xie et al. 2008). After early age heat treatment, there is almost no shrinkage or creep, which makes RPC very suitable for applications in prestressed concrete. The use of this material for construction is simplified through the elimination or minimization of conventional reinforcing steel and the ability of the material to be

Table 5.1 Material characteristics of RPCs and Geopolymer concretes compared to normal strength (*NSC*) and high strength (*HSC*) Portland cement concrete (after Graybeal 2006; Muntingh 2006; Rangan 2008; Ng and Foster 2008; Poon et al. 2009; Voo and Foster 2010)

Characteristics	Unit	Code/standards	NSC	HSC	Geopolymer concrete	RPC
Specific density, ρ	kg/m^3	AS1012.12.1 (1998)	2,300–2,400	2,400–2,500	2,250–2,400	2,350–2,550
Cylinder compressive strength, f_{cy}	MPa	AS1012.9 (1999)	20–50	50–100	30–100	120–210
Creep coefficient at 28 days, ϕ_{cc}		AS1012.16 (1996)	2–5	1–2	<0.7	0.2–0.66
Post cured shrinkage	με	AS1012.13 (1992)	1,000–2,000	500–1,000	≈100	<100
Modulus of elasticity, E_c	GPa	AS1012.17 (1997)	20–35	35–40	20–35	40–53
Poisson's ratio, ν		AS1012.17 (1997)	0.2	0.2	0.15–0.2	0.18–0.2
Split cylinder cracking strength, f_t	MPa	BS:EN 12390–6 (2000)	2–4	2–4	N/A	5–12.4
Split cylinder ultimate strength, f_{sp}	MPa	AS1012.10 (2000)	2–4	4–6	2–7.5	10–26.5
Flexural first cracking strength, $f_{cr,\,4P}$	MPa	AS1012.11 (2000),	2.5–4	4–8	2.5–8	8–9.7
Modulus of rupture, $f_{cf,\,4P}$	MPa	ASTM C1018 (1997)	2.5–4	4–8	2.5–8	18–50
Toughness indexes, I_5		(four-point test on	1	1	1	4–6.2
Toughness indexes, I_{10}		un-notched	1	1	1	10–15
Toughness indexes, I_{20}		specimen)	1	1	1	20–35
Bending fracture energy, $G_{f,\delta=0.46\,mm}$	N/mm	JCI-S-001 (2003),	<0.1	<0.2	<0.2	1–2.5
Bending fracture energy, $G_{f,\delta=3.0\,mm}$	N/mm	JCI-S-002 (2003)	<0.1	<0.2	<0.2	10–20
Bending fracture energy, $G_{f,\delta=10\,mm}$	N/mm		<0.1	<0.2	<0.2	15–30
Rapid chloride permeability	Coulomb	ASTM C1202 (2005)	2,000–4,000	500–1,000	N/A	<200
Chloride diffusion coefficient, D_c	mm^2/s	ASTM C1556 (2004)	$4–8\times10^{-6}$	$1–4\times10^{-6}$	$<0.003\times10^{-6}$	$0.05–0.1\times10^{-6}$
Water absorption	%	BS 1881:Part 122 (1983)	>3	1.5–3.0	<2	<0.2

Table 5.2 Mix design of typical (**a**) RPC and (**b**) geopolymer concrete

Ingredient	Mass (kg/m^3)	
	RPC	Geopolymer concrete
Portland cement	720	–
Silica fume	180	–
Fly ash	–	240
Ground granulated blast furnace slag	–	42
Fine aggregate	1,150	695
Coarse aggregate	–	1,120
Superplasticiser	40	–
High strength steel fibres	157	–
Free water	144	91
Sodium hydroxide (NaOH) solid	–	15.5
Sodium silicate solution (with $SiO_2/Na_2O=2$)	–	110

virtually self-placing or dry-cast. The comparison in Table 5.1 shows that RPC has superior mechanical properties over normal and high strength concretes.

5.2.2 Geopolymer Concrete

Geopolymer concretes have emerged as novel engineering materials with the potential to form a substantial element of an environmentally sustainable construction and building products industry (Provis et al. 2005; Duxson et al. 2007). Geopolymer concretes are commonly formed by alkali activation of industrial aluminosilicate waste materials such as fly ash and blast furnace slag, and, as will be discussed in detail in this paper, have lower greenhouse footprint when compared to traditional Portland cement concretes. Table 5.2 presents the mix design for a typical geopolymer concrete developed at the University of New South Wales, Australia.

With correct mix design and formulation development, geopolymer concrete can provide superior chemical and mechanical properties to Portland cement concrete, and be highly cost effective. Geopolymer concrete can gain 70% of the final compressive strength in the first four hours of setting (Li et al. 2004; Rangan 2008). Rangan (2008) and at the University of New South Wales, fly ash based geopolymer concretes have been developed with an achievable compressive strength ranging from 8 to 100 MPa depending on the mix composition and curing method. Similar to RPC, structural members made of geopolymer concrete are recommended to be heat cured (Rangan 2008).

Comparing geopolymer concrete with conventional concrete, heat treated geopolymer concrete has low shrinkage and creep (van Jaarsveld et al. 1997; Rangan 2008) and has a superior chemical resistance against chlorides, sulphates and acids (Palomo et al. 1999; Muntingh 2006; Song 2007; Rangan 2008). Geopolymer

concrete is also found to have high fire resistance in accordance with the studies of Gourley and Johnson (2005) and Kong and Sanjayan (2010). Importantly though, geopolymer concrete is found to have moderate to low elastic modulus for its strength (Fernández-Jiménez et al. 2006; Rangan 2008; Ng and Foster 2008).

5.3 Sustainability Design Approach

The concept of sustainability design, commonly known as "green design" as defined by the US Green Building Council (USGBC), consists of three components: environmental, economic, and health and community benefits. All three of these components can benefit from choices made in the structural design and construction phases of a project. The following is a list of the environmental, economic, and health and community benefits offered through sustainable structural design and construction as defined by the USGBC:

- Improvement and protection of the environment and biodiversity;
- A decline of solid waste products;
- Conservation of natural resources;
- A decrease in energy consumption with an increase in energy savings;
- Improved durability of structures and savings in project life cycle costs;
- A reduction in maintenance costs; and
- Improvement of occupant health and comfort.

The approach used for the design of RPC and geopolymer concrete structures is presented in Fig. 5.2. The three fundamental criteria for assessment of a sustainable design are:

1. An environmental impact calculation (EIC);
2. Design for longevity (i.e. durable structures);
3. Limit states design.

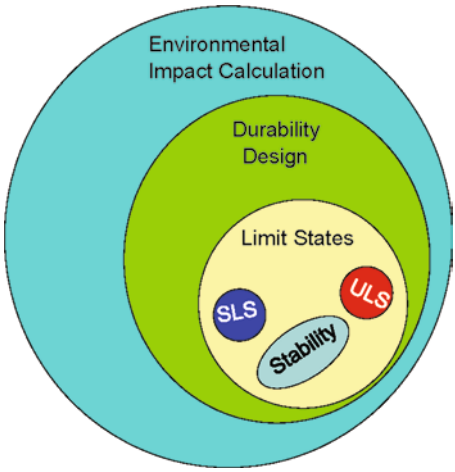

Fig. 5.2 Design model

Table 5.3 Environmental data for an EIC

	Units	RPC (2% steel Fibres)[a]	Grade-60 (15% PFA)	Grade-60 (15% PFA)	Geopolymer concrete	Steel Reinforcement
Density	kg/m^3	2,400	2,350	2,350	2,350	7,840
EE	GJ/m^3	7.77	2.70	2.27	0.57	185.8
CO_2	kg/m^3	10.65	487.2	406.8	318.2	17,123
NO_x	kg/m^3	4.86	1.66	1.66	–	55.4
CH_4	kg/m^3	0.76	0.12	0.12	–	30.7
100-year GWP	kg CO_2 eq./m^3	2,537	985	905	318	34,392
EE	MJ/kg	3.24	1.15	1.03	0.24	23.70
CO_2	kg/kg	0.45	0.21	0.17	0.14	2.18
NO_x	g/kg	2.03	0.71	0.71	–	7.06
CH_4	g/kg	0.32	0.05	0.05	–	3.91
100-year GWP	kg CO_2 eq./kg	1.06	0.42	0.38	0.14	4.39

[a]Environmental values include steel fibres contribution

To assess the performance of a structural design with regards to sustainability, objective measures are needed. For example, the EIC is a measure of the optimisation of the materials used with respect to the embodied energy, CO_2 emission and global warming potential when compared to existing practice. Durability can be defined as the capability of a structure to meet its defined design serviceability and strength limit state criteria over time. Durability design is important to ensure the designed structure meets the required design life, within a designed maintenance plan, thereby reducing the overall life-cycle cost, social impact and unplanned additional material consumption, which can bear heavily on future carbon impacts. Thus, in this paper durability design is categorized as a sub-set of environmental impact design. Finally, the limit state design should be used to design the structure to satisfy serviceability, stability and strength requirements. By fulfilling the aforementioned criteria, the overall cost and functionality of a designed structure will be optimised with respect to minimising its environmental impact.

5.3.1 Environmental Impact Calculation (EIC)

Undertaking a full EIC is a complex exercise and the data required for the calculation vary from country to country due to local practices and available technologies. Table 5.3 summarises the environmental data used in this comparative study. The table has been prepared for determining the equivalent CO_2 content of particular concrete mix designs and materials and the information may be updated frequently as the industry continues to improve its processes. The values of embodied energy (EE) and CO_2 emission in the production of the Portland cement concrete and steel for this study are extracted from the work of Struble and Godfrey (2004), while for geopolymer concrete the work of Witherspoon et al. (2009) is adopted. The energy

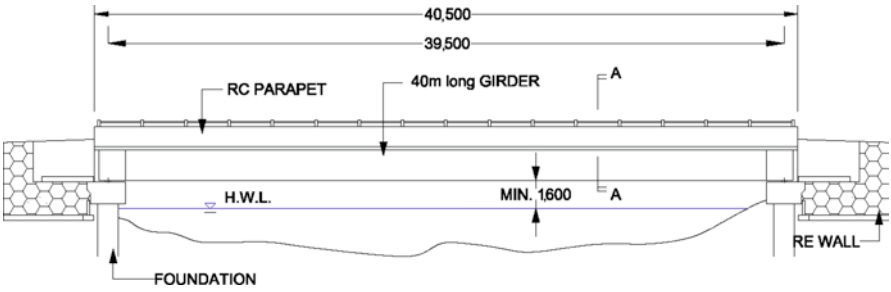

Fig. 5.3 Layout of a 40 m long span concrete road bridge

consumed in the production of Portland cement is estimated to be 4.88 MJ/kg and the total energy in the production of steel is estimated to be 23.7 MJ/kg (i.e. 185.8 GJ/m^3) (Struble and Godfrey 2004). For geopolymer concrete, the production of the alkaline source required to activate the fly ashes is the most energy intensive component in the manufacturing process. The energies consumed in the production of NaOH and sodium silicate are estimated to be 14.6 and 8.6 MJ/kg, respectively (Witherspoon et al. 2009). Based on these values, the EE values of Grade-40 and Grade-60 Portland cement concretes and that of geopolymer concrete and RPC with 1.5% and 2% of steel fibres can be determined and are presented in Table 5.3.

Elrod (1999) defines Global Warming Potential (GWP) as a measure of how a given mass of greenhouse gas is estimated to contribute to global warming over a given time interval. It is a relative scale that compares the gas in question to that of the same mass of CO_2 and a 100-year of time horizon is most commonly adopted, as per the Kyoto Protocol (Forster et al. 2007). The formulation of GWP can be ambiguous and the adequacy of the GWP concept has been widely debated since its introduction (Fuglestvedt et al. 2003). For simplicity, the 100-year GWP can be expressed as:

$$100-\text{year GWP} = CO_2 + 298\ N_2O + 25\ CH_4 \tag{5.1}$$

In the concrete industry, the production of Portland cement is the main contributor to the GWP. The greenhouse gas emission associated with the production of 1 tonne of Portland cement has been estimated at approximately 0.8 to 1 tonne of CO_2 and an average of 3.5 kg of Nitrogen oxides (NO_x) (Huntzinger and Eatmon 2009; US EPA 1994).

5.3.2 *Sustainability Design Example 1: Single Span 40 m Concrete Road Bridge*

Figure 5.3 shows the layout of a single span 40 m concrete bridge used by Voo and Foster (2010) to assess the GWP of RPC. In this paper, the design is supplemented by a geopolymer concrete and the I-girder section design (commonly adopted in

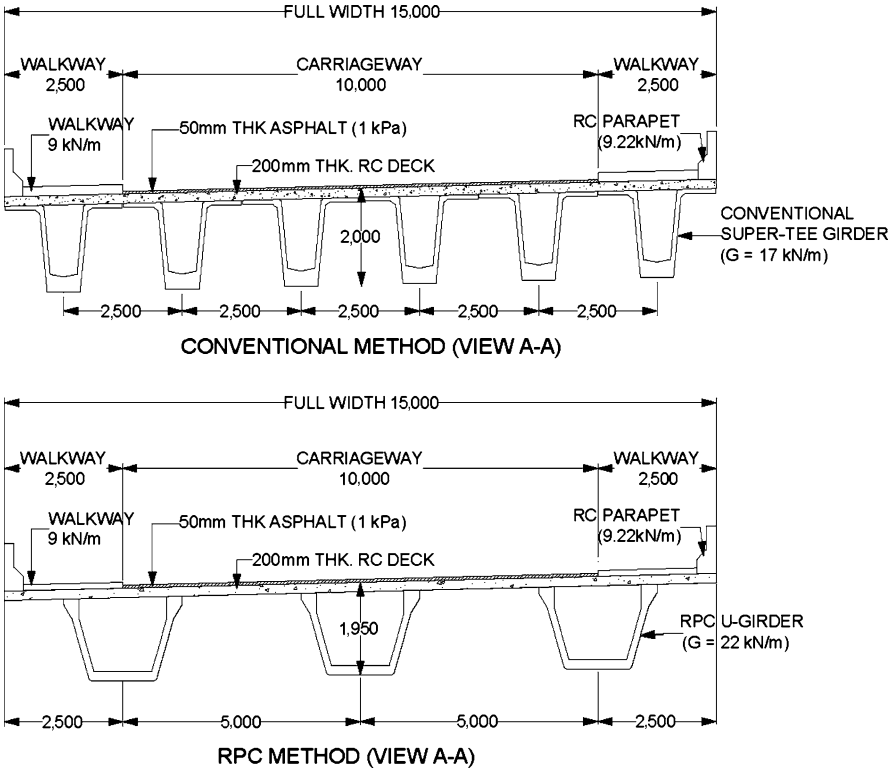

Fig. 5.4 Comparison of cross sectional view for conventional Super-T girders design and RPC U-girder design

Malaysia) is replaced with Australian super-tee sections. Note that the super-tee designs generally provide for the most economical solution using current practice. The total transverse width of the bridge is 15 m. Based on conventional concrete design, six precast pre-tensioned super-tee girders are needed. For the alternative RPC design, three U-girders are used (see Fig. 5.4). In this example, the precast girders are designed to be simply supported at their ends and are composite with a 200 mm thick Grade-40 in-situ RC deck slab. The RC deck is then covered with a 50 mm thick asphalt wearing surface as is common Australian practice.

The bridge is designed for the following specifications:

- Design life: 120 years
- Exposure class: XS1-exposed to airborne salt but not in direct contact with sea-water (Eurocode 2 (CEN 2004), Table 4.1)
- Imposed live load: Load models 1–4 with special vehicle 1800/150 (Eurocode 1-Part2 (CEN 2001))
- Minimum free-board clearance: 1.6 m
- Superstructure: Precast girders with 200 mm thick composite in-situ RC deck slab
- Bridge length: Single span of 40 m

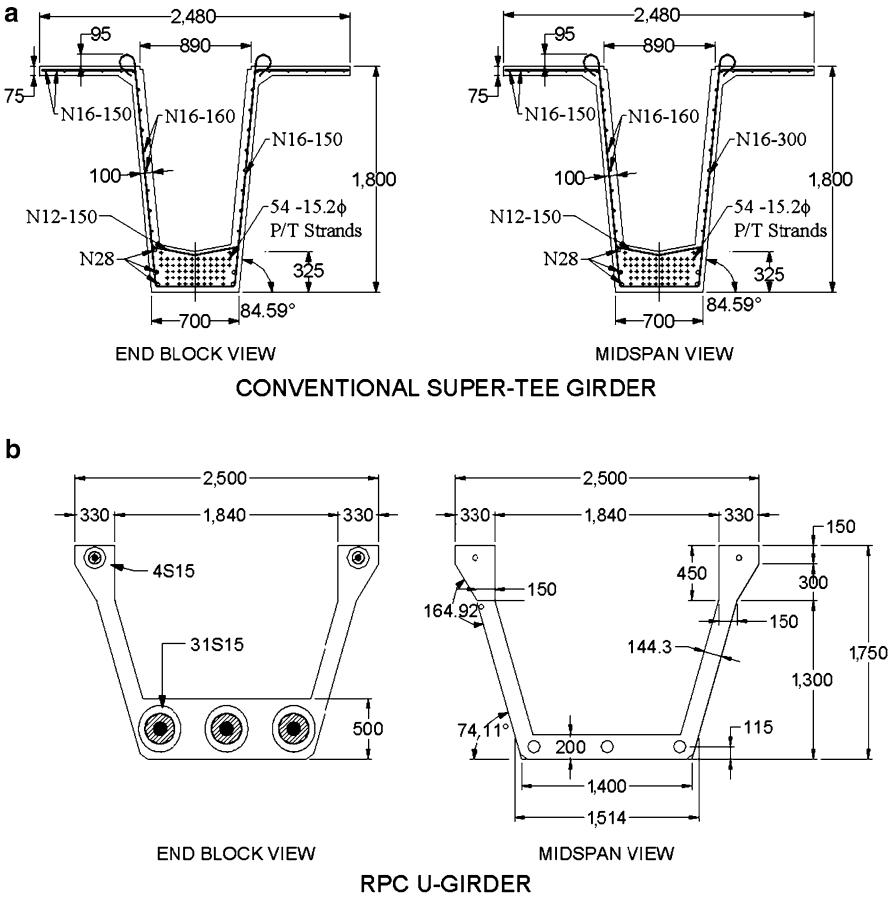

Fig. 5.5 Dimension of (**a**) conventional Super-T girders design and (**b**) RPC U-girder bridge

- Supported length: 39.5 m (centre-to-centre of bearings)
- Overall bridge width: 15 m
- Cross slope: 2.5%.

Figure 5.5a shows the cross section details for the 40 m long conventional super-tee girder design. The girders are designed to AS5100.5 (2004) Type 5 category and are pre-tensioned with 54 by seven wire low relaxation strands of nominal diameter 15.2 mm and nominal strength of 1,790 MPa and conformed to AS 4672.1 (2007). The strands are stressed to 75% of their guaranteed ultimate tensile strength (GUTS).

In this example, conventional steel reinforcing bars in the web are used to transfer shear forces and to resist transverse bending moment on the top flanges. The girder weighs approximately 1.7 tonnes per metre and gives a total weight of 68 tonnes per 40 m girder. In contrast, Fig. 5.5b gives the detail of the alternative

DURA® -U1750 RPC precast girder adopted for the RPC solution. The RPC girder consists of two 150 mm thick webs, a 200 mm thick base and it is post-tensioned using three tendons of 31 by 15.2 mm diameter strands at the base and two tendons of four by 15.2 mm diameter strands at the top flanges to ensure that the joints are in compression during transfer and in service. Each girder comprises five segments (three 8 m internal segments and two 8 m end-block segments). In addition, unlike a conventional precast concrete girder, the webs do not contain any reinforcement for transverse shear forces with steel fibres included to carry the tensile component of the internal forces generated by shear (Voo et al. 2006; Voo and Foster 2009). The girder weighs 2.2 tonne/m, which gives a total of 88 tonnes per girder.

Table 5.4 summarises the material quantities and the EIC of the two bridge girder designs. In the calculation of the material quantity, only the superstructure is considered herein. The amount of EE, CO_2 emissions and 100-year GWP are obtained from multiplying the amount of materials by the environmental data given in Table 5.3. A comparison of the EIC results is presented in Fig. 5.6. In terms of material consumption, the RPC design solution consumed 37% less material than the conventional solution. In terms of environmental impact, the RPC solution has 14% less embodied energy and 12% less CO_2 emissions. In terms of the 100-year GWP, the RPC solution provides for a reduction of 10% over that of the conventional solution.

For the geopolymer concrete solution, the design is similar to that Portland cement concrete and, therefore, the total material consumption is similar. However, in terms of natural resources or virgin materials consumption, geopolymer concrete is 8% lower that Portland cement concrete as it utilises industrial waste products such as fly ashes and slags that would otherwise be dumped into landfill sites or flushed into the sea. The geopolymer concrete solution consumes 15% less energy and gives 14% lower CO_2 emissions than the conventional Portland cement concrete design. Its 100-year GWP is 35% and 25% lower than that of Portland cement concrete and RPC solutions, respectively.

In regards to the above calculations for sustainability, it also needs to be recognised that only the savings at the level of the superstructure have been considered. For the RPC design solution, significant further savings will result from the lighter weight of the super-structure giving a smaller sub-structure, foundations and lower transport costs.

5.3.3 Sustainability Design Example 2: 1.5 m High Retaining Wall

A 180 m long by 1.5 m high retaining wall was recently developed as a pilot application of RPC technology in the construction of a 90 m long monsoon drain for a housing development project in Ipoh, Malaysia (Fig. 5.7a). The design surcharge load is 10 kPa at service and 15 kPa at ultimate. For a conventional reinforced concrete L-shaped wall, the wall will have a minimum of 150 mm thick footing and 100–150 mm thick stem (Fig. 5.7c). For the RPC solution, the L-shaped wall

Table 5.4 Material quantities and EIC for 40 m long road bridge

	RPC (m^3)	Grade-60 OPC concrete (m^3)	Grade-40 OPC concrete (m^3)	Geopolymer concrete	Steel reinforcement
Conventional design (OPC concrete)					
Precast 40 m super-tee girders	0	173.26	0	0	53.17
End crosshead (inc. wing-wall, approach slab and diaphragm)	0	0	124.9	0	16.61
RC deck (total) – 1.5% Reo.	0	0	120	0	14.1
RC Parapet – 1.0% Reo.	0	0	31.3	0	2.45
Sub-total	0.0	173.3	276.2	0.0	86.4
Mass of material used (tonne)	0	407.2	649.1	0	86.4
Embodied energy (GJ)	0	468	627	0	2,046
CO_2 (tonne)	0	84	112	0	188
GWP (tonne CO_2 eq.)	0	171	250	0	379
Conventional design (Geopolymer concrete)					
Precast 40m super-tee girders	0	0	0	173.26	53.17
End crosshead (inc. wing-wall, approach slab and diaphragm)	0	0	0	124.9	16.61
RC deck (total) – 1.5% Reo.	0	0	0	120	14.1
RC Parapet – 1.0% Reo.	0	0	0	31.3	2.45
Sub-total	0.0	0.0	0.0	449.5	86.4
Mass of material used (tonne)	0	0	0	1056.3	86.4
Embodied energy (GJ)	0	0	0	602	2,046
CO_2 (tonne)	0	0	0	143	188
GWP (tonne CO_2 eq.)	0	0	0	143	379
RPC design					
Precast 40m DURA-U1750 girders	108	0	0	0	17.1
End crosshead (inc. wing-wall, approach slab and diaphragm)	0	0	103	0	16.61
RC deck (total) – 1.5% Reo.	0	0	120	0	14.1
RC Parapet – 1.0% Reo.	0	0	31.3	0	2.45
Sub-total	108.0	0.0	254.3	0.0	50.3
Mass of material used (tonne)	257.9	0	597.6	0	55
Embodied energy (GJ)	835.0	0	577	0	1,304
CO_2 (tonne)	115.5	0	103	0	120
GWP (tonne CO_2 eq.)	274	0	230	0	220

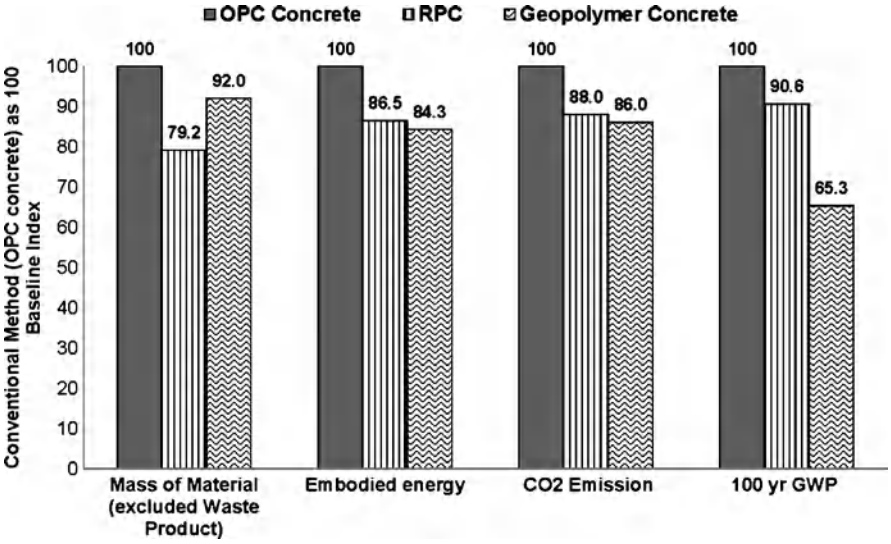

Fig. 5.6 EIC comparison for 40 m span bridge

required only thin panels of 30–50 mm thick (Fig. 5.7d) and weighs just 260 kg/m, a factor of four times lighter than the conventional reinforced concrete solution. The RPC wall was proof loaded with back filled soil up to 1.5 m and with an additional surcharge load of 25 kPa (Fig. 5.7e), 66% greater than the strength limit requirement and still it did not fail!

A comparison of the EIC results of the RPC retaining wall system against the conventional L-shaped retaining wall using Portland cement concrete and geopolymer concrete is given in Voo and Foster (2010) and presented in Fig. 5.8. In terms of material consumption, the RPC retaining wall consumes 76% less material than the conventional Portland cement concrete wall. In terms of the environmental indexes, the RPC wall requires less embodied energy and produces 48% less CO_2 emissions. In terms of the 100-years GWP, the RPC solution provides a reduction of 35%.For the geopolymer concrete solution, again less virgin materials are consumed than for the Portland cement design, it has 25% lower embodied energy and 20% less CO_2 gases are emitted. The geopolymer concrete solution has the least 100-year GWP in comparison with conventional Portland cement concrete and RPC solution.

5.4 Durability Design

The current design method for durability of concrete is based on deem-to-satisfy rules (i.e. minimum cover and crack width limitations) and the assumption that if these rules are met, the structure will have an adequate service life. However, many reinforced concrete structures deteriorate due to premature corrosion of steel

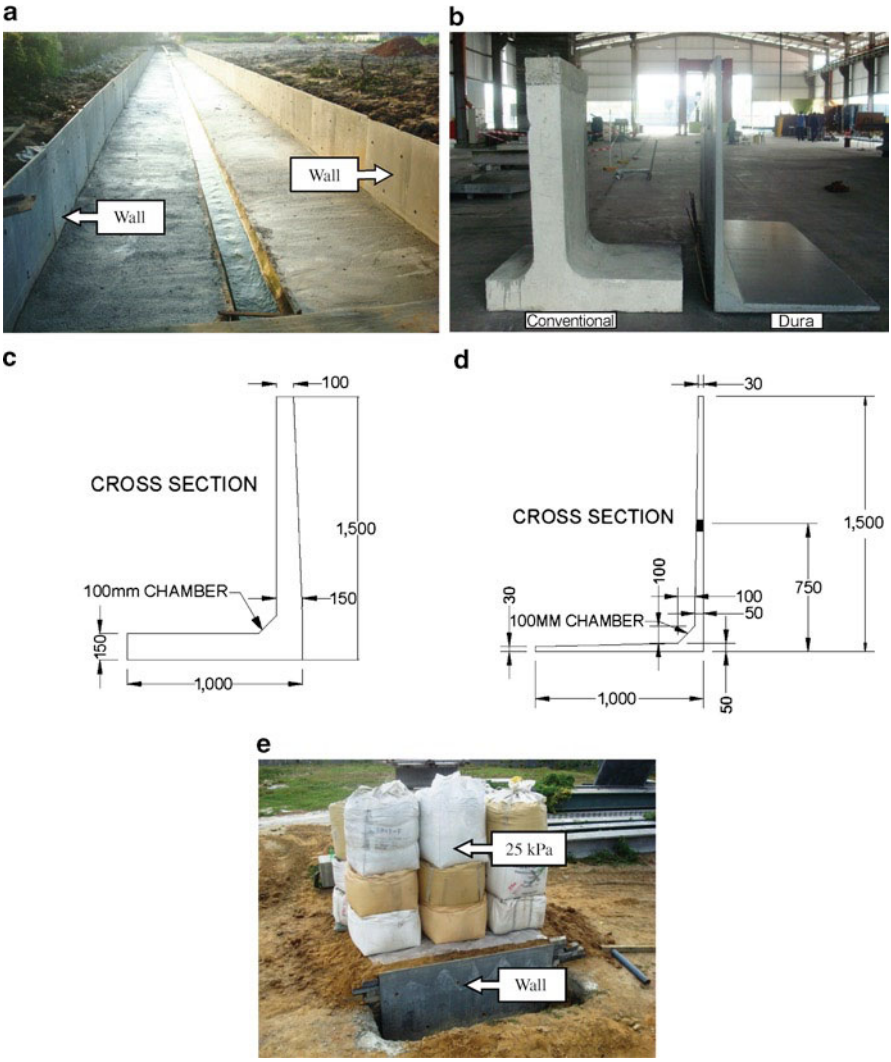

Fig. 5.7 (**a**) 90 m long monsoon drain using RPC retaining wall in Malaysia, (**b**) comparison of conventional precast L-shape retaining wall against RPC light weight retaining wall, (**c**) cross sectional details for conventional precast L-shape retaining wall, (**d**) cross sectional details for RPC retaining wall, and (**e**) load proof test of the RPC wall back filled and with a 25 kPa surcharge load

reinforcement, especially structures near coastal areas and in marine environments. Many bridges have been demolished due to heavy corrosion at ages of just 20–30 years and, in some cases, the maintenance costs far outweighed the initial construction costs (Tanaka et al. 2001).

Corrosion of steel reinforcement in concrete is due to an electrochemical process and must be taken into account in design and is dependent on the material quality

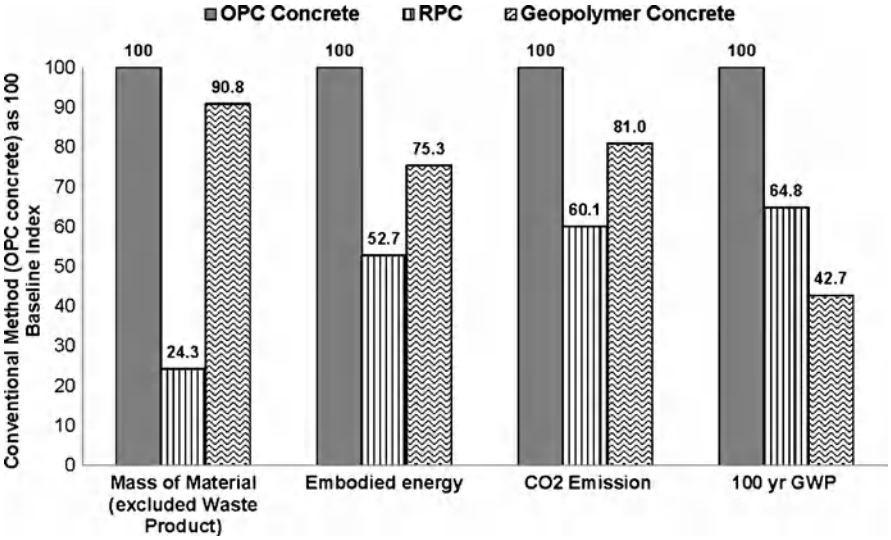

Fig. 5.8 EIC comparison for 1.5 m high retaining wall

and the environmental conditions. The high alkalinity nature of concrete passivates the reinforcement and protects it from corrosion (Tuutti 1982). However, if the concrete is permeable to the extent that carbonation reaches the concrete in contact with the steel or soluble chlorides can penetrate right up to the steel reinforcement, the reinforcement will be depassivated. Pitting corrosion and/or uniform surface corrosion will subsequently initiate.

The concept of chloride attack due to chloride ions permeating into reinforced concrete is illustrated in Fig. 5.9. The matrix of conventional concrete is analogous to that of a sponge (Fig. 5.9a) where the air voids, micro-pores, gel-pores and capillaries are inter-connected to each another. These micro-pores and gel water, which are generally formed in the concrete matrix, serve as routes for the movement of chloride ions. The pore structure in concrete depends on the type of concrete, mix proportion, type of formwork, placing technique, curing method, heat of hydration and material quality.

Unlike conventional concrete, RPC has a densely packed microstructure (Fig. 5.9b) in which the water/binder ratio is lowered to below the hydration limit (Water to Binder (W/B) ratio of 0.16 or less). Thus air voids are significantly reduced and are discontinuous in the matrix. Table 5.1 shows the chloride diffusion coefficient (D_c) of RPC is about an order less than for conventional concrete. For geopolymer concrete, the binder has densely packed microstructure with discontinuous air voids and micro pores. Only relatively few chloride diffusion studies have been published to-date for geopolymer concrete. Muntingh (2006) found that the D_c of geopolymer concrete is lower than 3×10^{-9} mm^2/s, i.e. more than 300 times lower than that of Portland cement concrete. Therefore in the presence of chloride ions at the surface of the concrete, the amount of time needed for the chloride ions to diffuse through geopolymer concrete and RPC's cover and initiate depassivation of the steel increases

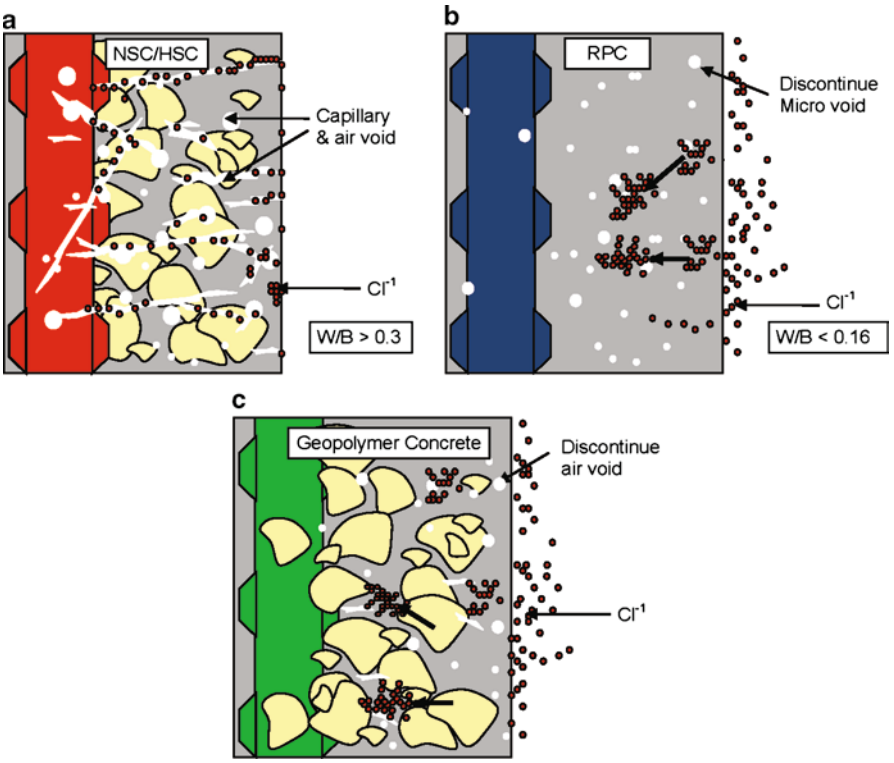

Fig. 5.9 Comparison of concrete matrix of (**a**) normal and high strength Portland cement concrete, (**b**) RPC, and (**c**) Geopolymer concrete

Table 5.5 Durability calculation in marine environment (for air-borne salt)

	HSC		Geopolymer concrete	RPC
Concrete cover, X (mm)	50	200	50	50
Airborne chloride concentration, C_s (kg/m^3)	6.4	6.4	6.4	6.4
Chloride threshold concentration, C_{ox} (kg/m^3)	1.2	1.2	1.2	1.2
Chloride diffusion coefficient, D_c (mm^2/s)	3×10^{-6}	3×10^{-6}	3×10^{-9}	6.7×10^{-8}
Time (years), t	**7.6**	**120**	**>1,000**	**340**
Time/120 years design life (%)	6.33	100	>1,000	283

dramatically. Of course, this assumption is only valid provided the geopolymer concrete and RPC is uncracked.

Taking the 40 m long bridge example discussed in the previous section, Voo and Foster (2010) provided a comparison between the durability of high strength concrete and RPC. The duration needed for chloride ions to diffuse through the concrete to initiate the reinforcement corrosion was undertaken using Fick's second law of diffusion. In this paper, diffusion time for geopolymer concrete is also assessed

and the results are presented in Table 5.5. For a 50 mm concrete cover, corrosion initiation of the reinforcing steel in a Grade 60 high strength concrete girder will occur after just after 7.6 years, on the other hand, a depassivation in RPC girder will not start for 340 years. More interestingly, for geopolymer concrete, depassivation will not theoretically begin for at least a 1,000 years if the concrete is uncracked (such as may occur in members in compression or in prestressed construction). This may partly explain why the ancient buildings built using geopolymer concrete technology such as the Roman's Coliseum and Pantheon are still standing even after 2,000 years! To meet a 120 year no maintenance criteria, a cover, in theory, of 200 mm would be required for high strength concrete girder. Thus without regular maintenance, or passive or active corrosion protection systems, many concrete structures in marine environments fail at an early age. In comparison, geopolymer concrete and RPC structures have potential for significant savings in maintenance costs and a longer working life leading to more sustainable solutions.

5.5 Conclusions

An overview is presented on the sustainability design approach. This design approach not only accounts for the limit states design but also takes into consideration the environmental impact and durability of the designed structures. Two examples of environmental impact calculations (EIC) for typical structures is provided for conventional Portland cement concrete, geopolymer concrete and RPC solutions. The EIC results show that geopolymer concrete and RPC structures are able to give immediate savings in terms of primary material consumption, embodied energy, CO_2 emissions and reduce the global warming potential (GWP). With regard to durability design, geopolymer concrete and RPC structures are shown to be superior over conventional Portland cement concrete. Geopolymer concrete and RPC structures have potentially significantly longer service life and design life without impacting on the integrity or safety of the structure. The geopolymer concrete and RPC technologies are confirmed to be greener construction materials and support the vision of a sustainable construction future.

The authors are of the opinion that in the future, geopolymer concrete and RPC technologies will contribute significantly to the realisation of sustainable development. These technologies will lower the impact on the environment while providing efficient structural performance and provide a minimum total life-cycle cost solution. In summary, geopolymer concrete and RPC technologies can provide the following benefits:

- Encourage the use of recycled materials (such as silica fume, fly ash and grounded granulated blast furnace slag);
- Prolong the service and design life of structures (and thus delay the need of new replacement that requires consumption of new materials, new budgeting costs and construction interruptions to the public);

- Minimum maintenance due to superior durability (providing immediate savings in costs for repair and rehabilitation);
- Reduction in overall CO_2 emissions, embodied energy and GWP through savings in material consumption for RPC and total elimination of the use of Portland cement for geopolymer concrete; and
- Saving in the total life-cycle cost, which helps to relieve the future national economies.

It is also recommended that objective measures using embodied energy and 100-year global warming potential (GWP) are introduced to enable designers to evaluate, quantify and compare relative environmental implications of their designs.

References

AS 1012.9 (1999) Determination of the compressive strength of concrete specimens. Standards Australia

AS 1012.10 (2000) Methods of testing concrete – determination of indirect tensile strength of concrete cylinders (Brazil or splitting test). Standards Australia

AS 1012.11 (2000) Methods of testing concrete – determination of the modulus of rupture. Standards Australia

AS 1012.12.1 (1998) Methods of testing concrete – determination of mass per unit volume of hardened concrete – rapid measuring method. Standards Australia

AS 1012.13 (1992) Methods of testing concrete – determination of the drying shrinkage of concrete for samples prepared in the field or in the laboratory. Standards Australia

AS 1012.16 (1996) Determination of creep of concrete cylinders in compression. Standards Australia

AS 1012.17 (1997) Methods of testing concrete – determination of the static chord modulus of elasticity and Poisson's ratio of concrete specimens. Standards Australia

AS 4672.1 (2007) Steel prestressing materials – general requirements. Standards Australia

AS5100.5 (2004) Bridge design, Part 5: Concrete. Standards Australia

ASTM C1202 (2005) Standard test method for electrical indication of concrete's ability to resist chloride ion penetration. ASTM, West Conshohocken

ASTM C1556 (2004) Standard test method for determining the apparent chloride diffusion coefficient of cementitious mixtures by bulk diffusion. ASTM, West Conshohocken

ASTM-C1018 (1997) Standard test method for flexural toughness and first crack strength of fiber reinforced concrete (using beam with third point loading). ASTM, West Conshohocken

BS1881-Part 122 (1983) Testing concrete – Method for determination of water absorption. British Standard, London

BS EN 12390-6 (2000) Testing hardened concrete – Tensile splitting strength of test specimens. British Standard, London

CEN (2001) EN 1991-2:2001. Eurocode 1: actions on structures. Part 2: Traffic load on bridges. Comite Europeen de Normalisation, Brussels

CEN (2004) EN 1992-1-1:2004. Eurocode 2: design of concrete structures – Part 1.1: General rules and rules for buildings. Comite Europeen de Normalisation, Brussels

Duxson P, Fernández-Jiménez A, Provis JL, Lukey GC, Palomo A, van Deventer JSJ (2007) Geopolymer technology: the current state of the art. J Mater Sci 42(9):2917–2933

Elrod M (1999) Greenhouse warming potential model. J Chem Educ 76(12):1702–1705

Fernández-Jiménez AM, Palomo A, López-Hombrados C (2006) Engineering properties of alkali-activated fly ash. ACI Mater J 103(2):106–112

Fling RS (1975) Energy consumption in cement and concrete. J Am Concr Inst 72(11):N3–N4
Forster P, Ramaswamy V, Artaxo P, Berntsen T, Betts R, Fahey DW, Haywood J, Lean J, Lowe DC, Myhre G, Nganga J, Prinn R, Raga G, Schulz M, Van Dorland R, Bodeker G, Boucher O, Collins WD, Conway TJ, Dlugokencky E, Elkins JW, Etheridge D, Foukal P, Fraser P, Geller M, Joos F, Keeling CD, Kinne S, Lassey K, Lohmann U, Manning AC, Montzka S, Oram D, O'Shaughnessy K, Piper S, Plattner GK, Ponater M, Ramankutty N, Reid G, Rind D, Rosenlof K, Sausen R, Schwarzkopf D, Solanki SK, Stenchikov G, Stuber N, Takemura T, Textor C, Wang R, Weiss R, Whorf T (2007) Changes in atmospheric constituents and in radiative forcing. In: Solomon S et al (eds) Climate change 2007: the physical science basis. Contribution of working group I to the 4th assessment report of the intergovernmental panel on climate change. Cambridge University Press, Cambridge
Fuglestvedt JS, Berntsen TK, Godal O, Sausen R, Shine KP, Skodvin T (2003) Metrics of climate change: assessing radiative forcing and emission indices. Climatic Change 58:267–331
Gourley JT, Johnson GB (2005) Developments in geo-polymer precast concrete. Proceeding of the fourth World Congress Geopolymer, France, pp 133–137
Graybeal BA (2006) Material property characterization of ultra-high performance concrete. US Department of Transportation, Federal Highway Administration, Publication No. FHWA-HRT-06-103
Huntzinger DN, Eatmon TD (2009) A life-cycle assessment of Portland cement manufacturing: comparing the traditional process with alternative technologies. J Clean Prod 17(7):668–675
JCI-S-001 (2003) Method of test for fracture energy of concrete by use of notched beam. Japan Concrete Institute
JCI-S-002 (2003) Method of test for load-CMOD curves of fibre reinforced concrete using of notched beam. Japan Concrete Institute
JSCE (2006) Recommendations for design and construction of ultra-high strength fiber reinforced concrete structures (draft). Concrete Committee of Japan Society of Civil Engineers (JSCE), JSCE Guideline for Concrete, No. 9
Kong DLY, Sanjayan JG (2010) Effect of elevated temperatures on geopolymer paste, mortar and concrete. Cement Concrete Res 40(2):334–339
Li Z, Ding Z, Zhang Y (2004) Development of sustainable cementitious materials. International workshop on sustainable development and concrete technology, Beijing, 20–21 May
Muntingh Y (2006) Durability and diffusive behaviour evaluation of geopolymeric material. M.Sc. Thesis, University of Stellenbosch, South Africa
Ng TS, Foster SJ (2008) Development of high performance geopolymer concrete. In: Futures in mechanics of structures and materials. Taylor & Francis Group, Toowoomba
Palomo A, Blanco MT, Granizo ML, Putertas F, Vazquez T, Grutzeck MW (1999) Chemical stability of cementitious materials based on Metakaolin. Cement Concrete Res 29(7):997–1004
Poon WK, Voo YL, Yap SK (2009) Thin protective wall panel made from 150 MPa ultra-high performance ductile concrete (UHPdC-DURA®). In: Proceedings of the 10th international conference on concrete engineering and technology 2009 (CONCET 2009), Shah Alam, Kuala Lumpur, 2–4 March
Provis JL, Lukey GC, van Deventer JSJ (2005) Do geopolymers actually contain nanocrystalline zeolites? - A re-examination of existing results. Chem Mater 17(12):3075–3085
Rangan BV (2008) Fly ash based geopolymer concrete. Research Report GC 4, Curtin University of Technology, Perth
Richard P, Cheyrezy MH (1994) Reactive powder concretes with high ductility and 200–800 MPa compressive strength. ACI SP 144(24):507–518
Song X (2007) Development and performance of class F fly ash based geopolymer concretes against sulphuric acid attack. PhD dissertation, University of New South Wales, Sydney
Struble J, Godfrey J (2004) How sustainable is concrete? In: International workshop on sustainable development and concrete technology, Beijing, 20–21 May, pp 201–211
Tanaka Y, Kawano H, Watanabe H, Nakajo T (2001) Chloride-induced deterioration and its influence on load carrying capacity of post-tensioned concrete bridges. Proceedings of 3rd international conference on concrete under severe conditions, Vancouver, pp 495–502

Tuutti K (1982) Corrosion of steel in concrete. Swedish Cement and Concrete Research Institute, Stockholm

US EPA (1994) Alternative control techniques document – NO_x emissions from cement manufacturing, U.S. Environmental Protection Agency, Office of Air and Radiation, Office of Air Quality Planning and Standards, Report No. EPA-453/R-94-004, North Carolina

van Jaarsveld JGS, van Deventer JSJ, Lorenzen L (1997) The potential use of geopolymeric materials to immobilize toxic metals: Part I. Theory and applications. Miner Eng 10(7):659–669

Voo YL, Foster SJ (2009) Reactive powder concrete: analysis and design of RPC girders. Lambert Academic Publishing, Saarbrücken

Voo YL, Foster SJ (2010) Characteristics of ultra-high performance 'ductile' concrete and its impact on sustainable construction. IES J A Civ Struct Eng 3(3):168–187

Voo YL, Foster SJ, Gilbert RI (2006) Shear strength of fiber reinforced reactive powder concrete prestressed girders without stirrups. J Adv Concrete Technol 4(1):123–132

Witherspoon R, Wang H, Aravinthan T, Omar T (2009) Energy and emissions analysis of fly ash based geopolymers. Society for sustainability & environmental engineering international conference – solutions for a sustainable planet, Melbourne, 22–24 Nov

Xie Y, Liu Y, Long G (2008) Long term durability of cement based materials with very low w/b. J Wuhan Univ Tech – Mater Sci Ed 23:303–308

Chapter 6
Low-Carbon Concrete Using Ground Granulated Blast-Furnace Slag and Fly Ash

Koji Sakai, Takeju Matsuka, and Yasunori Suzuki

Abstract In this study, the effect of ground granulated blast-furnace slag and fly ash on fresh properties, strength properties and durability was examined. In addition, the effect of those admixtures on the reductions of CO_2 was clarified. From the test results, it can be concluded that when the ground granulated blast furnace slag and fly ash were used (1) the early strength of concrete decreased compared with the concrete without the admixtures, (2) regarding the fresh properties, the compressive strength of concrete at the age of 28 days and the durability, the same performance as concrete without admixtures was obtained. The amount of CO_2 emission per 1 N/mm^2 of concrete compressive strength decreased when the amount of fly ash and ground granulated blast-furnace slag increased.

6.1 Introduction

In recent years, the target of reducing greenhouse gas emissions has been set at world level. Therefore, the importance of environmental considerations is increasing more and more in every field. In Japan, a legally binding commitment to reduce

K. Sakai (✉)
Safety Systems Construction Engineering, Kagawa University, 2217-20 Hayashi-cho, Takamatsu, Kagawa 761-0396, Japan
e-mail: sakai@eng.kagawa-u.ac.jp

T. Matsuka
Technical Research Institute, Hazama Corporation, 515-1 Karima, Tsukuba, Ibaraki 305-0822, Japan
e-mail: matsuka@hazama.co.jp

Y. Suzuki
Cement/Concrete Research Laboratory, Sumitomo Osaka Cement Co., Ltd, 585 Houfu-cho, Funabashi, Chiba, Japan
e-mail: yasuzuki@soc.co.jp

M.N. Fardis (ed.), *Innovative Materials and Techniques in Concrete Construction: ACES Workshop*, DOI 10.1007/978-94-007-1997-2_6,

Table 6.1 Combination of admixture replacement ratio

		Ground granulated blast-furnace slag replacement ratio (%)				
		0	10	20	30	40
Fly ash replacement ratio (%)	0	○	○	○	○	○
	10	○	○	○	○	–
	20	○	○	○	○	–

the overall standard emission of greenhouse gases by 6% by 2012 with respect to the level of 1990 was established as a short-term goal. Reductions of over 25% by 2020 and 80% by 2050 have also been adopted as mid-term and long-term goals. Amid the active efforts of all industries toward the development of low carbon technology to achieve these goals, it is clear that the construction and concrete sectors alone cannot continue their activities with present greenhouse gas emission values. It is now necessary to consider environmental performance as one of the essential performance requirements.

High strength and high durability have been regarded as the ultimate goals of conventional concrete. However, concrete generates extremely large environmental loads. Therefore, 'low-carbon performance' is required as a new performance in addition to conventional high strength and high durability when developing new concrete. Cement is a material that emits the largest amount of CO_2 among the constituent materials of concrete. Reducing the cement content per unit amount of concrete is an effective means of reducing CO_2. One such example is the use of admixtures such as ground granulated blast-furnace slag and fly ash. However, the concrete of high replacement ratios of the admixture is considered to remarkably decrease the performance of early strength and the crack resistance. Thus, it is realistic for reducing CO_2 to versatilely use cement with low replacement ratios of admixture. That is, it will become more important to comprehensively evaluate the basic and environmental performance of concrete in various cases.

In this study, the effect of ground granulated blast-furnace slag and fly ash on fresh properties, strength properties and durability was examined. In addition, the effect of those admixtures on the reduction of environmental impact was clarified.

6.2 Outline of Experiments

Table 6.1 gives the combinations of admixture replacement ratio. Cement from 0% to 20% and from 0% to 40% in mass was replaced with fly ash and ground granulated blast-furnace slag, respectively.

6.2.1 Materials

Table 6.2 shows the types and physical properties of concrete materials used in this study.

Table 6.2 Constituent materials of concrete

Materials	Type	Symbol	Physical properties
Cement	Ordinary portland cement	C	Density: 3.15 g/cm³ Specific surface area: 3,430 cm²/g
Fly ash	Class II fly ash	FA	Density: 2.25 g/cm³ Specific surface area: 4,150 cm²/g Ignition loss: 0.7%
Ground granulated blast-furnace slag	Ground granulated blast-furnace slag 4,000	BS	Density: 2.89 g/cm³ Specific surface area: 4,170 cm²/g
Fine aggregate	River sand	S	Density: 2.62 g/cm³ Absorption: 1.12% Finess modulus: 2.91
Coarse aggregate	Sand stone	G1	Maximum size: 20 mm Density: 2.72 g/cm³ Absorption: 0.58% Finess modulus: 7.07
		G2	Maximum size: 15 mm Density: 2.71 g/cm³ Absorption: 0.77% Finess modulus: 5.98
Chemical admixture	High-range AE water reducing agent	–	Polycarboxylic acid ether-system
	Air entraining agent	–	Denatured rosin acid compound-system anionic surface active agent

6.2.2 *Production and Mix Proportions of Concrete*

Concrete was produced in a laboratory at a temperature of 20°C. With a 100-liter twin-shaft batch mixer, concrete of 60 l in mixing volume was produced.

The water-binder ratio (*W*/*B*) and fine aggregate percentage (*s*/*a*) were kept constant at 40% and 46%, respectively. The high-range air-entraining (AE) water reducing agent was also constant at 0.8% of the binder content. Table 6.3 indicates the mix proportions of the concrete. When mixing concrete, the slump target was 12.0 ± 2.5 cm, the air content target was 4.5 ± 1.0%.

6.2.3 *Experimentally Measured Properties*

Slump, air content, bleeding and setting tests were conducted for fresh concrete. These tests were carried out in compliance with Japanese Industrial Standard (JIS).

For hardened concrete, compressive strength, splitting tensile strength, autogenous shrinkage, drying shrinkage and carbonation were tested. The tests were carried out in compliance with JIS and Japan Concrete Institute (JCI) standard (Japan Institute of Concrete 1996). In addition, when the autogenous shrinkage strain was

Table 6.3 Mix proportions of concrete

W/(C+FA+BS) (%)	Fly ash replacement ratio (%)	Ground granulated blast-furnace slag replacement ratio (%)	s/a (%)	Quantity of material per unit volume of concrete (kg/m³)										
				Water	Cement	Fly ash	Ground granulated blast-furnace slag	Fine aggregate	Coarse aggregate		High-range AE water reducing agent		Air entraining agent (100 times dilution)	
				W	C	FA	BS	S	G1	G2	(C+FA+BS)×%	(kg/m³)	(C+FA+BS)×%	(kg/m³)
40	0	0	46.0	140	350	0	0	848	620	412	0.80	2.80	0.12	0.42
		10		138	311	0	35	851	623	414	0.80	2.77	0.12	0.42
		20		136	272	0	68	855	625	415	0.80	2.72	0.12	0.41
		30		135	238	0	102	853	624	415	0.80	2.72	0.12	0.41
		40		133	200	0	133	859	628	417	0.80	2.66	0.12	0.40
	10	0		135	304	34	0	854	624	415	0.80	2.70	0.25	0.85
		10		130	260	33	33	864	632	420	0.80	2.61	0.25	0.82
		20		128	224	32	64	867	634	421	0.80	2.56	0.25	0.80
		30		126	189	32	95	871	637	423	0.80	2.53	0.20	0.63
	20	0		131	262	66	0	858	627	417	0.80	2.62	0.40	1.31
		10		127	223	64	32	865	633	420	0.80	2.55	0.40	1.28
		20		124	186	62	62	871	637	423	0.80	2.48	0.40	1.24
		30		121	152	61	91	877	641	426	0.80	2.43	0.35	1.06

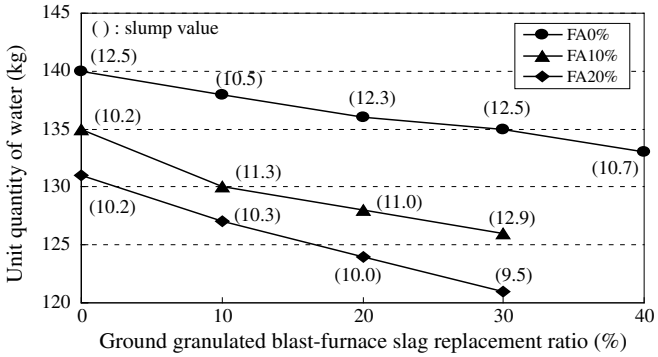

Fig. 6.1 Unit quantity of water

measured, an embedded low-rigidity strain gage was used. The autogenous strain was taken as the measured strain minus the temperature strain (thermal expansion coefficient: 10 μ/°C). The measurement of autogenous shrinkage began at the initial setting time of concrete.

6.3 Results and Discussion

6.3.1 Fresh Concrete

6.3.1.1 Unit Water Content

Figure 6.1 shows the unit water content of each mix proportion. The values in parentheses are the slump values. When the fly ash and ground granulated blast-furnace slag replacement ratios increase, the unit water content decreases. This was caused by the ball-bearing effect of fly ash, and the fact that the specific surfaces of fly ash and ground granulated blast-furnace slag were higher than that of cement.

6.3.1.2 Amount of AE Agent

Figure 6.2 shows the amount of the air-entraining (AE) agent of each mix proportion. The values in parentheses are the air content. When the fly ash was used, the AE agent increased. It is known that, when mixing fly ash, it is necessary to increase the amount of AE agent to secure a certain amount of air due to the adsorption of unburned carbon contained in fly ash. When both fly ash and ground granulated blast-furnace slag were used, however, the amount of AE agent tended to decrease with an increase in the ground granulated blast-furnace slag replacement

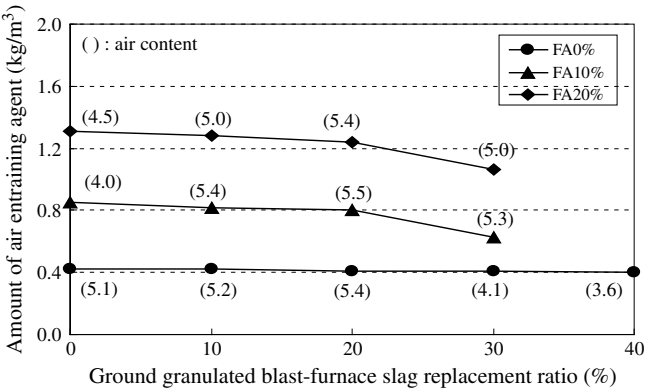

Fig. 6.2 Amount of air entraining agent

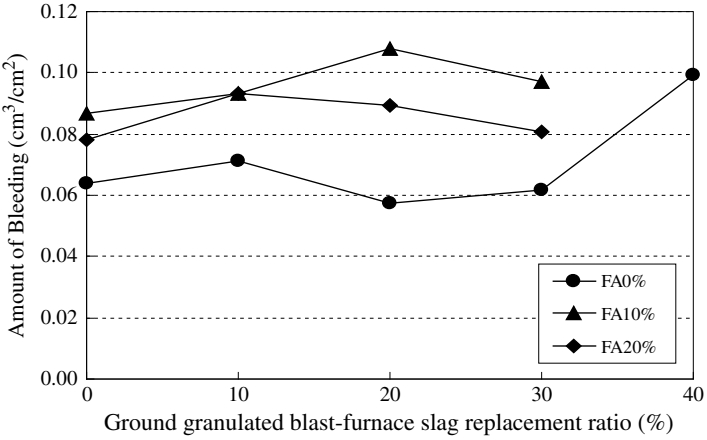

Fig. 6.3 Amount of bleeding

ratio. This is because the fly ash content per unit volume of concrete decreases with an increase in the ground granulated blast-furnace slag replacement ratio.

6.3.1.3 Bleeding

Figure 6.3 presents the results of the bleeding test. Bleeding ranges from 0.057 to 0.108 cm^3/cm^2. As to the effects of combinations of admixtures on the amount of bleeding, the contribution of each material is unclear. The effect of the increase in the ground granulated blast-furnace slag and fly ash replacement ratio on bleeding was believed to be due to the unit water content, unit powder content and moisture adsorption of each binder, although it is difficult to evaluate the extent of their respective effects quantitatively.

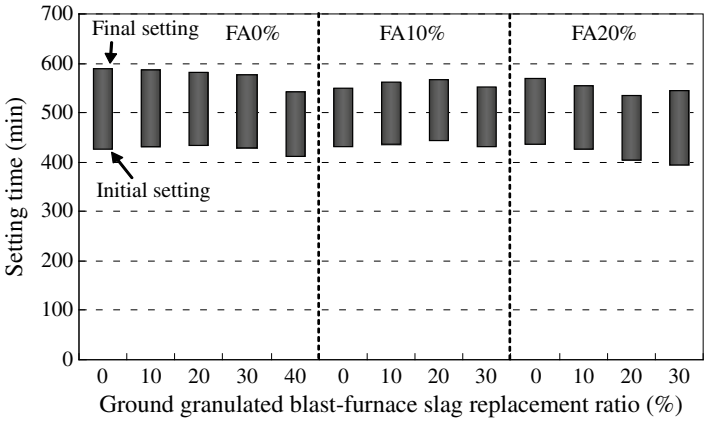

Fig. 6.4 Setting time

6.3.1.4 Setting Time

Figure 6.4 presents the setting time. When the ground granulated blast-furnace slag was used, initial and final setting show a tendency to take [lace earlier when the ground granulated blast-furnace slag replacement ratio increases. Since the setting times are generally reported to increase with an increase in the ground granulated blast-furnace slag replacement ratio (Architectural Institute of Japan 1992), the results in this study do not agree with the generally reported tendencies. It is thought that this is because the unit cement content in the present study is very low. However, a significant difference was not observed in the comparison in the presence of admixture. The initial and final setting times of all mix proportions are in the range of 395–444 min and 535–590 min, respectively.

6.3.2 Hardened Concrete

6.3.2.1 Compressive Strength

Figure 6.5 shows the results of the compressive strength test for concrete. Figure 6.6 shows the rate of change in the compressive strength of each mix proportion at an age of 3 days with respect to that of concrete containing no admixtures at the same age.

The compressive strength of concrete at 3 days decreases with an increase in the fly ash and ground granulated blast-furnace slag replacement ratio. The compressive strengths of concrete with the fly ash replacement ratio of 20% with no ground granulated blast-furnace slag are lower by 26% than those of concrete without admixtures. The compressive strengths of concrete with a ground granulated blast-furnace slag replacement ratio of 40% with no fly ash are lower by 36%. When fly ash and ground granulated blast-furnace slag replacement ratios of 20% and 30%,

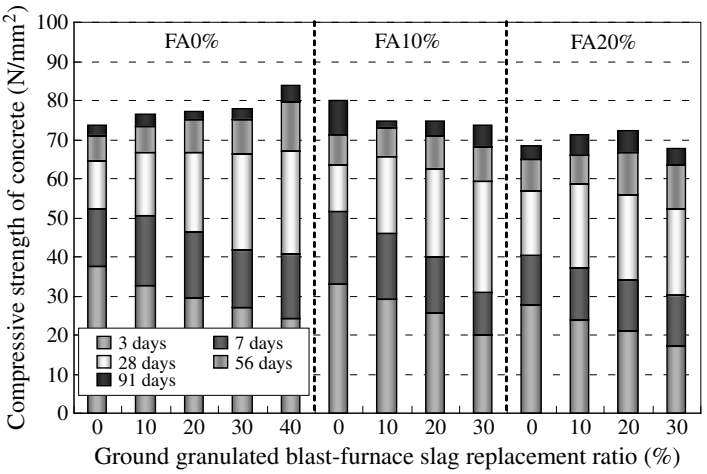

Fig. 6.5 Compressive strength

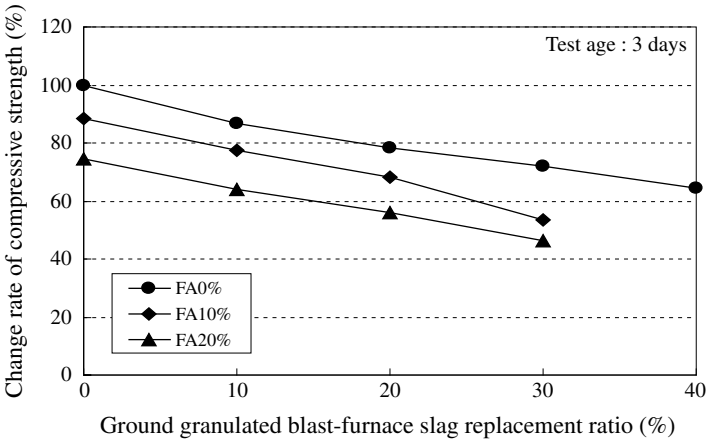

Fig. 6.6 Change rate of compressive strength (at 3 days)

respectively, were used, the loss in the compressive strength of concrete is greatest. The compressive strength of concrete is lower by 54% compared with that for no admixtures. The loss in the compressive strength at 3 days due to the inclusion of admixtures results from the reduction in cement content.

Figure 6.7 shows the rate of change in the compressive strength of concrete at 28 days. The loss in the compressive strength due to the inclusion of fly ash and ground granulated blast-furnace slag is smaller at 28 days than at 3 days. This can be attributed to the pozzolanic reaction of fly ash and latent hydraulicity of ground granulated blast-furnace slag. In addition, the compressive strength of concrete with fly ash and slag replacement ratios of 20% and 30%, respectively, is 19%. lower than in the case without the admixtures.

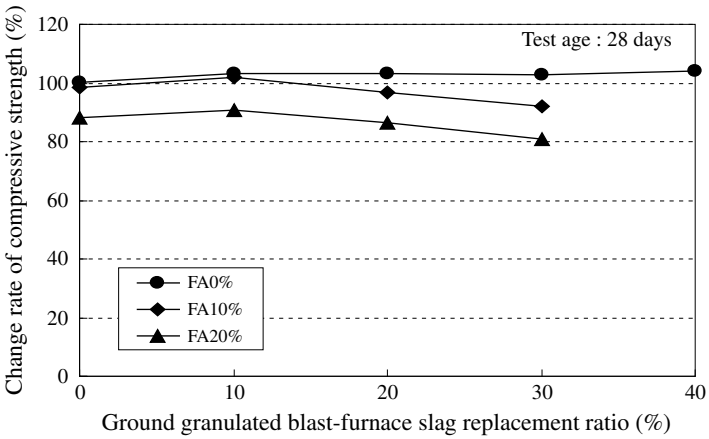

Fig. 6.7 Change rate of compressive strength (at 28 days)

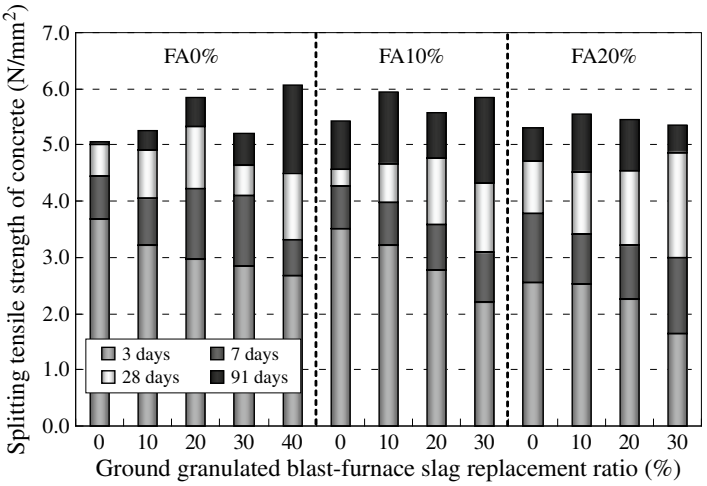

Fig. 6.8 Splitting tensile strength

6.3.2.2 Splitting Tensile Strength

Figure 6.8 depicts the results of the splitting tensile test for concrete. The results show tendencies similar to those of compressive strength. When fly ash and ground granulated blast-furnace slag replacement ratios of 20% and 30%, respectively, were used, the splitting tensile strength of concrete after 3 days and after 28 days was lower by 55% and 3% than for concrete without the admixtures.

Figure 6.9 shows the relationship between the splitting tensile strength and the compressive strength of concrete. This figure also shows the results calculated using the formula in the Standard Specifications of the Japan Society of Civil Engineers

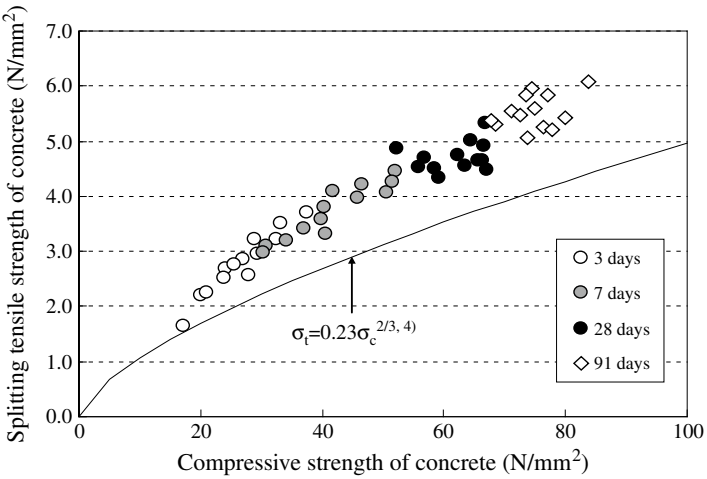

Fig. 6.9 Relationship of splitting tensile strength and compressive strength

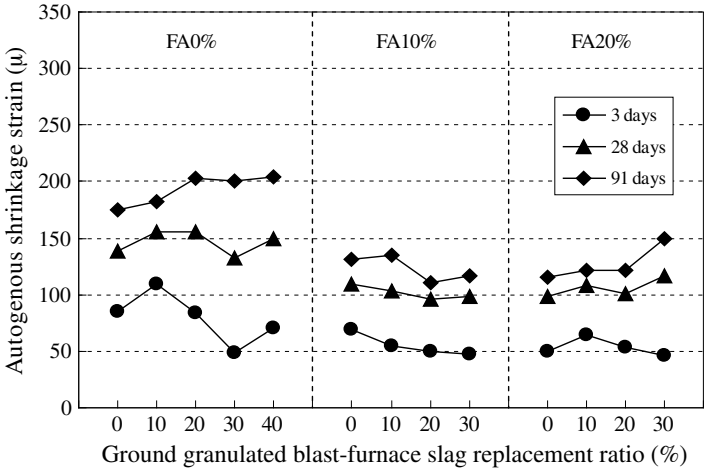

Fig. 6.10 Autogenous shrinkage strain

(Japan Society of Civil Engineers 2007). The values obtained in this study were greater than those obtained using the standard formula.

6.3.2.3 Autogenous Shrinkage Strain

Figure 6.10 shows the autogenous shrinkage strain of concrete. While the use of fly ash tends to reduce the autogenous shrinkage strain, the use of ground granulated blast-furnace slag tends to increase it. Ground granulated blast-furnace slag densifies the microstructure of concrete, presumably reducing the curvature radius of menisci formed in pore water, thereby increasing the autogenous shrinkage strain (Miura et al. 1995).

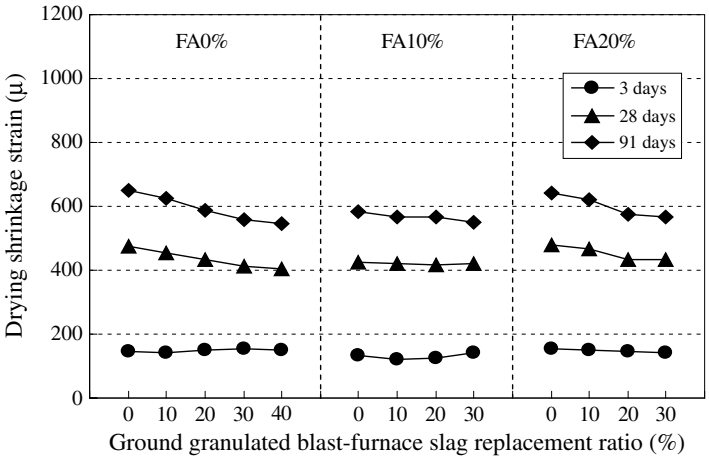

Fig. 6.11 Drying shrinkage strain

6.3.2.4 Drying Shrinkage Strain

Figure 6.11 shows the drying shrinkage strain of concrete. Whereas the effect of fly ash is not clear, the drying shrinkage strain of concrete tends to decrease with an increase in the ground granulated blast-furnace slag replacement ratio. This is presumably because the unit water content was reduced with an increase in the ground granulated blast-furnace slag replacement ratio and the microstructure of concrete was densified by the latent hydraulicity of ground granulated blast-furnace slag.

6.3.2.5 Carbonation Depth

Figure 6.12 presents the results of the accelerated carbonation test up to 91 days. As shown in this figure, the carbonation depth increases with an increase in the fly ash and ground granulated blast-furnace slag replacement ratios. This was thought to be due to the decrease in the amount of calcium hydroxide in the concrete.

6.3.3 Environmental Assessment of the Use of Admixtures

6.3.3.1 Calculation Method

The inventory data used in this study were referred to the Recommendations of Environmental Performance Verification for Concrete Structures (Japan Society of Civil Engineers 2005). Table 6.4 gives the unit-based CO_2 emission of concrete materials. In this study, because the amount of the AE agent used was minimal, the AE agent was excluded from the calculation of the CO_2 emission.

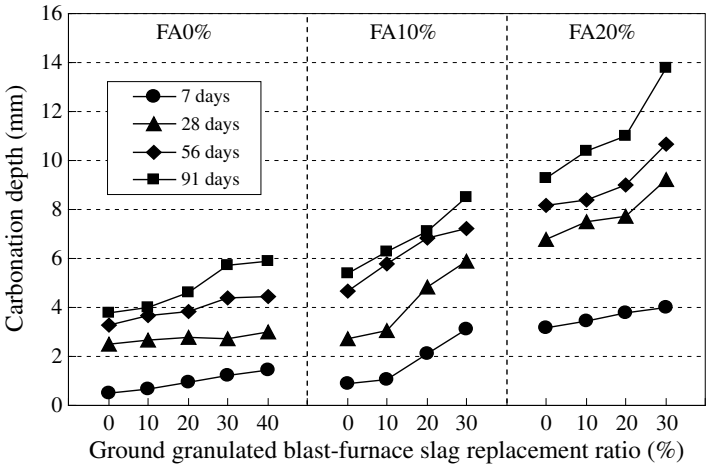

Fig. 6.12 Carbonation depth

Table 6.4 Unit-based CO_2 emission of concrete materials

Materials	Ordinary portland cement	Fly ash	Ground granulated blast-furnace slag	Fine aggregate	Coarse aggregate	High-range AE water reducing agent
CO_2 emission (kg-CO_2/t)	765.5	17.9	26.5	3.7	2.9	187.5

6.3.3.2 CO_2 Emission

Figure 6.13 shows the CO_2 emissions of each mix proportion. The CO_2 emission decreases with an increase in the fly ash and ground granulated blast-furnace slag replacement ratio. The CO_2 emissions were in the range of 127–275 kg/m^3.

Figure 6.14 shows the ratios of CO_2 emissions to the compressive strength of concrete, which express the amount of CO_2 emission to obtain a compressive strength of 1 N/mm^2. A smaller value therefore represents a concrete with a smaller environmental load. At 3 days, no significant differences are observed in the ratios of CO_2 emissions to the compressive strength of concrete. At later ages, however, the inclusion of admixtures reduces these ratios. From 7 days onwards, the ratio decreases with an increase in the fly ash and ground granulated blast-furnace slag replacement ratios. This means that, by using both fly ash and ground granulated blast-furnace slag, the environmental load reduction effect can be maximized over time. If early compressive strengths can be ensured, then it is possible in the future to reduce the CO_2 emission of concrete per unit compressive strength from an early age of concrete.

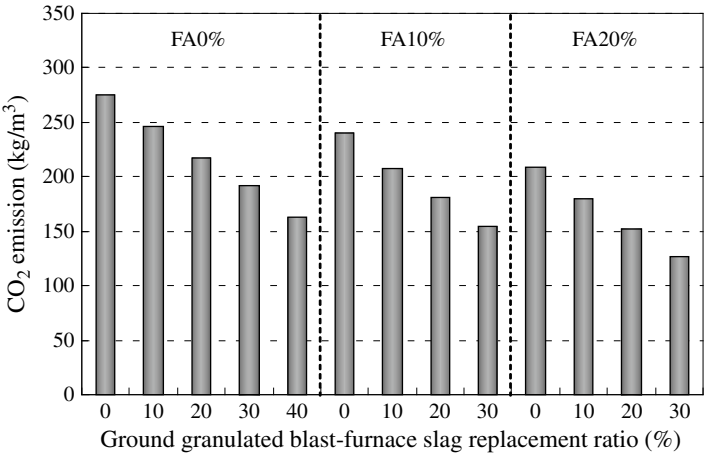

Fig. 6.13 CO_2 emission

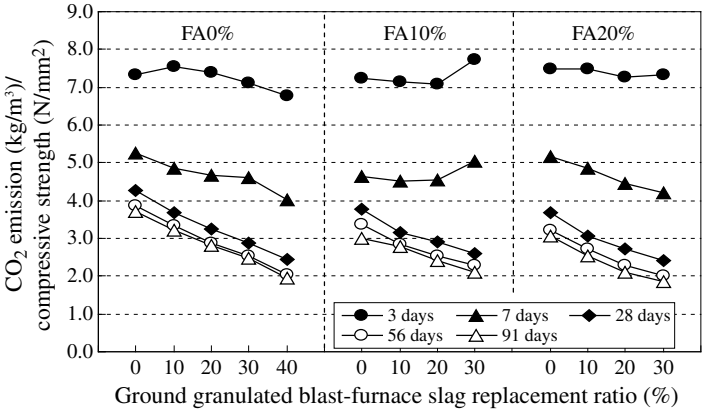

Fig. 6.14 Ratio of compressive strength to CO_2 emission

6.4 Conclusions

From this study, the following conclusions can be drawn:

1. The use of both fly ash and ground granulated blast-furnace slag allows significant reduction in the unit water content but increases the amount of necessary air-entraining agent.
2. The use of both fly ash and ground granulated blast-furnace slag affects the amount of bleeding but scarcely affects the setting times of concrete.
3. The use of both fly ash and ground granulated blast-furnace slag reduces the compressive and splitting tensile strengths of concrete by at most 54% and 55%,

respectively, at 3 days, but these losses are reduced to at most 19% and 3%, respectively, at 28 days.

4. The use of both fly ash and ground granulated blast-furnace slag reduces the autogenous shrinkage strain and drying shrinkage strain but increases the carbonation depth of concrete, when compared with concrete without these admixtures.
5. The use of both fly ash and ground granulated blast-furnace slag decreases the amount of CO_2 emission per 1 N/mm^2 of concrete compressive strength.

References

Architectural Institute of Japan (1992) State of the art report on concrete using ground granulated blast furnace slag

Japan Institute of Concrete (1996) Report of committee for autogenous shrinkage research

Japan Society of Civil Engineers (2005) Recommendation of environmental performance verification for concrete structures (Draft), Concrete Library 125

Japan Society of Civil Engineers (2007) Standard specifications for concrete structures-design

Miura T, Tazawa E, Miyazawa S, Yasutoshi A (1995) Influence of ground granulated blast-furnace slag on autogenous shrinkage of concrete. Collect Concr Eng Pap 17(1):359–364

Chapter 7
Recycled Aggregate Concrete for Structural Use – An Overview of Technologies, Properties and Applications

Snežana B. Marinković, Ivan S. Ignjatović, Vlastimir S. Radonjanin, and Mirjana M. Malešev

Abstract By the end of the twentieth century generation of huge amounts of waste became one of the biggest environmental problems in the majority of the world. Construction and demolition waste (C&D) makes almost half of the total industrial waste. On the other hand, consumption of natural aggregate as the largest concrete component is constantly and rapidly increasing with the increase in the production and utilization of concrete. Recycling represents one way to convert a waste product into a resource. It has the potential to reduce the amount of waste disposed of in landfills and preserve natural resources while limiting environmental disturbance. This paper presents a review of traditional and advanced production technologies that make recycling of concrete in a completely closed loop technically feasible. The specific features of recycled aggregate concrete (RAC) mix proportioning methods affected by the recycled aggregate (RA) properties are presented. The mechanical, rheological and durability properties of RAC based on up-to-date research are discussed from the point of the potential of its utilization in structural concrete. The current state of technical rules and standards in this area is briefly presented. The future research and necessary actions in facilitating the more extensive use of RAC in concrete structures are also pointed out.

S.B. Marinković (✉) • I.S. Ignjatović
Faculty of Civil Engineering, University of Belgrade, Bulevar kralja Aleksandra 73, Belgrade 11000, Serbia
e-mail: sneska@imk.grf.bg.ac.rs; ivani@imk.grf.bg.ac.rs

V.S. Radonjanin • M.M. Malešev
Department for Civil Engineering, Faculty of Technical Sciences, University of Novi Sad, Trg Dositeja Obradovića 6, Novi Sad 21000, Serbia
e-mail: radonv@uns.ac.rs; miram@uns.ac.rs

M.N. Fardis (ed.), *Innovative Materials and Techniques in Concrete Construction: ACES Workshop*, DOI 10.1007/978-94-007-1997-2_7,

7.1 Introduction

Production and utilization of concrete as a building material is constantly increasing nowadays. This results in increase of the consumption of natural aggregate as the largest concrete component. It is estimated that today's world concrete production is about six billion tons per year, i.e. one ton per person per year (ISO 2005). According to a European Environment Agency Report (European Environment Agency 2008), three billion tons of aggregate are produced each year in the countries of the European Union. In the United States two billion tons of aggregate are produced each year and the production is expected to increase to more than 2.5 billion tons per year by the year 2020 (FHWA 2004). This situation leads to a question about the availability of natural aggregate's sources and many European countries have already placed taxes on the use of virgin aggregates.

On the other hand, demolishing old and deteriorated infrastructures and replacing them with new ones are frequent phenomena especially in urban areas today. The main reasons for demolishing existing buildings are change of their purpose, ageing of structures, expansion of traffic directions and increase in traffic loads, natural disasters etc. For example, about 850 million tons of construction and demolition (C&D) waste are generated in the EU per year, which represent 31% of the total waste generation (Fisher and Werge 2009).

The most common method of managing this material is through its disposal of in landfills. According to ETC/SCP Working Paper (Fisher and Werge 2009), recycling rates differ a lot between European countries, ranging from over 90% in Denmark, Finland and Netherlands to less than 20% in Spain, the Czech Republic and Hungary (here the recycling rate is the amount of recycled C&D waste in percentage of the total amount of generated waste). Despite the fact that concrete makes a large part of C&D waste, it makes a small part of the waste that is recycled (20% in Netherlands, 5% in Hungary, 2% in Poland). Only in the Czech Republic concrete makes about 45% of the recycled C&D waste. As the recycling rates on average are small, huge deposits of C&D waste are created and consequently farmland and other types of available land are decreasing. For that reason in developed countries, restrictive laws in the form of prohibitions or special taxes for creating waste areas were brought into practice.

Recycling waste concrete for producing recycled aggregates represents one way to convert a waste product into a resource. It has the potential to reduce the amount of C&D waste disposed of in landfills and to preserve natural resources. But despite all the research performed in this area, recycled aggregates from waste concrete are being mostly used in lower quality product applications such as backfills and road sub-base materials. Although in some countries standards do allow the utilization of recycled aggregates from waste concrete in structural concrete, it remains limited to less than 1% of the amount of aggregates used in structural concrete (fib Task Group 3.3 2004).

This paper presents a review of traditional and advanced production technologies for recycling demolished concrete and producing recycled concrete aggregate (RCA). The specific features of mix proportioning methods for concrete made with such recycled aggregate-recycled aggregate concrete (RAC) are presented.

The mechanical, rheological and durability related properties of RAC based on up-to-date research are discussed from the point of the potential of its utilization in structural concrete. The current state of technical rules and standards in this area is briefly presented. The future research and necessary actions in facilitating the more extensive use of RAC in concrete structures are also pointed out.

7.2 Production Technologies and Properties of Recycled Concrete Aggregate (RCA)

Recycled aggregates from demolished concrete (RCA) are generally produced by crushing, screening and removing the contaminants such as reinforcement, paper, wood, plastics, gypsum (by magnetic separation, water cleaning, air-sifting). Crushing (primary and secondary) is performed using a combination of compressive-type and impact-type crushers, such as the jaw crusher and impact crusher. Figure 7.1 shows the typical recycling process in stationary recycling plants, which are suitable as recycling centers in urban areas.

Mobile recycling plants are typically used for demolition sites with large amount of homogenous waste which is going to be reused on site (rebuilding of roads and

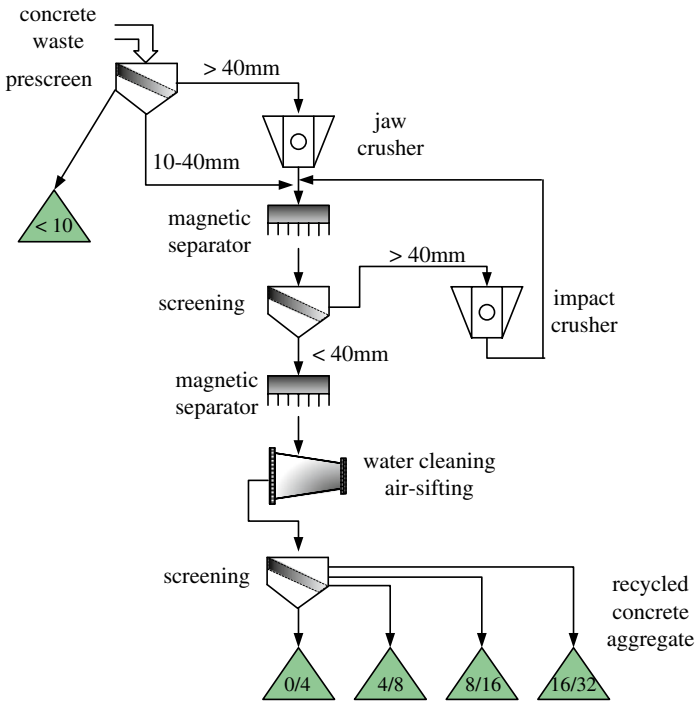

Fig. 7.1 Production technology in stationary recycling plant

highways, large industrial facilities). In mobile recycling plants processing is limited to one-stage crushing, magnetic separation and screening.

When demolished concrete is crushed, a certain amount of mortar and cement paste from original concrete remains attached to stone particles in recycled aggregate. Because of that attached mortar, recycled aggregates have lower density, higher porosity and higher water absorption than natural aggregates, and these properties of recycled aggregates affect the properties of concrete as well. To improve the quality of RCA and to make it comparable to natural aggregate it is necessary to reduce or completely remove the attached mortar. This is possible to achieve with increasing the number of treatment processes in recycling plants as it increases, the content of attached mortar decreases. But at the same time the recovery percentage of RCA decreases as large amount of powder by-products is produced. Therefore, special technologies for efficient production of high quality RCA without the attached mortar are needed.

Most of these advanced recycling technologies are developed in Japan (Shima et al. 2005; Tomosawa et al. 2005). They are based on grinding or rubbing of the concrete lumps crushed to a smaller size of 40–50 mm and heated to a temperature of 300°C. At that temperature cement paste dehydrates and becomes brittle and it can be separated from the original aggregate particles in the mill. For example, in the heating and rubbing method proposed by Shima et al. (2005) the average ratios of aggregate recovery and powder generation are 35% of coarse aggregate, 30% of fine aggregate and 35% of fine powder, respectively. Another similar technology was proposed by Mulder et al. (2006), but with higher heating temperature. This technology involves a rotary kiln in which the uncontaminated small pieces of concrete rubble are thermally treated at a temperature of about 700°C. This temperature is necessary to completely dehydrate the cement paste. After treatment, only 2% of cement paste remains attached to original coarse and fine aggregate, practically original components are set free. The recovery percentage is 45% of coarse aggregate, 35% of fine aggregate, 13% of cement paste, 1% is steel reinforcement and 6% is hydration water emitted as vapour.

As with natural aggregates (NA), the quality of RCA in terms of size distribution, water absorption, abrasion etc. needs to be assessed before using it as aggregate for structural concrete. Based on up-to-date research, general conclusions about the properties of RCA obtained by traditional two-stage crushing process, compared to the properties of NA are:

- RCA generally fulfils the size distribution requirements for natural aggregate (Yang et al. 2008; Hansen 1992; Exteberria et al. 2007; Sagoe-Crentsil et al. 2001; Poon and Lam 2008; Khatib 2005),
- density is decreased up to 10% compared to NA (Hansen 1992; Sagoe-Crentsil et al. 2001; Poon and Lam 2008; Sanchez de Juan and Gutierrez 2004),
- water absorption of coarse RCA ranges from 2.0% (Marinkovic et al. 2010) to 9.2% (Xiao et al. 2005); for fine RCA it ranges from 5.5% (Yang et al. 2008) to 13% (Evangelista and Brito 2007). These values are significantly higher than those of the NA whose water absorption is about 0.5–1.0%. High porosity of RCA can mainly be attributed to the remains of mortar adhering to the original

aggregate; the content of attached mortar ranges from 25% to 65% by weight (Sanchez de Juan and Gutierrez 2004),
- Los Angeles abrasion loss is increased up to 70% compared to NA (Poon and Lam 2008; Poon et al. 2003, 2004).

7.3 Mix Proportion and Properties of Recycled Aggregate Concrete (RAC)

Standard methods used for the mix design of NAC can be used for the design of RAC mixes too. However, there are two important differences. Firstly, the coefficient of variation of compressive strength between different RAC mixes can be high if the RCA is of non-uniform quality. This situation for example happens when RCA is delivered from a recycling plant that accepts concrete rubble from different demolition sites. Because of that, acceptance criteria for RAC should be based on a higher standard deviation or coefficient of variation of compressive strength test results than for NAC (Balasz et al. 2008).

Secondly, RCA has a high water absorption which affects the workability of the RAC mix. To obtain the desired workability of RAC it is necessary to add a certain amount of water to saturate recycled aggregate, before or during mixing. Results of some researchers indicate that better properties of RAC are obtained if RCA is presoaked before mixing (Hansen 1992), while according to others (Poon et al. 2004), better properties of RAC are obtained if dried RCA is used and additional water is added during mixing. Additional water demand can be determined from the short term water absorption of the aggregate (e.g. 20 min after mixing) or if necessary by taking into consideration the workability in 1 h. However, the additional water quantity can be reduced if water-reducing admixtures are used for achieving the desired workability.

Available test results on the properties of concrete made with recycled concrete aggregate vary in wide limits and sometimes are even opposite. Based on the analysis of published experimental evidence, it can be concluded that the concrete with recycled coarse aggregate, compared to concrete with natural aggregate (NAC) with the same water-to-cement (w/c) ratio, has the following properties:

- decreased compressive strength up to 25% (Yang et al. 2008; Hansen 1992; Rahal 2007; Poon et al. 2003; Ajdukiewicz and Kliszczewicz 2002),
- decreased splitting and flexural tensile strength up to 10% (Yang et al. 2008; Hansen 1992; Ajdukiewicz and Kliszczewicz 2002; Malesev et al. 2007),
- decreased modulus of elasticity up to 45% (Yang et al. 2008; Rahal 2007; Xiao et al. 2005; Ajdukiewicz and Kliszczewicz 2002),
- increased drying shrinkage up to 70% (Li 2008; Domingo-Cabo et al. 2009; Gomez-Soberon 2002a),
- increased creep up to 50% (Hansen 1992; Gomez-Soberon 2002b),
- increased water absorption up to 50% (Li 2008; Malesev at al. 2007),
- similar depth of carbonation (Otsuki et al. 2003; Levy and Helene 2004),

- decreased freezing and thawing resistance (Salem et al. 2003; Zaharieva et al. 2004),
- same or slightly increased chloride penetration (Shayan and Xu 2003; Olorunsogo and Padayachee 2002).

Here it should be emphasized that there is much more published test data on the mechanical properties of RAC than on durability related properties. Also, values given on various properties are the upper bounds of all the analyzed research data. Unfortunately, there is a large experimental data scatter because the quality of RAC depends mostly on the quality of recycled aggregate, i.e. the quality of waste concrete which is used for recycling. The common situation in practice is that RCA is obtained from stationary recycling plants, in which case it is a mix of different quality waste concretes originating from different demolishing sites. Such a RCA is usually of non-uniform quality. However, according to most of the published research (Ajdukiewicz and Kliszczewicz 2002; Malesev at al. 2007; Dosho et al. 1998; Hansen and Narud 1983) low to middle strength RAC with coarse recycled aggregate (with compressive strength up to 30–35 MPa) can be obtained regardless of the quality of recycled aggregate. From the point of view of practical applications and production conditions at recycling plants, this is a very important conclusion.

On the other hand, properties of RAC with both fine and coarse recycled aggregate are even lower than the properties of RAC with only coarse recycled aggregate. The fine RCA has very high water absorption values (up to 13%) and high cohesion which make the concrete quality control very difficult. Therefore, utilization of fine recycled aggregate in RAC for structural use is generally not recommended in available standards and specifications (Rilem TC 121-DRG 1994). Because of decreased compressive strength and modulus of elasticity, and increased creep and shrinkage, RAC shouldn't be applied in structural elements for which high stresses and deformations are expected. Also, this type of concrete shouldn't be used for structures exposed to aggressive environmental conditions without appropriate previous testing, as there are opposing conclusions about durability related properties in existing literature. But its utilization for low to middle strength structural concrete, low-to-middle span and load structural elements and non-aggressive exposure conditions is technically feasible.

7.3.1 RAC Mix Design Example

One example of possible RAC mix design is presented in this chapter. The aim of this research was to determine NAC and corresponding RAC mix proportion so that both concrete types have approximately the same compressive strength and workability. NAC was made entirely with natural river aggregate, while RAC was made with natural fine (river sand) and recycled coarse aggregate. Coarse recycled aggregate was obtained from demolished reinforced concrete structure which has been exposed to weather conditions for more than 30 years (Fig. 7.2). The crushing of the demolished concrete and screening into three fractions: 4/8, 8/16 and 16/31.5 mm was performed in the mobile recycling plant (Fig. 7.3).

Fig. 7.2 Demolition of a 30 years old concrete structure

The properties of recycled concrete aggregate were tested according to Serbian standards for natural aggregates, as there are no standards for testing and quality requirements for recycled aggregates in Serbia. Obtained results showed that RCA properties satisfy quality requirements for natural aggregates except for the content of weak grains and "Los Angeles" abrasion loss value, which was expected. Both content of weak grains and abrasion loss were slightly larger than allowed values for grain sizes 8/16 and 16/31.5 mm (Marinkovic et al. 2010). Also, water absorption of RCA measured 30 min after mixing was 6% for 4/8 mm fraction, 4% for 8/16 mm fraction and 2% for 16/31.5 mm fraction (Marinkovic et al. 2010). Such high values are typical because of the high content of cement paste in RCA and special measures must be undertaken to provide the required workability of concrete.

The target concrete strength class for both types was C25/30, nomenclature according to Eurocode 2 (characteristic compressive cylinder/cube strength equal to 25/30 MPa) and the target slump 20 min after mixing for both types was 6 ± 2 cm. The component materials used were:

- Portland cement EN 197-1 – CEM I 42.5 R
- fine aggregate, fraction 0/4 mm (river aggregate, Morava river)
- two types of coarse aggregate, fractions 4/8, 8/16 and 16/31.5 mm: river aggregate (Morava river) for NAC and recycled aggregate for RAC
- water.

Fig. 7.3 Recycling of demolished concrete in mobile recycling plant

Table 7.1 NAC and RAC mix proportion for concrete strength class C25/30

	Cement	Aggregate (kg/m^3)				Water		
	(kg/m^3)	0/4 mm	4/8 mm	8/16 mm	16/31.5 mm	(kg/m^3)	w/c[a]	a/c[b]
NAC	315	658	338	282	601	180	0.571	5.965
RAC	330	601	240[c]	343[c]	532[c]	181 + 40[d]	0.548	5.200

[a]Free water-to-cement ratio
[b]Aggregate-to-cement ratio
[c]Recycled aggregate
[d]Additional water quantity

As it was already mentioned, to obtain the desired workability of RAC it is necessary to add a certain amount of water to saturate recycled aggregate before or during mixing, if no water-reducing admixture is applied. In this case, dried recycled aggregate was used for RAC production and additional water was added during mixing. The amount of this water was calculated on the basis of recycled aggregate water absorption after 30 min. Cement content, i.e. w/c ratio was then determined on the basis of required compressive strength. No water-reducing admixtures were used. Laboratory tests with various mix proportions were performed to determine the mix proportion of RAC which will have the same compressive strength and the same slump as NAC. The results, i.e. obtained mix proportions and properties of NAC and RAC, are shown in Tables 7.1 and 7.2 (Marinkovic et al. 2010).

Table 7.2 Tested properties of NAC and RAC

	Density (kg/m^3)	Slump after 20 min (cm)	Compressive strength at 28 days (MPa)
NAC	2,396	5.5	39.2
RAC	2,259	7.0	38.6

Water-to-cement ratio shown in Table 7.1 refers to free water content, excluding the amount of additional water.

In order to obtain approximately the same workability and strength, a slightly larger amount of cement (about 5%) i.e. slightly smaller free water-to-cement ratio is required for RAC than for corresponding NAC (Table 7.1). Similar results were obtained by other investigators (González-Fonteboa and Martínez-Abella 2008). Also, density of RAC is slightly lower (about 6%) than density of corresponding NAC, because of the lower density of recycled concrete aggregate.

7.4 Standards and Recommendations

European norm EN 12620:2002 (CEN 2002) regarding aggregates for concrete allows the utilization of recycled aggregate for concrete production if it fulfils all the requirements for natural aggregate, i.e. there is no particular standard on recycled aggregates. Some of the European countries like Germany, UK, Netherlands and Hungary have issued standards or technical guidelines on recycled aggregates as complementary standards to EN (BSI 2006) or as separate standard or technical guidelines (Balasz et al. 2008; DIN 2002). In Japan standards on recycled aggregates (JIS 2006) were issued in 2006 as well as in China in 2007 as a regional Shanghai standard (Li 2008). RILEM published the recommendation on recycled aggregates in 1994 (Rilem TC 121-DRG).

In available standard specifications on recycled aggregates from C&D waste it is usually recommended to classify the recycled aggregate into different types according to composition and density and to impose maximum allowable limits on the content of the contaminants. Also, the replacement percentage of certain aggregate type is limited depending on the concrete strength class and exposure conditions.

RILEM recommendations (Rilem TC 121-DRG) from 1994 are presented here as an example. Recycled aggregate is classified into three types according to composition and density, and the maximum content of various contaminants is limited, Table 7.3. Table 7.4 shows the maximum allowed replacement percentage of recycled aggregate depending on aggregate type, concrete strength class and exposure conditions.

The utilization of fine recycled aggregate in structural concrete is not recommended in most of the standards and recommendations. Maximum allowed replacement percentage of coarse recycled aggregate differs and for the type of aggregate originating from concrete rubble it ranges from 20% to 100%. Maximum allowed concrete strength class depends on aggregate type and replacement percentage, and for the type of aggregate originating from concrete rubble it ranges from C30/37 to C50/60, nomenclature according to EC2 (CEN 2004). Similarly, utilization of

Table 7.3 Specifications for the properties of recycled aggregates for concrete (Rilem TC 121-DRG 1994)

	Type 1	Type 2	Type 3
Composition	Aggregates from masonry rubble	Aggregates from concrete rubble	Mixture of natural (min 80%) and recycled (max 20%) aggregate
Oven dry density (kg/m^3)	1,500	2,000	2,400
Maximum content of foreign matter (glass, bitumen) (%)	5	1	1
Maximum content of metal (%)	1	1	1
Maximum content of organic materials (%)	1	0.5	0.5
Maximum content of fines (<0.063 mm) (%)	3	2	2
Maximum content of sand (%)	5	5	5
Maximum content of sulfate (%)	1	1	1

Table 7.4 Requirements on concrete with recycled aggregate (Rilem TC 121-DRG 1994)

	Type 1	Type 2	Type 3
Replacement percentage of coarse recycled aggregate (> 4 mm)	Up to 100%	Up to 100%	Up to 20%
Use of fine recycled aggregate (< 4 mm)	Not recommended		
Maximum strength class	C16/20	C50/60	No upper limit
Exposure conditions	• No additional testing for concrete used under dry conditions or in non-aggressive soils and/or water, not exposed to frost • Additional testing for concrete used under other exposure conditions		

concrete with recycled aggregates is limited to non-aggressive exposure conditions, like XC0 and XC1 according to EC2 (CEN 2004).

It should be kept in mind that for replacement percentage of coarse recycled aggregate up to 30–40% it can be considered that the properties of RAC are not significantly different from the properties of corresponding NAC. But for higher replacement ratios, properties are significantly changed and the design provisions and equations in existing codes for NAC are no longer applicable for RAC.

7.5 Examples of Application

Some examples of buildings constructed with RAC used as structural concrete are presented in this chapter.

Figure 7.4 shows the office building with the open multi-storey garage Vilbeler Weg built in Darmstadt, in 1997/1998 (BIM 2010). Complete reinforced concrete structure was constructed using RAC, approximately 480 m^3 of RAC was built in.

Fig. 7.4 Vilbeler Weg office building, Darmstadt, Germany, 1997/1998 (BIM 2010)

Table 7.5 Concrete mix proportion and basic properties, Vilbeler Weg (BIM 2010)

Component	Type	Quantity (kg/m^3)
Recycled aggregate	0/2 mm	585
	2/8 mm	545
	8/16 mm	568
Portland cement	CEM I 42,5 R	310
Free water		170
Additives	pulverised fuel-ash	40
Superplasticiser		5–18 ml/kg of cement
Workability (flow table value)		550 mm
Compressive strength (28 days)		45 MPa on average

This project showed that the practical application of RAC in structural elements is possible, if it is combined with rigorous quality management system, especially in the concrete production phase.

Table 7.5 shows the mix proportions and basic properties of the applied RAC.

In residential building Waldspirale built in Darmstadt in 1998, RAC was applied for all in-door structural elements, as well as for foundation slab (BIM 2010). Two different quality concretes were used; C30/37 and C25/30 with a total amount of built-in concrete around 12,000 m^3. The sketch of the building is shown in Fig. 7.5, while the mix proportions and basic properties of the concrete are shown in Table 7.6.

The Environmental Building is a BRE office facility in Watford, UK, Fig. 7.6. This building represents the first-ever use in the UK of recycled aggregates in ready-mixed concrete (Collins 2000). Only coarse recycled aggregate was used in over 1,500 m^3 of RAC supplied for foundations, floor slabs, structural columns and waffle floors. For the foundations, a C25 mix (75 mm slump) was used with a minimum

Fig. 7.5 Waldspirale residential building in Darmstadt, Germany, 1998 (BIM 2010)

Table 7.6 Concrete mix proportions and basic properties, Waldspirale (BIM 2010)

Component	Type	Quantity (kg/m^3)	
		C30/37	C25/30
Recycled aggregate	0/2 mm	616	615
	2/8 mm	530	290
	8/16 mm	569	334
	16/32 mm		554
Portland cement	CEM I 42,5 R	300	
Portland cement	CEM I 32,5 R		290
Additives	pulverised fuel-ash	50	40
Superplasticiser		1.5 kg/m^3	
Workability		Normal (according to DIN 1045)	
Compressive strength (on average at 28 days)		42.9 MPa	36.4 MPa

cement content of 350 kg/m^3 and a maximum free water/cement ratio of 0,50 was required. For floor slabs, a C35 mix, also with 75 mm slump was specified.

7.6 Necessary Actions in Promoting Utilization of RCA and RAC

Major barriers in promoting a broader use of recycled aggregates and recycled aggregate concrete in construction industry can be divided into two groups: social barriers and technical barriers.

Fig. 7.6 The BRE office building in Watford, UK, 1995/96 (Collins 2000)

Within social barriers, the most important ones are lack of awareness about the environmental implications of using only natural aggregates and lack of government support. Creating awareness and dissemination of knowledge about recycling possibilities and potentials of RAC to be applied in structural concrete can mobilize public opinion towards the recycling option. On the other hand, developing appropriate policy supported by proper legislation can provide necessary impulses. For example, increasing the dumping costs and imposing taxes on the use of natural aggregates are possible actions. Also, favouring of those contractors who offer recycling of C&D waste in bidding competitions can help.

Within technical barriers, lack of knowledge about some properties of RAC, and lack of proper standards are the most important ones. Despite all the research performed in this area, durability related properties of RAC and long-term behavior of structural elements made of RAC are not well known yet. These uncertainties lead to a situation that very few countries have issued the standards on RCA and RAC and to a very limited allowed application of RAC in structural concrete. Further research into these areas is therefore needed.

7.7 Conclusions

Recycled aggregates from demolished concrete (RCA) are generally produced today by two-stage crushing, screening and removing the contaminants by water cleaning, air-sifting, magnetic separation. Recycled aggregates obtained in this manner are usually of lower quality compared to natural aggregates (significantly higher porosity and water absorption, decreased density and abrasion resistance), because of the certain amount of mortar and cement paste that remains attached to original aggregate grains. The best method for improving the RCA quality is to remove the attached mortar and some advanced technologies are already developed

mostly in Japan. With these procedures it is possible to achieve a high recovery ratio of aggregate with a very small percentage of attached mortar, comparable to natural aggregates. However, for the time being these advanced recycling technologies are probably more costly and energy demanding than traditional ones which are not much different from crushed aggregate production.

According to up-to-date state of research in the area, utilization of recycled aggregates from demolished concrete in structural concrete is technically feasible but limited. Firstly, it's limited to utilization of only coarse recycled aggregate, the use of fine recycled aggregate in concrete for structural use is generally not recommended. Secondly, the quality of RAC made of fine natural and coarse recycled aggregate is limited to low-to-middle strength structural concrete for practical applications. It is not recommended to apply this type of concrete for structural elements which are expected to have high stresses and deformations in service, because the long-term behaviour is not well-known yet. Finally, the application of such a RAC in aggressive environment conditions (risk of corrosion induced by carbonation and chlorides or risk of freeze/thaw and chemical attack) is not recommended because of its uncertain durability performance.

Even with all these limitations, the utilization of recycled aggregates in structural concrete should help improve the environmental performance of concrete. To enable a broader use of recycled aggregate concrete in structural applications it is necessary to widen our knowledge about all the relevant properties of this material, and to mobilize public opinion towards recycling concrete as a sustainable option of managing C&D waste and preserving the natural resources.

References

Ajdukiewicz A, Kliszczewicz A (2002) Influence of recycled aggregates on mechanical properties of HS/HPC. Cem Concr Compos 24(2):269–279

Balász GL, Kausay T, Simon TK (2008) Technical guideline for recycled aggregate concrete in Hungary. Concr Struct 2008:45–55

BIM (2010) Projekte-Hinweise zur Bedienung. http://www.b-i-m.de/projekte/projframe.htm. Accessed 22 Nov 2010

BSI (2006) Concrete Complementary British Standard to BS EN 206-1; Part 2: Specification for constituent materials and concrete. BS 8500-2:2006. BSI

CEN (2002) EN 12620:2002. Aggregates for concrete. Comite Europeen de Normalisation, Brussels

CEN (2004) EN 1992-1-1:2004. Eurocode 2: design of Concrete Structures – Part 1.1: General rules and rules for buildings, Comite Europeen de Normalisation, Brussels

Collins R (2000) The environmental building at BRE, United Kingdom. Use Recycl Mater Aggr Constr Ind 2(3–4) http://www.eco-serve.net/uploads/ETN_NL2.pdf. Accessed 20 Nov 2010

DIN (2002) Aggregates for mortar and concrete; Part 100: Recycled aggregates. DIN 4226 – 100. DIN

Domingo-Cabo A, Lázaro C, López-Gayarre F et al (2009) Creep and shrinkage of recycled aggregate concrete. Constr Build Mater 23(7):2545–2553

Dosho Y, Kikuchi M, Narikawha M et al (1998) Application of recycled concrete for structural concrete – Experimental study on the quality of recycled aggregate and recycled aggregate concrete. ACI Spec Publ 179-61A:1073–1101

Etxeberria M, Vasquez E, Mari A et al (2007) Influence of amount of recycled coarse aggregates and production process on properties of recycled aggregate concrete. Cem Concr Res 37(5): 735–742

European Environment Agency (2008) Effectiveness of environmental taxes and charges for managing sand, gravel and rock extraction in selected EU countries. EEA Report No 2. http://www.eea.europa.eu/publications/eea_report_2008_2. Accessed 17 Aug 2009

Evangelista L, Brito J (2007) Mechanical behaviour of concrete made with fine recycled concrete aggregate. Cem Concr Compos 29(5):397–401

FHWA (2004) Transportation applications of recycled concrete aggregate, state of the practice national review. Federal Highway Administration, Washington, DC. http://www.rmrc.unh.edu/Research/tools/RCAREPORT.pdf. Accessed 15 Sep 2010

fibTask Group 3.3 (2004) Bulletin 28 environmental design. Sprint-Digital-Druck, Stuttgart

Fisher C, Werge M (2009) EU as a recycling society. ETC/SCP working paper 2/2009. http://scp.eionet.europa.eu.int. Accessed 20 June 2009

Gómez-Soberón JMV (2002a) Shrinkage of concrete with replacement of aggregate with recycled concrete aggregate. ACI Spec Publ 209–26:475–496

Gómez-Soberón JMV (2002b) Creep of concrete with substitution of normal aggregate by recycled concrete aggregate. ACI Spec Publ 209–25:461–474

González-Fonteboa B, Martínez-Abella F (2008) Concretes with aggregates from demolition waste and silica fume. Materials and mechanical properties. Build Environ 43(4):429–437

Hansen TC (1992) Recycling of demolished concrete and masonry. Taylor & Francis, London/New York

Hansen TC, Narud H (1983) Strength of recycled concrete made from crushed concrete coarse aggregate. Concr Inter Des Constr 5(1):79–83

ISO (2005) Business plan. ISO/TC 71 Concrete, reinforced concrete and prestressed concrete.http://isotc.iso.org/livelink/livelink/fetch/2000/2122/687806/ISO_TC_071__Concrete__reinforced_concrete_and_pre-stressed_concrete_.pdf?nodeid=1162199&vernum=0. Accessed 21 Aug 2009

JIS (2006) Recycled aggregate for concrete – class H. JIS A 5021. JIS

Khatib JM (2005) Properties of concrete incorporating fine recycled aggregate. Cem Concr Res 35(4):763–769

Levy SM, Helene P (2004) Durability of recycled aggregates concrete: a safe way to sustainable development. Cem Concr Res 34(11):1975–1980

Li X (2008) Recycling and reuse of waste concrete in China; Part I. Material behavior of recycled aggregate concrete. Resour Conserv Recycl 53(1–2):36–44

Malesev M, Radonjanin V, Marinkovic S (2007) Recycled concrete as aggregate for producing structural concrete. In Bragança L et al (eds) Sustainability of constructions – integrated approach to life-time structural engineering, Lisbon, 2007

Marinkovic S, Radonjanin V, Malesev M et al (2010) Comparative environmental assessment of natural and recycled aggregate concrete. Waste Manag 30(11):2255–2264

Mulder E, De Jong TPR, Feenstra L (2006) Closed cycle construction: an integrated process for the separation and reuse of C&D waste. In: Proceedings of WASCON 2006 sixth international conference on the environmental and technical implications of construction with alternative materials science and engineering of recycling for environmental protection, Belgrade, 30 May–2 June 2006

Olorunsogo FT, Padayachee N (2002) Performance of recycled aggregate concrete monitored by durability indexes. Cem Concr Res 32(2):179–185

Otsuki N, Asce M, Miyazato S et al (2003) Influence of recycled aggregate on interfacial transition zone, strenght, chloride penetration and carbonation of concrete. J Mater Civ Eng 15(5):443–451

Poon CS, Lam CS (2008) The effect of aggregate-to-cement ratio and types of aggregates on properties of pre-cast concrete blocks. Cem Concr Compos 30(4):283–289

Poon CS, Azhar S, Kou SC (2003) Recycled aggregates for concrete applications. In: Proceedings of the conference materials science and technology in engineering, Hong Kong, January 2003

Poon CS, Shui ZH, Lam L et al (2004) Influence of moisture states of natural and recycled aggregates on the slump and compressive strength of concrete. Cem Concr Res 34(1):31–36

Rahal K (2007) Mechanical properties of concrete with recycled coarse aggregate. Build Environ 42(1):407–415
RILEM TC 121-DRG (1994) RILEM recommendation: specifications for concrete with recycled aggregates. Mater Struct 27:557–559
Sagoe-Crentsil KK, Brown T, Taylor AH (2001) Performance of concrete made with commercially produced coarse recycled concrete aggregate. Cem Concr Res 31(5):707–712
Salem RM, Burdette EG, Jackson NM (2003) Resistance to freezing and thawing of recycled aggregate concrete. ACI Mater J 100(3):216–221
Sanchez de Juan M, Gutierrez PA (2004) Influence of recycled aggregate quality on concrete properties. In: Vázquez E et al (eds) The use of recycled materials in building and structures, Barcelona, 8–11 Nov 2004
Shayan A, Xu A (2003) Performance and properties of structural concrete made with recycled concrete aggregate. ACI Mater J 100(5):371–380
Shima H, Tateyashiki H, Matsuhashi R et al (2005) An advanced concrete recycling technology and its applicability assessment through input-output analysis. J Adv Concr Technol 3(1):53–67
Tomosawa F, Noguchi T, Tamura M (2005) The way recycling should be. J Adv Concr Technol 3(1):3–16
Xiao J, Li J, Zhang C (2005) Mechanical properties of recycled aggregate concrete under uniaxial loading. Cem Concr Res 35(6):1187–1194
Yang KH, Chung HS, Ashour A (2008) Influence of type and replacement level of recycled aggregates on concrete properties. ACI Mater J 105(3):289–296
Zaharieva R, Buyle-Bodin F, Wirguin E (2004) Frost resistance of recycled aggregate concrete. Cem Concr Res 34(10):1927–1932

Chapter 8
Mix Proportioning Method for Lightweight Aggregate SCC (LWASCC) Based on the Optimum Packing Point Concept

Michael Kaffetzakis and Catherine Papanicolaou

Abstract In this paper a mix design methodology for Lightweight Aggregate Self-Compacting Concrete (LWASCC) is presented based on the packing density theory. The proposed methodology targets: (i) the minimization of the voids volume associated to the packing of the coarse aggregate fractions (4–16 mm); (ii) the maximization of the packing density of the cementitious materials in the paste; (iii) the minimization of the water-to-cementitious materials volumetric ratio (V_w/V_{cm}) in the mortar; and (iv) the optimization of the measurable workability features of the produced LWASCC mixtures. Points (ii) and (iii) are achieved using the "wet packing method" in the cementitious paste and mortar phases, along with standard consistency tests (mini slump-flow for the cementitious paste; mini slump-flow and mini V-funnel for the mortar). The final mixture proportions are attained by determining the optimum mortar-to-aggregates packing voids ratio.

8.1 Introduction

Lightweight aggregate self-compacting concrete comprises a high performance material that combines the advantages of structural lightweight aggregate concrete (LWAC), such as reduced dead loads and formwork pressure, high insulation capacity, improved durability, resistance against fire and chemical attack, with self-compacting characteristics that are reflected into the material's filling and passing ability and segregation resistance. The apparent contrast between properties such as low density (that is low dynamic energy of the mixture during flow) and self-compactness (which depends on the dynamic features of the mixture) renders the production of LWASCC rather unfavourable. However, the current

M. Kaffetzakis (✉) • C. Papanicolaou
Civil Engineering Department, University of Patras, 26504 Patras, Greece
e-mail: mkaffetzakis@upatras.gr; kpapanic@upatras.gr

M.N. Fardis (ed.), *Innovative Materials and Techniques in Concrete Construction: ACES Workshop*, DOI 10.1007/978-94-007-1997-2_8,

state-of-knowledge for this material (Papanicolaou and Kaffetzakis 2011; Mechtcherine et al. 2001; Shi and Wu 2005; Hwang and Hung 2005) and the experience gained from its application in structural works prove that properly designed and produced LWASCC fulfils a challenging combination of performance requirements at a high level of quality, comprising a significant step forward for the art and science of concrete technology.

The majority of LWASCC-related studies implement the use of artificial LWA (expanded shale, expanded clay etc.). In 2009 Uygunoğlu and Topçu (2009) and Papanicolaou and Kaffetzakis (Papanicolaou and Kaffetzakis 2009) first introduced natural LWA (pumice) in LWASCC. Uygunoğlu and Topçu (2009) investigated the effect of the aggregate type on the coefficient of thermal expansion by comparing normal weight SCC (NWSCC) and pumice aggregate SCC (PASCC) mixtures. In general, PASCC proved to be more durable, having higher coefficient of thermal expansion, due to the porous system of the pumice aggregates. Papanicolaou and Kaffetzakis (Papanicolaou and Kaffetzakis 2009) presented the development of PASCC (all-LWASCC) falling in the LC20/22 strength class and D1.4 density class (as per EN 206-1 (CEN 2000a)) focusing on the effect of coarse-to-fine aggregates ratio on the material's rheological and mechanical properties.

The present study aims to introduce a mix design methodology for LWASCC based on packing density and workability criteria. The LWASCC is separated in three phases (paste, mortar and concrete); each one is evaluated in terms of least voids content and self-compacting features. Special consideration is given to the method used for measuring the packing density in the paste and mortar phases. Finally, some empirical mixing instructions are provided based on former studies and the authors' experience on LWASCC production, and the suitability of the well-established normal-weight SCC fresh-state test limit values for the case of LWASCC is discussed.

8.2 Methods for Measuring Packing Density

According to European standards (CEN 1998, 1999, 2000b) packing density of fine or coarse aggregates is measured under dry conditions as the ratio of the bulk density of the granular mixture (measured in a container of known volume) to particle density (measured by a pyknometer). However, the magnitude of the applied compaction in the container can significantly affect the measured packing density (e.g. increased compaction increases the packing density).

Wong and Kwan (2008) have introduced a most interesting and simple method – the 'wet packing method' – to measure the packing density in cement pastes and mortars. This method calculates the air voids content, the minimum water demand and the maximum solid concentration by measuring the weight of the paste in a container of given volume. An optimized mixing procedure is suggested in order to achieve a saturated mixture for as long as possible: first, the entire water quantity is mixed with half of the cementitious materials and with half of the superplasticizer (SP) for 3 min; then the rest of the cementitious materials and the SP are divided

into four portions and each portion is added after an extra 3 min of mixing (total mixing time 15 min).

8.3 Experimental Program

In this study the mix design methodology followed for LWASCC involves the investigation of all three phases of the material: paste, mortar and concrete. Pastes and mortars are assessed in terms of their packing density by the 'wet packing method' described in the previous section. First, the weight of a cement paste (or mortar) of given water-to-cementitious materials volumetric ratio (V_w/V_{cm}) is measured; the container of the paste (or mortar) is of known volume (V_{total} = 1.5 l). Then, the contents of the total voids u and air voids u_α (expressed as the voids-to-solid materials volumetric ratios) and the solid concentration factor ϕ are calculated according to Eqs. 8.1–8.3. Solid materials for pastes include cementitious materials, sand powder (with maximum aggregate size < 125 μm) and admixtures' solid contents. In mortars solid materials also include sand (maximum aggregate size < 4 mm). Total voids stand for the sum of air and water voids.

$$u = (V_{total} - V_{solids}) / V_{solids} \tag{8.1}$$

$$u_\alpha = (V_{total} - V_{solids} - V_w) / V_{solids} \tag{8.2}$$

$$\phi = V_{solids} / V_{total} \tag{8.3}$$

The procedure starts by selecting a rather high value of V_w/V_{cm} (e.g. 0.8), which is gradually reduced in a series of trial pastes until the measured solid concentration factor ϕ starts to decrease. From this point, further decrease of the V_w/V_{cm} ratio yields pastes that fail to form. The results can also be shown in a u vs. V_w/V_{cm} curve, where the least total voids ratio corresponds to maximum packing. Figure 8.1 illustrates a typical u vs. V_w/V_{cm} curve (picked randomly from the experimental results produced by this study) with the highest packing and lowest voids ratio values corresponding to V_w/V_{cm} = 0.65.

The investigation aimed at determining: (i) the proportions of powder materials in the paste; and (ii) the sand content, the SP dosage and the V_w/V_{cm} ratio in the mortar that yield the optimum packing in both phases. It should be noted that the optimum packing concept employed in this work is not associated to the maximum attainable solid concentration of the mixture (maximum packing point – MPP), but it corresponds to the highest possible solid concentration that satisfies specific criteria associated to self-compactness (optimum packing point – OPP). These additional criteria differentiate this method from other SCC proportioning methods, which assume that the least voids volume of a mixture corresponds to the optimum flowability in the paste and mortar phases.

For every investigated combination of materials' proportions a series of mixtures is produced, each corresponding to a point in the u–V_w/V_{cm} diagram. The OPPs of all produced mixtures are then compared on the basis of least total voids volume (i.e. maximum solids concentration) and lowest V_w/V_{cm} (highest strength).

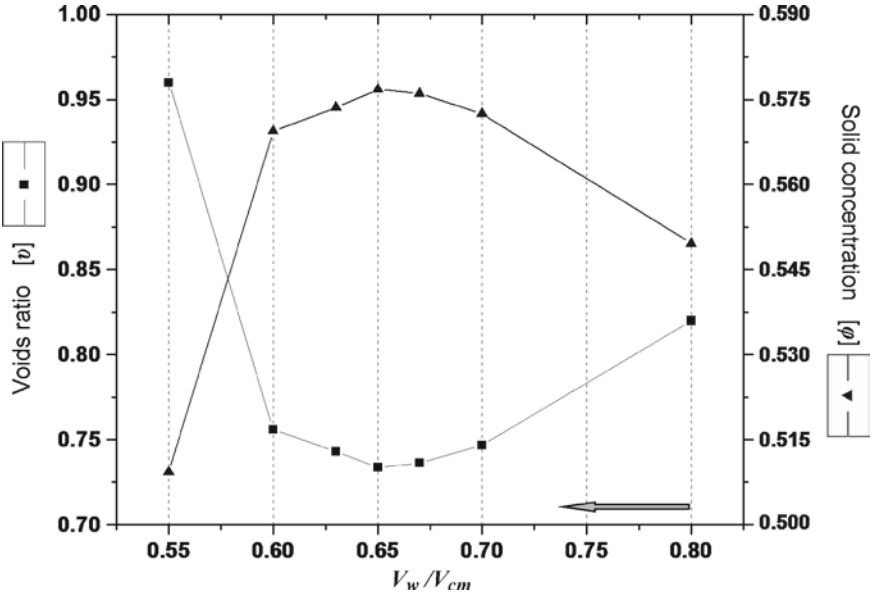

Fig. 8.1 Typical curves of total voids u and solid concentration factor ϕ versus V_w/V_{cm}

For pastes the OPP corresponds to the mixture which yields a 240–260 mm spread diameter using the mini slump-flow test. The OPP of mortars is derived through assessment of both their mini slump-flow (Fig. 8.2a) and the mini V-funnel test scores (Fig. 8.2b). High values of relative flow area Γ_m and relative funnel speed R_m are sought combined with absence of segregation. The relative flow area Γ_m gives an indication of the mixture's unconfined flowability (deformability) and equals to $(d_1 d_2 - d_0^2)/d_0^2$, with d_1 and d_2 being the flow diameters (measured in directions perpendicular one to the other) and $d_0 = 100$ mm (base diameter of the flow cone). The relative funnel speed R_m is indicative of the mortar's viscosity and equals to $10/t$, t being the measured time for the mortar to flow through the mini V-funnel.

In the concrete phase, the aggregate apparent and particle densities ($\rho_{apparent}$ and $\rho_{particle}$, respectively) are first measured (according to (CEN 1998, 1999, 2000b)) in order to determine the aggregate packing index C, where $C = \rho_{apparent}/\rho_{particle}$. Maximum aggregate packing (i.e. with zero inter-particle voids volume) is theoretically achieved at $C = 1$. In case two aggregate fractions are used, the fractions' volumetric ratio corresponding to the maximum C index value is determined. Then, based on Jacobsen (Jacobsen and Arntsen 2008), the LWASCC mixture's proportioning is finalized by careful adjustment of the mortar-to-aggregates' voids volumetric ratio, K (8.4), so that the pre-set desired workability features (assessed by Slump-flow, V-funnel, L-box tests, etc.) are reached.

$$K = V_{mortar} / \left[(1 - C) V_T \right], V_T = 1\, m^3 \tag{8.4}$$

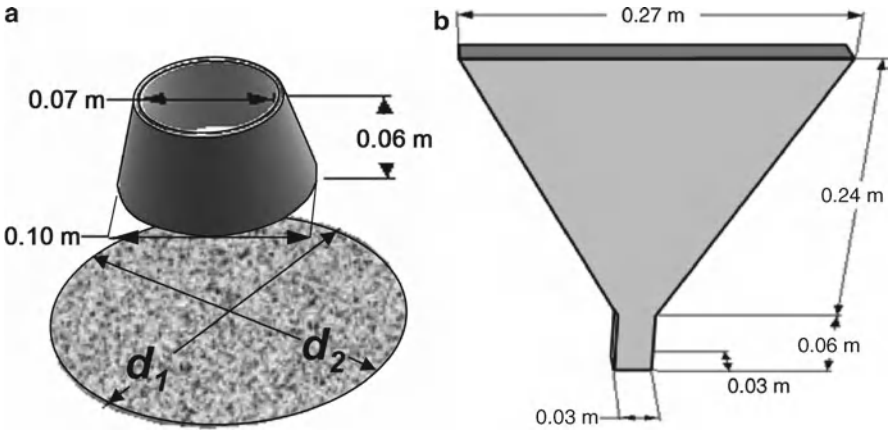

Fig. 8.2 (**a**) Mini slump-flow and (**b**) Mini V-funnel for mortar tests (Okamura and Ouchi 2003)

Table 8.1 Physical properties of cement and mineral additives

	Apparent density [kg/m^3]	Particle density [kg/m^3]	Mean grain size [μm]
CEM II42.5N	1,100	3,100	15.0
LF_{120}	1,400	2,700	25.0
LF_{10}	800	2,700	3.0
SF	250	2,200	0.7

For K larger than 1.0 an excess paste starts to form; for increasing K the thickness of the excess paste (which in turn is related to the workability of the mixture) is increased. Following this procedure the trial SCC mixes for fine tuning are distinctively limited. An initial value of K can be set to 1.3.

8.3.1 Materials

In this study four powder materials were used: a commonly used Portland cement (CEM II 42.5N), two limestone fillers (LF_{120} with a mean and maximum grain size equal to 25 μm and 120 μm, respectively, and LF_{10} with a mean and maximum grain size equal to 3 μm and 10 μm, respectively) and silica fume (SF) of a mean grain size equal to 3.5 μm. The physical properties of all powder materials are given in Table 8.1.

Constituent materials for various mixtures also included: normal-weight river sand [0–4 mm], natural pumice aggregates in three fractions [sand 0–4 mm, fine 4–8 mm and coarse 8–16 mm], polycarboxylic ether polymer superplasticizer (density: 1,060 kg/m³, solid content: 30%, by weight), and stabilizer (with a slight retarding

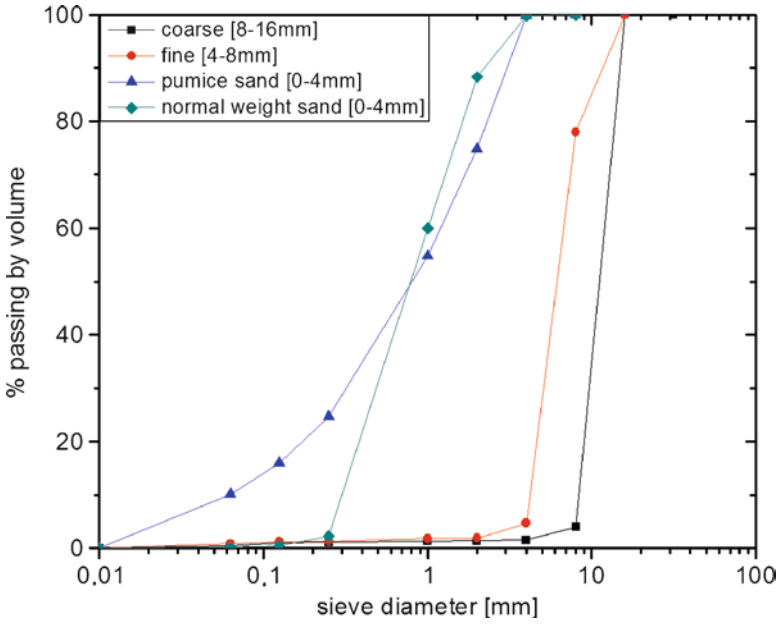

Fig. 8.3 Sieve analysis of all pumice fractions and normal-weight sand

Table 8.2 Physical properties of aggregates

Aggregates	Apparent density [kg/m^3]	Particle density [kg/m^3]	Water absorption[a] [% by weight]	Crushing resistance [MPa]
Normal-weight sand (0–4 mm)	1,516	2,420	3.0	-
Pumice sand (0–4 mm)	899	1,280	23.3	-
Fine pumice (4–8 mm)	587	1,082	25.0	3.44
Coarse pumice (8–16 mm)	570	1,034	25.0	3.19

[a]After 24 h of water immersion

action). The gradation curves and the physical properties of all aggregates are given in Fig. 8.3 and in Table 8.2, respectively.

8.3.2 Cement Paste Mixtures

In the cement paste phase 20 different mix designs were investigated resulting in a total of 144 tested mixtures. The additives used were LF_{120}, LF_{10} and SF. The scope of this part of the experimental campaign was to determine the optimum packing points of multi-additive (MA) pastes. Prior to the assessment of MA paste mixtures a series of single-additive (SA) trial pastes was produced in order to relate the results produced by the wet packing method to the effect of cement replacement by a single

Table 8.3 Mix proportions of paste mixtures

Mixtures' designation	Cement a%[a]	SP b%[b]	LF_{120} c%[c]	LF_{10} c%[c]	SF c%[c]	Pumice powder[d] c%[c]
$CEM_{0\%\ SP}$	100.0	–	–	–	–	–
$CEM_{1.0\%\ SP}$	99.9	1.0	–	–	–	–
$CEM_{1.5\%\ SP}$	99.8	1.5	–	–	–	–
$LF_{120\_12.5\%}$	88.8	1.5	12.5	–	–	–
$LF_{120\_25\%}$	79.9	1.5	25.0	–	–	–
$LF_{120\_50\%}$	66.6	1.5	50.0	–	–	–
$LF_{10\_12.5\%}$	88.8	1.5	–	12.5	–	–
$LF_{10\_25\%}$	79.9	1.5	–	25.0	–	–
$LF_{10\_50\%}$	66.6	1.5	–	50.0	–	–
$SF_{10\_12.5\%}$	88.8	1.5	–	–	12.5	–
$SF_{10\_25\%}$	79.9	1.5	–	–	25.0	–
$SF_{10\_50\%}$	66.6	1.5	–	–	50.0	–
$LF_{120}+X2_{\_0\%}$	71.4	1.5	40.0	–	–	–
$LF_{120}+LF_{10\_6\%}$	68.4	1.5	34.3	5.7	–	6.2
$LF_{120}+LF_{10\_9\%}$	68.4	1.5	30.8	9.2	–	6.2
$LF_{120}+LF_{10\_11.5\%}$	68.4	1.5	28.5	11.5	–	6.2
$LF_{120}+LF_{10\_17\%}$	68.4	1.5	22.8	17.2	–	6.2
$LF_{120}+SF_{\_7\%}$	68.4	1.5	33.0	–	7.1	6.2
$LF_{120}+SF_{\_11\%}$	68.4	1.5	28.7	–	11.3	6.2
$LF_{120}+SF_{\_14\%}$	68.4	1.5	25.9	–	14.1	6.2
$LF_{120}+SF_{\_21.5\%}$	68.4	1.5	18.6	–	21.4	6.2
$LF_{10}+SF_{\_11\%}$	68.4	1.5	–	28.7	11.3	6.2

[a]a%: by total solids volume
[b]b%: by cement weight
[c]c%: by cement volume
[d]<125 μm

powder on the paste's properties in the fresh- and hardened-state. The effect of superplasticizer content increase was also investigated in cement pastes (with no additive); these pastes are designated as $CEM_{Z\%SP}$, Z corresponding to the content of superplasticizer by cement weight.

The SA paste mixtures are denoted as $X_{\_Y\%}$, X being the abbreviation of the additive used (LF_{120}, LF_{10} or SF) and Y corresponding to the volumetric replacement of cement by additive X, namely 12.5%, 25% and 50%. The MA paste mixtures receive the following notation: $X1+X2_{\_Y\%}$, X1 being the first (coarser) additive, X2 the second (finer) one and Y the content of additive X2 by cement volume (Y corresponds to 5%, 8%, 10% and 15% of X2 by cement weight). It should be noted that in all MA paste mixtures the total additive percentage (X1 + X2) was kept constant at 40% of cement volume. Additionally, MA pastes included a constant amount of pumice powder (pumice sand fines < 125 μm), equal to 6.25% by cement volume. Finally, all paste mixtures (but $CEM_{0\%SP}$ and $CEM_{1.0\%SP}$) received a dosage of 1.5% (by cement weight) superplasticizer. All paste mix proportions are listed in Table 8.3. Each mix design represents a number of paste mixtures of varying V_w/V_{cm} ratios that were tested in order to pin-point the OPP.

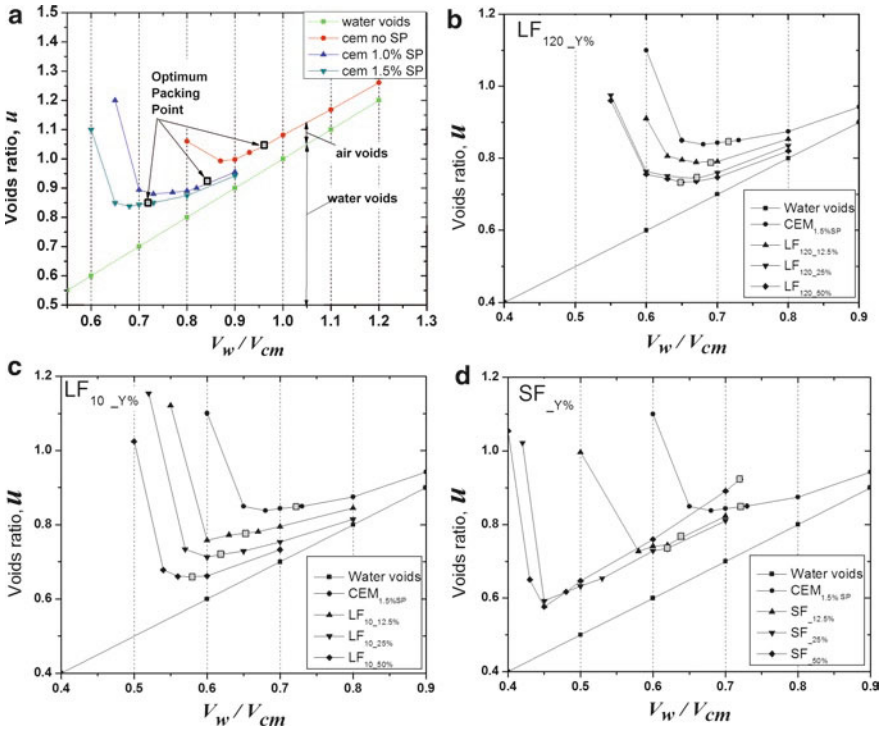

Fig. 8.4 Determination of OPPs for cement-only and SA pastes: (**a**) cement-only pastes with varying SP dosages; SA pastes comprising: (**b**) LF_{120}, (**c**) LF_{10} and (**d**) SF

For the estimation of mechanical strengths three prismatic specimens of 40×40×160 mm were sampled from each OPP mixture and stored in water until 3 h before testing.

8.3.2.1 Fresh-State Test Results and Discussion

Figures 8.4 and 8.5 present for each of the paste mixtures included in Table 8.3 the resulting values of total voids u for varying V_w/V_{cm} ratios. Optimum packing points for each paste mixture are also noted on the u versus V_w/V_{cm} curves (grey-filled squares). The water voids line is drawn in each of the Figs. 8.4 and 8.5 graphs, in order to facilitate the estimation of air-filled voids content of every single paste mixture. Water-to-cementitious materials ratios and solid concentration factors at MPP and OPP for all paste mixtures are listed in Table 8.4.

From Fig. 8.4a and Table 8.4 it becomes clear that the increase of SP dosage in cement-only pastes (without additions) allows for the reduction of V_w/V_{cm}, leading to the decrease of the total voids content (or, equivalently, to the increase of the mixture's packing density), while maintaining the workability at a specified level

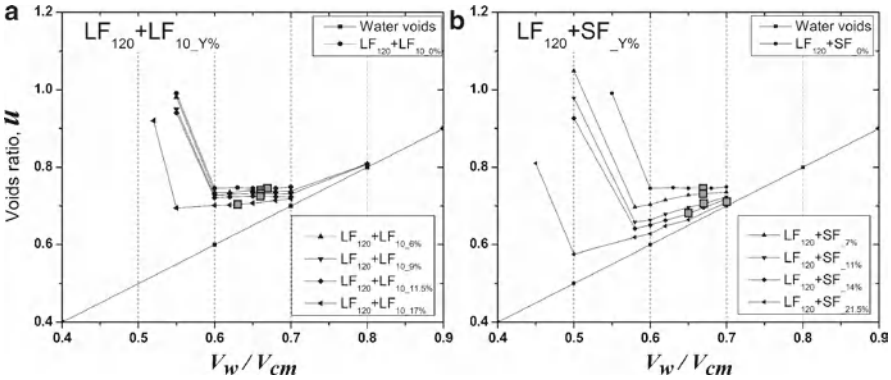

Fig. 8.5 Determination of OPPs for multi-additive mixtures comprising: (**a**) cement, LF_{120} and LF_{10}, and (**b**) cement, LF_{120} and SF

Table 8.4 Fresh- and hardened-state results of all produced cement paste mixtures

Paste mixtures	V_w/V_{cm} @ MPP [–], (ϕ)	V_w/V_{cm} @ OPP [–], (ϕ)	W_w/W_{cm} @ OPP [–]	$f_{c-28\,days}$ @ OPP [MPa]	$f_{t,fl-28\,days}$ @ OPP [MPa]
$CEM_{0\%\ SP}$	0.87 (0.502)	0.96 (0.489)	0.310	80.9	6.5
$CEM_{1.0\%\ SP}$	0.77 (0.531)	0.84 (0.524)	0.265	88.0	7.3
$CEM_{1.5\%\ SP}$	0.68 (0.544)	0.72 (0.542)	0.226	91.6	7.6
$LF_{120\_12.5\%}$	0.67 (0.559)	0.69 (0.559)	0.238	89.2	5.7
$LF_{120\_25\%}$	0.67 (0.573)	0.67 (0.573)	0.240	87.0	5.6
$LF_{120\_50\%}$	0.65 (0.577)	0.64 (0.575)	0.280	76.8	5.4
$LF_{10\_12.5\%}$	0.60 (0.569)	0.65 (0.562)	0.225	104.3	6.6
$LF_{10\_25\%}$	0.60 (0.584)	0.62 (0.581)	0.241	103.7	5.9
$LF_{10\_50\%}$	0.56 (0.602)	0.58 (0.602)	0.254	104.1	5.8
$SF_{10\_12.5\%}$	0.58 (0.579)	0.65 (0.565)	0.195	102.7	10.1
$SF_{10\_25\%}$	0.45 (0.628)	0.63 (0.573)	0.180	113.8	13.5
$SF_{10\_50\%}$	0.45 (0.634)	0.72 (0.520)	0.190	93.1	10.6
$LF_{120}+X2_{\_0\%}$	0.60 (0.573)	0.67 (0.573)	0.280	80.0	5.5
$LF_{120}+LF_{10\_6\%}$	0.60 (0.576)	0.66 (0.575)	0.280	89.4	5.4
$LF_{120}+LF_{10\_9\%}$	0.60 (0.579)	0.66 (0.577)	0.278	82.9	5.3
$LF_{120}+LF_{10\_11.5\%}$	0.60 (0.581)	0.66 (0.580)	0.276	89.4	6.6
$LF_{120}+LF_{10\_17\%}$	0.55 (0.590)	0.63 (0.587)	0.265	86.5	7.2
$LF_{120}+SF_{\_7\%}$	0.58 (0.589)	0.67 (0.578)	0.255	86.2	5.9
$LF_{120}+SF_{\_11\%}$	0.58 (0.605)	0.67 (0.587)	0.247	104.8	9.2
$LF_{120}+SF_{\_14\%}$	0.58 (0.609)	0.65 (0.595)	0.232	107.9	9.5
$LF_{120}+SF_{\_21.5\%}$	0.50 (0.635)	0.70 (0.585)	0.234	103.8	9.6
$LF_{10}+SF_{11\%}$	0.58 (0.609)	0.62 (0.605)	0.228	93.5	10.4

(that of the OPP – see grey-filled squares in Fig. 8.4a). Even when the same V_w/V_{cm} ratio is used, higher SP content results in lower voids ratios u and, hence, in higher solid concentration indices, ϕ; this observation comes into agreement with the findings of (Şhamaran et al. 2006; Jones et al. 2003).

The effect of additives on the packing density of SA pastes is more pronounced, especially for finely-grained ones. The addition of LF_{120} (Fig. 8.4b), as cement replacement (by volume), produces pastes with OPPs that correspond to lower V_w/V_{cm} ratios and higher packing densities compared to addition-free pastes ($CEM_{1.5\%SP}$). With varying percentage of cement replacement by LF_{120} (up to 25% by volume) there appears to be a linear relationship between V_w/V_{cm} and u (hence, ϕ) at the optimum packing points. However, for cement replacement percentages larger than 25%, voids volume decreases marginally (for any given V_w/V_{cm} ratio) and packing at OPP reaches a maximum attainable value. For the same V_w/V_{cm} ratio, the increase of the packing density of a paste with increasing quantity of cement replaced by a coarser powder comprises – by intuition – a contradiction. Nevertheless, the gradual substitution of cement with LF_{120} results in the modification of the solid particles' grading curve so that better packing is achieved.

In regards to LF_{120}, the effect of cement replacement by the finer LF_{10} limestone powder was qualitatively the same but more noticeable in terms of packing density increase at the OPPs with increasing cement replacement ratios (see Fig. 8.4c). In this case, a maximum attainable value of packing density at OPP was not reached, even for cement replacement percentages as high as 50%.

Cement replacement by silica fume resulted in considerable increase of the pastes' packing densities at MPPs (Fig. 8.4d), whereas the respective increase at OPPs was of lower magnitude. This was owed to the fact that increase of cement replacement percentages by silica fume resulted in pastes of progressively higher cohesion and stickiness. This was especially noticed for a cement replacement percentage equal to 50% (a percentage not practically applicable from a commercial point of view); in this case, the V_w/V_{cm} ratio corresponding to the OPP was equal to 0.72 (i.e. higher than the ones at OPPs for $SF_{12.5\%}$ and $SF_{25\%}$ pastes and considerably higher than the one corresponding to the MPP of $SF_{50\%}$).

The first set of MA pastes comprising limestone fillers, showed limited capacity for packing density increase at the OPPs for increasing content of additive LF_{10} up to 11.5% by cement volume. For these mixtures optimum packing density was achieved at an approximately constant V_w/V_{cm} ratio equal to 0.66 (see Fig. 8.5a and Table 8.4). The paste with LF_{10} content equal to 17% by cement volume (15% by cement weight) exhibited the highest packing density. The effect of SF content increase in MA pastes comprising LF_{120} and SF was analogous to the one for (SA) $SF_{Y\%}$ pastes. Again, with increasing SF content, packing density at OPPs increased at a much lesser extend in regards to the achieved increase of packing density at MPPs. As in the case of $LF_{120}+LF_{10\_Y\%}$ pastes (where $6\% \le Y\% \le 11.5\%$), optimum packing density in the $LF_{120}+SF_{\_Y\%}$ ones (where $7\% \le Y\% \le 14\%$) was achieved at the same V_w/V_{cm} ratio (with a mean value of 0.66). Further increase in SF content ($LF_{120}+SF_{21.5\%}$) resulted in a dramatic decrease of packing density at the OPP. A final MA paste mixture comprising finely ground powders ($LF_{10}+SF_{11\%}$) was investigated (Table 8.4); this mixture resulted in the maximum achieved packing density at the OPP compared to all other tested paste mixtures (and at a value of V_w/V_{cm} ratio lower than 0.66).

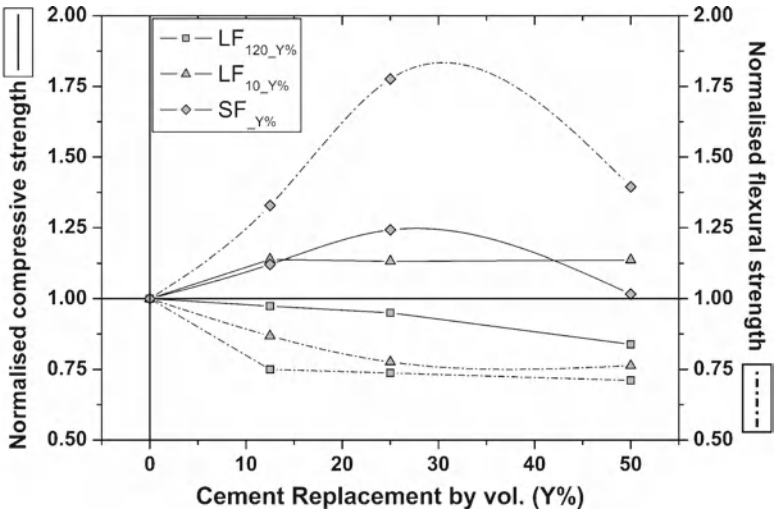

Fig. 8.6 Normalized compressive and flexural strengths of SA pastes v cement replacement ratio

8.3.2.2 Hardened-State Test Results and Discussion

Twenty-eight-day compressive and flexural strengths for all paste mixtures (sampled at their OPPs) are given in Table 8.4. As expected, the increase of SP dosage in cement-only pastes resulted in increased compressive and flexural strengths due to improved particle dispersion that lead to the reduction of the V_w/V_{cm} ratios and, hence, of the water-to-cement mass ratios (W_w/W_{cm}).

Figure 8.6 illustrates the variation of the normalized compressive and flexural strength for every SA paste mixture sampled at its OPP (i.e. the 28-day compressive or flexural strength of paste $X_{Y\%}$ over that of the control mixture $CEM_{1.5\%SP}$) as a function of the cement replacement percentage, Y%. For a specified level of workability, the strength of a paste is dependent on both the achieved packing density and the respective water-to-cementitious materials mass ratio: strength (especially compressive strength) increases with increasing ϕ and decreasing W_w/W_{cm}. This condition was achieved for $SF_{Y\%}$ pastes and for cement replacement ratios up to 25%; when half of the cement was replaced by silica fume the reduction of ϕ (unavoidable at the OPP) lead to strength loss. For increasing cement replacement ratios the increase of packing density in limestone-modified (SA) pastes was followed by increase of the respective W_w/W_{cm} ratios. [It is noted that the efficiency factors used for the calculation of W_w/W_{cm} of pastes with limestone fillers (regardless of grading) and silica fume were equal to 0.2 and 2.2, respectively.] In this context, both the compressive and the flexural strengths of $LF_{120\_Y\%}$ pastes were lower than the ones of the control paste ($CEM_{1.5\%SP}$) and decreased with increasing cement replacement ratios. On the contrary, it was possible to achieve higher compressive strengths for $LF_{10\_Y\%}$ pastes (in comparison to the one of the control paste) for all cement replacement ratios applied. This is ought to the lower W_w/W_{cm} ratios and to the considerably higher ϕ values

reached at the OPPs, compared to the counterpart $LF_{120\_Y\%}$ pastes, for each cement replacement ratio. Hence, it was possible to produce pastes of comparable workability and higher compressive strength to the ones of a cement-only paste by substituting as much as half of the cement with finely grained limestone filler. On the other hand, flexural strengths of $LF_{10\_Y\%}$ pastes (that are dependent more on W_w/W_{cm} ratios than on ϕ), though higher than the ones of $LF_{120\_Y\%}$ pastes, were lower than the flexural strength of the addition-free paste and decreased with increasing cement replacement ratios.

The limited packing density increase achieved in the $LF_{120}+LF_{10\_Y\%}$ paste series for increasing content of additive LF_{10} (keeping the sum of limestone additives at 40% by cement volume at all times) had practically no effect on the compressive strength of the pastes. On the contrary, when SF was used as the finer additive the compressive strength increased with increasing SF content due to the noticeable respective increase of packing density. Flexural strength increased with increasing content of the finer additive in both paste series. Paste $LF_{10}+SF_{\_11\%}$ achieved the highest flexural strength in the MA paste series.

8.3.3 Mortar Mixtures

The mortar phase of LWASCC was investigated through the assessment of two series of mortar mixtures, each series comprising ten different mix designs; paste compositions for these designs (but SP dosage) were identical to the two outperforming pastes of each series from the preceding part of the investigation in terms of tensile strengths, namely $LF_{120}+LF_{10\_17\%}$ and $LF_{10}+SF_{11\%}$ (henceforth referenced as M1 and M2, respectively). Two parameters were varied within each mortar series (keeping the sum of additives at 40% by cement volume at all times): the sand content (40%, 45% and 50% by mortar volume) and the SP dosage (1.5%, 1.8% and 2.1% by cement weight) resulting in nine different mortar mix designs within each mortar series. The optimum mortar mixture of each series in terms of mechanical strengths was reproduced with complete substitution of pumice sand with normal-weight river sand. All types of sands were used in an initially oven-dry state and were mixed at the beginning of the mixing procedure for 1 min with the total water quantity of the batch in order to reach a saturated state.

Mix proportions for all mortar mixtures are given in Table 8.5. The mixtures are denoted as $Mi\_X_{Y\%SP}$, where: i is set to either 1 or 2 for pastes (on which the mortars are based) M1 or M2, respectively; X and subscript Y correspond to the sand content (% by mortar volume) and superplasticizer content (by cement weight), respectively. Superscript NS (where applicable) denotes mortars comprising normal-weight sand.

As in the case of the paste phase, for every single mortar mix design (Table 8.5) a series of mixtures was produced with varying V_w/V_{cm} ratios, in order to identify the OPP as the point at which ϕ, Γ_m (the mini slump cone test result) and R_m (the mini V-funnel test result) are maximized. This procedure resulted in the production and fresh-state assessment of 101 individual mortar mixtures. Mechanical strengths of

Table 8.5 Mix proportions of mortar mixtures

Mortar mixtures	Cement (a%[a])	SP (b%[b])	LF_{120} (c%[c])	LF_{10} (c%[c])	SF (c%[c])	Sand (c%[c])
$M1\_50_{1.5\%\ SP}$	24.0	1.5	22.8	17.2	–	276.8
$M1\_50_{1.8\%\ SP}$	24.0	1.8	22.8	17.2	–	276.8
$M1\_50_{2.1\%\ SP}$	24.0	2.1	22.8	17.2	–	276.8
$M1\_45_{1.5\%\ SP}$	26.2	1.5	22.8	17.2	–	242.2
$M1\_45_{1.8\%\ SP}$	26.2	1.8	22.8	17.2	–	242.2
$M1\_45_{2.1\%\ SP}$	26.2	2.1	22.8	17.2	–	242.2
$M1\_40_{1.5\%\ SP}$	28.8	1.5	22.8	17.2	–	207.6
$M1\_40_{1.8\%\ SP}$	28.8	1.8	22.8	17.2	–	207.6
$M1\_40_{2.1\%\ SP}$	28.8	2.1	22.8	17.2	–	207.6
$M1^{NS}\_40_{2.1\%\ SP}$	28.8	2.1	22.8	17.2	–	207.6
$M2\_50_{1.5\%\ SP}$	24.0	1.5	–	28.7	11.3	276.8
$M2\_50_{1.8\%\ SP}$	24.0	1.8	–	28.7	11.3	276.8
$M2\_50_{2.1\%\ SP}$	24.0	2.1	–	28.7	11.3	276.8
$M2\_45_{1.5\%\ SP}$	26.2	1.5	–	28.7	11.3	242.2
$M2\_45_{1.8\%\ SP}$	26.2	1.8	–	28.7	11.3	242.2
$M2\_45_{2.1\%\ SP}$	26.2	2.1	–	28.7	11.3	242.2
$M2\_40_{1.5\%\ SP}$	28.8	1.5	–	28.7	11.3	207.6
$M2\_40_{1.8\%\ SP}$	28.8	1.8	–	28.7	11.3	207.6
$M2\_40_{2.1\%\ SP}$	28.8	2.1	–	28.7	11.3	207.6
$M2^{NS}\_40_{2.1\%\ SP}$	28.8	2.1	–	28.7	11.3	207.6

[a]a%: by total solids volume
[b]b%: by cement weight
[c]c%: by cement volume

mortars sampled at their OPPs were measured using prismatic specimens (40×40×160 mm).

8.3.3.1 Fresh-State Test Results and Discussion

Table 8.6 summarizes all mortar test results related to the assessment of the mixtures' workability at the OPPs. It should be highlighted at this point that the workability tests performed on mortars lacked any specific target value. The validity of recommended target values (see Okamura and Ouchi (Okamura and Ouchi 2003) – $4.75 \le \Gamma_m \le 5.76$ and $R_m \ge 1$) established for normal-weight SCC is challenged in the case of LWASCC. Therefore, an additional goal of this study was to define suitable ranges of Γ_m and R_m values that would ensure self-compactness for lightweight aggregate mortars, following the wet packing density method.

Figure 8.7 illustrates the solid concentration factor ϕ as a function of pumice sand and superplasticizer content in $M1\_X_{Y\%\ SP}$ and $M2\_X_{Y\%\ SP}$ mortars. It is observed that packing density increases with decreasing pumice sand content and increasing SP dosage; moreover, this increase in packing density is achieved at lower water-to-cementitious materials ratios. For both mortar series, ϕ was maximized at a pumice sand content equal to 40% by mortar volume and an SP dosage

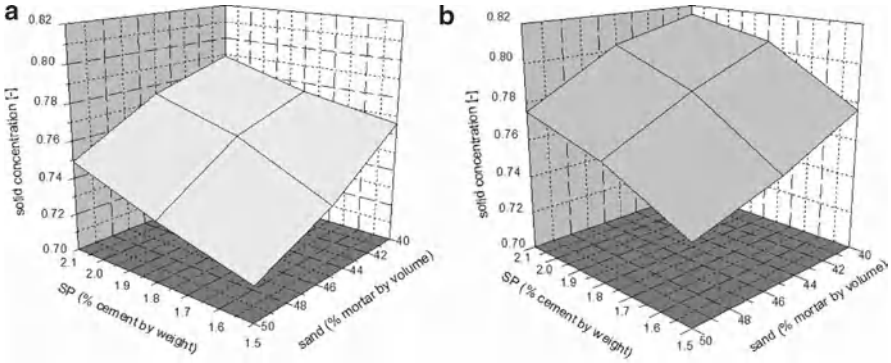

Fig. 8.7 Solid concentration factor ϕ as a function of sand and superplasticizer content in: (**a**) M1_$X_{Y\%\ SP}$ and (**b**) M2_$X_{Y\%\ SP}$ mortars

equal to 2.1% by cement weight. In most mixtures the magnitude of SP effect on packing density decreased with increasing dosage.

Slump-flow scores at the OPP for all mortar mixtures showed limited fluctuation ranging between 330 and 365 mm ($10.0 \leq \Gamma_m \leq 12.3$). Moreover, there was no clear distinction between mortars M1_$X_{Y\%\ SP}$ (with all-limestone additives) and M2_$X_{Y\%\ SP}$ (with additives comprising limestone and silica fume) in terms of slump-flow scores achieved (see Fig. 8.8a). On the contrary, the two mortar series produced mini V-funnel flow times of distinctively different ranges (see Fig. 8.8b). SF-modified mortars (M2_$X_{Y\%\ SP}$) resulted in shorter flow times (12.3–15.1 s) compared to mortars with additives consisting exclusively of limestone powders (M1_$X_{Y\%\ SP}$ with flow times ranging between 15.1 and 18.6 s). This was attributed to the inter-particle shear forces within the additives which were much weaker in SF blends due to the high sphericity of silica fume particles; limestone particles, on the other hand, were significantly more angular. Mini V-funnel flow times for all mixtures generally tended to decrease with increasing sand content, whereas Γ_m/R_m ratios tended to increase with increasing SP dosage.

Complete substitution of pumice sand with normal-weight river sand with rounder grains ($Mi^{NS}\_40_{2.1\%\ SP}$ mixtures) resulted in more flowable mixtures, especially when silica fume additive was employed.

8.3.3.2 Hardened-State Test Results and Discussion

Twenty-eight-day compressive and flexural strengths for all mortar mixtures (sampled at their OPPs) are given in Table 8.6. For all mixtures strength increased (almost linearly) with increasing packing density, that is with decreasing pumice sand content and increasing SP dosage. The compressive and flexural strength in the M1_$X_{Y\%\ SP}$ mortar series ranged from 58 to 70 MPa and from 5.7 to 7.6 MPa, respectively. Mortars containing silica fume (M2_$X_{Y\%\ SP}$ series) reached higher strengths with compressive and flexural strength spanning between 64 and 78 MPa and 6.7

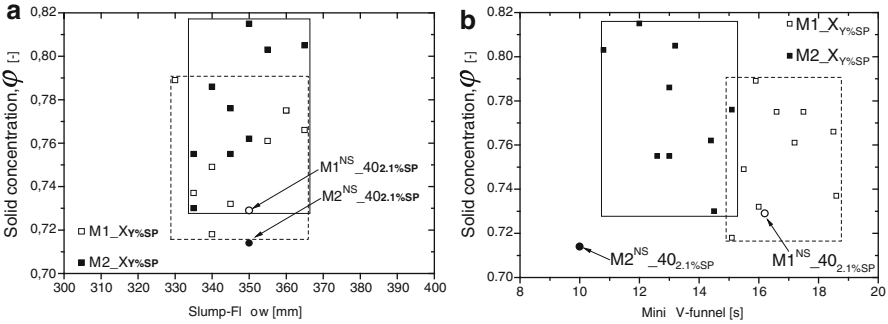

Fig. 8.8 Solid concentration factor ϕ at OPP for all mortars in respect to: (**a**) mini slump-flow and (**b**) mini V-funnel test results

Table 8.6 Fresh- and hardened-state results of all mortar mixtures produced

Mortar mixtures	Slump-flow [mm]	Γ_m [–]	V-funnel [s]	R_m [–]	V_w/V_{cm} @ OPP [–], (ϕ)	$f_{c\text{-}28\ days}$ @ OPP [MPa]	$f_{t,fl-28\ days}$ @ OPP [MPa]
$M1\_50_{1.5\%\ SP}$	320×355	10.4	15.1	0.66	0.70 (0.718)	58.1	5.7
$M1\_50_{1.8\%\ SP}$	330×340	10.2	18.6	0.54	0.62 (0.737)	61.0	7.3
$M1\_50_{2.1\%\ SP}$	370×360	12.3	18.5	0.54	0.58 (0.766)	63.4	7.6
$M1\_45_{1.5\%\ SP}$	340×350	10.9	16.0	0.63	0.64 (0.732)	61.2	6.5
$M1\_45_{1.8\%\ SP}$	345×365	11.6	17.2	0.58	0.55 (0.761)	63.4	6.7
$M1\_45_{2.1\%\ SP}$	370×350	12.0	17.5	0.57	0.52 (0.775)	69.8	7.0
$M1\_40_{1.5\%\ SP}$	340×340	10.6	15.5	0.65	0.51 (0.749)	62.9	6.4
$M1\_40_{1.8\%\ SP}$	365×360	12.1	16.6	0.60	0.48 (0.775)	67.5	7.5
$M1\_40_{2.1\%\ SP}$	340×325	10.1	15.9	0.63	0.45 (0.789)	67.7	7.6
$M1^{NS}\_40_{2.1\%\ SP}$	355×340	11.1	16.2	0.62	0.59 (0.729)	94.0	11.2
$M2\_50_{1.5\%\ SP}$	330×340	10.2	14.5	0.69	0.63 (0.730)	64.1	6.7
$M2\_50_{1.8\%\ SP}$	340×350	10.9	13.0	0.77	0.57 (0.755)	67.9	7.7
$M2\_50_{2.1\%\ SP}$	350×340	10.9	15.1	0.66	0.53 (0.776)	65.5	7.1
$M2\_45_{1.5\%\ SP}$	350×350	10.9	14.4	0.69	0.53 (0.762)	66.3	7.4
$M2\_45_{1.8\%\ SP}$	340×340	10.6	13.0	0.77	0.48 (0.786)	74.8	8.2
$M2\_45_{2.1\%\ SP}$	360×370	12.3	13.2	0.76	0.44 (0.805)	76.7	8.3
$M2\_40_{1.5\%\ SP}$	345×320	10.0	12.6	0.79	0.47 (0.755)	76.7	7.1
$M2\_40_{1.8\%\ SP}$	360×350	11.6	12.3	0.81	0.40 (0.803)	74.3	8.4
$M2\_40_{2.1\%\ SP}$	340×360	11.2	13.0	0.77	0.38 (0.815)	77.9	8.6
$M2^{NS}\_40_{2.1\%\ SP}$	340×360	11.2	10.0	1.00	0.62 (0.714)	101.4	11.4

and 8.6 MPa, respectively. In general, flexural to compressive strength ratio varied between 10% and 12%.

Mortars comprising normal-weight river sand exhibited higher strengths compared to their counterparts comprising pumice sand. Larger strength gains were recorded for mortars with all-limestone additives (approx. by 45%) in comparison to SF-modified mortars (strength gain being in the order of 30%). It is interesting to note that mortars $M1^{NS}\_40_{2.1\%\ SP}$ and $M2^{NS}\_40_{2.1\%\ SP}$ were almost equivalent in terms of strength.

Table 8.7 Mix proportions of LWASCC mixtures (all constituent materials in kg/m³)

LWASCC mixtures	Cement	LF_{120}	LF_{10}	SF	SP	Pumice			Total water	W_w/W_{cm}
						Sand	Fine	Coarse		
LF_1.20	326.0	65.0	49.0	–	4.9	297.0	139.0	310.0	316.0	0.47
LF_1.30	349.5	69.5	52.5	–	5.2	318.0	129.0	287.0	321.0	0.45
LF_1.40	377.0	75.0	56.5	–	5.7	343.0	114.0	253.0	326.0	0.44
LF_1.50	400.0	79.0	60.0	–	6.0	364.0	103.0	229.0	330.0	0.43
LF_1.55	428.0	85.0	64.0	–	6.4	398.5	91.0	202.0	332.5	0.41
SF_1.35	379.0	–	94.0	30.5	5.4	344.5	120.5	268.0	309.0	0.33
SF_1.40	400.0	–	100.0	32.0	6.0	363	114.0	253.0	305.0	0.31
SF_1.55	454.5	–	113.5	36.5	6.8	413.5	93.5	208.0	301.0	0.27

8.3.4 LWASCC Mixtures

Following the determination of lightweight aggregate mortars' compositions that ensure self-compactness, the mix design of LWASCC mixtures involved the derivation of the coarse-to-fine pumice aggregates ratio that corresponded to the least voids volume; this ratio was found to be equal to 70/30 (Papanicolaou and Kaffetzakis (Papanicolaou and Kaffetzakis 2011)). Then, the finalization of LWASCC mixtures' proportions was realized through determining the mortar-to-aggregates volumetric ratio (*K* factor) that produced the highest fresh- and hardened-state performance ratings.

Two mortar compositions were chosen as the 'core' material for the pumice aggregate SCC trial mixtures: $M1\_40_{1.5\%SP}$ and $M2\_40_{1.5\%\,SP}$. Mixtures receive the following notation: A_*K*, where A denotes the type of mortar composition used (LF for $M1\_40_{1.5\%SP}$ with all additives comprising limestone powders and SF for $M2\_40_{1.5\%SP}$ with additives consisting of limestone powder and silica fume); *K* is equal to the value of the *K* factor. All mixtures received a small quantity of stabilizer (0.5% by cement weight). Starting from a value of 1.20 the *K* factor was increased in each trial LF_*K* mixture until satisfactory workability test scores were achieved. The starting *K* factor value for the SF_*K* mixture series (produced after the completion of the LF_*K* mixtures) was equal to the optimum *K* factor derived for the LF_*K* series; this value was then decreased in each trial SF_*K* mixture, until satisfactory self-compactness was again reached. The proportions of all produced mixtures are presented in Table 8.7.

The mixing procedure (which is also proposed by the authors) started by mixing the aggregates (sand excluded) with the 2/3 of the total water quantity for 2 min in order for the aggregates to absorb water under dynamic conditions during mixing. For the same reason the lightweight sand was then added to the rest of the aggregates and mixed for one extra minute. Next, the cementitious materials (pre-mixed at a dry state for 2 min) and the rest of the water (in which the admixtures were deluded) were gradually added in the mix and mixing continued for 5–7 min.

All mixtures produced were assessed in both fresh and hardened state. The tests used in order to rate the self-compacting performance of the mixtures included: the Slump-flow test, the V-funnel test, the L-box test (blocking ratio H_2/H_1), the J-ring

test (spread and step values) and the Sieve Stability Test (SST), whereas a Visual Stability Index (VSI, ASTM C1611/C1611M - 09be1 2009) was also assigned for each mixture. All the aforementioned tests were performed at 30 min time intervals (up to 90 min after mixing completion) provided that they produced 'passing' scores (i.e. Slump-flow ≥ 550 mm, V-funnel test ≤ 30 s, $H_2/H_1 \geq 0.8$, J-ring$_{spread}$ ≥ 550 mm and J-ring$_{step}$ ≤ 10 mm). The air content of each fresh mixture was also measured using a volumetric air meter (as per the ASTM C173 standard (ASTM C173/C173M - 10b 2010)). The compressive strength of the mixtures was assessed at 7, 28 and 56 days after casting using 150 mm cube specimens. The 28-day compressive and splitting tensile strengths (as well as the modulus of elasticity) were also determined using 150 × 300 mm cylinders. All specimens were stored until testing in an environmental chamber under constant temperature (21°C) and relative humidity (95%).

8.3.4.1 Fresh-State Test Results and Discussion

The results of the fresh-state tests are presented in Table 8.8. During the testing period ambient and concrete temperatures ranged from 22.3°C to 25.2°C and from 24.0°C to 28.0°C

High aggregate contents in the LF_*K* series of mixtures ($K = 1.20$ or $K = 1.30$) resulted in increased inter-particle shear forces and, thus, failed to produce adequate workability right after mixing completion (for example, $H_2/H_1 = 0.6$ and 0.73 for LF_1.2 and LF_1.3, respectively, at t = 0′). Mixtures LF_1.4 and LF_1.5 performed better and retained self-compactness for 60 min with a low L-box value for the LF_1.4 mixture ($H_2/H_1 = 0.76$ at t = 60′) and a high V-funnel flow value for LF_1.5 mixture (13.5 s at t = 60′). The final mixture (LF_1.55) exhibited self-compacting ability up to at least 90 min after mixing completion (758 mm, 8.5 s and 1.0 for Slump-flow, V-funnel and L-box tests, respectively, at $t = 90'$).

Overall, the most demanding tests for limestone-modified pumice aggregate SCC were: (i) the L-box test (due to the low dynamic energy of the sampled material in the vertical compartment of the apparatus, which in turn is owed to the low density of the mix); and (ii) the V-funnel test (due to the high inter-grain friction in the mortar, owing to the angular shape of limestone fillers and pumice sand). Favorable J-ring test results were achieved provided that slump-flow exceeded 800 mm and V-funnel efflux time was between 7 and 10 s (at $t = 0'$). The air content ranged from 2.5% to 3.0%.

The SST results suggest a limited tendency to segregation for $K = 1.30$ and $K = 1.40$; these results are correlated to the VSI ratings (albeit subjective and ranging from 0 to 1.5) assigned to each mixture. However, it was observed that in the case of LWASCC, where highly porous aggregates continue to absorb part of the mixing water after mixing completion, an initial SST score of 18% should not be regarded as an alarming indication for segregation susceptibility.

In comparison to the LF_*K* series of mixtures the SF_*K* ones were significantly more cohesive resulting in lower SST and VSI values. SF_1.55 mixture (the mixture produced first in the SF_*K* series) performed poorly in terms of both unrestricted

Table 8.8 Fresh-state results of LWASCC mixtures

Mixture	SST [%]	Air [%]	VSI [0–4]	Slump-flow [mm]				V-funnel [sec]				L-box [H_2/H_1]				J-ring [mm]			
				t=0′	t=30′	t=60′	t=90′	t=0′	t=30′	t=60′	t=90′	t=0′	t=30′	t=60′	t=90′	t=0′	t=30′	t=60′	t=90′
LF_1.2	5	2.50	0.5	550	–	–	–	10.3	–	–	–	0.60	–	–	–	520[a]	–	–	–
																15[b]	–	–	–
LF_1.3	20	2.50	1.5	718	650	–	–	30	23.0	–	–	0.73	0.64	–	–	613	–	–	–
																12	–	–	–
LF_1.4	18	2.50	1.0	845	835	780	720	9.9	6.6	9.2	11.4	0.89	0.91	0.90	0.76	730	685	640	570
																6	5	8	10
LF_1.5	15	3.00	0.5	810	763	785	765	6.8	7.8	7.8	13.5	1.00	1.00	1.00	0.90	770	730	665	605
																3	2	7	10
LF_1.55	16	2.75	1.0	850	815	790	758	7.1	6.4	6.7	8.5	1.00	1.00	1.00	1.00	763	700	655	630
																2	2	2	8
SF_1.35	10	3.50	0.5	575	–	570	–	3.0	–	7.0	–	0.82	–	0.61	–	–	–	–	–
																–	–	–	–
SF_1.4	12	3.50	0.5	650	–	–	–	6.4	–	–	–	0.73	–	–	–	–	–	–	–
																–	–	–	–
SF_1.55	8	4.00	0.0	485	–	–	–	9.8	–	–	–	0.37	–	–	–	–	–	–	–
																–	–	–	–

[a] Spread value
[b] Step value

Table 8.9 Hardened-state properties of LWASCC mixtures

Mixture	Density [kg/m³]		Compressive strength [MPa]				Specific strength[a] [MPa/(kg/m³)×10⁻³]	$f_{t,sp28d}$ [MPa]	E_{28d} [GPa]
	ρ_{fresh}	$\rho_{oven\text{-}dry}$	$f_{c7d,cube}$	$f_{c28d,cube}$	$f_{c28d,cyl}$	$f_{c56d,cube}$			
LF_1.2	1,581	1,423	19.1	27.4	26.3	28.9	19.3	1.5	10.9
LF_1.3	1,596	1,490	20.1	30.3	26.4	30.6	20.3	1.7	11.1
LF_1.4	1,618	1,507	22.8	29.9	26.5	31.2	19.8	2.0	11.4
LF_1.5	1,680	1,550	23.6	32.3	28.7	33.4	20.8	1.9	11.7
LF_1.55	1,705	1,595	25.0	33.2	29.8	35.3	20.8	2.0	12.0
SF_1.35	1,634	1,483	27.0	34.5	29.9	35.5	23.3	2.0	12.2
SF_1.4	1,653	1,519	30.7	37.5	32.9	40.1	24.7	2.0	13.2
SF_1.55	1,668	1,576	33.3	41.1	34.9	45.0	26.1	2.1	14.3

[a] $f_{c28d,cube}/\rho_{oven\text{-}dry}$

and restricted flowability; as a result, a reduction of the paste content was deemed necessary. For $K=1.35$ the SF-modified pumice aggregate concrete showed moderate self-compacting potential (at t=0′), which was not retained for more than one hour past mixing completion. Further decrease of the K factor was not attempted as it led to mixtures of progressively lower densities and unacceptably low passing ratios.

Mixtures LF_1.55 and SF_1.35 (i.e. the outperforming ones from both series of mixtures in terms of self-compacting features) may be classified according to the appendix of EC2 (CEN 2000a) pertinent to SCC, as follows: (i) for LF_1.55 SF3 (slump-flow diameter class), VF1 (viscosity class V-funnel), PL2 (passing ability class L-box), PJ2 (passing ability class J-ring) and (marginally) SR2 (Sieve segregation resistance class); (ii) for SF_1.35 SF1, VF1, PL2 (passing ability class J-ring cannot be assigned for SF_1.35) and SR2.

8.3.4.2 Hardened-State Test Results and Discussion

All measured mechanical properties of the mixtures are given in Table 8.9, alongside their densities (fresh and oven-dry). All mixtures fall in the D1.6 density class per EN 206-1 (CEN 2000a). As expected, the compressive strength increased for increasing K values, while the SF_K mixtures reached higher compressive strengths compared to the LF_K mixtures (although a direct comparison is not entirely valid due to mix proportioning differences). The mean ratio of the 7-days' compressive strength ($f_{c7d,cube}$) to the 28-days' one ($f_{c28d,cube}$) was found to be equal to 0.7 and 0.8 for LF_K and SF_K mixtures, respectively. The 56-days' compressive strength ($f_{c56d,cube}$) compared to $f_{c28d,cube}$ increased by a percentage not exceeding 10% for any mixture. The mean ratio of the 28-days' compressive strength measured using cylindrical specimens ($f_{c28d,cyl.}$) to that measured using cubic specimens was equal to 0.9. The splitting tensile strengths ($f_{t,sp.28d}$) of all mixtures accounted for 6.5% of $f_{c28d,cyl}$ on average. The modulus of elasticity was significantly lower than in normal-weight SCC mixtures of comparable W_w/W_{cm} ratios

and may be estimated with adequate accuracy through multiplying the square root of $f_{c28d,cube}$ by a factor equal to (1.4 $\rho_{oven\text{-}dry}$). Finally, the 28-days' specific strength ($f_{c28d,cube}/\rho_{oven\text{-}dry}$) ranged from 19.3×10^{-3} MPa/(kg/m^3) to 26.1×10^{-3} MPa/(kg/m^3) while the mean value of LWASCC mixtures found in the literature is 24×10^{-3} MPa/(kg/m^3) (Papanicolaou and Kaffetzakis (Papanicolaou and Kaffetzakis 2011)).

8.4 Conclusions

The production of LWASCC requires a well-designed mortar, cohesive enough to inhibit aggregates' segregation due to buoyancy. The methodology presented herein includes the determination of: (i) the fines proportioning in the paste phase and the sand, water and SP proportioning in the mortar phase following the wet packing method, (ii) the optimum aggregates' fractions ratio and the volumetric mortar-to-aggregates ratio in the concrete phase. Highly fluidic LWASCC mixtures with enhanced stability and workability retention capacity are possible to produce. Ceiling strengths are posed by the inherently low crushing resistance of naturally occurring lightweight aggregates, such as pumice.

The mix design of LWASCC should not be exclusively focused on maximizing packing density. The optimum packing points in paste and mortar reached through both wet packing method and standard consistency tests are in most cases far from the maximum packing points. Relative flow areas and relative flow speeds for lightweight aggregate mortars assessed by the wet packing method were found to lie in the following ranges: $10.0\le\Gamma_m\le12.3$, $0.55\le R_m\le1.00$ and differ from the ones suggested for normal-weight self-compacting mortars.

Aggregates' absorption and subsequent workability loss in LWASCC mixtures may be successfully mitigated by pre-mixing the aggregates with part of the batch water at the beginning of the mixing procedure. Both filling and passing ability in self-compacting concrete mixtures are strongly related to their density. Self-compacting features (and especially passing ability) may be difficult to be achieved for low-density concrete ($\rho_{oven\text{-}dry}\le1{,}600$ kg/m^3), this difficulty increasing for decreasing unconfined flowability capacity of the mixture. High slump-flow scores (≥750 mm or SF3 class) and fast flowing mixtures (V-funnel efflux time ≤ 9 s, or VF1 viscosity class) are recommended for LWASCC, especially when a prolonged workability retention period is aimed for.

References

ASTM C1611/C1611M – 09be1 (2009) Standard test method for slump flow of self-consolidating concrete – Appendix X1, ASTM International, West Conshohocken, PA. doi: 10.1520/C1611_C1611M-09BE01, www.astm.org

ASTM C173/C173M – 10b (2010) Standard test method for air content of freshly mixed concrete by the volumetric method, ASTM International, West Conshohocken, PA. doi: 10.1520/C0173_C0173M-10B, www.astm.org

CEN (1998) EN 1097-3:1998. Tests for mechanical and physical properties of aggregates. Determination of loose bulk density and voids. Comite Europeen de Normalisation, Brussels
CEN (1999) EN 1097-4:1999. Tests for mechanical and physical properties of aggregates – part 6: determination of the voids of dry compacted filler. Comite Europeen de Normalisation, Brussels
CEN (2000a) EN 206-1:2000. Concrete – part 1: specification, performance, production and conformity. Comite Europeen de Normalisation, Brussels
CEN (2000b) EN 1097-8:2000. Tests for mechanical and physical properties of aggregates – part 6: Determination of particle density and water absorption. Comite Europeen de Normalisation, Brussels
Hwang CL, Hung MF (2005) Durability design and performance of self-consolidating lightweight concrete. Constr Build Mater 19:619–626
Jacobsen S, Arntsen B (2008) Aggregate packing and -void saturation in mortar and concrete proportioning. Mater Struct 41:703–716
Jones MR, Zheng L, Newlands MD (2003) Estimation of the filler content required to minimize voids ratio in concrete. Mag Concr Res 55(2):193–202
Mechtcherine V, Haist M, Hewener A, Muller HS (2001) Self-compacting lightweight concrete – a new high-performance building material. In: Proceedings of the 2nd international symposium on self-compacting concrete, Kochi, Japan
Okamura H, Ouchi M (2003) Self-compacting concrete. J Adv Concr Technol 1:5–15
Papanicolaou A, Kaffetzakis M (2009) Pumice aggregate self-compacting concrete. In: 16th National conference on concrete, Cyprus, Pafos (in Greek)
Papanicolaou C, Kaffetzakis M (2011) Lightweight aggregate self-compacting concrete: state-of-the-art & pumice application. J Adv Concr Technol 9(1):15–29
Şhamaran M, Christianto HA, Yaman İÖ (2006) The effect of chemical admixtures and mineral additives on the properties of self-compacting mortars. Cem Concr Compos 28:432–440
Shi C, Wu Y (2005) Mixture proportioning and properties of self-consolidating lightweight concrete containing glass powder. ACI Mater J 102(5):355–363
Uygunoğlu T, Topçu IB (2009) Thermal expansion of self-consolidating normal and lightweight concrete at elevated temperature. Constr Build Mater 23:3063–3069
Wong HHC, Kwan AKH (2008) Packing density of cementitious materials: part 1 – measurement using a wet packing method. Mater Struct 41:689–701

Chapter 9
Fibres in Concrete Structures

György L. Balázs

Abstract Fibres in concrete opened new ways of thinking in design and application of concrete as a structural material. Short fibres provide efficient ways to improve some specific properties of concrete members such as ductility, deformability, durability, as well as load bearing capacity. Parallelly bonded long fibres may form FRP reinforcements that can be applied internally like conventional prestressed or non-prestressed reinforcements. Otherwise they can be applied as externally bonded (EBR) or near surface mounted (NSM) reinforcements. Many applications show successful use. The present chapter intends to give an overview of the principal aspects of fibre-reinforced concrete, and on the other hand the main characteristics of EBR or NSM strengthening methods by using FRP. Specific details are given both on material and design aspects.

9.1 Introduction

Fibres have become important for concrete structures. A large variety of fibre applications in various members and for various purposes using different fibres is known from the last decades. These engineering applications often followed early empirical applications but are extended for further optimization of material properties.

Fibres are very thin compared to the dimensions of concrete elements, but still they may provide considerable improvements of material properties if used in reasonable ways. Fibres can be used either in their long form or cut into pieces and mixed into the concrete. These are often the same fibres. Bonded fibres can be

G.L. Balázs (✉)
Budapest University of Technology and Economics, Faculty of Civil Engineering, Department of Construction Materials and Engineering Geology, Muegyetem rkp 3, H-1111, Budapest, Hungary
e-mail: balazs@vbt.bme.hu

M.N. Fardis (ed.), *Innovative Materials and Techniques in Concrete Construction: ACES Workshop*, DOI 10.1007/978-94-007-1997-2_9,

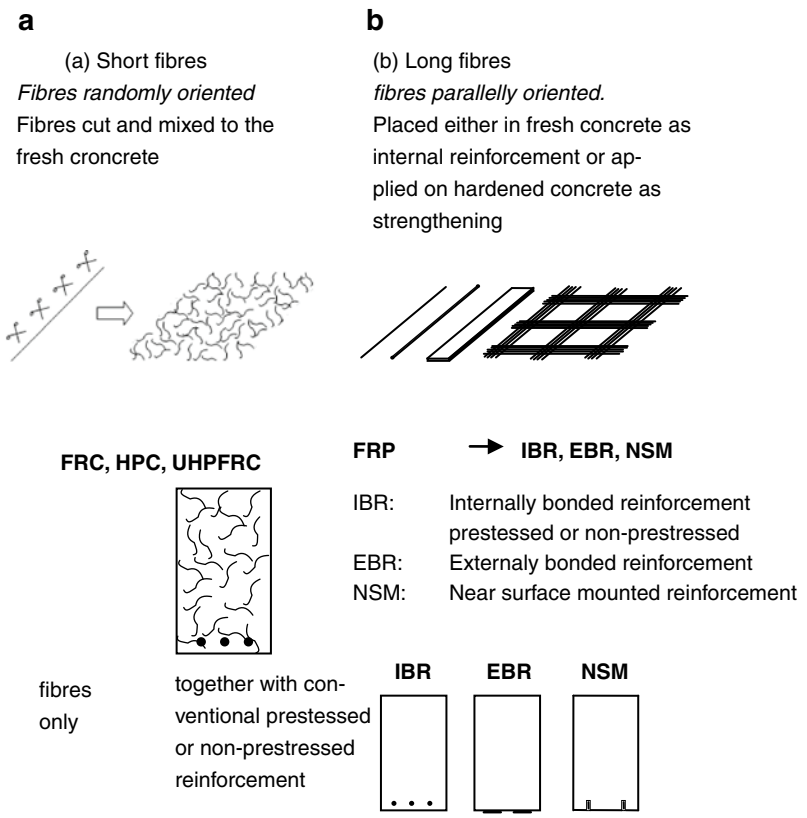

Fig. 9.1 Principles of using fibres for concrete structures: (**a**) short fibres (randomly oriented), and (**b**) long fibres (oriented)

formed similar to reinforcements like conventional prestressed or non-prestressed reinforcements.

Two different principles of using fibres for concrete structures are presented in Fig. 9.1. Fibres originally appear in long from, i.e. their length to diameter ratio is high.

The most traditional way of using fibres is when the fibres are cut or broken into short pieces and are mixed in a matrix where good bond between the fibres and the matrix is possible (Fig. 9.1a).

An adobe brick is shown in Fig. 9.2a as an example that natural fibres are able to keep the clay together even after cracking (if water is excluded).

This idea of fibre applications has been also adopted for concrete structures with or without simultaneous application of conventional prestressed or non-prestressed reinforcement.

The other way of using fibres (Fig. 9.1b) is to keep them in their long from (as far as they fit into the element) and place them accordingly to follow the high tensile stresses. A traditional application of this idea is shown in Fig. 9.2b, where

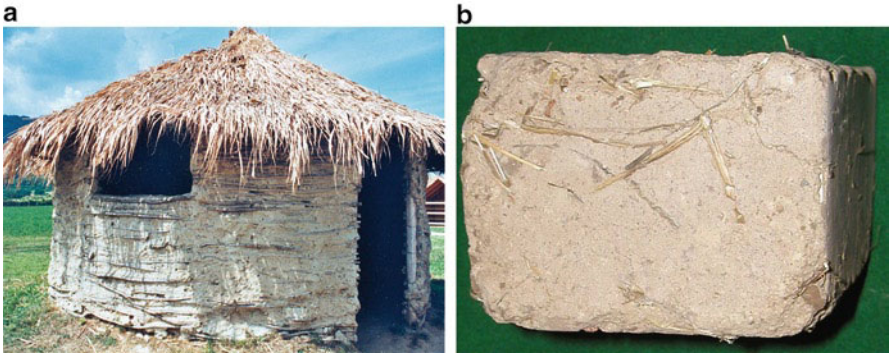

Fig. 9.2 Traditional applications of fibres: (**a**) Adobe brick, and (**b**) rural house: clay wall with wooden reinforcement

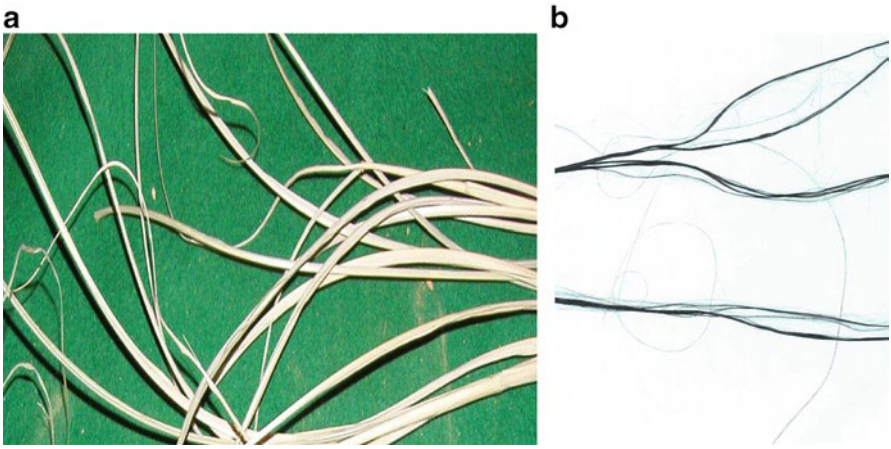

Fig. 9.3 Natural and artificial fibres: (**a**) long grass, and (**b**) carbon fibres

long pieces of tree branches are applied circumferentially in a simple clay wall in order to provide continuity against cracks and confinement for the whole wall. The reinforcement follows the circular tensile forces and is easy to apply during the production of the wall. This way of application may be considered as the origin of embedded reinforcement or of additional strengthening. The idea is still put into practice today by forming FRP (fibre reinforced polymer) reinforcements made of many fibres that are parallelly bonded together. It is then possible to apply them as internally bonded reinforcement (IBR) or externally bonded reinforcement (EBR) for strengthening or near surface mounted (NSM) reinforcements also for strengthening purposes (Fig. 9.1b).

Figure 9.3 shows the similarities between natural (long grass) fibres and artificial (CFRP) fibres.

9.2 Short Fibres in Concrete

The simplest fibre application is to mix short fibres (metallic or non-metallic) into conventional concrete. This concrete is then called fibre-reinforced concrete (FRC). Fibres (especially steel fibres) improve ductility and deformability as well as serviceability and durability.

A more advanced way of application is obtained by reducing both the maximum aggregate size and the length of the fibres. It generally leads to a mix that is often called ultra high performance reinforced concrete (UHPFRC), owing to the considerable improvement in material properties (especially in tensile strength) if a high amount of fibres is used.

Application of steel fibres in plain concrete improves material properties such as toughness, ductility, fatigue, and impact resistance (Naaman 1992; Balaguru and Shah 1992; Reinhard and Naaman 1999). For this reason, fibre concrete is especially applied for concreting industrial floors, roads and pavements, airfield runways, bridge decks, tunnels, and other concrete and reinforced concrete structures. Fibre reinforcement can be effectively used as retrofitting material as well. However, as previous tests indicated, steel fibre reinforcement is not effective at improving the moment capacity of reinforced concrete members. However, fibres may have a significant effect on the shear resistance of reinforced concrete beams and slabs (Falkner et al. 1994) (punching shear). Fibres may reduce the amount of stirrups and the congestion of the reinforcement in high shear regions. Fibres do not only increase shear capacity but also provide substantial post-peak resistance and ductility (Kovács and Balázs 2003). Moreover, by using steel fibres in plain concrete, a substantial decrease of the crack width can be achieved.

9.2.1 Performance of Fibre-Reinforced Concrete

Figure 9.4 intends to give a summary in a special way of the influences of steel fibres in concrete for various contents of steel fibres. The abscissa is the fibre content starting from zero and reaching the level of fibre contents for UHPFRC. The ordinate indicates the performance of concrete in all possible ways that can be positively influenced by fibres. The heading of the figure presents the words CONCRETE, FRC and UHPFRC parallel to abscissa. Concrete is the reference with no fibres. FRC means typically 20 kg/m³ (0.25 vol.%) up to about 80 kg/m³ (1 vol.%) fibre contents, UHPFRC normally indicates higher fibre dosages that are still possible to produce in conventional concrete mixers.

Regarding the improvement in performance of concrete as the steel fibre content increases, low amounts of fibres already produce an increase of toughness that is also mentioned as increase in the energy absorption of concrete. Fibres help to transform tensile forces through the initially small cracks, something that is often called cracks bridging mechanism. These include improved deformation capacity, especially the increase in the failure strain of concrete in compression. Fatigue and impact resistance can be also improved. At this phase, the existence of residual

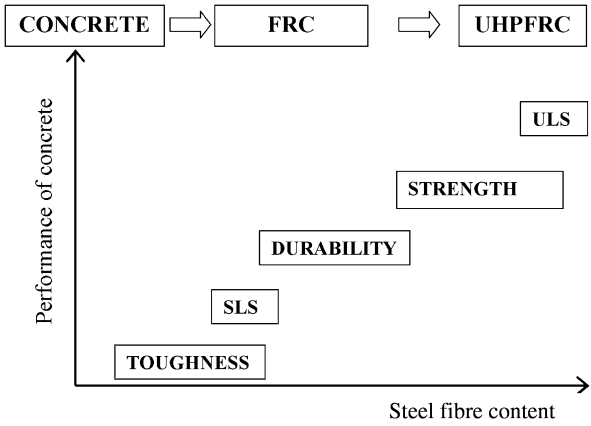

Fig. 9.4 Improved performance of concretes by increasing the content of steel fibres (schematic diagram)

tensile strength of fibre concrete after the appearance of cracks is very important. All these may lead to an improved behaviour both in terms of serviceability and of durability. The higher is the fibre content the greater the improvement.

A higher fibre dosage may produce even more considerable improvements. The strain softening behaviour (FRC) may change to strain hardening behavior (UHPFRC), thus improving also the ultimate (ULS) behaviour. At this level of fibre dosage, improvement in tensile as well as in compressive strength is possible (Naaman and Reinhardt 1995).

Residual tensile strength after cracking is one of the most important design parameters for FRC members. A typical flexural test is shown in Fig. 9.5, which conforms to the conditions set out by DAfStb (2010). The specimen has a section of 150 × 150 mm and a length of 700 mm with a span of 600 mm (Fig. 9.5a). Specimens were loaded in 4-point bending in deflection control. Figure 9.5b, c present two cases where the number of steel fibres in the failed cross-sections were considerably different (22 or 40 fibres) even if the same mix was used (the specimens were cast on the construction site by the construction company). Figure 9.5d indicates that the number of fibres in the failed section has a very important influence on the level of residual tensile capacity. By presenting all of the test results (Fig. 9.5d), an almost linear tendency is observed between the number of steel fibres in the failed cross-section and the so-called equivalent residual flexural tensile strength.

9.2.2 Tests with Steel Fibre-Reinforced Prestressed Concrete Beams

Three prestressed pretensioned concrete beams of 80 × 120 mm cross-section and 2 m length were prestressed by a simple seven-wire strand (∅12.9 mm, $f_{ptk} = 1{,}770$ N/mm², $f_{p,0.1} = 1{,}550$ N/mm², $A_p = 100$ mm²) at the core point of the section (Fig. 9.6). Specimens were prestressed simultaneously along a single strand, and did not contain any other non-prestressed reinforcement (not even stirrups) except the prestressing strand. The prestressing force was released gradually by hydraulic jacks. DRAMIX ZC 30/.5 hooked-end fibres were applied in 0 V%, 0.5 V% and 1.0 V% fibre contents.

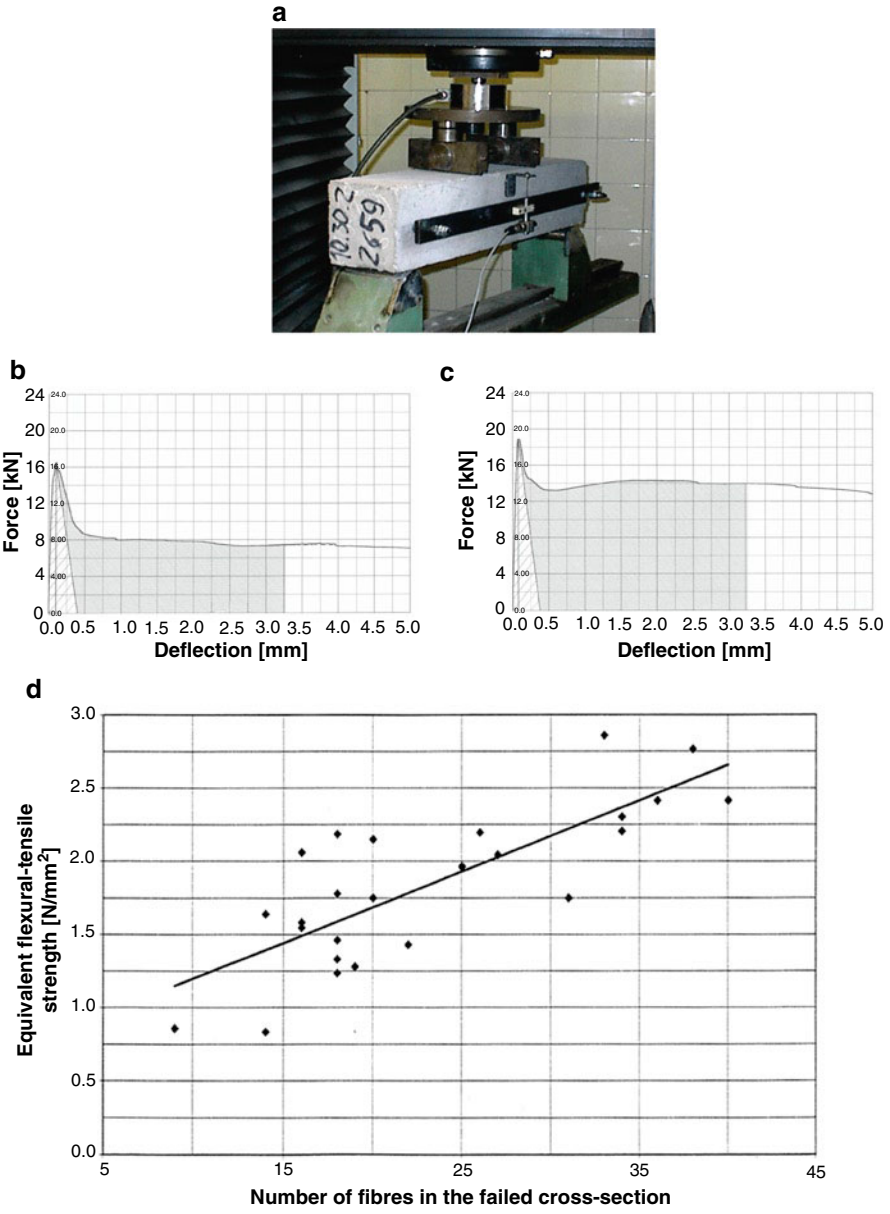

Fig. 9.5 Flexural tests on steel fibre-reinforced beams in deflection control: (**a**) test setup, (**b**) load-deflection curve for 22 fibres in the failed section, (**c**) load-deflection curve for 40 fibres in failed section, and (**d**) equivalent flexural tensile strength vs. number of fibres in the failed section

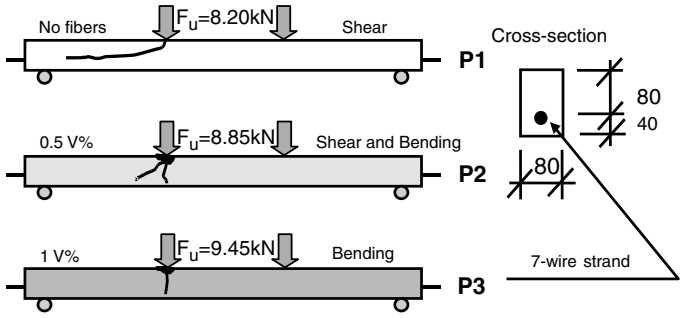

Fig. 9.6 Failure modes of prestressed pretensioned fibre-reinforced concrete beams (fibre reinforcement: Dramix ZC 30/.5)

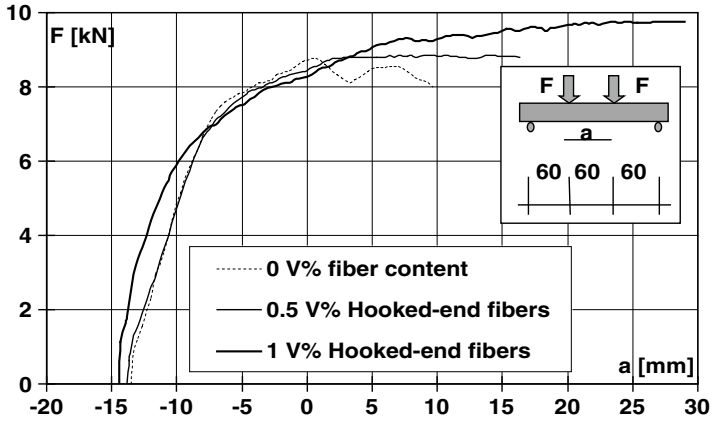

Fig. 9.7 Load versus mid-span deflection in four point bending of prestressed concrete beams

Four-point bending tests were carried out on the prestressed pretensioned concrete beams (Figs. 9.6 and 9.7). Failure loads and failure modes are presented in Fig. 9.6. Results indicate that the fibre content influences the failure load and even the failure mode. By increasing the fibre content the failure load increases and the failure mode may change from one due to shear (*top*) to a combined one in shear and bending (*middle*) and further to a clearly flexural failure mode (*bottom*). Failure of the beam without fibre reinforcement was very brittle and explosive.

9.3 Long Fibres in Concrete

If long parallel fibres are embedded into a resin matrix, they can be formed into reinforcement (FRP reinforcement) that looks similar to conventional prestressed or non-prestressed steel reinforcement. Alternatively, they may be formed as a mesh.

The advantages are especially their high strength, high fatigue strength and electrolytic insensitivity. However, their sensitivity against lateral forces needs special care during application. These FRP reinforcements can be placed into concrete before casting as internally bonded reinforcement; on the other hand they can be externally bonded on the surface of the concrete member (EBR) or into grooves that are cut in the concrete cover (NSM) as was shown in Fig. 9.1b. With internal application a new member is produced; external application is common in strengthening.

Concrete structures may need strengthening due to the deterioration of material properties (including excessive cracking or deflection), the increase in loads or the modification of the strengthening system. Strengthening should fulfill the following requirements:

- easy applicability even by keeping the live load (at least partly)
- short period of time required for strengthening work
- considerable increase in service life with limited maintenance after strengthening
- aesthetic solution not disturbing the appearance of the structure
- economic solution, at least in relative terms.

In general, we can choose from the following strengthening materials and techniques:

- supporting construction
- concrete overlay
- shotcrete layer
- SCC layer
- external prestressing
- steel jacketing
- steel plate bonding
- externally bonded FRP
- near surface mounted reinforcement.

The present contribution discusses the last two cases.

External bonded strengthening with FRP goes back to the end of ‘80s (*fib* 2001). The near surface mounting type of strengthening was first published by Asplund (1949) but became widely known after the research by Blaschko (2001). A generic description of NSM strengthening is presented by Szabó and Balázs (2008).

9.3.1 Design Principles

The design principles of CFRP strengthening are:

- the design of strengthening should be based on the stresses and deformations of the structure before strengthening (Fig. 9.8),
- strengthening elements are stressed only from loads applied after the strengthening procedure,

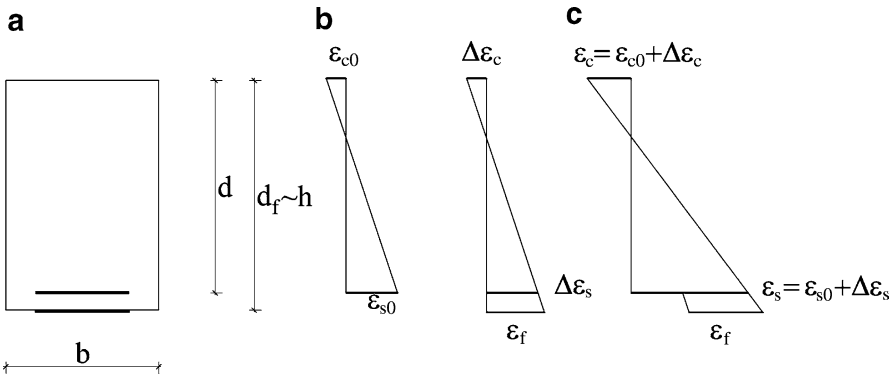

Fig. 9.8 Strain profiles before and after strengthening: (**a**) strains before strengthening, (**b**) strains from loads above strengthening, and (**c**) strains of strengthened member

– the design of strengthening should include the analysis of all possible failure mechanisms,
– flexural strengthening is not always enough; shear strengthening may also be required.

Possible failure modes of the strengthened members are given in various publications, e.g. *fib* (2001) and *fib* (2006), including initiation of failure by any constituent. All possible failure modes should be analysed during design. Special attention should be given to the debonding failure modes (Hollaway and Leeming 1999).

The safety concept for design is that the governing failure mode should be relatively ductile, i.e. steel yielding or concrete crushing prior to rupture or debonding of the FRP strengthening material.

9.3.2 Case Study

A typical example is shown in Fig. 9.9. The reinforced concrete grain silo lost its capacity to resist the circumferential tensile forces that was originally provided by prestressing strands (Balázs and Almakt 2000). The bottom part of the silo was constructed of 12 prefabricated concrete pieces. The most reasonable way of strengthening was to apply CFRP strips that are insensitive to electrolytic corrosion. The application step in Fig. 9.9 indicates the closing of strengthening strips by overlapping. The design included analysis of forces and deformations. The final design criterion was not the maximum tensile force but the maximum allowable opening between the prefabricated concrete pieces.

Fig. 9.9 Strengthening of a grain silo with CFRP strips

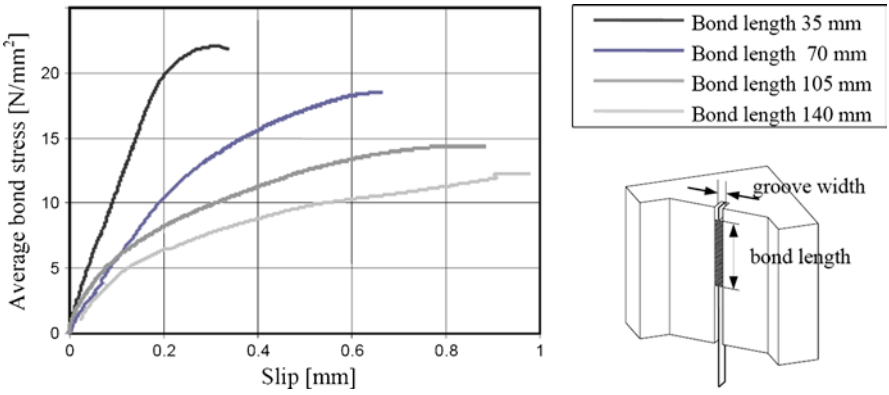

Fig. 9.10 Characteristic average bond stress-slip curves for various bond lengths

9.3.3 Bond along NSM Reinforcement

For proper study of the force transfer of the near surface strengthening, an L shaped pull-out specimen was developed (Szabó and Balázs 2008). The specimen (Fig. 9.10) was designed to reduce eccentricities during loading. The special form of the concrete specimen enabled proper view of the likely failure surface. It also provided the possibility of measuring the displacement of both loaded and unloaded ends of the bond length. In the case of FRP strips, the bond on lateral surfaces is considerably influenced by the lateral confinement of the specimen induced also by frictional stresses developed at supporting planes. Therefore, the bond length was shifted as much as possible to the top of the specimen. In addition, the bond length was kept

Table 9.1 Long-term properties of strengthenings

Mechanical properties	Environmental	Hazards
Relaxation	Alkalis	Impact
Fatigue	Water	Fire
	Chloride ions	Vandalism
	Freeze-thaw	
	UV radiation	

to a certain distance from the bottom edge of the specimen. Over that distance the strip was kept free to avoid fastening type of failure.

Typical average bond stress vs. slip diagrams are shown in Fig. 9.10. Slip at the loaded end was examined in the case of four bond lengths. At small bond lengths, the steep ascending branch of the average bond stress vs. the slip curve was recorded in the first stage of loading. Approaching the failure load the tangent of the curve decreased showing gradual failure of the connection. The inclination of the curve decreased when increasing the bond length, thus showing an average bond stress decrease and an increase in the deformation capacity of the connection. The characteristic failure was a shearing failure of the adhesive near the FRP surface. The residual stress was the result of friction between the sheared adhesive surfaces. The diagram also shows that the average bond strength deceases by increasing the bond length, thus indicating the non-uniform distribution of bond stresses along the bond length. The existence of an effective bond length, i.e. a bond length beyond which increasing the length does not result in a considerable increase of the anchorage capacity of the FRP strip, is noticeable.

9.3.4 Future Work on Long-Term Properties of FRP Strengthenings

Long-term material properties of FRPs (relaxation, fatigue) are considered favourable especially for carbon fibres embedded into epoxy resin. Environmental influences should be also considered for specific cases. Special consideration may be required if impact, fire or vandalism cannot be excluded (Table 9.1).

9.4 Conclusions

Fibres have become important for concrete structures. The engineering applications often followed early empirical applications, but are extended for further optimization of material properties. Fibres can be used either in their long form or cut into pieces and mixed into the concrete. These are often the same fibres. Bonded fibres can be formed similarly to reinforcement, like conventional prestressed or non-prestressed reinforcement.

The most traditional way of using fibres is when the fibres are cut into short pieces and are mixed in a matrix. This idea of fibre application has been also adopted for concrete structures with or without simultaneous application of conventional prestressed or non-prestressed reinforcement. Short fibres provide efficient ways to improve some specific properties of concrete members such as ductility, deformability, durability as well as load bearing capacity.

Parallelly-bonded high-strength non-corrosive fibres may form FRP reinforcements that can be applied internally like conventional prestressed or non-prestressed reinforcements. Otherwise they can be applied as externally bonded (EBR) on the surface of the element or near surface mounted (NSM) reinforcements bonded into pre-cut grooves.

The present chapter gives specific details on how the performance of the elements may increase in the case of fibre-reinforced concretes. Test results are shown for the improvement of failure load and failure mode of prestressed pretensioned concrete elements by applying steel fibres.

Design aspects and general considerations are given for EBR as well as for NSM strengthening with FRP including test results on the bond capacity of NSM reinforcements.

Acknowledgements Special thanks to Porr Construction Ltd. Hungary for supporting the present research.

References

Asplund SO (1949) Strengthening bridge slabs with grouted reinforcement. J ACI 45(1):397–406

Balaguru PN, Shah SP (1992) Fiber-reinforced cement composites. McGraw-Hill Inc, New York, p 531

Balázs LG, Almakt MM (2000) Strengthening with carbon fibres – Hungarian experience. J Concr Struct 2:52–60

Blaschko MA (2001) Load bearing capacity of concrete elements with CFRP strips glued into grooves. PhD Thesis, TU Munich (in German)

DAfStb (2010) Technical guidance document for fibre-reinforced concrete (Richtlinie Stahlfaserbeton - in German), Deuthscher Ausschuss für Stahlbeton, Berlin

Falkner H, Kubat B, Droese S (1994) Durchstanzversuche an Platten aus Stahlfaserbeton (Punching tests on steel fibre reinforced plates). Bautechnik 71(8):460–467

fib (2001) Externally bonded FRP reinforcement for RC structures. *fib* bulletin 14. Federation internationale du beton, Laussane. ISBN 2-88394-054-1

fib (2006) Retrofitting of concrete structures by externally bonded FRP with emphasis on seismic applications. *fib* bulletin 35. Federation internationale du beton, Laussane, ISBN 2-88394-075-4

Hollaway LC, Leeming MB (eds) (1999) Strengthening of reinforced concrete structures – using externally bonded FRP composites in structural engineering. CRC Press, Boca Raton. ISBN 1855733781

Kovács I, Balázs GL (2003) Structural behaviour of steel fibre reinforced concrete. J Struct Concr 3:57–63

Naaman AE (1992) Tailored properties for structural performance. High performance fibre reinforced composites. In: RILEM Proceedings 15. Chapman and Hall, London

Naaman AE, Reinhardt HW (1995) High performance fibre reinforced cement composites 2. In: Proceedings of the second international RILEM Workshop, Ann Arbor, USA, (EFN Spon, Suffolk)

Reinhard HW, Naaman AE (1999) High performance fiber reinforced cement composites 3. In: Proceedings of the third international RILEM/ACI Workshop, Mainz, Germany, 17–19 May

Szabó KZs, Balázs GL (2008) Advanced pull-out tests for near surface mounted CFRP strips. In: Marques A, Juvandes L, Henriques A, Faria R, Baross J, Ferreira A (eds) Proceedings of eight CCC2008, challenges for civil construction , Porto, pp 192–193. ISBN: 978-972-752-100–5

Chapter 10
Sustainable Roof Elements: A Proposal Offered by Cementitious Composites Technology

Marco di Prisco, Liberato Ferrara, Marco Lamperti, Simone Lapolla, Anna Magri, and Giulio Zani

Abstract The use of High Performance Fibre Reinforced Cementitious Composites (HPFRCC) allows the designer to reduce the dead weight of roofing keeping concrete covering structures still more competitive in relation to steel structures in terms of costs, thermal and acoustic insulation and fire resistance. Thin slabs can be used as tertiary elements in roof decks beside the spandrel beams and the simply supported prestressed precast roof elements. Two metres wide elements, simply supported along a 2.5 m span were devised as a possible application in this paper: the high performances are mainly used for the bending behavior along the 2.5 m span and in order to drastically simplify the detailing of the support regions. The idea is that of coupling textile and Ultra High Performance Fibre Reinforced Concrete (UHPFRC) technology, by means of an interposed polystyrene layer.

A wide experimental investigation is in progress to mechanically characterize the materials in uniaxial tension and compression, in order to identify all the data needed for design like toughness, bending resistance, fire resistance and durability. As for the UHPFRC, in the research, the check of the ductility and the identification of the mechanical characteristics in tension are performed by means of bending tests carried out on unnotched specimens according to Italian Recommendations CNR DT-204 and of a new test (Double Edge Wedge Splitting test) recently proposed, while third point bending test as suggested in EN14651 is used to classify the material production.

With reference to textile materials, they are reinforced with glass fabric and randomly dispersed glass or PVA fibres. The mechanical characteristics are deduced in uniaxial tension.

M. di Prisco (✉) • L. Ferrara • M. Lamperti • S. Lapolla • A. Magri • G. Zani
Department of Structural Engineering, Politecnico di Milano, Piazza Leonardo da Vinci, 32, Milano 20133, Italy
e-mail: marco.diprisco@polimi.it; liberato.ferrara@polimi.it; lamperti@stru.polimi.it; simone.lapolla@gmail.com; magri@stru.polimi.it; zani@stru.polimi.it

M.N. Fardis (ed.), *Innovative Materials and Techniques in Concrete Construction: ACES Workshop*, DOI 10.1007/978-94-007-1997-2_10,

10.1 Introduction

Precast concrete roof systems are often disadvantaged compared with other structural solutions, made of timber or steel, because of the higher ratio of dead weight to live loads. An average dead weight close to 2 kN/m^2, that can be regarded as a common value for a concrete roof system consisting of precast Reinforced Concrete (RC) elements, is quite large compared to the snow load, that is close to the value of 1.5 kN/m^2 in many parts of the world. An acceptable compromise in terms of costs and weight can be achieved by adopting ultra high performance materials (Naaman and Reinhardt 2003; Reinhardt and Naaman 2007) which are more expensive, but can be much lighter. The reduction of the total weight can also result in reduced global structural cost. Preliminary results considering a composite slab made of High Performance Fibre Cementitious Composite (HPFRCC) and Textile Reinforced Concrete (TRC) are here presented to be used as secondary structural element in a prefabricated structure (Fig. 10.1).

The plate is conceived as a layered composite structure, with a High Performance Cementitious Composite in the top layer and Textile in the bottom layer. The two layers are coupled by means of a high density Polystyrene panel (Fig. 10.2), that is structurally employed to transmit very small shear stresses and is used also for thermal insulation. The low permeability of the composite (Moro et al. 2011) suggests preventing the use of a waterproofing layer over the structure, by allowing a solution that makes use only of a suitable gasket between the plates. The plates are also characterized by high fire resistance: in fact, when a fire occurs, polystyrene sublimates because the melting temperature of EPS (Expanded Polystyrene) is close to 160°C. Polystyrene is a thermoplastic substance, which is in solid (glassy) state at room temperature, but flows if heated above its glass transition temperature, and becomes solid again when cooled. If a suitable fixing device is designed to hang the

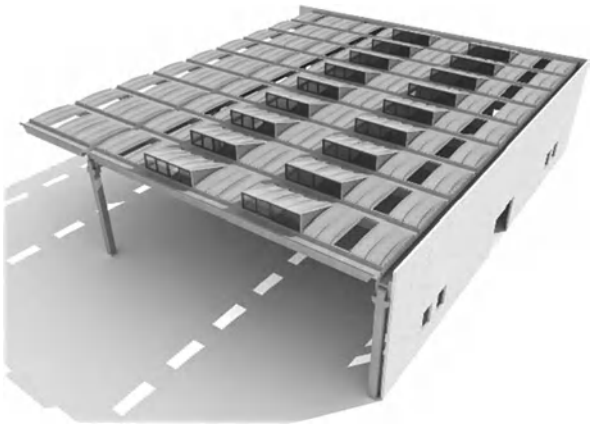

Fig. 10.1 Sketch of the prefabricated roofing adopted as a reference

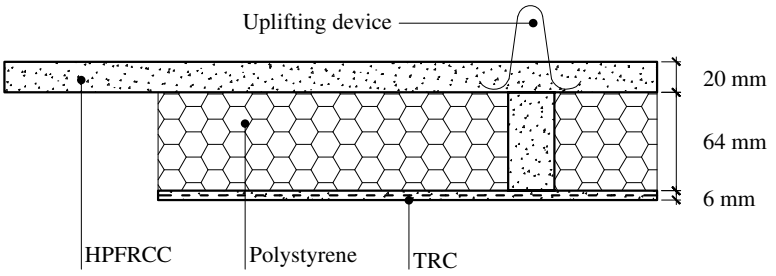

Fig. 10.2 Geometrical description of the multilayer thin plate for roofing

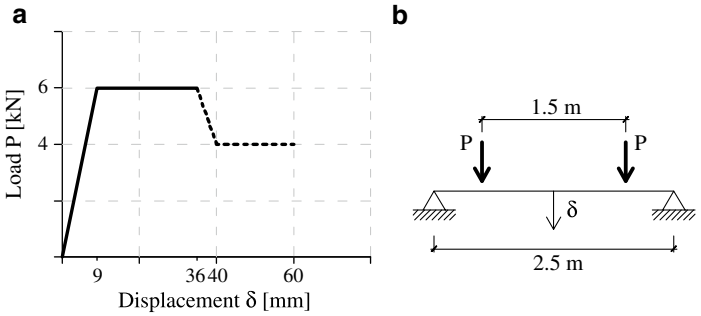

Fig. 10.3 Performance target for the roof element

textile thin layer to the upper HPFRCC plate, the empty space formed with the polystyrene melting becomes an ideal barrier against fire and the TRC panel works as a fire shield preserving the structural bearing resistance of the top HPFRCC plate. Of course a suitable escape for the smoke has to be introduced.

10.2 Research Significance

The research aims at investigating the mechanical behaviour of a layered composite structure designed to achieve the following goals: light weight, low cost, good thermal insulation, reliable waterproofing and high fire resistance. The bending resistance of the plate should guarantee a higher load for serviceability limit states and a lower load in case of fire because in that case snow load can be neglected and the bending is caused only by the structure self weight. In Fig. 10.3 a qualitative sketch of the designed bending moment performance required for a plate 2 m wide, 2.5 m long and 90 mm thick respectively at serviceability ($M=6$ kNm) and fire load ($M=4$ kNm) action combinations is shown.

10.3 Materials

10.3.1 High Performance Steel Fibre Cementitious Composite (HPSFRC)

The mix design of the cementitious composite (Table 10.1) was selected by comparing different solutions starting from the aggregates generally used by the precast manufacturer and limiting their maximum size to 2 mm. The composite was a self compacting cementitious material (Fig. 10.4) and some data on its fresh behaviour are available in (di Prisco et al. 2008; Ferrara et al. 2011). The steel fibre content was equal to 100 kg/m^3 (1.2% by volume); straight high carbon steel fibres, 13 mm long and with an aspect ratio (l_f/d_f) equal to 80 were used. Preliminary tests on free and restrained shrinkage (di Prisco et al. 2008), allowed estimation of the quite large strain, that was not unexpected due to the significantly large paste volume fraction which characterizes the mix composition. A cubic compressive strength of 143 MPa and an elastic modulus close to 40 GPa were measured in the preliminary material qualification. Unnotched prism specimens with a square 50 mm side cross section were tested in three point bending (span 125 mm). An average bending strength equal to 27.4 MPa was obtained, with standard deviation

Table 10.1 Mix composition

Component	Dosage (kg/m^3)
Cement type I 52.5	600
Slag	500
Water	200
Superplasticizer	33 (l/m^3)
Sand 0–2 mm	983
Fibres (l_f = 13 mm; d_f = 0.16 mm)	100

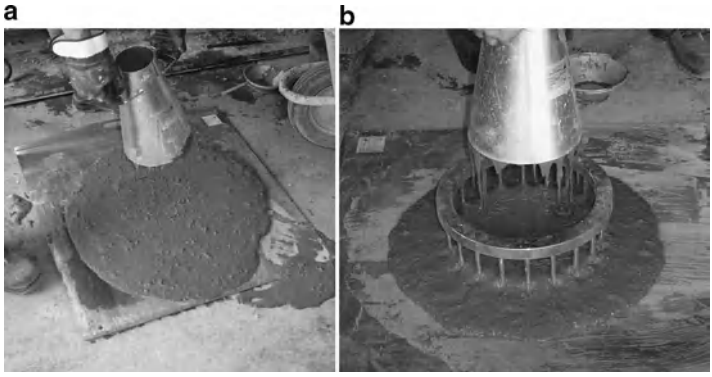

Fig. 10.4 Fresh concrete performance: (**a**) slump flow and (**b**) J-ring tests

Table 10.2 Nominal strength in bending according to UNI 11039

$f_{IF,av}$ (st.dev.) [MPa]	$f_{eq1,av}$ (st.dev.) [MPa]	$f_{eq2,av}$ (st.dev.) [MPa]
7.10 (0.14)	12.06 (1.36)	9.77 (1.83)

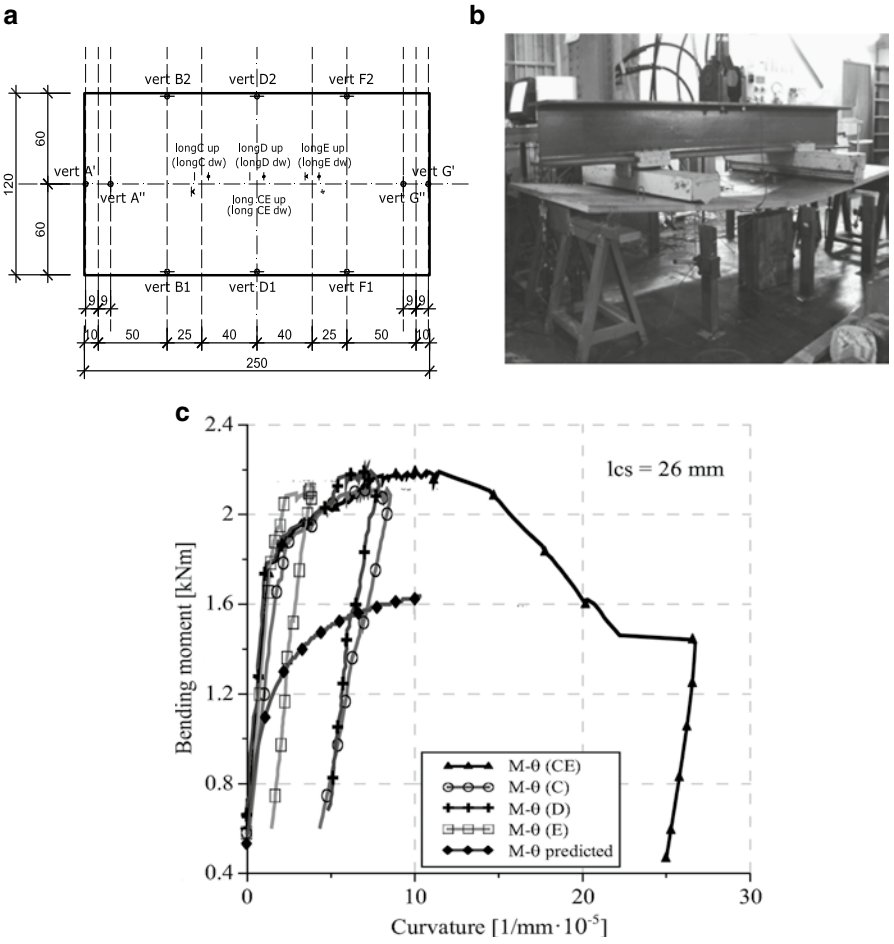

Fig. 10.5 Bending of HPFRC thin plate: (**a**) plate set-up; (**b**) deformed shape at collapse; (**c**) bending moment vs. curvature

of 1.5 MPa. To qualify the material according to Italian Standards (CNR-DT 204 2006) also four point bending tests on notched prism specimens 600 mm long, with a 150 mm side square cross section were carried out: the bending residual strength are summarized in Table 10.2. In order to ascertain the effectiveness of the bending behaviour with reference to large plates, also some tests on rectangular 1.2 m × 2.5 m plates 26 mm thick were carried out (Fig. 10.5).

Table 10.3 LOP strength and ultimate ($w = 1.8$ mm) residual strength in bending at high temperature (Caverzan et al. 2009a, b)

	Fibres	$T = 20$ °C	$T = 200$ °C	$T = 300$ °C	$T = 400$ °C	$T = 600$ °C	$T = 900$ °C
$f_{lf,av}$	Aligned	11.30	9.10	–	4.93	4.64	–
[MPa]	Random	11.05	–	8.20	–	4.15	0.64
$f_{eq2,av}$	Aligned	22.81	23.42	–	23.23	4.36	–
[MPa]	Random	14.00	–	14.03	–	4.99	0.34

The results obtained without any attempt to orient steel fibres highlight the favourable deflection hardening behaviour which can be achieved. Furthermore, as also highlighted in the *fib* Model Code 2010, a large safety margin can be observed when the response in bending is predicted by employing material constitutive laws identified from 4-point bending tests on notched specimens, as used for the classification of the material. A better prediction can be achieved when a tensile constitutive law is identified from bending tests performed on a "structural" unnotched specimen, characterized by the same thickness and the same casting procedure as for the structural element to be (di Prisco et al. 2009). The material used showed also very good performance with reference to fire resistance: detailed results are shown in (Caverzan et al. 2009a, b) with reference to both not aligned and aligned steel fibres: Table 10.3 provides a summary of the peak and residual strengths when the material is exposed to different high temperatures.

10.3.2 Textile Reinforced Mortar

Textile Reinforced Mortar is a relatively new material which allows producing thin structural layers characterized by a high tensile strength mainly given by an Alkali Resistant glass fabric (Hinzen and Brameshuber 2007; Brameshuber 2006; Peled and Bentur 2000; Peled et al. 1999). The reinforcement is scantly affected by aggressive environment and therefore no cover needs to be respected. This feature allows the designer to consider a reinforced skin that can exploit the largest lever arm for bending. One of the most interesting aspects is the small variability of the response when good bond between the reinforcement and the matrix is developed (Fig. 10.6; Colombo et al. 2011). Multiple cracking allows spreading the deformation as in RC structures, but a very small crack spacing prevents large crack opening up to the failure. In this preliminary study, an E-glass fabric and a commercial mortar were used. Their characteristics are specified in Tables 10.4 and 10.5.

10.3.3 Polystyrene

A careful mechanical characterization of Polystyrene was carried out (Colombo et al. 2008). The specimens were prismatic ($90 \times 90 \times 45$ mm) and both uniaxial tension and compression tests were performed. In Fig. 10.7 the strain has been

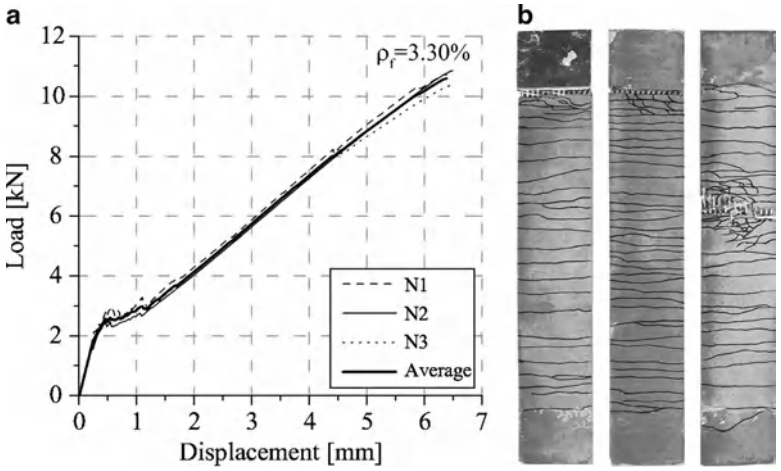

Fig. 10.6 Mechanical characteristics of a strip 400 mm long, 70 mm wide and 6.2 mm thick achieved with TRC made of AR glass fabrics: (**a**) load vs. total displacement in a uniaxial tension test; (**b**) crack pattern (Colombo et al. 2011)

Table 10.4 Geometrical characteristics of E-glass fabric used

Warp wire spacing [mm]	4.5
Weft wire spacing [mm]	5.0
Warp [Tex]	136 + 136
Weft [Tex]	320
Fabrication technique	Leno weave
Average Peak load [kN/m]	40

Table 10.5 Mortar mechanical characteristics

γ_{av} (st.dev.) [g/cm^3]	$R_{cm,av}$ (st.dev.) [MPa]	E_{av} (st.dev.) [GPa]	$f_{ct,fl}$ (st.dev.) [MPa]
2.19 (0.07)	77.50 (6.87)	29.67 (0.04)	9.52 (0.38)

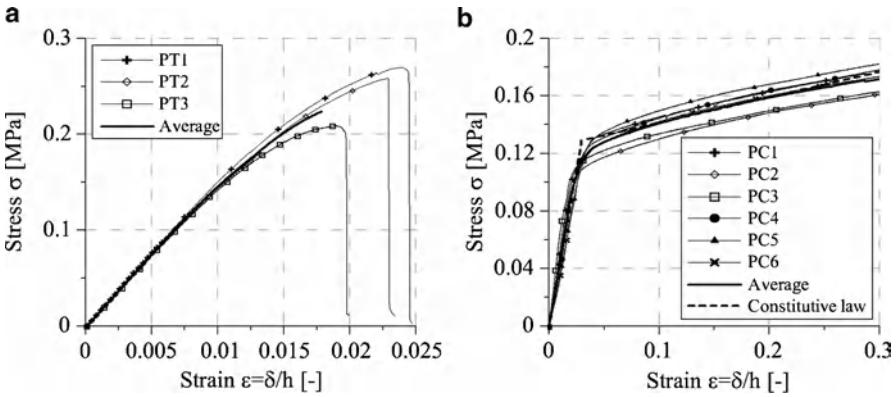

Fig. 10.7 Polystyrene mechanical characteristics: (**a**) uniaxial tension; (**b**) uniaxial compression (Colombo et al. 2008)

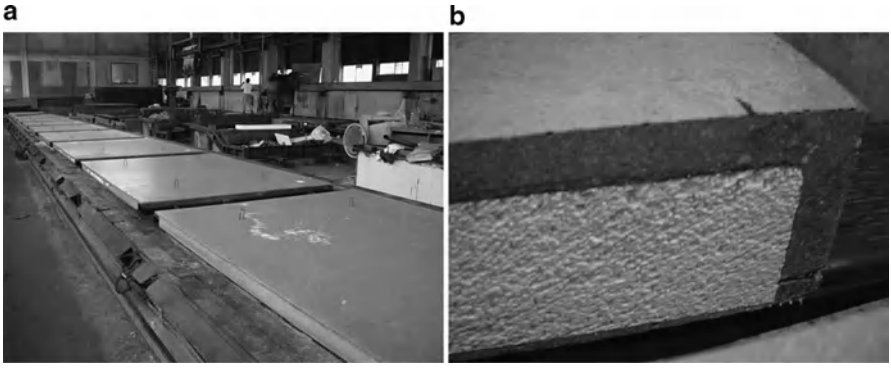

Fig. 10.8 Casting of full scale multilayer plates

calculated dividing the relative displacement of the press platens by the total specimen length. As expected, the material exhibits a quite low strength, but while in compression its behaviour is elastic–plastic, in uniaxial tension is elastic-brittle, with a strong non-linearity close to the peak. It is interesting to observe that the compressive yield strength (f_{py} = 0.12 MPa; Fig. 10.7b) is lower than the tensile one (f_{pt} = 0.2 MPa; Fig. 10.7a), even if the compressive behaviour guarantees a larger ductility due to the hardening branch that plays the key role in the mechanical behaviour of the layered panel. Furthermore, also the Young's modulus in tension is larger than in compression (E_{Pc} = 4.35 MPa; E_{Pt} = 14.7 MPa).

10.4 Experimental Investigation

In order to understand if the conceptual design, as highlighted in the Research Significance Section, could achieve the declared goal, a preliminary experimental investigation on small prismatic specimens and full scale plates was carried out. This investigation was instrumental to anticipate the rising of unexpected structural problems, if any, related to delamination, shear failure, deformability or other mechanical problems concerning the use of unconventional materials. The specimen production was also instrumental to highlighting any constructive difficulty. Ten plates 2.0 m × 2.7 m and 90 mm thick were produced (Fig. 10.8a). The thickness of the three layers was 20, 64 and 6 mm respectively for HPFRCC, polystyrene and TRC materials (Fig. 10.8b). Two different E-glass fabrics and different devices to guarantee the transmission of shear stresses between the two cementitious layers were investigated. A plate was first sawn to obtain several prismatic specimens devoted to investigate the specific behaviour of the composite structure. This procedure guarantees the most realistic situation in the sense that the material properties as well as the casting procedure are exactly the same of the full scale manufactured slab, and for this reason the representativeness of these test specimens is very high.

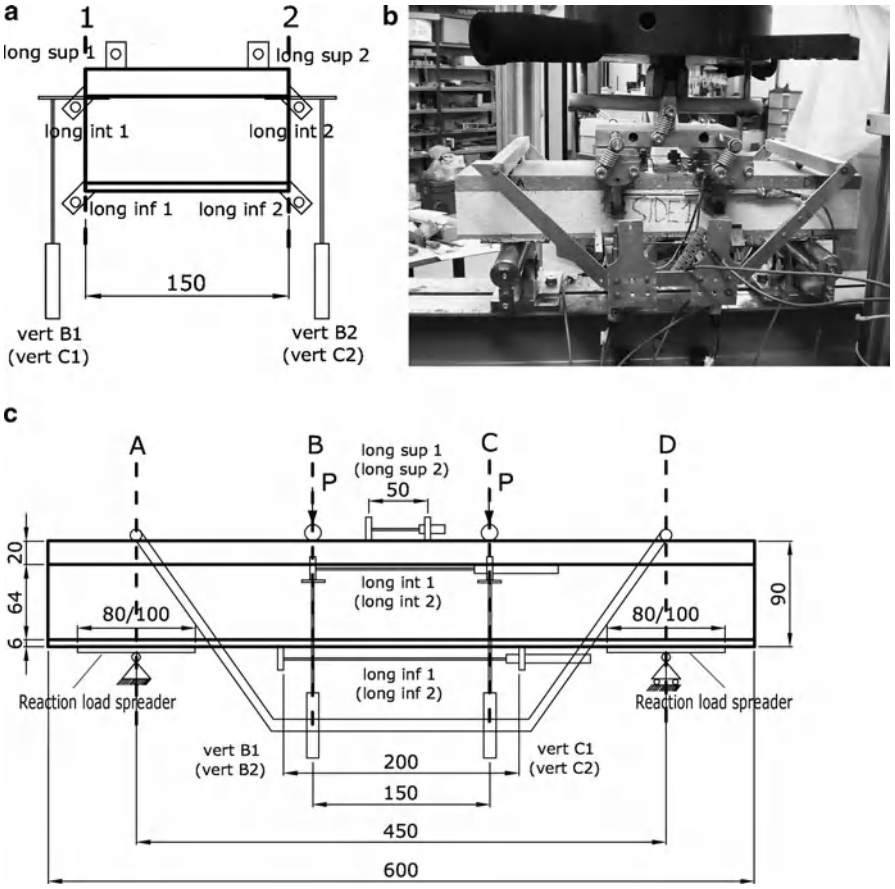

Fig. 10.9 Composite beam specimen: (**a**) geometry; (**b**) test set-up; (**c**) instrumental equipment

10.4.1 Composite Beam Specimen test

Fifteen tests were carried out on prismatic layered specimens 150 mm wide according to a four point bending set-up: the details of the geometry and of the instrument equipment are shown in Fig. 10.9. Two thin steel plates were glued to the TRC bottom layer in the zones close to the supports in order to diffuse the localized stress and prevent any spurious localization due to the reduced load span here adopted with respect to the one introduced in the full scale plate test (Fig. 10.9c). The vertical displacements of two points close to the intrados of the UHPFRCC layer and in correspondence with the loading knives were recorded; besides vertical deflections, also the relative horizontal displacements between two points located close to the top and the bottom fibres to evaluate the curvature in the central zone between the loading knives were used. The tests were also instrumental in the evaluation of the scattering in the response, both in relation to the peak and the ductility.

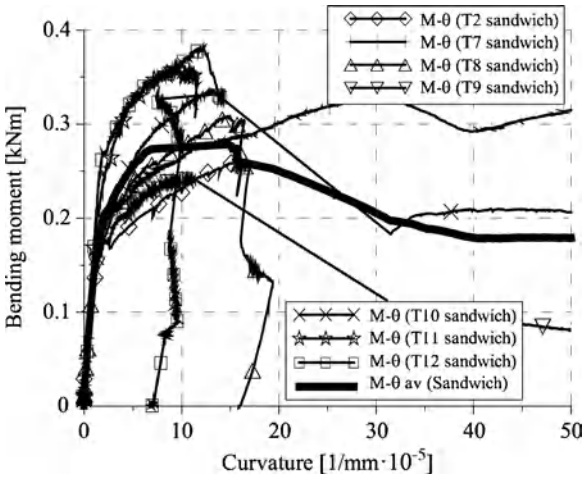

Fig. 10.10 Bending moment vs. curvature of composite beam specimens

The comparison between seven tests carried out on sandwich prismatic specimens with the same E-glass fabric and described in terms of bending moment versus curvature are shown in Fig. 10.10. A double plateau is clearly observed: the first one corresponding to the bending contribution of the TRC and the second one corresponding to the bending of the HPFRCC layer alone, which remains active when the crack propagates through the polystyrene layer. Although the small sizes of the prism specimens cannot guarantee a good repeatability of the response, the global ductility obtained with the use of a brittle glass fabric is quite high, since a peak curvature equal to 10^{-4} mm^{-1} has been reached, while the curvature measured at the failure of the top HPFRCC plate is much higher, reaching a value close to five times the peak one. The average was computed by a first normalization of each curve with respect to each peak. The initial stiffness is not affected by any tolerance or defect and is always the same, thus showing that no sliding or delamination occurs up to the onset of cracking of the TRC layer, that is for a bending moment close to 55% of the average peak value.

10.4.2 Full Scale Structure Tests

The full scale plate tests were carried out at different ages in order to evaluate the effect of aging on the mechanical degradation of the E-glass material used in the TRC layer, even if a careful protection made of a suitable dressing was adopted. The four point bending set-up used is described in Fig. 10.11: five cross sections (A–E) were instrumented to measure vertical deflections at the supports, at midspan and under the loading knives at the slab intrados. Four LVDT transducers were positioned at the supports (long A2(E2)sup, long A2(E2)inf; Fig. 10.11) to measure the relative sliding of the top and bottom cementitious layers to the polystyrene one. No significant sliding was observed up to the peak. The test was displacement controlled and the feedback parameter was the midspan deflection. The employed hydraulic jacket

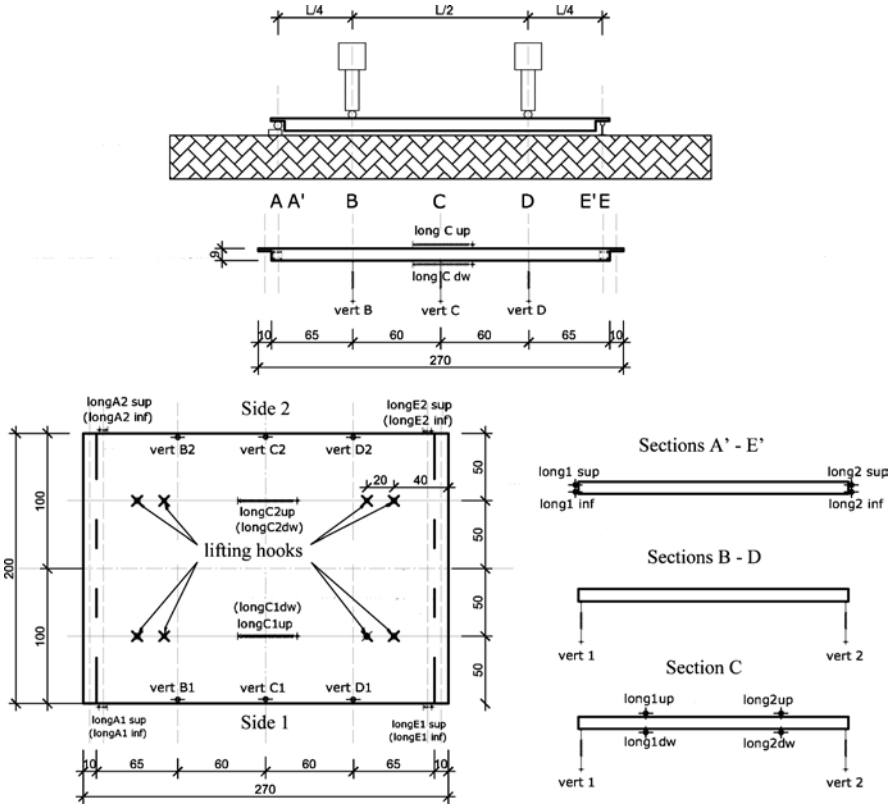

Fig. 10.11 Full scale plate set-up

(MTS®) had a load capacity of 250 kN available at the Department of Structural Engineering; two loading knives 120 cm long and acting over suitable timber beams were used in order to distribute over the whole plate width the total load. The two load devices guaranteed separately both the rotations around a knife axis (roller) and about longitudinal axis parallel to the longitudinal symmetry one (Fig. 10.12a).

Three load stages were imposed: an adjustment stage by imposing a loading and unloading cycle up to 6 kN (corresponding to a moment given by a uniformly distributed load of 1.25 kN/m^2); a second stage with three loading and unloading cycles between zero and a maximum load respectively equal to 3.0, 6.0, and 9.0 kN. In this phase the structural response remains quasi-linear. This was followed by a monotonic loading stage, in which a peak load equal to 15.26 kN was reached at a deflection equal to 40 mm. A further cycle in the cracked regime was imposed up to a deflection of 60 mm. Finally a third stage characterized by a progressive reduction of the load displacement controlled was imposed. The final load reached corresponded to about 20% of the peak load. It is worth remarking that all the tests were performed at an environment temperature equal to about 28°C. The graphs here proposed concern only the first two stages. The E-glass fabric, as expected progressively lost its

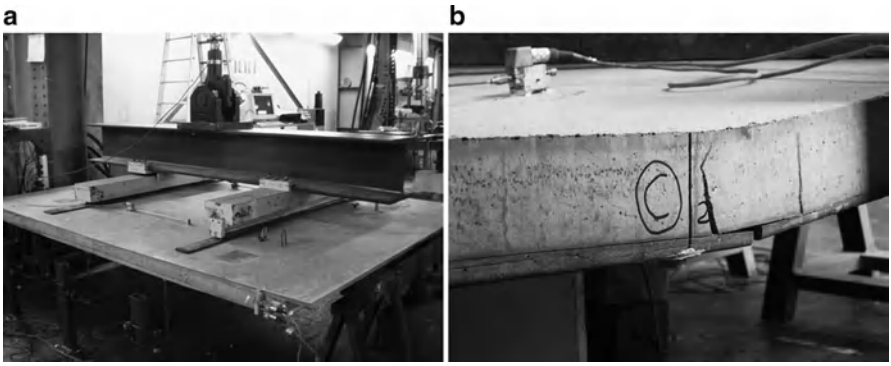

Fig. 10.12 Full scale plate testing: (**a**) bending test arrangement; (**b**) localization at failure

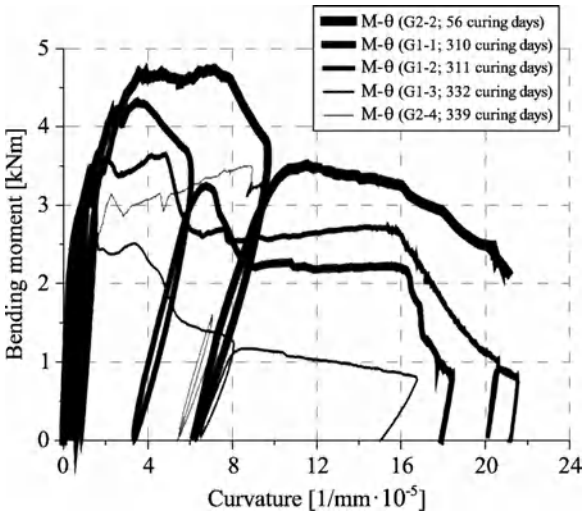

Fig. 10.13 Bending tests carried out at different ages

tensile strength due to Alkali attack, despite the suitable dressing used (Fig. 10.13). The best behavior was obtained in the earliest test and the load vs. vertical displacements as well as the load vs. longitudinal relative displacement, useful to compute the load vs. curvature response, are shown in Fig. 10.14. The total load is equal to about twice as much as the serviceability loads anticipated as design target. As remarked above, the double plateau values correspond first to the bearing capacity of the composite plates and, after the crack propagation, only to that of the top HPFRCC plate. Although the E-glass fabric was elastic-brittle, a suitable coupling of the layers allowed a ductile behaviour as planned in the preliminary design.

The comparison between composite beam and plate behaviour (Fig. 10.15a) highlights that the plate, due to its larger size and consequently to its higher expected defect distribution, shows a reduced ductility and a smaller bending strength. Moreover it is also worth noting that the larger shear load introduced in the beam due to its reduced span, does not at all affect the bending behaviour.

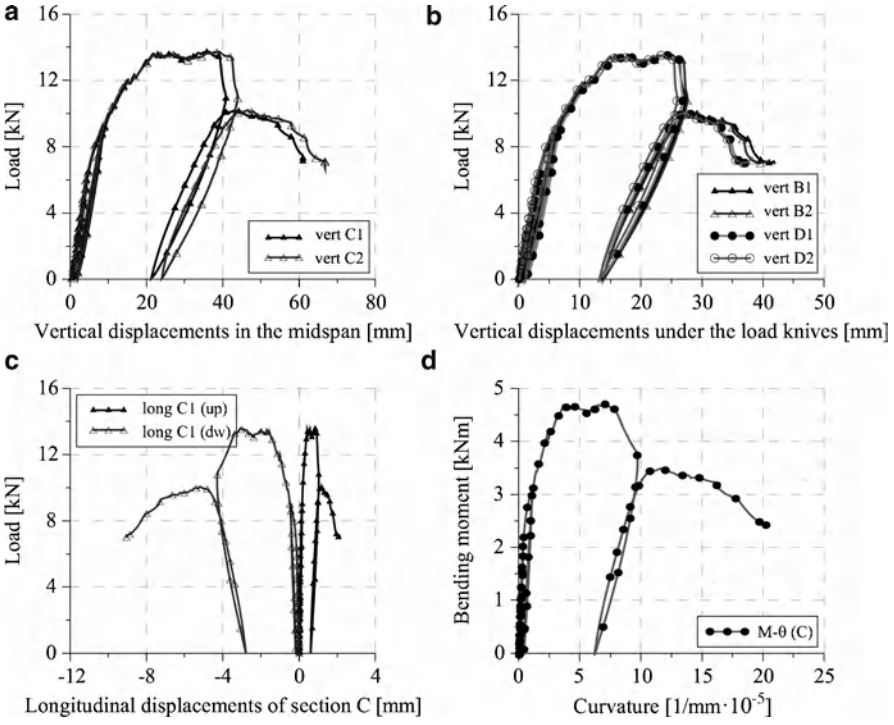

Fig. 10.14 Bending behaviour of full scale composite plate G2-2 (56 curing days): (**a**, **b**) load vs. deflection in the midspan and under the load knives; (**c**, **d**) load vs. longitudinal displacements and bending moment vs. average curvature at midspan

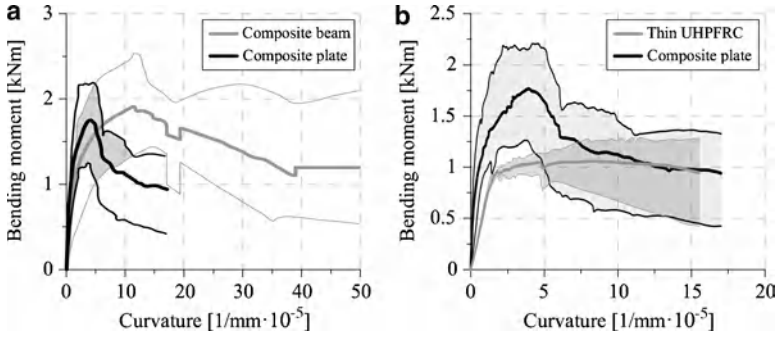

Fig. 10.15 Test comparisons on bending behaviour: (**a**) composite beam vs. composite plate; (**b**) thin UHPFRC vs. composite plate

Finally, the comparison between the behaviour of composite and simple UHPFRCC plates (Fig. 10.15b; (di Prisco et al. 2008)) highlights the TRC contribution, which is limited to a larger initial stiffness and the first plateau bending performance.

10.5 Technological and Design Problems

During the production of full size composite plate, several technological problems were met. The most crucial concerns with the ability to guarantee the robustness of the fresh state performance of the employed HPFRCC, which is, as a matter of fact, necessary not only for successful casting but also with reference to the expected day by day variability of mechanical performance (Ozyurt et al. 2009). As known, it is mainly affected by the actual water/binder ratio, which needs a careful control of the aggregate moisture content. Some difficulties also arose with reference to filling all the gaps between the moulds and the polystyrene panels; these gaps, because of the fibre length, cannot be made thinner than 10 mm. In the proposed experimental campaign no effort to orientate the fibres in the top plate was performed. During the production a special care has to be devoted to shrinkage, especially when the mortar used in TRC is not the same used for HPFRCC material.

10.6 Concluding Remarks

An original idea to build light, waterproofing, thermal insulated and fire resistant roof plates has been presented in this paper. The main result is the possibility to use layered plates without any special gluing, obtained just using the chemical and mechanical bond strength obtained between polystyrene and high performance mortars due to hydration of Portland cement. In the tests no delamination problems were met and the results confirm the achievement of the declared goals. The mechanical response of the overall composite structures shows a quite good ductility, while it has been proved once again that E-glass fabrics must be substituted by AR glass fabric to prevent significant performance decreases in the time of the structural behaviour. Further research aimed at improving bending performance by means of oriented fibres in the top layer as well as larger reinforcement ratios of AR glass fabrics in the bottom layer is in progress.

Acknowledgements The authors thank FUMAGALLI Edilizia Industrializzata S.p.A., BASF and Gavazzi companies for their financial support and the help received from their technicians in the production of the whole set of specimens.

References

Brameshuber W (ed) (2006) Textiles reinforced concrete, Report 36. Rilem Publications S.A.R.L, Bagneux

Caverzan A, Colombo M, di Prisco M, Lapolla S (2009a) On high-temperature behaviour of HPFRC thin plates. In: Proceedings of the 4th international conference on construction materials CONMAT'09, Nagoya, Japan, pp 444–449

Caverzan A, Colombo M, di Prisco M (2009b) High performance steel fibre reinforced concrete: residual behaviour at high temperature. In: Proceedings of the 2nd international conference on performance, protection and strengthening of structures under extreme loading PROTECT2009, Hayama, Japan, 2009, on CD

CNR-DT 204 (2006) Instruction for design, execution and control of fibre reinforced concrete structures, Italian Standards

Colombo M, di Prisco M, Zecca C (2008) On the coupling of soft materials with thin layers of glass fibre reinforced mortar. In: Proceedings of challenges for civil constructions, Porto

Colombo I, Colombo M, Magri A, Zani G, di Prisco M (2011) Tensile behaviour of textile: influence of multilayer reinforcement, accepted by HPFRCC6 international workshop, Ann Arbor

di Prisco M, Lamperti M, Lapolla S, Khurana RS (2008) HPFRCC thin plates for precast roofing. In: Proceedings of second international symposium on ultra high performance concrete, Kassel, pp 675–682

di Prisco M, Plizzari G, Vandewalle L (2009) Fibre reinforced concrete: new design perspectives. Mater Struct 42:1261–1281

Ferrara L, Ozyurt N, di Prisco M (2011) High mechanical performance of fiber reinforced cementitious composites: the role of "casting-flow induced" fiber orientation. Mater Struct 44:109–128

Hinzen M, Brameshuber W (2007) Influence of short fibres on strength, ductility and crack development of textile reinforced concrete. In: Reinhardt HW, Naaman AE (eds) Proceedings of the fifth international RILEM workshop HPFRCC5 PRO53, Mainz. RILEM Publications S.A.R.L, Bagneaux, France, pp 105–112

Moro S, di Prisco M, Barragan B, Magarotto R, Roncero J (2011) Ultra high performance concrete: from material optimization to structural applications, SEWC international conference, Como

Naaman AE, Reinhardt HW (eds) (2003) High performance fiber reinforced cement composites (HPFRCC4), PRO 30, Rilem publication S.A.R.L, Bagneaux, France

Ozyurt N, Teregger N, Ferrara L, Sanal I, Shah SP (2009) Adapting fresh state properties of fiber-reinforced cementitious material for high performance thin-section elements. In: Wallevik OH et al (eds) Proceedings of the 3rd international RILEM symposium on rheology of cement suspensions, Reykjavik, Iceland. RILEM PRO 68, pp 313–321

Peled A, Bentur A (2000) Geometrical characteristics and efficiency of textile fabrics for reinforcing composites. Cem Concr Res 30:781–790

Peled A, Bentur A, Yankelevsky D (1999) Flexural performance of cementitious composites reinforced by woven fabrics. Mater Civil Eng (ASCE) 11(4):325–330

Reinhardt HW, Naaman AE (eds) (2007) High performance fiber reinforced cement composites (HPFRCC5), PRO 53, Rilem publication S.A.R.L

Chapter 11
Heterogeneous Fiber-Particle Composite Subjected to Principal Stress Rotation

Benny Suryanto, Kohei Nagai, and Koichi Maekawa

Abstract Test results of 20 Engineered Cementitious Composite (ECC) plates under 4-point bending are reported. 13 plates were pre-cracked to allow rotation of the principal stress directions, in order to permit the study of shear and tensile stress transfer at multiple cracks. Coarse aggregates were investigated as a possible means to improve shear-transfer. When subjected to principal stress rotation, ECC exhibited a nearly orthogonal crack pattern, indicating little contribution from the shear transfer mechanism. A reduction in flexural capacity was observed, depending on the relative angles of principal tensile stress applied. When coarse aggregate was added to ECC, significant reductions in flexural capacity and flexural ductility were observed. In a situation when principal stress direction rotated, however, the test results show that coarse aggregate in the amount of 15% of the maximum packing density of the aggregate used was effective to control the orientation of secondary cracks in cracked ECC and to maintain a comparable level of flexural capacity irrespective of the reorientation angle of principal stress field and the angle of pre-existing cracks.

11.1 Introduction

Nowadays it is not uncommon to add fibers to improve the properties of concrete in tension. Fibers are expected to reduce the brittleness of concrete and to maintain its integrity after cracking. Depending on the behavior of fiber-reinforced concrete under direct tension and bending tests, Naaman and Reinhardt proposed four

B. Suryanto (✉) • K. Nagai • K. Maekawa
Department of Civil Engineering, The University of Tokyo, 7-3-1 Hongo, Bunkyo-ku, Tokyo 113-8656, Japan
e-mail: benny@concrete.t.u-tokyo.ac.jp; nagai@concrete.t.u-tokyo.ac.jp; maekawa@concrete.t.u-tokyo.ac.jp

M.N. Fardis (ed.), *Innovative Materials and Techniques in Concrete Construction: ACES Workshop*, DOI 10.1007/978-94-007-1997-2_11,

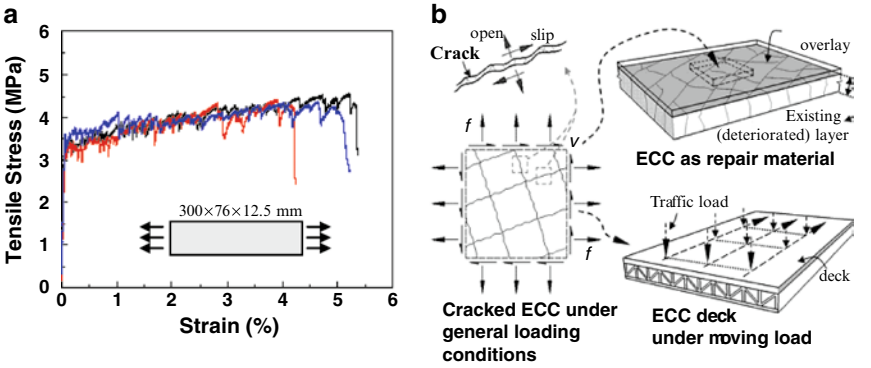

Fig. 11.1 (**a**) ECC with 2% PVA fibers in tension (Li 2003), and (**b**) Illustration of cracked ECC subjected to general loading conditions, allowing not only tensile stress, but also shear stress developed across cracks (Suryanto et al. 2010)

categories: namely, deflection-softening, deflection-hardening, strain-softening, and the outmost remarkable strain-hardening response (Naaman and Reinhardt 1996).

To achieve strain-hardening response in a cement-based composite, (Li and Wu 1992; Li et al. 2001) demonstrated its possibility with a moderate amount of short random polymeric fibers only, a material later known as the Engineered Cementitious Composite (ECC). The strain-hardening response is attributed to the formation of multiple cracks. To achieve this remarkable tensile response, an ECC mixture typically contains fine-graded materials such as cement, fine sand, fly ash, and PVA fibers in a volume ratio of 2% (Li et al. 2001). Example applications of ECC include thin overlays (Kunieda and Rokugo 2006), coupling beams for high-rise buildings (Kunieda and Rokugo 2006), and bridge decks (Kunieda and Rokugo 2006; Li et al. 2005).

In using ECC for general applications, investigation of its post-cracking behavior when subjected to general loading conditions is necessary. Under service loading, cracked ECC may undergo complex behaviors, involving opening, closing, and slip of pre-existing cracks and formation of new cracks. While many investigations have been devoted to investigate the behaviour of ECC relating to the crack-opening (Li 2003), little has been made to investigate the behaviour relating to crack-shear transfer and slip. Crack-shear slip can occur, for example, at the diagonal cracks in shear-critical beams, at the cracks in a bridge deck due to traveling-wheel load, or in an overlay material that has cracked and is under the influence of surrounding damaged parts (Fig. 11.1). In such cases, the rotation of the principal stress fields in the ECC is usually apparent and may proceed to a greater extent. The rotation of stress fields implies that not only tensile stress, but also shear stress develops across cracks. Due to the absence of coarse aggregate, however, it is of concern that cracked ECC may exhibit low interface shear resistance, especially when the crack surface is under repeated shear slip.

To investigate this issue, the authors recently performed bidirectional multiple cracking tests on eight pre-cracked ECC plates (Suryanto et al. 2010). To initiate shear stress at cracks, the test considered two constitutive principal stress directions. The ability of the ECC to transmit tensile and stresses across cracks is evaluated from the remaining flexural capacity, after being pre-cracked, and the final cracking

pattern. The test showed that the flexural capacity of the plates, where the cracks opened and slipped simultaneously, was about 30% (at worst) less than the plates whose cracks were in the opening-mode only. A nearly orthogonal crack pattern was observed irrespective to the difference between the two principal stress directions applied. This suggests that cracked ECC is an orthotropic material, and hence orthogonal cracks resulted. Results of the tests are described in detail in (Suryanto 2009) and are briefly summarized in the following sections.

In response to this finding, this contribution explores the possibility of adding coarse aggregate – referred to as particles in this paper – in ECC with the aim of improving its crack-shear transfer property. Coarse aggregates are recognized as a cheap and potentially available material for use in the fabrication of such a cement-based composite. The scope of this contribution is to come up with a possible mixture proportioning of ECC with coarse aggregate, to check its feasibility, and to investigate the influence of coarse aggregate to the properties of ECC. A more detailed report on the results of a larger series of ongoing investigations on the merit of coarse aggregate in ECC will be given elsewhere. Considering the practical applicability, the current investigation is limited to ECC reinforced with PVA fibers 2% by volume.

11.2 Experimental Program

The experimental program involved the testing of 20 ECC plates produced in three batches. In each batch, there were two types of plate, namely control plates and main plates [see Fig. 11.2a]. The control plates had dimensions of $400 \times 250 \times 20$ mm, whereas the main plates had dimensions of $550 \times 420 \times 20$ mm. The control plates were directly tested in 4-point bending so as to obtain the flexural capacity of the undamaged state. For the main plates, flexural cracks were induced prior to testing. The plates were then sawn with certain orientations to facilitate reorientation of the stress fields and were finally retested in bending to failure. An overview of the experimental program is given in Table 11.1.

11.2.1 Testing Procedure

The overall testing procedure is shown in Fig. 11.2c. To facilitate reorientation of the stress fields, the course of the testing was divided into two testing stages: preloading (stage I) and final loading (stage II). The preloading stage (stage I) was the damage initialization stage and was applied only to the main plates. At this loading stage, the inclination of the principal stress direction was altered by cutting a larger, preloaded plate. This testing technique was inspired by those previously implemented by (Maekawa 1983) and (Van Mier 1985). The damage level was set at 40% of the average ultimate tensile strain of the control plates. The main variable was the orientation of pre-cracks at the plate soffit as listed in Table 11.1. For this purpose, the plate was cut based on the layout given in Fig. 11.2b, with five different orientations: 0°, 20°, 45°, 70°, and 90°.

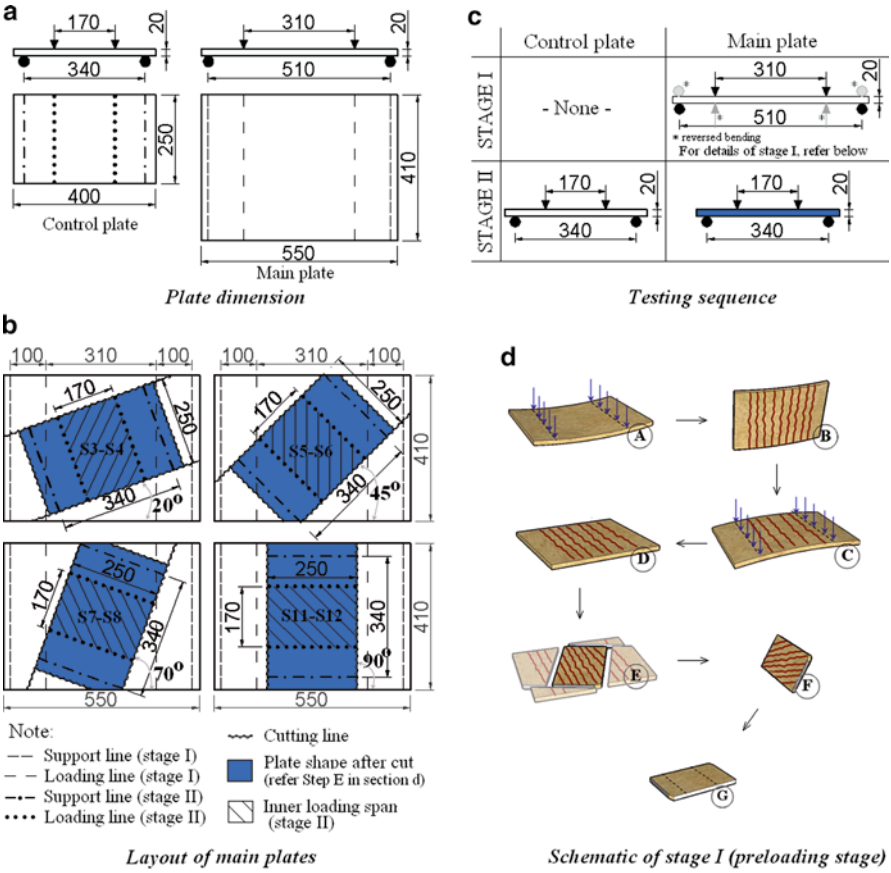

Fig. 11.2 Details of the plates and the testing procedure (Suryanto et al. 2010): (**a**) plate dimension, (**b**) layout of main plates, (**c**) testing procedure, and (**d**) schematic of stage I (preloading stage)

Table 11.1 Overview of test specimen

	Dimension			Initial damage		
ID	W (mm)	L (mm)	H (mm)	Orientation[a](°)	Level (%ε_{tPmax})	Plate type
0C1,2	250	400	20	–	–	Control
0CR						
1C1,2; 2C1,2						
1M0; 2M0	420	550	20	0	40	Main
0M20; 1M20; 2M20				20	40	
0M45; 1M45; 2M45				45	40	
0M70; 1M70; 2M70				70	40	
1M90; 2M90				90	40	

[a] Measured from the plane parallel to the width of the plate after cut 0-, 1-, and 2- implies Group 0, Group 1, and Group 2 plates, respectively

Table 11.2 Mix proportion of ECC and properties of PVA fibers (JSCE 2007)

W/(C+FA) (%)	Water (kg/m^3)	S/(C+FA) (%)	PVA Fibers (% by volume)	Fiber dia. (mm)	Fiber length (mm)	Fiber tensile strength (MPa)
42.2	350	70	2.0	0.04	12	1,600

Table 11.3 Sieve analysis of the coarse aggregate

Sieve size (mm)	Cumulative passing (%)
19	100
13.2	95
4.75	5.7

The complete procedure for the preloading stage is illustrated by the letters A to F in Fig. 11.2d. A step-by-step description of the procedure is as follows:

Step A: The plate was first loaded in a 4-point bending test with a span of 510 mm and an inner span of 310 mm. As loading proceeded, multiple flexural cracks gradually formed at the plate soffit and propagated upwards.

Step B: After reaching the target-damage level, the plate was unloaded and flipped.

Steps C-D: Reversed loading was applied to flatten the plate. As a result of this reversed loading, a few cracks were also observed at the top plate surface. These cracks might slightly reduce the initial stiffness of the plate during the final loading stage.

Step E: The plate was cut so as to align the cracks into the predefined orientation given in Table 11.1 and resize the plate to match the control plate. It was easy to make the cuts while preserving the pre-existing cracks undisturbed.

Step F: At the end of the preloading stage, the plate was flipped again, making it ready for the final loading stage (Step G).

The final loading stage (stage II) was the conventional 4-point bending test and was applied to both control and main plates.

11.2.2 Material Selection and Plate Fabrication

A pre-mixed ECC material (JSCE 2007), of which the mix proportion is listed in Table 11.2, was used. It contained PVA fibers in the volume of 2%. This premix ECC was packed in 25 kg paper bags, and sent to Concrete Laboratory, University of Tokyo, for fabrication of the test plates.

The coarse aggregate was a crushed type available in the market. Its gradation is shown in Table 11.3. Considering the thickness of the test plates, the aggregate size larger than 9.5 mm was omitted. Prior to casting, the aggregate was washed properly and made in the saturated surface dry (SSD) condition. The amount of aggregate included in the Group 1 and 2 was about 30% and 15% of γ_{max}, respectively, where

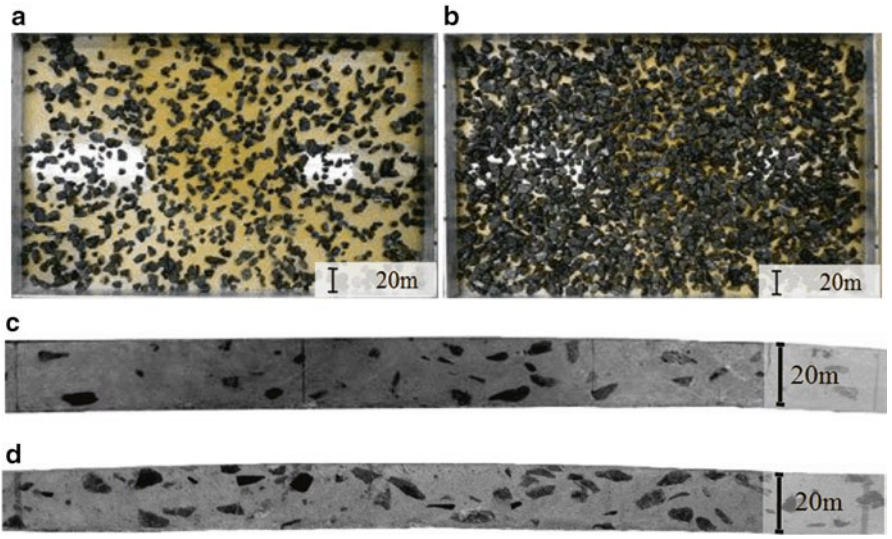

Fig. 11.3 Illustration of the aggregate used in Group 1 and 2 plates: (**a**), (**b**) in 9-mm depth, (**c**) and (**d**) in a sliced section

γ_{max} is the maximum packing density of the aggregate used (about 63%). These two aggregate amounts were decided based on the distribution of the aggregate and the workability when mixed with the ECC paste. Note that the aggregate distribution is important to ensure the presence of aggregate at any potential crack interface, whilst the workability is related to the ease of production. The aggregate used in the Group 2 plates had a minor impact on the workability, while the relatively large amount used for Group 1 had a significant effect. Relatively large addition of aggregate in Group 1 plates was intentionally made for the purpose of investigating the improvement of crack-shear transfer.

Mixing of the ECC was in all cases done as specified in Reference 9 for about 10 min. The air content and slump flow was then measured to ensure the property of the ECC matrix after hardening. The slump flow and air content was 490 mm and 9% for plates in the first batch, 510 mm and 15% for the second batch, and 515 mm and 7% for the third batch. After this measurement, coarse aggregate was added slowly to the ECC slurry in the third bath. They were then remixed for about 2 min.

After mixing, the ECC slurry was poured at once to the middle of each framework, made of plywood with aluminum frames. The slurry was then shredded in a radial pattern, rodded, finished with a steel trowel and finally covered with a plastic sheet. After 2 days, the plates were demolded and air-cured under 60% relative humidity and 20°C until the test date (started from the 28th day after casting). The average compressive strength and modulus elasticity were 33 MPa and 15 GPa, and 39 MPa and 20 GPa respectively, for ECC in the first and third batch, respectively. No measurements were made for ECC in the second batch.

The aggregate included in a 9-mm depth framework is shown in Figs. 11.3a and b. It should be noted that this is a 2D illustration; the distribution in a 3D space was

much sparser. To better illustrate the actual distribution, shown in Figs. 11.3c and d are the aggregate distributions at cut sections of two representative plates. Since the aggregate amount is much less than that used in ordinary concrete, the aggregates appeared to be suspended well in the ECC matrix.

11.3 Macroscopic Response of the Tested Plates

The first part of Sect. 11.3 describes the results of control plates where the influence of coarse aggregate is evaluated in bending under a fixed stress direction. The second part describes the performance of cracked ECC under the rotation of stress fields, which the cracks have to sustain shear and tensile stress actions.

11.3.1 Control Plates (C-Series)

The load-midspan displacement response of all control plates is presented in Fig. 11.4. All control plates exhibited ductile, deflection hardening response. This ductile response attributed to the formation of multiple cracks and the opening of pre-existing cracks. This condition continued until the weakest few cracks were unable to bear the applied tensile stress. Hence, one major localized crack formed across the plate soffit. This was the moment when the plate reached the maximum load.

Although the control plates were made of the same ECC mixture, variation of the first cracking load was observed. This may be attributed to the quality of the ECC matrix caused by the variation of air content for each casting batch. Group 0 control plates (0C1,2) cracked at a load of about 1.6 kN, while Group 1 and Group 2 plates

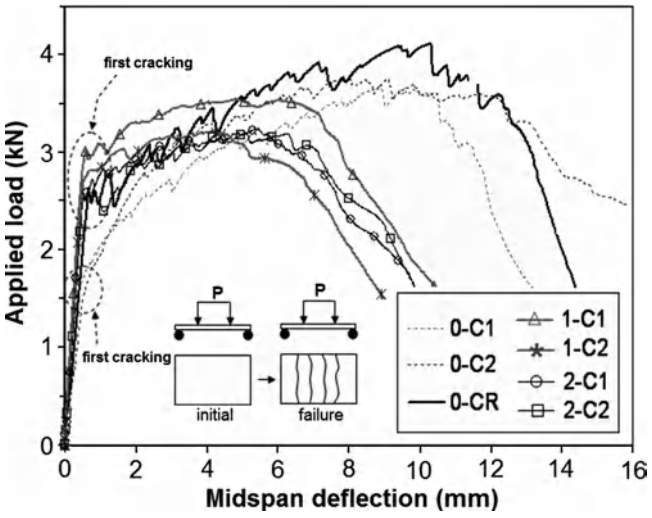

Fig. 11.4 Measured responses of control plates

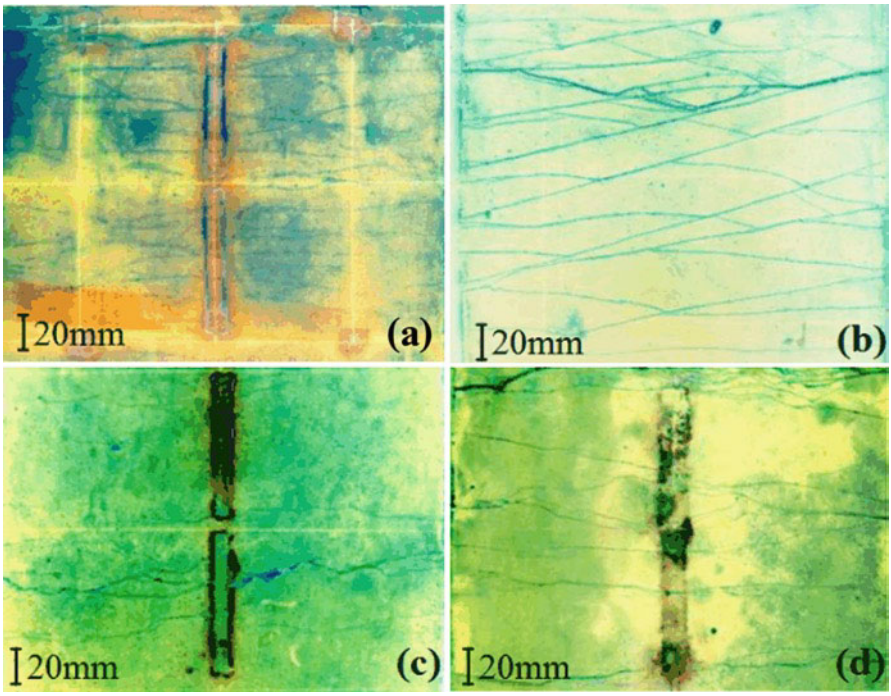

Fig. 11.5 Typical crack pattern after failure: (**a**) Plate 0 C1 (no aggregate); (**b**) Plate 0CR (no aggregate); (**c**) Plate 1 C1 (20%γ_{max}); and (**d**) Plate 2 C1 (10%γ_{max})

[Plates 0CR(no aggregate), 1C1,2, and 2C1,2] were in the range 2.6–2.9 kN. The largest first cracking load was shown by the Group 1 plates with the aggregate addition of 30% γ_{max}. This perhaps indicates the hindrance of aggregate in developing a full-length crack across the plate width.

The post-cracking response of Plates 1C1,2 and 2C1,2 (with aggregate) showed a much flatter response than Plate 0CR (no aggregate). From the response presented in Fig. 11.4 it can be observed that the addition of aggregate decreases the ratio between flexural capacity and cracking load. Flexural capacities of Plates 1C1,2 and 2C1,2 were only about 20% higher than their corresponding cracking load and 20% less than that of Plate 0CR. Moreover, significant reductions in flexural ductility were observed. The average flexural ductility of Plates 1C1,2 and 2C1,2 was about 5.5 mm, half of that of Plate 0CR. The same trend can be seen for the tensile strain measured at the plate soffit at the maximum load. The average strain value was 1.2%, 1.1%, and 0.5% for the first, second, and third batch plates, respectively. These strain values were then used as reference values for determining the initial strain of the main plates. The flexural performance degradations may be attributed to the combination of several factors, including fewer numbers of fiber bridging and increase of the ECC matrix toughness.

Figure 11.5 shows the crack pattern of all control plates over the constant moment span (170 mm). It appears that the higher the aggregate content, the less was the crack

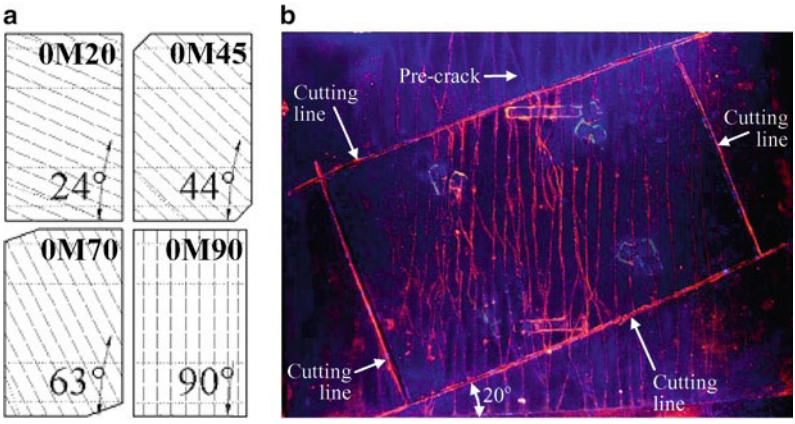

Fig. 11.6 (**a**) Schematic of pre-crack pattern of Group 0 plates, and (**b**) Crack pattern at the soffit of Plate 0 M20 after being pre-cracked and cut

number and the crack width. The crack numbers decreased from about nine cracks in Group 0 [Fig. 11.4b] to six cracks in Group 2 [Fig. 11.4d] and three cracks in Group 1 [Fig. 11.4c] plates. Several microcracks were observed in Group 1 plates.

In general, it appears that the addition of coarse aggregate is accompanied by a decrease in flexural properties including flexural capacity, flexural ductility, and less crack numbers. Perhaps this poor performance explains why coarse aggregate is always omitted in the design of ECC.

11.3.2 Main Plates (M-Series)

The preloading stage resulted in well-established, uniform multiple cracks over the soffit of the main plates. Figure 11.6 illustrates the schematic of the crack pattern for the Group 0 plates prior to the final test. The pre-cracks at the constant moment span prior to the final loading stage were in the range of 10–15 cracks. For Group 1 and 2 plates, no direct observation was made. Judging from the final crack pattern after failure, which will be shown later on in this paper, there were 5–7 cracks prior to the final loading stage.

The load-midspan displacement of Group 0 main plates are compared in Fig. 11.7. Plotted also in the figure are the results of pre-cracked plates that were subjected to higher initial damage level (70% ε_{tu}). Overall, the results indicate that the presence of pre-cracks alters the flexural capacity and initial stiffness of the plates. Notable reductions in flexural capacity were observed in both Plates 0M45 and 0M70. The initial stiffness rises with increasing initial crack orientation up to 90°, indicating the increase contribution of the uncracked ECC between the cracks.

The crack pattern of Group 0 plates are shown in Fig. 11.8. Three typical cracking patterns are observed. First, the cracks appeared in a bi-directional pattern.

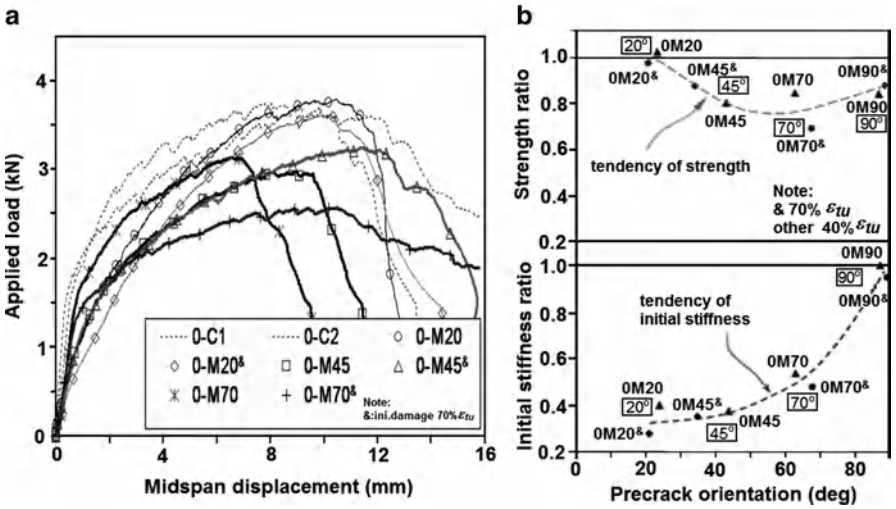

Fig. 11.7 (**a**) Load-midspan deflection of Group 0 plates with no coarse aggregate, and (**b**) Normalized flexural capacity and stiffness of the plates

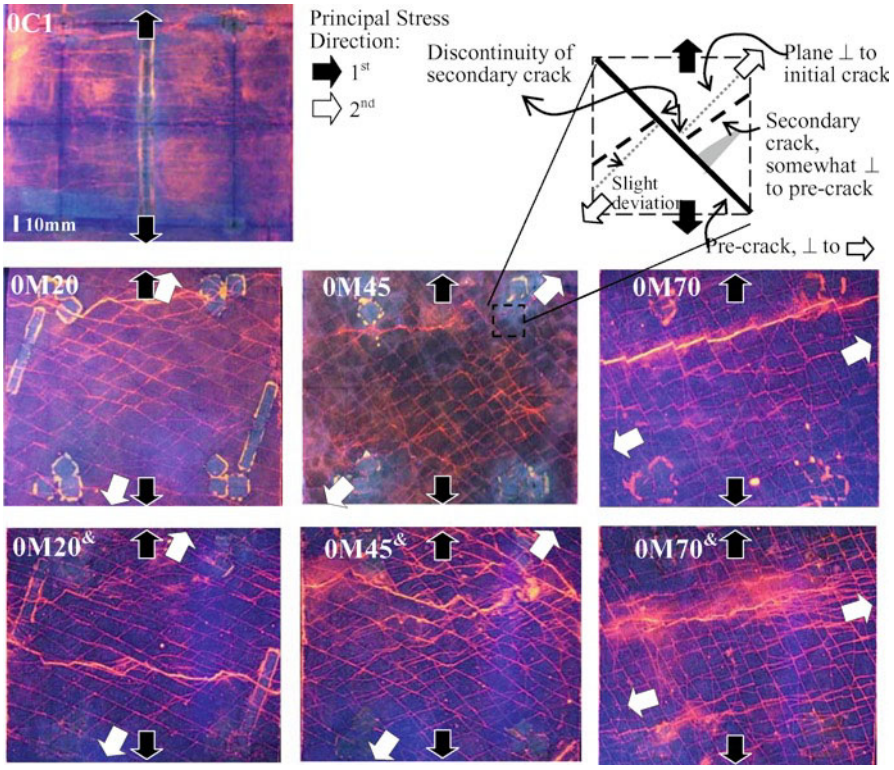

Fig. 11.8 Crack pattern of Group 0 plates after failure

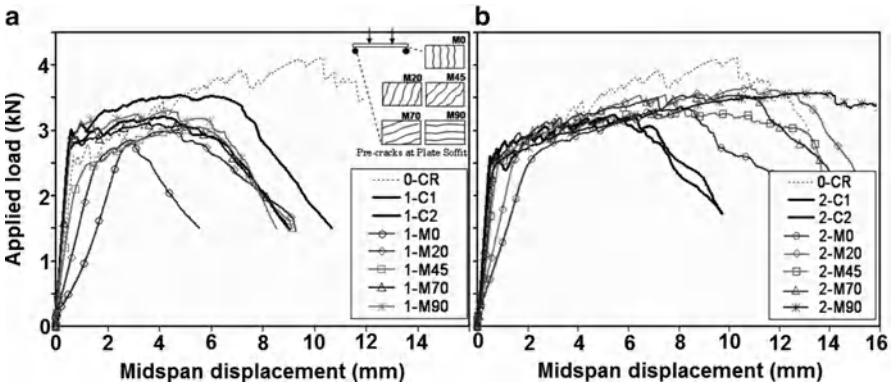

Fig. 11.9 Response of: (**a**) Group 1 plates (aggregate 30%γ_{max}) and (**b**) Group 2 (15%γ_{max})

Second, pre-cracks were uniform and continuous, while secondary cracks were discontinuous. They were uniformly spaced between 5 and 15 mm apart. Third, the pre-cracks were orthogonal to the principal stress direction of the preloading stage, while the secondary cracks always appeared near the orthogonal to the pre-cracks, with variations of up to 15°. No secondary cracks were formed orthogonal to the principal stress direction applied during the final loading stage. It should be noted that the orientation of the secondary cracks, in fact, indicates the in-plane stress-carrying mechanism of cracked ECC. The orthogonal pattern of the pre- and secondary cracks implies that the mechanism of stress transfer was relying more on the stresses developed parallel and orthogonal to the pre-cracks and less on the shear along the pre-cracks. Hence an orthogonal crack pattern resulted.

The load-midspan deflection responses of the pre-cracked plates of Group 1 and 2 are compared in Fig. 11.9. In Group 1 plates, only in Plate 1M0 was the response brittle due to premature failure at the pre-crack. The other plates in Group 1 showed a deflection-hardening response. Plates 1M20, 1M45 and 1M70 showed a comparable ductility in the range of about 4–6 mm. Slight reductions in flexural capacity were observed, of about 5–10%. This result suggests that the rotation of the principal stress direction had less impact on its macroscopic response. Nevertheless, flexural capacity and ductility of the plates were significantly below those of Plate 0CR [for clarity, see Fig. 11.10b]. Therefore, it could be surmised that the addition of excessive amount of coarse aggregate in ECC is ineffective.

Figure 11.11 shows the comparison of the crack pattern of the plates in Groups 0, 1, and 2. Note that the cracking pattern of Group 0 plates previously shown in Fig. 11.8 is again shown at the first row for a better comparison. The second and third rows indicate the cracking pattern of Group 1 and 2 plates with coarse aggregate amount of 30% and 15%γ_{max}, respectively. The different columns indicate various pre-crack orientations. Significant differences in secondary crack orientation can be observed. In all cases, the secondary cracks in Group 0 plates showed the largest deviation angle θ with respect to the plane normal to the new principal stress direction. Interestingly, θ appears to be the most acute for Group 2 plates, indicating

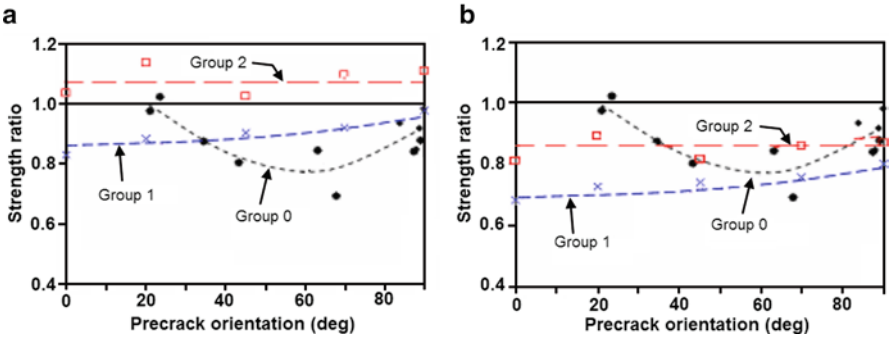

Fig. 11.10 Normalized strength based on: (**a**) the companion control plates and (**b**) Plate 0CR

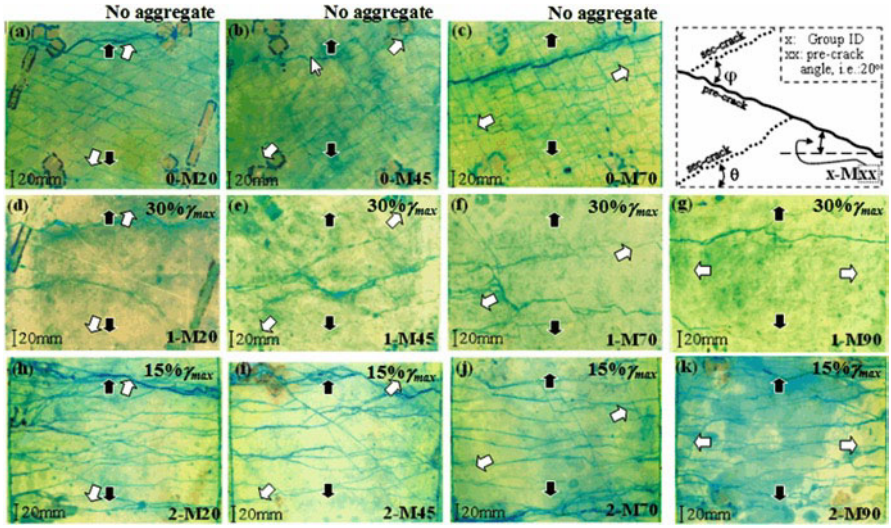

Fig. 11.11 Comparison of crack pattern among the plates with and without coarse aggregates

a better stress transfer along the pre-cracks than the other two groups. The indication is that, although the amount of coarse aggregate in Group 2 was less than that used in Group 1, the stresses across the cracks were transmitted more effectively. This might be attributed to the interaction between fiber bridging and aggregate: while the fibers confined the pre-cracks from reopening, the aggregate transmitted the occurring shear stress and limited the crack slip. The trade-off between the two should be optimized and addressed in further research.

Further observations of the cracking pattern of each plate shown in Fig. 11.11 also show that the number of secondary cracks in each plate of Group 0 and 1 is comparable to that of the corresponding control plates shown previously in Fig. 11.5. In Group 2 plates, the crack number tends to increase slightly. The increase might

be benefitted from internal microcracking that formed around the aggregate during the pre-cracking stage.

Another potentially interesting observation is that the orientations of secondary cracks θ tend to vary even in one plate, something that particularly appeared in Group 2 plates. In Plate 2 M45, for example, θ tends to increase in regions where the crack spacing is larger. This implies that the orthogonal crack pattern observed was not merely attributed to the stresses occurring at cracks, but also to the area of the uncracked parts. Further research in this area should address the effectiveness of coarse aggregate when it is used in ECC with smaller crack spacing than the one investigated herein.

11.4 Summary and Conclusions

Results from bending tests on pre-cracked ECC plates with and without the addition of coarse aggregate, subjected to principal stress rotation, are presented. From the results presented, the following conclusions can be drawn:

1. Tests on pre-cracked ECC plates subjected to principal stress rotation enable a more thorough investigation of post-cracking behavior of ECC subjected to complex stress states, involving tensile stress and shear stress transfer across multiple cracks.
2. Reorientation of the principal stress direction was found to have a significant effect on the response of cracked ECC. As the angle between the principal stress direction and the orientation of pre-existing cracks becomes larger (up to 70°), the strength apparently decreases up to about 30%. Initial stiffness appears to consistently increase with increasing angle between principal tensile stress and pre-cracks orientation.
3. When subjected to a stress rotation, ECC exhibited a nearly orthogonal crack pattern. The orthogonal pattern implies that the mechanism of stress transfer was relying more on the stresses parallel and orthogonal to the pre-existing cracks and less on interface shear transfer.
4. The addition of coarse aggregate demonstrates significant reductions in flexural capacity and flexural ductility when the applied stress direction does not rotate. In a situation when principal stress direction rotates, the test results show that the addition of aggregate can improve the performance of cracked ECC.
5. The viability to improve the performance of cracked ECC is achieved by the addition of coarse aggregate of $15\%\gamma_{max}$. The improvement is judged by the orientation of secondary cracks that became less dependent on the orientation of the pre-existing cracks, comparable flexural capacity irrespective of the reorientation of the stress fields, and ductile response. It is surmised that the addition of coarse aggregate in ECC helps the fibers in transmitting shear stress across cracks, provided that the fibers still hold the cracks from further opening.
6. The addition of an excessive amount of coarse aggregate (e.g. larger than $30\%\gamma_{max}$) is ineffective, possibly due to the significant reduction of fiber bridging at a crack and the considerable increase in the ECC matrix toughness.

References

JSCE (2007) Recommendations for design and construction of High Performance Fiber-Reinforced Cement Composite with multiple fine cracks (HPFRCC). Concrete Libr 127:129–135 (in Japanese)

Kunieda M, Rokugo K (2006) Recent progress on HPFRCC in Japan – required performance and applications. J Adv Concrete Technol 4(1):19–33

Li VC (2003) On Engineered Cementitious Composites (ECC). J Adva Concrete Technol 1(3): 215–230

Li VC, Wu HC (1992) Conditions for pseudo strain-hardening in fiber reinforced brittle matrix composites. J Appl Mech Rev 45(8):390–398

Li VC, Wang S, Wu C (2001) Tensile strain-hardening behavior of PVA-ECC. ACI Mater J 98(6): 483–492

Li VC, Lepech M, Li M (2005) Field demonstration of durable link slabs for jointless bridge decks based on strain-hardening cementitious composites. Michigan Department of Transportation Research Report no. RC-1471, p 110

Maekawa K (1983) Flow rule and plane stress constitutive equations of concrete. Concrete Eng 21(8):103–121 (in Japanese)

Naaman AE, Reinhardt HW (1996) Characterization of High Performance Fiber Reinforced Cement Composites – HPFRCC. High Performance Fiber Reinforced Cement Composites 2 (HPFRCC 2), In: Naaman AE, Reinhardt HW (eds) Proceedings of the second international RILEM workshop, E&FN Spon, London, pp 1–24

Suryanto B (2009) Mechanics of high-performance fiber-reinforced cementitious composite under principal stress rotation. PhD thesis, University of Tokyo, Japan

Suryanto B, Nagai K, Maekawa K (2010) Bidirectional multiple cracking tests on high-performance fiber-reinforced cementitious composite plates. ACI Mater J 107(5):450–460

Van Mier JGM (1985) Influence of damage orientation distribution on the multiaxial stress strain behavior of concrete. Cement Concrete Res 15:849–862

Chapter 12
Effect of Steel Fibers on the Flexural Ductility of Lightly Reinforced Concrete Beams

Avraham N. Dancygier and Erez Berkover

Abstract It is well known that one way to increase concrete toughness is the use of steel fibers, where increasing of material toughness is done with an aim to enhance structural ductility. However, in a former test series, reduced flexural ductility was observed in high strength concrete (HSC) beams with relatively low reinforcement ratios that included steel fibers. The motivation for the current study was to examine whether similar behavior of reduced flexural ductility occurs also in Fibrous Normal Strength Concrete (FNSC). For this purpose, a series of flexural tests of beam specimens was planned. The specimens were made of NSC, with and without fibers, with various reinforcement ratios. This paper shows preliminary results that indicate a similar phenomenon to the one observed in HSC. That is, reduced flexural ductility, which occurred in NSC specimens with a low reinforcement ratio and with steel fibers. Yet, ductility of the FNSC beams increased with increasing reinforcement ratio. A possible reason for these results, which involves localization of steel-concrete slip, is discussed.

12.1 Introduction

One of the design aspects of flexural members is maintaining an adequate ductility at ultimate limit state. For example, design principles for Fiber Reinforced Concrete (FRC) in the draft of the New Model-Mode require that the ultimate and peak-load displacements would be (respectively) at least 20 and 5 times larger than the displacement at service load (fib 2010).

A.N. Dancygier (✉) • E. Berkover
Department of Structural Engineering and Construction Management, National Building Research Institute, Technion – Israel Institute of Technology, Technion City, Haifa 32000, Israel
e-mail: avidan@technion.ac.il; eberk@technion.ac.il

M.N. Fardis (ed.), *Innovative Materials and Techniques in Concrete Construction: ACES Workshop*, DOI 10.1007/978-94-007-1997-2_12,

FRC is known to be a material with increased toughness compared to plain concrete (fib 2010). High strength concrete (HSC) is characterized by its high compressive strength but also by its relatively high brittleness (fib 2008). Therefore, addition of steel fibers to concrete is considered an efficient way to increase the material toughness and obtain high performance concrete (HPC).

Thus, the effects of applying steel fibers in HSC on the flexural behavior of beam specimens were examined in a series of tests (Dancygier and Savir 2006). Experimental observations from these tests showed that the displacement ductility of HSC beams with steel fibers and with moderate to high ratios of flexural reinforcement (higher than ~0.5%) had increased displacement ductility compared to similar reinforced HSC specimens without fibers, as expected. However, these tests also showed that when steel fibers were used in beams with relatively low reinforcement ratios (0.3%) they had a significantly lower ductility, compared to similar beams without fibers (Dancygier and Savir 2006). The plain reinforced concrete (RC) specimens in these tests responded according to the classical RC behavior, with flexural cracks whose widths developed with an increasing deflection of the beam. The initial response of the fibrous specimens involved also the development of flexural cracks at spacing similar to that of the plain specimens. Yet conversely to the plain specimens, as the deflection increased, the width of only a single crack continued to develop whereas widths of the other cracks remained almost unchanged.

This local response of a crack, which widened more than the others, led to high strains of the longitudinal steel in its vicinity. Consequently, the steel at the location of this crack reached its rupture strain. This occurred at a relatively low deflection – about one third of the ultimate deflection of similar plain specimens, exhibiting lower displacement ductility.

The current study is aimed at examining whether it was the concrete high strength that caused the above result or was it because of another reason. That is, the current experiments were planned to test whether similar behavior would occur also in normal strength concrete (NSC) specimens. Initial results of these tests are described herein.

12.2 Experimental Program

Four-point loading tests were performed of beam specimens made of NSC. The beams had different reinforcement ratios, starting at 0.15%. Most specimens included steel fibers. Some of the beams that served as control specimens were also cast with plain concrete mixes.

12.3 Materials

Concrete mixes included Portland cement type CEM I-52.5N, dolomite coarse aggregates of 19 mm maximum size, and natural quartz sand (Table 12.1). Average compressive strengths from 100 mm cubes at 28 days are given in Table 12.2.

Table 12.1 Concrete mix composition (nominal quantities)

Type	Cement (kg/m^3)	Sand (kg/m^3)	Aggregate (kg/m^3)	Water (kg/m^3)	W/C Ratio	Steel fibers (kg/m^3)	WRA[a] (Kg/m^3)
NSC	259	730	1,171	203	0.78	–	1.03
FNSC	251	709	1,137	198	0.79	60	1.51

[a]Water reducing agent

Table 12.2 Specimen details and material properties

Tension reinforcement								
Specimen	Concrete compressive strength (MPa)[a]	Fibers[b]	Details	Yield strength (MPa)	Ultimate strength (MPa)	Reinf. ratio	*d* (mm)	Shear reinforcement within shear span (mm)
NF-0-015	34.4	–	2 ϕ 8	496	698	0.15%	273	ϕ 8 @ 200
NF-1-015	29.5	+	2 ϕ 8	496	698	0.15%	273	ϕ 8 @ 200
NF-1-063	29.8	+	2 ϕ 16	412	668	0.63%	267	ϕ 8 @ 100
NF-0-126	34.0	–	4 ϕ 16	412	668	1.26%	267	ϕ 10 @ 100
NF-1-126	31.5	+	4 ϕ 16	412	668	1.26%	267	ϕ 10 @ 100

[a]Average strength at 28 days from 100 mm cubes
[b]60 kg/m^3 of hooked-end steel fibers

The fibrous mixes included hooked-end steel fibers that were given in a constant weight of 60 Kg/m^3 of mixture (volume ratio of 0.75%). The fibers were 35-mm long and 0.55 mm in diameter with an aspect ratio of 64 and a minimum tensile strength of 1,000 MPa (manufacturer's data).

12.3.1 Specimens

The beam specimens had 240 × 300 mm^2 cross-sections with different tension reinforcement ratios (Table 12.2). The longitudinal reinforcement consisted of deformed rebars with yield and ultimate strengths that are given in Table 12.2. The length of the shear span was 0.85 m and the span was 3.2 m, leaving a 1.5 m length for the constant moment zone between the two loads (Fig. 12.1). Spacing of the ties was reduced within the shear span in order to ensure flexural response of the beams. Concrete cover (of the ties) was 15 mm.

12.3.2 Measurements

Measurements included the external load, mid-span displacement and strains along the beam length. Strains at the top part of the beam were measured directly by strain gages. Indirect strain measurements were obtained from pairs of Linear Variable Displacement Transducers (LVDT) that were attached on both sides of the beam at

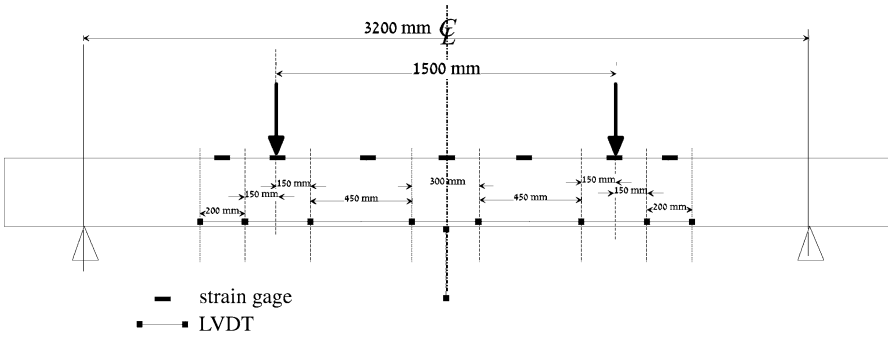

Fig. 12.1 Scheme of a beam specimen and measurements

the level of the longitudinal tension steel (Fig. 12.1). Thus, top and bottom strains were recorded at seven locations along the beam. The curvature at these locations was calculated by applying the Euler-Bernoulli theory, as the linear vertical gradient of the measured longitudinal strains along the cross-section where they were measured (i.e., sum of the absolute values of the top and bottom strains divided by the vertical distance between measurement points).

12.3.3 Test Procedure

The tests were performed with a manually stroke-controlled loading, which led to mid-span displacement rates that ranged from 0.5 to 1.0 mm/min up to post-yield. Experiments of the fibrous specimens included 1–2 repetitions of each specimen type.

12.4 Results

All specimens reached failure in a flexural mode as expected. Failure was characterized by concrete crushing at the top fiber of the beams. However, in the NF-1-015 specimens, which included steel fibers and had a 0.15% reinforcement ratio, it was followed by rupture of the tension rebars (rupture of one of the rebars occurred also in one of the beams without fibers and 0.15% of tension reinforcement, but it was at a much larger beam deflection). Load-mid-span displacement curves of the beams that had a low reinforcement ratio of 0.15% show that while the plain concrete specimens (NF-0-015) reached a maximum deflection of 120–150 mm the maximum deflections of similar beams with fibers were only 30–50 mm (Fig. 12.2a). Addition of fibers in the beams with higher longitudinal reinforcement ratios led to increased ultimate displacements, as demonstrated in Fig. 12.2b.

Another similarity to the response that was observed in FHSC beams was the development of cracks, where only a single crack continued to widen with increasing

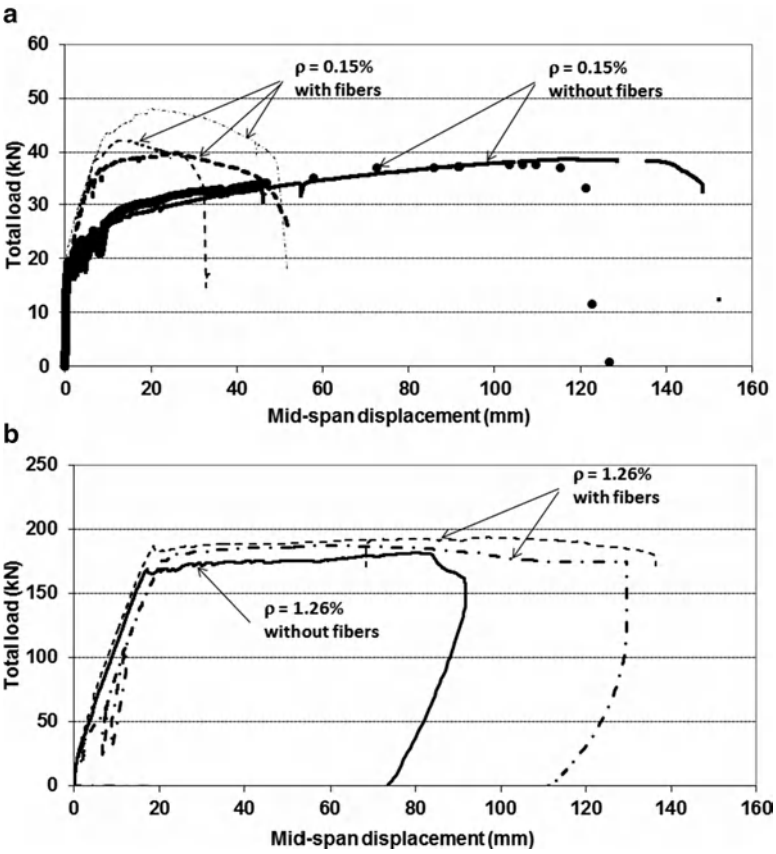

Fig. 12.2 Load-mid-span displacement curves of beams with reinforcement ratios of (**a**) 0.15% and (**b**)1.26%

deflection in the lightly reinforced beams that include fibers (as opposed to relatively uniform widening of the cracks within the constant moment zone in the similar plain RC beams).

Flexural capacities according to the measured maximum total load P_{max} were similar in the beams with and without fibers. Yet it is interesting to note that with decreasing reinforcement ratio there was an increase in the fibrous-to-plain concrete capacity ratios: P_{max}(with fibers)/P_{max}(plain concrete) ratios were 1.13 and 1.05 for the specimens with 0.15% and 1.26% reinforcement ratios (respectively).

12.4.1 Curvature Distribution

Measurements of longitudinal strains at the top and near-bottom of the cross-sections at seven locations along the beam (refer to Fig. 12.1) were converted to curvatures at these locations. Figure 12.3 shows the curvature distribution between

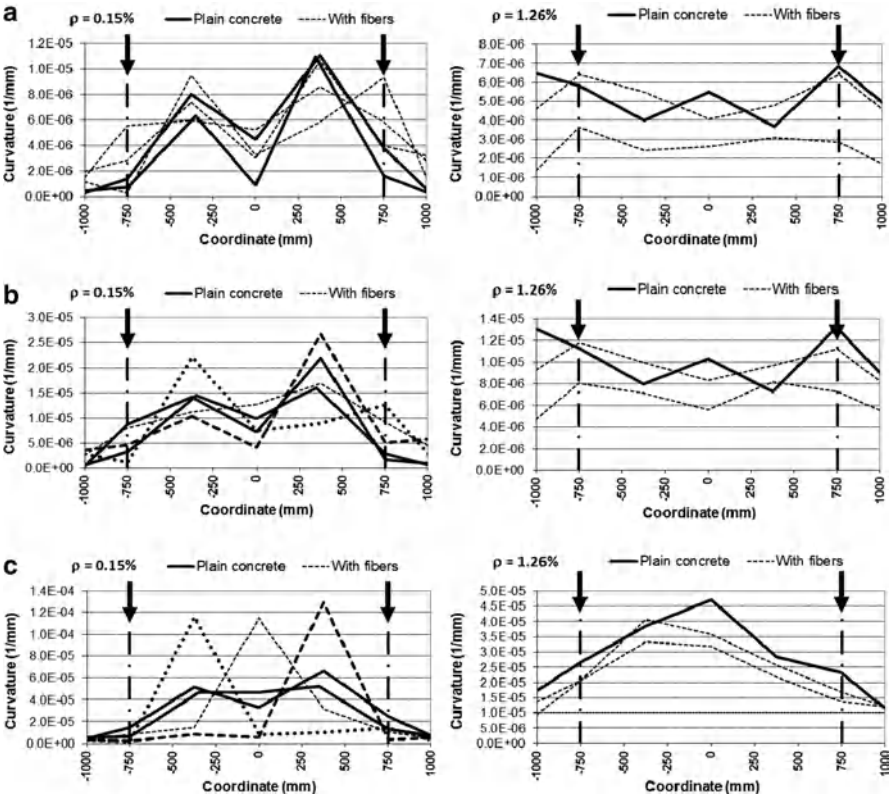

Fig. 12.3 Curvature distribution of fibrous and plain concrete specimens between points of loading at mid-span deflections of (**a**) *L*/500, (**b**) *L*/250 and (**c**) *L*/75 (*L* = span)

the two points of loading (within the constant moment zone) at various levels of mid-span displacement.

It can be seen that in both specimen types shown in Fig. 12.3 ($\rho = 0.15\%$ and $\rho = 1.26\%$) and at a relatively low displacement of *L*/500 (*L* = span), curvature distribution in beams that included fibers and in beams made of plain RC was similar (compare solid and dashed lines in Fig. 12.3a). However, as the beam deflection increased there was a difference between the curvature distribution in the lightly reinforced specimens and the beams with a higher amount of longitudinal steel (compare $\rho = 0.15\%$ and $\rho = 1.26\%$ in Fig. 12.3b): While the distribution remained relatively uniform in the beams with $\rho = 1.26\%$ (with or without fibers) it had distinct peaks in the beams with $\rho = 0.15\%$ that included fibers (refer to the three dashed lines of three specimens in the left Fig. 12.3b). This observation was more pronounced at larger deflections (Fig. 12.3c). Comparison of the locations of the curvature peaks in the fibrous specimens with pictures taken during the tests showed that the peak location coincided with the location of the crack whose width was significantly larger than the others.

12.5 Discussion

It is noted that a longer part of a beam, along which the curvature is larger than the yield curvature, denotes larger plastic hinge length and thereby enhanced beam ductility. The distribution of the curvature within the constant moment zone (i.e., between the loading points) is expected to have peaks at the cracked cross-sections. Yet, in case of a fairly uniform pattern of cracks of similar widths the distribution of these peaks as well as their size is likely to be relatively uniform. At increased deflections, curvature values near or at the maximum moment zone are likely to be high and it is therefore expected that a more uniform distribution of these curvature values would indicate longer plastic hinge and increased structural ductility. Thus, the relatively non-uniform distribution of the curvature within the constant moment zone, at large deflections of the beams with low reinforcement ratio and with fibers (ρ=0.15%, Fig. 12.3c) conforms to their reduced ductility, as displayed in Fig. 12.2a.

A more quantitative measure of the uniformity of the curvature distribution is the ratio between the standard deviation of the curvature values and their average (Stdv/Avg, i.e., the coefficient of variation) within the constant moment zone (a perfectly uniform distribution would result in a ratio of zero). This ratio is shown in Fig. 12.4 at three levels of the mid-span displacement. Figure 12.4 shows that as the reinforcement ratio increased the Stdv/Avg ratio decreased as well, indicating a more uniformly distributed curvature. These ratios were clearly higher in the specimens that included fibers at relatively low reinforcement ratios and at mid-span deflection of *L*/75 (~43 mm) (ρ=0.15%, Fig. 12.4c). This result reflects in a quantitative manner the localization of cracking and curvature in lightly reinforced beams with steel fibers.

Another measure of the ductility is the mid-span deflection at maximum load. Figure 12.5 shows mid-span displacements (normalized with respect to the span) that were measured at maximum load in the current tests and in a previous series of tests of HSC beams without fibers and with steel fibers (FHSC), which also included control NSC specimens (Dancygier and Savir 2006). It can be seen in Fig. 12.5 that the plain specimens showed the expected trend of increasing peak-load deflection with decreasing reinforcement ratio (Fig. 12.5a). However, in lightly reinforced beams the specimens that included fibers had a different trend, where the peak-load deflection decreased with decreasing reinforcement ratios that were lower than about 0.75% (Fig. 12.5b).

The current results together with those of a previous series of tests of HSC and FHSC specimens (Dancygier and Savir 2006) show that when fibers are added to concrete in a lightly reinforced concrete beam its response is different than that of RC beam without fibers. Cracking pattern at early stages of loading is similar in both types of beams (Fig. 12.3a). However, while in plain RC beams the widths of cracks under the same moment develop in a relatively uniform manner, in fibrous RC beams the response is localized to one of the cracks, which keeps widening more than the other cracks. This leads to a reduced length of the "plastic" behavior (or length of the plastic hinge), and to localization of the strains in the longitudinal reinforcement.

It may be thought that this phenomenon is a result of the effect of fibers on bond strength. However, a study, which consisted on a series of pullout tests of NSC, FNSC,

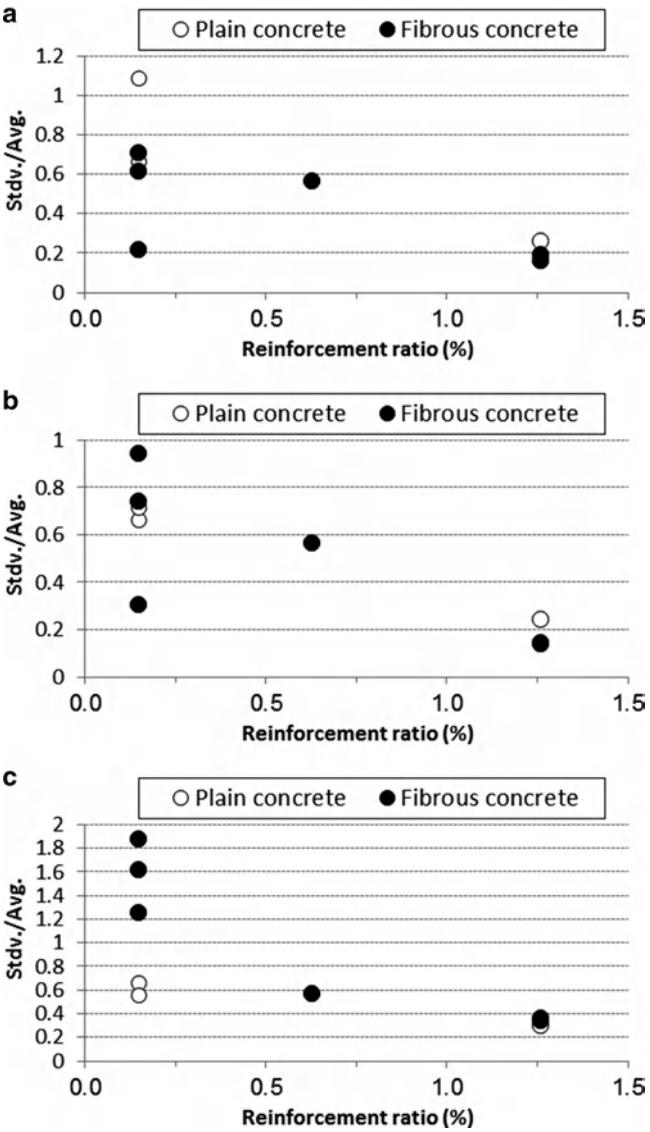

Fig. 12.4 Ratios of standard deviation to average of curvature values (coefficient of variation) measured between points of loading at mid-span deflections of (**a**) *L*/500, (**b**) *L*/250 and (**c**) *L*/75 (L = span)

HSC and FHSC specimens with deformed bars of different diameters, showed that there was no clear difference in bond strength when fibers were added (Dancygier et al. 2010). Moreover, it was shown that fibers had a more pronounced effect on bond in HSC than in NSC, while the above result was similar in both types of concrete.

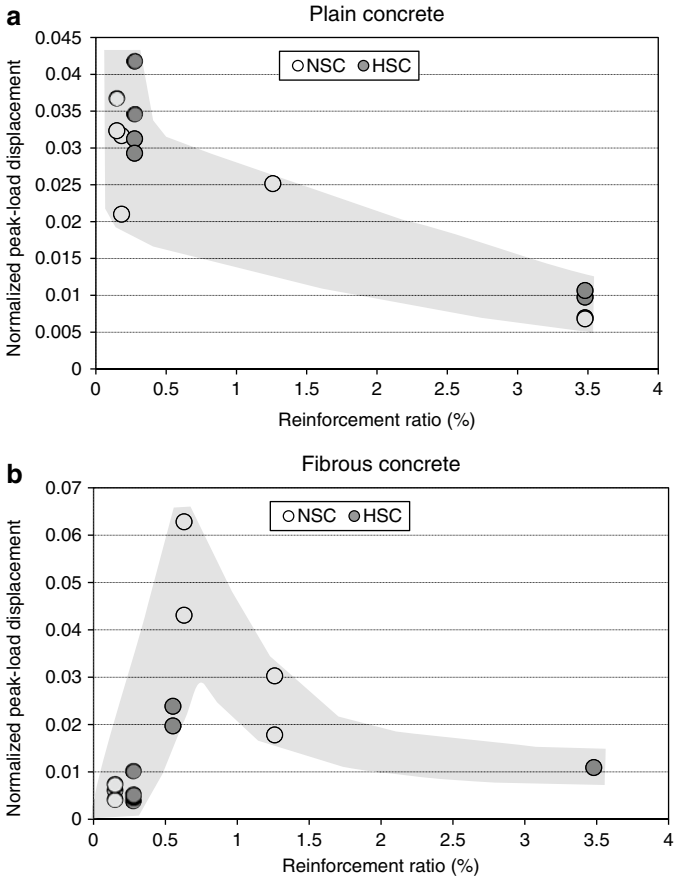

Fig. 12.5 Normalized mid-span displacements measured at maximum load in (**a**) plain and (**b**) fibrous beam specimens (in current tests and in tests reported by Dancygier and Savir 2006)

Yet, it is interesting to note that unlike bond strength, slip was reported to be higher in the fibrous specimens at peak and at post-peak pullout load (Dancygier et al. 2010).

Yuguang et al. (2009) tested reinforced concrete bars in uniaxial tension and analyzed their response. Some of the specimens in their study included steel fibers. They noted that "with increasing fiber content, localization is more likely to occur in one crack" and they associated this conclusion to the scatter in fiber content along the specimen.

Hence, for a given fiber volume there is a scatter of residual tensile strengths at the cracked cross-sections. This scatter is likely to be more significant as the amount of tension reinforcement decreases. For example, it would be most significant in fibrous concrete without steel rebars and almost insignificant in the presence of relatively high reinforcement ratios. The effect that this scatter may have on the slip of the tension steel at a particular crack could eventually cause larger strains of the rebars and, thereby, their premature rupture, as observed in the current tests.

12.6 Conclusions

Four-point loading tests were performed of beam specimens made of NSC, with and without steel fibers and with different reinforcement ratios, starting at 0.15%. In addition to the load and mid-span displacement, curvature distribution along the beam was evaluated according to measurements of longitudinal strains and displacements at seven cross-sections.

The tests were aimed to examine whether a phenomenon of reduced structural ductility, which was observed in lightly reinforced fibrous beams in a former series of tests of HSC, would repeat in NSC beams.

Reduced flexural ductility was observed in the current test specimens with low reinforcement ratios that included steel fibers. This result was characterized by relatively low maximum deflections accompanied by rupture of the tension rebars in the beams with fibers and low reinforcement ratio. Maximum displacements of these fibrous beam specimens were about one third of maximum displacements of the corresponding beam specimens with the same low amount of reinforcement but without fibers. Reduced structural ductility was also indicated by the relatively non-uniform curvature distribution within the constant moment zone, at large beam deflections, as compared to the curvature distribution in similar beam specimens, which did not include fibers. Ductility of fibrous RC beams increased though with increasing reinforcement ratios.

A possible reason for these results may be localization of slip of the tension rebars in the presence of fibers. Application of fibers leads to scatter in residual tensile strength at the cracks (more than in plain concrete). The effect of this scatter is likely to be stronger in the presence of low amounts of reinforcement (and vice versa). Hence, at low (e.g., minimum) reinforcement ratios, it would lead to locally larger strains of the reinforcing steel, which can be as large as its rupture strain.

These results may raise a question to whether larger amounts of minimum reinforcement ratios should be specified in FRC beams. This question is not based on the common concern for minimum moment capacity at cracking. It is raised in order to ensure their adequate ductility.

Acknowledgments This study was partially supported by the Israeli Ministry of Construction and Housing.

References

Dancygier AN, Savir Z (2006) Flexural behavior of HSFRC with low reinforcement ratios. Eng Struct 28(11):1503–1512

Dancygier AN, Katz A, Wexler U (2010) Bond between deformed reinforcement and normal and high strength concrete with and without fibers. Mater Struct 43(6):839–856

fib (2008) Constitutive modelling of high strength/high performance concrete, *fib* Bulletin 42. Federation internationale du beton, Lausanne

fib (2010) Model code 2010, First complete draft, vol 1, *fib* Bulletin 55. Federation internationale du beton, Lausanne

fib (2010) Model code 2010, First complete draft, vol 2, *fib* Bulletin 56. Federation internationale du beton, Lausanne

Yuguang Y, Walraven JC, den Uijl JA (2009) Combined effect of fibers and steel rebars in high performance concrete. HERON 54(2/3):205–224

Chapter 13
Innovative Textile-Based Cementitious Composites for Retrofitting of Concrete Structures

Thanasis Triantafillou

Abstract The author reviews experimental studies which have provided fundamental knowledge on the use of a new generation of composite materials, namely textile-reinforced mortars (TRM), as strengthening and seismic retrofitting materials of concrete structures. TRMs are investigated as a means: to provide confinement in plain and reinforced concrete (RC), to increase the deformation capacity of old-type RC columns subjected to simulated seismic loading and to increase the shear and flexural resistance of RC members. In all cases, the effectiveness of TRM systems is quantified through comparison with equivalent fiber-reinforced polymer (FRP) ones. Based on the results it is concluded that TRM jacketing is an extremely promising new technique, which will enjoy the attention of the research community and will be employed in numerous applications in the next decades.

13.1 Introduction

The increasing popularity of fiber-reinforced polymers (FRP) as a means of strengthening and seismic retrofitting of existing concrete structures derives from numerous attractive features of these materials, such as: high specific strength (i.e. strength to weight ratio), corrosion resistance, ease and speed of application and minimal change of cross section dimensions. Despite these well-established advantages over other methods, the FRP strengthening technique entails a few drawbacks, which are mainly attributed to the organic resins used to bind and impregnate the fibers. The replacement of organic binders with inorganic ones, e.g. cement-based polymer-modified mortars, would seem as the logical course of action, targeting at the alleviation of all resin-related

T. Triantafillou (✉)
Department of Civil Engineering, University of Patras, 26504 Patras, Greece
e-mail: ttriant@upatras.gr

M.N. Fardis (ed.), *Innovative Materials and Techniques in Concrete Construction: ACES Workshop*, DOI 10.1007/978-94-007-1997-2_13,

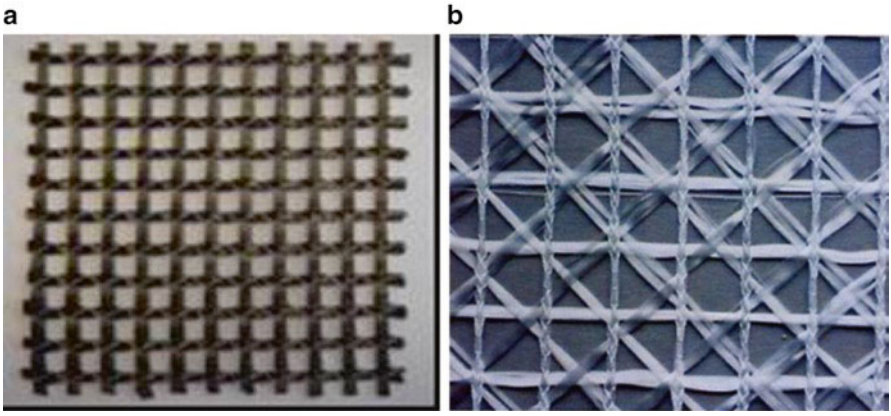

Fig. 13.1 Typical textiles: (**a**) two-directional carbon fibers; (**b**) three directional glass fibers

problems. Nevertheless, the substitution of FRP with fiber-reinforced mortars would be inhibited by the relatively poor bond conditions in the resulting cementitious composite as, due to the granularity of the mortar, penetration and impregnation of fiber sheets is very difficult to achieve. Enhanced fiber-matrix interactions could be achieved when continuous fiber sheets are replaced by textiles, resulting in a new generation of materials, which may be called Textile-Reinforced Mortars (TRM), and may be thought of as an alternative to FRP in the field of strengthening and seismic retrofitting.

Textiles comprise fabric meshes made of long woven, knitted or even unwoven fiber rovings in at least two (typically orthogonal) directions (Fig. 13.1). The quantity and the spacing of rovings in each direction can be independently controlled, thus affecting the mechanical characteristics of the textile and the degree of penetration of the mortar matrix through the mesh openings. The latter is a measure of the composite action achieved for the mortar-grid structure through mechanical interlock. For the polymer-modified cementitious matrix of externally applied TRM overlays used for strengthening purposes, the following requirements should be met: no shrinkage; high workability (application should be possible using a trowel); high viscosity (application should not be problematic on vertical or overhead surfaces); low rate of workability loss (application of each mortar layer should be possible while the previous one is still in a fresh state); and sufficient shear (hence, tensile) strength, in order to avoid premature debonding. In case E-glass fiber textiles are used, the cement-based matrix should be of low alkalinity.

In this paper, the author reviews experimental studies which have provided fundamental knowledge on the use of TRM as strengthening and seismic retrofitting materials: to provide confinement in plain and reinforced concrete (RC); to increase the deformation capacity of old-type RC columns subjected to simulated seismic loading; and to increase the resistance of RC members in shear and flexure. In all cases, the effectiveness of TRM systems is quantified through comparison with equivalent FRP ones. Based on the results it is concluded that TRM jacketing is an extremely promising new technique, which will enjoy the attention of the research community and will be employed in numerous applications in the next decades.

13.2 Confinement

13.2.1 Axially Loaded Concrete

First we study experimentally the effectiveness of TRM versus FRP jackets as a means of confining unreinforced or reinforced concrete members subjected to concentric compression. The test plan included the following groups of specimens: (i) unreinforced cylinders with diameter 150 mm and height 300 mm (Series A); (ii) short column-type prisms of both reinforced and unreinforced concrete, with rectangular cross section 200 × 200 mm and height 375 mm (Series B). Each specimen series was cast using the same ready-mix concrete batch (but slightly different from series to series, in terms of water to cement ratio). The steel used for both longitudinal and transverse reinforcement in Series B specimens (see configurations in Fig. 13.2) had an average yield stress equal to 560 MPa. The four corners of all rectangular prisms were rounded at a radius equal to 25 mm.

All specimens received textile sheets as externally bonded reinforcement, except for some of the Series B specimens in which the epoxy resin-impregnated jackets consisted of fabrics (unidirectional fiber sheets). All confining systems were applied "as usual", that is with a single textile (or fabric) sheet wrapped around each specimen until the desired number of layers was achieved. The bonding agent was either epoxy resin or polymer-modified cement mortar, applied to the concrete surface, in between all layers and on top of the last layer. Application of the mortars was made in approximately 2 mm thick layers with a smooth metal trowel.

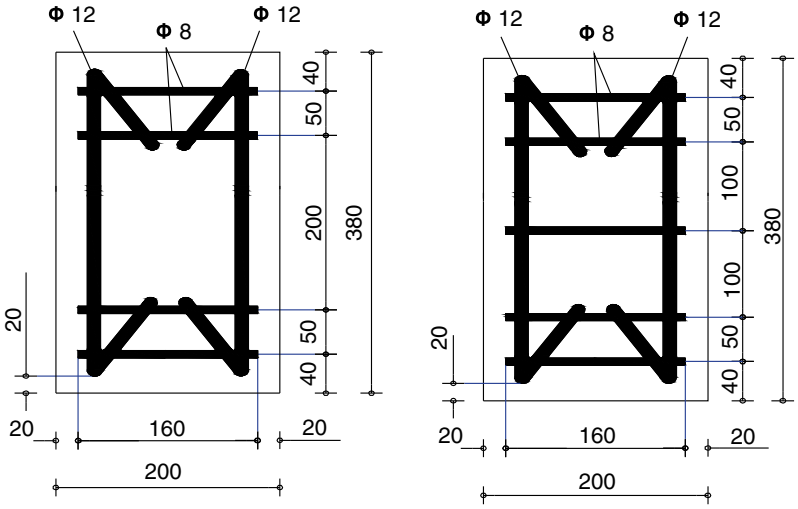

Fig. 13.2 Reinforcement configurations for specimens in Series B (dimensions in mm)

Specimens are given the notation Y_XN, where: Y denotes the series designation (A, B); X denotes the type of jacket (C for the unjacketed/control specimens, M_A for Series A cylinders with mortar jackets, M_B for Series B prisms with mortar jackets mortar quality in this case being different from mortar M_A, and R for resin-based jackets FRP); N denotes the number of layers.

Two different commercial unwoven textiles with equal quantity of high-strength carbon fiber rovings in two orthogonal directions were used. The mass of fibers in the textile used for all specimens of Series A (Tex1) was 168 g/m² and the nominal thickness of each layer (corresponding to the equivalent smeared distribution of fibers) was 0.047 mm. The corresponding values in the textile used in Series B receiving mortar were double (in this case, i.e. in Tex2, the rovings were impregnated with a low-strength polymer). The fabric used for specimens of Series B receiving epoxy resin had a unit mass of 300 g/m² and a nominal thickness of 0.17 mm. The guaranteed tensile strength of the fiber sheets in each direction was 3,350 MPa for Tex1, 3,545 MPa for Tex2 (when the nominal thickness is used) and 3,790 MPa for the fabric; the elastic modulus for all carbon fiber materials ranged between 225 and 230 GPa. Mortars M_A and M_B were commercial dry polymer-modified cement-based binders with a 28-day compressive and flexural strength equal to 30.6 and 4.2 MPa, respectively, for M_A and 22.1 and 6.8 MPa, respectively, for M_B.

The response of all specimens in uniaxial compression was obtained by monotonically applied loading in displacement control. Loads were measured from a load cell and displacements were obtained using external displacement transducers. From the applied load and average displacement measurements the stress-strain curves were obtained for each test (selected results are given in Fig. 13.3). All stress-strain plots for TRM- and FRP-confined reinforced concrete specimens are characterized by an ascending branch, which nearly coincides with that for unconfined concrete, followed by a second nearly linear one, which drops at a point where the jacket ruptured due to longitudinal bar buckling at specimen's corners. Past the peak load, FRP-confined specimens exhibited an explosive type of failure which was not preceded by any kind of visible jacket damage, due to the release of a large amount of strain energy stored in the column. On the contrary, prior to strength loss, TRM jackets experienced gradual fracture and a post-peak behaviour that was distinctively more compliant than their resin-based counterparts.

Based on the response of confined specimens made of plain concrete, it is concluded that: (a) TRM confining jackets provide substantial gain in compressive strength and deformation capacity. This gain is higher as the number of confining layers increases and depends on the shear strength of the polymer-modified mortar, which determines whether failure of the jacket will occur due to fiber fracture or debonding. (b) Compared with their resin-impregnated counterparts (FRP), TRM jackets may result in reduced effectiveness, depending on the type of mortar. (c) Failure of mortar-impregnated textile jackets is less abrupt compared to that of their resin-impregnated counterparts, due to the slowly progressing fracture of individual fiber bundles. A more detailed analysis of the results as well as some modeling aspects of TRM-confined concrete may be found in Triantafillou et al. (2006) and Bournas et al. (2007). Generally, similar conclusions apply for the case of reinforced

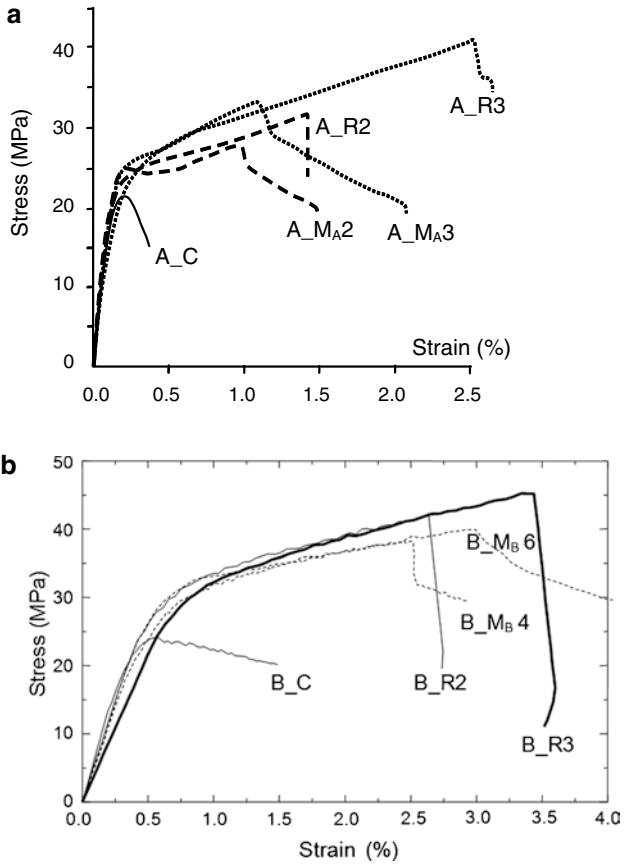

Fig. 13.3 Typical stress-strain curves for (**a**) Series A (plain concrete cylinders) and (**b**) Series B (RC prisms with stirrups every 100 mm)

concrete specimens; TRM jackets seem to be slightly less effective in terms of both strength increase and deformation capacity, by approximately 10%.

13.2.2 Seismic Retrofitting

In this section selected results are presented as part of an experimental investigation of the effectiveness of TRM jacketing in plastic hinge confinement of old-type RC columns designed with poorly detailed reinforcement. The increase in ductility provided by TRM jackets is compared with the one provided by equivalent (that is with the same amount of fibers in the circumferential direction) FRP ones. Three full-scale reinforced concrete columns were cast using ready-mix concrete. The columns measured 1.80 m in height and had a cross section of 250×250 mm. Testing was done in a cantilever

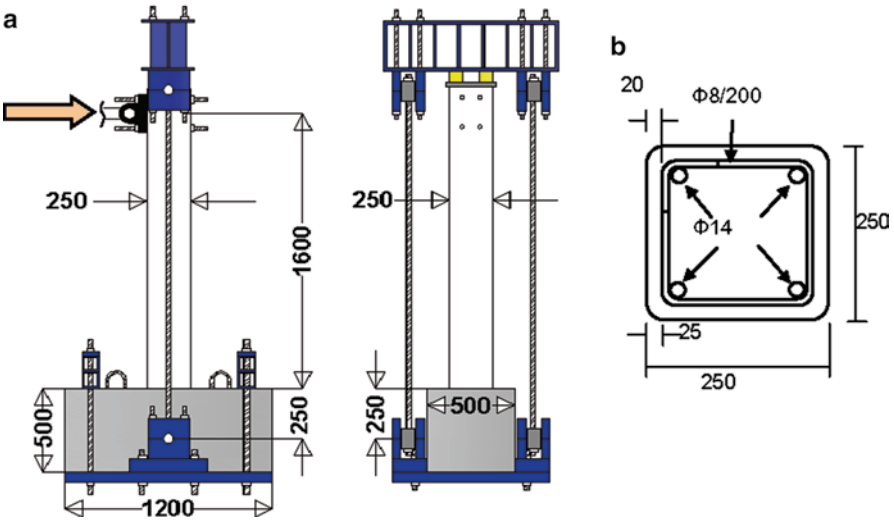

Fig. 13.4 (**a**) Geometry of columns and (**b**) details of cross section (dimensions in mm)

configuration, with a shear span of 1.60 m. The geometry of the columns, the reinforcement detailing and the general set-up of the test are shown in Fig. 13.4. Details are provided in Bournas et al. (2007) and an in-depth experimental investigation for columns with lap-splices is given in Bournas and Triantafillou (2011).

The columns were cast using concrete of mean 28-day compressive strength equal to 25 MPa. The steel used for both longitudinal and transverse reinforcement (both smooth) had an average yield stress equal to 372 MPa. Special attention was given to the appropriate anchoring of longitudinal reinforcement into the specimen's footings in order to minimize slippage. One column was unstrengthened (control specimen), another one received a four-layer TRM jacket in the plastic hinge region (jacket height being equal to 430 mm, accounting for the calculated height of the plastic hinge) and a third column was jacketed with two-layers of resin-impregnated carbon fiber fabric (FRP). The materials used for jacketing were identical to the ones used for strengthening specimens of Series B in the previously described experimental investigation. The columns were subjected to lateral cyclic loading under a constant axial load of 460 kN corresponding to 30% of the member's compressive strength. The lateral load was applied using a horizontally positioned actuator and the axial load was exerted by a set of four hydraulic cylinders. Displacements at the plastic hinge region were monitored using six rectilinear displacement transducers. The load versus piston displacement curves for all specimens are given in Fig. 13.5.

The performance and failure mode of all tested columns was controlled by flexure. The unretrofitted column (Fig. 13.5a) attained a drift ratio (tip displacement divided by height) at failure of about 3.6%. The concrete cover and part of the core over the lower 200 mm of the column disintegrated and bar buckling initiated after the concrete cover spalled off at a drift ratio of about 3%. The behavior of the two retrofitted columns was very similar (Figs. 13.5b and c for columns M4 and R2, respectively),

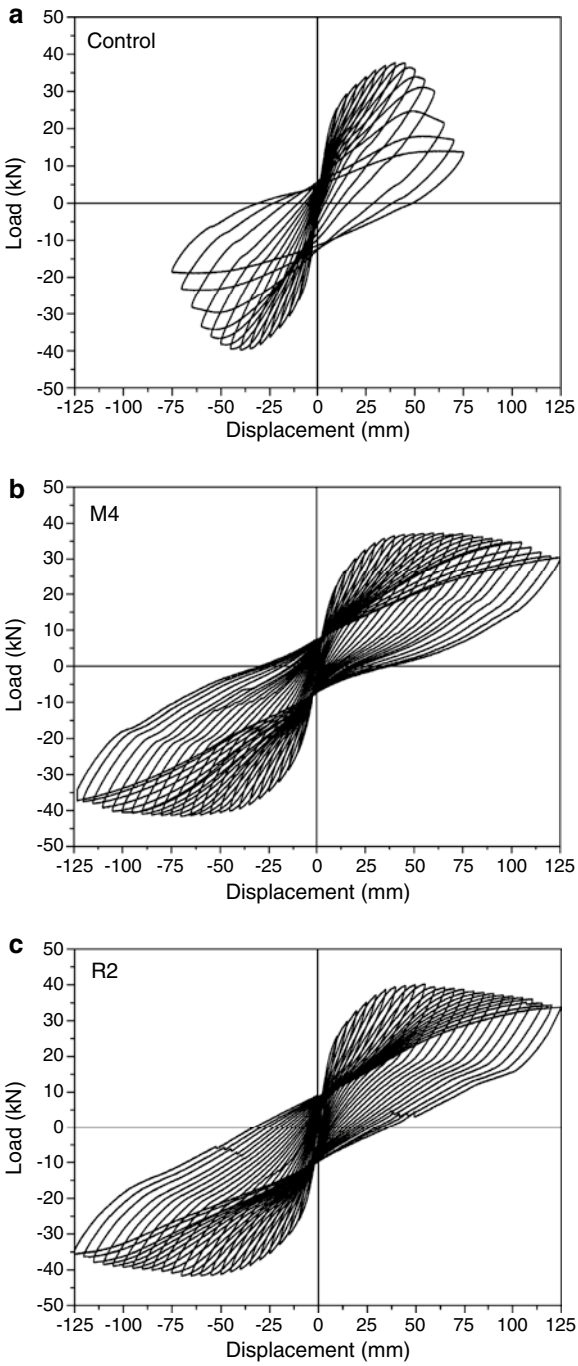

Fig. 13.5 Load-displacement curves for (**a**) the control specimen, (**b**) the TRM-confined specimen (M4), and (**c**) the FRP-confined specimen (R2)

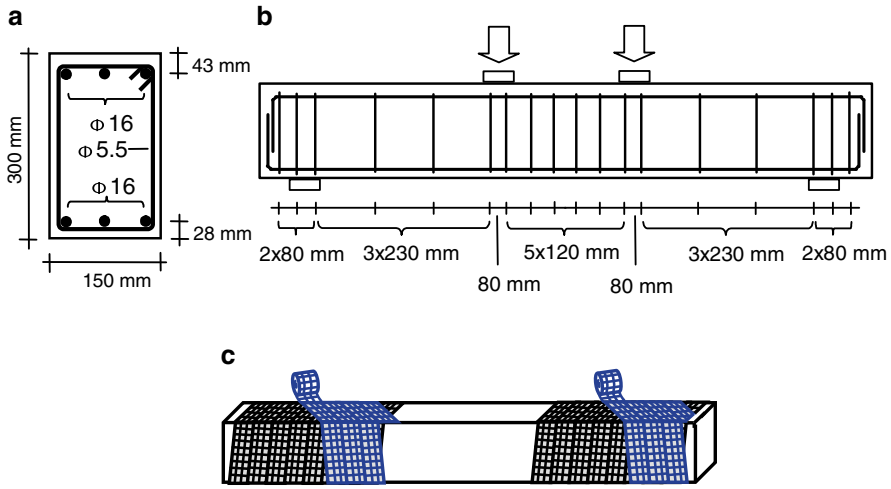

Fig. 13.6 (**a** and **b**) Geometry of beams; (**c**) spiral application of strips at the shear spans

but quite different from and far better than their unretrofitted counterpart. Member deformation capacity increased by a factor of more than two, corresponding to a drift ratio at failure of about 7.5%; peak resistance was practically the same as in the unretrofitted column; and the post peak response was quite stable, displaying gradual strength degradation. Whereas the CFRP jacket in column R2 exhibited limited rupture over the lower 50 mm at 7.2% drift ratio (in the pull direction), the TRM jacket remained intact until the test was terminated at 7.8% drift ratio. When the jackets were removed in both retrofitted columns after the end of the tests, a completely disintegrated concrete core was exposed, one that had been kept in place by the heavy confinement provided by the jackets (both FRP and TRM).

13.3 Shear Strengthening

The aim of this part of the experimental program was to examine the effectiveness of TRM jackets as strengthening reinforcement of shear-critical RC members. The investigation was carried out on six beams deficient in shear (i.e. with a large spacing of stirrups in the shear span) in four point bending. The beams measured 2.60 m in length and had a cross section of 150×300 mm. The geometry of the beams, the reinforcement detailing and the general set-up of the test are shown in Figs. 13.6a and b. A more detailed description of this study is given in Triantafillou and Papanicolaou (2006).

The beams were cast using a ready-mix concrete of mean 28-day compressive strength equal to 30.5 MPa. The steel used for transverse and longitudinal reinforcement had an average yield stress equal to 275 and 575 MPa, respectively. Textile, mortar

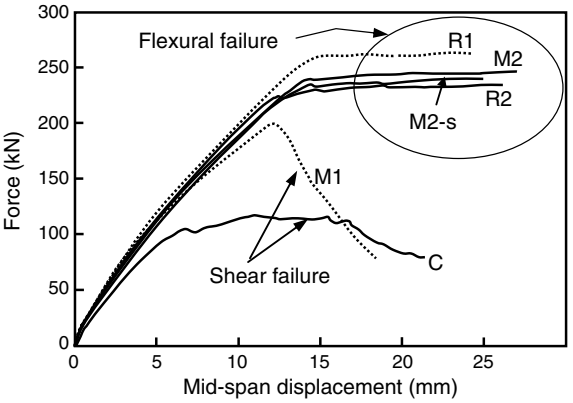

Fig. 13.7 Force – mid-span displacement curves for all beams tested (for beams M1 and R1 subjected to cyclic loading the envelope curves in the push direction are given)

(type M_A) and resin matrices were the same materials as those in the experimental study involving confined specimens made of plain concrete. The influence of three parameters was considered in the experimental investigation, namely the use of inorganic mortar versus resin-based matrix material for the textile reinforcement, the number of layers (one versus two) and the use of conventional wrapping versus "spirally applied" textiles. Here, "conventional wrapping" corresponds to a single textile sheet being wrapped around the shear span until the desired number of layers is achieved. The bonding agent was either epoxy resin or polymer-modified cement mortar, applied to the concrete surface in between all layers and on top of the last layer. "Spirally applied" jacketing (Fig. 13.6c) was implemented in one beam only and involved the formation of each layer through the use of a single strip, approximately 150 mm wide. The first strip was wrapped around the member in a spiral configuration, starting from one end of the shear span and stopping at the other; the next strip was wrapped in the same configuration but in a direction opposite to that of the first strip. Both strips formed a 10° angle with respect to the transverse to the member axis.

Four of the beams were tested monotonically and two of them were subjected to cyclic loading. One of the four monotonically tested beams served as a control specimen (C); a second one was wrapped with two layers of mortar-based jacket in the shear span (M2); a third beam was identical to the second but with a resin-based matrix material for the textile reinforcement (R2); and a fourth beam was strengthened with jackets formed by spirally applied strips (M2-s). The next two specimens (subjected to cyclic loading a few months later than the previous four) were identical to the second and third, but with one layer (instead of two) of textile in a mortar-based (M1) and a resin-based (R1) matrix, respectively. Specimens C, M2, R2 and M2-s were tested monotonically, whereas the remaining two were subjected to quasi-static cyclic loading, all in displacement control. The load was applied using a vertically positioned actuator and the displacements were measured at mid-span using two external linear variable differential transducers mounted on both sides of the specimens. The load versus mid-span displacement curves for all specimens are given in Fig. 13.7.

The control beam (C) failed in shear, as expected, through the formation of diagonal cracks in the shear spans; the ultimate load was 116.5 kN. No sudden drop in the load was recorded after diagonal cracking, as considerable contribution to shear

resistance was provided by both the stirrups crossing the crack and the strong dowel action (activated by the three Ø16 mm longitudinal rebars).

The behavior of beams R2, M2, M2-s and R1 indicated that shear failure was suppressed and that failure was controlled by flexure: cracks in the constant moment region became wide and yielding of the tension reinforcement resulted in a nearly horizontal branch of the force versus displacement curve. The maximum loads in specimens R2, M2 and M2-s were 233.4, 243.8 and 237.7 kN, respectively, that is nearly the same. This confirms the fact that the shear strengthening scheme selected in this study did not affect the flexural resistance. But the increase in shear resistance was dramatic (more than 100%), regardless of the strengthening scheme: two layers of textile reinforcement (either in the form of continuous sheets or in the form of spirally applied strips) with the cementitious binder performed equally well to the epoxy-bonded (FRP) jacket (with two layers of textile reinforcement). Specimen R1 experienced a flexural yielding failure mode with unequal capacities in the push and pull directions (261.9 and 201.4 kN, respectively), possibly due to the unintentionally larger concrete cover at the top of each beam compared to the bottom. Specimen M1 failed in shear (at a peak load of 200.1 kN); this was evident by diagonal cracking in the shear span as well as by the rather sudden strength and stiffness degradation. In this case, the application of a single-layer TRM jacket resulted in a substantial increase in the specimen's shear capacity with respect to the control specimen, in the order of 70%. It should be noted that for specimen M1: (i) fracture of the fibers in the cement-based jacket was gradual, starting from a few fiber bundles and propagating slowly in the neighboring fibers; and (ii) contrary to conventional FRP jackets, beam cracking was clearly visible on the TRM jacket, a feature that facilitates damage assessment.

Overall, it may be concluded that the TRM jackets employed in this study were quite effective in increasing the shear resistance of reinforced concrete members. Two layers of textile reinforcement (with a nominal thickness per layer equal to only 0.047 mm in each of the principal fiber directions) were sufficient to prevent sudden shear failure, whereas one layer proved less effective compared to its resin-bonded counterpart, but still sufficient to provide a substantially increased shear resistance.

13.4 Flexural Strengthening

13.4.1 Beams

In this part of the investigation, the effectiveness of TRM as externally applied flexural strengthening reinforcement of RC beam-type members was examined. The results reported here refer to testing of three under-reinforced beams in four-point bending, at a span length of 2.0 m and a shear span of 0.75 m. The beams had a cross section of 150×250 mm and were reinforced with 2Ø12 longitudinal rebars on each side (top and bottom), at a cover equal to 25 mm. The shear reinforcement comprised Ø8

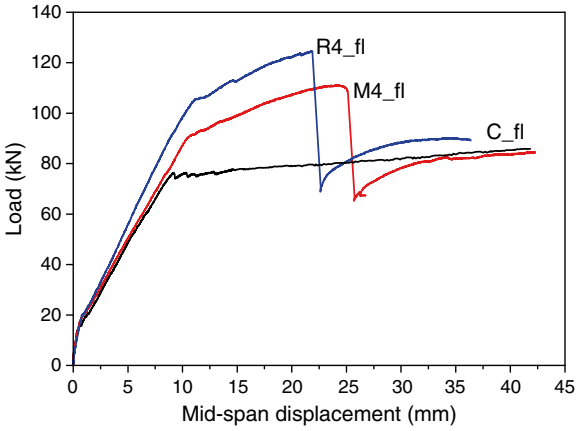

Fig. 13.8 Load – displacement response of beams strengthened in flexure

stirrups at a small spacing equal to 100 mm, to ensure that failure would be controlled by flexural yielding. Self-compacting concrete was used for casting of the beams (mix design and production were performed in the laboratory within the framework of a parallel experimental investigation); mean 28-day compressive strength was equal to 34.5 MPa. The steel reinforcement had an average yield stress equal to 530 MPa. Textile, polymer-modified mortar (type M_A) and epoxy resin matrices were the same materials as those in the experimental study involving confined cylinders made of plain concrete.

One of the three beams was tested without strengthening, as a control specimen (C_fl); a second one was strengthened with four layers of textile bonded with cement-based mortar (M4_fl); the third beam was identical to the second but with an epoxy resin-based matrix material for the textile reinforcement (R4_fl). The externally bonded reinforcement had a width and a length equal to 120 mm and 1.90 m, respectively, so that its distance from each support was equal to 50 mm. All beams were tested monotonically with the load applied using a vertically positioned actuator and a heavy spread beam; the displacements were measured at mid-span using two external linear variable differential transducers mounted on both sides of the beams. The load versus mid-span displacement curves for all beams are given in Fig. 13.8.

The control specimen (C_fl) displayed the standard nearly-bilinear response characteristics of under-reinforced beams. Strengthening with the epoxy-impregnated textile (beam R4_fl) resulted in increased strength (by approximately 50%) and increased stiffness, as expected; failure in this case was rather sudden, due to the tensile fracture of the externally bonded reinforcement at mid-span (at a load of 125 kN). The TRM-strengthened beam (M4-fl) displayed similar characteristics to its epoxy-bonded counterpart, with four distinct differences: its response was a little more ductile; yielding initiated at a lower load; the ultimate load was lower (111 kN); and the failure mechanism was governed by debonding at the end (anchorage) of the external reinforcement due to inter-laminar shearing. It is believed that the slightly lower stiffness and higher ductility characteristics of beam M4_fl compared to R4_fl are attributed to the lower stiffness of the bond between the external reinforcement and the

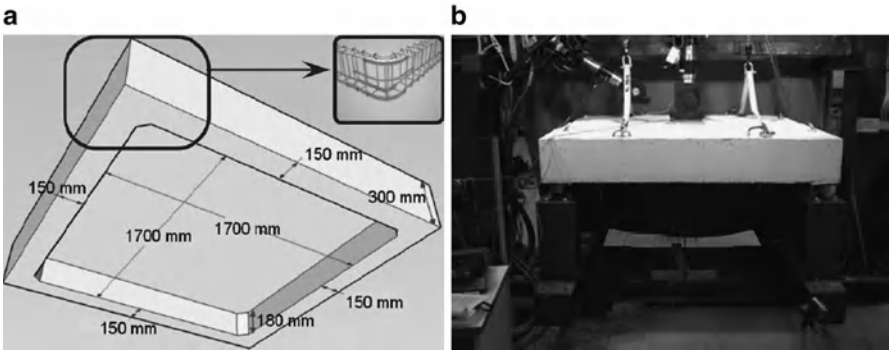

Fig. 13.9 (**a**) Geometry of two-way slabs tested; (**b**) test set-up

concrete, which may have resulted in reduced composite action. Overall, the TRM-based strengthening system used in this study was approximately 30% less effective in terms of strength but 30% more effective in terms of (displacement) ductility.

13.4.2 Two-Way Slabs

Here we aim to assess the effectiveness of TRM overlays as a measure of increasing the strength and deformation capacity of centrally loaded two-way RC slabs. To examine this, four specimens were tested under monotonic flexure. The specimens were square in plan with a side length of 2,000 mm and a slab thickness of 120 mm. The slabs were uniformly cast with perimeter beams measuring 300 mm in height and 150 mm in width; therefore, the slab section of each specimen measured 1,700 × 1,700 mm in plan. One specimen was used as a control specimen, and the others were strengthened. The specimen's geometry is shown in Fig. 13.9a.

All slabs were fabricated with identical structural steel reinforcement simulating lightly reinforced or, alternatively, moderately corroded slabs. Two welded wire fabrics (WWF) were used: the first comprised a T139 WWF [i.e. 100 × 100-W13.8 × W13.8 (mm × mm-mm² × mm²)] and was placed at the bottom (tension) surface of the slabs, whereas the second one was a T92 WWF [i.e. 150 × 150-W13.8 × W13.8 (mm × mm-mm² × mm²)] and was placed at their top (compression) surface. The tensile reinforcement ratio was equal to 0.14%. The WWF placed at the compression side of the specimens was regarded as non-structural and was used to avoid cracking during handling and transportation of the slabs to the testing rig. The slabs were cast using a ready-mix concrete of mean 28-day compressive strength equal to 25.6 MPa (31.2 MPa at the day of testing). The steel had a conventional yield stress of 645 MPa (at plastic strain 0.2%).

For the specimens receiving TRM overlays, commercial textiles with either high-strength carbon or E-glass fiber rovings arranged in two orthogonal directions were used. Both types of textiles shared the same geometry and comprised equal

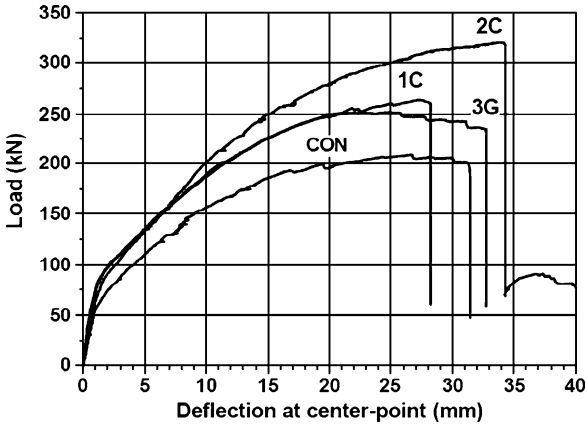

Fig. 13.10 Load – centre point deflection curves

(but different between textiles) quantities of fibers in each direction. Each fiber roving (1,650 Tex for carbon and 2,400 Tex for E-glass) was 3 mm wide and the clear spacing between rovings was 7 mm. The weight of fibers in the textiles was 350 g/m² and 500 g/m² for the carbon fiber and the E-glass fiber textile, respectively. The nominal thickness of each layer (based on the equivalent smeared distribution of fibers) was 0.18 mm, for both types of textile. The guaranteed tensile strength of the fibers (as well as of the textile, when the nominal thickness is used) in each direction was taken from data sheets of the producer equal to 3,500 and 1,750 MPa for carbon and E-glass fibers, respectively; the elastic modulus of the fibers was 220 GPa (carbon) and 72 GPa (E-glass). It becomes clear that in terms of axial rigidity one layer of carbon fiber textile is equivalent to three layers of E-glass fiber textile. The inorganic binder had a 28-day flexural and compressive strength equal to 6.5 and 24.6 MPa, respectively.

Three specimens were strengthened in total, whereas one served as the control specimen (designated as CON). One specimen received one layer of carbon fiber textile (specimen 1C), another one received two (specimen 2C), whereas the third specimen was strengthened with three layers of E-glass fiber textile (specimen 3G) having the same axial rigidity (i.e. equal product of fibers modulus of elasticity and textile thickness) with the single-layered carbon fiber textile (in both directions). These strengthening schemes were selected in this study so that they would provide useful insight into the effects of the fiber reinforcement ratio and the number of TRM layers (of equivalent axial rigidity).

All specimens were subjected to monotonic compressive loading at mid-span – in a displacement-control mode – using the stiff steel frame and support steelwork shown in Fig. 13.9b. The specimens were simply supported at their corners on ball-bearing hinges (thus, they were free to rotate at these points).

The load versus centre-point deflection for all specimens is shown in Fig. 13.10. All specimens responded in a similar manner in terms of crack development and failure mode. In the uncracked stage the initial stiffness of all strengthened specimens was higher than the one of the control specimen. For all slabs first cracking due to flexure occurred – as expected – directly below the load application area and

at approximately the same load value. With increasing imposed displacement, more flexural cracks formed in both directions along the bars of the tensile steel reinforcement grid (this being more visible in the control specimen) and diagonal cracks were generated propagating from the centre of the specimens to the corners. As recorded by strain gauges, yielding of tensile reinforcement in both directions was delayed in all strengthened specimens.

The failure mechanism involved sudden punching out of a pyramoid concrete plug at the centre of the slabs, accompanied by immediate and significant drop in load. The punched concrete plug was steeper (in the narrower direction) in the control specimen in comparison to the strengthened ones. Failure is characterised as "flexural punching" since punching occurred shortly after yielding of the flexural reinforcement (in both directions) near the load application point.

The increase in textile layers (1C–2C) did not lead to an undesirable failure mode (debonding of the TRM overlays from the soffit common for FRP strengthening). Furthermore, increasing the overlay thickness while keeping the same axial rigidity resulted in an almost identical response of specimens 1C and 3G; for the latter, premature failure in the form of inter-layer delamination was avoided (this was attributed to the high shear strength of the mortar and to the relatively short span of the slab). Stepwise load reduction following the achievement of maximum load-carrying capacity for specimen 3G denotes gradual fiber fracture, whereas the enhanced deformation capacity of this specimen (in relation to specimen 1C) is the result of inter-laminar slippage. It is notable that the deformation capacities of specimens 1C and 2C are practically identical. The load-carrying capacity of the strengthened slabs was increased by 26%, 53%, and 20% over that of the control specimen for slabs 1C, 2C and 3G, respectively, as the external TRM reinforcement delayed tensile steel yielding. Further details on test results as well as a comparison with analytical predictions are given in Papanicolaou et al. (2009).

It is concluded that TRM overlays are successful in increasing the load-carrying capacity of flexure-critical RC slabs acting as external reinforcement with improved bonding conditions to the substrate. Load-carrying capacity increases with increasing fiber reinforcement ratio, overlays of equal axial rigidity per direction result in comparable increase in the elements ultimate strength, and inter-layer relative slippage in multi-layered systems seems to enhance the deformation capacity of the slabs. Although all strengthened specimens in this study failed due to flexural punching, the failure mode is likely to change into a brittle shear punching one should TRM overlays of higher axial rigidity be used.

13.5 Conclusions

An innovative strengthening technique (TRM) is described in this study for strengthening and seismic retrofitting of reinforced concrete members through confinement; the technique is also used in shear and flexural strengthening. Key feature of this technique is the combination of textiles with inorganic binders, hence it may be

considered as an alternative to FRP strengthening. From the results presented in this study it was shown that TRM jacketing of RC is nearly as effective as FRP jacketing. The author strongly believes that TRM jacketing is an extremely promising solution for increasing the confinement as well as the shear and flexural capacity of reinforced concrete members, which are all of crucial importance in strengthening and seismic retrofitting.

References

Bournas D, Triantafillou TC (2011) Bond strength of lap spliced bars in concrete confined with composite jackets. ASCE J Comp Constr 15(2):156–167

Bournas DA, Lontou PV, Papanicolaou CG, Triantafillou TC (2007) Textile-reinforced mortar (TRM) versus FRP confinement in reinforced concrete columns. ACI Struct J 104(6):740–748

Papanicolaou C, Triantafillou TC, Papantoniou I, Balioukos C (2009) Strengthening of two-way slabs with textile-reinforced mortars (TRM). Proceedings 11th international fib symposium, London

Triantafillou TC, Papanicolaou CG, Zissimopoulos P, Laourdekis T (2006) Concrete confinement with textile-reinforced mortar jackets. ACI Struct J 103(1):28–37

Triantafillou TC, Papanicolaou C (2006) Shear strengthening of RC members with textile reinforced mortar (TRM) jackets. Mater Struct RILEM 39(1):85–93

Chapter 14
Strength and Deformability of Concrete Members Wrapped with Fibre-Reinforced Polymer Composites with a Large Rupture Strain

Jian-Guo Dai and Tamon Ueda

Abstract Recently, a new category of fibre-reinforced polymer (FRP) composites has emerged as a potential alternative to conventional FRPs, whose reinforcing fibres are usually made of carbon, glass or aramid. These new FRP composites are made of Polyacetal fibres (PAF), Polyethylene Naphthalate (PEN) fibres, or Polyethylene Terephthalate (PET) fibres, which are characterised by a large tensile rupture strain (LRS) (usually larger than 5%) and a relatively low elastic modulus. Compared to conventional FRPs, LRS FRPs are much cheaper and more environmentally friendly since they can be made of recycled plastics (e.g. PET bottles). This paper presents a summary of several completed/on-going research projects conducted in the authors' research groups on the structural performance of concrete members wrapped with LRS FRP composites, including the compressive behaviour of LRS FRP-confined concrete, the deformability of RC columns confined or internally shear-reinforced with LRS FRP composites under seismic loading, and the shear strengthening of RC members with LRS FRP composites. It is demonstrated that, despite their relatively low elastic modulus, LRS FRP composites can become a very attractive option particularly for the seismic retrofit of RC columns. Besides, LRS FRP composites also have a good potential to be used as the internal shear reinforcement in RC members since their use can lead to a ductile shear failure.

J.-G. Dai (✉)
Department of Civil and Structural Engineering, The Hong Kong Polytechnic University, Hung Hom, Hong Kong
e-mail: cejgdai@polyu.edu.hk

T. Ueda
Division of Engineering and Policy for Sustainable Environment, Faculty of Engineering, Hokkaido University, Sapporo 060-8628, Japan
e-mail: ueda@eng.hokudai.ac.jp

M.N. Fardis (ed.), *Innovative Materials and Techniques in Concrete Construction: ACES Workshop*, DOI 10.1007/978-94-007-1997-2_14,

14.1 Introduction

In spite of the many advantages of FRP composites over conventional steel reinforcement, a significant fact restraining a more widespread use of conventional FRPs in construction is their high material cost. Compared to steel reinforcement, the brittleness and small tensile rupture strain of conventional FRPs may also become a concern sometimes, since they may lead to a non-ductile failure manner. In recent years, a new category of FRP composites has emerged as an alternative to conventional FRP composites (Ueda and Sato 2002). These new FRP composites are made of Polyacetal fibres (PAF), Polyethylene Naphthalate (PEN) fibres, or Polyethylene Terephthalate (PET) fibres, which are characterised by a large tensile rupture strain (LRS) (usually larger than 5%), but a relatively low elastic modulus (see Fig. 14.1). Compared to conventional FRPs, LRS FRPs are much cheaper and more environmentally friendly since they can be made of recycled plastics (e.g. PET bottles). Table 14.1 summarizes the material properties of the above-mentioned LRS fibres in comparison with conventional carbon, glass and aramid fibres.

To facilitate the practical applications of LRS FRP composites in concrete structures, an in-depth understanding of the strength and ductility behavior of concrete members incorporating them is necessary. This paper aims to present a review of the authors' recent research work, which has been investigating the structural performance of concrete members wrapped with LRS FRP composites in terms of the compressive behaviour of LRS FRP-confined concrete columns, the deformability of RC columns confined or internally shear-reinforced with LRS FRP composites under seismic loading, and the shear strengthening of RC members using LRS FRP composites.

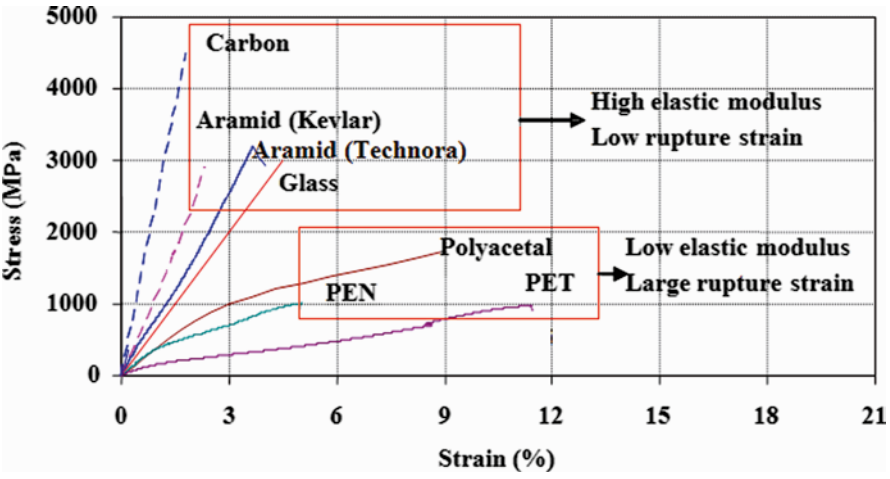

Fig. 14.1 Tensile stress-strain relationships of conventional and *LRS FRP* composites

Table 14.1 Properties of conventional and LRS fibers

Fiber		Tensile strength (MPa)	Young's modulus (GPa)	Fracturing strain (%)	Density (g/mm^3)
Carbon (PAN)	High strength type	2,600–4,500	200–240	1.3–1.8	1.7–1.9
	High elasticity type	2,000–2,800	350–450	0.4–0.8	1.8–1.9
Carbon (Pitch)	Ordinary type	780–1,000	38–40	2.1–2.5	1.6–1.7
	High strength and elasticity type	3,000–3,500	400–800	0.4–1.5	1.9–2.1
Aramid	High strength type	2,800	130	2.3	1.45
	High elasticity type	3,110	77	4.4	1.39
Glass	E-glass	3,500–3,600	74–75	4.8	2.6
	Alkali-resistance	1,800–3,500	70–76	2–3	2.27
Polyacetal		1,730	20*	6–9	1.45
Polyethylene Naphthalate		790	15 ± 2*	>5.0	1.41
Polyethylene Terephthalate		740	10 ± 1*	>7.0	1.44

* Polyacetal, PEN and PET fibers all exhibit some material nonlinearity
Their initial elastic modulus is usually higher than the values given in Table 14.1

14.2 Compressive Behaviour of LRS FRP-Confined Concrete

The most efficient and popular application of fiber-reinforced polymer (FRP) materials is to use them to confine reinforced concrete (RC) columns for strength and ductility enhancement. To achieve a reliable design for FRP strengthening of such columns under the action of axial loading or combined axial and lateral loading, an in-depth understanding of the compressive stress-strain behavior of FRP-confined concrete is very important. At present, a large number of experimental studies have been conducted particularly on FRP-confined circular concrete columns. Theoretical stress-strain models, either design-orientated ones (e.g. Lam and Teng 2003) or analysis-orientated ones (e.g. Jiang and Teng 2007), have been developed to predict the compressive strength, the ultimate compressive strain, as well as the full-range compressive stress-strain behavior of FRP-confined concrete. However, no experimental work has been conducted on the compressive stress-strain behavior of concrete confined with LRS FRPs. It remains unclear if the existing confinement models are applicable for LRS FRP-confined concrete.

Given the above context, compressive tests were conducted on a total of 42 cylindrical concrete specimens, comprising 36 FRP-wrapped specimens and 6 control specimens, which were prepared and tested under monotonic uni-axial compression (Dai et al. 2011). Each specimen was 152 mm in diameter and 305 mm in height. Among the 36 specimens, 9 specimens were wrapped with AFRP FRP jackets, other 9 specimens were wrapped with PET FRP jackets, and the rest were wrapped with PET FRP jackets. AFRP jackets were used in the test program because the existing compressive tests on AFRP-confined concrete are very limited and the rupture strain

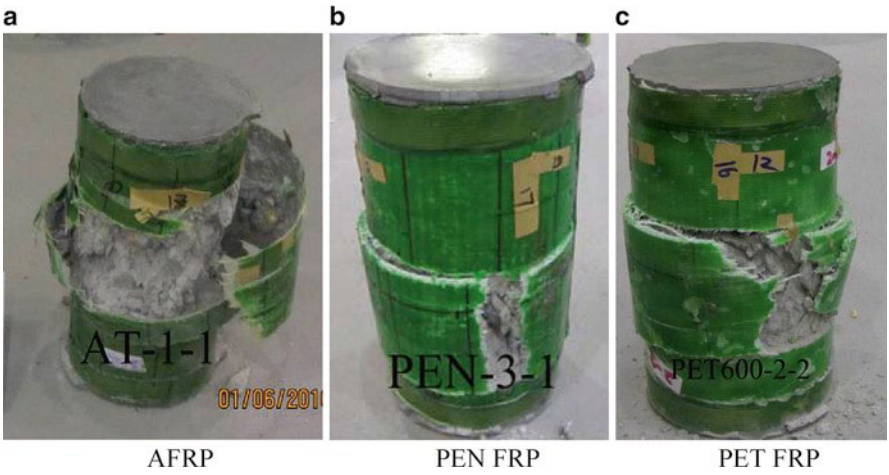

Fig. 14.2 Typical failure of FRP-confined concrete (**a**) AFRP (**b**) PEN FRP (**c**) PET FRP

of AFRP lies between those of CFRP and PEN FRP (see Fig. 14.1), representing a transition state of rupture strain from high modulus FRPs to low modulus FRPs.

It was found that the typical failure of LRS FRP-confined concrete was still due to the hoop tensile rupture of the FRP jacket outside the overlapping zone as observed in conventional FRP-confined concrete (see Fig. 14.2). But the failure at the ultimate state was smooth and quiet, unlike the explosive one observed in AFRP-confined concrete. The average hoop rupture strain of FRP jackets from these compression tests was found to be 3.0%, 4.5% and 7.5%, respectively, for AFRP, PEN FRP and PET FRP, while most existing tests on concrete confined by GFRP and CFRP exhibited hoop rupture strains of around 2% and 1%, respectively (Lam and Teng 2004). Similar to those of conventional FRP-confined concrete with a sufficient level of FRP confinement, the stress-strain curves of LRS FRP-confined concrete also exhibited a monotonically ascending bilinear shape with rapid softening in a transition zone around the stress level of unconfined concrete strength. Both the compressive strength and the ultimate axial strain were significantly enhanced (see Fig. 14.3).

To see if existing confinement models, which have been developed based on tests of conventional FRP-confined concrete, can describe appropriately the compressive behavior of LRS FRP-confined concrete, an analysis-orientated model, which was proposed by Jiang and Teng (2007) and was reported to be the most accurate among similar models, was used to predict the experimental compressive stress-strain curves of LRS FRP-confined concrete following an incremental iteration calculation process (Dai et al. 2011). This analysis-oriented model is, in principle, applicable to concrete confined by all sorts of materials as long as the relationship between the hoop strain (or lateral strain) and the confining pressure of the confining jacket is established. The predictions from Jiang and Teng's model are in close agreement with the test results in terms of the compressive strength, but overestimate the ultimate axial strain of LRS FRP-confined concrete as shown in

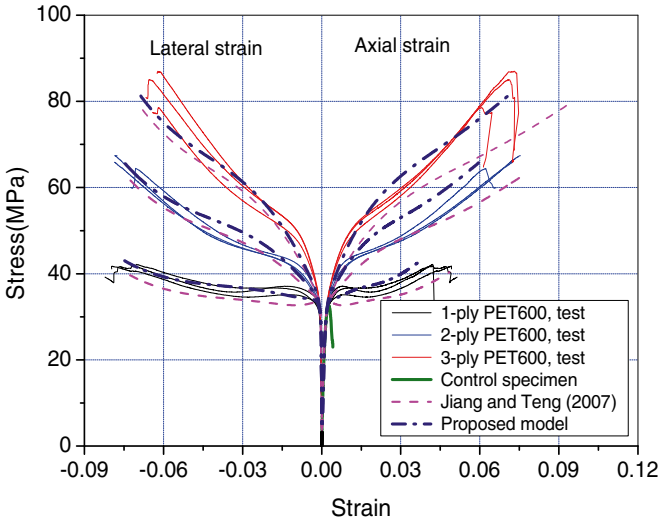

Fig. 14.3 Compressive stress-strain relationships of LRS FRP-confined concrete

Fig. 14.3, in which PET FRP-confined concrete has been taken as an example. This discrepancy indicates that the lateral strain-axial relationship in Jiang and Teng's model is inaccurate for strains larger than that normally experienced by conventional FRP jackets. Based on regression of the test results, a new lateral strain-axial strain equation was proposed for LRS FRP-confined concrete as follows (Dai et al. 2011):

$$\frac{\varepsilon_c}{\varepsilon_{co}} = \left(1+8\frac{\sigma_l}{f_{co}}\right)\cdot\left[1.024\left(\frac{\varepsilon_l}{\varepsilon_{co}}\right)^{0.350} + 0.089\left(\frac{\varepsilon_l}{\varepsilon_{co}}\right)\right] \tag{14.1}$$

where ε_c is the axial strain of concrete; ε_l is the lateral strain of concrete; ε_{co} is the axial strain at the peak axial stress of unconfined concrete; σ_l is the lateral confining pressure; and f_{co}' is the compressive strength of unconfined concrete.

Based upon the proposed model, a simple comparison among concrete confined with FRP jackets made of five different fiber sheets (CFRP, GFRP, AFRP, PEN and PET) was also made as shown in Fig. 14.4 (Dai et al. 2011). A concrete cylinder with an unconfined concrete strength of 38 MPa was assumed for such a comparison and the rupture strain of fibers used in the analysis were assumed to be 0.095%, 1.7%, 3.0%, 4.5%, and 7.5%, which are typical values for CFRP, GFRP, AFRP, PEN FRP, and PET FRP, respectively. Provided that all FRP-confined concrete achieves the same energy absorption, which is evaluated using the area underneath the compressive stress-strain curve, at the rupture of the fiber sheet, the needed tension stiffness of PEN FRP and PET FRP jackets are found to be 19.0% and 13.3%, respectively, of that of CFRP jackets. Apparently, LRS FRP jackets lead to a more economic and attractive confinement solution in terms of the energy absorption capacity.

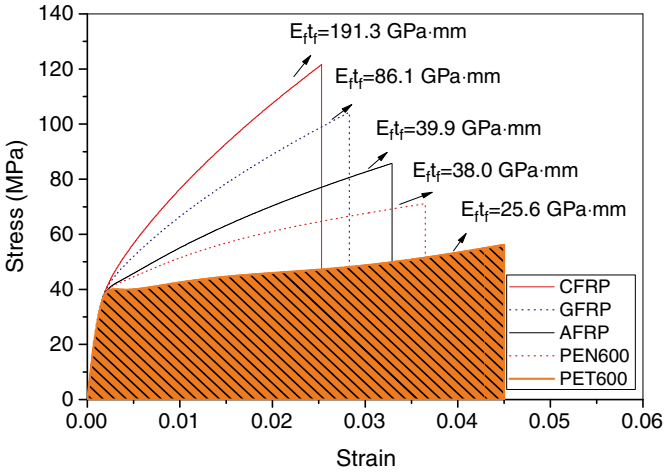

Fig. 14.4 Energy absorption comparison of conventional and LRS FRP-confined concrete

14.3 Deformability of RC Columns Confined or Internally Shear-Reinforced with LRS FRP Composites Subjected to Seismic Loading

Retrofit of RC columns by the provision of FRP jackets with the main fibres in the hoop direction is an effective means for improving their seismic performance. This is not only because of the additional shear capacity contributed by the FRP which reduces the risk of brittle shear failure, but also because of the increasing strain capacity of concrete in compression as a result of the FRP confinement, leading to a significant enhancement in the member ductility. To observe the deformability of RC columns confined with LRS FRP-jacketed RC columns under seismic loading, a program including tests of 15 RC specimens was conducted (Anggawidjaja et al. 2006). Each specimen consisted of a square column and a column base to represent a bridge pier with footing (see Fig. 14.5). The cross sectional dimensions of the columns were 400×400 mm for 10 of the specimens and 600×600 mm for the rest. Information in details about the 15 specimens can be found in Anggawidjaja et al. (2006).

The test program involved a new jacketing method, called the A-P Jacketing (duplex jacketing) method, in which two kinds of FRPs were used: one with a high stiffness AFRP outside the plastic hinge zone and another with a high rupture strain PEN FRP or PET FRP within the plastic hinge zone (see Fig. 14.5). In one specimen, high strength AFRP jackets were also used in the plastic hinge zone for comparison purposes. The plastic hinge zone was assumed to have a length of 1*D* above the pier base, in which *D* is the dimension of the square pier section.

It was found that a significant characteristic of RC columns jacketed with PET FRP composites is that the fibres hardly rupture at the ultimate state (see Fig. 14.6).

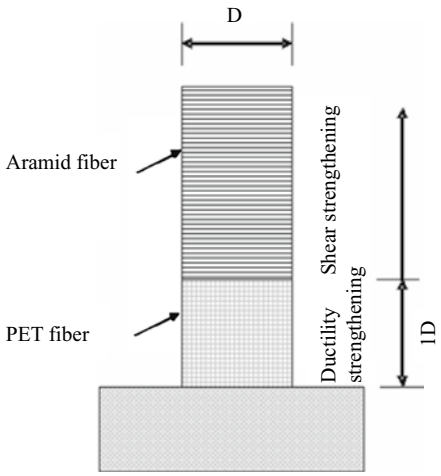

Fig. 14.5 Duplex jacketing for seismic retrofit of RC columns

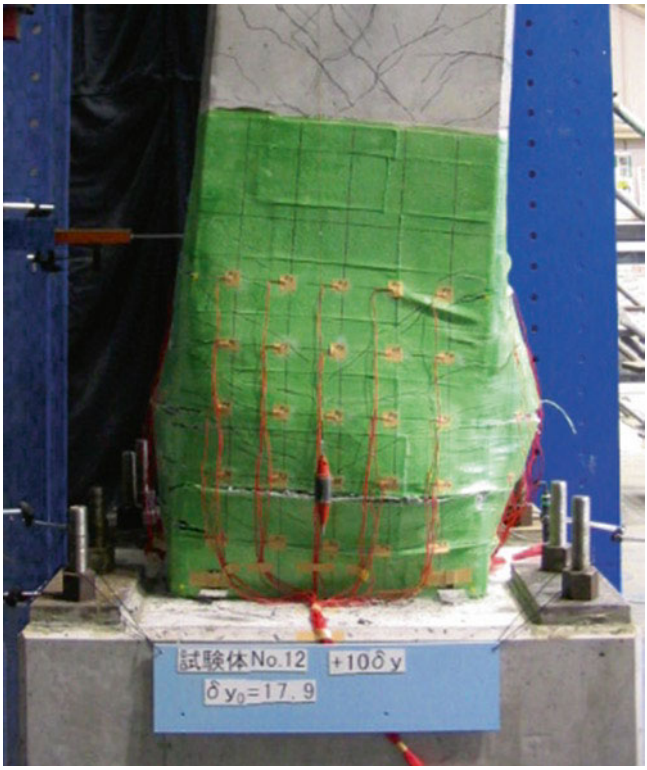

Fig. 14.6 Typical failure of RC columns jacketed with PET composites within the hinge zone at the ultimate state

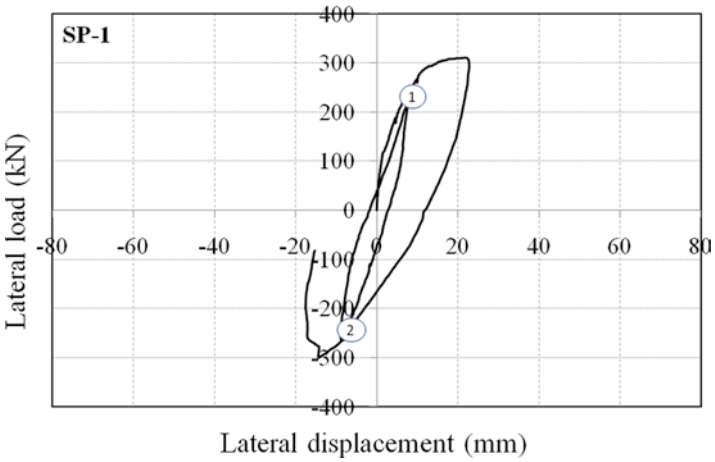

Fig. 14.7 Load-lateral displacement responses of the reference RC pier under reversed cyclic lateral loading

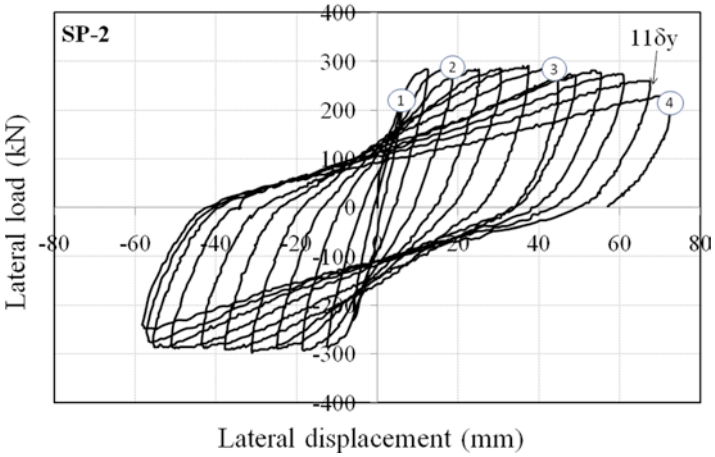

Fig. 14.8 Load-lateral displacement responses of the RC pier jacketed with high-strength AFRP composites within the hinge zone under reversed cyclic lateral loading

By contrast, the ultimate state of conventional FRP (particularly CFRP) jacketed RC columns is usually caused by the sudden rupture of fibres (i.e. at the corner of the column) followed by the complete loss of concrete cover in an explosive manner, which is certainly not desirable for structures in earthquakes. Compared to the reference RC pier (see Fig. 14.7), the ductility of RC columns jacketed with AFRP and PET FRP composites within the plastic hinge zones all led to a significant increase in the member ductility under the reversed cyclic loading (see Figs. 14.8 and 14.9).

The numbers marked on Figs. 14.7–14.9 represent the responses at: (1) initial yielding of longitudinal reinforcement, (2) initial yielding of transverse reinforcement,

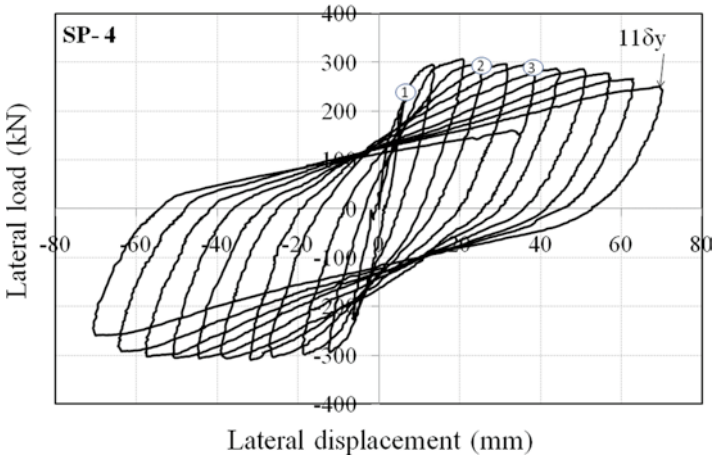

Fig. 14.9 Load-lateral displacement responses of the RC pier jacketed with PET FRP composites within the hinge zone under reversed cyclic lateral loading

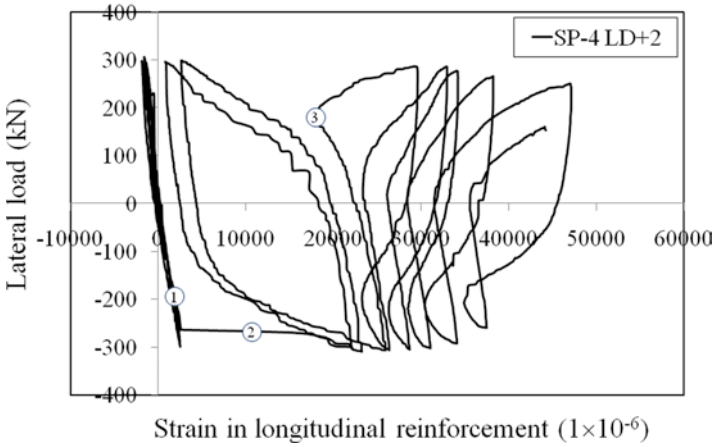

Fig. 14.10 Progressive buckling of longitudinal steel reinforcement in an RC column jacketed with PET FRP composites within the hinge zone

(3) buckling of longitudinal reinforcement, and (4) fracture of fibers. In order to achieve similar ductility (see 11 δ_y, where δ_y is the lateral displacement at the initial yielding of longitudinal tensile reinforcement, in Figs. 14.8 and 14.9), the tension stiffness of PET FRP composites used in the plastic hinge zone was only one quarter of that used for high strength AFRP.

Further investigations on the structural behaviour of the plastic hinge zones of PET FRP jacketed RC columns revealed that the LRS property of FRP jackets allows progressive bulking of longitudinal steel reinforcement as shown in Fig. 14.10. In conventional FRP-jacketed RC columns, the bulking of longitudinal steel

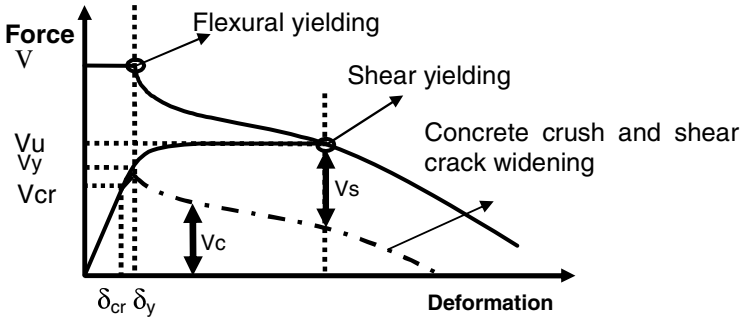

Fig. 14.11 Flexure/shear interactions in RC columns

reinforcement is usually associated with the rupture of conventional FRP composites (Ogata and Osada 2000), leading to the arrival of the ultimate state of the whole member. However, the use of LRS FRP jackets allows a further development of the lateral displacement without a significant loss of the load-carrying capacity even after the initial bulking of longitudinal steel reinforcement. It is usually recommended to use a high stiffness FRP jacket to suppress the bulking of longitudinal steel reinforcement within the hinge zone (i.e. Seible et al. 1997). But this may not necessarily be a very efficient solution particularly in RC columns with a square/rectangular section because the out-plane bending stiffness of FRP jackets is quite small. Without a certain level of expansion of the concrete cover, the FRP jackets are not able to provide substantial confining force. In other words, it may not be very efficient to increase the tension stiffness of FRP jackets (i.e. the amount of fibre sheets) in order to restrain the out-plane bulking. Instead, the use of LRS FRP jackets may become a more cost-effective and optimal solution.

The study of Anggawidjaja et al. (2006) also aimed to develop design equations for predicting the ductility of LRS FRP jacketed RC columns. In the 15 specimens tested, the ratio between the shear strength and the flexural strength of the RC columns (referred to as "shear strength ratio" for brevity) was treated as the key experimental parameter. The reason is that the seismic performance of an RC bridge pier, regardless of its failure mode, can be related to the shear strength ratio at a given displacement level (see Fig. 14.11). This concept is adopted in the current "JSCE Recommendation for Upgrading Concrete Structures with Use of Continuous Fiber Sheets" (2001). Following such a concept and through analysis of the test data, semi-empirical equations were proposed to predict the ductility of RC columns jacketed with LRS FRP composites as follows:

$$\theta_u = \theta_m + \eta\left(1 - \frac{M_y}{M_{\max}}\right) \tag{14.2}$$

$$\theta_m = \theta_{me} + \theta_{pull-out} + \theta_{shear} + \theta_{mp} \tag{14.3}$$

$$\theta_{mp} = \frac{0.021 k_s K_o \rho_w + 0.013}{0.79\rho_t + 0.153} \tag{14.4}$$

$$\eta = 1.22 K_u + 0.04 \tag{14.5}$$

$$K_o = 0.0019 E_{frp} . \rho_{frp} + 3.65 \tag{14.6}$$

$$K_u = \frac{V_w + V_c}{V_{mu}} \cdot \frac{E_{frp} \cdot \rho_{frp}}{E_w . \rho_w} \tag{14.7}$$

where θ_u = the drift ratio of the member at the ultimate state; θ_m = the drift ratio of the member at the maximum load; θ_{mp} = the drift ratio of the member due to the plastic member rotation at the maximum load; θ_{me} = the drift ratio of the member due to elastic flexural member rotation at the maximum load; $\theta_{pull\text{-}out}$ = the drift ratio of the member due to the rotation caused by the pull-out slips of longitudinal reinforcement at the footing-to-pier interface; θ_{shear} = the drift ratio of the member due to the shear deformation in the plastic hinge zone; M_y = the moment at the yielding load; M_{max} = the moment at the peak load; ρ_w = the ratio of lateral reinforcement (%); ρ_t = the ratio of tensile reinforcement (%); η = a factor to take into account the slope of the linear descending branch of the load-displacement responses; K_o = a factor representing the confinement effects of FRP jackets; k_s = a factor to take into account the strength of transverse reinforcement; and K_u = a factor to represent the FRP strengthening ratio.

In Eq. 14.2, the drift ratio, θ_{me}, due to elastic flexural member rotation at the maximum load is calculated using Euler's beam theory and Branson's equation to account for the effective moment of inertia of cracked RC columns (Anggawidjaja et al. 2006). The drift ratio, $\theta_{pull\text{-}out}$, is calculated using Ishibashi et al.'s (2002) approach, which is also adopted in JSCE Standard Specifications for Seismic Performance Verification of Concrete Structures (2005). In Anggawidjaja et al. (2006), the drift ratio, θ_{shear}, is estimated to be 5 ~ 12% of the total drift ratio at the ultimate state. In a more recent work, Ueda and Anggawidjaja (2007) developed a universal model to predict the shear deformation of RC columns jacketed with FRP composites as well as the shear strength degradation of concrete taking into account the complex flexural/shear interactions as indicated in Fig. 14.11, so that the descending branches of the load-lateral displacement responses of RC columns jacketed with LRS FRP composites can be predicted in a more generic way.

LRS FRP composites can also been used as the internal tie reinforcement to partially replace conventional steel stirrups. A series of tests including six reinforced concrete columns with the use of steel stirrups alone and a mixed use of steel and PAF tie reinforcement were conducted under reversed cyclic loading (Ueda and

Fig. 14.12 PAF sheets as the internal tie reinforcement of an RC column

Sato 2002; Tuladhar et al. 2003). The PAF sheets could be easily winded around the longitudinal reinforcement in RC columns due to their flexibility as shown in Fig. 14.12. Results from such tests indicated that PAF sheets as the internal reinforcement of RC columns increase the ultimate flexural deformation. Comparison of the load-deformation curves between the specimen including both PAF (volumetric reinforcing ratio of 0.58%) and steel tie reinforcement (volumetric reinforcing ratio of 0.17%) and the specimen with steel tie reinforcement only (volumetric reinforcing ratio 0.68%) is shown in Fig. 14.13. Although the total tie reinforcement ratios of the two specimens are similar, it is clearly shown that the ultimate deformation of the specimen with the PAF tie reinforcement is significantly greater than that of the specimen with the steel tie reinforcement only. The reason is that the PAF reinforcement provided a good confinement effect to the core concrete. In the latter case, the yielding of transverse steel reinforcement caused a decrease of the member shear stiffness, and consequently the degradation of the shear contribution of concrete jeopardized the member ductility. In the former case, however, the existence of LRS PAF sheets prevented loss of member shear stiffness due to the yielding of conventional steel stirrups, and in the meantime, the shear degradation of concrete was compensated by a consistently increased shear resistance contributed by the linear PAF sheets, which did not encounter any fracture that conventional FRP composites might have experienced at that moment.

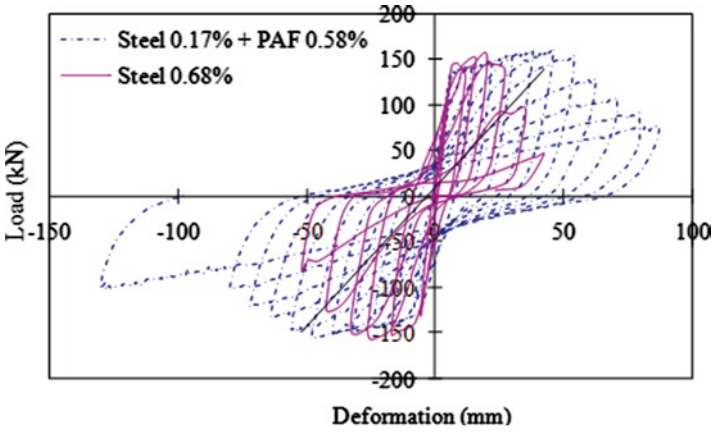

Fig. 14.13 Load-displacement response of RC columns including PAF sheets as the internal tie reinforcement under reversed cyclic lateral loading

14.4 Shear Strengthening of RC Members with LRS FRP Composites

LRS FRP composites can be used to strengthen RC members in shear as conventional FRPs do. In fact, the low elastic modulus of LRS FRP composites is not a critical concern because this can be compensated by providing more FRP materials, while the low tensile rupture strain of conventional FRPs cannot. To see how RC members strengthened with LRS FRP composites in shear behave, two series of tests were conducted (Ueda and Sato 2002; Senda and Ueda 2009).

The first test series involved five RC columns (Ueda and Sato 2002). Among them one was the reference specimen with a volumetric ratio of steel tie reinforcement of 0.151%, another was shear-strengthened with high strength carbon fiber sheets (E_f=230 GPa) with a volumetric ratio of 0.017%, and the remaining three specimens were shear-strengthened with PAF sheets at volumetric ratios of 0.077%, 0.153% and 0.291%, respectively. It was found that use of PAF sheets could increase significantly the shear strength of the columns and, particularly, that the latter could maintain this strength (see Fig. 14.14a) until a large shear deformation had occurred (see Fig. 14.15a). Although these PAF-strengthened RC columns failed in shear (without yielding of longitudinal reinforcement), a ductile shear failure manner was observed, which is significantly different from those brittle ones often observed in the reference and CFRP sheet shear-strengthened RC columns (see Fig. 14.14a). The main reason is that the PAF sheets were far from their rupture strain when the shear capacity was experienced.

The second test series (Senda and Ueda 2009) involved ten RC beams, one of which was the reference specimen and the remaining nine were strengthened with

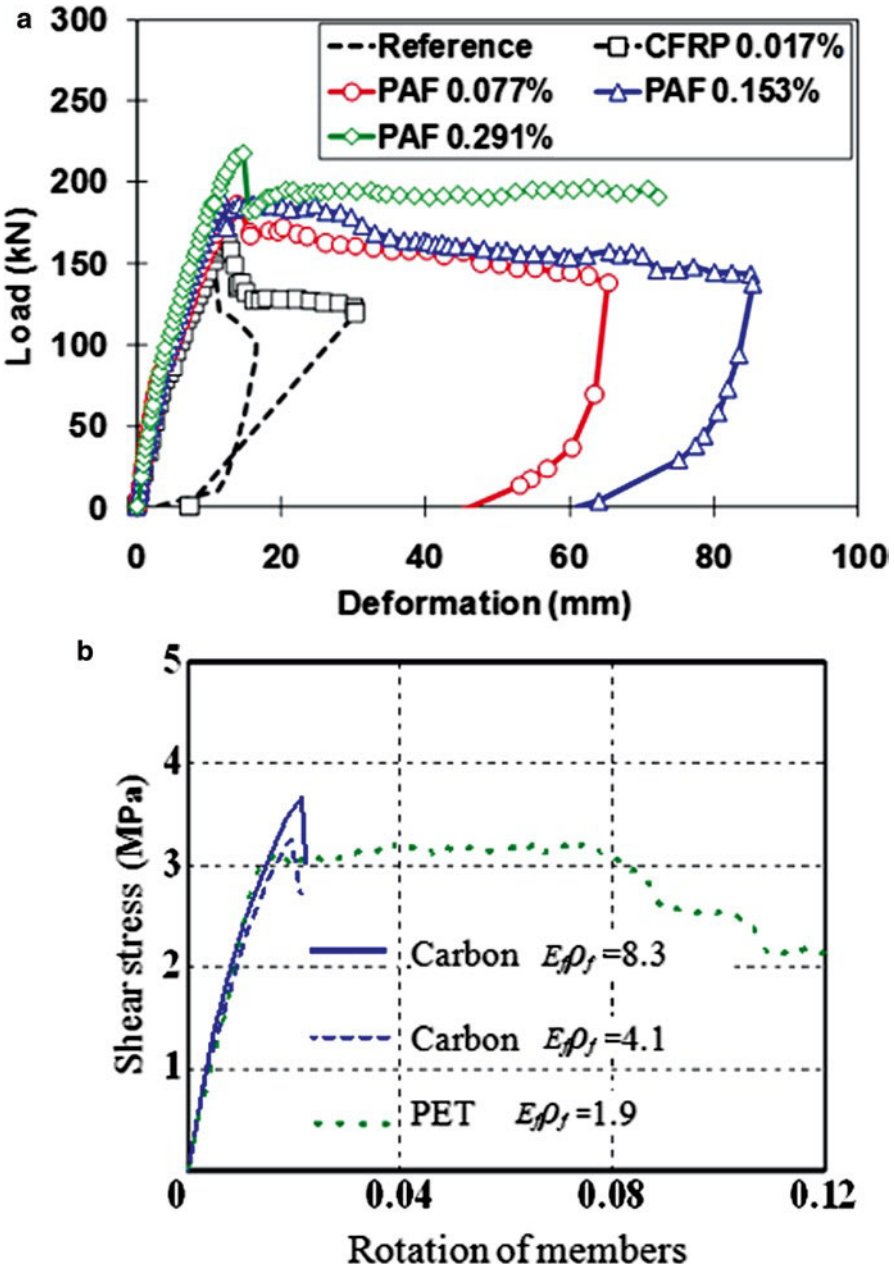

Fig. 14.14 Load–displacement responses of RC members shear-strengthened with LRS FRP composites (**a**) PAF shear strengthened RC columns (**b**) PET FRP shear-strengthened RC beams

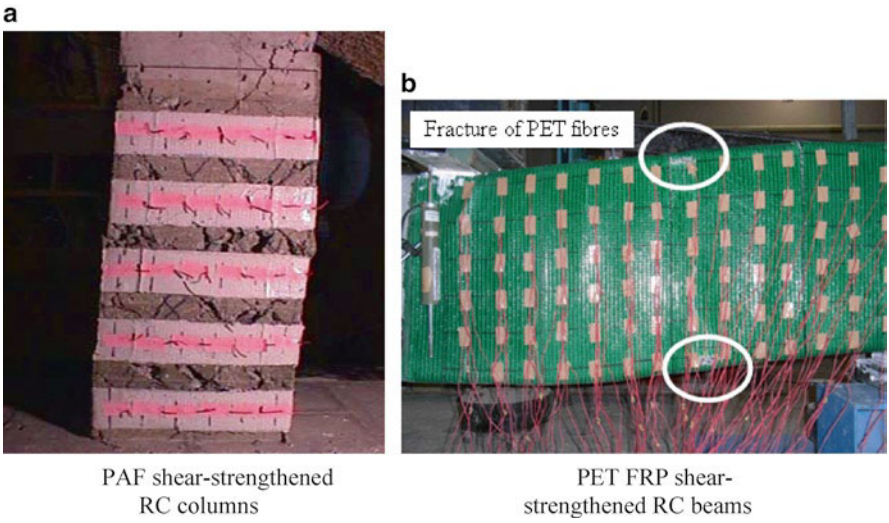

Fig. 14.15 Shear failure of RC members wrapped with LRS FRP composites (**a**) PAF shear-strengthened RC columns (**b**) PET FRP shear- strengthened RC beams

PET FRP composites at different volumetric ratios. Similarly, a ductile shear failure manner of PET FRP-strengthened RC beams was observed (see Fig. 14.14b) in association with a large shear deformation at the ultimate state (see Fig. 14.15b). The load-carrying capacity was well-maintained even after the rupture of PET FRP composites had initiated at the corner of the RC beam (see Fig. 14.15b). However, the shear failure of conventional FRP- (i.e. CFRP-) strengthened RC beams is brittle and a sudden drop of load-carrying capacity is often seen after the shear strength is reached (see Fig. 14.14b), as reported by many previous researchers (i.e. Sirbu 1998).

14.5 Conclusions

This paper presents a review on the structural behaviors of concrete members wrapped with fiber-reinforced polymer composites with relatively low elastic modulus, but a much larger rupture strain than conventional FRP composites. The LRS FRP composites had been used as the confining jackets to enhance the strength and deformability of concrete and the rotation capacity of the plastic hinge zone of RC columns, as well as the tie reinforcement to strengthen the shear capacity of RC

columns/beams. Through observations, the following conclusions have been made for this new category of fiber-reinforced polymer materials:

1. LRS FRP composites are superior to normal rupture strain FRP composites, particularly for seismic retrofit purposes, since the material stiffness required for the latter is much less, provided that the same displacement ductility and energy absorption are desired.
2. Existing confinement models for conventional FRP-wrapped concrete are not suitable for describing the compressive stress-strain behavior of LRS FRP-confined concrete, mainly because the existing dilation models of concrete under axial loading were calibrated from tests on normal rupture strain FRP-confined concrete.
3. LRS FRP composites are well-suited for confining the plastic hinge zones of RC columns to increase their rotation capacity. But in LRS FRP-jacketed RC columns subjected to seismic loading, the initiation of the buckling of longitudinal steel reinforcement usually precedes the ultimate state of the column, at which rupture of LRS FRP composites hardly occurs either. In conventional FRP-jacketed columns, however, the ultimate state of the column is often associated with the bulking of the longitudinal steel reinforcement and/or the rupture of FRP jackets.
4. LRS FRP composites have a good potential for use as the internal tie reinforcement to partially replace the steel stirrups in RC members; their use can lead to a ductile member shear failure and they hardly reach their rupture strain when the shear strength is reached.

Acknowledgements The authors are grateful for the financial support received from Grants-in-Aid for Scientific Research of Japan Society of the Promotion of Science (JSPS) (Project Code: 12555123), Hokkaido University and The Hong Kong Polytechnic University (Project Code: A-PC1L). The authors are also thankful to Mr. H. Nakai, Maeda Kosen Co. Japan for his help in organizing the experimental tests and providing experimental materials, and to Mr. D. Anggawidjaja, Mr. H. Jaqin, Mr. M. Senda and Mr. Y. L Bai for their contributions to the listed projects in various aspects.

References

Anggawidjaja D, Ueda T, Dai JG, Nakai H (2006) Deformation capacity of RC columns wrapped by new fiber-reinforced polymer with large fracture strain. Cem Concr Compos 28:914–927

Dai JG, Bai YL, Teng JG (2011) Behavior and Modeling of Concrete Confined with FRP Composites of Large Deformability, Journal of Composites for Construction, ASCE, http://dx.doi.org/10.1061/(ASCE)CC.1943–5614.0000230

Ishibashi T, Tsuyoshi T, Kobayashi K, Yoshida T, Umihara T (2002) Study on ductility evaluations on reinforced concrete columns subjected to reversed cyclic loading with large deformations. Proc JSCE 56(711):79–96

JSCE Research Committee on Upgrading of Concrete Structures with FRP Reinforcement (2001) "Recommendation..... sheets", Concrete Engineering Series, No. 41, Japanese Society of Civil Engineers, Tokyo

Jiang T, Teng JG (2007) Analysis-oriented stress-strain models for FRP-confined concrete. Eng Struct 29:2968–2986

JSCE Subcommittee on English Translation of the Standard Specifications (2005) Standard specifications for concrete structures – 2002 'Seismic Performance Verification', JSCE Guidelines for Concrete, No. 5, Japan Society of Civil Engineers, Tokyo

Lam L, Teng JG (2003) Design-oriented stress-strain model for FRP-confined concrete. Constr Build Mater 17(6–7):471–489

Lam L, Teng JG (2004) Ultimate condition of fiber reinforced polymer-confined concrete. J Compos Constr ASCE 8(6):539–548

Ogata T, Osada K (2000) Seismic retrofitting of expressed bridges in Japan. Cem Concr Compos 22:17–27

Seible F, Priestley MJ, Hegemier GA, Innamorato D (1997) Seismic retrofit of RC columns with continuous carbon fiber jackets. J Compos Constr 1(2):52–62

Senda M, Ueda T (2009) Experimental study on shear strengthening by continuous fiber with high fracturing strain. Proc Concr Struct Scenar JSMS 8:249–256, in Japanese

Sirbu G (1998) Resisting shear capacity of a reinforced concrete pier retrofitted with carbon fiber sheet. Master thesis, Hokkaido University, Sapporo

Tuladhar R, Utsunomiya Y, Ueda T (2003) New flexible system of transverse reinforcement for RC piers. Adv in Struct Eng 6(3):215–230

Ueda T, Anggawidjaja D (2007) Universal model for predicting ultimate deformation of concrete columns retrofitted by FRP jacketing. In: Proceedings of 8th international symposium on fiber reinforced polymer reinforcement for concrete structures (FRPRCS-8), (CD-ROM, Paper number: 10–11), Patras, pp 10

Ueda T, Sato Y (2002) New approach for usage of continuous fiber as non-metallic reinforcement of concrete. Struct Eng Int 12(2):111–116

Chapter 15
Innovative Techniques for Seismic Retrofitting of RC Joints

Idris Bedirhanoglu, Alper Ilki, and Nahit Kumbasar

Abstract The main target of this study is to develop simple, realistic and applicable retrofitting techniques by using innovative materials in existing deficient beam-column joints. Retrofitting is targeted at overcoming deficiencies such as usage of low-strength concrete, absence of stirrups in the joint and poor anchorage of beam longitudinal bars at the joint.

15.1 Introduction

The use of low-strength concrete, smooth (plain) reinforcing bars and insufficient transverse reinforcement in beam-column joints may cause severe damage to buildings during earthquakes. While structures with these deficiencies are common in developing countries, research on these types of joints is limited.

Early attempts to retrofit joints were made by using different types of steel and reinforced concrete jackets. More recently researches have concentrated on innovative techniques such as FRP (fibre reinforced polymers) retrofitting. On the other hand, the use of cementitious composites for joint retrofitting is very rare. The main purpose of this study is to investigate the behaviour of reference and retrofitted exterior beam-column joints constructed with low-strength concrete and smooth

I. Bedirhanoglu (✉)
Department of Civil Engineering, Structural Engineering Laboratory, Engineering Faculty, Dicle University, 21280 Diyarbakir, Turkey
e-mail: ibedirhanoglu@dicle.edu.tr

A. Ilki • N. Kumbasar
Faculty of Civil Engineering, Istanbul Technical University, Ayazaga Campus, 34469 Maslak, Istanbul, Turkey
e-mail: ailki@itu.edu.tr; kumbasarn@itu.edu.tr

M.N. Fardis (ed.), *Innovative Materials and Techniques in Concrete Construction: ACES Workshop*, DOI 10.1007/978-94-007-1997-2_15,

(plain) round bars. For the retrofitting of joints, innovative materials such as FRP sheets and precast HPFRCC (high performance fibre reinforced cementitious composite) panels are used. Beam-column joint specimens tested in most of the available studies are T-type joints without transverse beam and slab. In this study, joint specimens with transverse beam and slab are tested with the aim to represent the actual geometry more realistically.

15.2 Experimental Details

15.2.1 Specimens

Three large-scale specimens were tested to investigate the behaviour of reference and retrofitted beam-column joints against simulated earthquake excitations. Details of the reference and retrofitted specimens are given in Table 15.1. The specimens were designed to represent the exterior joint of a column and two beams at a corner of an intermediate floor in a reinforced concrete building. As can be seen in Fig. 15.1a, half of the column represented the lower half of the upper-story column and the other half of the column represented the upper half of the lower-story column. In laboratory conditions, the specimens were tested with the columns in horizontal position. Lateral displacement reversals were applied to the tip of the beam. The intersection between the column and the beam will be referred to as the beam-column joint. While there was no transverse reinforcement in the joint core, columns and beams were designed following recommendations given in the Turkish Seismic Design Code (DBYBHY-07 2007) and Reinforced Concrete Design Code TS 500 (TS 500 2000) to avoid their failure under shear forces, and enforce damage to occur in the joint core (Fig. 15.1b).

Specimens were constructed with low-strength concrete (the mean measured cylinder strength was $f_c = 8.3$ MPa for the testing days), and smooth (plain) round reinforcing bars. Sixteen mm and 8-mm smooth round bars were used as longitudinal and transverse reinforcement, respectively. The yield stresses of longitudinal

Table 15.1 Specimen details

Specimen	Explanation	Welding of hooks of beam longitudinal bars	Retrofitting		
			Amount of FRP		Plies and designation
			Total (m^2)	ρ_{FRP}[a]	
JO	Reference	No	–	–	–
JWC-D-5	Weld, repair mortar and FRP	Yes	5.4	0.0010	5 plies CFRP-200 mm diagonal strips
JWH	Weld, repair mortar and HPFRCC	Yes	40 mm thick precast HPFRCC panel		

[a]Ratio of cross-sectional area of FRP in the joint to the area of the joint in the diagonal direction

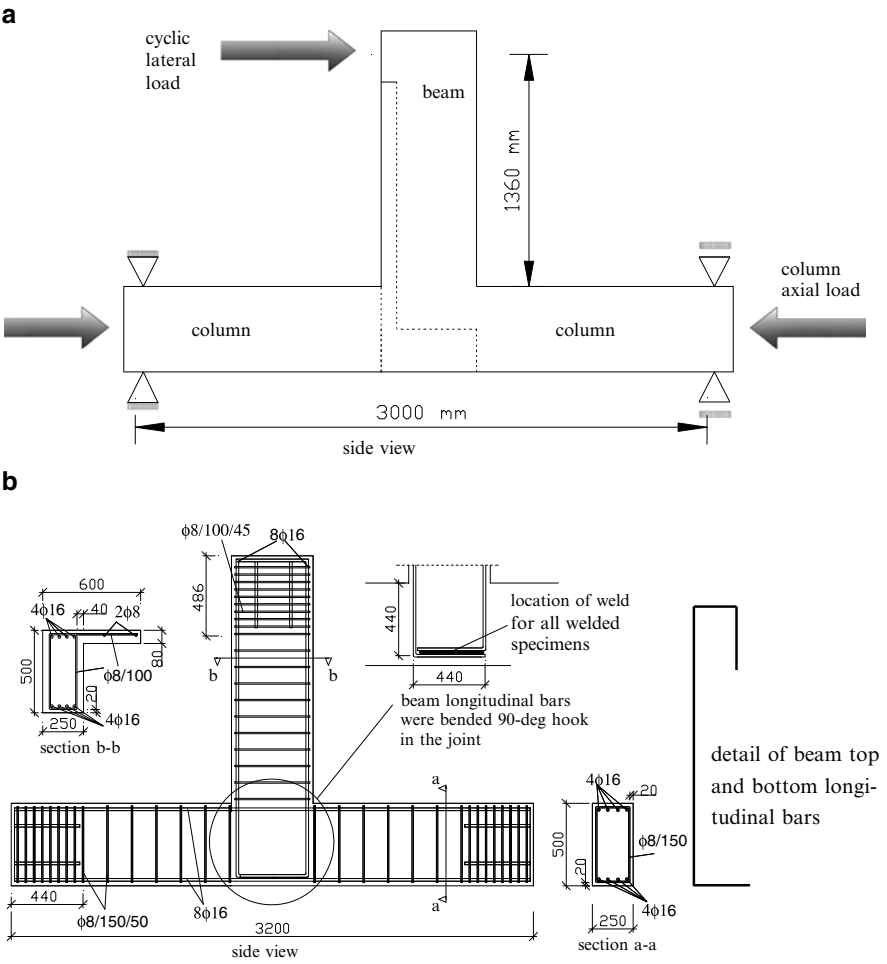

Fig. 15.1 Geometry, test setup and reinforcement details (**a**) Specimen at the test setup (**b**) Reinforcement details (dimensions are in mm and clear cover is 20 mm for all members)

and transverse bars were 333 and 315 MPa, respectively. Maximum stresses were measured to be 470 and 430 MPa and the rupture strains were 0.34 and 0.33 for longitudinal and transverse bars, respectively. These values are the average of five coupon tests for each series. It should be noted that the columns were stronger than the beam.

In all specimens, the longitudinal reinforcement of the column was continuous and the longitudinal reinforcement of the beam was anchored in the joint using 90° hooks (Fig. 15.1b). The anchorage length (including the length of the hook) was 880 mm, which corresponds to 55 bar diameters. According to TS 500 (TS 500 2000), the

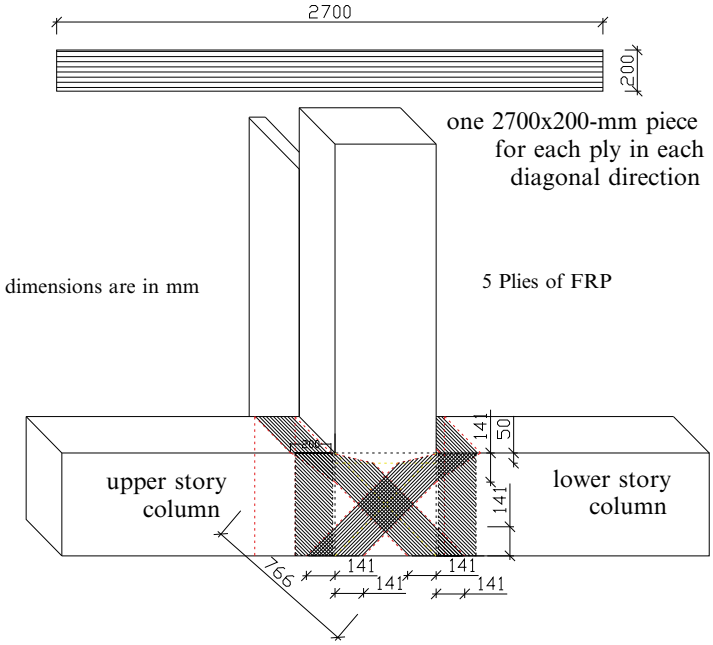

Fig. 15.2 FRP application details of specimen JWC-D-5

development length (l_{dh}) for smooth (plain) round bars with 90° hooks is 0.18 times the ratio of design yield strength of the bar to the design tensile strength of the concrete, where this length should not be smaller than $40d_b$ (d_b is the bar diameter). This definition yields a required anchorage length of 633 mm which corresponds to $40d_b$ for the tested specimens considering the design practice of the 1970s–1980s (i.e. considering a design yield strength of the bar of 220 MPa and a design compression strength of the concrete of 14 MPa).

15.2.2 Retrofitting

After testing the reference specimen, other undamaged joints were retrofitted by welding hooks of beam longitudinal bars and by shear strengthening the joint core, either with FRP sheets or with precast HPFRCC panels (Figs. 15.2 and 15.3). The design philosophy of retrofitting is to achieve a ductile failure through flexural failure of the beam. Slip of beam longitudinal bars and potential shear failure of the joint if the slip of beam longitudinal bars is to be avoided were observed to be the probable premature failure modes through the testing of a reference specimen and analytical predictions.

To prevent the slip of beam longitudinal bars in the joints, the hooks of top longitudinal bars were welded to the hooks of bottom bars in the joint. To place these

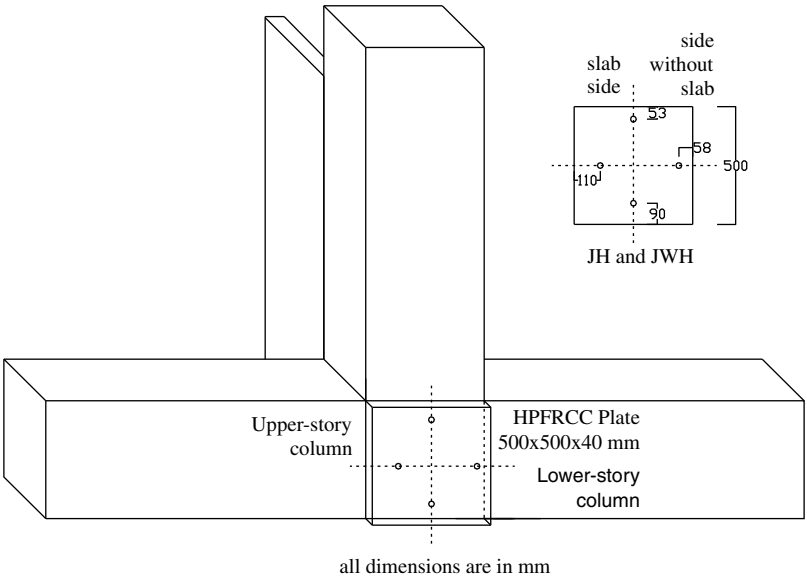

Fig. 15.3 Details of HPFRCC retrofitting (specimen JWH)

welds, a 130-mm thick layer of concrete was removed after constructing these specimens. After welding, the removed concrete was replaced with Emaco S88 high-strength repair mortar produced by BASF.

To prevent brittle shear failure of the joints, either FRP sheets or HPFRCC panels were bonded over the external surface of the joint. One of the specimens (JWC-D-5) was retrofitted with 200-mm wide FRP sheets in two diagonal directions of the joint core as can be seen in Fig. 15.2. FRP sheets were bonded only on the external side of the joints since on the other side the beam was framing into the joint (Fig. 15.2). In order to prevent stress concentrations, all corners were rounded before FRP application. Tensile strength, elasticity modulus, rupture strain, effective thickness and unit weight of carbon FRP sheets were 3,800 MPa, 240 GPa, 1.55%, 0.176 mm and 330 g/m^2, respectively. In HPFRCC retrofitting (specimen JWH), the prefabricated HPFRCC panel was bonded on the external side of the joint by an epoxy-based adhesive (Fig. 15.3). The tensile and compressive strength of the adhesive were 25 and 75 MPa, respectively, at an age of 7 days. As seen in Fig. 15.3, the dimensions of the HPFRCC panel (500×500×40 mm) were tuned to match the joint dimensions. The thickness of the bonding material between the HPFRCC panel and the joint surface was 3 mm. The contact surface was cleaned carefully before bonding and the epoxy adhesive was applied on the prepared surface with a trowel to ensure a uniform thickness of 3 mm of the epoxy adhesive layer. In addition, as a further precaution for appropriate connection of HPFRCC panel to the joint surface, four 16-mm diameter rods were used to anchor the HPFRCC panel to the joint. The embedment depths of these steel roods were 200 mm into the joint

core. The bolts were fixed in the joint using an epoxy based anchorage mortar. For fixing the panels, 12 Nm torque was applied to the bolts.

The HPFRCC panel was cast in a wooden form and the form was placed on a vibration table to ensure a satisfactory compaction. It should be noted that relatively longer mixing time (≈30 min) with respect to normal concrete was necessary to obtain a workable HPFRCC. The panel was removed from the formwork after 1 day and was cured in 90°C water for 3 days and in 20°C water for 25 days. To obtain the optimum mix-proportion and high tensile strength, an extensive experimental study had been carried out beforehand. The HPFRCC mix-proportions are 925 kg cement, 204 kg water, 186 kg microsilica, 557 kg silica sand, 278 kg sand, 314 kg steel fibres and 33.6 kg admixture per cubic meter. The total volumetric ratio of steel fibres was 4%. The diameter, aspect ratio and tensile strength of the steel fibres were 0.55 mm, 55 and 1,100 MPa, respectively. The microsilica was produced by Elkem Materials with a mean particle size smaller than 500 μm and specific gravity of 2.3 kg/dm^3. The admixture was Glenium 51 hyperplasticizer produced by BASF.

In order to obtain the mechanical characteristics of HPFRCC mixture, standard cylinder compression and splitting tests were carried out at the ages of 28, 90, 180 and 360 days. The average compressive and splitting tensile strengths of the HPFRCC mixture around testing days were found to be approximately 129 and 17 MPa, respectively, and the modulus of elasticity was around 41,000 MPa (the age of the HPFRCC panels was around 60 days at the days of experiments). As shown in Figs. 15.2 and 15.3, special attention was paid for the retrofitting methods to be simple and practically applicable. Further details can be found elsewhere (Bedirhanoglu 2009; Bedirhanoglu and Ilki 2009).

15.2.3 Test Setup and Displacement History

The specimens were tested under the combined action of constant column axial load and static lateral displacement reversals were imposed on the tip of the beam. The test setup is shown in Fig. 15.1a. Nearly constant axial load of 130 kN was applied by a 600 kN-capacity hydraulic jack at one end of the column. Reversed cyclic lateral displacements were applied in the horizontal direction to the free end of the beam using a 250-kN servo-controlled hydraulic actuator. All tests were conducted under displacement control. The measuring system consisted of displacement transducers (LVDTs), electrical resistance strain gages bonded on steel bars, concrete surfaces and load cells.

Each test started with gradual application of the axial load. Subsequently, lateral displacements were imposed until the pre-defined drift ratios were reached. Drift ratios reported herein are the ratios of the displacements measured at the free end of the beam to the length of the beam. These ratios were then corrected by subtracting the rigid-body rotation associated with deformations of the supports. Specimens were subjected to 10 cycles at drift ratios increasing gradually from 1/4,000 to 1/25.

15.3 Test Results and Discussion

Test results are summarized in Table 15.2, and Figs. 15.4 and 15.5. The main deficiency observed during testing of the reference specimen was the slip of beam longitudinal bars together with shear damage at the joint after large drift ratios, such as 4%. Cracks showing slip of beam longitudinal bars at the intersection of the column and the joint and parallel to the beam longitudinal axis were observed during the test of reference specimen JO. The slip of beam longitudinal bars was also verified through a wide crack

Table 15.2 Test results

Specimens	Maximum load at tip of beam		Drift ratio at first		Diagonal deformation at 4% drift ratio (from LVDT over 480 mm gage length)	ε_{lmax}[a]	τ_v (MPa)[b]	Δ_L (%)[c]	V_{jh}/f_c[d]
	SWT (kN)	SWC (kN)	Flexural crack at beam	Inclined crack in the joint core					
JO	65.8	53.3	1/1,000	4/1,000	0.0064	0.0011	1.53	6.3	0.19
JWC-D-5	80.8	71.4	1/2,000	20/1,000	0.0013	0.0020	1.86	10.0	0.23
JWH	85.3	84.0	1/1,000	20/1,000	−0.0048	0.0017	1.97	8.5	0.24

SWT slab works in tension, *SWC* slab works in compression

[a]Maximum strain of beam longitudinal reinforcement at maximum lateral load

[b]Joint shear stress (slab works in tension)

[c]Δ_L: drift ratio corresponding to the 85% of the lateral load capacity on the descending branch

[d]Joint shear strength in horizontal direction, V_{jh} (slab works in tension). f_c is the mean measured cylinder strength

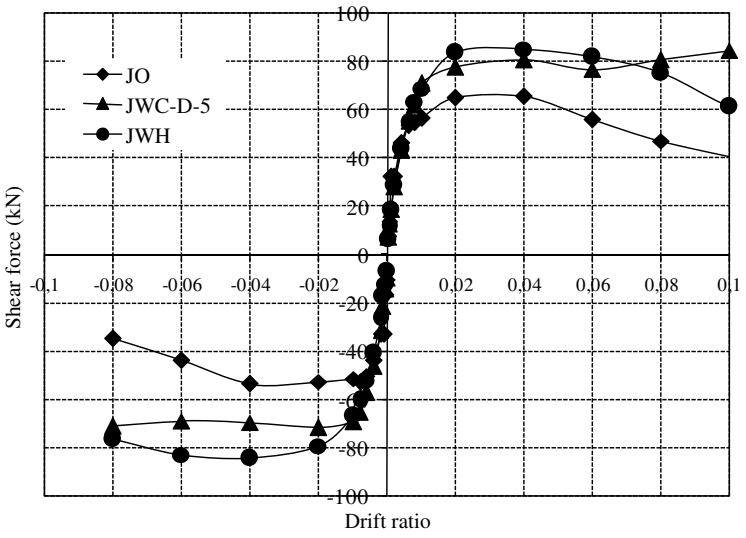

Fig. 15.4 Comparison of envelopes of shear force-drift ratio relationships of all specimens

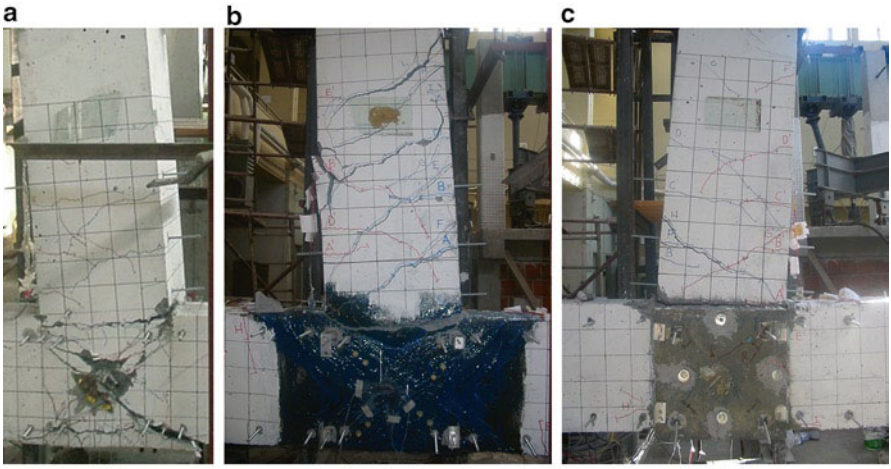

Fig. 15.5 Photos of damaged specimens (**a**) JO (**b**) JWC-D-5 (**c**) JWH

at the intersection of the beam and the joint, although the beam flexural capacity was not reached. However, the slip was not associated with the brittle failure of the specimen, and the specimen reached 4% drift ratios without any strength decay. The mechanism of slip can be explained briefly as follows. As lateral load is applied to the tip of the free end of the beam, beam longitudinal bars exert compression stress to the concrete around the corners of the 90° hooks of beam longitudinal bars. As this load increases and reaches a certain limit, gradual crushing of concrete around the corners of the 90° hooks begins and the crushing causes slip out of the beam longitudinal bars.

The slip of beam longitudinal bars, observed while testing reference specimen JO, was prevented by welding hooks of beam longitudinal bars at their hooks at the joint (Bedirhanoglu et al. 2010). As explained by Bedirhanoglu et al. (Bedirhanoglu et al. 2010), while the welding prevented slip of beam longitudinal bars, it did not improve the shear capacity of the joint core. Consequently, a ductile failure mechanism through beam hinging could not be obtained.

Therefore, in order to improve further the behaviour of the joint by preventing joint shear damage, the other specimens were retrofitted by bonding either FRP sheets or HPFRCC panel to the external face of the joint in addition to welding. Envelopes of shear force-drift ratio relationships both in positive and negative loading directions are given for all specimens in Fig. 15.4. As seen in this figure, bonding FRP sheets or HPFRCC panel to the external face of the exterior joint is a very effective way to prevent strength decay due to shear damage at the joint. The retrofitted specimens did not show any sign of strength degradation until the large drift ratios of 7–10%.

Since the amount of FRP used was significantly more than needed in specimen JWC-D-5, no damage was observed either in the middle of the joint or at the anchorage zones of carbon FRP sheets. As shown in Fig. 15.5, no important damage was observed on the HPFRCC panel, apart from a few very fine cracks.

It should be noted that the details of the behaviour of FRP retrofitted specimens can be found elsewhere (Ilki et al. 2011).

15.4 Concluding Remarks

The behaviour of existing typical deficient reinforced concrete joints before and after retrofitting was investigated. The main conclusions are summarized below:

All the specimens sustained their capacities to carry lateral loads during static displacement reversals with maximum drift ratios of up to 4% where the maximum strength degradation was less than 10%. The pseudo-ductile behaviour of the reference specimen is mainly due to local gradual crushing of low strength concrete around the 90° hooks of beam longitudinal bars.

It was clearly seen that through adequate design and detailing of FRP or HPFRCC retrofitting of joint cores together with rehabilitation of the anchorage of beam longitudinal bars through welding, the specimens could reach their flexural capacity and could keep their strengths until the drift ratios of 7–10%.

References

Bedirhanoglu I (2009) The behaviour of reinforced concrete members with low strength concrete under earthquake loads: an investigation and improvement. Dissertation, Istanbul Technical University, Istanbul

Bedirhanoglu I, Ilki A (2009) HPFRCC for rehabilitation of reinforced concrete members with low-strength concrete. ITU J/d Eng 8(6):146–156, in Turkish

Bedirhanoglu I, Ilki A, Pujol S, Kumbasar N (2010) Seismic behavior of joints built with plain bars and low-strength concrete. ACI Struct J 107(3):300–310

DBYBHY-07 (2007) Regulations for buildings to be constructed in earthquake prone areas, Turkish seismic design code, Ankara, Turkey

Ilki A, Bedirhanoglu I, Kumbasar N (2011) Behavior of FRP-retrofitted joints built with plain bars and low-strength concrete. ASCE J Compos Constr 15(3):312–327

TS 500 (2000) Requirements for design and construction of reinforced concrete structures. Turkish Standards Institute (TSE). Ankara, Turkey

Chapter 16
External Strengthening of Continuous RC Beams with CFRP

Pieter Desnerck, Lander Vasseur, Stijn Matthys, and Luc Taerwe

Abstract The structural behaviour of reinforced beams strengthened in flexure with externally bonded FRP (Fibre Reinforced Polymer) reinforcement has been extensively investigated with respect to isostatic beams. Design methods are given in guidelines and standards, and failure modes are described. However, limited information is available on the behaviour of continuous beams, strengthened with composite reinforcement. For flexural strengthening of a 2-span continuous beam, the FRP reinforcement can be applied on top of the central support, at the bottom-side of the two spans or at both locations. By means of an analytical study, the non-linear behaviour of this type of beam is investigated. The failure modes are studied and it is verified to which degree moment redistribution is still present when applying this strengthening technique which makes use of a linear elastic polymeric material.

16.1 Introduction

Structures may need to be strengthened for different reasons, among which is a change in function, the implementation of additional services, or the repair of damage. Different strengthening techniques are possible, but often used nowadays is the application of an externally bonded reinforcement (EBR) consisting of a fibre-reinforced polymer (FRP), the so-called FRP EBR. FRP ('Fibre Reinforced Polymer'

P. Desnerck (✉) • S. Matthys • L. Taerwe
Department of Structural Engineering, Magnel Laboratory for Concrete Research, Ghent University, Technologiepark-Zwijnaarde 904, B-9052 Zwijnaarde, Belgium
e-mail: pieter.desnerck@ugent.be; stijn.matthys@ugent.be; luc.taerwe@ugent.be

L. Vasseur
ECC NV Belgium, Terbekehofdreef 50-52, B-2610 Antwerp, Belgium
e-mail: lander.vasseur@ecc-belgium.be

M.N. Fardis (ed.), *Innovative Materials and Techniques in Concrete Construction: ACES Workshop*, DOI 10.1007/978-94-007-1997-2_16,

or 'Fibre Reinforced Plastic') is a composite material consisting of non-metallic fibres imbedded in a polymeric matrix. Generally a thermoset material such as polyester, vinyl ester or epoxy resin is used as matrix. The types of fibres mostly applied for civil constructions are: glass fibres (GFRP), aramid fibres (AFRP) and carbon fibres (CFRP), the latter type being used in this study.

FRP EBR can be used for the strengthening of existing structures in order to enhance their flexural and shear capacity. This paper discusses the flexural strengthening of 2-span reinforced concrete beams. CFRP (Carbon FRP) laminates are glued on the soffit of spans and/or on the top at the mid-support (Nanni 1993; NBN-EN-1504-5 2005). Besides the more regular failure modes of beams in flexure (concrete crushing, rebar yielding, etc.), the efficiency of the FRP EBR strengthening technique is limited by the capability to transfer stresses at the bond interface. Often debonding of the laminate will lead to overall failure of the element. Hence, the aim of this study is to gain a better insight into the behaviour and failure mode of reinforced multispan concrete beams strengthened in flexure with CFRP.

16.2 Moment Redistribution

Performing an analysis of a structure according to the linear elastic theory, a linear relationship between the moment and the curvature is assumed, i.e.

$$\chi = \frac{1}{r} = \frac{M}{EI} \tag{16.1}$$

with l/*r* the curvature, *M* the bending moment and *EI*=*K* the flexural rigidity, which is often assumed to be constant and therefore independent of the value of the bending moment. However, for the cross-section of a concrete beam the moment-curvature diagram is non-linear, which corresponds to a variable flexural rigidity. This is illustrated in Fig. 16.1, where the non-linear behaviour is simplified by three straight branches each characterized by a specific flexural rigidity.

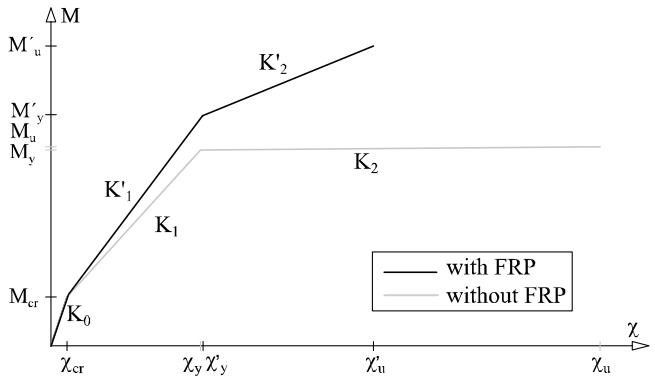

Fig. 16.1 Moment-curvature diagram: influence of flexural strengthening

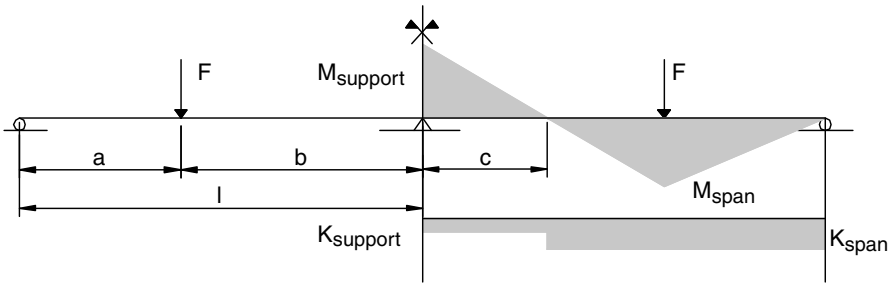

Fig. 16.2 Two-span beam with stepwise constant flexural rigidity

Figure 16.1 compares the M-χ relationship of an unstrengthened and an FRP flexural strengthened RC cross-section. K_0 represents the flexural rigidity of the uncracked concrete section, K_1 of the section after cracking and K_2 of the cracked section after yielding of the steel reinforcement. In a cross-section with both steel and externally bonded FRP reinforcement, higher values of K (especially K_2 and K'_2) are obtained in comparison with the same beam without FRP. Due to strengthening a higher bending moment capacity is obtained whereas the ultimate curvature is reduced. This different behaviour will influence the moment redistribution of a continuous beam.

Considering a continuous beam with two identical spans and two symmetric point loads (Fig. 16.2), three zones can be identified:

- The central mid-support zone with hogging moments.
- The span zones with sagging moments.

It is assumed that in each zone, the flexural rigidity is constant. The flexural rigidity of the mid-support zone and the span zones is designated respectively as $K_{support}$ and K_{span}. Referring to Fig. 16.2, the non-dimensional variables m (moment ratio), k (flexural rigidity ratio) and λ (location of point loads) are introduced:

$$m = \frac{M_{support}}{M_{span}} \quad k = \frac{K_{support}}{K_{span}} \quad \lambda = \frac{a}{b} \tag{16.2}$$

Using equilibrium equations, requiring the rotation above the mid-support to be zero and fixing λ to 2/3 (see tests discussed in Sect. 16.4), the following relationship between the two basic variables can be derived:

$$36m^3 + (45 - 8k)m^3 - 34km - 35k = 0 \tag{16.3}$$

Given the k-m relationship which is valid for the specific beam geometry and loading configuration, the bending moment ratio m can be derived from the known flexural rigidity ratio k, which depends on the internal and the external reinforcement ratios and on the load level.

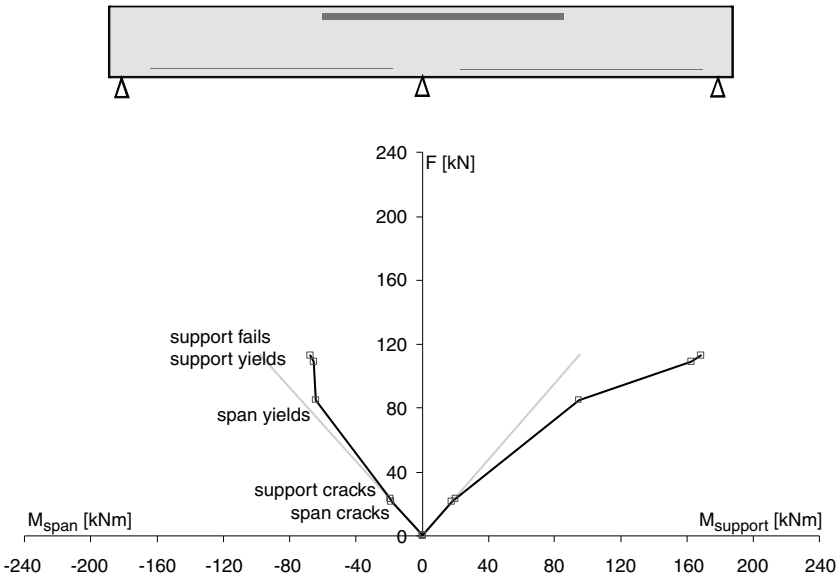

Fig. 16.3 Redistribution graphs for unstrengthened 2-span beam

In Fig. 16.3 a comparison is made between a strengthened and an unstrengthened 2-span beam with *a* equal to 2 m and *b* equal to 3 m. The span and support moments are plotted as a function of the loads F. The span section being the most critical, the first plastic hinges occur in the spans. All additional loading is taken by the mid-support (Fig. 16.3). By using FRP EBR at both locations (Fig. 16.4), it is noticed that after yielding of both critical cross-sections the moment distribution is parallel to the linear elastic moment distribution.

A comparable situation is seen when the reinforcement in the spans of the beam is increased and the first plastic hinge is formed at the mid-support. Applying FRP EBR at the top of the beam at the mid-support allows for the suppression of the formation of a plastic hinge at that location and the bending moments are closer to the elastic curve. The theoretically obtained redistribution curves show a good to excellent agreement with the experimentally obtained moment redistribution (see Sect. 16.4).

16.3 Debonding Mechanisms

For the design of an externally strengthened beam at the ultimate limit state (ULS), guidelines recommend a two stage analysis (fib 2001; Matthys 2000; ACI 2002). First, the strengthened beam is designed assuming a full composite action (meaning

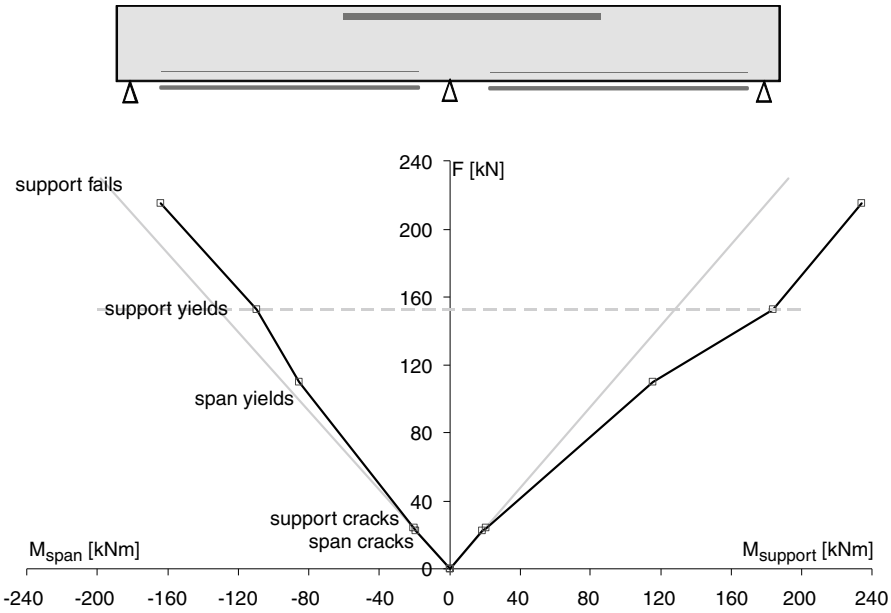

Fig. 16.4 Redistribution graphs for FRP EBR strengthened 2-span beam

no debonding of the FRP EBR material from the concrete is taken into account). One of the following failure modes occurs:

- Steel yielding followed by concrete crushing
- Steel yielding followed by FRP fracture
- Concrete crushing without steel yielding.

In the second design stage of an externally strengthened beam at the ultimate limit state (ULS), the loss of composite action between the concrete and the FRP reinforcement has to be checked. This type of failure typically occurs in a sudden and brittle way.

In practice, debonding in the adhesive or FRP is generally not noticed because the tensile and shear strength of the resin or adhesive are mostly higher than that of the concrete. Hence, it can be concluded that debonding normally occurs in the concrete, near to the surface or along the embedded reinforcement. The exact location of debonding in the concrete cover is dependent on the type of debonding mechanism which is typical for a certain type of beam and strengthening configuration. According to *fib* Bulletin 14 (2001) and Matthys (2000) different bond failure types can be distinguished, i.e.:

- Debonding at flexural cracks (crack bridging)
- Debonding at shear cracks (crack bridging)
- Curtailment or anchorage length failure
- End shear failure.

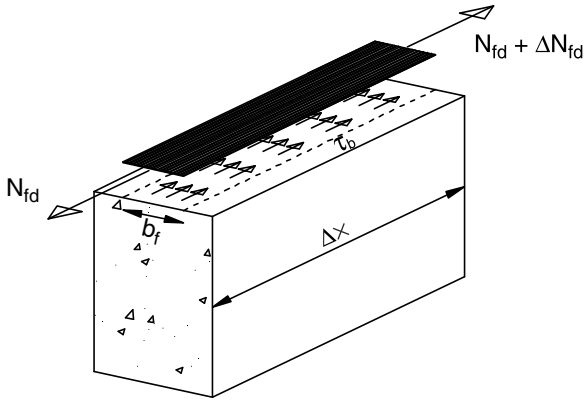

Fig. 16.5 Shear stresses along FRP laminate element

16.3.1 Crack Bridging

For the debonding phenomena by crack bridging, a distinction is made between the bridging of flexural cracks and the bridging of shear cracks by the FRP laminate.

Flexural cracks are characterized by a horizontal crack opening. At both sides of a crack, high peak shear stresses occur. When the peak shear stress exceeds the maximum shear stress $\tau_{b,max}$, a gradual debonding is noticed, initiated by micro-cracking and finally continuing in macro-cracking.

When debonding is initiated, the shear stress redistributes and a smoothing effect occurs for the ideal case of pure flexure. From this smoothing of the shear stresses, one could conclude that this debonding failure mode is less critical than crack bridging at flexural cracks in regions with additional shear forces and hence vertical crack displacement (Matthys 2000). As indicated by several authors (Teng et al. 2003; Oller et al. 2007; Chen et al. 2007), debonding at the location of a flexural crack can result in a complete debonding of the FRP laminate and has to be checked consequently. According to *fib* Bulletin 14 (2001), checking of peeling off failure at flexural cracks can be performed according to several approaches.

One of these methods is the verification of the bond stresses due to force transfer. The variation of the tensile force in the FRP initiates bond shear stresses τ_b at the interface. To avoid debonding of the laminate by this mechanism, the shear stress between the FRP and the concrete, resulting from the change of tensile force along the length of the laminate, has to be limited. This shear stress is calculated as follows, based on the equilibrium of forces as can be seen in Fig. 16.5 and assuming a uniform bond stress over the distance Δx.

$$\tau_b = \frac{\Delta N_{fd}}{b_f \Delta x} \tag{16.4}$$

In the ULS, this acting shear stress has to be limited to the design bond shear strength f_{cbd}, which is given by the following equation:

$$f_{cbd} = 1.8 \frac{f_{ctk}}{\gamma_c} \tag{16.5}$$

When the width of the bond interface b_f is sufficient, this limitation of the shear stress will not be critical in most cases. However, in case the internal steel reinforcement is yielding, the increase in tensile force under increasing bending moment is uniquely provided by the FRP laminate resulting in higher values of ΔN_{fd} and τ_b. In this case debonding may become critical.

In regions with significant shear forces, the shear cracks are inclined, and are associated with both horizontal and vertical crack displacements. Crack bridging models for shear cracks explicitly consider the combined effect of horizontal and vertical displacements. Due to the horizontal crack displacement, peak shear stresses are induced. On the other hand, the vertical crack displacement results in an additional peeling-off effect of the laminate by inducing interfacial tensile stresses perpendicular to the FRP laminate.

To evaluate this latter debonding mechanism, several models can be found in the literature (fib 2001; Matthys 2000). As these methods result in a rather complex calculation of the resisting shear force, an alternative Eq. 16.6 is proposed in (Matthys 2000):

$$V_{Rp} = \tau_{Rp} bd \tag{16.6}$$

$$\tau_{Rp} = 0.38 + 151 \rho_{eq} \text{ with } \rho_{eq} = \rho_s + \rho_f \frac{E_f}{E_s} \tag{16.7}$$

with E the FRP's Young modulus and ρ the reinforcement ratio of the FRP reinforcement (subscript f) and the longitudinal reinforcement (subscript s).

This equation is calibrated on experimental results obtained from 4-point bending tests for concrete strengths C25/30 and C30/37. Both CFRP prefab and wet lay-up types are considered.

16.3.2 Curtailment and Anchorage Length Failure

Theoretically the FRP reinforcement can be curtailed when the axial tensile force can be carried by the internal steel only. The remaining force in the FRP at this point needs to be anchored. Nevertheless, the FRP may need to be extended to zones corresponding to even lower FRP tensile stresses, as the anchorage capacity of the interface is limited (see Fig. 16.6).

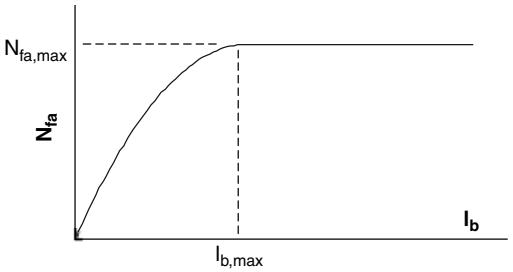

Fig. 16.6 Maximum FRP force which can be anchored in function of the bond length

Based on fracture mechanics considerations (Holzenkämpfer 1994), the values of the maximum FRP force which can be anchored, $N_{fa,max}$, and the maximum anchorage length, $l_{b,max}$ (as can be noticed in Fig. 16.6) can be calculated from (fib 2001):

$$N_{fa,\max} = \alpha.c_1.k_c.k_b.b_f.\sqrt{E_f.t_f.f_{ctm}} \tag{16.8}$$

$$l_{b,\max} = \sqrt{\frac{E_f.t_f}{c_2.f_{ctm}}} \tag{16.9}$$

In this equation the geometry of the FRP strip is incorporated in the thickness t_f and the width b_f. Furthermore, α is a reduction factor, approximately equal to 0.9, to account for the influence of inclined cracks on the bond strength; k_c is a factor accounting for the state of compacting of concrete and k_b is a geometrical factor.

16.3.3 End Shear Failure

By curtailing a laminate at a certain distance from a support, a shear crack can appear at the FRP-end. The propagation of this crack is hindered by the internal steel reinforcement (both the stirrups and the longitudinal reinforcement) and the aggregate interlocking. Although, due to the lack of internal steel stirrups between the internal steel reinforcement and the external FRP reinforcement (see Fig. 16.7), this shear crack may propagate as a debonding failure at the level of the internal steel reinforcement. In this case the laminate as well as a thick layer of concrete will rip off.

An important parameter in the mechanism of concrete rip-off is the distance between the plate end and the support. Related to continuous beams, the latter has to be seen as the distance between the plate end and the point of contraflexure.

Based on the concept of the fictitious shear force zone a_L (Fig. 16.8), it is possible to estimate the resisting shear force at the location of the plate end (fib 2001):

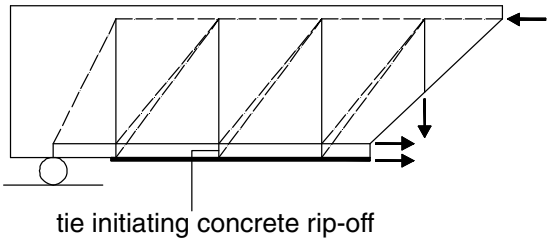

Fig. 16.7 Truss system in order to explain the tie initiation of concrete rip-off

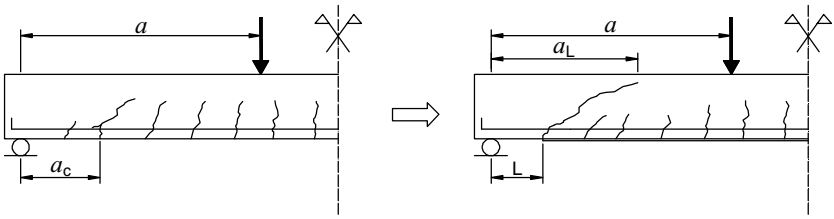

Fig. 16.8 Checking of concrete rip-off

$$a_L = \sqrt[4]{\frac{\left(1-\sqrt{\rho_s}\right)^2}{\rho_s} L^3 d} \tag{16.10}$$

$$V_{Rd} = \tau_{Rd} b d \tag{16.11}$$

with τ_{Rd1} the design value of the nominal maximum shear stress.

In these equations only the internal reinforcement is taken into account. Moreover, it has to be mentioned that the model is applicable only if the following conditions are fulfilled $a > L + d$ and $a_L < a$. From experimental research it can be concluded that this model is an accurate lower bound limit for the prediction of concrete rip-off.

16.3.4 Failure Modes in Case of Continuous Beams

By investigating the above-mentioned mechanisms in continuous beams, certain differences with isostatic beams have to be mentioned. A first aspect which may influence the debonding mechanisms in continuous RC beams is that moments of opposite signs occur along the beam. In contrast to reinforced isostatic beams, this allows to anchor the FRP laminates in compression zones. By extending a laminate into these compression zones, two out of the four debonding mechanisms will be avoided: debonding by a limited anchorage length and debonding by end shear failure (concrete rip-off). Care should be taken to limit the length along which the laminate is extended in the compression zone, so as to restrict the compressive stress in the laminate and reduce the chance of local laminate buckling.

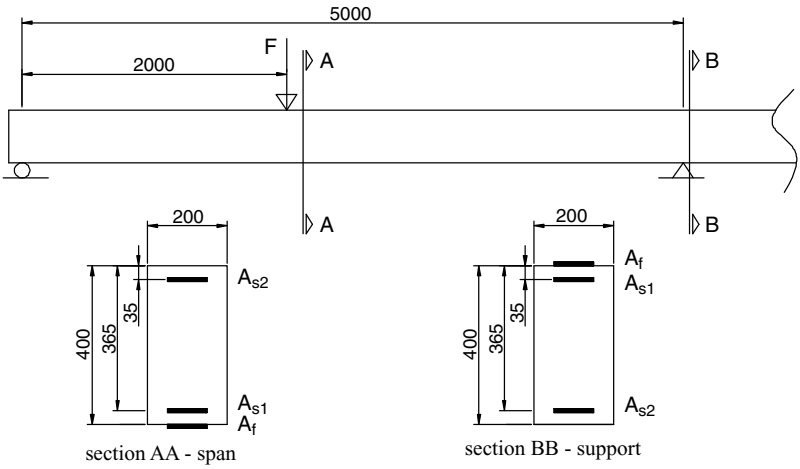

Fig. 16.9 Indication of reinforcement position at critical sections

16.4 Tests on Continuous Beams

16.4.1 Beam Characteristics

For the experimental study of CFRP strengthened continuous beams, three different full-scale 2-span beams were tested up to failure, each with a specific internal steel configuration (Fig. 16.9). Despite the different internal and external reinforcement configurations, a similar failure load is obtained for all beams.

The total depth of the tested beams equals 400 mm, the width equals 200 mm and the span length equals 5 m. The beams are loaded with one point load in each span. The locations of the point loads are at a distance of 3 m from the mid-support and at 2 m from the end supports. Hence $\lambda = 2/3$ (referring to Eq. 16.2). This test set-up is equal to the beam configuration used in the theoretical approach (see Sect. 16.2). The reinforcement ratios according to Eq. 16.7 are given in Table 16.1. As external reinforcement, CFRP laminates with section 100 mm $\times$ 1.0 mm are applied in the zones with low internal reinforcement sections.

Beam CB1 is reinforced with a small amount of internal reinforcement in the spans and a large amount at the mid-support. To compensate the small amount in the spans, externally bonded reinforcement (EBR) is applied only in the spans. A second beam (CB2) has a large amount of internal reinforcement in the spans and a small amount at the mid-support (opposite to CB1). As external reinforcement, EBR is only applied at the top of the beam above the mid-support. The third beam (CB3) has internal reinforcement based on the linear elastic theory. In this case almost the same amount of internal reinforcement is used in the spans and the mid-support. As external reinforcement, laminates are glued on top of the beam above the mid-support as well as at the soffit of the beam in the spans.

Table 16.1 Reinforcement ratios used at mid-support and span [in%]

	Mid-support			Span		
	$\rho_{sup,s}$	$\rho_{sup,f}$	$\rho_{sup,eq}$	$\rho_{span,s}$	$\rho_{span,f}$	$\rho_{span,eq}$
CB1	1.43	–	1.43	0.53	0.13	0.65
CB2	0.31	0.13	0.43	0.75	–	0.75
CB3	0.67	0.13	0.79	0.75	0.13	0.87

Table 16.2 Material properties

	Concrete	Reinforcement span	Reinforcement support	CFRP
f_c (MPa)	38.0	–	–	–
Yield stress (MPa)	–	601	530	–
Yield strain	–	0.28%	0.25%	–
f_{ct} (MPa)	3.4	677	701	2,770
Failure strain	0.35%	12.4%	12.4%	1.46%
E-modulus (GPa)	35.5	218	216	190

The same concrete composition was used for the different beams. A cement type CEM I 52,5 N (300 kg/m³), a sand 0/5 (655 kg/m³), two gravel types 2/8 (190 kg/m³) and 8/16 (1,120 kg/m³) and 165 l of water was used. The main material properties of the concrete, the reinforcing steel and the CFRP laminates are given in Table 16.2.

16.4.2 Test Results

In Fig. 16.10, the experimental and analytical moment redistributions of CB1 are compared. Regarding the unstrengthened beam (dashed line), the formation of a plastic hinge can be noticed (vertical part of the moment distribution curve). In case of the strengthened beam, although the strengthened spans still start to yield first, the FRP allows the spans to continue resisting the additional load and a so-called restrained hinge is formed. The internal restrain is due to the fact that the CFRP laminate shows an elastic behaviour. At increasing load, when the mid-support starts to yield, a plastic hinge occurs at the mid-support.

Shortly after this plastic hinge formation, debonding of one of the span laminates occurred at 153 kN. Good agreement is observed between the experimental curve and the calculated curve.

The experimental and analytical moment redistributions of CB2 are compared in Fig. 16.11. For the unstrengthened beam, the formation of a plastic hinge can be noticed at the mid-support (vertical part of the dashed moment distribution curve). In case of the strengthened beam, although the strengthened mid-support section still starts to yield first (as mentioned above), the FRP allows the mid-support to continue resisting the additional load (restrained hinge formation). At increasing load, when the spans start to yield, a plastic hinge is formed in the spans. At a slightly higher load, the laminate debonded at 152 kN.

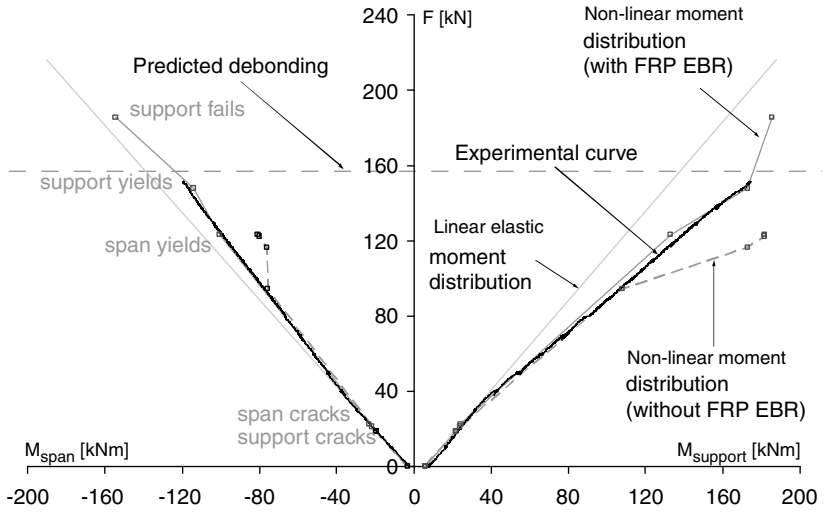

Fig. 16.10 Moment redistribution of beam CB1

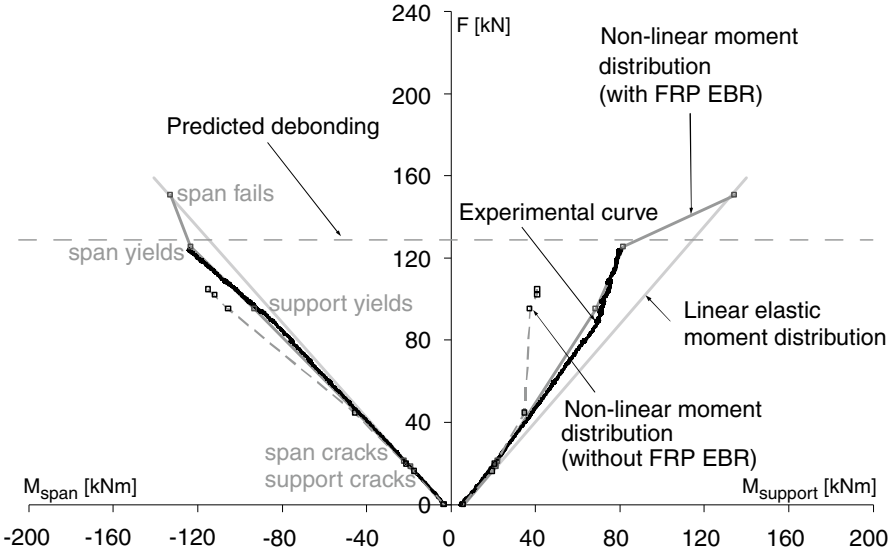

Fig. 16.11 Moment redistribution of beam CB2

Unfortunately no information about the moment redistribution for F>122 kN is available, due to a technical problem by which the signals from the load cells were not recorded beyond 122 kN. Concerning the available experimental data, a good agreement is observed with the calculated curve.

In Fig. 16.12, the experimental and analytical moment redistributions of CB3 are compared. Both for the unstrengthened and for the strengthened beam a moment

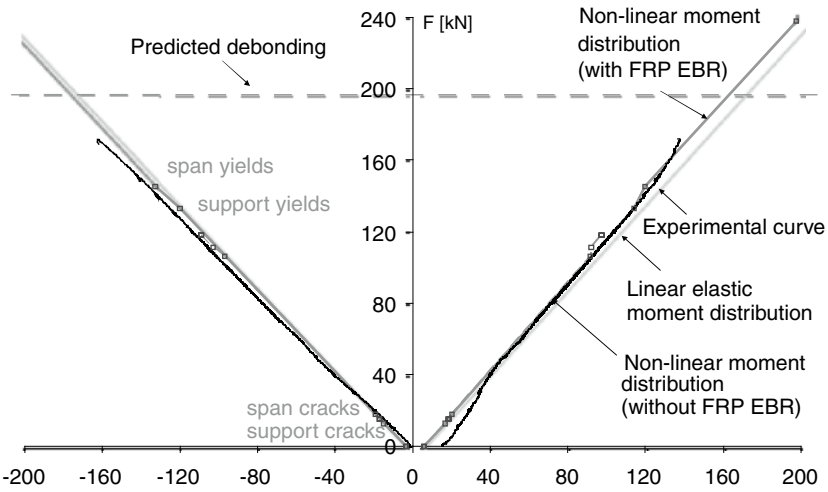

Fig. 16.12 Moment redistribution of beam CB3

distribution is observed similar to the distribution obtained from the linear elastic theory. At increasing load, when the spans and mid-support sections start to yield, the FRP allows both the spans and the mid-support to continue resisting the additional load (restrained hinge formation).

Concerning the available experimental data, a good agreement is observed with the calculated curve. Debonding of the laminate occurs at 170 kN, after both mid-support and spans already yield.

16.5 Conclusions

The use of EBR to strengthen reinforced concrete structures implies the possible occurrence of debonding of the laminates. In the design of a strengthened member, often full composite action is assumed to start with. In a second stage, different debonding mechanisms are considered or verified in the design. The different debonding mechanisms which can appear in the strengthened regions of a continuous beam are similar to the mechanisms which appear in isostatic beams. However, with proper design end shear failure and anchorage failure can be avoided.

In unstrengthened 2-span beams, plastic hinges are expected in the zones with low internal reinforcement ratios (compared to the linear elastic reinforcement ratios). By strengthening only these zones with FRP EBR, the possibility exists to move the location of the plastic hinge to the zones with high internal reinforcement ratios (compared to the linear elastic reinforcement ratios).

The analytically obtained moment redistribution based on a non-linear analysis, shows good to excellent agreement with the experimentally obtained moment redistribution.

The models allow prediction of the debonding failure load with a fairly high accuracy.

Acknowledgements The authors would like to thank the Fund for Scientific Research in Flanders (FWO) for the financial support.

References

ACI (2002) Guide for the design and construction of externally bonded FRP systems for strengthening concrete structures, ACI 440.2R-02. American Concrete Institute, Farmington Hills

Chen JF, Yuan H, Teng JG (2007) Debonding failure along a softening FRP-to concrete interface between two adjacent cracks in concrete members. Eng Struct 29(2):259–270

fib (2001) Externally bonded FRP reinforcement for RC structures. International federation for structural concrete. fib bulletin 14, Lausanne, 138 pp

Matthys S (2000) Structural behaviour and design of concrete members strengthened with externally bonded FRP reinforcement. PhD thesis, Department of Structural Engineering, Ghent University, Ghent, p 345

Nanni A (1993) Fibre-Reinforced-Plastic (FRP) reinforcement for concrete structures: properties and applications, vol 42. Developments in Civil Engineering, Amsterdam, 450 pp

NBN-EN-1504-5 (2005) Products and systems for the protection and repair of concrete structures – definitions, requirements, quality control and evaluation of conformity – part 5: concrete injection = EN 1504–5:2004

Oller E, Cobo D, Mari AR (2007) A new design proposal to prevent failure in beams strengthened by plate debonding. Proceedings, 8th international symposium on fibre reinforced polymer reinforcement for concrete structures (FRPRCS-8), Patras, July 2007

Teng JG et al (2003) Intermediate crack-induced debonding in RC beams and slabs. Constr Build Mater 17(6–7):447–462

Chapter 17
Prestressed FRP Fabrics for Flexural Strengthening of Concrete

Marco Menegotto, Giorgio Monti, and Marc'Antonio Liotta

Abstract The feasibility and advantages of strengthening reinforced concrete (RC) beams by prestressed Fibre-Reinforced-Polymer (FRP) fabrics are examined. Actually this is possible, as a prestressing machine has been designed, suitable to properly seize and prestress the fabric, without risk of ripping it. The device is illustrated and the case of RC beams with inadequate steel reinforcement for bending is treated. A method is proposed and the analytical verifications are shown, that make use of closed-form equations and follow the usual steps commonly taken when strengthening, i.e. to assess the resisting moment capacity of the existing beam, to evaluate the demanded strength increase and to design the amount and prestress level of the strengthening. A design example is also given.

17.1 Introduction

The use of prestressed FRP reinforcement in the shape of laminated strips, for flexural strengthening of RC members, has broadly increased over the past decade.

In some cases, it may be advantageous to bond the external FRP reinforcement onto the concrete surface in a prestressed state. Both laboratory and analytical research (e.g. Triantafillou and Deskovic 1991; Triantafillou et al. 1992; Deuring 1993) show that prestressing represents a significant contribution to the improvement of the FRP strengthening technique, and that procedures have been developed to prestress the FRP composites under real life conditions (Luke et al. 1998).

M. Menegotto (✉) • G. Monti • M. Liotta
Department of Structural Engineering and Geotechnics, Sapienza University of Rome, via A. Gramsci, 53, I-00197 Rome, Italy
e-mail: marco.menegotto@uniroma1.it; giorgio.monti@uniroma1.it; liotta@uniroma1.it

M.N. Fardis (ed.), *Innovative Materials and Techniques in Concrete Construction: ACES Workshop*, DOI 10.1007/978-94-007-1997-2_17,

Prestressing the strips prior to bonding has several advantages: it provides stiffer behaviour, as at low loading most concrete is under compression, thus better contributing to the inertia. Crack formation is delayed and, when it appears, cracks tend to be thinner and more finely distributed. Prestressing also favours the closure of pre-existing cracks, improving both serviceability and durability, while it also enhances the shear resistance.

Further, the same strengthening can be achieved with smaller areas of FRP, if pre-stressed, and, with adequate anchorage, prestressing may increase the ultimate resisting moment by avoiding peeling-off at crack locations and at the strips ends. Finally, prestressing significantly increases the load level which makes the steel reinforcement yield.

Prestressing also has drawbacks: it is more expensive than normal strip bonding, due to the number of operations and the equipment required, and it requires the prestressing force to remain in place longer, until the adhesive has hardened enough.

Were the prestressing force too high, failure of the beam would occur due to the release of the prestressing force at the ends, inducing excessive shear stresses in concrete just above the FRP. Hence, design, detailing and execution of the end zones require special care. Tests and analyses have shown that FRP strips shear off (from the ends) if no special anchorages are provided at the ends and prestress levels are above 5–6% of their tensile strength (for CFRP). But technically and economically, a considerably higher degree of prestressing would be effective – around 50% of the FRP tensile strength – which can be achieved only by use of special confining anchorages. These have been developed, for research purposes as well as for practical applications.

So far, devices that are effective in seizing and prestressing *laminated strips*, thanks to their high transverse stiffness, have been produced, and field applications have been already carried out. However, the use of prestressed FRP reinforcement in shape of *fabrics* has not developed as much. This is mostly due to the difficulty of seizing the fabric when prestressing it without ripping the fibres. In fact, significant problems have been encountered in developing appropriate devices. This paper tries to contribute in this respect, by presenting a tensioning machine for FRP fabrics. The concept and a design scheme are illustrated. Some considerations regarding the design of a strengthening intervention through prestressed FRP are also discussed, along with an example.

17.2 Current Research

Quite limited experimental research on external strengthening of RC with prestressed FRP has been carried out to the authors' knowledge. Regardless of the type of strengthening, two main ways of prestressing may be distinguished: indirect or direct. In the first, strips or sheets are prestressed by cambering the flexural member (Saadtmanesh and Ehsani 1991); in the latter, either by jacking against an external reaction frame (Deuring 1993) or against the beam itself (Andrä and Maier 1999; Wight et al. 2001).

In the indirect method, one cambers the flexural region of a member using hydraulic jacks inducing opposite curvature. FRP plates are attached to the lower (tensile) face and, when the FRP is fully bonded to the concrete, the jacking force is removed, the member deflects and a tensile stress rises in the strengthening. The prestress level generated in this way is quite low, compared to the FRP tensile strength.

In the direct method, proposed by Triantafillou et al. (1992) and Deuring (1993), the FRP-strengthening is tensioned over a stressing bed independent of the beam. Again, it is attached to the lower face of the concrete member and, after it is fully bonded, the tensioning force is removed. Due to the higher level of prestress that can be reached, the transfer of prestress to concrete mobilizes quite a severe shear stress state in the interface region at the end of the strengthening; therefore, to avoid peeling failure, additional restraining must be provided. If the FRP-strengthening is tensioned by reacting directly on the beam, an advantage may be offered by the tensioning device itself, which can be left in place as a mechanical end restraint.

17.3 Technological Issues

The main technological challenge of prestressing FRP fabrics consists in seizing the fabric itself. At present, the only reliable way to prestress a fabric seems to be the following: to preliminarily wrap it several times around a resin-impregnated steel rod at its ends; then to allow appropriate time for the resin to cure; finally, to pull the fabric end(s) for tensioning. The fabric may also be bonded to the surface of the concrete member, in order to gain the effects of a full interaction. Several layers can be subsequently applied in a similar way, with a partial loss of prestress in the previously bonded ones, as no additional tension can be given to them. The solution may be cost-effective, but it takes time to apply it.

The fabric is wrapped around a rod with suited curvature, because it cannot be seized with simple devices (as for the laminated strips), due to its extremely low thickness and absence of resin: that is the only way to avoid the risk of ripping it.

17.4 The FRP-Prestressing Device

A new tool has been devised (Monti and Liotta 2006) to effectively seize and prestress FRP fabrics. One of its main features is that it may allow for differential prestressing of the fabric along the beam length, thus inhibiting the risk of debonding at the ends, in case the fabric is not mechanically restrained.

The device (Figs. 17.1–17.4) is a machine outfitted with a cylinder of appropriate diameter (coloured in red), around which the fabric can be wrapped without the need of resin. The cylinder is mounted on a moving sledge (light blue), that can slide into a second, fix sledge (dark blue), mounted directly onto the beam surface to strengthen. The cylinder rotates on its axis, wraps around the fabric length needed

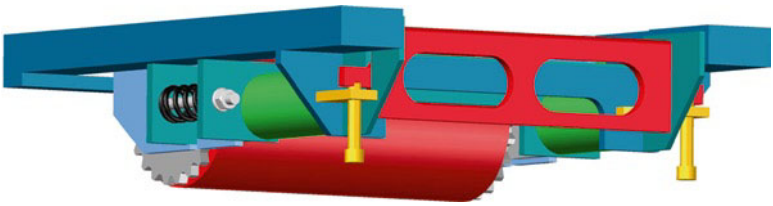

Fig. 17.1 Sketch of the FRP prestressing machine, seen from the beam midspan side

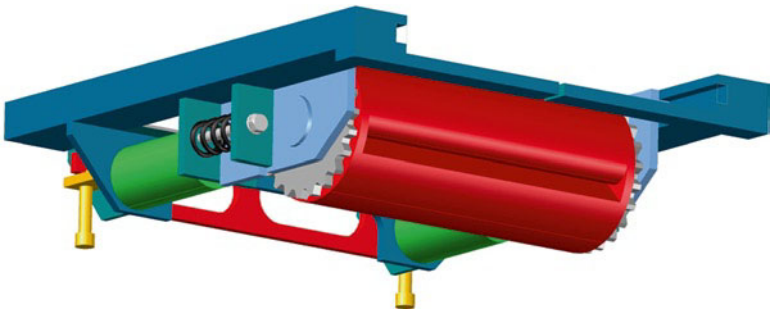

Fig. 17.2 Sketch of the FRP prestressing machine, seen from one beam end side

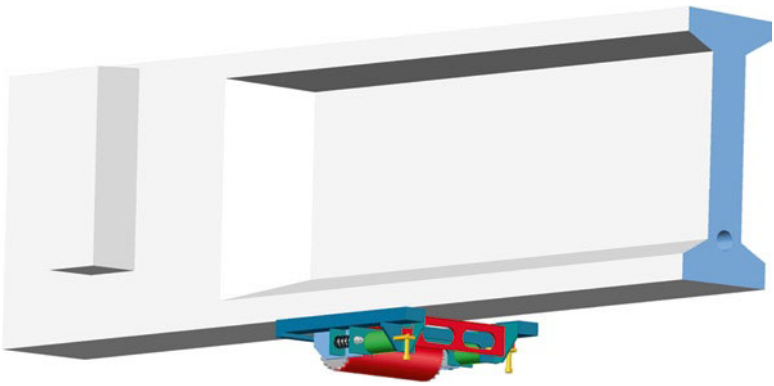

Fig. 17.3 Sketch of the FRP prestressing machine applied under a bridge beam

to properly restrain it by simple friction, without glue, and to put it in a slight tensional state.

By adjustment of the rotation, the cogs of the gears lock, thus inhibiting any further rotation. After locking, the hydraulic jacks (in green on the device sides, Figs. 17.1–17.3) are activated and shift backwards the rods, thus tensioning the whole FRP fabric strengthening. The jacks are equipped with load cells. By monitoring the oil pressure in the jacks and the load cells, the stress applied in the FRP is continuously controlled, up to the design level.

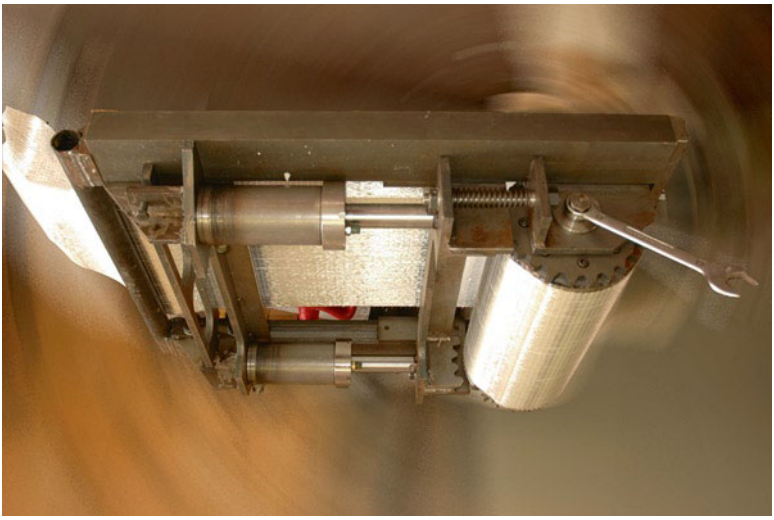

Fig. 17.4 An FRP prestressing machine prototype with GFRP fabric mounted for tests

During all those phases, some space is always allowed between the fabric and the beam soffit, in order to prevent the risk of ripping against possible concrete unevenness.

Finally, the FRP fabric is pushed against the beam surface by the rubber edged guillotine (in red) moved by the bolts (in yellow), then epoxy resin is glued and/or mechanical restraints are applied (if needed). The exceeding final part of the fabric may then be wrapped around the beam end or simply cut off, and the machine removed.

Generally, two such machines are put in place, symmetrically. Alternatively, one end of the fabric can be previously fastened to the beam.

The use of two machines also allows for a symmetrically differential prestressing to be applied to each FRP layer. Tension is first applied to the whole length of the fabric at the design level referred to midspan and it is fastened (mechanically or glued) only along a central segment; then, by controlled lowering of the pressure in the jacks, tension is reduced in the remaining portions of the fabric toward the beam ends and, by fastening them stepwise, tuned prestress can be applied. This procedure allows for the fabric to be strained at midspan to its ultimate design level, instead of the debonding design level, which is usually lower.

17.5 ULS Design of Flexural Strengthening with Prestressed FRP

The case of an RC beam with inadequate steel bending reinforcement is dealt with. The analytical developments follow the steps commonly taken when aiming at strengthening, i.e.: once the existing moment capacity of the beam has been assessed,

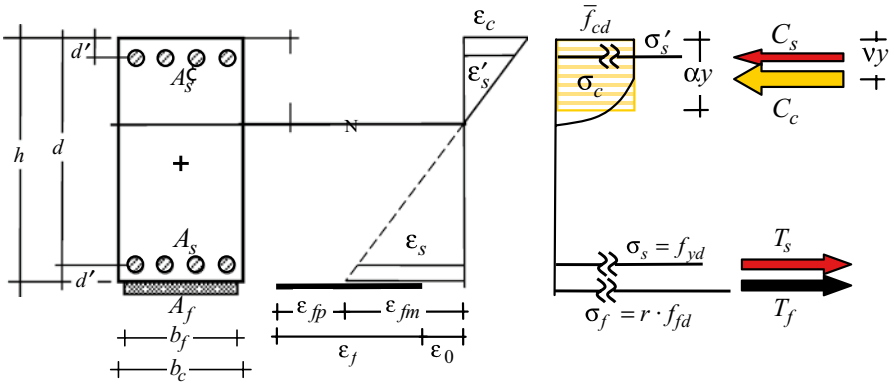

Fig. 17.5 Beam geometry, with strain and stress profiles

the difference with respect to the demand is evaluated; then the required amount of strengthening material and its prestress level is designed, using closed-form equations.

17.5.1 Geometry and Material Properties

Figure 17.5 shows an RC cross-section (which can be rectangular, T- or I-shaped) under bending, with a prestressed FRP sheet bonded to the bottom edge; strain and stress distributions along the depth are also shown, with their corresponding resultant forces.

Geometric and material properties are:

b_c section width
h section depth
d' concrete cover thickness
$d = h - d'$ effective depth
A_s tensile steel area
$A_s' = u \cdot A_s$ compressive steel area
f_{ck} concrete characteristic strength
$f_{cd} = \alpha_{cc} f_{ck} / \gamma_c$ concrete design strength
with $\gamma_c = 1.5$; $\alpha_{cc} = 1$ (CEN 2004, par. 3.1.6)
$E_c = 22000(f_{cm}/10)^{0.3}$ [N/mm^2] concrete modulus (CEN 2004, Table 3.1)
$f_{cm} = f_{ck} + 8$ [N/mm^2] concrete mean strength (CEN 2004, Table 3.1)
$\varepsilon_{cu} = 0.0035$ concrete ultimate strain
f_{yk} steel characteristic yield strength
$f_{yd} = f_{yk} / \gamma_s$ steel design yield strength

with $\gamma_s = 1.1$
$\varepsilon_{yd} = f_{yd} / E_s$ steel yield strain

No check on ultimate strain is performed, as stated in EN1992-1-1 § 3.2.7.

17.5.2 Non-dimensional Formulation

For the purpose of the analytical developments, it is expedient to define the following non-dimensional parameters:

(a) neutral axis depth ratio (unknown):

$$\xi = \frac{y}{d} \tag{17.1}$$

(b) concrete cover ratio:

$$\delta = \frac{d'}{d} \tag{17.2}$$

(c) beam depth ratio:

$$\eta = h / d = 1 + \delta \tag{17.3}$$

(d) compressive/tensile steel ratio and its complement:

$$u = A_s' / A_s \text{ and } w = 1 - u \tag{17.4}$$

(e) mechanical ratios of tensile and compressed steel, respectively:

$$\mu_s = \frac{A_s f_{yd}}{f_{cd} b_c d} \text{ and } \mu_s' = \frac{A_s' f_{yd}}{f_{cd} b_c d} = u \cdot \mu_s \tag{17.5}$$

where:
A_f = area of the FRP sheet/plate (having width b_f and thickness t_f),
$f_{fd} = E_f \varepsilon_{fd}$ = design strength of the FRP sheet (where: E_f = FRP modulus, ε_{fd} = design ultimate strain of FRP).

Finally, all bending moments can be normalized as follows:

$$m = \frac{M}{f_{cd} b_c d^2} \tag{17.6}$$

Throughout the following, non-dimensional notation will be used, yielding more compact and readable equations. The physical sense of those equations is immediately evident when one refers to Fig. 17.6, where the same cross-section of Fig. 17.5 is redrawn, with all relevant parameters replaced with the corresponding non-dimensional ones.

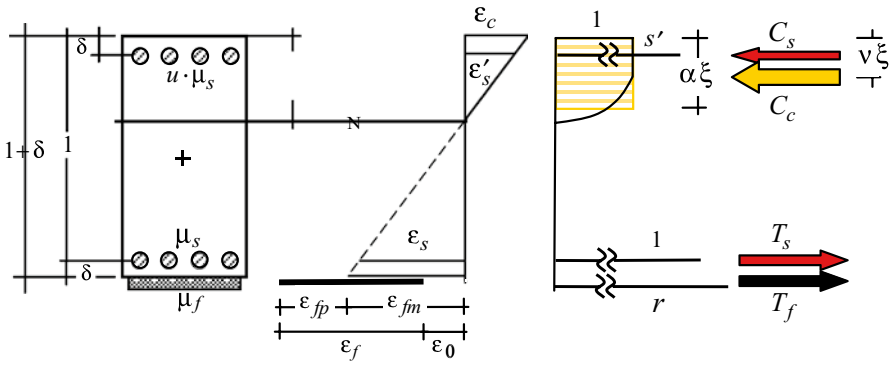

Fig. 17.6 Geometry, strain and stress profiles, as in Fig. 17.5, non-dimensional

17.5.3 Compatibility

Given that failure occurs when $\varepsilon_c = \varepsilon_{cu}$, the corresponding strains at the tension and compression steel bars are easily found, respectively:

$$\varepsilon_s(\xi) = \varepsilon_{cu}\frac{d-y}{y} = \varepsilon_{cu}\left(\frac{1}{\xi}-1\right) \tag{17.7}$$

$$\varepsilon'_s(\xi) = \varepsilon_{cu}\frac{y-d'}{y} = \varepsilon_{cu}\left(1-\frac{\delta}{\xi}\right) \tag{17.8}$$

while the stress of the compression steel in the non-dimensional form is:

$$s'(\xi) = \frac{\sigma'_s}{f_{yd}} = \min\left[\frac{\varepsilon_{cu}}{\varepsilon_{yd}}\left(1-\frac{\delta}{\xi}\right),1\right] \tag{17.9}$$

17.5.4 Stress State Before Strengthening

In the non-dimensional form, the existing resisting moment is found by solving the equilibrium equation for the neutral axis depth ξ:

$$0 = \alpha\cdot\xi + s'(\xi)\cdot u\cdot\mu_s - \mu_s \tag{17.10}$$

where $\alpha = 0.8$ is the concrete stress diagram shape factor.

The solution of Eq. 17.10 is used to find the non-dimensional resisting moment, by replacing it in the following:

$$m_{Rd} = s'(\xi)\cdot u\cdot\mu_s(\nu\,\xi-\delta)+\mu_s(1-\nu\,\xi) \tag{17.11}$$

where $\nu = 0.4$ is the concrete compression centroid factor and $s'(\xi)$ is computed by Eq. 17.9; u by Eq. 17.4; μ_s by Eq. 17.5; δ by Eq. 17.2.

17.5.5 Strain State Before Strengthening

Before applying the FRP strengthening, it is necessary to know the strain state at the beam soffit. In case of propped beam, this is equal to zero, whereas if the beam is left under the characteristic (mean) value of the permanent service load G_k, the initial strain ε_0 is:

$$\varepsilon_0 = \min(\varepsilon_{0,cr}, \varepsilon_{0,tr}) \tag{17.12}$$

where $\varepsilon_{0,cr}$ and $\varepsilon_{0,tr}$ are the initial strain, evaluated using either the conventionally cracked or the transformed cross-section stiffness, respectively. The former is obtained by dividing the gross section stiffness by $2.0 \div 2.5$, while the latter by considering the section made of the compressed concrete and the "homogenized" steel areas. The strain is found as:

$$\varepsilon_0 = \frac{M_{G_k}}{E_c I_{(cr \text{ or } tr)}}(h - y) \tag{17.13}$$

where M_{G_k} is the bending moment due to the characteristic (mean) value of the permanent load under service conditions (=0, if beam is propped), $I_{(cr \text{ or } tr)}$ is the moment of inertia, evaluated with either the cracked or the transformed stiffness. Generally, the former yields better predictions than the latter, with less algebraic effort.

17.5.6 FRP-Strengthening Design Target

The aim of the strengthening procedure through prestressed FRP must comply with the requirement:

$$m_{Rd,f} = incr \cdot m_{Rd} \geq m_{Sd} \tag{17.14}$$

i.e. it has to increase by a factor *incr* the assessed resisting moment m_{Rd} of Eq. 17.11, for obtaining a final resisting moment $m_{Rd,f}$ higher than the applied design moment m_{Sd}.

The condition must be fulfilled, that the FRP strain ε_f does not exceed the design maximum strain ε_{fd}, possibly reduced by an efficiency (or uncertainty) factor $r \leq 1$ (its value is assigned based on the prestressing device used):

$$\varepsilon_f(\xi) = \varepsilon_{fm}(\xi) + \varepsilon_{fp} \leq r \cdot \varepsilon_{fd} \tag{17.15}$$

where the total FRP strain is obtained as the sum of the mechanical strain $\varepsilon_{fm}(\xi)$ plus the initial prestress strain ε_{fp}. The former is induced by the moment increase $(M_{Rd,f} - M_{G_k})$, after reduction by the initial strain ε_0 of Eq. 17.12, and it is found according to compatibility, as follows:

$$\varepsilon_{fm}(\xi) = \varepsilon_{cu}\left(\frac{\eta}{\xi} - 1\right) - \varepsilon_0 \tag{17.16}$$

17.5.7 Strengthening with Prestressed FRP

The first step is to choose the appropriate FRP material, on the basis of the design ultimate strain ε_{fd}. Other properties, such as strength and modulus, will be selected after the design procedure is completed.

Then, the device efficiency (or uncertainty) factor can be expressed as:

$$r = \frac{\varepsilon_{fm}(\xi)}{\varepsilon_{fd}} + p_f \leq 1 \tag{17.17}$$

where $\varepsilon_{fm}(\xi)$ is found by Eq. 17.16, while:

$$p_f = \frac{\varepsilon_{fp}}{\varepsilon_{fd}} \tag{17.18}$$

is the pre-strain ratio in FRP, with respect to its ultimate strain.The above parameter is the design target, together with the FRP-strengthening ratio μ_f, defined as:

$$\mu_f = \frac{A_f f_{fd}}{f_{cd} b_c d} \tag{17.19}$$

where f_{fd} is the FRP design strength.

The equilibrium equations, in this case, are:

$$0 = \alpha \cdot \xi + s'(\xi) \cdot u \cdot \mu_s - \mu_s - r \cdot \mu_f \tag{17.20}$$

$$m_{Rd,f} = s'(\xi) \cdot u \cdot \mu_s (\nu\, \xi - \delta) + \mu_s (1 - \nu\, \xi) + r \cdot \mu_f (\eta - \nu\, \xi) \tag{17.21}$$

where the target value $m_{Rd,f}$ depends on the value chosen for *incr* in Eq. 17.14, and η is given by Eq. 17.3.

By solving the above equations, together with the limitation of *r* from Eq. 17.17, the three unknowns: μ_f, p_f, ξ, are found.

17.5.8 Design Through Closed-Form Equations

Simple design equations can be obtained by making the assumption: $s'(\xi)=1$. Such an assumption is non-restrictive, because: (i) the contribution from the compression steel is generally sensibly lower than that of tensile steel plus FRP; (ii) the compression steel is generally yielded:

$$\varepsilon_s'(\xi)=\varepsilon_{cu}\left(1-\frac{\delta}{\xi}\right)\geq\varepsilon_{yd} \tag{17.22}$$

that is when:

$$\xi\geq\frac{\varepsilon_{cu}}{\varepsilon_{cu}-\varepsilon_{yd}}\delta \tag{17.23}$$

which is almost always the case.

The equilibrium Eqs. 17.20 and 17.21 become:

$$0=\alpha\cdot\xi-w\cdot\mu_s-r\cdot\mu_f \tag{17.24}$$

$$m_{Rd,f}=\mu_s\cdot(1-u\cdot\delta-w\cdot\nu\,\xi)+r\cdot\mu_f(\eta-\nu\,\xi) \tag{17.25}$$

where Eqs. 17.3 and 17.4 have been used.

From Eq. 17.24, the expression of ξ is found, as:

$$\xi=\frac{w\,\mu_s+r\,\mu_f}{\alpha} \tag{17.26}$$

which can be substituted in Eq. 17.25 to obtain:

$$m_{Rd,f}=\mu_s(1-u\,\delta)+r\,\mu_f\eta-\frac{\nu}{\alpha}(w\,\mu_s+r\,\mu_f)^2 \tag{17.27}$$

from which the amount of FRP μ_f can be found:

$$\mu_f=\frac{1}{2\nu r}\left[\alpha\cdot\eta-2\nu\,w\cdot\mu_s-\sqrt{\alpha^2\cdot\eta^2-4\nu\,\alpha[m_{Rd,f}-\mu_s(u-\delta)]}\right] \tag{17.28}$$

along with the prestress p_f to be applied:

$$p_f=r-\frac{\varepsilon_{cu}}{\varepsilon_{fd}}\left(\frac{\alpha\cdot\eta}{w\,\mu_s+r\,\mu_f}-1\right)+\frac{\varepsilon_0}{\varepsilon_{fd}} \tag{17.29}$$

17.5.9 Dimensioning the FRP

Having determined the non-dimensional FRP-strengthening ratio μ_f, the FRP area is found by selecting the FRP design strength f_{fd} (and implicitly the FRP modulus, as: $E_f = f_{fd} / \varepsilon_{fd}$):

$$A_f = \frac{\mu_f f_{cd} b_c d}{f_{fd}} \tag{17.30}$$

The applied prestress is:

$$\sigma_{fp} = p_f \cdot r \cdot f_{fd} \tag{17.31}$$

and the force to apply to the FRP strengthening:

$$P_{fp} = \sigma_{fp} \cdot A_f \tag{17.32}$$

17.5.10 Time-Dependent Effects

To the authors' knowledge, long term effects can be relevant in the case of high level of prestress to beams where the strengthening is not mechanically restrained, but only bond-restrained. Experimental evidence of creep behaviour and exposure to cyclic thermal conditions under heavy stress levels is not well established. Further studies should be carried out in this respect.

17.6 Design Example

17.6.1 Geometry and Material Properties

With reference to Fig. 17.5, a rectangular reinforced concrete cross-section with the following geometric and material properties are considered:

$b_c = 300$ mm
$h = 400$ mm
$d' = 30$ mm $\quad d = h - d' = 370$ mm
$A_s = 4\phi 16 = 804$ mm^2 $\quad A'_s = 2\phi 16 = 402$ mm^2
$f_{ck} = 20$ N/mm^2
$f_{cd} = 13.3$ N/mm^2
$E_c = 30{,}000$ N/mm^2
$f_{cm} = 28$ N/mm^2
$\varepsilon_{cu} = 0.0035$

$f_{yk} = 380$ N/mm^2
$f_{yd} = 345.5$ N/mm^2
$\varepsilon_{yd} = 0.0017$.

17.6.2 Non-dimensional Parameters

Using the above numbers, the non-dimensional parameters, defined in Sect. 17.5.2 for the analytical developments, become:

$\delta = 0.081$
$\eta = 1.081$
$u = 0.5$
$w = 0.5$
$\mu_s = 0.188$

17.6.3 Stress State Before Strengthening

The neutral axis depth, found by solving Eq. 17.10, is: $\xi = 0.136$. This allows to determine the stress ratio in the compression steel from Eq. 17.9: $s'(\xi) = 0.84$ (which means that before strengthening the compression steel is in the elastic range) and the strain in the tension steel from Eq. 17.7: $\varepsilon_s(\xi) = 0.022$. The non-dimensional assessed resisting moment is: $m_{Rd} = 0.175$.

17.6.4 Strain State Before Strengthening

In order to determine the value of the bending moment M_{G_k} due to the characteristic (mean) value of the permanent load, it is assumed that the (factorized) dead/live load ratio at the ULS is: $ratio = 0.5$.

Thus, considering a G-load factor $\gamma_G = 1.4$, the non-dimensional moment is:

$$m_{G_k} = \frac{ratio \cdot m_{Rd}}{\gamma_G} = 0.063 \tag{17.33}$$

from which the dimensional bending moment, from Eq. 17.6 is:

$$M_{G_k} = 34.3 \text{ kNm}.$$

The moment of inertia of the cross-section, evaluated with either the cracked or the transformed cross-section stiffness (where the neutral axis depth has been found as: $y = 126$ mm) is, respectively:

$$I_{cr} = \frac{1}{2.0} \cdot \frac{1}{12} b_c h^3 = 8 \times 10^8 \text{ mm}^4 \tag{17.34}$$

$$I_{id} = \frac{1}{3} b_c y^3 + n \cdot u \cdot A_s (y - d')^2 + n \cdot A_s (d - y)^2 = 9.7 \times 10^8 \text{ mm}^4 \quad (17.35)$$

A bottom initial strain ε_0 is therefore obtained by using I_{id}:

$$\varepsilon_0 = \frac{M_{G_k}}{E_c I_{id}} (h - y) = 0.00032 \quad (17.36)$$

17.6.5 FRP-Strengthening Design Target

In this example, it is required that the resisting moment be increased by a factor *incr* = 150%, by applying prestressed FRP sheets:

$$m_{Rd,f} = 1.5 \cdot 0.175 = 0.263 \quad (17.37)$$

17.6.6 Strengthening with Prestressed FRP

As a first step, the FRP sheets are selected, having a design ultimate strain: $\varepsilon_{fd} = 0.02$. The prestressing device efficiency (or uncertainty) factor is taken as: $r = 0.8$.

17.6.7 Design Through Closed-Form Equations

The amount of FRP μ_f is found from Eq. 17.28 as:

$$\mu_f = 0.116 \quad (17.38)$$

while the prestress p_f to be applied is found from Eq. 17.29 as:

$$p_f = 0.18 \quad (17.39)$$

i.e. the FRP sheets are prestressed to reach 18% of the design ultimate strain, reduced by the efficiency factor *r*.

The neutral axis depth can be found from Eq. 17.26 as: $\xi = 0.233$, which fulfils the limitation of Eq. 17.23.

Note that, in this particular case, the tensile contributions to the total resisting moment are: 65% from the reinforcing steel and 35% from the prestressed FRP strengthening.

17.6.8 Dimensioning the FRP

The selected FRP design strength is: $f_{fd} = 3{,}500$ N/mm^2 and its elastic modulus results in: $E_f = 175$ GPa.

The FRP area from Eq. 17.30 is therefore equal to: $A_f = 49.1$ mm^2.
If one chooses a sheet with
width: $b_f = 0.5 \cdot b_c = 150$ mm,
thickness: $t_f = 0.167$ mm,
area: $(150 \cdot 0{,}167) = 25{,}05\, mm^2$ per layer,
the number of layers needed is then: $n_f = 2$.

The applied prestress is found from Eq. 17.31 as: $\sigma_{fp} = 506$ N/mm^2, for a total force applied, from Eq. 17.32: $P_{fp} = 24.8$ kN. Note that this increases the compressive stress in concrete by only 0.2 N/mm^2.

17.7 Concluding Remarks

A machine has been illustrated, able to properly seize and prestress with accuracy FRP layers in the shape of fabrics. The device is easily handled, reusable and adjustable to the local work conditions and design needs.

Prestress level and total stress in the fabric are continuously monitored and easily adjustable to the specific design needs. They can be varied along the length of the member to be strengthened.

A design procedure of immediate use for professionals is proposed, which allows for determining, by use of closed-form equations, the amount of FRP and the prestressing level that provide weak RC flexural members with the required moment resistance increase.

Acknowledgments The support of Roberto Marnetto and T.I.S. SpA, for the development and the realization of the machine, is appreciated. This work has been funded by the Italian government program "DPC – Consorzio RELUIS".

References

Andrä HP, Maier M (1999) Poststrengthening of RC structures by prestressed externally bonded CFRP strips. Structural faults and repair 99 M.C. Forde ed, 8th International Conference "Extending the Life of Bridges, Civil + Building Structures" London

CEN (2004) EN 1992-1-1:2004. Eurocode 2: design of concrete structures – part 1.1: general rules and rules for buildings, Comite Europeen de Normalisation, Brussels

Deuring M (1993) Bericht Nr 224. Verstarken von Stahlbeton mit gespännten Faserverbundwerkstoffen. EMPA, Dubendorf

Luke PS, Leeming MB, Skwarski AJ (1998) Robust results for carbon fibre. Concr Eng Int 2(2):19–21

Monti G, Liotta MA (2006) Pretension of externally bonded FRP sheets for flexural reinforcement of RC beams: methods and design equations. In: 2nd fib congress, Naples, 2006, pp 5–8

Saadtmanesh H, Ehsani MR (1991) RC beams strengthened with GFRP plates. I: experimental study. J Struct Eng ASCE 117(11):3417–3433

Triantafillou TC, Deskovic N (1991) Innovative prestressing with FRP sheets: mechanics of short-term behavior. J Eng Mech 117(7):1652–1672

Triantafillou TC, Deskovic N, Deuring M (1992) Strengthening of concrete structures with prestressed fibre reinforced plastic sheets. ACI Struct J 89(3):235–244

Wight RG, Green MF, Erki MA (2001) Prestressed FRP sheets for postrengthening reinforced concrete beams. J Compos Constr 5:215–220

Chapter 18
Assessment of the Fire Damage of Concrete Members after Fire Exposure

Emmanuel Annerel and Luc Taerwe

Abstract An adequate assessment of the fire damage of concrete structures exposed to fire is necessary for calculating the remaining load bearing capacity and for executing an appropriate repair. This paper describes several techniques to assess the internal concrete damage, such as colorimetry, microscopy and water immersion. On the other hand, the residual compressive strength is studied. This strength is influenced by the post-cooling storage conditions and may suffer from additional strength losses of up to 20%. Once the temperature distribution in the concrete is known, the residual capacity of a concrete element can be calculated. The use of the finite element program TNO DIANA in combination with simple calculations is illustrated for a concrete girder exposed to a real fire and afterwards repaired with shotcrete.

18.1 Introduction

Generally, concrete structures have a very good fire resistance. Although damage to the concrete gradually appears with increasing temperature, it is possible to repair the structure after an adequate assessment. To do this in a systematic way, knowledge is necessary concerning residual material properties and methods to assess this strength. Since the residual strength is temperature dependent, methods may be used to assess the strength indirectly by measuring the alteration in the material as a function of the temperature. A paper by Annerel (Annerel and Taerwe 2007) illustrates how cracks appear and the colour of the concrete changes from red (300–600°C) to whitish grey (600–900°C) and buff (900–1,000°C). Once these temperatures are

E. Annerel (✉) • L. Taerwe
Faculty of Engineering and Architecture, Department of Structural Engineering, Magnel Laboratory for Concrete Research, Ghent University, Technologiepark-Zwijnaarde 904, B-9052 Zwijnaarde, Belgium
e-mail: emmanuel.annerel@ugent.be; luc.taerwe@ugent.be

M.N. Fardis (ed.), *Innovative Materials and Techniques in Concrete Construction: ACES Workshop*, DOI 10.1007/978-94-007-1997-2_18,

Table 18.1 Concrete mix design [m³]

	SCC Siliceous	TC siliceous	TCk calcareous
Sand [kg/m³]	782	640	663
Gravel 2–8 mm [kg/m³]	300	525	–
Gravel 8–16 mm [kg/m³]	340	700	–
Limestone 2/6	–	–	450
Limestone 6/20	–	–	759
Portland cement 52.5 [kg/m³]	400	350	350
Water [kg/m³]	192	165	165
Limestone powder [kg/m³]	300	–	–
Superplasticizer 1 [l/m³]	2.90	–	–
Superplasticizer 2 [l/m³]	–	–	–
W/C [-]	0.48	0.47	0.47
$f_{c,cub,\ 28\ days}$ [N/mm²]	65.9	56.5	60.3

obtained, simple calculations based on EN 1992-1-2 (CEN 2004) may be used to determine the residual capacity of concrete elements, as elaborated in a paper by Taerwe et al. (2006) and Annerel and Taerwe (2009a).

18.2 Concrete Mix

Table 18.1 summarizes the mix design of a self-compacting concrete (SCC), a traditional vibrated concrete with siliceous aggregates (TC) and calcareous aggregates (TCk). Cubes of 150 mm were cured for 4 weeks in an air-conditioned room at a RH>90% and a temperature of 20 ± 1°C, after which they were stored at 60% RH and 20 ± 1°C for drying until testing age (>17 weeks).

18.3 Residual Strength

During the 3 weeks before the heating test, the SCC cubes were dried at 105°C to avoid explosive spalling. Two cubes of SCC and TC were heated for each of the examined temperature levels (till 800°C), occurring at a heating rate of 3.5°C/min. The target temperature was kept constant for 750 min, after which the cubes were slowly cooled in ambient air after removal from the furnace.

Figure 18.1 shows compares the results with the curves in EN 1992-1-2 (CEN 2004).

Tests are executed to determine separately the influence of the heating rate, duration and cooling method on the residual strength at 0 days after heating to 350°C and 550°C (Annerel and Taerwe 2007). The heating rate is changed to 10°C/min for TC and 20°C/min for SCC. The duration at the target temperature is altered to

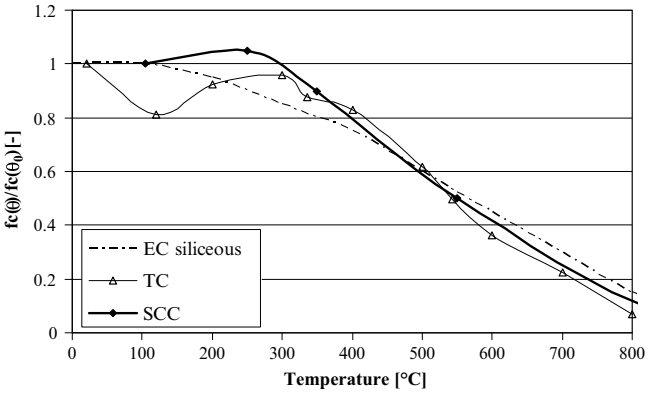

Fig. 18.1 Residual compressive strength

3,600 min and the cooling regime is modified into a rapid cooling by quenching under water. Results show that only the cooling method is an important parameter to consider, resulting in an extra drop of the residual strength of 30–35%.

The residual strength is also influenced by the storage conditions after fire. Therefore, 150 mm cubes of TCk are heated to different target temperatures according to the standard conditions as mentioned before. The cubes are tested for compressive strength immediately after cooling and after a storage period of 28 days at RH 60% and 20 ± 1°C. Furthermore, TC cylinders (with a diameter of 113 mm and height of 320 mm) are heated at a rate of 1°C/min, kept for 750 min at target temperature and slowly cooled in the oven. These cylinders are tested for compressive strength immediately after cooling and after storage for 12 weeks at RH 60% and 20 ± 1°C.

The results of the compressive tests are given in Fig. 18.2. Above 200°C an additional strength decrease compared to the strength loss immediately after cooling of about 20% is found for both the TCk cubes and TC cylinders. These experiments have been repeated for 350°C and 550°C, after which they were stored under water and ambient air (Annerel and Taerwe 2007). Again an additional strength decrease of 20–30% was perceptible after approximately 7 days of storage, from which point onwards the strength slowly recovers. Strength recovery of up to 10% was found when storing for 56 days.

Notice that during heating the concrete expands, according to its thermal expansion coefficient. After cooling, a part of this expansion is irrecoverable. The deformation is measured after cooling with a ruler. For TC2k-5 the deformation is measured for 0 and 28 days after cooling. During this storage period under constant climate conditions of 60% RH and 20 ± 1°C, the concrete has absorbed an amount of moisture and the volume has increased further. A linear relationship is found between both alterations ($R^2 = 0.998$). The absorbed water and volume increase are both around 0.40% in the temperature range 200–400°C and 0.70% in the range 500–600°C when compared to a non-heated reference cube.

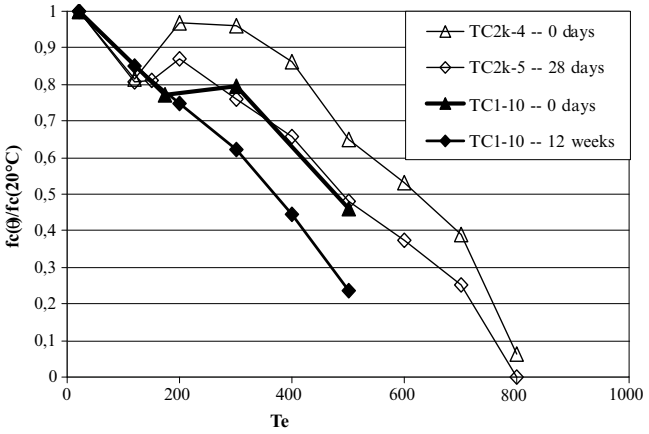

Fig. 18.2 Further strength decrease and recovery of TC2k cubes and TC1 cylinders due to storage (60% RH and 20 ± 1°C) after heating

18.4 Assessment of the Temperature Profile

18.4.1 Colorimetry

The colour is measured with an X-rite SP60 spectrophotometer (aperture 8 mm) according to the CIE Lab-colour space. In this colour system 'L' is the lightness with values between 0 (black) and 100 (white), 'a' is spread between magenta (positive values) and green (negative values) and 'b' is positioned between yellow (positive values) and blue (negative values). Figure 18.3 shows how the colour measured on heated TC concrete describes a path in the a*b*-colour space. The measurements are executed immediately after cooling down to ambient temperature.

If the concrete cubes are stored under RH 60% and at temperatures of 20 ± 1°C for several weeks, a shift towards the inner part of the ellipse is found (Annerel and Taerwe 2007). This shift can probably be attributed to the moisture absorption, because a linear relationship between the colour change (L*, a*, b*) and the weight increase exist with a R^2-value of 0.7–0.8. Further studies are executed on TC and SCC samples cut from drilled cores, after polishing and masking of the colourful aggregates (Annerel and Taerwe 2007).

18.4.2 Microscopy

Microscopy can also help to determine the fire damage caused at a concrete structure. According to (Larbi and Nijland 2001; Annerel and Taerwe 2009b) several degradation periods can be seen under the polarising and fluorescent microscope.

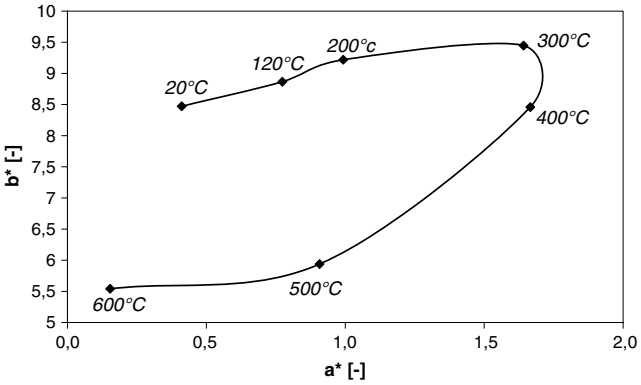

Fig. 18.3 Elliptical colour path in a*b*

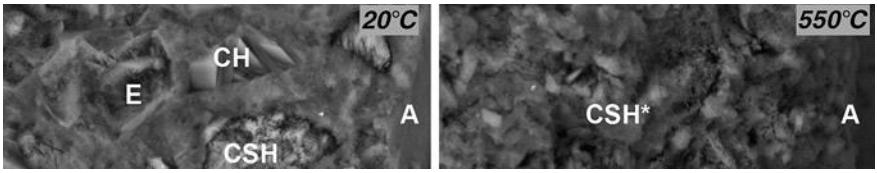

Fig. 18.4 ESEM images of ordinary Portland concrete at 20°C (*left*) and heated up to 550°C (*right*). E = ettringite, CH = portlandite, CSH* = temperature modified CSH and A = aggregate

Not only the change in fluorescence intensity above 100°C, the dissociation of ettringite (>70°C), but also the oxidation of the iron in the siliceous aggregates at 350°C and the disappearance of the portlandite in the temperature region 450–500°C can be clearly noticed. However, under the electron microscope this dissociation process can be seen in more detail (Fig. 18.4).

These images are taken at the interfacial transition zone of traditional, Portland cement based concrete. At 20°C the bonding between the cement matrix and the aggregate is good and shows a lot of portlandite, CSH and ettringite. At 350°C the ettringite is dissociated and an interfacial crack is visible, while at 550°C even the portlandite is depleted in the cement matrix resulting in a more porous matrix.

18.4.3 Water Immersion

Heating of concrete introduces stresses, resulting in cracks. Meanwhile, chemical alterations, such as dehydration and decarbonation, lead to disappearing of the hydration products, which increase the pore space (Fig. 18.4). Both effects lead to an increase in the porosity when heating concrete. Note that immersion of concrete under water will fill the pores and cracks with water. The weight increase can then be used to assess the internal damage due to heating.

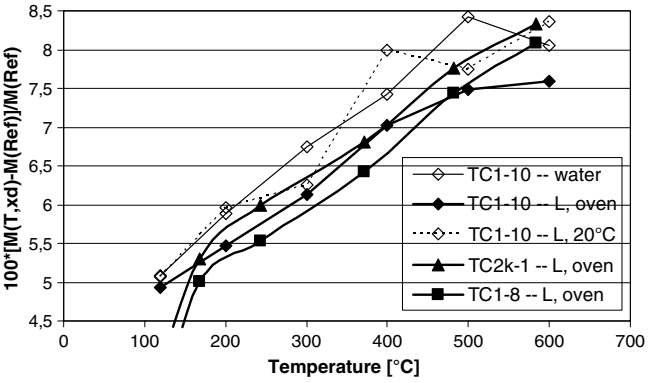

Fig. 18.5 Water immersion

The total water absorption can be defined as the difference in weight after storage under water and a reference weight, for instance the weight at uniform target temperature ($M_{0d,hot}$). After 7 days the weight increase flattens. $M_{0d,hot}$ can be determined from the heated sample itself by drying it till constant mass is achieved. Drying is necessary to eliminate the moisture due to climatic circumstances. New-made hydration products which may fill some small cracks and thus may hinder the water absorption are neglected in this method. Under lab conditions, this weight is measured during the test when the concrete is at target temperature or after cooling down to 60°C.

Figure 18.5 illustrates the water immersion of half cubes (TC1-8, TC2k-1) and small discs (TC1-10) with 80 mm diameter and 15 mm height. These results are transformed in percentages by dividing with the reference weight $M_{0d,hot}$. For the discs, different cooling methods are used: (1) slowly cooling in the oven ('L, oven'); (2) cooling outside the oven at ambient air ('L, 20°C'); (3) cooling by quenching into water ('Water'). The results on half cubes and small discs are comparable, as is visible on the water absorption for specimens slowly cooled in the oven.

18.5 Finite Element Temperature Simulation

In the 1970s an industrial hall in precast concrete elements was erected especially to submit it to a real scale fire test. This experiment was executed in order to gain knowledge about the behaviour of such a building. During the test, the temperature was recorded with several thermocouples. After the fire, a pretensioned concrete girder was removed from the building, was repaired by shotcreting and submitted to a static loading test up to failure. The girder collapsed at a maximum bending moment of 1,632 kNm, corresponding to four point loads of 162 kN. Figure 18.6 shows the fire damage of the girder, before repair.

The roof girder is modelled in the finite element program TNO DIANA to obtain the temperature distribution inside the concrete. This 2D heat flow analysis is

Fig. 18.6 Fire damage of pretensioned IV girder

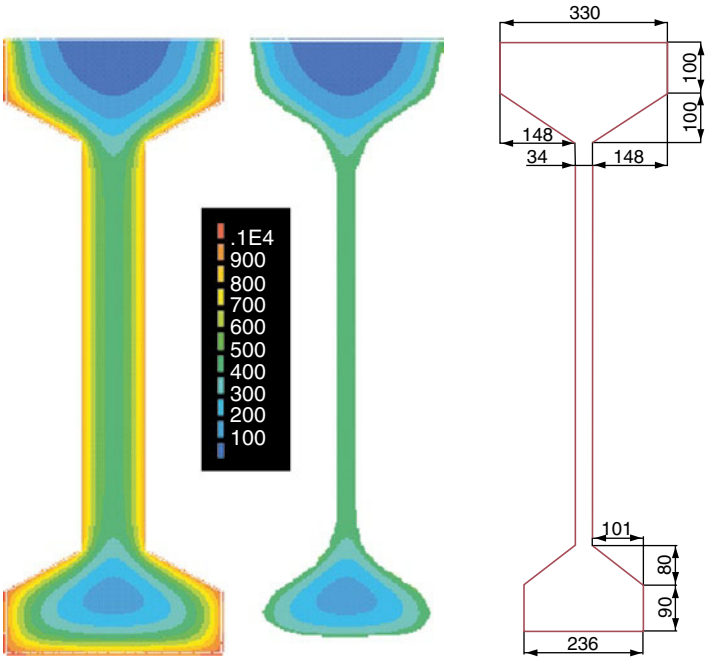

Fig. 18.7 Temperature distribution in girder (*left*) and area with temperatures lower than 500°C (*centre and right*)

simulated by using the thermal material properties as outlined in EN 1992-1-2 (CEN 2004) for siliceous concrete. The fire load taken to occur conform to the ISO834 curve and also according to the surface temperature of the roof beam measured during the fire test. Figure 18.7 (left) illustrates the temperatures reached inside the concrete after 90 min of fire exposure. Rough interpolation yields that the real fire after 90 min has almost the same effect inside the cross section as the ISO curve after 85 min.

The maximum bending moment before, during and after the fire is calculated according to EN 1992-1-2 by using reduction coefficients $k_p(\theta)$. Before the fire, the calculated resistance capacity is 1,855 kNm. During the fire, this capacity drops to

57% when using the 500°C method (Fig. 18.7, centre and right). After repairing and for the four point loads, the calculated capacity is 1,604 kNm, which is comparable to the result obtained from the loading test. This experiment illustrates how after repair a girder can recover 86% of its original strength.

18.6 Conclusions

The residual strength is mainly influenced by the temperature during heating, the way of cooling and the time of storage after fire. Water cooling may induce an additional reduction of the compressive strength of 30–35%, whereas post-cooling storage also results in strength loss of up to 20–30%.

When concrete has been heated, the colour changes according to a colour path in the a*b*-colour space and shifts to the inner part as a function of moisture absorption. Colour analysis provides an adequate basis to assess the temperature history of concrete.

The change in porosity, measured by water immersion, seems to be a good indicator to estimate the maximum temperature which was reached in the heated concrete.

Combination of finite element techniques and simple calculations show how the strength of a girder evolves before, during and after a fire.

Acknowledgements The authors would like to thank the Fund for Scientific Research in Flanders (FWO) for the financial support through the research grant "Damage assessment and estimation of the residual strength of concrete members after exposure to fire".

References

Annerel E, Taerwe L (2007) Approaches for the assessment of the residual strength of concrete exposed to fire. In: Proceedings of the international workshop fire design of concrete structures, from materials modelling to structural performance, Coimbra, 8–9 Nov 2007, pp 489–500

Annerel E, Taerwe L (2009a) Load bearing capacity of precast elements after fire. In: 1st international workshop on concrete spalling due to fire exposure: from real life experiences and practical applications to lab-scale investigations and numerical modeling, Leipzig, 2009, pp 41–51

Annerel E, Taerwe L (2009b) Revealing the temperature history in concrete after fire exposure by microscopic analysis. Cem Concr Res 39(12):1239–1249

CEN (2004) EN 1992-1-2:2004. Eurocode 2: design of concrete structures – Part 1.2: structural fire design. Comite Europeen de Normalisation, Brussels

Larbi JA, Nijland TG (2001) Unravelling the temperature distribution in fire-damaged concrete by means of PFM microscopy: outline of the approach and review of potentially useful reactions. HERON 46(4):253–264

Taerwe L, Poppe AM, Annerel E, Vandevelde P (2006) Structural assessment of a pretensioned concrete girder after fire exposure. In: Proceedings of the 2nd fib Congress, Naples, 5–8 June 2006

Chapter 19
Robustness of Shrinkage-Compensating Repair Concretes

Pierre-Vincent Certain, Benoît Bissonnette, Josée Bastien, Jacques Marchand, and Marc Jolin

Abstract Drying shrinkage is one of the least desirable properties of repair concrete, because in restrained conditions, it may lead to shrinkage cracking and thus adversely affect its durability. Shrinkage compensating concretes (ShCCs) made with expansive mineral admixture represent an attractive alternative to prevent shrinkage cracking. This paper outlines a project devoted to the study of ShCC repair material robustness as a function of selected parameters. Two types of expansive agents were used, a calcium sulfoaluminate-based admixture (Type K) and a calcium oxide-based (Type G) one. The assessment of robustness addressed the influence of both the mixture design parameters (cement composition, type and dosage of expansive agent, w/cm ratio) and the curing conditions (moist curing conditions, temperature) upon the ShCC expansive behavior, the bond between ShCC repairs and concrete substrates, and ShCC frost durability. Overall, the results yielded in this study demonstrate interesting potential of ShCCs as crack-resistant and durable repair materials.

19.1 Introduction

A study by the U.S. Army Corps of Engineers (McDonald and Campbell 1985) showed that about 50% of concrete repairs do not achieve satisfying performance and need to be redone after a short period of time. One of the main problems impairing repair durability is cracking induced by drying shrinkage.

P.-V. Certain
Département de génie civil, LCM, École Polytechnique Fédérale de Lausanne,
1015 Lausanne, Switzerland
e-mail: pierre-vincent.certain@epfl.ch

B. Bissonnette (✉) • J. Bastien • J. Marchand • M. Jolin
Département de génie civil, CRIB, Université Laval, Québec, QC G1K 7P4, Canada
e-mail: benoit.bissonnette@gci.ulaval.ca; josee.bastien@gci.ulaval.ca;
jacques.marchand@gci.ulaval.ca; marc.jolin@gci.ulaval.ca

M.N. Fardis (ed.), *Innovative Materials and Techniques in Concrete Construction: ACES Workshop*, DOI 10.1007/978-94-007-1997-2_19,

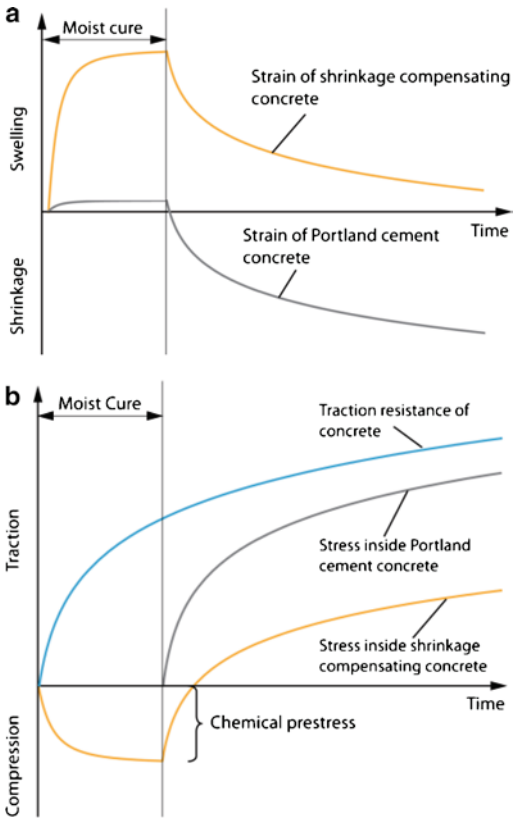

Fig. 19.1 Typical length change evolution and stress development in ordinary concrete and ShCC: (**a**) unrestrained length change behavior; (**b**) stress development in restrained conditions

Actually, dimensional compatibility is among the greatest challenges with regards to concrete repair materials. The bond between old and new concrete creates a confined environment where the individual dimensional variations are restrained. This situation can lead to significant distresses in the repair, such as cracking, debonding and delaminating. During the process of selecting the right repair material, Emmons (1994) states that drying shrinkage is a critical factor and that whenever possible, repair materials subject to as low as possible drying shrinkage should be opted for.

In fact, the use of shrinkage-compensating concrete (ShCC) allows achieving a zero dimensional balance with respect to drying shrinkage, through the use of a mineral expansive agent (Fig. 19.1) (Bissonnette et al. 2008). During hydration, the expansive agent reaction induces expansive forces within the cement paste, leading to a net macroscopic volume increase. When the material is exposed to drying, shrinkage gradually offsets the initial expansion, resulting in a close-to-zero dimensional balance if the expansive agent content is properly adjusted. In restrained movement conditions, the expansion induces a compressive stress ("*chemical prestress*"), which subsequently is relieved by the tensile stress induced by the drying shrinkage when the material is exposed to a lower relative humidity. This allows to prevent or

at least limit the occurrence of net tensile stresses in the repair material, and thereby to reduce the risk of crack development.

19.2 Experimental Program

The experimental program aimed at assessing the robustness of ShCC used as repair material with respect to the following three aspects:

- shrinkage compensation effectiveness (dimensional and stress balance) of various mixture designs;
- bond development in a repair system;
- frost durability.

19.2.1 Dimensional Balance

The first phase of the project consisted in evaluating the influence of specific mixture design characteristics and curing conditions upon ShCC shrinkage compensation.

The investigated mixture design variables were the cement composition, the expansive agent type and dosage, and the water to binder ratio. The influence of the Portland cement composition was investigated using ASTM Type I cements from different manufacturers (cement "a", cement "b", cement "c"). Two types of expansive agents were used: a calcium sulfoaluminate-based admixture (Type K) and a calcium oxide-based one (Type G). For each type, a low and a high dosage was used, i.e. 10% and 16% for Type K, and 3% and 8% for Type G respectively. The various binder-expansive agent combinations were studied for two different water to binder ratios, 0.40 and 0.50.

The influence of exposure conditions after demolding was studied by curing the specimens for 7 days in lime-saturated water at different temperatures (5°C, 23°C or 38°C). In this part of the work (exposure conditions), only the mixtures prepared with cement "a" were tested.

The unrestrained and restrained dimensional balances have been evaluated in accordance with test procedures adapted from ASTM C 157 and ASTM C 878. The test modification essentially concerns the time of demolding, the specimens being demolded 8 ± 1 h after initial water/cement contact.

19.2.2 Bond Development in Repair Systems

In a repair, the influence of ShCC material expansion upon bond development can draw legitimate concerns. To investigate bond development between ShCC repairs and ordinary concrete, a range of ShCC mixtures were placed on concrete base

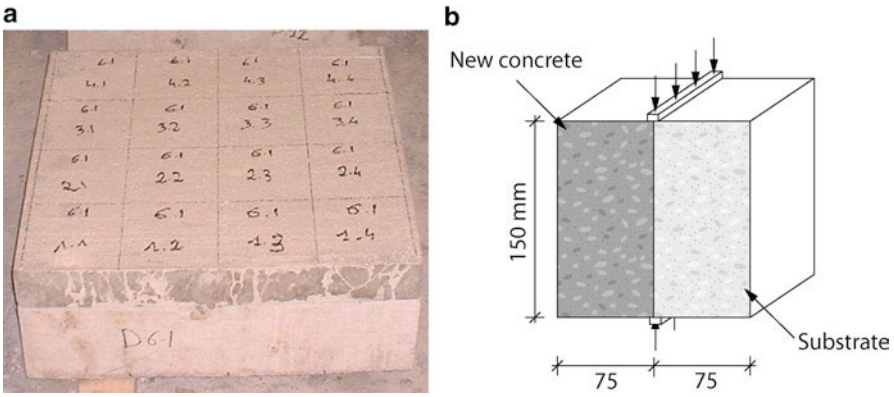

Fig. 19.2 Splitting-tensile bond strength testing: (**a**) repaired concrete slab (repaired slab was subsequently sawn into 150×150×150 mm test cubes); (**b**) splitting-tensile bond strength experiment scheme

slabs (600×600×150 mm slabs cast with the same concrete mixture from a single batch and conditioned for 1 year before the experiments).

The following ShCC-mixture proportions were studied:

- w/cm ratio (0.40 or 0.50);
- cement composition (cement "a" and cement "b");
- type and dosage of expansive agent(no agent, Type G [3%, 8%], Type K [16%]).

Prior to the addition of ShCC, all substrate surfaces were slightly roughened by means of high-pressure water jetting. Given the influence of water availability upon ShCC expansion, each of the tested mixtures was laid on a "wet" and a "dry" substrate. The "wet" substrates were humidified during 5 days prior to ShCC placement. In case of the "dry" substrates, the storage of the slabs at approximately 50% RH (20°C) was extended for at least 1 week following the water jetting procedure.

After the ShCC placement (layer thickness: 75 mm), the specimens were cured under wet burlaps and plastic sheets during 1 week. They were then air-cured at approximately 50% RH (20°C) for three more weeks. At the end of the curing period, the specimens were sawn into 150×150×150-mm composite cubes. Bond strength was determined subsequently on these cubes by means of tensile-splitting bond tests (Fig. 19.2).

The mixture design identification key used in this part is the following:

Cement	*w/c* ratio	Expansive agent type and dosage
Gua: cement "a"	4:0.40	G3:Type G 3%
Gub: cement "b"	5:0.50	G8:Type G 8%
Guc: cement "c"		K10:Type K 10%
		K16:Type K 16%
Example: **Gua 4 G8**		

19.2.3 Frost Durability

In order to assess the durability of ShCC with regards to freezing and thawing resistance, modified ASTM C 666 tests were performed. Again, the modification essentially concerns the time of demolding, the specimens being demolded 8 ± 1 h after initial water/cement contact. The investigated variables were the type of expansive agent and the moist curing conditions. ShCC mixtures were prepared with the high dosage of expansive agent (16% of Type K, and 8% of Type G), cement "a", and a w/cm ratio of 0.40. The test specimens were moist cured for 7 days at 23°C, either in lime-saturated water or at 50% RH.

19.3 Results and Discussion

19.3.1 Dimensional Balance

The test results showing the influence of the cement composition upon the free expansion are presented in Fig. 19.3. Concerning the ShCC mixtures prepared with low dosages of either expansive agent, the cement composition seems to exert some influence on the development of expansion, but it is overall moderate. When the dosages are in fact increased to the maximum recommended dosages, the results show that there is virtually no effect of the cement composition, either with Type K or Type G.

It can be noticed that the two types of expansive agents yield quite different expansion kinetics. With Type G, the expansion takes place within approximately 2 days, while in Type K-based mixtures, the expansion potential does not seem to be fully exhausted at the end of the 7-days curing period.

The results related to the influence of the curing temperature upon free expansion are presented in Fig. 19.4. Temperature influences both the magnitude and the rate of expansion. The slope of the curve during the expansion phase increases with the temperature. The ultimate expansion also depends on temperature. For the Type K-based ShCC mixture, the expansion in the specimens cured at 38°C occurs faster and vanishes sooner than in the specimens cured at 23°C and 5°C. In the Type G-based mixture specimens cured at 38°C, the final strain at the end of the curing time is just shy of 4,500 μm/m, nearly three times the maximum expansion strain recorded for that mixture at 23°C.

The results of the free length change tests performed under different moist curing conditions are presented in Fig. 19.5. The influence of water curing on the expansive reaction is clearly demonstrated for both expansive systems investigated. It is actually more critical in Type K-based ShCCs, as virtually no net expansion is generated under 50% RH moist conditions. In the Type G-based mixture, the expansion still occurs at 50% RH, but the magnitude is three times lower than the value reached in water.

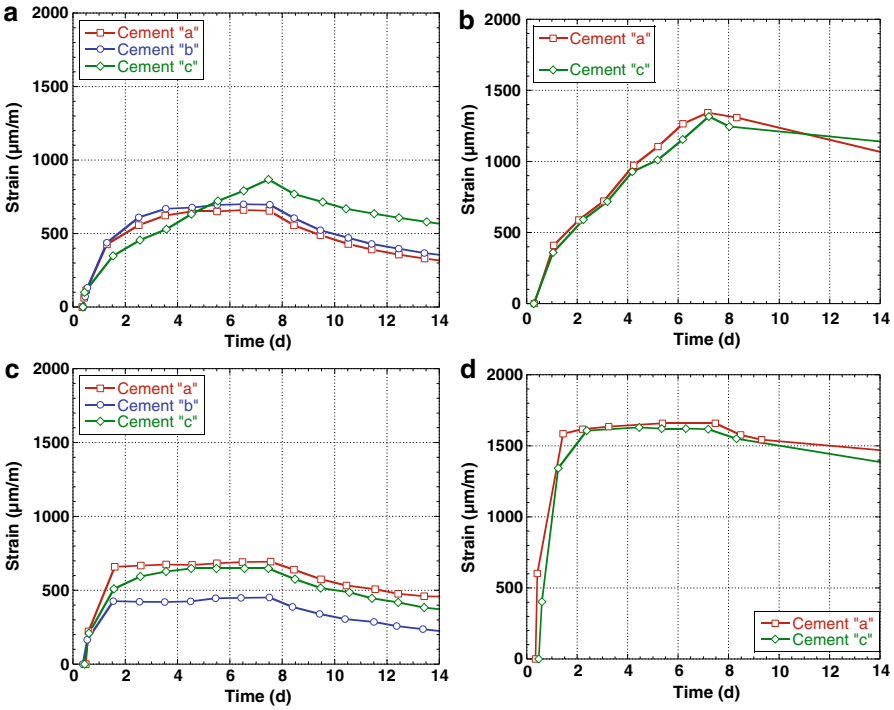

Fig. 19.3 Influence of cement composition upon free expansion: (**a**) Type K 10%; (**b**) Type K 16%; (**c**) Type G 3%; (**d**) Type G 8% (note: data with Cement "b" data are not available for high expansive agent dosages)

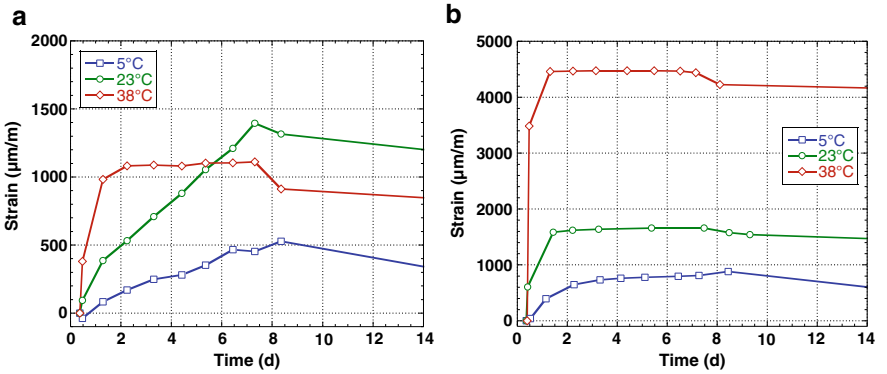

Fig. 19.4 Influence of curing temperature upon free expansion: (**a**) Type K 16%; (**b**) Type G 8%

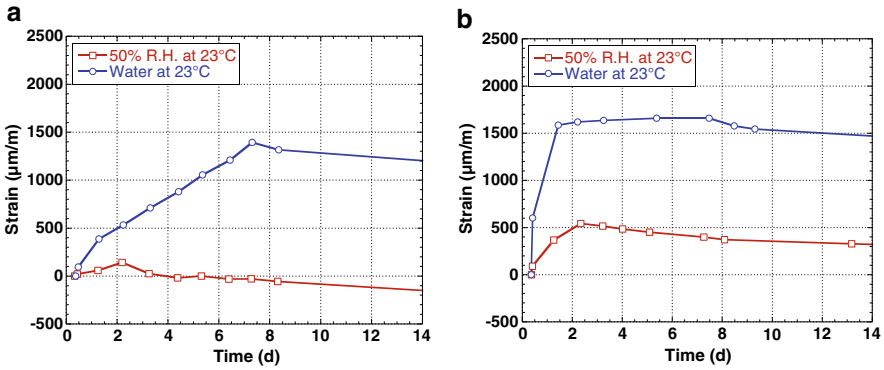

Fig. 19.5 Influence of moist curing condition upon free expansion: (**a**) Type K 16%; (**b**) Type G 8%

Table 19.1 Influence of curing temperature upon ShCC stress balance

Concrete mixture	Curing temperature (°C)	Stress balance (MPa)
Type K (16%)	5	+0.10
	23	−0.01
	38	−0.30
Type G (8%)	5	+0.09
	23	−0.09
	38	−0.18

The stress balance was evaluated using the results of restrained length change tests. The stress is calculated with the following equation:

$$\sigma_c = -\frac{A_s}{A_c} E_s \varepsilon_s \tag{19.1}$$

In this expression, σ_c is the stress induced in the concrete sample, A_s is the reinforcing steel cross-sectional on area, A_c is the concrete specimen cross-sectional area, E_s is the steel elastic modulus, and ε_s is the recorded steel strain.

The stress balance is calculated as the difference between the stress at the end of the moist curing period ("chemical prestress") and the long-term stress (at the end of the drying period), based on the restrained length change test results.

The calculated stress balance data are summarized Tables 19.1 and 19.2. A positive stress balance indicates that the concrete specimen is in tension, whereas a negative balance indicates compression. In a properly designed ShCC mixture, the stress balance should ultimately be negative or close to zero, which would indicate that drying shrinkage is fully compensated.

The influence of temperature on the stress balance is consistent with the trends observed for the free length change data. At the lowest temperature (5°C), the drying shrinkage stresses are not fully compensated.

Table 19.2 Influence of curing moisture upon ShCC stress balance

Concrete mixture	Moist curing conditions	Stress balance (MPa)
Type K (16%)	50% RH	+0.18
	Water	−0.01
Type G (8%)	50% RH	+0.04
	Water	−0.07

Table 19.3 Compressive strength test results at 28 days (ShCC with cement "a" and 0.40 w/cm)

		28 day compressive strength (MPa)	
		Moist curing conditions	
		7 days in water	
Concrete mixture	Curing temperature (°C)	21 days at 50% RH	28 days in water
Type K (16%)	5	30.5	51.0
	23	36.0	52.0
	38	44.0	56.5
Type G (8%)	5	34.0	44.5
	23	38.5	41.0
	38	36.5	40.5

The calculated stress balance values indicate that in specimens moist cured at 50% RH, irrespective of the type of expansive agent, the stress induced during the expansion phase is not high enough to fully compensate the effect of drying shrinkage.

The 28 day compressive strength test results for the ShCC mixtures prepared with cement "a", 0.40 w/cm and high expansive agent dosages are summarized in Table 19.3. In prolonged moist curing conditions, Type K-based mixtures develop higher compressive strength values, but when the specimens are exposed to drying at 7 days, it is comparable to those recorded for the Type G-based mixtures. Overall, temperature has little influence on the compressive strength of these systems, except maybe for Type K-based mixtures where moist curing is interrupted at 7 days. In such case, the acceleration of hydration due to temperature in the first few days results in a higher 28 day compressive strength. It can be further concluded that continued expansion in water with Type K expansive agent is not detrimental to the material integrity and strength, at least when it occurs in the first 28 days.

19.3.2 Bond Development in Repair Systems

The test results are presented in a bar chart in Fig. 19.6. In most cases (352 of the 384 tensile splitting test composite cubes), failure occurred partly or completely in the substrate. The result variability is quite low and the tensile splitting bond strength values recorded for the composite specimens are actually very close to the substrate

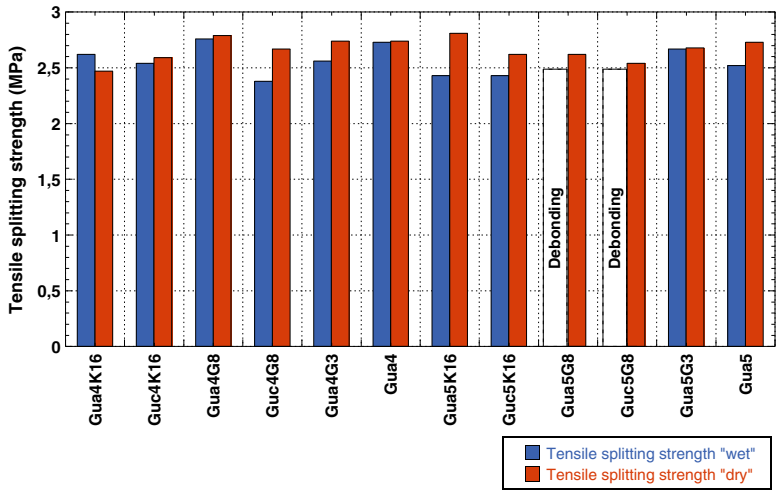

Fig. 19.6 Tensile splitting bond strength recorded on composite test cubes (old/new concrete)

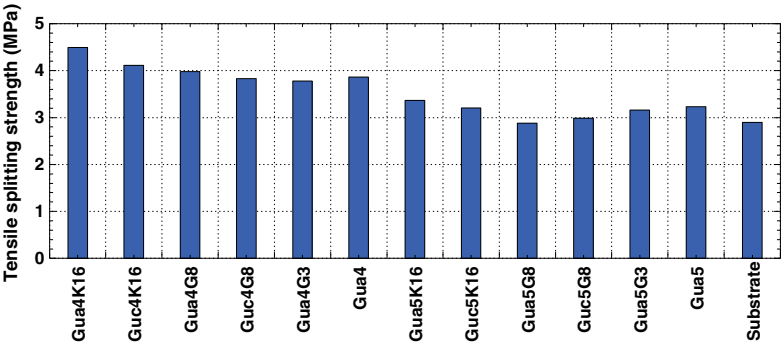

Fig. 19.7 Tensile splitting strength results for the base slab mixture and the ShCC mixtures

concrete tensile splitting strength (Fig. 19.7). It means that bond development was overall very effective (except for the specific combination discussed in the previous paragraph) and ultimately, since the tensile strength of the substrate concrete is lower than that of the repair concretes, failure is predominantly initiated in the substrate.

For the following parameter combination, the ShCC layer debonded completely prior to sawing the slabs into cubes:

- Type G agent at 8%;
- $w/c = 0.50$;
- "wet" substrate.

One of the substrate slabs on which debonding occurred was re-used to repeat the experiment (same parameter combination), after adequate surface preparation was achieved to restore similar surface characteristics. The same outcome was reached.

Table 19.4 Freeze/thaw resistance test results (after 300 cycles)

Concrete mixture		Air content (%)	Dynamic modulus (%)	Deformation (%)
Type K (16%)	Air curing (50% RH)	6.5	96.2	0.072
	Moist curing	6.5	67.6	0.055
Type G (8%)	Air curing (50% RH)	7.0	89.5	–0.016
	Moist curing	6.5	58.0	–0.004
Allowable limits[a]		**4–8**	**60.0**	**0.06**

[a]ASTM C 666

Based on impact-echo test monitoring data recorded from the time of casting, it could be assessed that "debonding" occurred during the wet-curing period. Possible explanations are therefore that debonding was caused by the early high-magnitude expansion or, more likely, that this specific combination of conditions (high lime-based agent dosage and high water contents in both the mixture and the substrate) led to very extensive precipitation of Portlandite over the surface and hindered bond formation between the forming CSH and the substrate.

19.3.3 Frost Durability

The freeze-thaw resistance test results are presented in Table 19.4. All tested mixtures had an air content above 6.5%.

The recorded dynamic modulus values suggest that moist curing is harmful towards ShCC's frost durability, with values close to the limits allowed by the ASTM C 666 standard. These results suggest that early-age expansion has a negative impact on the freeze/thaw resistance of ShCC, as the air-cured samples, which exhibited limited expansion (Fig. 19.5), fared better in the tests. Nevertheless, caution is required in analyzing these results, as the hardened concrete air-void characteristics were not assessed. Further testing is required for more conclusive assessment.

Regarding the deformations recorded after 300 cycles, it should be stressed that the Type K-based mixtures underwent signicant expansion during the test duration, essentially as a result of continued expansive agent hydration.

19.4 Conclusion

Overall, the results of this study demonstrate the potential of ShCCs as crack-resistant and durable repair materials. The main findings of this study are the following:

- Both the Type K and Type G agents are effective in fully compensating drying shrinkage. However, the curing temperature significantly influences the expansion kinetics and magnitude, such that at low temperatures, the generated expansion is

not sufficient to compensate the subsequent drying shrinkage. Besides, the absence of moist curing negatively affects the expansion and thus the degree of shrinkage compensation.

- Except for one specific extreme case involving the Type G agent, the tensile splitting strength tests performed on composite test cubes showed adequate bonding between ShCC and the concrete substrate.
- The ShCC mixture designs tested showed acceptable resistance to freeze/thaw cycles, but further testing for conclusive assessment.

Acknowledgments This project has been financially supported by the Natural Sciences and Engineering Research Council of Canada (NSERC), the Québec FQRNT Research Fund and the industrial partners of the Industrial Chair on Durable Repair and Optimized Maintenance of Concrete Infrastructures at Laval University (BASF Building Systems, City of Montreal, City of Québec, Euclid, Holcim, Hydro-Québec, Kerneos, King Packaged Materials, Lafarge, Ministry of Transportation of Québec, W.R. Grace & Co.).

References

McDonald JE, Campbell RL (1985) The condition of corps of engineers civil works concrete structures, technical report REMR-CS-2, US army corps of engineers, Waterways Experiment Station, Vicksburg

Emmons PH (1994) Concrete repair and maintenance illustrated: problem analysis, repair strategy, techniques. R.S. Means Company, Kingston

Bissonnette B, Perez F, Blais S, Gagné R (2008) Évaluation des bétons à retrait compensé pour les travaux de réparation. Can J Civ Eng 35(7):716–726

Chapter 20
Design of Marine Concrete Structures

Tor Ole Olsen

Abstract Offshore concrete structures are durable and behave well, if properly built and properly designed. The importance of the early design phases is significant; this is when the competitiveness is established, and also the robustness of the structure to meet changes at later stages. The structures will float during stages. Redundancies are therefore expensive, and the meaning of robustness needs to be clearly understood. Generally, offshore concrete structures are heavily reinforced. Construction planning and management is important, and so is the close integration of construction and design. Offshore structures are subjected to very severe loadings, and increasingly more so as arctic frontiers are developed.

20.1 Introduction

There are some 50 offshore concrete structures servicing the oil and gas industry, most of them in the North Sea, but also in Asia, Australia and North America. Offshore concrete structures are durable and behave well, if properly built and properly designed. Many platforms have passed their intended design lives, many have got their functional duties enlarged, and many have shown a remarkable strength towards abnormal events. References (fib 2009; Sandvik et al. 2005) give a relatively general description of these structures.

Reference (Olsen et al. 2009) "Offshore Concrete Structures for tough Environments" was presented at the *fib* Symposium in London 2009. The presentation described the work being done by *fib* Task Group 1.5, which last year resulted in the *fib* state-of-the-art report "Concrete structures for oil and gas fields in hostile marine environments" (fib 2009).

T.O. Olsen (✉)
Dr.techn.Olav Olsen a.s., Dicks vei 10, 1325 Lysaker, Norway
e-mail: too@olavolsen.no

M.N. Fardis (ed.), *Innovative Materials and Techniques in Concrete Construction: ACES Workshop*, DOI 10.1007/978-94-007-1997-2_20,

Structural design is an important part of offshore concrete projects, and is performed stepwise with increasing accuracy and increasing extent. Before the structure is built, a comprehensive detailed design including reinforcement drawings and bar bending schedules will be performed. Before that, however, typically several design phases have been performed.

The importance of the early design phases is significant. This is when the competitiveness is established, and also the robustness of the structure to meet changes at later stages. Offshore structures are subjected to very severe loadings, and increasingly more so as arctic frontiers are developed. The structures will float during stages. Redundancies are therefore expensive, and the meaning of robustness needs to be clearly understood.

Typically, construction contracts are design-and-build contracts. Where this is the case, the quality of design performed in former phases is important.

The two latest completed offshore concrete projects are the two Sakhalin II platforms (installed in 2005) and the Adriatic Liquefied Natural Gas (LNG) Terminal (installed in 2008). Different structures with different specifications, they will hopefully fulfill the needs of their owners and of the society at large.

Plans for further oil and gas exploitation in ever increasing harsh environments have accelerated the focus and interest for the efficiency of offshore concrete structures, this being the prime reason for *fib* to do the work of Task Group 1.5 (Olsen et al. 2009). Currently a new project is under construction: the Sakhalin I platform, in Russia.

20.2 History and Background

Since the Ekofisk Tank was installed in 1973, 49 other major offshore concrete structures have been built or are being built. *fib* Bulletin 50 (fib 2009) provides a list of these structures.

Figure 20.1 shows the tow of Beryl A in 1975, from its construction in sheltered Norwegian fjords on its way to the harsh environment of the North Sea, illustrated in Fig. 20.2. Figures 20.1 and 20.2 illustrate some of the design criteria for offshore structures, and at the same time indicate why concrete may be the best choice of construction material.

Figure 20.2 illustrates that it is not possible to build structures offshore. They must be installed, however, and may have to be completed offshore with respect to the foundation (piling, grouting) and topside installation. The degree of inshore completion influences the cost and safety of the field development.

The typical offshore concrete structure is of the caisson type, often termed Concrete Gravity Structure (CGS). The caisson provides buoyancy in the construction and towing phases, and a foundation structure in the operational phase. In addition, the caisson may also provide storage volume for oil. This multiple usage of the structure may prove very economic, particularly when oil storage is required.

Steel structures may, of course, also be built to provide buoyancy and storage, but buoyancy at large water depth is demanding and expensive when using steel structures.

Fig. 20.1 Beryl A under tow to installation site, in 1975

Fig. 20.2 The environment of the sea

The nature of hydrodynamic loads is such that they are greatly reduced with increasing water depth. Therefore, a buoyancy structure deeply submerged may be far more efficient than one just below sea level. Most countries of the world have a construction industry for concrete structures; few have for large steel structures. This is a competitive edge for offshore concrete structures.

The inshore construction of concrete offshore structures provides good conditions for quality construction. The construction site of Norwegian Contractors at Hinna, near Stavanger in Norway, was likely the best and most professional and effective construction site in the world, including onshore sites. The design and construction of 15 Condeeps created a large amount of expertise. Figure 20.3 illustrates the Condeeps built by Norwegian Contractors. Dr.techn.Olav Olsen designed them, sometimes in collaboration with others.

Probably the most impressive Condeep is the Troll A platform, shown in Fig. 20.4. The platform is not used for oil storage, and was complete with topside when towed

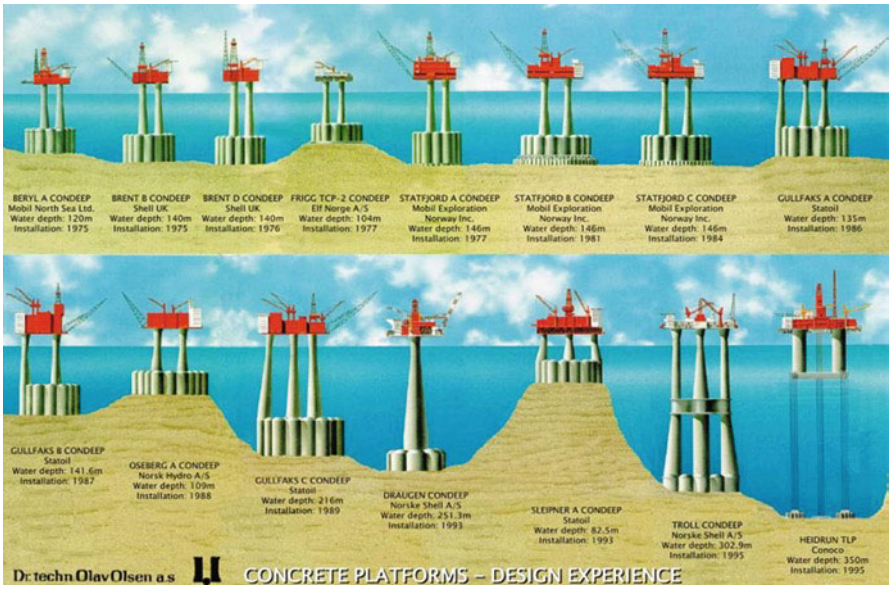

Fig. 20.3 The Condeeps

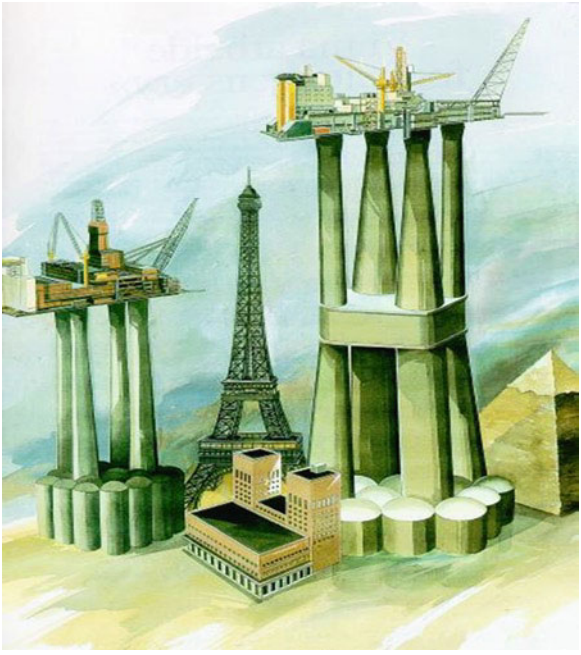

Fig. 20.4 The Troll A Condeep, compared with other structures

Fig. 20.5 The Troll A Condeep during tow-out

out and installed at 303 m water depth in the North Sea in 1995. Parts of the Troll A structure were subject to a water pressure of 3.5 MPa during construction, and carried the topside weight of 22,000 t 150 m above the sea level during tow-out, as shown in Fig. 20.5 above.

The deadweight of the platform is clearly of importance. A vessel must carry its own weight plus a payload. For the concrete platform the payload is the topside and equipment, as well as any ballast required for hydrostatic and/or geotechnical stability.

The significance of weight and strength is illustrated in Fig. 20.6 for a "unit" structure subjected to hydrostatic pressure (Jakobsen et al. 1987). The figure also demonstrates the importance and potential benefits of research. The pay-off of this research is tremendous. Jan Moksnes (Moksnes 2002) presents some of the results of Norwegian research on concrete over the past 20 years.

High strength concrete is required for efficient offshore concrete structures, at least when the loading is high. Equally important with structural efficiency is the performance of the material over time. It is evident from Fig. 20.2 that the environmental impact in terms of spray and seawater is extreme. Fortunately, high strength/high performance concrete is durable, and has proven so after many years in the North Sea and elsewhere.

A major project in Norway named "Bestandige Betongkonstruksjoner" (Durable Concrete Structures) has documented the very good quality of the offshore concrete structures of the North Sea. The project was primarily aimed at bridges, in particular those in the marine environment. For comparison and correlation a number of platforms were included, some of them with service lives up to 25 years in one of the harshest areas of the world, which were in fact longer than their intended design lives.

Inspections and measurements document that the concrete in the offshore platforms is not flawless. But when the intended quality of concrete and cover to

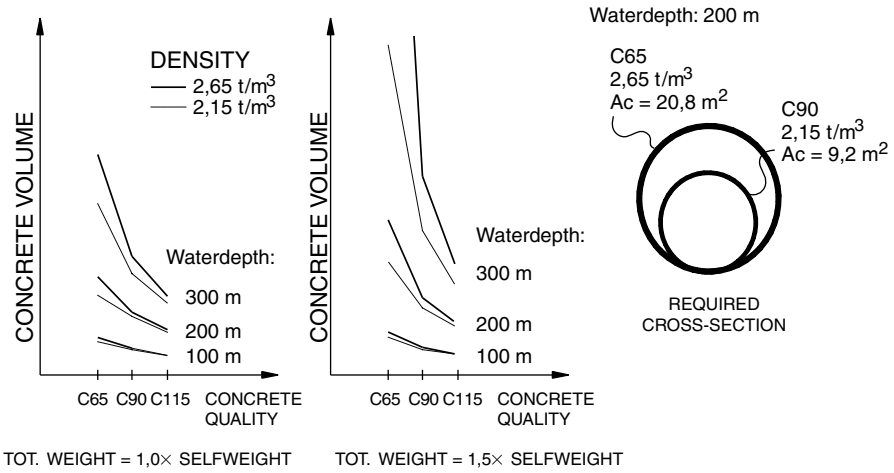

Fig. 20.6 The effect of strength and weight of concrete on concrete volume required for a "unit" vessel (Jakobsen et al. 1987)

reinforcement are achieved, the concrete is very durable and serves its function very well. Based on measurements of chlorides in the cover zone, anticipated life of such concrete is more than 200 years (Bech and Carlsen 1999; Fjeld and Røland 1982).

There are virtually no costs associated with the maintenance of offshore concrete structures (Sandvik et al. 2005). As an example, an early Condeep platform installed in the mid 1970s has been compared to a neighbouring steel jacket platform installed at the same time. The steel platform has had maintenance costs exceeding the entire cost of the concrete substructure. Modern steel structures may be different, so the difference may not be as striking, but it will still favor the concrete by far. This aspect will become clearer when modern methods of calculating economic return (i.e. Life Cycle Cost) become more common or mandatory.

20.3 Decommissioning of the Offshore Platforms

Even though the offshore platforms, steel or concrete, may be fit for many years, international regulations will put constraints on the use of the oceans. Particularly important here is the OSlo PARis Convention (OSPAR). In July 1998 it was decided that all platforms in the North Sea shall be removed after completing their duties.

An exemption was made for concrete platforms, because of the believed complexity of the operation. But in an addendum to the Convention it was stated that there are no plans for future use of concrete platforms. This may be interpreted as an obstacle to competition.

fib initialized work on the subject in their Task Group 3.2 "Recycling of Offshore Concrete Structures", reported as *fib* Bulletin 18 (fib 2002).

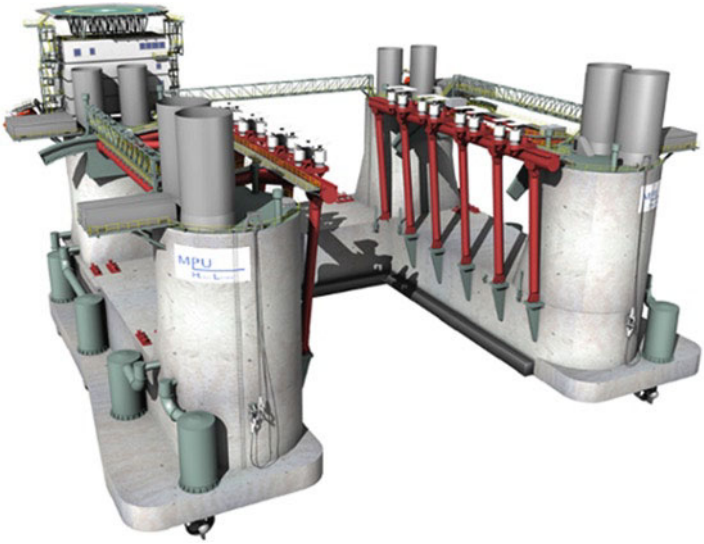

Fig. 20.7 The MPU Heavy Lifter

The conclusions of the work were:

- It is feasible to remove offshore concrete structures.
- Removing the entire installation is most likely the safest and most cost efficient way to remove the topside.
- The OSPAR Convention requires that the topside of the concrete platforms must be removed.

The work of TG 3.2 is described in (Olsen 2001; Høyland and Olsen 1998). The steel platforms will also have to be removed. A concrete vessel was designed to perform these removals.

For the North Sea alone this represents a market value of some US $20 billion, and what would be better than a robust, inexpensive heavy lifting vessel that utilizes the simple principle of Archimedes in order to lift the structure directly off its foundations?

The proposed vessel is a concrete U-shaped semi-submersible vessel, commercially named Heavy Lifter, (Maage and Olsen 2000; Olsen 2000b). Dr.techn. Olav Olsen developed the design; however, the owner of the vessel went bankrupt and the project was terminated before the construction was complete (Fig. 20.7).

20.4 Recent Concepts

In response to the need for deep water production and storage, further concepts have been developed for this purpose. The Semisubmersible monohull (Semo) is illustrated in Fig. 20.8. The overall design philosophy is indicated in Fig. 20.9.

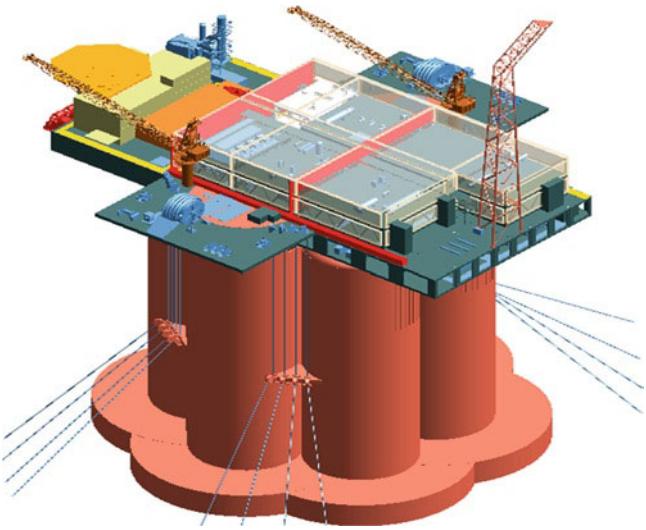

Fig. 20.8 The Semo

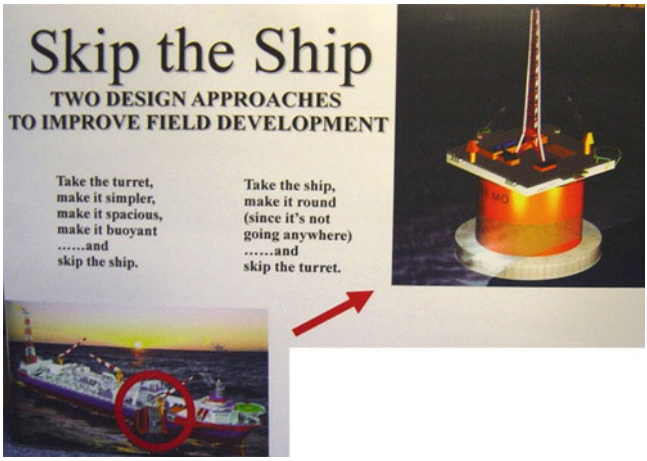

Fig. 20.9 The design philosophy behind the Semo

Figure 20.9 shows two design approaches leading to the same result, and a very logical result indeed. A lot of work has been performed on the concept. Floating structures are more complex to design load wise, there are a lot of parameters that need to be accounted for. Analyses show that the Semo concept is feasible, robust and flexible with regard to most types of offshore developments.

Advanced motion analyses and simulations verify that the concept has superior sea motion characteristics. To further document the motion characteristics, the

Semo was tested in the ocean basin at Marintek, Trondheim. The results from these tests were as expected very positive. So, aspects regarding second-order motions are now considered as solved.

A very simple FSO has been developed lately, as a result of the need for oil storage offshore. The concept has significant similarities to the Semo, but has different design specifications. These concepts have sparked enthusiasm among medium sized ship/offshore yards which do not have their own dry-dock facilities available. They see the concepts as an opportunity to enter the "FSO/FPSO market" which so far has been dominated entirely by ship-shaped solutions.

Local content will be more important in the future, and concrete creates interesting opportunities with regards to local fabrication and assembly. For many countries it is important to build new industry and to further develop the economy. The fabrication of a concrete structure can give significant amounts of work locally, which could give a political advantage compared to structures built in other countries.

20.5 LNG Terminals

The future will see an increased use of offshore LNG terminals, even in ice-infested waters. The worldwide LNG trade has increased steadily and the trend is expected to continue. Concrete offers a unique combination of advantages over steel.

Figure 20.10 shows a picture of the Adriatic LNG Terminal. This terminal was built in Spain and Italy, and installed outside Venice in the summer of 2008. It facilitates safe import of energy far away from inhabited areas. Figure 20.11 shows the first ship berthing, in August 2009.

Fig. 20.10 The Adriatic LNG terminal under construction in Spain

Fig. 20.11 The Adriatic LNG terminal, first ship berthing, August 10th, 2009

Fig. 20.12 Sakhalin II platforms during construction in Nahodka, Russia

20.6 The Arctic

One quarter of the undiscovered reserves of hydrocarbons are expected to be in ice-infested waters, predominantly in the Arctic, but also in the Caspian Sea and other cold waters.

Concrete is a very well-suited material to build structures for the Arctic. Several structures are recently built for the Sakhalin field. Figure 20.12 shows these platforms when constructed in Nahodka (south of Vladivostok, Russia). Figure 20.13 shows one of them after installation, prior to deck installation.

Fig. 20.13 Sakhalin II

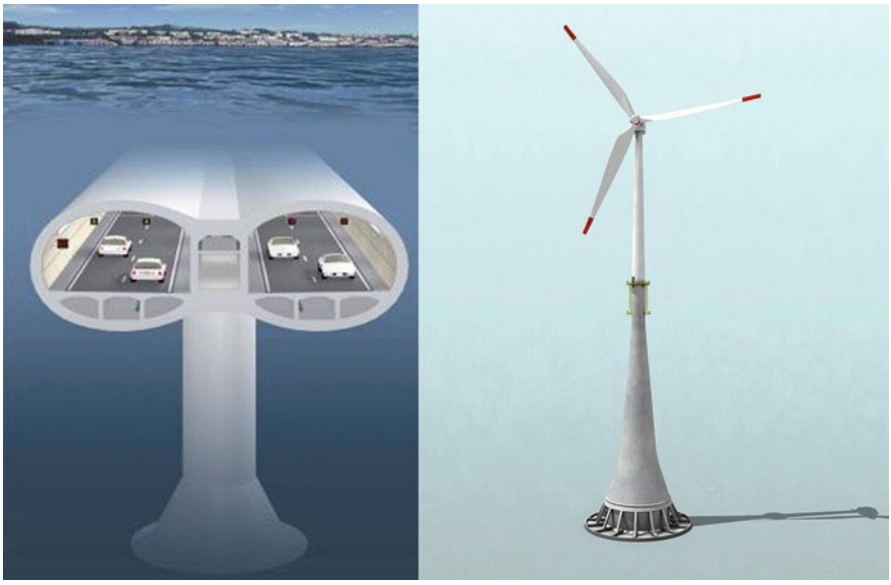

Fig. 20.14 Submerged floating tunnel and offshore windmill

20.7 Outlook

The oil and gas projects may benefit our future by way of providing experience, in order to achieve robust and safe structures for other applications of concrete in marine environments. The examples above (Fig. 20.14) show a concept for a

submerged floating tunnel (Muttoni et al. 2001; Haugerud et al. 2001), and for offshore windmill substructures.

Experiences with realized offshore concrete structures are very good, the structures are tough and they require little or no maintenance. The future sees a development in even harsher areas, where the concrete structures are well apt to do a good job for safe operations.

References

Bech S, Carlsen JE (1999) Durability of concrete offshore structures. In: 5th international symposium on utilisation of high strength/high performance concrete, Sandefjord, 1999

fib (2002) Recycling of offshore concrete structures– State-of-the-Art Report. *fib* Bulletin 28. Federation internationale du beton, Lausanne

fib (2009) Concrete structures for oil and gas fields in hostile marine environments. *fib* Bulletin 50. Federation internationale du beton, Lausanne

Fjeld S, Røland B (1982) In-service experience with eleven offshore concrete structures. In: Offshore Technology conference, Houston, 1982

Haugerud SA, Olsen TO, Muttoni A (2001) The Lake Lugano crossing – technical solutions. In: 4th symposium on strait crossings, Bergen, 2001

Høyland K, Olsen TO (1998) Recycling of offshore concrete structures. In: International workshop, Consec '98, Tromso, 1998

Jakobsen B, Eikenes Å, Olsen TO (1987) Recent development and potentials for high-strength offshore concrete platforms. NB, SINTEF, FIP, NIF, Symposium on utilization of high strength concrete, Stavanger, 1987

Maage M, Olsen TO (2000) LETTKON A major joint Norwegian research programme on light weight aggregate concrete. In: Second international symposium on structural lightweight aggregate concrete, Kristiansand, 2000

Moksnes J (2002) 20 years of R&D into HPC – has it been a profitable investment? In: 6th international symposium on utilization of high strength/high performance concrete, Leipzig, 2002

Muttoni A, Haugerud SA, Olsen TO (2001) The new AlpTransit railway across the Alps. A crossing proposal for the Lake Lugano. In: 4th symposium on strait crossings, Norway, 2001

Olsen TO (2001) Recycling of offshore concrete structures. Structural concrete, Journal of the *fib* (3) Sept 2001

Olsen TO, Helland S, Moksnes J (2009) Offshore concrete structures for tough environments. In: *fib* symposium "Concrete: 21st Century Superhero", London, 2009

Sandvik K, Eie R, Advocaat J-D, Godejord A, Hæreid KO, Høyland K, Olsen TO (2005) Offshore structures – a new challenge. In: XIV national conference on structural engineering, Acapulco, 2005

Chapter 21
Composite Bridges with Corrugated Steel Webs to Meet Environmental Needs by Innovative Bridge Engineering

Jun Yamazaki

Abstract A composite bridge type incorporating corrugated steel webs fits beautifully into the surroundings, as Dole bridge or Maupre viaduct near Charolles do. The weight of the structure and the clear flow of forces in it give designers the possibility to improve structural details and construction methods in order to meet various environmental needs. The innovation of creating a structural element by folding a flat plate into a corrugated shape took place in France. A folded plate is compliant in compression while exhibiting high in-plane shear resistance. This function is ideal in order to enhance the moment capacity of prestressed box girder bridges. The assembly of corrugated steel webs into box girders and the anchorage of external prestressing tendons required novel connecting techniques. Extradosed prestressing enhances the moment capacity of bridge girders and lightens the structure. Hence, extradosed prestressing and corrugated steel webs make an ideal match. Both cantilever construction and incremental launching have been used.

More than 100 bridges with corrugated steel webs have been built in Japan in one and a half decades. Durability was designed with care, in particular the durability of external prestressing tendons and interfaces between corrugated steel webs and concrete. A guide to maintain durability is now being prepared in Japan by the engineering association and one of the road companies. National and local government and the autonomous public authority for highway construction encouraged innovative design and construction methods. Their guidance to verify performance by tests gave industry confidence in reliability and helped it to develop progressively challenging projects. After the dissolution of JH (Japan Highway Public Corporation) in 2005, efforts to archive technical data are being made by three regional road companies, West-, Central- and East- NEXCO, their research institute, the engineering association, prestressed concrete contractors and an industry group.

J. Yamazaki (✉)
Department of Civil Engineering, Nihon University, Kanda-Surugadai 1-8-14, Chiyoda-ku, Tokyo 101-308, Japan
e-mail: yamazaki@civil.cst.nihon-u.ac.jp

M.N. Fardis (ed.), *Innovative Materials and Techniques in Concrete Construction: ACES Workshop*, DOI 10.1007/978-94-007-1997-2_21,

Innovation in bridge construction in Japan has been prompted by the progressive management methods of the public autonomous authority, which has 50 years of experience in this field. After JH was divided into the three NEXCOs, new schemes to encourage innovation were looked for. One attempt to that end is the creation of an innovative design guide. The new design guide yet to come may urge designers to create structures for high performance and specific targets.

21.1 Introduction

This paper reviews the innovation of composite bridge with corrugated steel webs, the technology of which was transferred from France to Japan, and its environmental impact.

21.2 Innovation and Function of Corrugated Steel Web

A composite bridge type incorporating corrugated steel webs fits beautifully into the surroundings, as Dole bridge or Maupre viaduct near Charolles do (Figs. 21.1 and 21.2). The innovation of creating a structural element by folding flat a plate into a corrugated shape was developed in France. It allows compliance in compression while maintaining large in-plane shear resistance. This function is ideal in order to enhance the moment capacity of prestressed box girder bridges (Combault et al. 1988, 1993; Capra and Leveille 1998).

Fig. 21.1 Dole bridge

Fig. 21.2 Maupre viaduct near Charolles

21.3 Performance of Bridge Girders with Corrugated Steel Webs

The function of corrugated steel webs enhances the moment carrying efficiency of girders. It reduces the dead weight of concrete webs; it saves prestress otherwise wasted in the cross sectional area of concrete webs not contributing to the moment capacity. Extradosed prestressing enhances the moment capacity of bridge girders by increasing the eccentricity of prestress. Hence, extradosed prestressing and corrugated steel webs are an ideal match.

The Oumi-ohtori bridge in Ritto, Shiga prefecture is a rigid frame. The span, with three traffic lanes, is 140 m from the tower to the abutment. The depth of the girder at the tower is 7.5 m, which is significantly less than in a concrete box girder prestressed by internal tendons (Figs. 21.3–21.5).

Corrugated steel webs are brought to the construction site and assembled into a box girder. The procedure of assemblage requires novel connecting techniques in addition to ordinary prefabrication techniques. These include connections of top and bottom edges of the webs to top and bottom concrete slabs and anchorage of external prestressing tendons to the concrete slabs. The anchorage zones need to be designed so as to withstand the tendon forces. Analyses of the behaviour or load tests of deviators or blisters are often required for design against potential cracking.

The connections of the top and bottom edges of the webs to the top and bottom concrete slabs are made by channel sections welded on top of the upper flange welded to corrugated webs. Several other methods of connections have been developed.

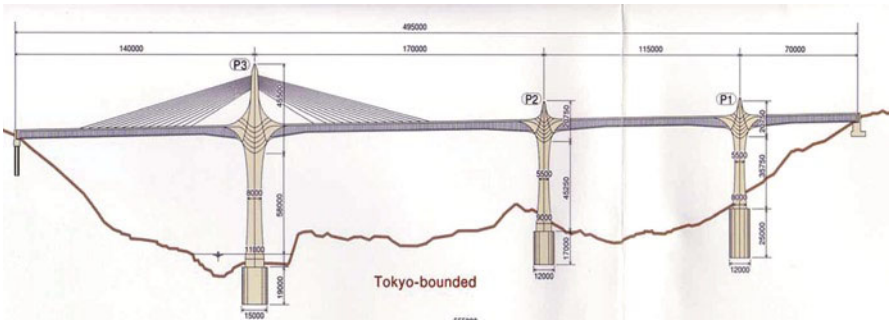

Fig. 21.3 Oumi-ohtori bridge in Ritto (CAD by JH and PS-Mitsubishi)

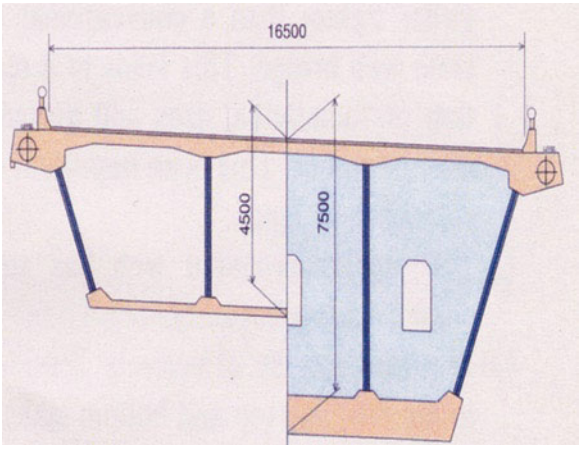

Fig. 21.4 Cross section, Oumi-ohtori bridge in Ritto (Courtesy of JH and PS-Mitsubishi)

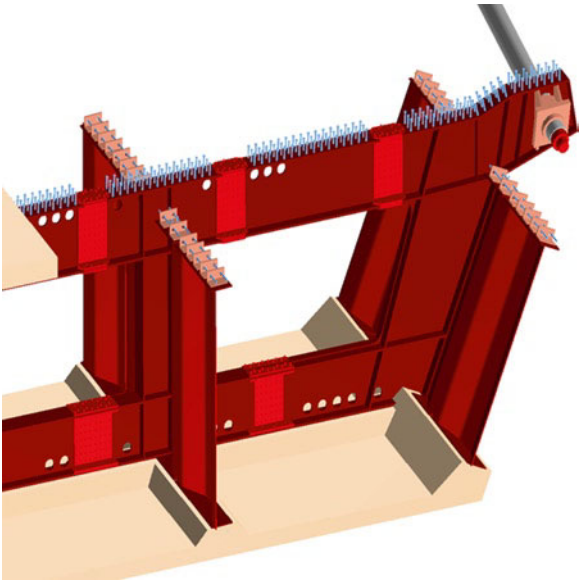

Fig. 21.5 Connections, Oumi-ohtori bridge in Ritto (Courtesy of JH and PS-Mitsubishi)

In combining extradosed tendons and corrugated steel webs in box girders, transverse diaphragms are inserted in the load path from extradosed tendons to concrete slabs.

21.4 Construction Methods

The clear flow of forces in this structure gives designers the possibility to improve structural details and construction methods so as to meet various environmental needs. Both cantilever construction and incremental launching are used.

The Akabuchi-gawa bridge is the newest one constructed by an improved cantilever method (Figs. 21.6 and 21.7). To reduce weight of fresh concrete during casting on the form traveler and corrugated steel webs, casting of sections of the top slab is set back relative to that of the bottom slab. This results in a lighter form traveler. Whether this procedure may be applied depends on local situations.

A similar idea was implemented in the Sunniberg bridge, Switzerland (Figs. 21.8 and 21.9). Casting the section of the slab was set back relative to the edge girders. The situation of Sunniberg bridge was said to allow suspension of the construction during winter. Flexibility in construction scheduling is nowadays desirable.

The Katsurashima-viaduct (Figs. 21.10 and 21.11) was built by incremental launching. The weight of the bridge girder during launching was significantly reduced by refined prefabrication techniques. The concrete of the deck slab was cast only after the girder has run a full a span. Transverse ribs and struts increased the rigidity (Aoki et al. 2006).

Fig. 21.6 Akabuchigawa bridge (Courtesy of JH and Sumitomo-Mitsui)

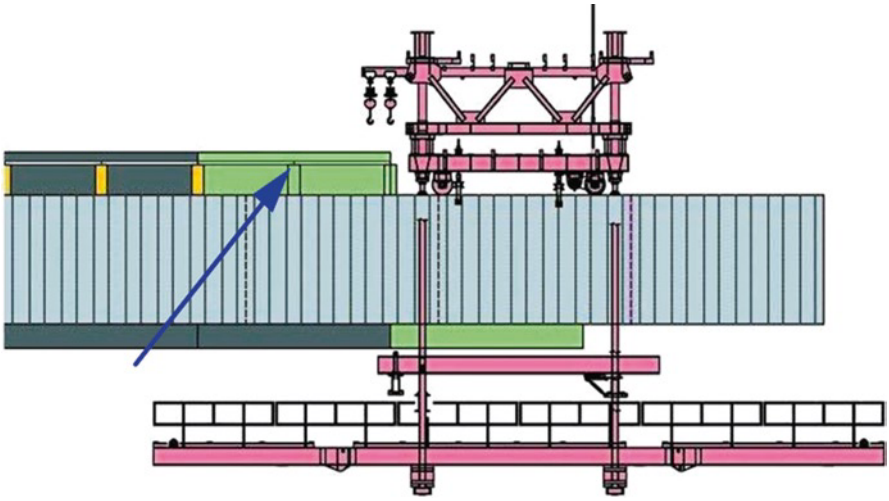

Fig. 21.7 Akabuchigawa bridge, form traveler (Courtesy of JH and Sumitomo-Mitsui)

Fig. 21.8 Sunniberg bridge

Fig. 21.9 Sunniberg bridge, form traveler

Fig. 21.10 Katsurashima viaduct (Courtesy of JH and Sumitomo-Mitsui)

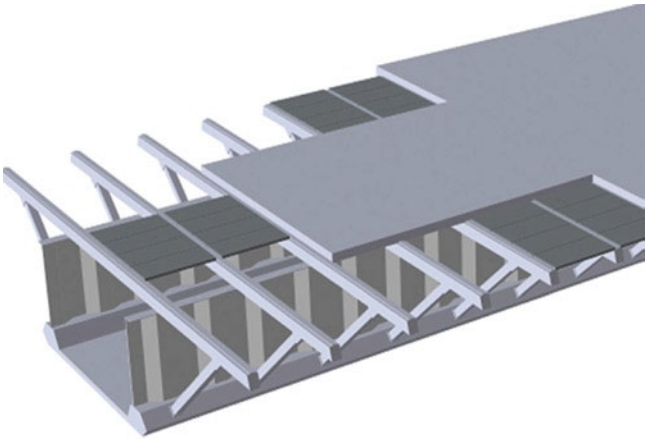

Fig. 21.11 Katsurashima viaduct, prefabrication (Courtesy of JH and Sumitomo-Mitsui)

Fig. 21.12 Torisaki-gawa viaduct, launching (Courtesy of JH, Taisei)

For the Torisaki-gawa viaduct (Figs. 21.12 and 21.13) a conventional launching nose, which is usually scrapped after completion, was not needed. The end span was made to be light enough but with the required strength and stiffness. Ultra high strength concrete (DUCTAL) was used in the prism attached to the bottom flange of the corrugated steel webs.

Fig. 21.13 Torisaki-gawa viaduct, launching nose (Courtesy of JH, Taisei)

21.5 Environmental Needs

The lightness of this bridge type meets environmental needs. The Oumi-ohtori bridge in Ritto, Shiga prefecture, is surrounded by forests. The freeway passes over hills and through tunnels. There are small communities around, whose traditional craft is pottery. (Wilcox et al. 2002). Figures 21.14 and 21.15 depict the image and the sensation of flight experienced by drivers and travelers driving over this bridge.

The Himi-yume bridge in Himi, Nagasaki prefecture, is built in a valley, fairly close to a settlement (Figs. 21.16 and 21.17). The bridge is seen daily by the local people from below. The slender girder has a constant depth of 4 m for a span of 180 m between towers, for two traffic lanes. The girder, towers and piers were given a well-rounded shape by the designer (Kuroiwa et al. 2006) (Figs. 21.18 and 21.9).

Access from freeways to local roads typically passes through communities. The surrounding area is usually a mixture of nature and man-made infrastructure. Farms for vegetable, rice, tea and orchards are much smaller in scale and most products are grown for local consumption. It is thus important to protect the environment, reduce disturbance and adjust to the local economy and slow way of life. A solution has been small sizing of man-made structures at various stages of construction and emission control.

Fig. 21.14 Oumi-ohtori bridge (Courtesy of JH, PS–Mitsubishi)

Fig. 21.15 Himi-yume bridge (Courtesy of JH, Sumitomo–Mitsui)

Fig. 21.16 Oumi-ohtori bridge, Frame joint

Fig. 21.17 Himi-yumei bridge, view from the community below

Fig. 21.18 Environment of the community, farms and man-made facilities 1

Fig. 21.19 Environment of the community, farms and man-made facilities 2

21.6 Environment for Progress

More than 100 composite bridges incorporating corrugated steel webs have been built in Japan in one and a half decades. National and local government and the autonomous public authority for highway construction encouraged innovative design and construction methods. Their guidance to verify performance by tests gave industry confidence in their reliability and helped it to progressively develop challenging projects. To meet the varying needs depending on the environment and the activities of local inhabitants, innovative techniques of assembly and construction were developed. The earlier state-of-practice and -design were documented by the Japan Prestressed Concrete Engineering Association (JPCEA). Subsequent developments were reported individually, some of which in the national reports at *fib* Congresses. Durability is designed with care, in particular the durability of external prestressing tendons and interfaces between corrugated steel webs and concrete. A guide to maintain durability is now being prepared in Japan by JPCEA and one of the road companies.

After the dissolution of JH in 2005, efforts to archive technical data are being made by three regional road companies, West-, Central- and East- NEXCO, their research institute, JPCEA, prestressed concrete contractors and an industry group.

21.7 Conclusion

Innovative bridge engineering was reviewed with respect to its effectiveness in meeting environmental needs. Innovation in Japan has been prompted by the progressive management of the public autonomous authority, which has 50 years of experience in this field. After JH was divided into the three NEXCOs, new schemes to encourage innovation were looked for. One attempt to that end is the creation of an innovative design guide. The new design guide – yet to come – may urge designers to create structures in pursuit of high performance for specified functions.

Acknowledgments A study tour to the Maupre viaduct near Charolles and the Dole bridge in France helped Japanese bridge engineers understand the innovation in corrugated steel webs. This study in 1997 was made possible thanks to Michel Virlogeux and Emmanuel Bouchon and the staff of SETRA, Service d'Etudes Techniques des Routes et Autoroutes, Paris. Site visits were assisted by Olivier Caplain and Alain Leveille of Campenon Bernard. Atsuo Ogawa, the director of engineering of Japan Highway Public Corporation (JH), was the leader of the study tour conducted by the Express Highway Research Foundation.

Shoji Ikeda, Prof. Emeritus at Yokohama National University, conducted earlier experiments at the university, chaired the committees set up for several important bridge projects (including Hondani bridge, JH's first bridge, and Oumi-ohtori bridge in Ritto), created design guides with the committees of the engineering association and organized studies of industry groups.

Takashi Ohura, PS-Mitsubishi, translated articles by Jacques Combault to Japanese and realized Shinkai bridge, the first bridge with corrugated steel webs, built in the Niigata prefecture.

Information contained in this paper was provided by JH and prestressed concrete contractors, PS-Mitsubishi (Oumi-ohtori bridge), Sumitomo-Mitsui (Akabuchigawa, Katsurashima, Himiyume bridge) and Taisei (Torisakigawa bridge).

Tsutomu Kadotani, the last director of engineering of JH, realized many important composite bridges with corrugated steel webs.

All of the individuals and groups mentioned were committed to the development of composite bridges with corrugated steel webs in Japan and are gratefully acknowledged.

References

Aoki K, Kasuga A, Nakamura A, Morohashi A (2006) Prestressed concrete corrugated steel web box girder with ribs and struts - Katsurashima viaduct. In: Recent works of prestressed concrete (National Report), Second fib congress 2006, Naples, pp 133–136, 2006

Capra A, Leveille A (1998) Fatigue test of a corrugated web girder. The French technology of concrete (National Report), FIP congress, Amsterdam, 1998, pp 19–24

Combault J, Virlogeux M, Causse G, de Matteis D et al (1988) Viaduc du vallon de Maupre, a Charolles. Travaux, Oct 1988

Combault J, Lebon JD, Pei G (1993) Box girders using corrugated steel webs and balanced cantilever construction. Proceedings, FIP symposium, Kyoto, 1993, pp 25–32

Kuroiwa T, Nishikawa K, Kasuga A, Tazoe K (2006) Extradosed bridge with corrugated steel web. In: Recent works of prestressed concrete (National report). Second *fib* congress 2006, Naples, pp 93–96, 2006

Wilcox T, Guarre JS, Berger FS (2002) Bridge in flight: harmony of style and structure. In: Proceedings, Session 14 aesthetics of concrete structures, First *fib* congress 2002, vol 8, Osaka, pp 125Ð134, 2002

Chapter 22
Segmental Concrete Bridges with Corrugated Steel Webs

Tsutomu Kadotani

Abstract A Prestressed Concrete (PC) bridge with corrugated steel webs is less expensive than a conventional PC bridge with concrete webs if the span is more than 50 m. This is due to the fact that the corrugated web bridge is 20–30% lighter than the concrete web bridge. Cost-effectiveness is also promoted by the accordion effect, by which the corrugated web has no stiffness against axial force. The emission of carbon dioxide (CO_2) has become a serious problem all over the world. The bridge with corrugated webs is an eco-friendly bridge which can reduce the emission of CO_2 greatly in comparison with conventional concrete or steel bridges. A bridge with corrugated steel webs carries the loads by out-of-plane deformation and requires no stiffeners. A structural analysis program incorporating elasto-plastic stiffness and geometric stiffness has been developed and verified by many loading tests.

A girder with corrugated steel webs can be integrated without a hinge with a steel box girder in the longitudinal direction. A newly developed connecting method between corrugated web girder and steel girder has made such a hybrid structure possible. A steel bridge with a span of over 400 m can be replaced by this hybrid bridge. The hybrid bridge is cost-effective and emits less CO_2. In Japan, more than 130 hybrid bridges have been constructed not only because they cost less but also because of lower CO_2 emissions. Such hybrid bridges may well replace the bridges that have all their components made of steel in the near future.

T. Kadotani (✉)
Hanamizuki Bridge Planning, INC, 2-13-16-504, Kamitsuruma Honcho,
Minami-ward, Sagamihara City 228-0818, Japan
e-mail: tsutomukadotani@gmail.com

M.N. Fardis (ed.), *Innovative Materials and Techniques in Concrete Construction: ACES Workshop*, DOI 10.1007/978-94-007-1997-2_22,

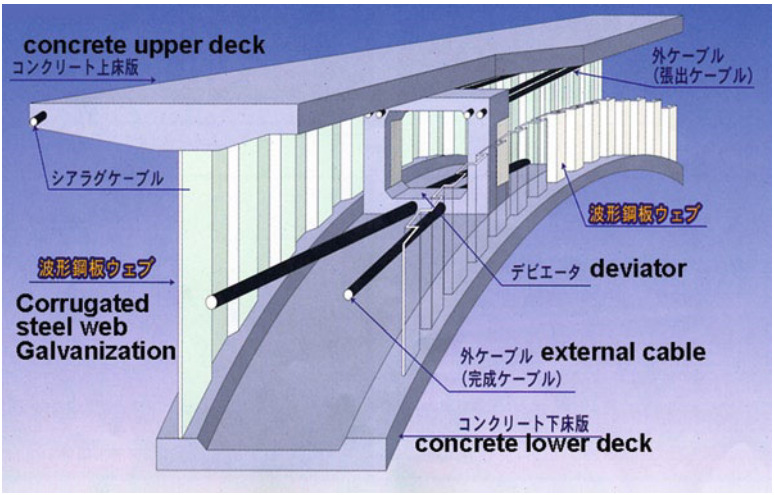

Fig. 22.1 PC bridge with corrugated steel webs

22.1 Introduction

A concrete bridge with a corrugated steel web is one where the concrete web of a conventional concrete box girder is replaced with corrugated steel webs, as shown in Fig. 22.1.

Inside the box of a bridge with corrugated steel webs, external prestressing is applied. The external tendons are deviated at deviators installed at the diaphragms. A typical concrete bridge with corrugated steel web is shown in Fig. 22.2.

22.2 Characteristics of a Bridge with Corrugated Steel Webs

22.2.1 Higher Shear Strength

The corrugated web carries the loads by out-of-plane deformation and requires no stiffeners, as shown in Fig. 22.3. Equilibrium in the undeformed configuration, based on the infinitesimal displacement theory, cannot be applied.

Incorporating Elasto-plastic stiffness and Geometric stiffness, the equilibrium equation in the deformed configuration, of F.E.M. non-linear analysis is shown as follows:

$$\Delta f^k = \mathrm{T}^k (\mathrm{K}^k + \mathrm{K}_G^k) \mathrm{T}^{k^T} \Delta d^k \tag{22.1}$$

Fig. 22.2 Concrete bridge with corrugated steel webs

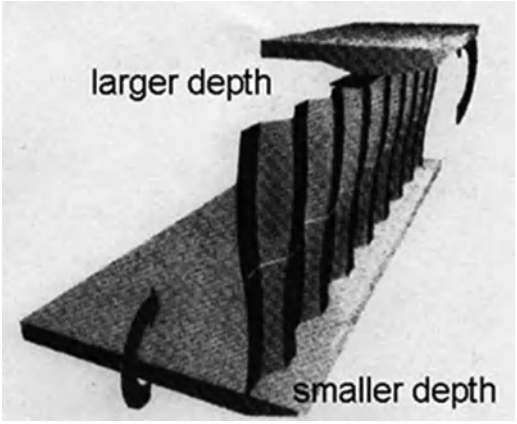

Fig. 22.3 Deformation of corrugated web

According a recently constructed non-linear F.E.M. analysis code incorporating geometric stiffness and elasto-plastic stiffness, the corrugated steel web has 10 times higher shear resistance per unit mass than a concrete web. This has been proved by the loading test shown in Fig. 22.4.

The higher shear resistance of a corrugated steel web allows a depth 10% smaller than that of the concrete web bridge, as shown in Fig. 22.5. The bridge with corrugated webs is 20% lighter than the bridge with concrete webs.

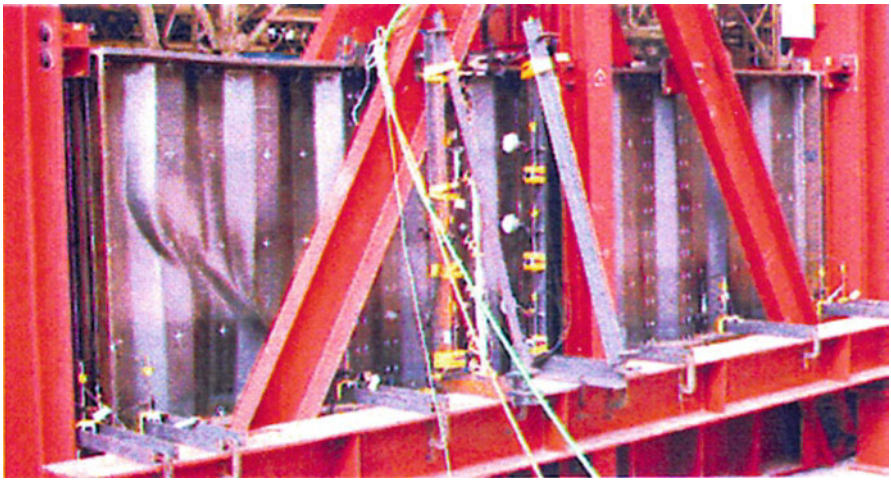

Fig. 22.4 Loading test of corrugated steel web

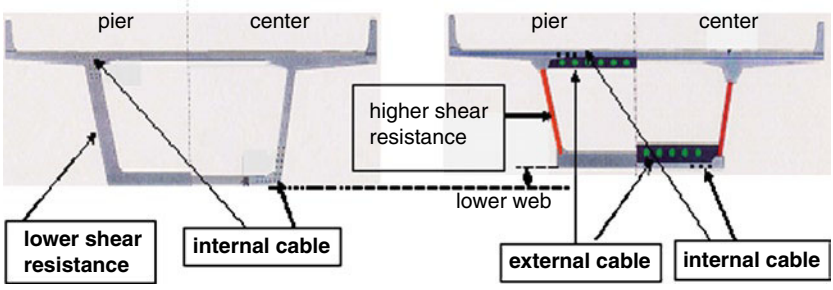

Fig. 22.5 Box girder bridge with concrete web and corrugated web

22.2.2 Accordion Effect

According to experiments, a corrugated web exhibits almost no stiffness or resistance to axial force. This is called Accordion Effect, shown in Fig. 22.6. The Accordion Effect enables the upper deck or the lower deck to be prestressed effectively, since there is no axial stiffness in the webs, unlike concrete webs (Fig. 22.7).

The Accordion Effect makes an extradosed bridge with a span of 180 m more economical. In an extradosed bridge with concrete webs, as shown in Fig. 22.8, the pylon will be taller than in an extradosed bridge with corrugated webs, because the prestress by the horizontal component does not work effectively, owing to the resistance of concrete webs. The foundation of an extradosed bridge with concrete webs will be larger, because of the increased weight and a larger seismic overturning moment. If one uses a steel box girder, like the one shown in Fig. 22.9, the pylon will be much taller than for an extradosed bridge because the horizontal force

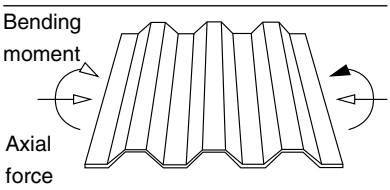

Fig. 22.6 Accordion effect

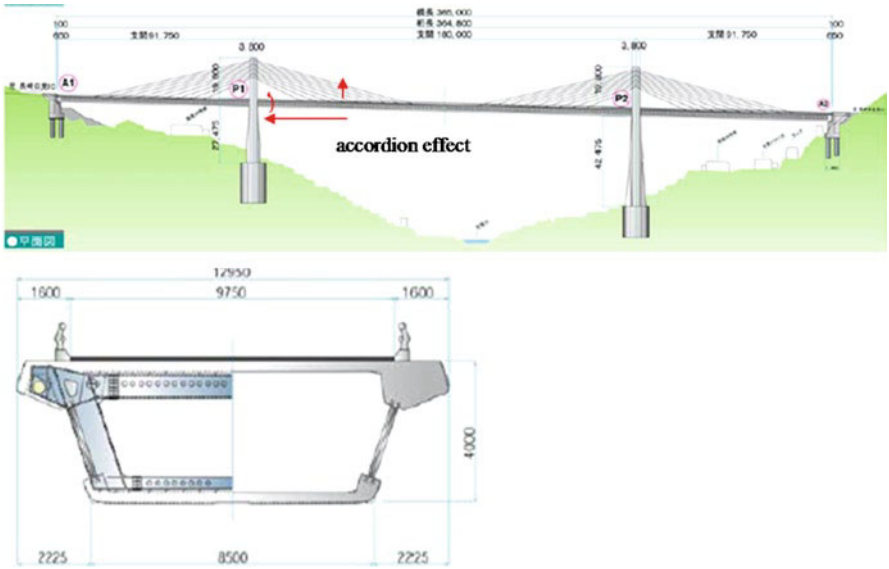

Fig. 22.7 Extradosed bridge with corrugated steel webs

component is greatly limited to avoid buckling. It is not considered an extradosed bridge but a cable stayed bridge. Figure 22.10 shows a conventional concrete box girder with center hinge which requires massive girder and foundations. The higher shear resistance and the accordion effect make a bridge with corrugated webs less expensive than conventional bridges.

22.2.3 Eco-Friendly Bridge

The greenhouse gas emissions (CO_2) was calculated for a five span continuous bridge with a span of 50 m, shown in Fig. 22.11. The calculation was made for a PC box girder with concrete webs, PC box girder with corrugated steel webs and steel box girder (Figs. 22.12–22.14).

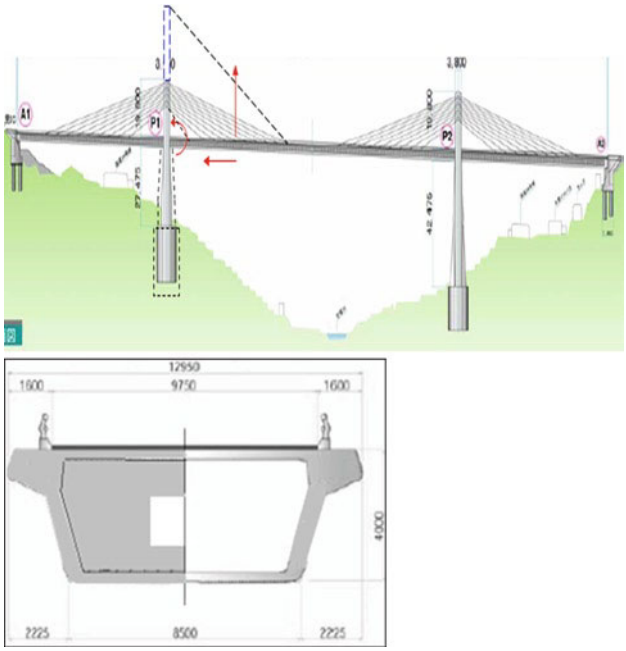

Fig. 22.8 Extradosed bridge with concrete webs

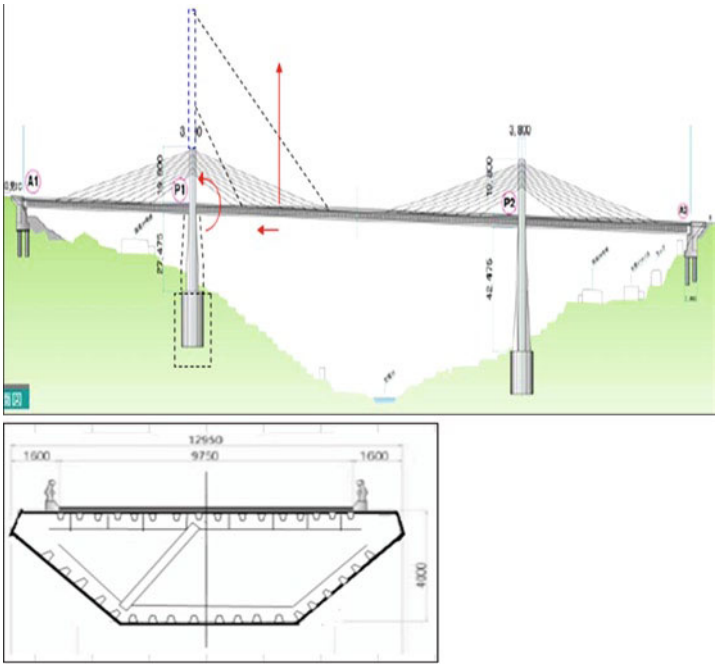

Fig. 22.9 Cable-stayed bridge with steel box girder

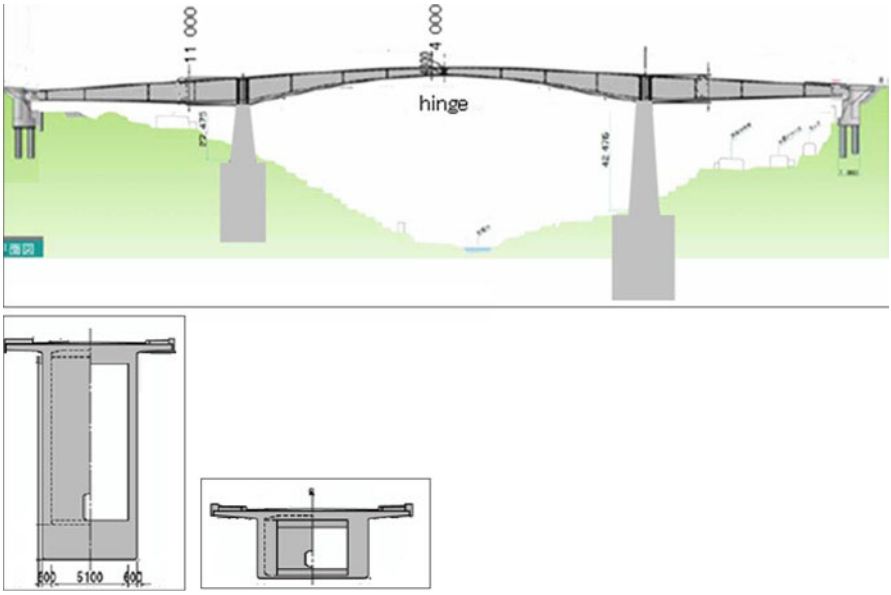

Fig. 22.10 Concrete box girder with center hinge

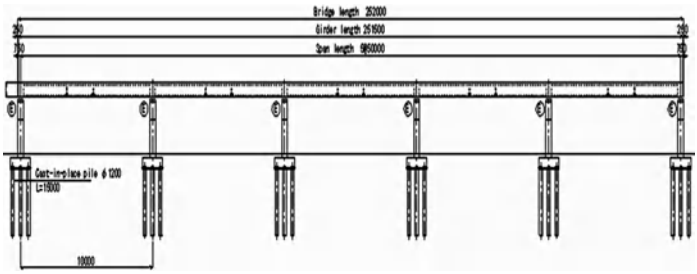

Fig. 22.11 Five span continuous bridge (span of 50 m)

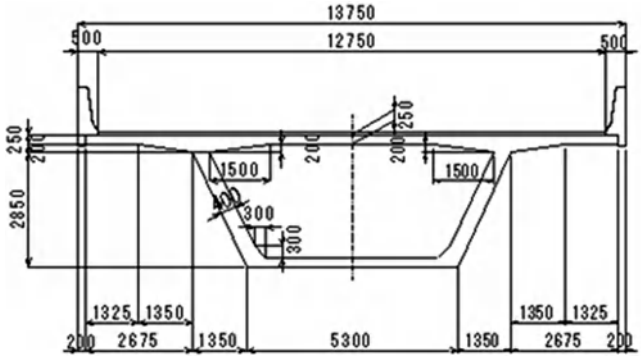

Fig. 22.12 Concrete webs (h = 2.85 m)

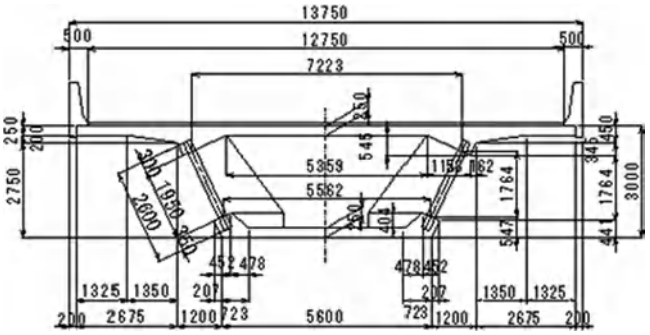

Fig. 22.13 Corrugated webs (h = 2.75 m)

Fig. 22.14 Steel box girder (h = 2.5 m)

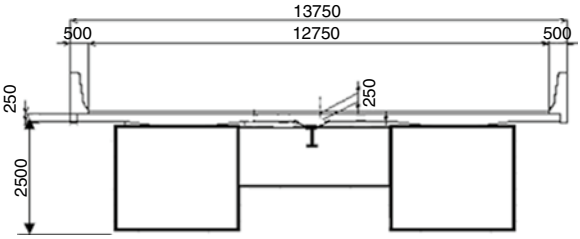

Fig. 22.15 CO_2 emission unit (kg-CO_2/kg)

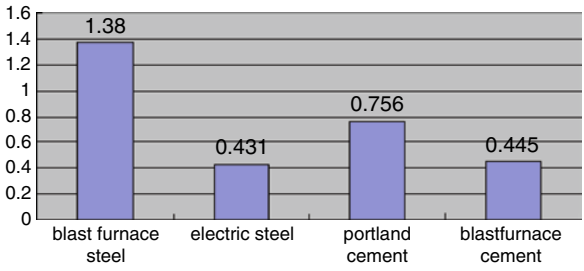

The calculation was carried out based on a CO_2 emission unit (kg-CO_2/kg), as shown in Fig. 22.15. The CO_2 emission of each bridge is shown in Fig. 22.16. The PC box with concrete web and the steel box girder have almost equal emissions. Since the concrete girder is heavier than the steel girder, the substructure is larger than that of steel box girder. On the other hand, the lighter steel superstructure leads to a smaller substructure, although steel emits almost twice as much CO_2 as portland cement does. Figure 22.16 shows that the bridge with corrugated steel web emits the least CO_2 and is more eco-friendly.

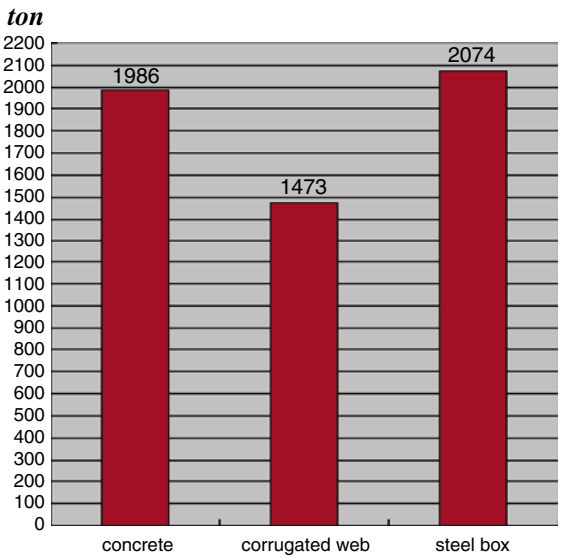

Fig. 22.16 CO_2 emissions

22.2.4 Simpler Fabrication

Corrugated steel webs are manufactured in a specially made press, which can fabricate a wide and longe panel easily, as shown in Fig. 22.17.

22.3 Application of the Corrugated Steel Webs to Longer Spans

Figure 22.18 shows a concrete bridge with corrugated steel web built by balanced cantilever segmental construction. The longest span is 97 m. Since the superstructure is 20% lighter than the bridge with concrete webs, the substructure becomes more slender. The length of a segment with corrugated web is larger than that with a concrete web, since the corrugated web is 20% lighter than a concrete one. This makes construction shorter.

Figure 22.19 shows a concrete extradosed bridge with corrugated steel webs constructed by the balanced cantilevering segmental method. The maximum span of 170 m for one pylon may be equivalent to 275 m for two pylons. The corrugated web has enabled the extradosed bridge to have such a long span.

Figure 22.20 shows an extradosed bridge with a corrugated steel web integrated with a 133 m long steel box girder. The integrated section between the concrete box girder and the steel box girder is also shown in Fig. 22.20. The maximum span is 235 m. If a concrete bridge with corrugated steel webs had not been developed, this bridge would have been a cable-stayed bridge of steel structure and would have cost 40% more.

Fig. 22.17 A sophisticated press and fabricated corrugated webs

Figure 22.21 shows the details of the cross-section around the cable anchor in the girder.

The span of 235 m for one pylon may be equivalent to $171 \times 2 = 342$ m for two pylons, as shown in Fig. 22.22. If integration between corrugated web girder and steel girder is applied, the equivalent span will be $342 + 67$ (steel box girder) $= 409$ m for two towers (Fig. 22.23).

Figure 22.24 shows a steel arch bridge with a span of 297 m which crossing a channel. The arch could be replaced by the extradosed bridge in Fig. 22.22 since the approach length is sufficient for the side spans of an extradosed bridge.

Figure 22.25 shows a steel cable-stayed bridge with a steel deck plate and a span of 410 m over a channel. The bridge could be replaced by the extradosed bridge with integration shown in Fig. 22.23. The 171 m of the girder of both sides of the towers might become a girder with corrugated webs. It may be less expensive and eco-friendly than the steel box girder.

Fig. 22.18 Concrete bridge with corrugated steel web by balanced cantilever segmental construction

Fig. 22.19 Concrete extradosed bridge with corrugated steel webs

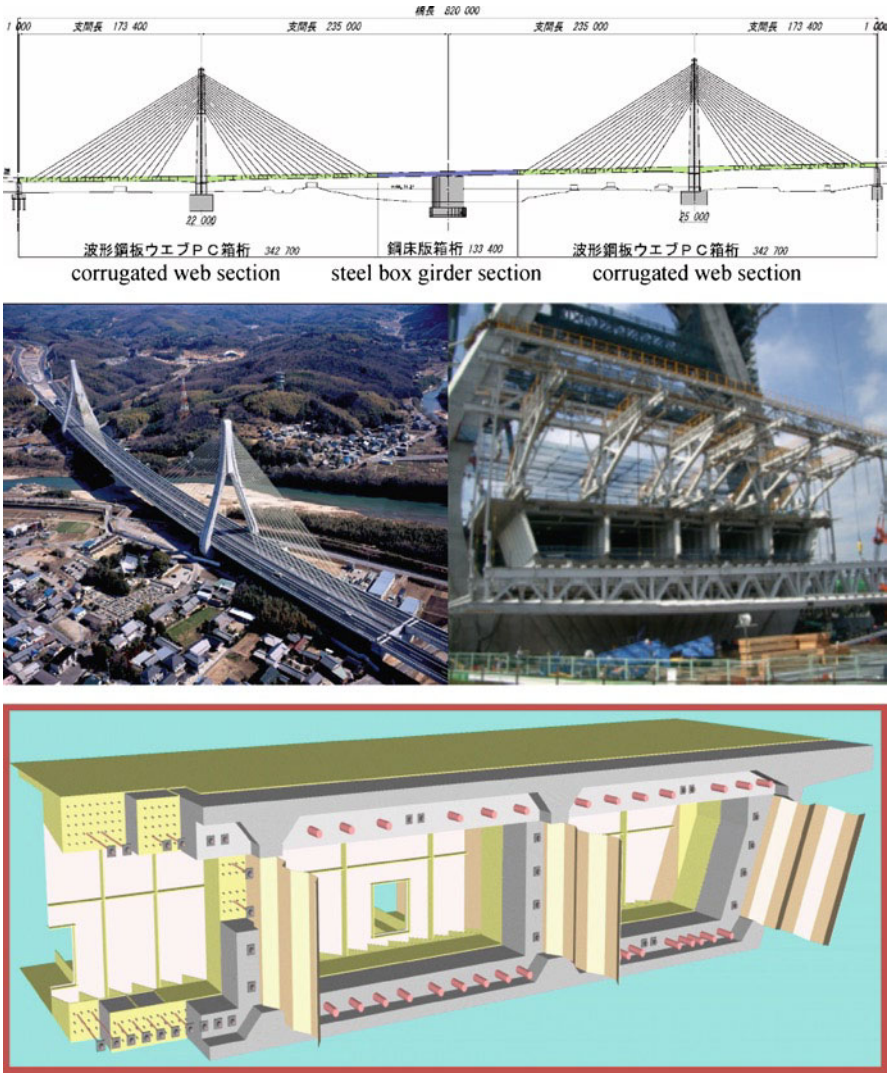

Fig. 22.20 Extradosed bridge with corrugated steel web integrated by steel box girder.

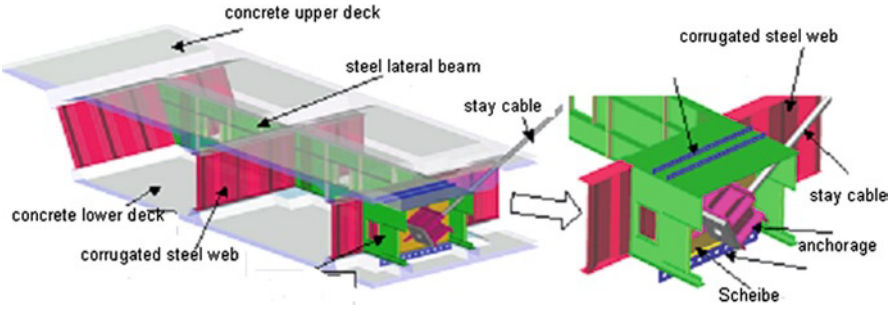

Fig. 22.21 Details of cross-section around cable anchor in the girder

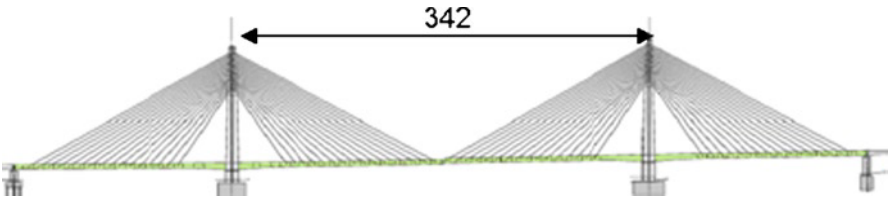

Fig. 22.22 Equivalent span for two towers

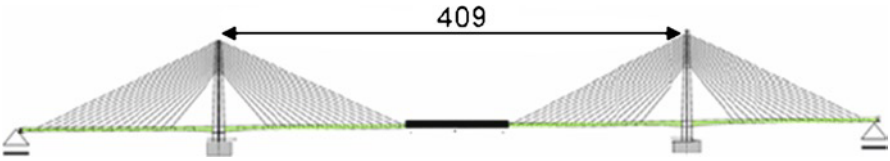

Fig. 22.23 Equivalent span with integration, for two towers

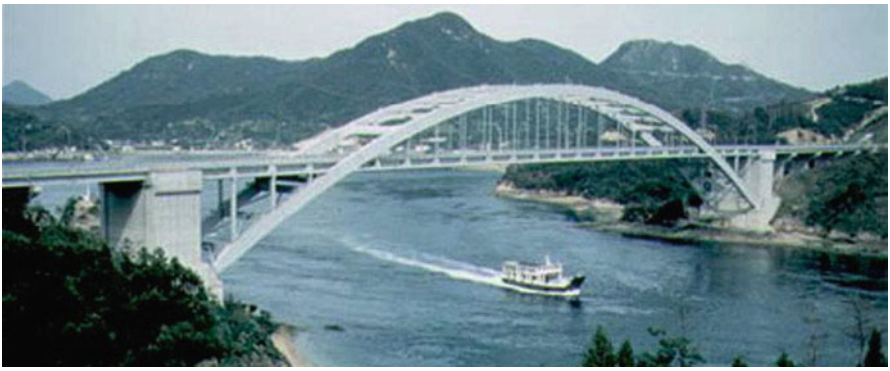

Fig. 22.24 The steel arch bridge (span 297 m) that could be replaced by the extradosed corrugated web bridge

Fig. 22.25 The steel cable-stayed bridge (span 410 m) to be replaced by the extradosed corrugated web bridge

22.4 Conclusions

The bridge with corrugated steel webs is one of the innovative technologies developed in the twenty-first century. The accordion effect and higher shear strength make the bridge with corrugated steel webs more economical than the conventional steel or concrete bridges if the span is more than 50 m. Especially if the ground condition is soft, the bridge with corrugated steel webs is even more favourable, since it is lighter than the conventional concrete bridge.

Connecting a girder having corrugated steel webs with a steel box girder might make a long span of 400 m a hybrid structure consisting of a girder of corrugated steel webs and a steel box girder. For girders with corrugated steel webs applied instead of steel box girders, lower carbon dioxide emissions will contribute to the protection of the environment.

Chapter 23
Innovation in Bridge Design and Construction: Composite Box Girder Bridge

Giuseppe Mancini

Abstract This paper illustrates how a traditional type of structure can be revisited in order to conform to the rules of environmental design. The outcome of such an approach is not only ecological but also less expensive and quicker to build than traditional structures. If we also take into account that the sustainable bridge which will be discussed is not a mere theoretical case-study, but has already been built and has the world span record in its category, we can truthfully state that a goal in life cycle design engineering has been probably achieved.

23.1 Introduction

For about 20 centuries construction was inspired by the requirements set by the Roman military man Marcus Vitruvius Pollio: Firmitas, Utilitas, Venustas. Such requirements may be translated today as Robustness and Safety (Firmitas), Serviceability and Functionality (Utilitas), Elegance and Beauty (Venustas).

During the past two decades these requirements have been integrated in a more general concept, named "Sustainability". According to the Brundtland Report (Burtland 1987), sustainable development is defined as "the development that meets the needs of the present without compromising the ability of future generations to meet their own needs."

The construction process has recently been substantially influenced by sustainability considerations, as envisaged in *fib* Bulletin 28 (fib 2004), in which the transformation from the old traditional construction process to the new sustainable

G. Mancini (✉)
Dipartimento di Ingegneria Strutturale e Geotecnica, Politecnico di Torino,
C.so Duca degli Abruzzi 24, Torino 10127, Italy
e-mail: giuseppe.mancini@polito.it

M.N. Fardis (ed.), *Innovative Materials and Techniques in Concrete Construction: ACES Workshop*, DOI 10.1007/978-94-007-1997-2_23,

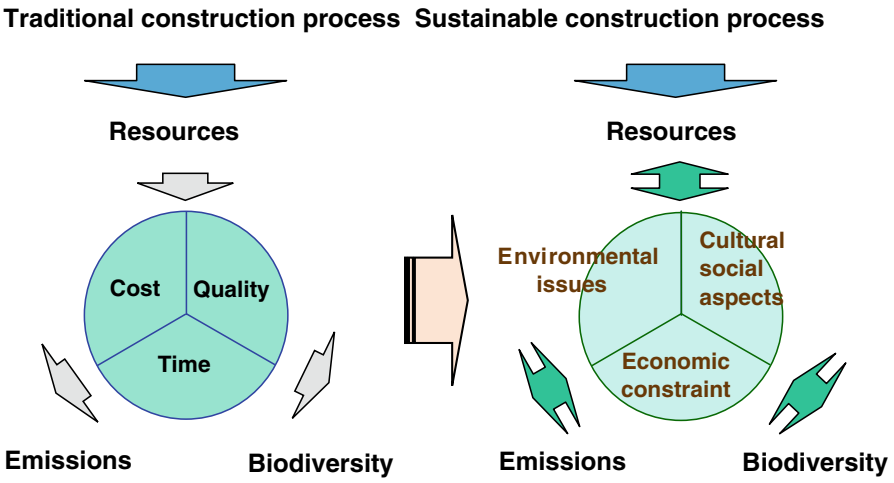

Fig. 23.1 Evolution from the traditional construction process to a sustainable one

approach is clearly pointed out. Figure 23.1 clearly shows to which extent environmental issues, cultural and social aspects and economic constraints can influence the construction process.

Sustainability requires a complete life-cycle assessment (LCA), which takes into account the environmental aspects and potential impacts of a product during its whole life cycle, with the goal of minimizing the negative environmental impact.

As far as concrete structures are concerned, consideration of all the life phases of a concrete product is required:

- Raw material acquisition: mining of aggregates, mining of stones for cement production, energy sources and energy production, water supply;
- Realization: production of concrete and concrete elements, design, construction;
- Utilization: use, maintenance, repair, renovation;
- End of service life: demolition, re-use, recycling, disposal, landfill

The potential to influence the degree of environmental impact (Ei) of a concrete structure throughout its life cycle has not been agreed on, but a general international consensus has been reached on the qualitative subdivision described in *fib* Bulletin 28 (Fig. 23.2): as clearly shown in this figure, the reduction of the environmental impact mainly relies on the:

- Conceptual design
- Technology concept
- Use/maintenance/repair
- Recycling

In view of the above considerations, it is obvious that sustainability requires a typical engineering method: to learn from the past experience with the aim to avoid wasting resources in the future, especially when correcting errors committed in the past.

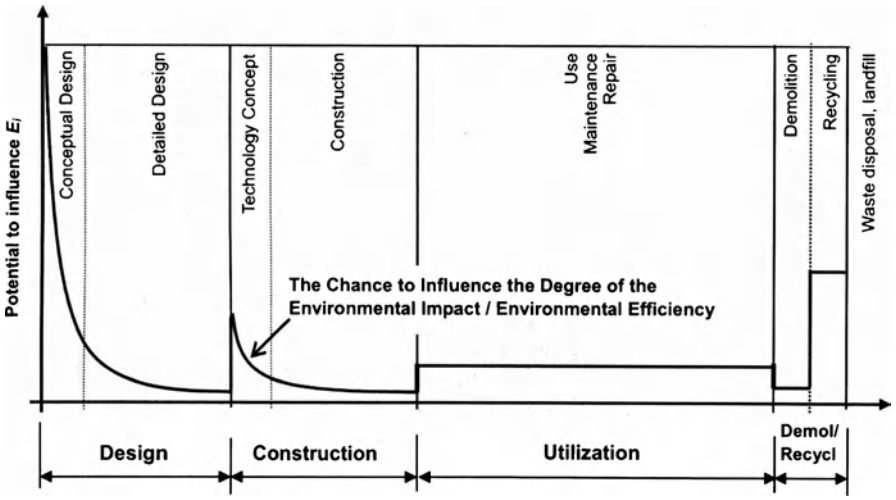

Fig. 23.2 Life cycle phases of a concrete structure (From *fib* Bulletin 28 fib 2004)

As far as bridges are concerned, durability plays a very important role. It currently attracts – and will continue to do so in the foreseeable future – large investment:

- About 60% of the investment in repair, strengthening and upgrading of existing infrastructures;
- About 40% of the investment in construction of new bridges.

The errors made in the past should be avoided. Therefore, both in upgrading existing infrastructures and in construction of new ones, the sustainability of the proposed interventions has to be carefully assessed.

A bridge that was recently constructed will be presented in detail. It meets the requirements of sustainability and, in particular, durability, which are considered fundamental in our days and should be satisfied to the greater possible extent. "Design for durability" should be considered as an essential step in any future designs, as it is closely linked with the service life of the structure, together with the verification of safety, serviceability and functionality.

23.2 Composite Box Girder Bridge

The use of external prestressing in the static scheme of a continuous beam has given a boost to the construction of composite steel concrete bridges. This new concept of a box-shaped deck bridge has turned out to be very interesting, because the use of steel is restricted only to the webs, and both top and bottom slabs are made of concrete. From a conceptual point of view, the compression stresses are essentially carried by concrete and the use of prestressing may lead to nil or very small tensile stresses in serviceability conditions (in the frequent combination of actions).

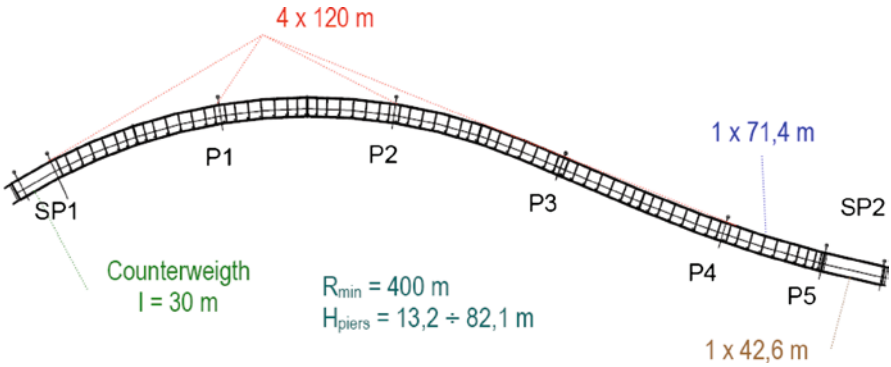

Fig. 23.3 Viaduct in plan

In addition, the extensive use of external prestressing enhances the durability and sustainability features of the bridge. In fact, it is easy to inspect its conservation in time, and to substitute, without limiting substantially the operability of the bridge, the tendons that were possibly damaged during their service life.

France, Germany and Japan boast several bridges of this kind, which sometimes use corrugated webs to avoid stiffeners for the steel plates, and to reduce the amount of prestressing that may migrate from the concrete to the steel parts of the section.

The first example of such type of deck in Italy is the Roccaprebalza Viaduct, located along the Parma-La Spezia highway. This bridge has established the world record for the entity of typical span (120 m) in the field of composite continuous beams with stiffened plated webs.

The viaduct has a total length of 624 m realized with a counterweight (30 m), four spans of 120 m, one span of 71.4 m, and a final isostatic (simply supported) span of 42.6 m. The reason for this last isostatic span is the expected movement of the ground by some millimeters per year in the vicinity of the last pier. The deck continuity has been interrupted, and multi-directional bearings have been used on the piers, integrated by adjustable transversal restraint under continuous monitoring.

Figure 23.3 displays the viaduct in plan, whereas Fig. 23.4 shows the transverse sections of the deck on the piers and at mid-span.

It can be easily seen that the layout in plan is very complex due to a minimum radius of curvature of only 400 m. The depth of the piers also varies, from a minimum of 13.15 m (P5) to a maximum of 82.07 m (P2).

The following options were considered during the conceptual design of the bridge:

- Segmental construction with match cast joints and use of a launching girder for the assembly, as it was practically impossible to supply segments of about 100 t weight from ground level in the valley.
- Classical cantilever with cast in situ segments and mixed prestressing: internal for construction phases, external for continuity tendons.
- Classical cantilever with composite deck and mixed prestressing: internal for construction phases, external for continuity tendons.

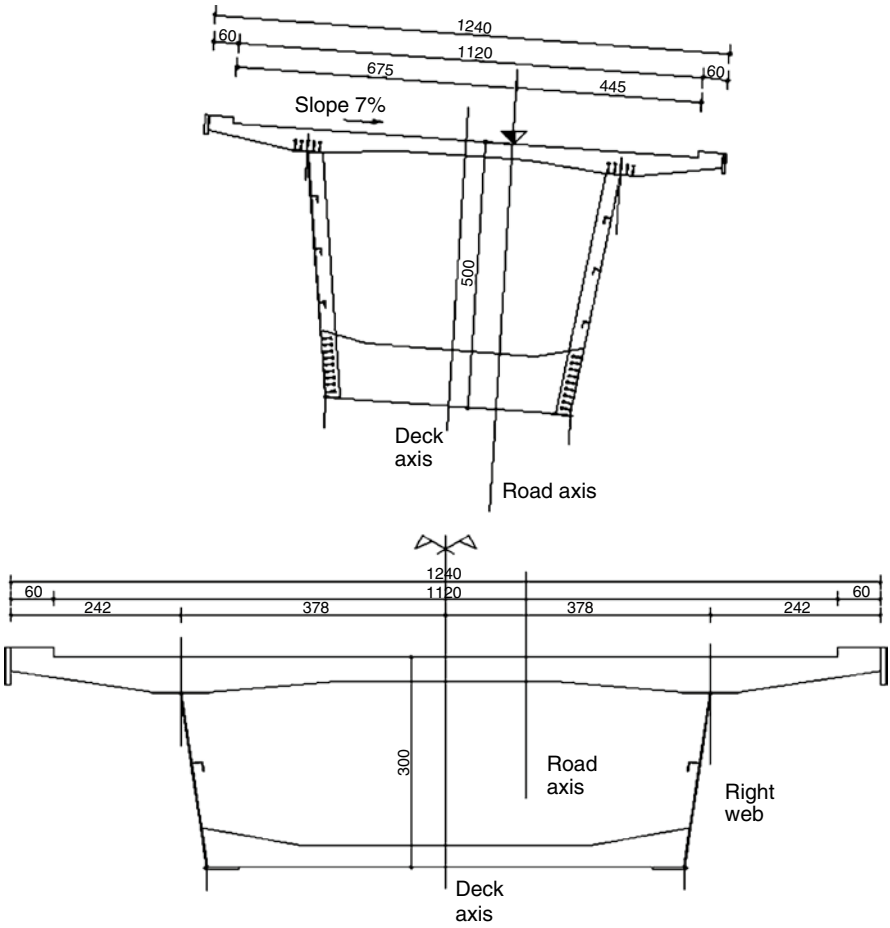

Fig. 23.4 Transverse sections above the pier (*top*) and at mid-span (*bottom*)

The first option was abandoned due to the very high cost of the launching girder, which would need a vertical hinge because of the ratio between span and horizontal curvature radius.

The second solution was also rejected due to the long construction time it required. In fact, only a couple of scaffolding would cost almost as much as the bridge itself.

The third solution was adopted in order to both reduce the execution time and to avoid the cost of the launching girder. In fact, as explained below, assembling the bridge only required a tower crane already used for the construction of the pier.

Fig. 23.5 Pier segment ready to be assembled

23.2.1 Construction Procedure

The construction sequence includes the following main steps:

- Positioning of the steel box of the pier segment, which is used as formwork for the subsequent concreting of the diaphragm and is able to both transfer the torque to the bearings and to anchor the cantilever to the pier by means of vertical prestressing tendons. The latter aspect is very important for the robustness of the deck during construction; if a segment falls, the cantilever should be able to keep its overall equilibrium as a rigid body on the pier. Figures 23.5 and 23.6, respectively, show the pier segment ready for the assembling and its positioning on the top of the pier.
- Assembling by bolts the webs of the following segments on both sides and their adjustment and stiffening by means of temporary steel ties, which are removed after casting the top slab.
- Placing precast slabs of 60 mm thickness, stiffened by a steel lattice, on the bottom flange of the steel webs. These slabs are used as formwork for the casting.
- Once the bottom flange is hardened, assembling the scaffolding and formwork for the top slab, whose internal surface lies on scaffolding directly supported by the bottom slab; the external scaffolding is tied to the webs by means of cross bolts. Figure 23.7 shows the bottom flange of the mid-span segment and the scaffolding and formwork of the top slab that has just been cast.

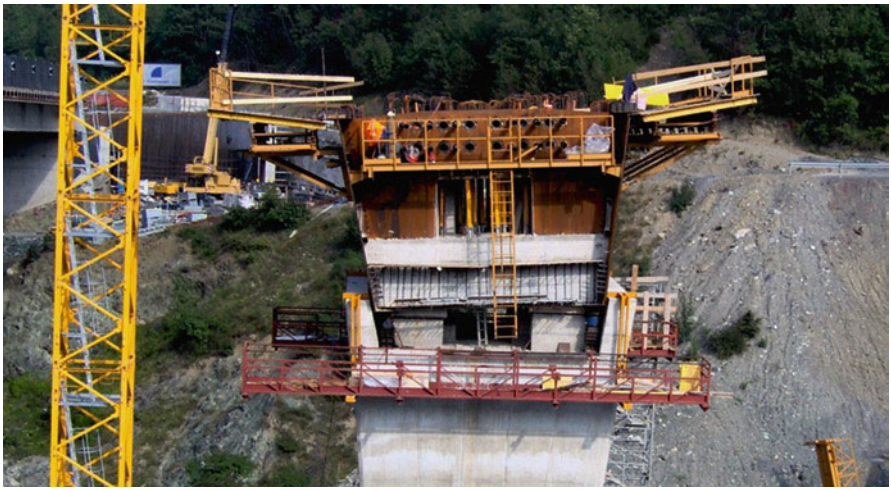

Fig. 23.6 Pier segment assembled on the pier

Fig. 23.7 Bottom and top flanges with formwork and scaffolding

- Insertion and tensioning of internal tendons, which are anchored on the pier segment of the hammers. In the case presented here, precast blisters were used for the anchorage of prestressing tendons. They were inserted in the formwork before casting. They had been designed using the indented construction joints model according to EN 1992-1-1 (CEN 2004a) and EN 1992-2 (CEN 2005) (see Fig. 23.8).
- The procedure illustrated above is repeated for all the remaining segments, working in parallel on different piers in order to build several hammers at the same time (Fig. 23.9). Figure 23.10 shows a completed cantilever.

Fig. 23.8 Precast anchorage blisters

Fig. 23.9 Parallel construction of several hammers

When two adjacent cantilevers are completed, a complex step is their adjustment in plan and elevation. During construction all the structure is supported on the pier by means of a system of hydraulic jacks, so that, at the end, it is possible to offset any positioning errors by moving the hammer as a rigid body before the casting of actual bearing connections. Then the two cantilevers are mutually connected by ties, and the final steel joint and the last casting are made (Fig. 23.11).

We should also keep in mind that during construction internal stiffeners (truss beams) and deviators are assembled inside the segments, as shown in Figs. 23.12 and 23.13, respectively.

Fig. 23.10 Completed cantilever spanning 60 m

Fig. 23.11 Completed cantilever spanning 60 m

It is now possible to place the external tendons, anchored at opposite sides of the pier segments, according to the layout shown in Figs. 23.14 and 23.15, and to apply 50% of the final prestressing force, after connecting each pair of hammers.

The remaining 50% of the prestressing is to be applied only on the final static scheme, in other words after the completion of the deck.

Fig. 23.12 Internal stiffeners

Fig. 23.13 External tendons' deviators

23.2.2 Main Aspects of Design

One of the most difficult design aspects is the definition of cumbering during construction so that the final configuration is reached under serviceability conditions. It has to be underlined that the cumbering system depends on the construction sequence which cannot be modified once the final cumbering has been calculated.

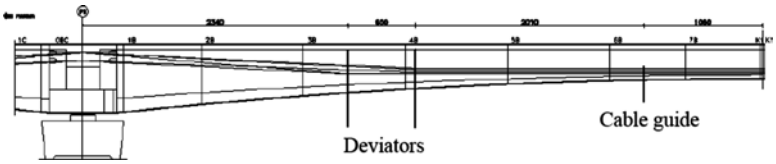

Fig. 23.14 Layout of external tendons

Fig. 23.15 Internal view of external tendons near the pier segment

A second important aspect is the evaluation of potential errors that should be compensated, such as:

- Geometrical errors in the cutting of the steel webs. They are generally very small, due to the accurate production technologies, and result in reduced tolerances.
- Geometrical errors in the thickness of the concrete slabs. They can be controlled with accurate construction, thus their consequences are limited.
- Scattering of shrinkage and creep parameters. Due to great uncertainties of these phenomena, their effects should be preliminarily investigated with sensitivity analyses.

Just to give an idea of the importance of cumbering, Fig. 23.16 shows the construction geometry of the hammer of pier P1. As it can be seen, on the left side, towards the counterweight, the tip of the cantilever is 30.86 mm higher than the pier segment, whereas the opposite end is only 9.25 mm higher. This asymmetry takes into account the assembling sequence of the hammer and the important displacements induced by the external prestressing, which is applied to the two cantilevers in a different static scheme.

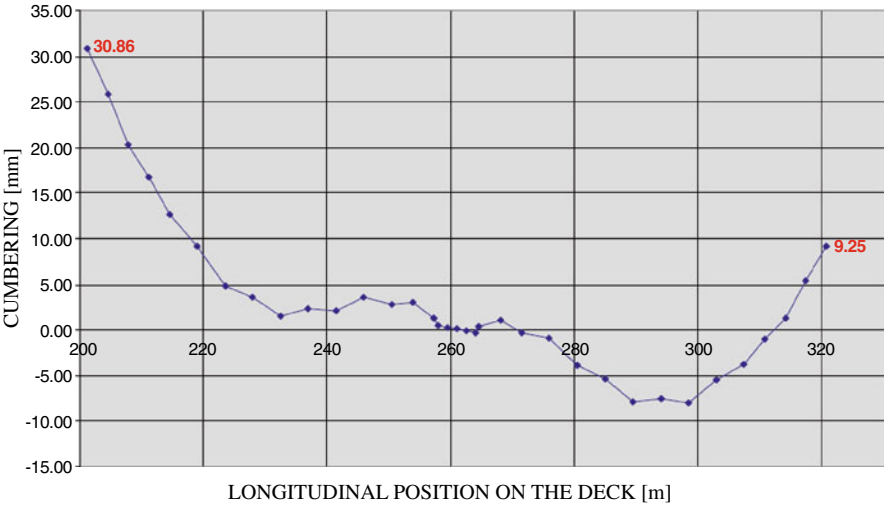

Fig. 23.16 Cumbering of hammer on pier P1

In the case under consideration, the final result of such cumbering has been the necessity to correct the resulting profile with a mean increase of the pavement thickness by 15 mm, which is fully acceptable considering the span and the plan layout of the viaduct.

The redistribution of internal actions due to the rheological behaviour of concrete, both within the section and in the whole structure, is another relevant aspect of design.

It is well-known that, dealing with a composite structure, the principles of linear viscoelasticity cannot be used. The general method for the evaluation of creep effects should be applied in agreement with EN 1992-2 (CEN 2005). The fundamental equation used for the analysis of such effects is:

$$\varepsilon_c(t) = \frac{\sigma_0}{E_c(t_0)} + \varphi(t,t_0)\frac{\sigma_0}{E_{c28}} + \sum_{i=1}^{n}\left(\frac{1}{E_{cti}} + \frac{\varphi(t,t_i)}{E_{c28}}\right)\Delta\sigma(t_i) + \varepsilon_{cs}(t,t_s) \quad (23.1)$$

in which the first term describes the instantaneous deformation due to stresses applied at time t_0, whereas the second term represents the viscous deformation due to the same state of stress, the third term the amount of instantaneous and viscous deformation that takes place at time $t_{i,}$ and the fourth term the shrinkage deformation. Equation 23.1 should be used in a time-history that follows the assembling operations, for instance the casting of a couple of symmetrical segments.

On the other hand, the losses of the external tendons are evaluated using the mean stress between two adjacent deviators, because under serviceability conditions no slip can take place in these devices.

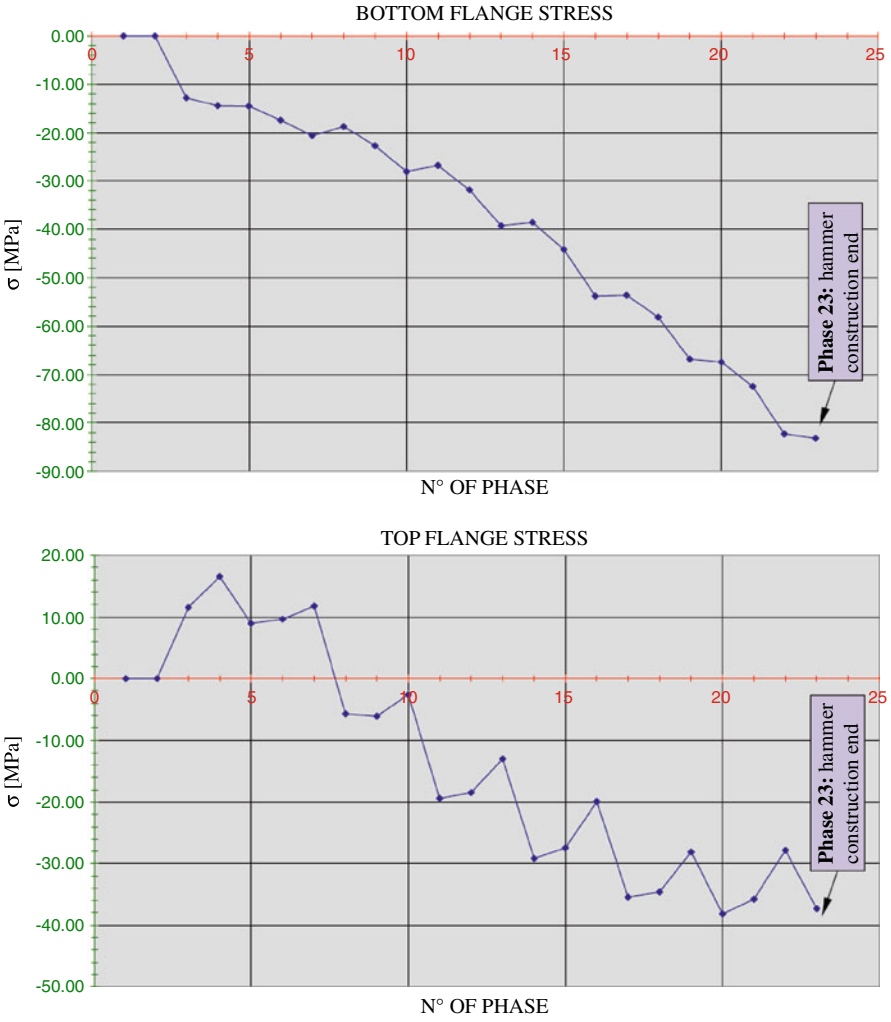

Fig. 23.17 Evolution of stresses in the top and bottom steel flanges of the first segment during the construction process

In such kind of structures, a strong redistribution of internal actions is expected with time from concrete to steel, particularly in relation to the effects of prestressing. An accurate analysis of the stability of steel plates and a careful design of bolted connections are therefore required.

Figure 23.17 illustrates the evolution, during construction, of stresses in the top and the bottom flange of the steel web of the first segment after the pier-diaphragm. As was very much expected, the bottom flange is compressed at every step, but also

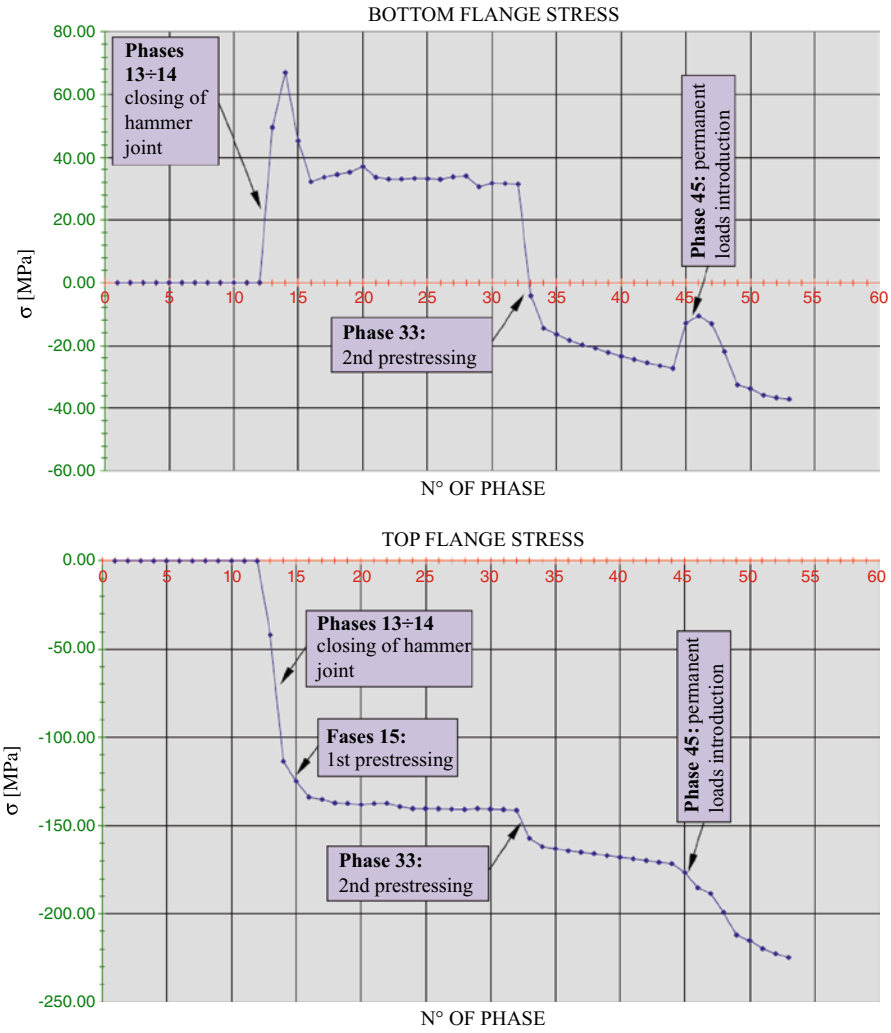

Fig. 23.18 Evolution of stresses in the top and bottom steel flanges of the mid-span segment during the construction process

the top flange is compressed after the introduction of prestressing in the second segment.

Figure 23.18 shows the same stresses at mid-span: both flanges are compressed in the very long term, but the upper one is in tension until the external prestressing is completed. After this operation, which is identified as phase 33, a significant migration of stresses from concrete to steel can be clearly observed.

This phenomenon reduces the residual compressive stresses in the concrete but, in any case, it is not able to increase the tensile stresses under serviceability conditions (under the frequent combination of actions).

This migration could be reduced to some extent if corrugated steel webs were used; an option that, nevertheless, implies an increase of about 50% in the amount of steel required.

Although it is elegant and reduces the amount of external prestressing, this solution is inconvenient nowadays from an economical point of view, in particular after the publication of EN 1993-1-5 (CEN 2004b). In fact this code, unlike the previous ones which are generally used in design, allows for a significant reduction in the stiffeners used in plated structural elements.

23.3 Conclusions

From the above discussion, we can draw the conclusion that the solution of composite steel-concrete deck with additional external prestressing is sustainable from several points of view:

- Durability: absence of longitudinal tensile stresses in the concrete under serviceability conditions, in particular in the frequent combination of actions.
- Economy: reduction of construction time and avoidance of the very expensive launching girder.
- Environmental impact reduction: the large areas that are usually necessary for the construction and storage of concrete precast segments are not needed.
- Maintenance: it is easy to inspect the external tendons.
- Rehabilitation: it is possible to substitute the external tendons without obstructing the traffic significantly.

It is also worth noting that this kind of deck is economical for spans of up to 160–170 m for continuous decks. Thus the scope of possible application of continuous concrete box girder bridges is enlarged. For longer spans, of up to 300 m, the proposed solution may be adjusted by adopting the static scheme of an extradosed bridge, as has been done in several structures in Japan.

Lastly, for the construction of the bridge under consideration, the following ratios show the materials used per square meter of the deck:

- Concrete: 0.85 m^3/m^2
- Steel: 220 kg/m^2
- Prestressing steel (internal and external): 60 kg/m^2
- Ordinary reinforcement 170 kg/m^2

Such data provide clear evidence that the chosen solution is economical.

References

Burtland GH (1987) Common future. The World Commission Environment and Development (WCED). Oxford University Press, Oxford

CEN (2004a) Eurocode 2: design of concrete structures – part 1.1: general rules and rules for buildings. Comite Europeen de Normalisation, Brussels. ISBN EN 1992-1-1:2004

CEN (2004b) Eurocode 3: design of steel structures – part 1.5: plated structural elements. Comite Europeen de Normalisation, Brussels. ISBN EN 1993-1-5:2004
CEN (2005) Eurocode 2: design of concrete structures – part 2: concrete bridges, design and detailing rules. Comite Europeen de Normalisation, Brussels. ISBN EN 1992-2:2005
fib (2004) Environmental design – state-of-the-art report. *fib* Bulletin 28. Federation internationale du beton, Lausanne

Chapter 24
Orthotropic Model for the Analysis of Beams with Corrugated Steel Webs

Gabriele Bertagnoli, Mario Alex Biagini, and Giuseppe Mancini

Abstract A flat orthotropic finite element model for steel and composite beams with corrugated webs is presented in this paper. The target of the authors is to improve computational efficiency and to reduce input time by means of material orthotropic equivalence. The results obtained with the simplified model proposed in the paper are compared to both the available outputs from experimental tests and other numerical analyses done with full 3D models. Both elastic and plastic behaviour is investigated. Buckling loads of corrugated steel webs under different loading cases are studied in detail. A parametric study of the 2D "flat" equivalent model is presented in order to investigate the influence of geometric parameters on the structural behavior and to check the robustness of the simplified method in predicting different failure modes. Finally, the effect of mesh size is studied on a control specimen. Good overall results of this procedure are demonstrated.

24.1 Introduction

Corrugated web girders represent a new structural system developed in the past two decades. The girder's flanges provide the bending strength; the corrugated webs provide almost no contribution to bending, but ensure the girder's shear capacity. Failure of the web occurs by steel yielding, buckling or interaction between the two. Lateral torsion and local flange buckling of corrugated web girders represent two other possible failure criteria.

G. Bertagnoli (✉) • M.A. Biagini • G. Mancini
Dipartimento di Ingegneria Strutturale e Geotecnica, Politecnico di Torino, C.so Duca degli Abruzzi 24, Torino 10127, Italy
e-mail: gabriele.bertagnoli@polito.it; mario_alex.biagini@libero.it; giuseppe.mancini@polito.it

M.N. Fardis (ed.), *Innovative Materials and Techniques in Concrete Construction: ACES Workshop*, DOI 10.1007/978-94-007-1997-2_24,

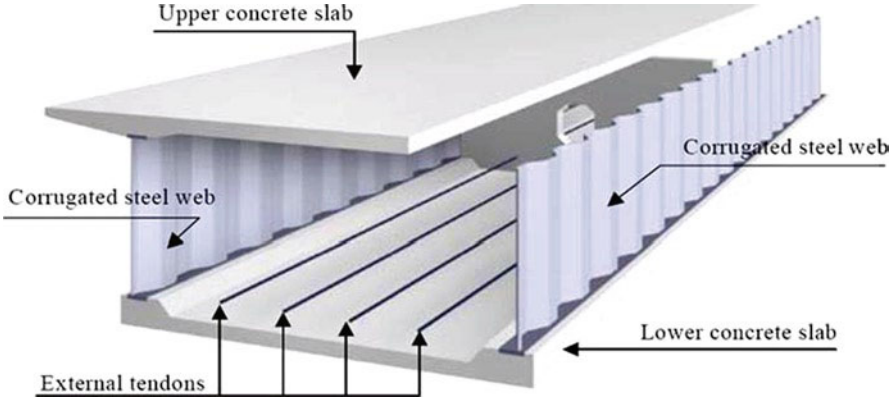

Fig. 24.1 Typical section of PC bridge with corrugated web

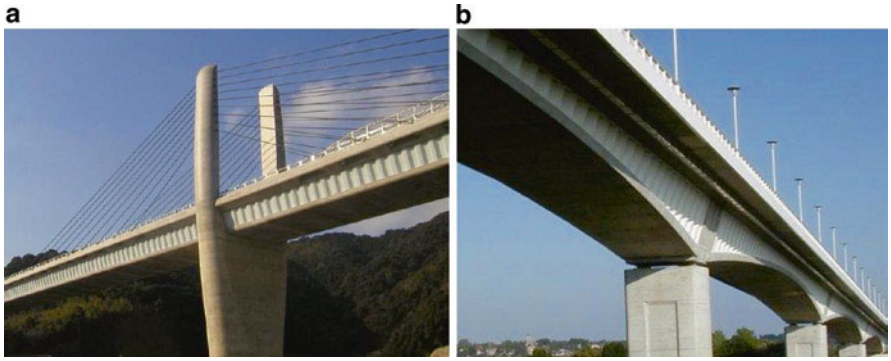

Fig. 24.2 (**a**) Himi Yuma Bridge, Japan, and (**b**) Pont de la Corniche, France

Corrugated steel webs are usually used on a composite girder bridge with concrete flanges because of their cost effectiveness. Concrete webs are replaced with corrugated steel plates to reduce the self-weight, which can also speed up construction and/or reduce construction costs. The corrugated steel webs can withstand shear actions without absorbing axial stresses due to prestressing, thus enabling efficient prestressing of top and bottom concrete deck slabs. Moreover, corrugated webs also provide high shear buckling resistance. Figure 24.1 shows the typical section of a prestressed concrete bridge with corrugated webs.

Many bridges with corrugated steel web were built in Japan. One of these is the Himi Yuma Bridge (Fig. 24.2a. It was finished in≠and it is the longest extradosed bridge with corrugated steel webs. It has Y-shaped intermediate piers and it is composed of three spans with the central one 180 m long. Its deck is box-shaped and composed by prestressed concrete flanges and corrugated steel webs. The extradosed prestressing concept is a type of structural system placed between cable-stayed bridges

and ordinary girder bridges with internal or external tendons. Tendons are installed outside the main girder and deviated by short antennas located over the piers.

Corrugated steel webs are also used in Europe on composite girder bridges. A great example is the Pont de la Corniche in France (Fig. 24.2b. It was the first bridge of this kind built with the cantilever method. It has a box-girder cross section with prestressed concrete flanges. The structure is composed of seven spans (48 m long edge spans and 80 m inner ones), and the girder is 14.5 m wide. The web height varies from 4.011 (on the piers) to 1.081 m (in the midspan) and its thickness ranges from 8 to 10 mm. Thickness is maximum where prestressing tendons are deflected and minimum at the abutments. The Pont de la Corniche is prestressed by three families of tendons, namely cantilever, continuous and external. Cantilever tendons were anchored to the top slab and tensioned after completion of each pair of symmetrical segments (hammer construction). After the cantilevers were assembled they were joined by continuous tendons. The whole structure is then prestressed by external tendons and the tendon profile is achieved using two concrete diaphragms per web.

24.2 Flat Approximated Model for Corrugated Webs

Many researchers have been studying the behaviour of girders realized with corrugated webs from the end of the ‘50s to date. The most famous works were by Fraser (1956), Basler (1961), Luo and Edlund (1996), Elgaaly et al. (1997), Johnson and Cafolla (1997), El-Metwally (1998), Ibrahim et al. (2006).

The bending behaviour of such panels has been described by Elgaaly and Seshadri (1997) whereas the shear behaviour has been approached by Lindner (1991).

Numerical analyses using finite element methods were performed by Luo and Edlund (1995) and by Elgaaly and Seshandri (1998).

The buckling behaviour of corrugated panels has been studied by Aravena and Edlund (1987), Dahlen and Krona (1983) and Easley and McFarland (1969).

The main purpose of the study is to propose an equivalence to simplify the 3D corrugated web in a 2D equivalent surface. Figure 24.3 explains the transformation of a basic web element from the real 3D corrugated shape to a fictitious flat unit.

There are several reasons to find out a proper equivalence. A flat simulation offers the opportunity to have a lighter f.e.m. model, an easier geometry to input and a quicker analysis, as the corrugated web may be treated as an equivalent orthotropic plate.

Orthotropy can be described both in terms of geometry properties and of material properties. In the first case, geometric equivalent areas and moments of inertia have to be calculated whereas the material may have isotropic properties. In the second case, a simple plate element with uniform thickness but different material properties (Young modulus and Poison coefficient) in the main in-plane directions. The second approach is presented in the present paper: the geometric approach was abandoned as it worked only with linear elastic material properties, while material equivalence could be extended to a non-linear field.

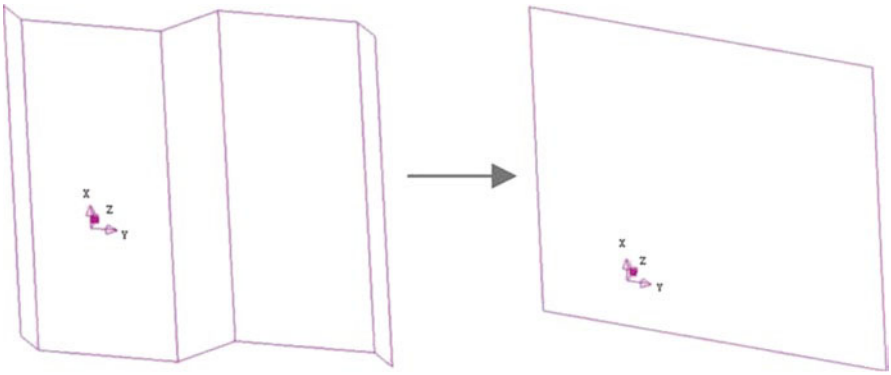

Fig. 24.3 Basic element equivalence

A flat geometric model is used. Geometric parameters such as areas and moments of inertia are therefore constant in all directions. Material's parameters such as Young's moduli, Poisson ratios and shear moduli are different depending on the axis. The complete three dimensional material stiffness matrix is shown in the following (see Timoshenko and Woinowsky-Krieger 1970):

$$\begin{Bmatrix} \sigma_{xx} \\ \sigma_{yy} \\ \sigma_{xy} \\ \sigma_{yz} \\ \sigma_{zx} \end{Bmatrix} = \begin{bmatrix} E_x & -\nu_{xy}E_x & 0 & 0 & 0 \\ -\nu_{xy}E_x & E_y & 0 & 0 & 0 \\ 0 & 0 & G_{xy} & 0 & 0 \\ 0 & 0 & 0 & G_{yz} & 0 \\ 0 & 0 & 0 & 0 & G_{zx} \end{bmatrix} \begin{Bmatrix} \varepsilon_{xx} \\ \varepsilon_{yy} \\ \gamma_{xy} \\ \gamma_{yz} \\ \gamma_{zx} \end{Bmatrix} \tag{24.1}$$

The relations between the material parameters shown in Eq. 24.1 can be derived for corrugated webs in an approximated way by means of stiffness equivalence.

We identify with y the longitudinal axis of the beam, with x the axis orthogonal to y and lying in the plane of the web, and with z the axis orthogonal to the plane of the web.

The thickness of the equivalent flat model is calculated in order to have in the 2D model the same volume of the web of the 3D "real" model, so as to have the same self-weight of the element.

The equivalence between the real 3D web and the flat element of the out of the plane bending stiffness of a portion of web of unit length in the y direction reads:

$$E \cdot I_{yy,3D} = E_x I_{yy,eq} = E_x \frac{t_{eq}^3}{12} \tag{24.2}$$

where: E is the elastic modulus of steel (i.e. 210 GPa)
$I_{yy,3D}$ is the inertia modulus of the real 3D web for out of the plane bending
E_x is the term in position 1,1 of the matrix in Eq. 24.1
t_{eq} is the thickness of the equivalent 2D web

In a similar way, the equivalence between the real 3D web and the flat element for the membrane force in the x direction reads:

$$EA_{xx,3D} = E_x I_{xx,eq} = E_x t_{eq} \tag{24.3}$$

where: E is the elastic modulus of steel (i.e. 210 GPa)
$A_{xx,3D}$ is the cross section of a portion of real 3D web of unit length
E_x is the term in position 1,1 of the matrix in Eq. 24.1
t_{eq} is the thickness of the equivalent 2D web

$A_{xx,3D}$ can be calculated by multiplying the actual thickness off the 3D web by the length of the steel plate needed to have a unit length corrugated panel.

Equations 24.2 and 24.3 can be written in a system to calculate the unknowns E_x and t_{eq}.

$$\begin{cases} E_x I_{yy,3D} = E_x \dfrac{t_{eq}^3}{12} \\ E_x A_{xx,3D} = E_x t_{eq} \end{cases} \tag{24.4}$$

The equivalent Young's modulus in the longitudinal direction y is calculated considering the accordion effect. This term describes the low axial rigidity in stretching and contracting in the direction of the corrugation as described by Huang et al. (2002).

Let's consider wavelength portion of web in the y direction and of unit side in the x direction, extrapolated from the beam and loaded with the boundary conditions shown in Fig. 24.4.

The ratio r_{eq} between the y-displacements of the 3D real model and the 2D equivalent flat model with an equivalent thickness t_{eq} was used to calculate E_y.

$$r_{eq} = \frac{\Delta_{y,3D}}{\Delta_{y,flat}} \tag{24.5}$$

$$E_y = \frac{E}{r_{eq}} \tag{24.6}$$

The ratio r_{eq} may be calculated with excellent accuracy using the simple beam model shown in Fig. 24.5. A wavelength of corrugated steel web is considered (Fig. 24.4a).

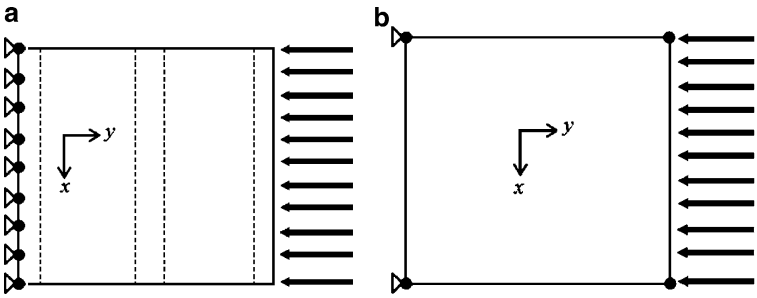

Fig. 24.4 Loading and boundary condition of the 3D (**a**) and equivalent flat (**b**) model

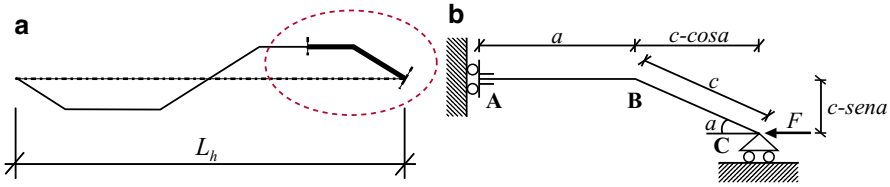

Fig. 24.5 A wavelength of corrugated steel web (**a**) and equivalent static scheme (**b**)

In order to depict the web deformation, proper symmetry constraints are applied to the substructure shown in Fig. 24.5b.

To derive a simple solution, it is assumed that the web is under pure bending moment and the axial deformation in each plate element of the corrugated web is negligible. The displacement of point C can be calculated as follows:

$$\begin{aligned}\delta_{3D} &= \int_s \frac{M_i M}{EJ} dS = \int_A^B \frac{Fc^2 \sin^2\alpha}{EJ} dx + \int_B^C \frac{Fc\sin\alpha}{EJ}\left(1-\frac{x}{c}\right) c\sin\alpha\, dx \\ &= \frac{Fc^2\sin^2\alpha}{EJ}\left(a+\frac{c}{3}\right)\end{aligned} \tag{24.7}$$

where a, c and α are shown in Fig. 24.4b.

The total horizontal displacement of a wavelength is four times the displacement calculated above. If we express the moment of inertia J of the panel as a function of the real thickness t, we get for a unit height $J = t^3/12$:

$$\Delta_{3D} = 48\frac{Fc^2\sin^2\alpha}{Et^3}\left(a+\frac{c}{3}\right) \tag{24.8}$$

The Δ_{3D} displacement calculated with Eq. 24.8 of single-wave element is compared with the x-displacement of a unit height isotropic flat model:

$$\Delta_{flat} = \frac{FL_h}{Et_{eq}} \tag{24.9}$$

where: F is the same load applied on the 3D model
L_h is the wavelength shown in Fig. 24.4
E is the elastic modulus of steel (i.e. 210 GPa)
t_{eq} is the thickness of the equivalent 2D web
It is then possible to calculate the accordion effect factor:

$$r_{eq} = \frac{\Delta_{y,3D}}{\Delta_{y,flat}} = 48\frac{c^2 \sin^2 \alpha t_{eq}}{L_h t^3}\left(a + \frac{c}{3}\right) \tag{24.10}$$

The Young's modulus in the longitudinal direction is calculated by the product of the real Young's module for the ratio r_{eq}, calculated above. The shear modulus has the same value for all directions and it is calculated as:

$$G_{xy} = G_{yz} = G_{xz} = G_{eq} = G\frac{t_{eq}}{t} = \frac{E}{2(1+\nu)}\frac{t_{eq}}{t} \tag{24.11}$$

where ν is the real Poisson ratio and it is assumed equal to 0.3. The equivalent Poisson ratio ν_{xy} is assumed null in all directions, since the web behaves in a very different way in x and y directions:

$$\nu_{xy} = 0 \tag{24.12}$$

24.3 Experimental Validation

The results obtained with numerical models, both full 3D and the approximated 2D proposed by the authors, are compared in this section to the results obtained in laboratory on tested specimens.

24.3.1 Ibrahim, El-Dakhakhni and Elgaaly (2006) Beam

The numerical simulation of the test made on a steel beam with trapezoidally corrugated webs by Ibrahim, El-Dakhakhni and Elgaaly (2006) is presented in this paragraph. The beam was made of 3 mm thick and 500 mm deep web, and 12 mm

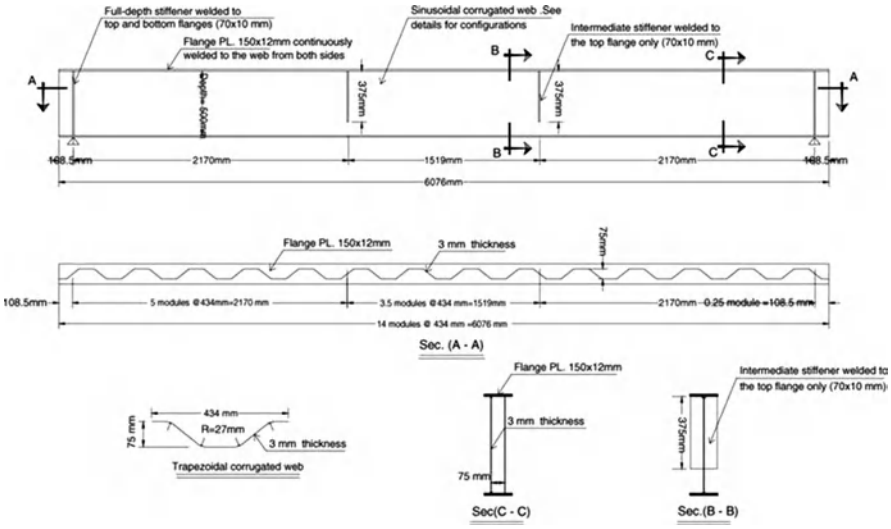

Fig. 24.6 Geometry of Ibrahim, El-Dakhakhni and Elgaaly (2006) test specimen

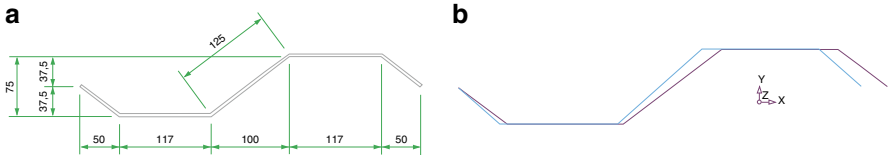

Fig. 24.7 Dimensions (in mm) of a single wave (**a**), deformation due to accordion effect (**b**)

thick and 150 mm wide flanges. The geometry and the load scheme of the experiment are shown in Fig. 24.6.

A single-wave portion of the web is shown in Fig. 24.7 together with the deformed shape due to the accordion effect.

The force has a value of −10 N in the negative X-direction, so it acts horizontally. The displacement in x-direction is $\Delta X = 9.18e-6$ m, as shown in Fig. 24.7b. Then, a second model is carried out. It has a rectangular shape of dimension 434 × 250 mm: the base is as long as the horizontal projection along x-direction of the 3D model, the height is half of the girder depth. The web thickness is equal to the equivalent thickness (105.2 mm). The specimen has the same stress-strain relationship, supports and load as the previous model. The displacement of the flat model in x-direction is $\Delta X' = 0.723 \times 10^{-8}$ m. The resulting ratio used to take into account the accordion effect is $r_{eq} = \Delta X/\Delta X' = 1{,}260$. It is now possible to model the whole girder with the equivalent flat model. As explained before, the equivalent thickness and the Young's module in the vertical direction are set

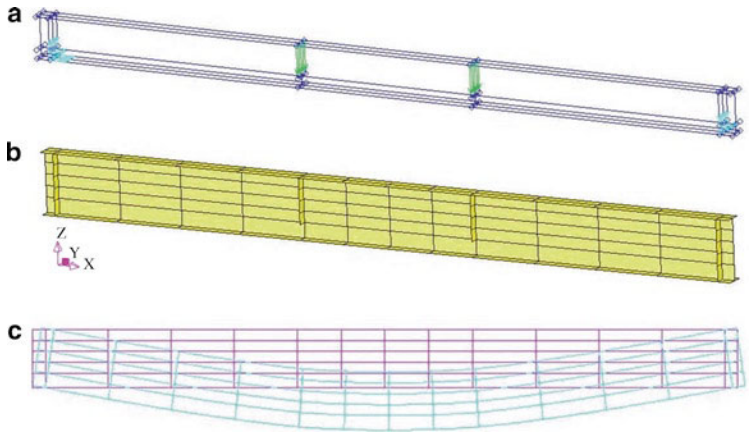

Fig. 24.8 Geometry, supports and loads of the flat model (**a**), its mesh (**b**) and deformed shape (**c**)

through axial and flexural rigidity equivalence between flat and 3D model. Resulting equations are:

$$\begin{cases} t_{eq} = \sqrt{\dfrac{12 I_{yy,3D}}{A_{xx,3D}}} = 0.1052m \\ E_{x,eq} = \dfrac{A_{xx,3D} E}{t_{eq} L_{x,eq}} = 6360 \dfrac{N}{mm^2} \end{cases} \tag{24.13}$$

where $I_{yy,3D} = 1{,}339{,}000\ \text{mm}^4$
$A_{xx,3D} = 1{,}450\ \text{mm}^2$
$E = 200{,}000\ \text{N/mm}^2$
$L_{x,eq} = 434\ \text{mm}$

The Young's modulus in the longitudinal direction is calculated dividing the real Young's modulus by the ratio r_{eq}, calculated above:

$$E_{y,eq} = \frac{E}{r_{eq}} = 158.4 \frac{N}{mm^2} \tag{24.14}$$

The shear modulus has the same value for all directions and it is calculated as:

$$G_{eq} = G \frac{t_{eq}}{t} = \frac{E}{2(1+\nu)} \frac{t_{eq}}{t} = 2200 \frac{N}{mm^2} \tag{24.15}$$

where ν is the real Poisson ratio and it is assumed equal to 0.3.

Once the material parameters are calculated, the model of the whole girder is implemented. A global view of the fem geometry is shown in Fig. 24.8a. The flat

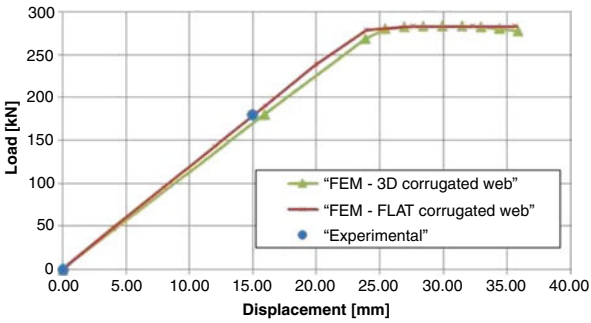

Fig. 24.9 Comparison of load-displacement curves

equivalent mesh is shown in Fig. 24.8b. It is clearly visible that this model requires fewer elements than the 3D one: in the flat web there are only 56 shell elements, while in the corrugated one there were 2,367 elements. The deformed shape obtained through the non-linear analysis is shown in Fig. 24.8c.

The load-displacement curve of the equivalent model is then compared with experimental values and with numerical results of the 3D model with corrugated webs (Fig. 24.9). A very good agreement is found: the yielding load of the flat model is 3.5% greater than the 3D one. There is no difference in the plastic range.

24.3.2 Prestressed Concrete Girder with Corrugated Steel Web

Prestressed concrete girders with corrugated steel webs are one of the most promising concrete-steel hybrid structures applied to highway bridges. As shown in the test carried out by Ata, prestress can be efficiently introduced into the concrete flanges due to the "accordion effect" of the corrugated web.

The geometry and boundary conditions of the large-scale specimen analyzed by Ata et al. (2001) are given in Fig. 24.10.

Since the main purpose of the experimental test program was to evaluate the fatigue performance of four different steel web joints located at positions J1–J4, the static loading tests were conducted before the fatigue test only within the elastic range.

The corrugated web in this case had the following characteristics: Young's modulus E_s =206 GPa, thickness of 9 mm, inclined and straight segments with the same length (430 mm), inclination angle θ=30°. The upper and lower steel flanges (320×16 mm) were welded to the corrugated web. However, the steel flanges were cut at four locations, J1–J4, to promote the accordion effect of corrugated web. External flanges were made of concrete with a compressive strength f'_c=37.9 MPa

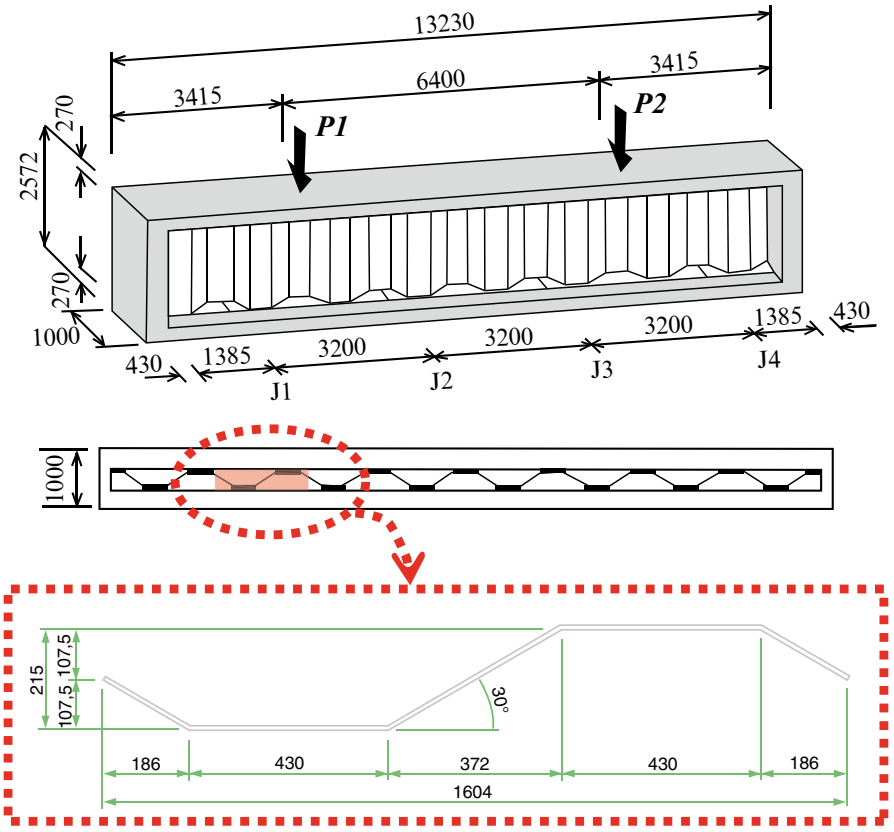

Fig. 24.10 Ata et al. (2001) test specimen (dimensions in mm)

and Young's modulus $E_c = 23.8$ GPa. The beam was simply supported and was subjected to two different load cases:

1. Two concentrated loads, $P1$ and $P2$, on each quarter span. Both loads were equal to 50 kN.
2. Concentric prestressing coming from four prestressing tendons (diameter 21.8 mm) located in the top and bottom concrete flanges of the specimen, and then stressed to 1,300 MPa.

The procedure shown in paragraph two is applied to the new web geometry. The ratio to take into account the accordion effect is $r_{eq} = \Delta X/\Delta X' = 9.94e2$. The material properties of the equivalent flat model are:

$$\begin{cases} t_{eq} = \sqrt{\dfrac{12 I_{yy,3D}}{A_{xx,3D}}} = 0.304m \\ E_{x,eq} = \dfrac{A_{xx,3D} \cdot E}{t_{eq} L_{x,eq}} = 6540 \dfrac{N}{mm^2} \end{cases} \tag{24.16}$$

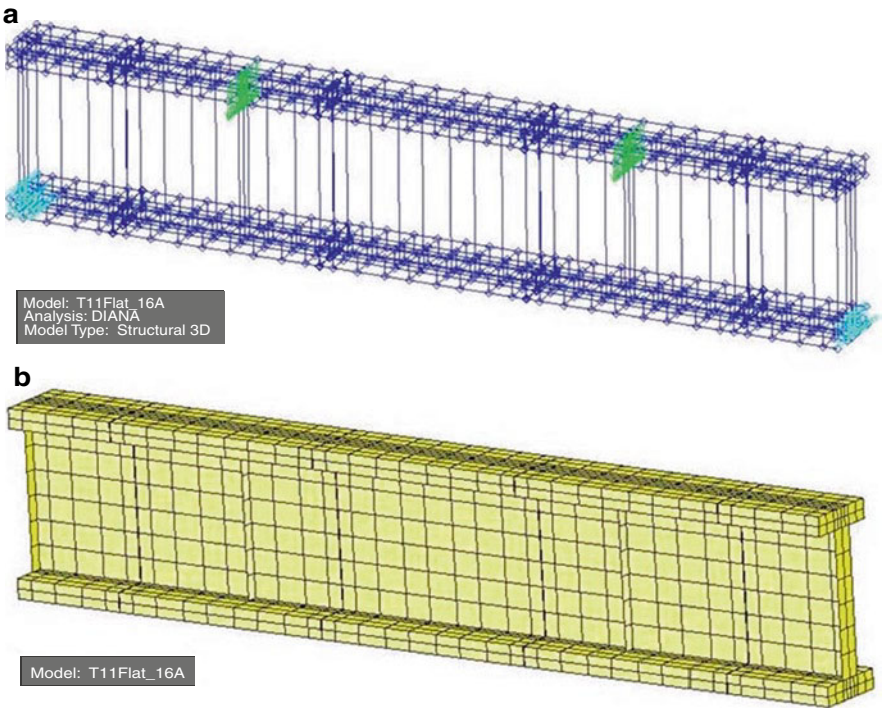

Fig. 24.11 Geometry, supports and loads of the flat model (**a**) and its mesh (**b**)

where $I_{yy,3D} = 1.192e8\ mm^4$
$A_{xx,3D} = 1.548e4\ mm^2$
$E = 2.06e5\ N/mm^2$
$L_{x,eq} = 1.604\ mm$
Then:

$$E_{y,eq} = Er_{eq} = 6136000\frac{N}{mm^2}$$
$$G_{eq} = G\frac{t_{eq}}{t} = \frac{E}{2(1+\nu)}\frac{t_{eq}}{t} = 2350\frac{N}{mm^2} \tag{24.17}$$

where ν is the real Poisson ratio and it is assumed equal to 0.3. The equivalent Poisson ratio is assumed null in all directions ($\nu_{xy} = 0$). A global view of the fem geometry is shown in Fig. 24.11a.

The mesh with flat web is shown in Fig. 24.11b. It is clear that the flat web model requires fewer elements than the 3D one: in the flat web there are only 245 shell elements, while in the corrugated one there were 3,647 elements. The deformed shape under load case 1 is shown in Fig. 24.12a. The load-displacement curve of the

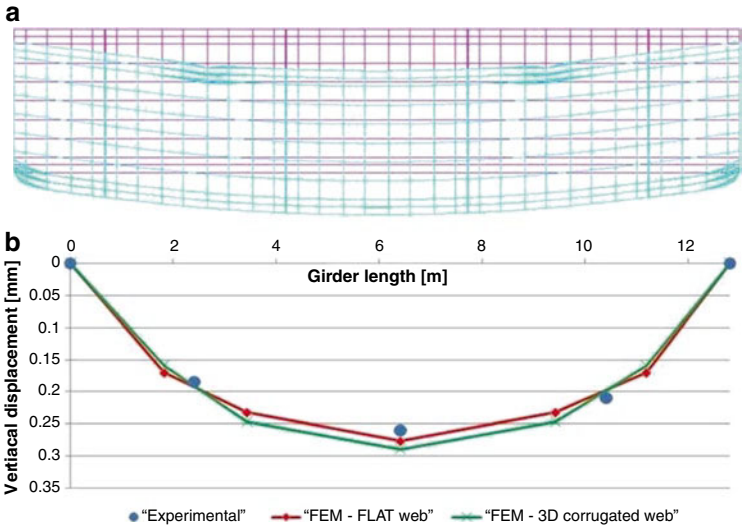

Fig. 24.12 Flat model deformed shape (**a**) and comparison of deflection curves due to symmetric loads (**b**)

equivalent model is then compared in Fig. 24.12b with experimental values reported in previous studies and with numerical results of the 3D numerical model with corrugated webs. A very good agreement is observed.

24.3.3 Influence of Mesh Dimension

In order to understand if mesh division can affect finite element outputs, the case of study analyzed in paragraph 24.3.2 was examined with load case 2 (axial prestressing) and three different meshes obtained with almost squared elements (flat equivalent web) changing web mesh division:

(a) small elements (the web is vertically divided in 24 parts);
(b) intermediate elements (the web is vertically divided in 12 parts);
(c) big elements (the web is vertically divided in 6 parts).

Horizontal (axial) displacements are calculated in three different points:

1. bottom flange surface at the midspan,
2. bottom flange surface under the load application point,
3. half web height over the right support.

Very good agreement was found in all comparisons, as reported in Table 24.1. The maximum divergence between results from the 3D web model and the equivalent one is equal to 5.06%. As a consequence, it is possible to state that mesh element

Table 24.1 Comparisons between 3D model and flat model displacements

	Point 1	Point 2	Point 3
3D model	1.32E-03	1.97E-03	2.57E-3
Mesh a	1.33E-03 0.76%	2.01E-03 2.03%	2.62E-03 1.95%
Mesh b	1.33E-03 0.76%	2.06E-03 4.57%	2.70E-03 5.06%
Mesh c	1.36E-03 3.03%	2.06E-03 4.57%	2.70E-03 5.06%

Table 24.2 Comparison between 3D and equivalent model computation times

	Nodes	Elements	Time [s]
3D model	68,000	16,128	780
Mesh a	18,333	4,216	72
Mesh b	8,850	1,854	37
Mesh c	8,358	1,707	30

dimensions are not relevant to analysis outputs and, on the other hand, that bigger elements allow quicker analysis.

It is worth noting that a major reduction in computation time is obtained by using bigger elements and flat web geometry. In order to understand this aspect, a comparison is proposed in Table 24.2 between the number of nodes, the number of elements and the computation times of the 3D web model and those of the equivalent flat web models described above. It can be estimated that the analysis of the model with small size mesh elements (case "a") is 11 times faster than the 3D web model analysis, and that the analysis done with big elements (case "c") is 26 times faster than the 3D web model analysis.

24.4 Conclusions

The proposed equivalent flat model can be an efficient tool for structural analyses of corrugated steel web girders.

It is built and tested on experimental results for web subjected to in-plane actions. Under this load conditions it works very well within the elastic field and is able to predict the plastic yielding if it occurs before buckling.

The equivalence is able to model the out of the plane stiffness also, but its performance outside the elastic field has still to be verified.

The main advantage of the solution proposed consists in the reduction of input time due to the simplified geometry, of the number of elements and degrees of freedom, and in the fact that the proposed equivalence is not affected by the size of the mesh. All these results lead to a remarkably greater computational efficiency.

Although the research presented in this thesis does not cover all the aspects related to the corrugated beams, it does lay a foundation for further studies. Based

on the research already done, it has been found that there are still a lot of topics which need to be carried out in the following areas:

- evaluation of the reduction of the prestressing action in comparison with plane webs;
- study of the rheological behaviour of composite corrugated steel-concrete;
- analyses of the transverse actions' influence on the web stability (folded plate);
- study of the behaviour of corrugated webs subjected to out-of-plane loads;
- analysis of the effects of corrugation line radius combined with the angle between the horizontal and inclined folds and thickness of the web;
- studies on the buckling strength, especially when the web shear buckling load is close to the flange yielding load.
- more experimental tests should be carried out to study the lateral torsional buckling behavior of corrugated steel webs.

References

Aravena L, Edlund B (1987) Trapezoidally corrugated panels-buckling behavior under axial compression and shear. Publ 87.1, Division of Steel and Timber Structures, Chalmers University of Technology, Sweden

Ata Y et al (2001) Static and fatigue test of beam specimens for prestressed concrete bridge with corrugated steel web. Prestress Concr J Japan 43(4):72–81

Basler K (1961) Strength of plate girders in shear. Proc ASCE 1 J Struct Div USA 87:151–180

Dahlen A, Krona KM (1983) Lokal intryckning av veckat liv provning av plàtbalkar med veckat liv under punktlast. Chalmers Tekniska Hogskola, Institutionen for Konstruktionsknik, Goteborg, Sweden

Easley JT, McFarland D (1969) Buckling of light, gage corrugated shear diaphragms. J Struct Div USA 95:1497–1516

Elgaaly M, Seshadri A (1997) Girders with corrugated webs under partial compressive edge loading. J Struct Eng ASCE Philadelphia 123(6):783–791

Elgaaly M, Seshadri A (1998) Depicting the behavior of girder with corrugated webs up to failure using non-linear finite element analysis. Elsevier, Philadelphia

Elgaaly M, Seshadri A, Hamilton RW (1997) Bending strength of steel beams with corrugated webs. J Struct Eng ASCE Philadelphia 123(6):772–782

El-Metwally AS (1998) Prestressed composite girders with corrugated steel web. Thesis for degree of master, University of Calgary, Alberta

Fraser AF (1956) Experimental investigation of the strength of multiweb beams with corrugated webs. National Advisory Committee for Aeronautics, Washington, DC

Huang L, Hikosaka H, Komine K (2002) Simulation of accordion effect in corrugated steel web with concrete flanges. Computer & Structures 82(23–26):2061–2069

Ibrahim SA, El-Dakhakhni WW, Elgaaly M (2006) Behavior of bridge girders with corrugated webs under monotonic and cyclic loading. Eng Struct 28:1941–1955, Canada

Johnson RP, Cafolla J (1997) Fabrication of steel bridge girders with corrugated webs. Struct Eng UK 75(8):133–135

Lindner J (1991) Shear capacity of beams with trapezoidally corrugated webs and openings. Proceedings of Structure Stability Research Council, Chicago, 1991

Luo R, Edlund B (1995) Numerical simulation of shear tests on plate girders with trapezoidally corrugated webs. Division of Steel and Timber Structures, Chalmers University of Technology, Göteborg

Luo R, Edlund B (1996) Ultimate strength of girders with trapezoidally corrugated webs under patch loading. Thin-Walled Struct 123(6):135–156
Timoshenko SP, Woinowsky-Krieger S (1970) Theory of plates and shells, 2nd edn. McGraw-Hill, New York

Index

M.N. Fardis (ed.), *Innovative Materials and Techniques in Concrete Construction: ACES Workshop*, DOI 10.1007/978-94-007-1997-2,